Proceedings of

2nd Japan – Taiwan Joint Workshop

Nagaoka, Niigata, Japan, May 18 – 20, 2006

Geotechnical Hazards from Large Earthquakes and Heavy Rainfall

ATC3 Committee, ISSMGE

Japanese Geotechnical Society

Proceedings of

2nd Japan – Taiwan Joint Workshop

Nagaoka, Niigata, Japan, May 18 – 20, 2006

Geotechnical Hazards from Large Earthquakes and Heavy Rainfall

ATC3 Committee, ISSMGE

Japanese Geotechnical Society

Geotechnical Hazards from Large Earthquakes and Heavy Rainfall

Proceedings of 2nd Japan – Taiwan Joint Workshop

Nagaoka, Niigata, Japan, May 18 – 20, 2006

Sponsored by

ATC3, Geotechnology for Natural Hazards, International Society for Soil Mechanics and Geotechnical Engineering

Published by

The Japanese Geotechnical Society

Sengoku 4-28-2, Bunkyo-ku, Tokyo 112-0011, Japan

ISBN 4-88644-814-3

Printed by WACO Co., Ltd.

CONTENTS

Preface ……………………………………………………………………………………………….. i

Organizing Committee ……………………………..…………………………………… ii

PAPERS

Special Lectures

Energy approach to slope failures and a case study in 2004 Niigata-ken Chuetsu Earthquake

Kokusho, T. and Ishizawa, T. ………………...……………………………… ...1

Debris flow hazards and mitigations in Taiwan

Lin, Meei-Ling ……………………………………………………..………13

(1) Earthquake induced slope instability

Hazards prediction and assessment of the landslides and debris flows in the mountain area of Ta-Chia River after Taiwan Chi-Chi Earthquake

Cheng, Chin-Tung ..…………………………………………………..…23

Landslide zonation of Hungtsaiping area based on aerial photograph and PIV technology

Lo, Chia-Ming, Lee, Kuo-Chang, Lee, Wei-Chu, Lin, Ming-Lang and Jeng, Fu-Shu ……………………………………………………30

Characteristics of damage of road embankment in the 2004 Mid Niigata Prefecture Earthquake

Tokida, K., Egawa, Y., Nakahira, A. and Okajima, Y. ………………………37

Earthquake induced slope failure and cyclic shear strength of bedding sandy soil

Onoue, A., Wakai, A., Ugai, K., Higuchi, K. and Kuroda, S. ….…………...43

Estimation of natural slope failures induced by the 2004 Niigata-ken Chuetsu Earthquake

Toyota, H. ………………………………………………………..…………...49

Run-out distances of landslides of reclaimed soil deposits at the residential hill in 2004 Niigata-ken Chuetsu Earthquake
Tsukamoto, Y., Ishihara, K. and Kobari, Y. …...…………………………..56
Impact of sediment yields from landslides and debris flows after Chi-Chi Earthquake on hydropower plants in Ta-Chia River and the strategies of geohazards mitigation
Yu, S.H., Yang, S.D., Wang, C.F., Chiao, C.H., Hwang, L.T., Chern, J.C., Cheng, C.T., Chang, Y.L., Ku, C.Y., Shu, S.M., Chiu, S.J. and Lin, Y.S. …………………..62

(2) Rainfall induced slop instability

Study on the influence of soaking effects to the shear strength of colluviums on Mt. Da-Lum
Chen, S., Chen, P.S. and Huang, H.C. ……………………………..………71
Predicting probabilities of landslides along mountain roads in Taiwan using Gaussian process model
Ching, Jianye and Liao, Hung-Jiun ……………………………………..….77
Case study on the variation of water content and matrix suction of unsaturated culluvium slope
Jeng, Ching-Jiang and Lin, Tai-An ……………………………………..…..85
Applicability of rainfall index R' for recent cases in 2004 - 2005
Nakai, S., Kaibori, M., Sasaki, Y., Moriwaki, T. and Kano, S. ……………...90
Stability of a model embankment subjected to artificial rainfalls
Gallage, C.P.K., Garcia, E.F. and Uchimura, T. ……………...…..…………..98
GIS-based nationwide evaluation of erosion rate potential in Japan
Hasegawa, K., Wakamatsu, K. and Matsuoka, M. ………..……………….108
Improvement of slope hazard assessment by using physical properties of local soil
Mizuhashi, M, Sato, J., Towhata, I. and Tsujimura, T. …………………….114
Field measurement for natural disasters due to slope failures caused by heavy rainfall
Sako, K., Fukagawa, R., Kitamura, R. and Yasukawa, I. ……………...…….120

(3) Liquefaction associated phenomena

Influence factors on damage to pile foundation by liquefaction ground flow

Adachi, Y., Miura, K., Morimasa, S., Mihara, M. and Urano, K. …………127

Study of ground treatment on improvement of pile foundation response in liquefiable soils

Chan, Sung-Ju and Su, Ting-Chiun ……………………...………………….135

Uncoupled numerical analyses for ground lateral spread effects on single pile

Lin, San-Shyan, Tseng, Y.J., Wang, C.H. and Lee, W.F. …………………...141

Uplift of buried manholes and pipes due to liquefaction of replaced soils

Yasuda, S. and Kiku, H. ……………………………………………..…..…146

Pile-soil interaction in liquefied soil ground of Kazakhstan

Zhusupbekov, A. Zh., Zhussupbekov, A. A. and Zhakulin, A.S. ………..150

(4) Soil liquefaction and remediation

EQWEAP ~ a simplified procedure to analyze dynamic pile-soil interaction with soil liquefaction concerns

Chang, D.W. and Lin, B.S. ……………..…………………...………………...155

Experimental study of liquefaction resistance of clayed sands by cyclic direct simple shear

Chang, W. J., Chou, B. Y., Lin, P. S., Huang, C. C. and Hong, M. L. ……..163

Liquefaction strength of sands containing fines compared with cone resistance in triaxial specimens

Kokusho, T., Hara, T. and Murahata, K. ……………………………………170

Dynamic centrifuge model test of road embankment

Nabeshima, Y., Tokida, K., Nakahira, A., Ohtsuki, A. and Nakayama, Y.

…………………………………………………………………..177

Evaluation of liquefaction resistance of gravel drain improved loose sandy ground considering the partially drained cyclic behaviour

Priyankara, N.H., Kazama, M., Sento, N. and Uzuoka, R. ……………......183

Pore pressure measurements in cyclic triaxial tests of sand with high fines contents

Ueng, T.S., Yeh, C.L. and Wu, S.H. ……………………………………..……191

Liquefaction of silty sand with micro-layered structure due to segregation

Yoshimine, M. and Koike, R. ………………………………………………195

(5) Performance based design and other related topics

Seimic microzonation of Taipei basin

Chen, C.H., Tsai, C.C. and Chiou, J.S. …………………...……………….201

Performance evaluation of geotechnical structures under different earthquake motions

Hazarika, H., Nozu, A., Sugano, T. and Suzuki, H. ……………………….209

Correlating DMT K_D and CRR of a silty sand through laboratory calibration tests

Huang, A.B., Tai, Y.Y. and Liu, C.H. ………………………………………..215

Evaluation of subsurface ground softness layers of the eastern area of Sendai City based on the bore-hole data

Mori, T., Kazama, M., Uzuoka, R. and Sento, N. ……………………...…...217

The performance-oriented aspects for the geotechnical engineering

Wang, C.H. and Chen, J.R. …………………...……………………………225

Framework of design procedures of pipeline structures against surface earthquake faulting

Yasuda, S. and Hori, M. ……………………………………………………232

(6) Damages during recent earthquakes

Cause of earthquake induced damage of Building No.3 at NNCT

Onoue, A., Fukutake, K., Hotta, H. and Nagai, H. ……………………..….237

Report on the sluice damage caused by the 2003 Tokachi-oki Earthquake

Kawai, M., Takebe, T., Satou, K., Minobe, N., Kakubari, S., Shiwa, M. and Sasaki, Y. ………………………………………………………………………..244

Restoration of a tilted three-story RC building via grouting

Lin, Yung-Kuang, Kuo, Chin-Jung, Hsieh, Hsii-Sheng and Lin, San-Shyan ………………………………………………………………………..252

Damage of embankment and reconstruction by the RRR method in Joetsu Line by Niigata-ken Chuetsu Earthquake in 2004

Kikkawa, M. and Aizawa, F., Saruya, K. and Morishima, H. …………….257

Damage of the Shinano river dike due to the Niigata-ken Chuetsu Earthquake

Oshiki, H. and Sasaki, Y. ………………………………………..………262

Analyses for the settlement of damaged embankments during the Niigataken-chuetsu Earthquake based on a unified stress-strain relationship of liquefied or softened soils

Yasuda, S., Inagaki, M., Itakiyo, K., Yamada, S. and Kasuda, K. …………270

Three dimensional analysis of liquefaction-induced flow at Koshien-hama during the 1995 Hyogoken-nambu (Kobe) earthquake

Yasuda, S., Yoshida, N. and Ohya, Y. ……………………………………….278

PREFACE

It is our great pleasure that the Second Japan - Taiwan Joint Workshop is held under the auspices of Asian Technical Committee on Geotechnology for Natural Hazards (ATC-3), of the International Society for Soil Mechanics and Geotechnical Engineering (ISSMGE), in Nagaoka in May, 2006. This workshop is also cosponsored by the Japanese Geotechnical Society and the Taiwan Geotechnical Society.

The themes of this workshop reflect the common geotechnical problems in Japan and Taiwan, associated with natural hazards resulting from large earthquakes and heavy rainfall during passages of typhoon. Our colleagues in Taiwan and Japan have been aware of those common interests, and have been recognizing with each other the importance of regularly exchanging knowledge and promoting technology in mitigating natural disasters. In this vein, the first joint workshop was organized and successfully held at National Centre for Research on Earthquake Engineering in Taipei in November, 2004. This workshop is an extension and expansion of the previous workshop to promote further development of natural hazard mitigation technologies. The location of this workshop coincides with the recent 2004 Niigata-ken Chuetsu Earthquake, enabling the workshop attendees to visit several sites associated with this earthquake.

On behalf of the organizing committee and ATC-3, I wish to express my sincere appreciation to the working members of ATC-3. Tremendous help received from Prof. Y. Tsukamoto of Tokyo University of Science, Prof. A. Onoue of Nagaoka National College of Technology and Prof. H. Toyota of Nagaoka University of Technology and from Dr. C.H. Wang and Dr. W.F. Lee in Taiwan is gratefully acknowledged.

T. Kokusho
Chairman ATC-3
Professor of Chuo University, Japan

ORGANIZING COMMITTEE

Chairman : Kokusho, T. (Chuo University, Japan)

Hazarika, H. (Port and Airport Research Institute, Japan)
Ishihara, K. (Chuo University, Japan)
Onoue, A. (Nagaoka National College of Technology, Japan)
Towhata, I. (University of Tokyo, Japan)
Toyota, H. (Nagaoka University of Technology and Science, Japan)
Tsukamoto, Y. (Tokyo University of Science, Japan)
Yasuda, S. (Tokyo Denki University, Japan)
Yoshida, N. (Tohoku Gakuin University, Japan)
Yoshimine, M. (Tokyo Metropolitan University, Japan)
Chen, Chen Hsin (Taiwan National University, Taiwan)
Huang, A. B. (National Chiao Tung University, Taiwan)
Jeng Fu-shu (Taiwan National University, Taiwan)
Lee, Wei F. (Taiwan Construction Research Institute, Taiwan)
Lin, Meei Ling (Taiwan National University, Taiwan)
Wang, C.H. (Taiwan Construction Research Institute, Taiwan)

Special Lectures

Energy Approach to Slope Failures and a Case Study in 2004 Niigata-ken Chuetsu Earthquake

T. Kokusho[1] and T. Ishizawa [2]
[1]Department of Civil Engineering, Chuo University, Tokyo, Japan
[2]PhD Student, ditto.

Abstract

So far, earthquake-induced slope stability has been evaluated by the force-equilibrium of soil mass in normal engineering practice, which cannot evaluate failure deformation once large failure occurs. The energy approach is proposed, in which the amount of earthquake energy is evaluated in conjunction with the gravitational potential energy to be dissipated in slope displacement including large flow deformations. An energy balance in a model of a rigid block resting on an inclined plane is examined. Then, shake table tests of dry sand slope are carried out in which the earthquake energy used for the slope failure can be successfully quantified. It is shown that the energy balance holds in the sand slope and its displacement can be evaluated from the rigid block model by modifying the friction coefficient of the slope. The energy approach is then applied to slope failures occurred during the 2004 Niigata-ken Chuetsu earthquake. Among a number of slope failures which can be classified into 3 types, one of the most typical large-volume failure is chosen and the equivalent friction coefficient is evaluated based on the energy balance.

Keywords—*slope stability, energy balance, shake table tests, case study*

ENERGY APPROACH

Seismically induced slope failures have normally been evaluated based on the equilibrium of forces acting on a potentially sliding soil mass. This force approach can evaluate the initiation of slide or the safety factor against the slope failure, but it cannot predict slide deformations, once failure occurs. From the viewpoint of the performance based design or the risk evaluation of slope failures, it is very important to know not only the safety factor but also how large the deformation will develop and how far the effect reaches down-slope. The Newmark method [1] can evaluate slope displacement along a fixed slip surface based on a double integration of acceleration of a potentially sliding soil block. In actual slope failures, sliding soil may not always behave as a rigid body but deforms continuously without fixed slip surfaces. It sometimes tends to become destructive due to a shift from slow slide to fast flow because the soil strength decreases drastically after the initiation of failure.

In this research, an energy approach is proposed to evaluate slope failures including flow failures from their initiation to termination. The basic idea, first proposed by the first author [2], is shown in Fig.1. In case of earthquake- induced slope failures, four energies; potential energy by the gravity E_p, kinetic energy E_k of sliding soil mass, earthquake energy contributing to the slope failure E_{EQ} and energy dissipated in soil due to the slope deformation E_{DP}, can be correlated by the following equation;

$$E_{DP} + E_k = E_{EQ} - \delta E_p \tag{1}$$

or in an incremental form as;

$$\triangle E_{DP} + \triangle E_k = \triangle E_{EQ} - \triangle\delta E_p \tag{1'}$$

Note that the potential energy change before and after failure δE_p in Eq.(1) or $\triangle\delta E_p$ in Eq.(1') is normally negative. If failures occur after the end of earthquake shaking as often observed in case histories, the energy balance becomes identical with that in slope failures due to rainfall or other non-seismic causes without the earthquake energy;

$$\triangle E_{DP} + \triangle E_k = -\triangle\delta E_p \tag{2}$$

In non-seismic cases, if $-\triangle\delta E_p$ is larger than $\triangle E_{DP}$ in Eq.(2), then $\triangle E_k > 0$ and failure starts. Namely the condition for initiation of failure is;

$$\triangle E_k = -\triangle\delta E_p - \triangle E_{DP} > 0 \text{ or } -\triangle\delta E_p > \triangle E_{DP} \tag{3}$$

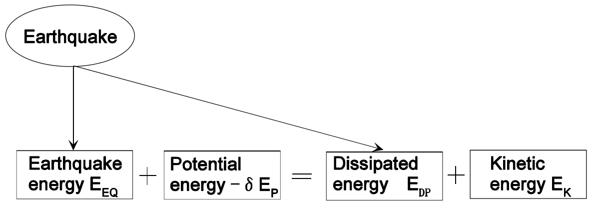

Fig.1 Energy balance during seismically induced slope failure

Once failure starts, the amount of the dissipated energy is critical to decide if it develops as a flow-type failure and how far it flows. If $\vartriangle E_{DP}$ is smaller than $-\vartriangle \delta E_p$ in some time increments, then $\vartriangle E_k$ is increased and the soil movement is accelerated. A shift from slow slide to fast flow may occur not only due to increase in $-\vartriangle \delta E_p$ but also due to drastic decrease of $\vartriangle E_{DP}$ caused by pore-pressure buildup in liquefiable soil, strength loss in high-sensitivity clay, etc. In fast flow failures, soil mass can keep flowing unless the kinetic energy at a time (E_k) plus the subsequent potential energy change ($-\delta E_p$) is all dissipated.

If $-\vartriangle \delta E_p$ is smaller than $\vartriangle E_{DP}$, then $\vartriangle E_k$ is negative, hence the soil mass decreases the speed and comes to a halt if reserved kinetic energy E_k is all consumed. If the failure mode and the energy dissipation mechanism in flowing soil mass are known, it is possible to evaluate how far the flow will reach in the down-slope direction.

ENERGY BALANCE IN RIGID BLOCK MODEL

The Newmark Method based on a rigid block model, a commonly accepted practice in geotechnical earthquake engineering to estimate seismically induced displacement of earth-structures, has recently been examined from the viewpoint of energy by Kokusho et al.[3]. The application of the energy approach to the rigid block model shown in Fig.2 gives the potential energy change δE_p and the dissipated energy due to the block slippage E_{DP} to be correlated with horizontal residual displacement δ_r as;

$$-\delta E_p = Mg\beta\delta_r \tag{4}$$

$$E_{DP} = \frac{\mu\left(1+\beta^2\right)}{1+\mu\beta} Mg\delta_r \tag{5}$$

Then, based on Eq.(1) and using $E_k = 0$ if compared before and after slope failure, the earthquake energy is correlated with δ_r as;

$$E_{EQ} = \frac{\mu-\beta}{1+\mu\beta} Mg\delta_r \tag{6}$$

The ratios of E_{EQ} to $-\delta E_p$ and E_{EQ} to E_{DP} are after Kokusho et al.[3];

$$\frac{-\delta E_p}{E_{EQ}} = \frac{\beta\left(1+\mu\beta\right)}{\left(\mu-\beta\right)} \tag{7a}$$

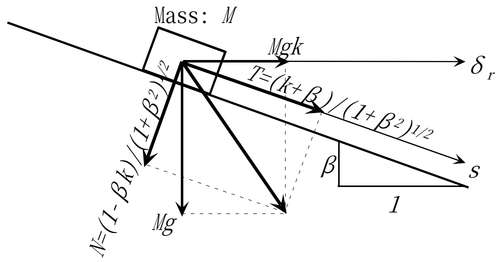

Fig.2: A block on a slope subjected to seismic effect

$$\frac{E_{DP}}{E_{EQ}} = \frac{\mu\left(1+\beta^2\right)}{\left(\mu-\beta\right)} \tag{7b}$$

The contribution of the earthquake energy in comparison to the dissipated energy or the potential energy depends only on slope inclination β and the friction coefficient μ . Also note that the contribution of E_{DP} becomes smaller with larger slope inclination β and smaller friction coefficient μ .

In these relationships, dynamic changes of seismic inertia force affect not only the driving force of the sliding block but also the shear resistance along the slip surface. If the soil mass is saturated, however, seismic inertia force is all carried by temporary pore-water pressure and does not change the effective stress normal to the slip plane and hence the shear resistance. Consequently, for saturated soil, Eqs.(6) and (7) is replaced by the next equation, in which σ_{n0} and σ'_{n0} are total and effective stresses normal to the slip plane, respectively, and E_{EQ}/A is the energy per unit area.

$$E_{EQ}/A = \left(1+\beta^2\right)\left(\mu\sigma'_{n0} - \beta\sigma_{n0}\right)\delta_r \tag{6'}$$

$$\frac{-\delta E_p}{E_{EQ}} = \frac{\beta\sigma_{n0}}{\left(\mu\sigma'_{n0} - \beta\sigma_{n0}\right)} \tag{7a'}$$

$$\frac{E_{DP}}{E_{EQ}} = \frac{\mu\sigma'_{n0}}{\left(\mu\sigma'_{n0} - \beta\sigma_{n0}\right)} \tag{7b'}$$

It is needless to say that the rigid block model on the slip plane, although it captures basic physics of slope failure mechanism, cannot directly reproduce the failure of sloping soil mass. One of the most significant differences is that, in actual slope failures, soil mass may not slide as a rigid body along a fixed slip plane but deforms continuously with or without movable slip planes. Furthermore, if the friction coefficient μ decreases due to pore pressure buildup or other mechanisms after the initiation of failure, it cannot predict the displacement of the failed soil mass anymore. Consequently, a shake table test of sand slope was carried out (Kokusho et al. [3]) to quantify energies involved in slope failures more realistic than the rigid block model.

SHAKE TABLE MODEL TESTS

A spring-supported shaking table shown in Fig.3 was utilized to apply vibrations to a model slope made from sand, called Model-A here, in a rectangular lucite box. The model slope (base length; L = 60 cm, height; H = 33 cm, width; B = 40 cm) was made by air-pluviating dry clean Toyoura sand to a prescribed relative density of $Dr \approx 40\%$. The slope angle was about 29 degrees. In order to evaluate the friction coefficient μ of the model slope, the slope was gradually inclined statically until the onset of slope failure. The static tests carried out three times with the same initial slope angle of 29 degrees and $Dr \approx 40\%$ gave the angle of repose 34.8 to 36.0 (average 35.3) degrees.

The table was initially pulled to a prescribed horizontal displacement and then released to generate damped free vibration. Dissipated energy, which can be calculated from the decay in displacement amplitude in each cycle depends not only on the energy dissipation due to slope deformation but also on other energy loss mechanisms such as radiation damping in the shake table foundation. In order to extract the dissipated energy due to slope deformation, a dummy model, called Model-B consisting of a pile of rigid concrete blocks, was made in the same lucite box and vibrated in the same way. The total weight and the center of gravity were adjusted to be almost identical in the two models.

The decay in amplitudes, measured by a LVDT displacement gauge in both Model-A and B are shown in Fig.4. Notes that, though the initial table displacement, 2.0 cm, and the vibration period of the table, are almost the same, the difference in amplitudes grows larger with increasing number of cycles. It may be reasonable to assume that this difference reflects the greater energy dissipated in Model-A (the model slope) due to its internal deformations, since almost negligible energy is dissipated in the rigid concrete blocks in Model-B.

The loss energy per cycle $\triangle W$ can be calculated as

$$\triangle W = 4\pi W D \tag{8}$$

in which W, representing the strain energy in the same cycle, can be evaluated from the spring constant and the displacement amplitudes of the shaking table. The earthquake energy increment in the model slope $\triangle E_{EQ}$ can then be evaluated from the loss energies per cycle in Model-A and Model-B, $\triangle W_A$ and $\triangle W_B$, respectively as;

$$\triangle E_{EQ} = \triangle W_A - \triangle W_B \tag{9}$$

The total earthquake energy E_{EQ} calculated as a sum of $\triangle E_{EQ}$ in each cycle represents the amount of earthquake energy involved in producing the final displacement in the model slope. To be more precise, E_{EQ} also includes the energy dissipated by soil damping in the model during vibration, which is neglected in the interpretation of the model test results.

Such decay vibration tests were carried out under different frequencies by changing the mass of the table in four steps in order to know the effect of the input frequency on the slope displacement.

The total input energy applied to the shaking table

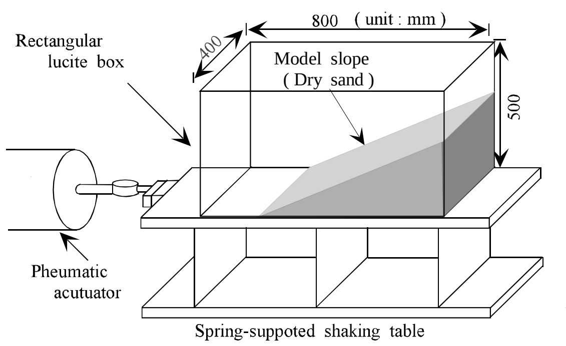

Fig.3 Shake table test apparatus for model slopes.

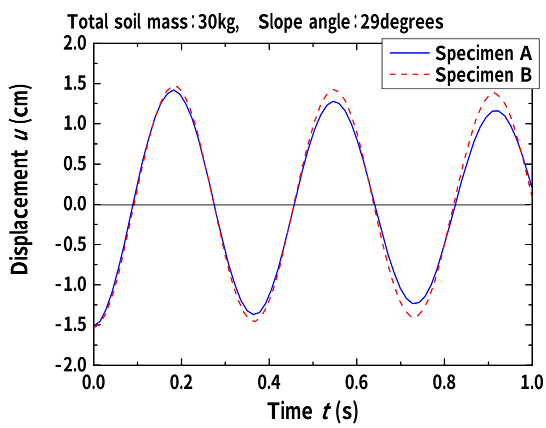

Fig.4 Decay vibrations measured by a LVDT displacement gauge in the Model-A and B.

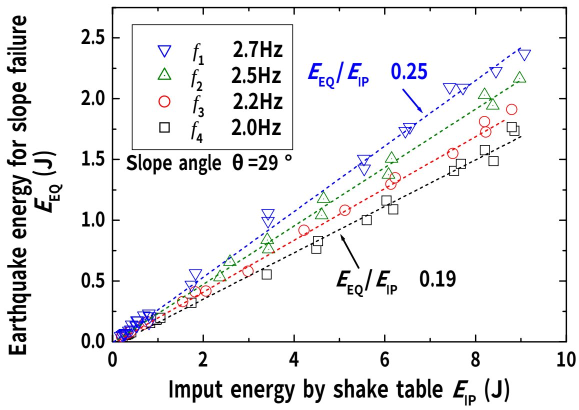

Fig.5 Decay vibrations measured by a LVDT displacement gauge in the Model-A and B.

E_{IP} can be calculated from the initial pull displacement u_o of the table and the spring constant κ as;

$$E_{IP} = \frac{1}{2}\kappa u_o{}^2 \tag{10}$$

Fig.5 shows the values of E_{EQ} actually measured by the above-mentioned method plotted versus the input energy of the shaking table calculated by Eq.(10). It is found that the relationship between E_{EQ} and E_{IP} is almost constant despite increasing input energy regardless of the vibration frequency. It indicates that the ratio of the earthquake energy actually used for slope failure to the total input energy may be assumed almost constant no matter how large the input seismic energy is or how much slope failure occurs.

The deformation of the model slope was observed by two video cameras, one from the side and the other from the above. Column-shaped markers made from colored sand were installed at the side of the model. On the slope face, dry noodle sticks of 5 cm length were set up in line. The interval of these markers was 10 cm in the slope direction. The down-slope surface deformation was almost uniform in the direction normal to the cross-section. The slope deformation was also measured before and after the end of tests by a laser beam displacement sensor and compared with the video data to check their reliability. In order to correlate the energies with the residual displacement of the slope, the horizontal residual displacement of the slope surface was evaluated here as an average of the displacements of the sticks. This calculation was implemented in each cycle of the input vibration to obtain the incremental residual displacement $\Delta\delta_{rs}$.

In Fig.6, $\Delta\delta_{rs}$ is plotted versus the number of cycles, N. The incremental earthquake energy ΔE_{EQ} and the potential energy change $-\Delta\delta E_p$ are also plotted against N in the same chart. From the change in the slope surface geometry $-\Delta\delta E_p$ is calculated cycle by cycle as;

$$\Delta\delta E_p = \Delta\left(\rho_d gB\int zdxdz\right) \tag{11}$$

where z is the vertical coordinate and ρ_d is the dry soil density (assumed constant). The integration is carried out over the cross-sectional area of the slope. It is confirmed that measurable slope deformation occurs only until about 5th cycle, which is almost consistent with the variation in the energies ΔE_{EQ} and $-\Delta\delta E_p$.

SLOPE DISPLACEMENT VERSUS ENERGY

The incremental energies, ΔE_{EQ} and $-\Delta\delta E_p$ calculated in each cycle are summed up to evaluate the corresponding total energies, E_{EQ} and $-\delta E_p$. The dissipated energy E_{DP} can be readily evaluated from Eq.(1) because E_k =0 if the energy balance before and after slope failure is compared. The total residual displacement δ_{rs} is also calculated by summing up all incremental displacements $\Delta\delta_{rs}$. In Fig.7 the residual displacements are plotted versus the vibration energy E_{EQ} used for slope deformations. Here, the results obtained under 4 different input frequencies for the same 29 degrees slope are plotted. It is remarkable that all plots can be approximated as a single curve despite the difference in the input frequency, indicating that the energy can serve as a determinant for slope displacement even under different shaking frequency. Also noted in Fig.7 is that there exists a threshold energy below which no residual displacement occurs.

In Fig.8, the values of $-\delta E_p$ and E_{DP} are plotted versus the earthquake energy E_{EQ} for numerous test data with different initial table displacements under different

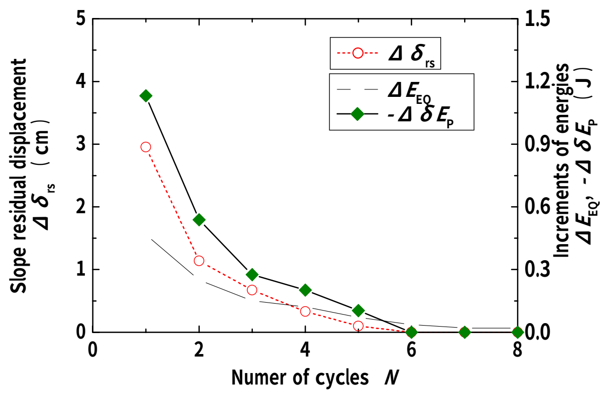

Fig.6 Displacement $\Delta\delta_r$, incremental energies, and $-\Delta\delta E_p$ plotted versus the number of cycles N.

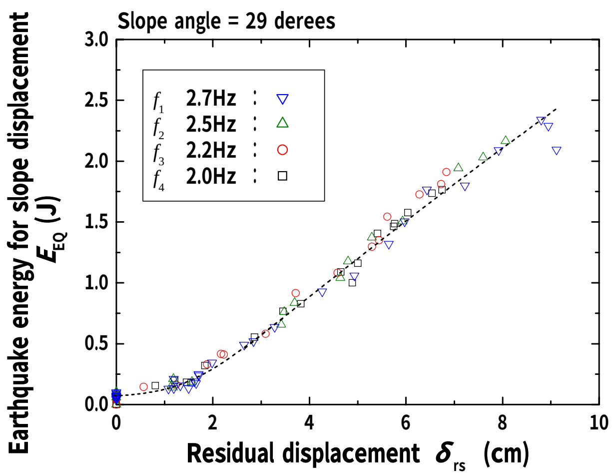

Fig.7 Earthquake energy E_{EQ} plotted versus resisual slope displacement for several test cases with different initial table displacement.

input frequencies. In the light of the energy considerations on the rigid block model discussed before, the ratios $-\delta E_p / E_{EQ}$ and E_{DP}/E_{EQ} can be calculated theoretically based on the rigid block model by Eqs.(7a) and (7b). The angle of the slope is 29 degrees ($\beta = 0.55$) and the angle of repose of the sand is about 35 degrees (μ =0.71). This value was obtained as an average of 4 tests, in which the same sand slope was statically inclined until failure to measure the angle of repose. Using these values in Eqs.(7a) and (7b), $-\delta E_p / E_{EQ}$ =5.0 and E_{DP}/E_{EQ} =6.0, which are drawn in Fig.8 by two dotted lines. Obviously there is a wide gap between the theory on the rigid body model using the angle of repose and the experimental results. However, it is noted that the experimental results can also be roughly approximated by

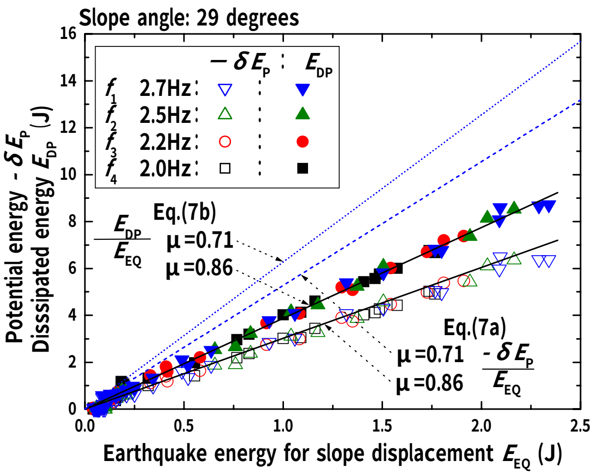

Fig.8 Earthquake energy E_{EQ} plotted versus potential e nergy or dissipated energy for several test cases with different initial table displacement.

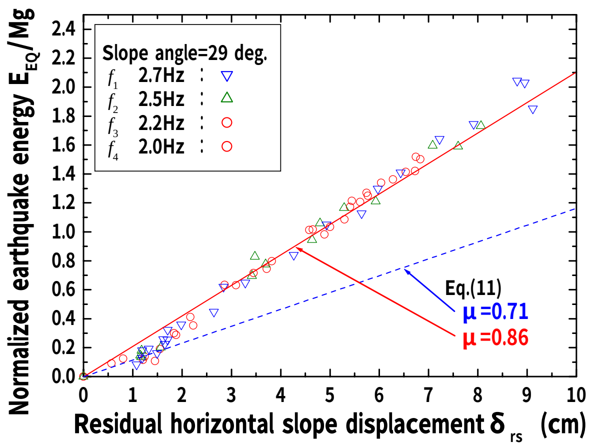

Fig.9 Relationships between residual displacement δ_r and earthquake energy E_{EQ}/Mg for different initial table displacements compared with the rigid block theory.

straight lines, indicating that $-\delta E_p$ and E_{DP} tend to increase almost in proportion with E_{EQ} irrespective of the intensity of shaking and the input frequency. Actually, if μ =0.86 is used instead of μ =0.71, the theoretical line can predict the test results almost perfectly as shown with the solid line in Fig.8. The gap between μ =0.71 and μ =0.86 may be explained by the difference in the failure mode of the sand slope. The depth of slipped sand was limited near the surface in the static test for the angle of repose, while in the dynamic test it extended to a depth with larger volume of sheared zone.

From Eq.(6) for the rigid block model, the residual slope displacement can be formulated as;

$$\delta_r = \frac{1+\mu\beta}{\mu-\beta}\frac{E_{EQ}}{Mg} \qquad (12)$$

In Fig.9, the residual displacement δ_{rs} , which is considered to be equivalent to δ_r in the rigid block model, obtained by numerous tests are plotted versus the normalized earthquake energy E_{EQ}/Mg . The weight of the displaced soil mass Mg was evaluated from Eq.(4) using the displacement δ_{rs} and the measured potential energy change $-\delta E_p$. The dashed line corresponding to the theoretical relationship of Eq.(12) by the rigid block model for μ =0.71 and $\beta = 0.55$ overestimates the observed residual displacement for the same normalized energy. However, another theoretical relationship by solid line for μ =0.86 and $\beta = 0.55$ can predict the residual slope displacement almost perfectly. This indicates that if an appropriate friction coefficient is chosen, the simple rigid block model, which apparently possesses different failure mechanism, can successfully simulate sand slope.

ENERGY BASED SLOPE FAILURE EVALUATION

Based on the theoretical considerations on the simplified block model and the model test explained above, a energy-based design method in which post earthquake residual slope displacements can be evaluated may be proposed as shown in Fig.10.

First, the input earthquake energy E_{IP} defined at the base of slopes or embankments is designated site by site. The energy E_{IP} can be evaluated [3] as;

$$E_{IP} = \rho_2 Vs_2 \int (du/dt)^2 dt \qquad (13)$$

where du/dt is the particle velocity of the design motions in terms of time t and $\rho_2 Vs_2$ is the impedance of the base layer as shown in Fig.11. By assuming the energy

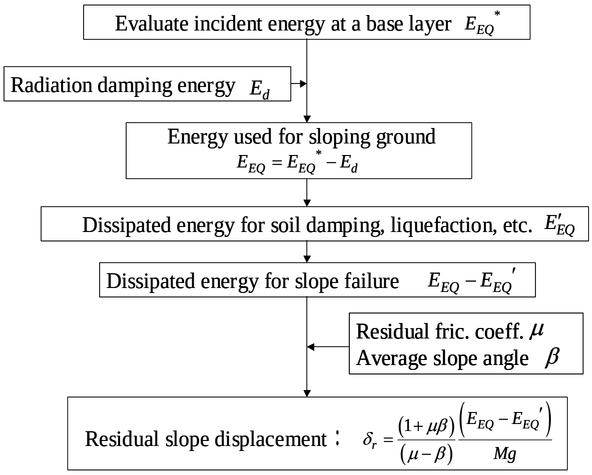

Fig.10 Flow chart for evaluation of slope displacement by energy approach

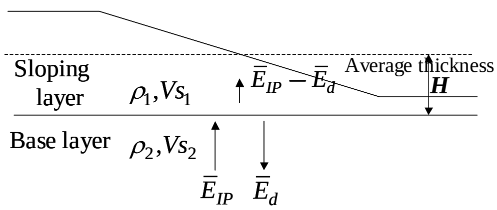

Fig.11 Definition of seismic wave energy at the base of a sloping layer

radiating downward through the base, E_d, the earthquake energy, E_{EQ}, which will be dissipated inside the slopes or embankments can be obtained as;

$$E_{EQ} = E_{IP} - E_d \tag{14}$$

In the present model test, E_{EQ}/E_{IP} was found almost constant (0.19-0.25) depending on the shaking frequency, 2.0-2.7 Hz, despite the difference of slope displacement as shown in Fig.5.

Theoretically, the energy ratio is controlled by the impedance ratio $\alpha = \rho_1 Vs_1 / \rho_2 Vs_2$ between the sloping ground and a base layer as illustrated in Fig. 11. Here a sloping ground is approximated by a horizontal 2-layers system with the average height H in the upper layer. Under stationary vibration by sinusoidal input motion, the ratio between the energy flux of downward radiation wave $\bar{E}_d$ and that of upward input wave $\bar{E}_{IP}$ can be formulated as Eq.(15) based on the one-dimensional SH wave propagation [3]. Here, the energy flux means the amount of harmonic wave energy transmitted per unit time.

$$\bar{E}_d / \bar{E}_{IP} = \left| \frac{(1-\alpha^*) + (1+\alpha^*) e^{-2ik_1^* H}}{(1+\alpha^*) + (1-\alpha^*) e^{-2ik_1^* H}} \right|^2 \tag{15}$$

Here, the wave number k_1^* is $k_1^* = \omega / Vs_1^*$ (ω is the angular frequency) and the complex impedance ratio α^* can be written as;

$$\alpha^* = \rho_1 Vs_1^* / \rho_2 Vs_2^* = \alpha \left\{ (1+2iD_1)/(1+2iD_2) \right\}^{1/2} \tag{16}$$

in which Vs_1^*, Vs_2^* = complex S-wave velocity and D_1, D_2 = damping ratios of the upper and lower layer, respectively. If the energy flow is stationary by harmonic wave propagation, the energy stored in the sloping layer is $W = \bar{E}_{IP} - \bar{E}_d$ and the energy dissipating downward by radiation is $\Delta W = \bar{E}_d$. From an analogous expression for a lumped mass linear viscous system which is in resonance with a harmonic input motion, the damping ratio due to wave radiation D_R may be defined as;

$$D_R = \Delta W / 4\pi W = \bar{E}_d / 4\pi (\bar{E}_{IP} - \bar{E}_d) \tag{17}$$

Consequently the energy flux ratio $\bar{E}_d / \bar{E}_{IP}$ can be correlated with the damping ratio by radiation D_R as;

$$\bar{E}_d / \bar{E}_{IP} = 4\pi D_R / (1 + 4\pi D_R) \tag{18}$$

If Eq.(17) can also be assumed for transient earthquake waves then;

$$E_d / E_{IP} = 4\pi D_R / (1 + 4\pi D_R) \tag{18'}$$

The rest of the energy $E_{EQ} = E_{IP} - E_d$ is the maximum energy which can potentially be used for deformation and failure of the sloping ground. If, for instance D_R =15% as sometimes used in embankment dams in Japan, then, E_d / E_{IP} =0.65 and E_{EQ} / E_{IP} =0.35.

More practically, the energy ratio E_{EQ} / E_{IP} may be quantified by a 1D multi-reflection analysis in which the design input motion is given at the base layer. It is assumed here that the 1D simple analyses can properly approximate 2D or 3D conditions in actual slopes.

The energy E_{EQ} is dissipated by residual slope deformation as well as by internal soil damping in the sloping layer. The present model tests indicate that the energy by internal damping E'_{EQ} seems small compared to E_{EQ}. If necessary, it is possible to evaluate the energy E'_{EQ} associated with internal soil damping based on the 1D analyses and thus the earthquake energy to be used for the residual slope deformation $\left(E_{EQ} - E'_{EQ}\right)$ can be differentiated.

Based on the rigid-block simple model, the residual horizontal displacement is expressed based on Eq.(6) as;

$$\delta_r = \frac{(1+\mu\beta)}{(\mu-\beta)} \frac{\left(E_{EQ} - E_{EQ}{}'\right)}{Mg} \tag{19}$$

This equation is applicable to unsaturated slopes where seismic inertia affects not only the driving force but also the shear resistance along the slip plane. If a slip plane is saturated, then the following equation based on Eq.(6') should be used.

$$\delta_r = \frac{\left(E_{EQ} - E'_{EQ}\right)/A}{\left(1+\beta^2\right)\left(\mu\sigma'_{n0} - \beta\sigma_{n0}\right)} \tag{19'}$$

The thickness or the mass of sliding soil may be determined by conventional slip surface analyses.

As previously mentioned, the test results was almost perfectly reproduced by the theoretical line, indicating that the rigid block model may be applicable by modifying the friction constant μ. In order to know how μ should be determined in actual design, the friction coefficient μ in Eq.(19) or Eq.(19') is back-calculated from recent case history during the 2004 Niigata Chuetsu earthquake.

CASE HISTORY DURING 2004 NIIGATAKEN CHUETSU EQ.

The Niigata-ken Chuetsu earthquake (M_J=6.8) occurred on October 23, 2004, which caused more than 1600 slope failures in the middle part of the main island of Japan due to the main shock and also several strong aftershocks.

The damaged area is known as a landslide-prone area of green-tuff, with geological structures of active folding which cover active faults underneath. Synclines and anticlines are running parallel in the north-south direction, among which rivers are flowing in the same direction. Mountains are about 400 m at the highest, and the slopes are composed of weak sedimentation rock of Neogene, alternative layers of strongly weathered mud stones and sand stones. Bedding planes had a strong effect on the slope failures.Some of the earthquake-induced slides were obviously influenced by previous landslides. Rainfalls in three days prior to the quake were 120 mm, which may have influenced the slope instabilities.

It was disclosed that similar disasters accompanying countless landslides in the green-tuff soft rock areas had occurred once in every 30 years on average in the north and central Main Island of Japan, the lessons of which had not been learned before.

Classifications of slope failures

The slope failures due to this particular earthquake are classified into 3 types as illustrated in Fig.12;

Type-A: Deep slips parallel to sedimentation planes (dip slip), in gentle slopes of around 20 degrees. In many cases, displaced soil mass had originally been destabilized by river erosions or road constructions, and glided as a rigid body along the slip plane. The displaced soil volumes were very large, translating ground surfaces with little disturbance.

Type-B: Shallow slips of 1~2 m depth not parallel to sedimentation planes at steep slopes (>30 degrees). This type far outnumbered Type-A, but the displaced soil volume was not so large. Soils normally fell down as

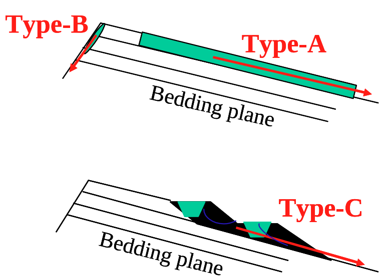

Fig.12 Three types of slope failures; A, B and C, during the 2004 Niigataken Chuetsu earthquake.

Fig.13 Type-A: Landslide mass in Higashi-Takezawa seen from the scarp

Fig.14 Spillway constructed on the natural dam in Higashi Takezawa

pieces, sometimes leaving trees with deep roots at original places.

Type-C: Deep slips in strongly weathered colluvial soils in places where koi-ponds and terraced paddy fields were located. This type seems very peculiar in this earthquake because countless koi-ponds were located in the damaged area. This failure type obviously involved ponds, which seems to have provided water for piping and caused delayed flow-type failure of the clluvial soils. Soil liquefaction or cyclic softening may have contributed to large ground deformation including cracks because sand boils were actually witnessed at some sites.

A number of slope failures stopped streams and made more than 80 natural reservoirs. Some of the largest ones belong to Type-A. The most typical one in Higashi-Takezawa, shown in Fig. 13, inundated houses and yards in a upstream village which were rapidly filled with washout sands. On the natural dams, emergency dewatering and spillway-constructions were implemented to prepare for flooding in the next spring as shown in Fig.14. This treatment will make the natural dam sustainable as long as engineered embankment dams. The other typical case of Type-A is shown in Fig. 15, where the upper rock mass slid down literally as a rigid body along the slip plane (inclined by 20-23 degrees) of weathered silty sand seam sandwiched in mudstone. In most Type-A failures, slope stabilities were deteriorated even before the earthquake because the slope toes had been cut by river flows (in Higashi-Takezawa) or road constructions (in Yokowatashi).

In Figs. 16 and 17, typical slope failures of Type-B are shown. The slip surfaces were generally shallow (about 1 m) leaving trees with deep roots. Though the number of slope failures of Type-B was extremely greater, the soil

Fig.15 Type-A: Rigid block slip along flat sedimentation plane of weathered silty sand seam in mudstone in Yokowatashi.

Fig.16 Type-B: Debris of shallow slip covered a railway track in Kita-Horinouchi.

Fig.17 Type-B: Dip slip by shallow toppling failure near Haguro tunnel.

Fig.18 Type-C: Deep failure in weathered soils caused by water seepage or piping from koi-ponds in Nicho-No.

Fig.19 Type-C: Dip slip of weathered soils along mudstone of developed mudflow of 1 km run-out distance in Oguri-Yama.

volume in each failure was much smaller than Type-A.

In Figs. 18 and 19, slope failures of Type-C are exemplified. Type-C failures were essentially controlled by the dip slip like Type-A, but the displaced soil mass had been very much weathered and utilized as koi ponds or terraced paddy fields. The koi ponds seem to have played an important role in triggering the failures; they kept the soil wet and prone to seismic instability, developing ground fissures and internal erosions by pond water which eventually caused large-volume failures. Some of the failures probably occurred no sooner than the earthquake shaking while the others seem to have occurred a few days or weeks later. There are still a lot remained before the exact mechanism of Type-C failures is solved.

Influencing factors of slope failures

Combining a map of slope failures published from the Geographical Survey Institute just after the earthquake (Fig.20) with geographical and geological maps, a statistical study was carried out to analyze key factors for the slope failures in this earthquake.

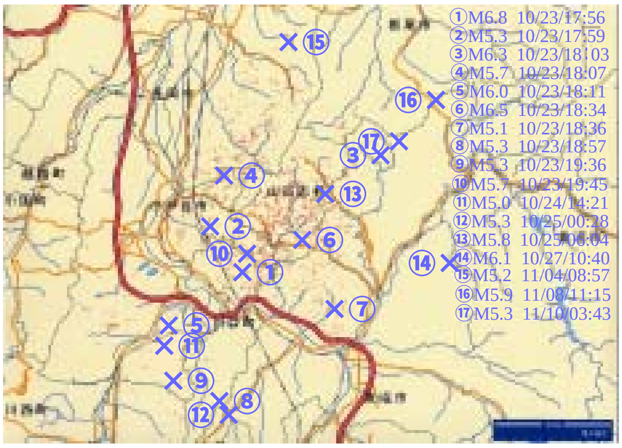

Fig.20 Map of slope failures (a number of red dots) published from Geographical Survey Institute together with epicenters of the main shock and larger aftershocks

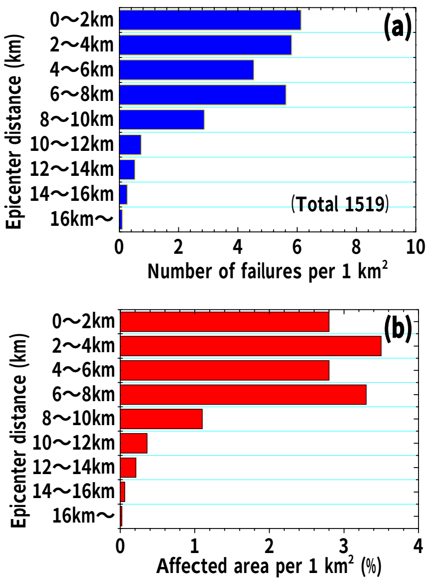

Fig.21 Epicenter distances versus numbers (a) and affected areas (b) of slope failures per 1 km^2.

Fig.21 shows histograms of slope failures versus epicenter distance in terms of the number of failures or in terms of affected areasper unit area of 1 km^2. It is clearly seen that a threshold epicenter distance for dense slope failures during the M_J=6.8 earthquake was around 8-10 km and the maximum percentage of the affected area was about 3.5%. This result seems to hold even when the epicenters of larger aftershocks of MJ=6.5 or 6.3 which occurred in less than 1 hour after the main shock are taken into consideration.

Histograms in Fig.22 show the influence of geology on the number or the affected areas of slope failures.

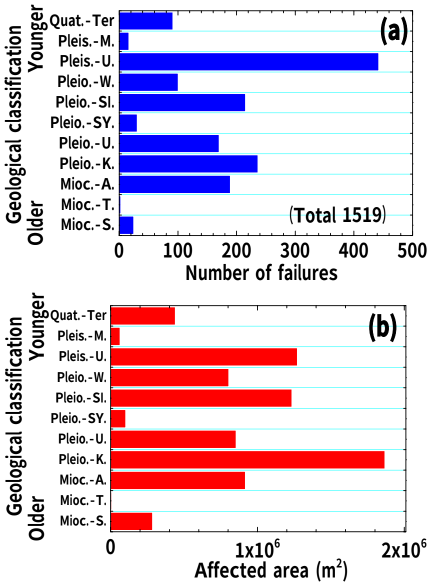

Fig.22 Geological categories versus numbers (a) and affected areas (b) of slope failures.

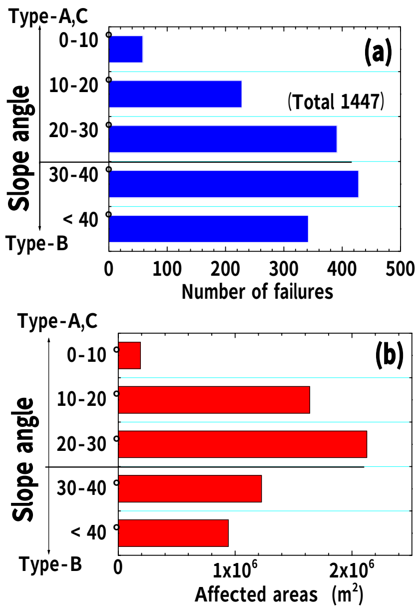

Fig.23 Slope angles versus numbers (a) and affected areas (b) of slope failures.

(a)

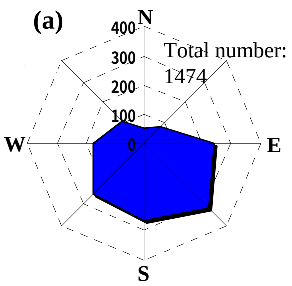

(b)

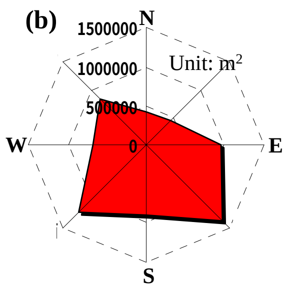

Fig.24 Sloping directions in terms of numbers (a) and affected areas (b) of slope failures

Geological ages of the slopes span wide from Pleistocene of Quaternary to Miocene of Tertiary. However there seems to exist no clear trend that the younger geologies suffered more failures than the older ones. It is probably because the area is so much affected by the active folding and weathering that the geological age has little to do with mechanical properties.

Fig.23 shows how steep the failed slopes were, indicating that slopes steeper than 30° (Type-C) were greater in number as shown in (a) while slopes gentler than 30° (Type-A,C) affected larger areas as in (b). This indicates that though Type-B failures outnumbered Type-A,C failures, the latter gave far serious effects on road traffics, river flows, etc.

Fig.24 depicts the effect of sloping directions on the number (a) and the affected areas (b) of slope failures. It can be said that the dominant direction are from east to south and south-west in (a) and (b). Note that the major shaking direction of the earthquake was east-west. The dominant directions of failed slopes probably reflect the directions of seismic shaking, axis of the folding, directions of river valleys, etc.

ENERGY APPROACH TO 2004 NIIGATA CHUETSU EQ

Among the slope failures during the earthquake, the Type-A failure in Higashi-Takezawa was the one of the largest which filled a valley and stopped a river flow, making a large natural reservoir (See Fig.13). This case was chosen here in order to apply the flow chart in Fig.8 to evaluate the equivalent friction coefficint. Figs.25(a) and (b) show the plan and the cross-section of the failure before and after the failure, respectively. The failure occurred along a sedimentation plane between mudstone and sandstone of Neogene. The inclinations of slope surface and slip plane were about 20 degrees. A sandstone soil block of 20 m in maximum depth and 300 m x 250 m in maximum horizontal dimensions slid along the sedimentation plane and plugged the valley. The total volume of displaced soil calculated three-dimensionally was 0.9 x 10^6 m^3 and 1.2 x 10^6 m^3 before and after the failure, respectively.

The failure was idealized here by simplifying the soil mass by a flat block of 6.9 x 10^4 m^2 (in horizontal area) by 15.2 m (in thickness) sliding down along the slip plane with the total mass unchanged. The center of gravity moved by 94.1 m laterally and 21 m vertically. The equivalent slip inclination connecting the center of gravity before and after the failure is 12.4°, which is considerably lower than the angle of slip plane, 20°, because the front portion of the failed soil mass crashed against the opposite side of the valley and piled up there.

(a)

(b)

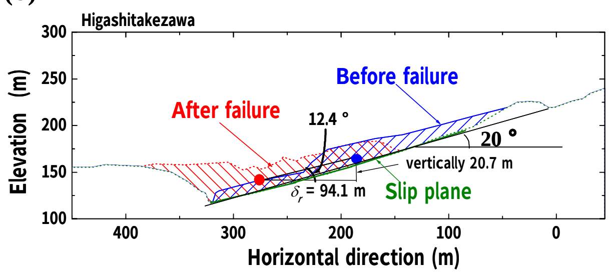

Fig.25 Plan (a) and cross-section (b) along blue chain-dotted line of Higashi-Takezawa slope failure along gentle slip plane of about 20 deg.

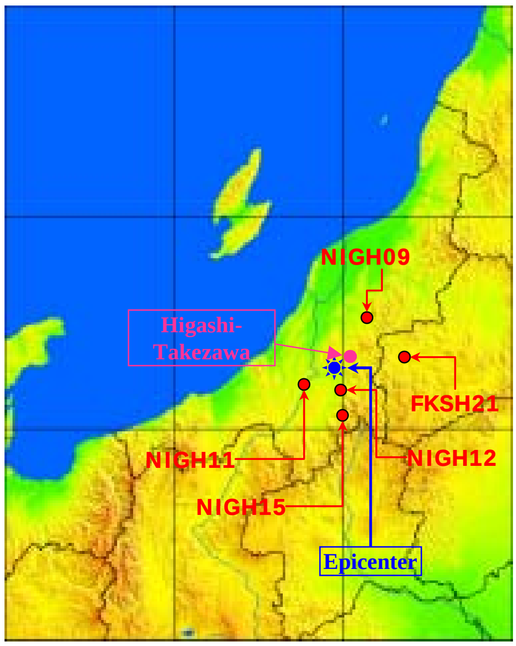

Fig.26 Locations of Higashi-Takezawa slope failure together with the epicenter and KIK-net sites.

Table-1 Evaluated energies and related values in nearby vertical array sites.

Site No.	ACCmax (gal)	Epic. / Foc. Dist. (km)	Base layer Depth (m)	Vs at base layer (km)	E_{IP}/A at base layer (kJ/m^2)
NIGH11	587.9	17 / 22	205	850	122
NIGH12	410.0	13 / 19	110	780	149
NIGH09	390.1	36 / 38	100	1380	33
FKSH21	361.7	40 / 42	200	1600	74
NIGH15	242.8	29 / 32	100	1540	5

The input earthquake energy E_{IP} defined at a base layer of the slope was extrapolated from several KIK-net vertical array records installed by NIED around the area. Fig.26 shows the locations of KIK-net sites around Higashi-Takezawa together with the epicenter of the main shock. Table 1 shows the calculated input energies per unit area E_{IP}/A at the base layers and pertinent parameters at the 5 vertical array sites. The S-wave velocities of the base layers in those sites span from 780 to 1600 m/s.

In Fig.27, the values of E_{IP}/A are plotted versus focal distances (focal depth=13.4 km) on a log-log chart. The solid line in the chart indicates the wave energy per unit area theoretically calculated from the spherical energy radiation of body waves,

$$E_{IP}/A = E\Big/\left(4\pi R^2\right) \tag{20}$$

where R = focal distance. The total wave energy E released at a point source is evaluated by an empirical equation of Gutenberg and Richter [4]

$$\log E = 1.5M + 11.8 \tag{21}$$

It is noted that the input energies E_{IP}/A calculated from earthquake records may be approximated by the dashed line parallel to the solid line, despite some scattered data points presumably due to fault mechanisms, indicating that the calculated energy is slightly smaller than the theoretical energy assuming the point source. The input energy at the base layer of Higashi-Takezawa can be obtained by substituting R=14 km to this dashed line in Fig.27 as E_{IP}/A =280 kJ/m^2. If the radiation damping D_R =15% is assumed in this site, then E_{EQ}/E_{IP} =0.35 as previously mentioned, and hence the maximum energy potentially dissipated in the slope in Higashi-Takezawa is E_{EQ}/A=98 kJ/m^2.

Estimating that the slip plane was saturated at the time of earthquake (water was actually running on the impervious mudstone plane when we visited after the earthquake), Eq.(19') is expressed here to back calculate equivalent friction coefficient μ or equivalent friction angle ϕ_{eq} as;

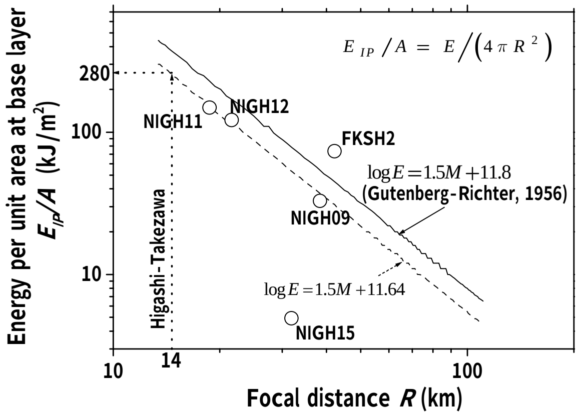

Fig.27 SH wave energy versus focal distance compared with the spherical energy radiation combined with Gutenberg-Richter relationship.

$$\mu = \tan\phi_{eq} = \left(E_{EQ} - E'_{EQ}\right)\Big/\left(AD_{av}\rho_t g\,\delta_r\right) + \beta \tag{22}$$

where A = horizontal area, D_{av} = thickness, $\rho_t g$ =unit weight of failed slope. The dissipating energy E'_{EQ} by liquefaction or soil damping is assumed negligibly small compared to other energies and ρ_t =1.8 t/m^3, assuming that the major portion of the solid soil block was unsaturated except along the slip plane. Then, substituting equivalent slip inclination $\beta = \tan 12.4°$ into Eq.(22), the friction angle ϕ_{eq} is 12.6°. This value represents an equivalent friction angle for failure modes combining the rigid block slide along the smooth slip plane (Type-A) and subsequent crash into the valley. The equivalent friction angle is much lower than the inclination of the slip plane 20°, indicating that the slope started to glide very easily. It seems that the large difference between 12.6° and 20° allowed the failed soil mass to accelerate and push the front soil mass piling up on the opposite side of the river terrace.

The exact mechanism why this low equivalent friction angle could be realized is not yet known. The sandstone overlying the slip plane of cemented mudstone was highly weathered and almost equivalent to decomposed dense sand. The relative density of intact soil is estimated as Dr > 55~70%. It may somehow be explained by high water pressure acting on the slip plane, although the dense sand deposit is unlikely to have completely liquefied.

CONCLUSIONS

The energy approach for slope failure evaluation has been developed by first examining the energy balance in the Newmark-type block model, comparing it to innovative shake table tests of a model slope of dry sand and then applying it to an actual slope failure during the Niigata-ken Chuetsu earthquake, yielding the following major findings.

1) The energy balance in the rigid block model indicates that the ratio of the earthquake energy E_{EQ} used for slope failure to the potential energy change $-\delta E_p$ of the slope depends only on slope inclination β and friction coefficient μ. The slope displacement can be formulated to be proportional to E_{EQ}.
2) In shake table tests of dry sand slope to quantify energies involved in slope failures more realistically than the rigid block model, the earthquake energy E_{EQ} can be successfully measured, quantifying the energy balance involved in the failure of the model slope. Comparison of the theory with the test results indicates that the simple rigid block model, which apparently possesses different failure mechanism, can satisfactorily simulate a continuously deforming sand slope if an appropriate friction coefficient μ is chosen.
3) Based on the theoretical considerations and the model tests, an energy-based design method in which post earthquake residual slope displacements can be evaluated is proposed.
4) Before applying the energy approach to the case history during the 2004 Niigata-ken Chuetsu earthquake, a number of slope failures was statistically classified into three types; Type-A (dip slip in gentle slopes of around 20 degrees), Type-B (shallow slip in steep slope of more than 30 degrees) and Type-C (Deep slips in strongly weathered colluvial soils invoving koi-ponds and terraced paddy fields)
5) In order to back-calculate the friction coefficient μ, the energy-based method was applied to a typical Type-A slip. The input earthquake energy E_{IP} defined at a base layer of the slope was extrapolated from several KIK-net records in the area. If the radiation damping D_R =15% is assumed based on dam engineering practice in Japan, the maximum energy potentially used for the slope failure in Higashi-Takezawa is E_{EQ}/A=98 kJ/m^2. The equivalent friction angle ϕ_{eq} = 12.6° was obtained. This friction angle is much lower than the inclination of the slip plane 20° of the sedimentation rock, indicating that the sliding soil block accelerated and pushed the front soil mass to the opposite side of the valley.

ACKNOWLEDGMENTS

Geological Survey Institute in Tsukuba, Japan, is gratefully acknowledged for compiling and disseminating the map of slope failures in the website shortly after the earthquake. NIED (National Research Institute for Earth Science and Disaster Prevention) in Tsukuba, who generously provided KIK-net data of the earthquake through internet, is gratefully appreciated.

REFERENCES

[1] Newmark, N. M. “Effects of earthquakes on dams and embankments,” Fifth Rankine Lecture, Geotechnique Vol.15, pp.139-159, 1965.

[2] Kokusho, T. and Kabasawa, K.: “Energy approach to flow failure and its application to flow due to water film in liquefied deposits,” Proc. of International Conference on Fast Slope Movement, Naples, May 2003.

[3] Kokusho, T., Ishizawa, T. and Harada, T. Energy approach for earthquake induced slope failure evaluation, Proc. 11th International Conference on Soil Dynamics & Earthquake Engineering and 3rd International Conference on Earthquake Geotechnical Engineering, Berkeley, California, Vol.2, 260-267, 2004.

[4] Kokusho, T., Motoyama, R. and Mantani, S.: H. Motoyama, “Seismic wave energy evaluation in surface layer for performance based design”. 13th World Conference on Earthquake Engineering, Vancouver, Paper No.3480, 2004.

[5] Gutenberg, B. and Richter, C. F.: “Earthquake magnitude, intensity, energy and acceleration (Second paper)” Bulletin of Seismological Society of America, Vol.46, pp.105-145, 1956.

Debris Flow Hazards and Mitigations in Taiwan

Meei-Ling Lin[1]
[1]*Department of Civil Engineering, National Taiwan University, Taipei, Taiwan*

Abstract

In order to effectively manage the debris flow hazard, it is important to understand the potential of the debris flow, to identify the potentially affected area, and to simulate the hazard scenario for drafting of mitigation program. In this paper, current status of the data inventory, potential analysis, and scenario simulation of debris flow developed in Taiwan will be introduced along with experiences of the application of the information for hazard management.

Keywords—*debris flow, hazard mitigation, potential analysis, scenario simulation*

INTRODUCTION

Due to the steep terrain and fragile geological conditions in Taiwan, heavy rainfall carried by typhoon often caused severe slope failures. Among all types of slope failure, debris flow often caused significant loss of human lives and damage to properties due to its high flow velocity and large deposition area. In 1996, typhoon Herb struck Taiwan, and caused severe debris flow in the Chen-You-Lan river watershed, which killed 27 people and 14 people was missing. After the Chi-Chi earthquake of 1999, more than 100 newly occurred debris flow locations were identified in the central Taiwan, which appeared to have been resulted from landslides caused by the earthquake. In 2001 and 2004 severe typhoons struck Taiwan, and caused significant losses of lives and properties. Various mitigation measures were conducted in efforts to reduce the impacts of debris flow hazard. In 1997 the National Science and Technology Program for Hazard Mitigation (NAPHM) was established, and the concepts of mitigation measures have taken different prospects. Since then, the researches and mitigation measures started emphasizing on hazard prevention and reduction. Inventory of database, being able to identify the potential and the affected areas, and assessing the possible risk caused by debris flow hazards could provide important information for drafting of an effective and realistic mitigation program, and to plan ahead for hazard management (Lin, 2001). The current status and efforts on such measures and related researches are presented in this paper.

DEBRIS FLOW HAZARDS IN TAIWAN

Severe hazard caused by debris flow has a long record in Taiwan. In 1990, typhoon Ofelia struck Taiwan, and 39 people were killed by the debris flow induced by typhoon in the Tung-Man area, Hualien County. In 1996, typhoon Herb struck Taiwan, and caused severe debris flow in the Chen-You-Lan river watershed, which killed 27 people and 14 people was missing. Some of the major debris flow hazard events are as listed in Table 1. After the Chi-Chi earthquake of 1999, more than 100 newly occurred debris flow locations were identified in the central Taiwan, which appeared to be closely related to the landslides induced by the earthquake. The Xiansane typhoon struck the northern Taiwan in 2000, and triggered severe debris flow hazard which caused more than 10 lives. In 2001, typhoon Toraji induced severe debris flow hazard in Nantou County, and more than 100 people were killed. Two months later, typhoon Nari struck Taiwan, and caused severe damages to Taipei MRT and about 20 persons died because of debris flow and landslides (Chen, et. al. 2001). In 2003, typhoon Mindule along with a weather system dumped more than 2000 mm of rainfall in the central Taiwan. Severe landslides and debris flow occurred especially in the Ta-Jia river watershed; several villages were flooded and damaged. The series of hydraulic power plants along the Ta-Jia river were flooded and damaged. In 2004 and 2005, debris flow occurred again in southern Taiwan and Tai-Tung; both caused severe damages to properties. However, since typhoon Toraji, emergency evacuation was enforced in potentially hazardous areas, which proved to be effective in reducing casualties. Such measures rely heavily on the accurate information derived from database, potential analysis, and scenario simulation.

INVENTORY OF POTENTIAL DEBRIS FLOW TORRENTS

The Soil and Water Conservation Bureau (BSWC) started investigation of the potential debris flow torrents since 1991, and 485 potential debris flow torrents in Taiwan were identified in 1996., Subsequently the potential analysis of the 485 potential torrents was performed by the NAPHM office (Lin, et. al. 1999). After the Chi-Chi earthquake of 1999, the reconnaissance conducted by the National Center for Research on Earthquake Engineering of National Science Council documented 438 landslides from ground-base investigations (NCREE, 2000). From the field investigations, the earthquake caused grounds

Table 1 Some case history of debris flow hazards

date and items	1959, typhoon Ellen	1982, typhoon Sieth	1990, typhoon Ofelia	1996, typhoon Herb
location	Pa-gua mountain debris flow	Lin-kou tableland debris flow	Tung-man area debris flow	Nantou County debris flow
No of death	1075	17	39	41
No of injury	295	7	10	65
Affected area	1244 km^2	110He.	>10 He.	600He.
House destroyed	22426	36	24	--
House damaged	18002	51	11	--
Property loss (NT$)	>34 billions	10 billions	>10 billions	>100 billions
48hrs. max rainfall (mm)	1034	365	491	1987

to loosen and produce fissures and cleavages. New landslides, rock falls, and debris flow may be easily triggered by aftershock or rainfall. Field investigations supported by NSC were conducted for the central Taiwan to identify the potential debris flow torrents, and models for evaluation of hazard potential and risk were developed. Risk assessments of the debris flow torrents of central Taiwan areas were performed accordingly (Lin, et. al. 2001). The debris flow torrents were rated as with high, intermediate, and low risk; the rated result is shown as Fig. 1. The rating results can be used for determining the remedial priority, and enforcing emergency evacuation during typhoon warning period.

A separate investigation was also conducted by BSWC after the earthquake of the central Taiwan, and the number of identified debris flow torrents in Taiwan increased to 722 based on watershed information. In 2001, typhoon Toraji induced severe debris flow hazard and a more comprehensive investigation was again conducted through out the whole Taiwan, and a total number of 1420 debris flow torrents were identified as shown in Fig.2 (BSWC, 2003). It appeared that follow-up investigation of the potential debris flow torrents was required due to drastic variations in the topography and items related to potential of debris flow. For the purpose of debris flow hazard mitigation, it is necessary to establish the database based on the field investigation. Due to the vast amount of potential debris flow torrents needed to be investigated, the whole area was divided into three regions as shown in Fig.2, and the field work was conducted accordingly. In order to ensure the consistency of investigation results, a standard format for data collection and operation manual were established.

The data were divided into four layer sheets. The first layer contains the fundamental information of the debris flow torrent, which includes: administrative region, ID number, coordinates positioned through global positioning system (GPS), original rating, and previous hazard record. The second layer sheet contains the descriptions of the current field conditions, which includes: types of failure, slope of triggering area, magnitude of landslide, grain size of depositing material, vegetation, possible hazard, preliminary rating of the potential, risk to the affected area, and preliminary rating of the susceptibility. The data were filled in according to the operation manual, and the rating of potential and susceptibility was classified as low, medium, high, and on observation. The third layer sheet contains the information of the potentially affected zone, which includes possible overflow location and its coordinates through GPS positioning, field observation of potentially affected area and geomorphologic characteristics. The fourth layer contains the information of mitigation measures and possible risk items, which includes buildings and roads at risk, their locations, mitigation structure, evaluation of its effectiveness and location, and other related items. The database and query system is illustrated in Fig.s 3 and 4. The inventory and database are currently under constant maintenance and renewal status.

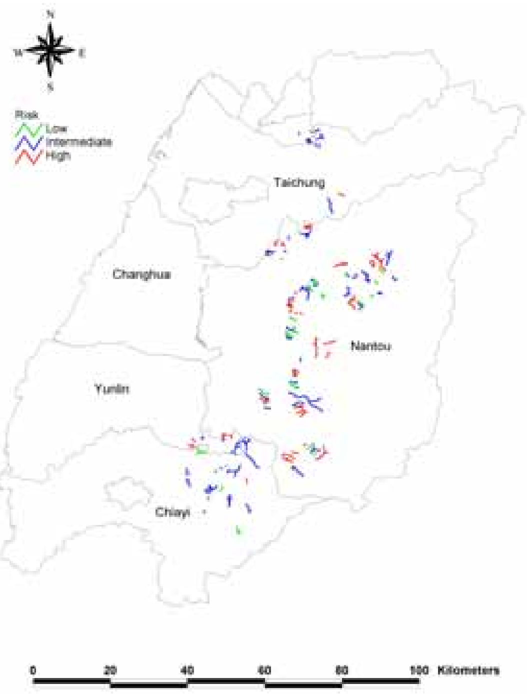

Figure 1. Distribution of the rated potential debris flow torrents in the central Taiwan after Chi-Chi earthquake.

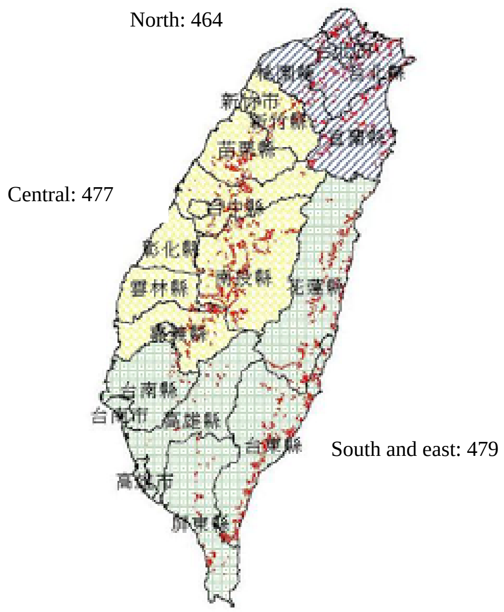

Figure 2. Distribution of debris flow torrents (BSWC, 2003)

Figure 3. Illustration of user interface for visualization of the second layer of data sheets.

Figure 4. Illustration of user interface for visualization of the fourth layer of data sheets.

POTENTIAL ANALYSIS OF DEBRIS FLOW TORRENT

.

To evaluate the potential of debris flow torrents based on the field investigation data, the parameters related to the potential were selected. The geo-environmental factors considered as related to the potential of debris flow were selected and assessment model was established.

The major environmental factors considered for causing debris flow were debris deposit, topographic condition, and water supply, and thus the factors should be related to the three conditions. Considering the data that could be extracted from the field investigation database, five factors were selected for assessment of debris flow potential according to the assessment model proposed by Lin, Yu, Lin, Fan, and Wang (2001). The five factors used in this study are: magnitude of landslide in the upstream area of debris flow, slope of the upstream area, grain size of deposit material, geological formations, and ground vegetation coverage. The rating of each factor and the preliminary breaking within each parameter were determined based on previous researches and distribution of the data. Cross-examinations were performed to verify the independency and significance of each factor. For the geological formation factor, the rating was determined according to the distribution of the 1420 potential debris flow torrents within each geological formation as number of potential torrents per thousand hectares as shown in Table 2. In Table 2, the Coastal Range zone, slate zone, and igneous rock zone are with the highest ratio of potential torrents per unit area, and thus are assigned with the highest score. The schist zone and laterite zone are with the second highest ratio of potential torrents per unit area, and are assigned with the second highest score. While the sedimentary rock zone and the other are with the lowest ratio of potential torrent per unit area, and thus are assigned the lowest score. For the basin with larger magnitude of landslides in the upstream area, the potential for triggering a debris flow is higher, and debris flow with larger grain size often induced more severe damage. For the assessment of the potential, a total score of 100 was assigned with an equal score of 20 for each factor initially.

The initial model was tested using the field database. The potential debris flow torrents identified as on observation were not included into the analysis, and thus the total number of potential debris flow torrents used in the analysis was 1210. The first test was made using the initial rating model, and the distribution of rating is as illustrated in Fig. 5, which is fairly close to normal distribution. Testing of the model was performed on each potential factor to determine the significance and weighting of the factor. The procedures for testing and adjustment are as illustrated in Fig. 6. For each factor, the distribution conditions of field rating versus the different classes within each parameter were examined for magnitude of landslide in the triggering area, slope of the triggering area, grain size of deposit material, geological formation, and vegetation coverage, respectively. During

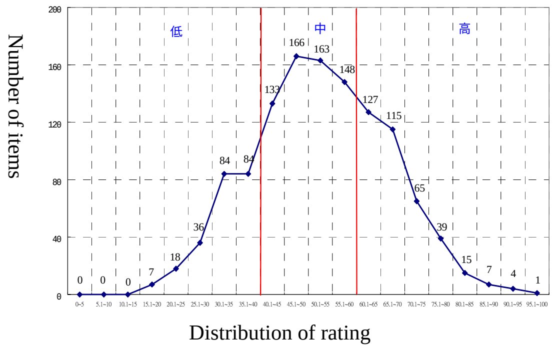

Figure5 Distribution of initial rating of debris flow torrent

the testing, it was found that a strong correlation existed between potential and magnitude of landslide factor, and also for slope of the upstream area. As for the grain size of depositing material, it appeared to have a good relationship with the potential, but is not as significant. The significance of the geological formation and vegetation coverage factors to the potential appeared to be the lowest. Thus the highest scores were assigned to the magnitude of landslide factor, and also for slope of the upstream area, and an intermediate score was assigned to the grain size of depositing material, and the lowest scores were assigned to geological formation and vegetation coverage factors. The overall rating and scores reassigned to each factor and breakage of classification within each factor were determined after several testing procedures, and the final scores and rating of the potential factors are as illustrated in Table 3.

Verifications of the rating model were made by comparing the model rating results with the field conditions of some case histories of debris flow hazard. It was found that the model rating provided more consistent representation of the field conditions and was more objective than field rating (Lin, Wen, and Jeng, 2004).

Table 2 Distribution of number of potential torrents within different geological formations

Type of formation	Area (10^3 he.)	No. of torrents	No. of torrents per 10^3 he.
A (Coastal Range)	248	190	0.77
B (Schist)	470	57	0.12
C (Slate)	1091	379	0.35
D (Sedimentary rock)	774	577	0.75
E (Laterite)	223	76	0.34
F (Igneous rock)	31	47	1.53
G (others)	789	94	0.12

Table 3 Final rating of potential factors

Factor	Class	Score
magnitude of landslide in the upstream area	large scale	30
	small scale	15
	not significant	5
slope of the upstream area	> 50°	30
	30°-50°	15
	< 30°	5
grain size of deposit material	> 30 cm	20
	7.5 cm- 30 cm	13
	< 7.5 cm	5
	not significant	0
geological formation	A, D, F	10
	C, E	6
	B, G	3
vegetation coverage	bare land	10
	sparse coverage	6
	medium coverage	3
	good coverage	1
total		100

ZONING OF POTENTIALLY AFFECTED AREA

Generally, the major consideration of the potential area affected by debris flow torrents are areas downstream of the overflow location with the consideration of local terrain, low-lying lands, scale of disaster, size of particles, and so on. The major principles of mapping followed the technical codes and regulations of laws of soil and water conservation and the influences of terrain variation on the scene. The terrain scanning method was developed for mapping of the first set of 485 debris flow torrents in 2000 (Lin, et.al., 2000), with the assumptions as follows:

1. It is assumed that the terrain of fan-shaped area downstream of overflow point is the dominating deposition area.

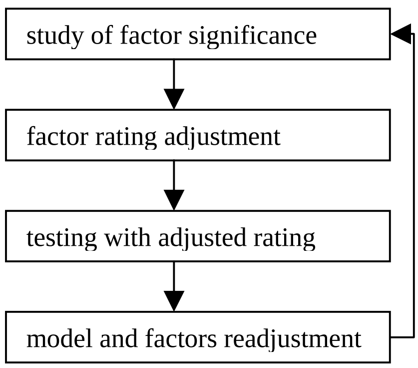

Figure 6. The procedures for model testing and adjustment

2. The overflow point of debris flow torrent is assumed to follow the technical codes of the Soil and Water Conservation. The apex of the potential fan-shaped area are determined as: (a) the outlet of a valley, (b) the sudden open space in valley, (c) the apex of alluvial fan of torrent, (d) the sudden changes of river width, or (e) the point where slope of riverbed is 10^{o}. 3. The fan-shaped area is assumed to extend from the overflow point toward the downstream area with the maximum extension angle of 105^{o}.

4. The topography of the fan-shaped area is the dominating factor which affects the flow direction and deposition of debris in the downstream area.

The process of mapping potential areas started by determining the overflow point of debris flow manually, and the 1/25000 topographic map published by Council for Economic Planning and Development was used for this purpose. With the overflow point as the apex of the fan-shaped area, a fan with an angle of 105 ° and centered along tangent direction of torrent was drawn toward the downstream area with proper radius or frontal gradient of 2 degree. In principle, the fan-shaped map only indicates potential deposit areas without adjustment for local terrain. The scanning method developed using ArcView then scanned the trajectory direction of the fan-shaped area after overflow by calculating the difference between the height of exit of debris flow and the elevation of the scanned location in the fan (Lin, et. al., 2000). Area with the steeper slope downstream was identified as more danger than other region after debris overflow from the exit. This method was used due to the limitation of not being able to conduct full field investigation. However, in 2003 with the up-dating field investigation, the field conditions were recorded and the affected area was modified accordingly. The mapping started with determination of overflow point and drafting of the 105 degree fan on the topographical map and aerial photo of 1/5000 as illustrated in Fig.7 for Taipei no.A295 debris flow torrent as a preliminary zone. The affected area and overflow point were then determined based on observation of in-situ topographic characteristics and their GPS positioning were then recorded during the field investigation. The final map of the affected area was then generated using the 1/5000 color aerial photo with modification based on the field data, and with local landmark and related information. An example of Taipei no.40 debris flow torrent is as shown in Fig. 8.

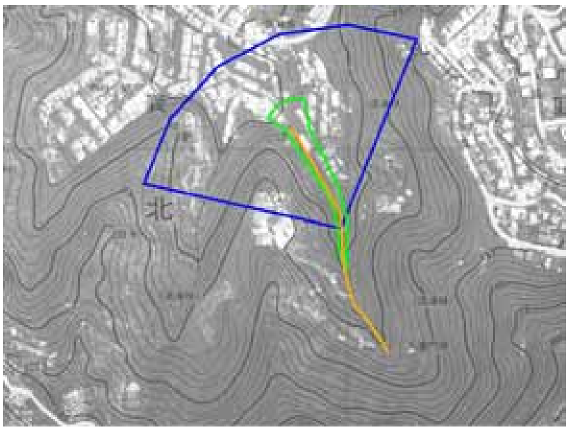

Figure 7 Drafting of 105 degree fan and modifications based on field topography on the 1/5000 aerial photo-topographical map for Taipei no.A295 debris flow torrent.

SCENARIO SIMULATION AND LOSS ESTIMATION

In order to identify the severity of debris flow in the affected area, the ability to simulate the flow route of debris is desirable. The procedures for using numerical model for simulation of debris flow deposition process had been established (Lin, et.al, 2001). For the numerical simulation, a commercially available flow model, FLO-2D (O'Brien&Julien, 1985), was used to analyze the two dimensional two-phase flow. Considering the effects on hazard, the deposition and propagation of debris flow in the deposition area are the main interest, therefore, even though FLO-2D model cannot take erosion into account (Hübl and Steinwendtner, 2001), still it serves the purpose of flow simulation. The model can simulate the deposition with giving a certain mass from the upstream. The stopping criterion comes from the governing equations, which take yield stress and viscosity into account. In order to establish the proper procedures for simulation and to ensure the appropriateness of the simulation results, case study of the debris flow event during typhoon Herb in the Chui-Sue river watershed was performed. The field deposition conditions were established through micro-geomorphologic analysis. The digital elevation models for the watershed before and after the events were constructed with a resolution of 10m by 10m, and the erosion and deposition areas were determined. To compare the field condition with the numerical results, the average thickness of deposition and erosion of each grid area was computed from the micro- geomorphologic analysis and was plotted as shown in Fig. 9. Numerical

Figure 8 The affected potential area map for Taipei no. 40 debris flow torrent

simulation of the Chui-Sue river watershed was performed with parameters determined from verifications and parametric study. For the simulation, the hydrological time history was produced for the basin based on the precipitation record of typhoon Herb, and the debris flow simulation was conducted by assigning sediment concentration and the resulting hydrograph starting from the overflow point identified in micro-geomorphologic analysis. Results of the numerical simulation are as shown in Fig.10. Comparing Fig.10 to the deposition area of micro-geomorphologic study, the affected area appeared to be fairly consistent, but the thickness of deposition varied. A more detailed comparison at certain locations along the Chui-Sue river revealed that the Chui-Sue river merged into the Her-Ser river downstream, and then was joined by Ai-Yu-Zi river further downstream. As the thickness of deposit derived from the model simulation was based on the debris flow from Chui-Sue River only, therefore the effects of effluence from other streams were not accounted for. However, in the micro-geomorphologic analysis, the terrain variations caused by other merging streams were included. It was likely that the effluence of

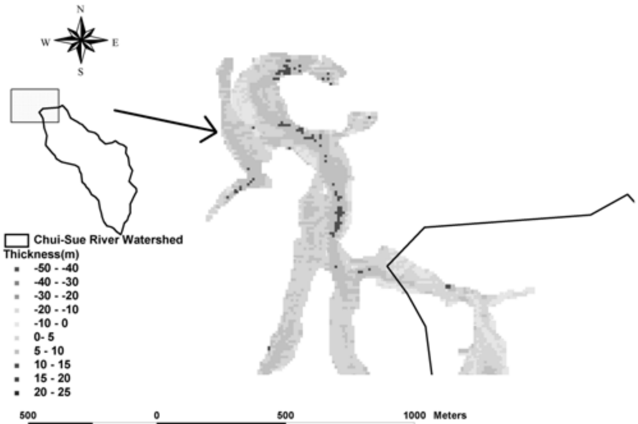

Figure. 9 Distributions of average thickness of deposition and erosion along Chui-Sue River from micro-geomorphologic study

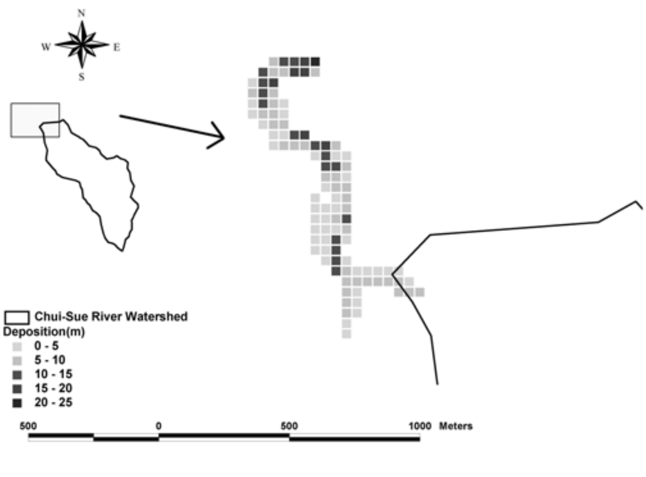

Figure.10 Results of the downstream debris flow simulation for Chui-Sue River Watershed

the other streams could affect the debris thickness because the two streams also produced debris flows. As moving further downstream of the Her-Ser River, the debris could be washed away by the river flow, for at such locations deposits resulting from model simulation displaying larger thickness than those from micro-geomorphologic study. For the Chui-Sue River Watershed, the total area of deposition from numerical simulation was about 18% larger than that of the micro-geomorphologic analysis, and may due to the reason as discussed above. The trend of thickness distribution and area of deposition obtained from the model simulation appeared to be fairly consistent with the micro-geomorphologic analysis especially for the area not affected by other inflow rivers (Lin, Wang, and Huang, 2005). Thus the procedures for simulating debris flow run-off and distribution of debris depositions could be established.

The results of the debris flow simulation provide information of the potential hazard area and the extent and severity of the debris deposit condition. However, the risk or hazard caused by the debris flow will depend on the actual damages to human lives and properties. Therefore, a risk assessment model was developed, which could quantify the damages caused by the deposition of debris to the land use, buildings, traffic, and human lives. Based on the socio-economic database constructed, layout of the land use, and by combining the layout of deposition condition and the maps of population distribution, damage and loss assessment could be calculated. For rating of damage, different thickness of deposit results in different degree of severity of damage, the thicker the deposit, the more severe the damage is. With the simulation result, the loss of buildings, number of people threatened, and damages to traffic, the loss could be estimated. The final results of the risk assessment could provide information for remedial measures for hazard reduction and preparedness.

On September 5, 2001, a weather system dropped heavy rainfall in a very short period of time. Within few hours, severe debris flow occurred at the Taipei no. 40 torrent in the Bei-Tou district of Taipei City, and killed 2 people. More debris flows occurred in the neighboring areas in Taipei County, and caused even more damages and casualties. The scenario simulation of Taipei no.40 torrent was performed using typhoon Nari as the simulation event as designated by the Hazard Prevention Council of the Taipei City, and a DEM with resolution of 4m by 4m was used. Results of the flow simulation are illustrated in Fig. 11 with the distribution of debris deposit thickness. The thickness of debris deposition is divided into three groups: for thickness larger than 3m, which is approximately higher than one floor (considered as high); with thickness between 1.5m to 3m, which is about higher than a person (considered as medium); and with thickness smaller than 1.5m (considered as low), respectively. It was noted that the deposition area from numerical simulation of debris flow consisted well with the mapped

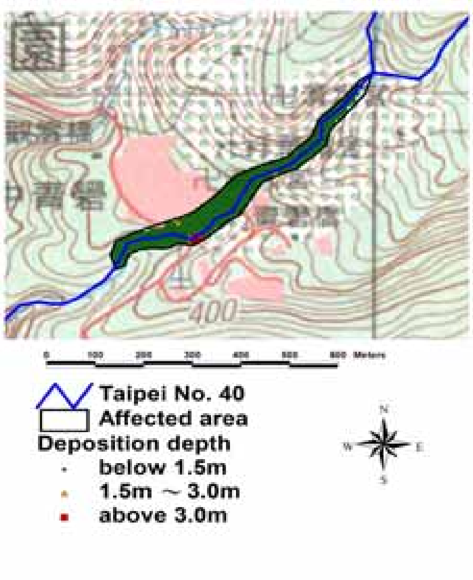

Figure 11. Results of debris flow simulation of the Taipei no.40 torrent with typhoon Nari precipitation.

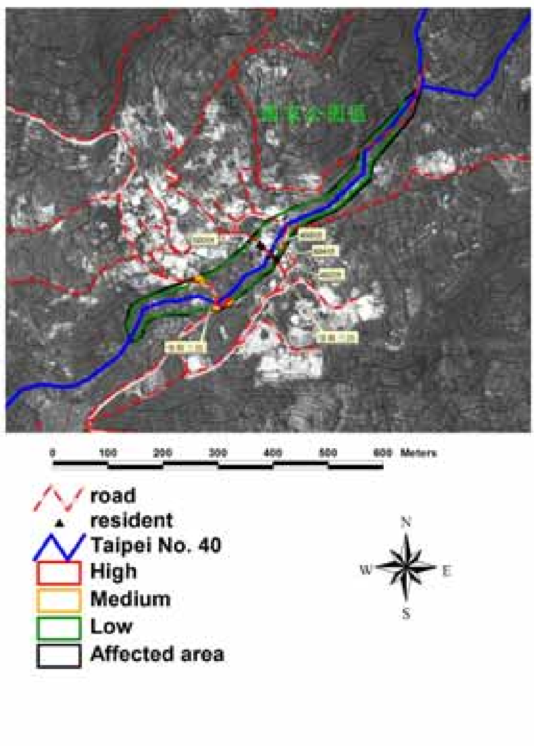

Figure 12. Results of Nari scenario of Taipei no.40 torrent.

potential affected area. With the flow simulation results, the damages and losses were estimated by overlaying the socio-economic data with deposition results as shown in Fig. 12. The estimations of direct loss and affected population are as listed in Table 4. Thus with the information listed in Table 4, further measures such as planning of evacuation route and shelter, evaluation of land-use, and effectiveness of mitigation structures could be performed accordingly.

The risk considered in this research was direct damages and losses to the population, buildings, and traffic. Further rating system of risk could be established and other factors could be added for more detailed rating of the risk. By inspection of the risk factors and possible damages by the debris flow, it was found that different classification of road could have a significant effect to subsequent recovery and further economic loss. Therefore, the classification of road should be given higher rating of risk. The risk assessment model could be combined with probability analysis for determining the scale and type of precipitation to be used for scenario simulation.

Table 4 Estimation of damages and losses for the Nari scenario of Taipei no.40 torrent

Deposition Area	26144m^2
Debris Volume	9824.64m^3
Landuse	Resident
Building Damage	
High	0
Medium	0
Low	4
Total	4
Affected Population	
High	0
Medium	0
Low	16
Total	16
Traffic Affection	
Type of road	Regular
Mileage	0.32km

EFFECTS OF CHI-CHI EARTHQUAKE

Due to the severe slope failures caused by the Chi-Chi earthquake, the slope material was loosened and with fissures and cleavages. New landslides, rock falls and debris flow may be easily triggered by other earthquakes or rainfall. Thus the immediate field investigations were conducted to identify the potential debris flow torrents, and models for evaluation of hazard potential and risk were developed as a measure to reduce secondary hazard. Potential analysis of the debris flow rivers of the Central Taiwan areas were performed and rated as with high, intermediate, and low potential as discussed previously and results are as shown in Fig. 1. Emergency remedial and reinforcing measures for slopes and debris flow torrents identified with high potential were conducted before the typhoon season in order to prevent further damages and secondary hazard.

In 2001, typhoon Toraji caused severe landslide and debris flow hazard, and it was found that most of the landslides and debris flows occurred at locations identified with previous landslides caused by the Chi-Chi earthquake as illustrated in Fig. 13. In 2004, typhoon Mindule again caused severe landslides and debris flow hazard in the Central Taiwan area. The reconnaissance (Lin, et. al., 2004) again indicated that a close relationship between the hazard induced by the typhoon Mindule and landslides induced by the Chi-Chi earthquake as illustrated in Fig.14. For both events, it was found that the magnitude and extend of failures of many reactivated landslides and debris flows increased significantly. Case histories of 14 debris flow torrents with known significant recurring debris flow hazards were documented by BSWC (2002) for major typhoon events from 1985 to 2001 as

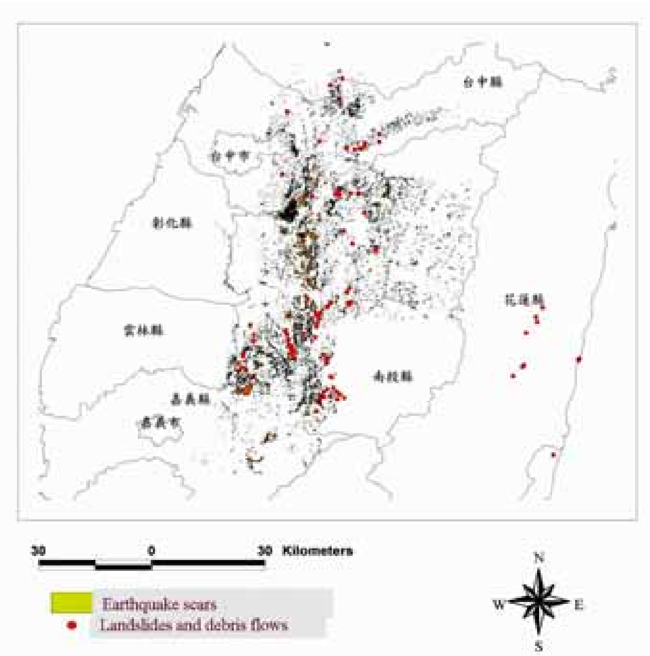

Figure 13 Landslides and debris flows induce by typhoon Toraji in 2001 versus landslides induced by the Chi-Chi earthquake

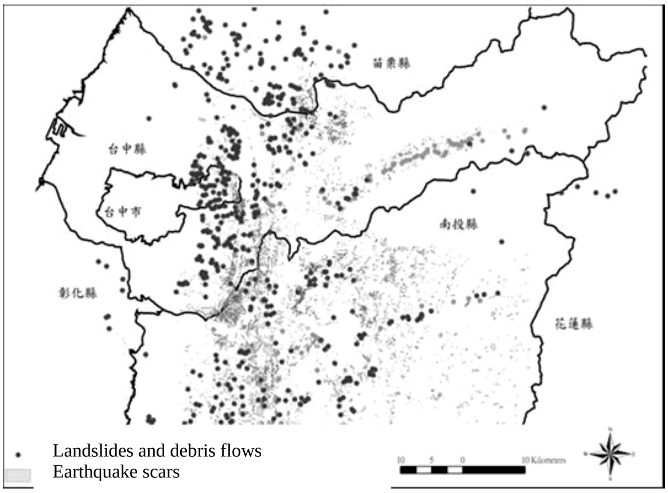

Figure 14 Landslides and debris flows induce by typhoon Mindule in 2004 versus landslides induced by the Chi-Chi earthquake

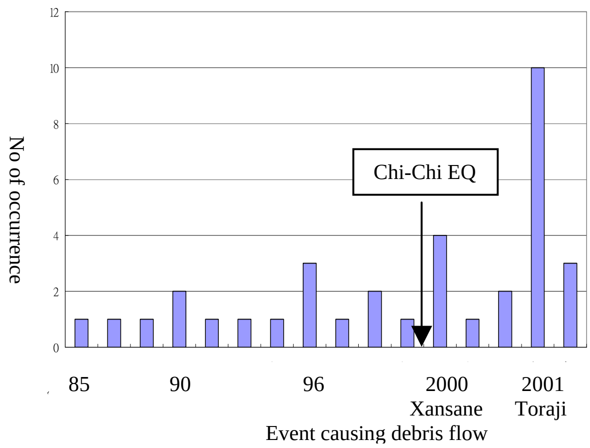

Figure 15 Number of debris flow occurrences for 14 torrents during major typhoon events.

shown in Fig.15. Observing Fig. 15, it was noted that the number of debris flow occurrence increased significantly after Chi-Chi earthquake.

Thus, a large magnitude earthquake could induced extensive failures and landslides, which lead to severe and prolonged secondary hazard such as subsequent landslides and debris flows. It is expected that more mitigation efforts will be required in order to reduce the effects of such secondary hazard in the near future.

CONCLUSIONS

The experiences of enforcing emergency evacuation based on the results of potential analysis and correct debris flow torrent database during emergency response stage has proved to be effective in reducing the amounts of casualty and losses since Typhoon Nari in 2001. Further applications and analysis of the data were also done for evaluating the priority of mitigation and set-up of monitoring and warning systems. The techniques of scenario simulation and damage assessment could provide information on the scale of impact caused by debris flow hazard. Accordingly, usage of the knowledge and technology of such kind could prove to be helpful for setting up of the area hazard prevention program, such as the routing of evacuation, location of shelter, rerouting of traffic, and planning of emergency response, etc. Further hazard reduction could be achieved through measures such as land use management, engineering structures, public educations, and forming of related public policies. However, due to the extensive failures caused by the Chi-Chi earthquake, the debris flow hazards could have significant prolonged effects, and further mitigation efforts will be essential.

ACKNOWLEDGMENTS

Parts of the research results presented in this paper were the joint efforts with the Office for National Science and Technology Program for Hazard Mitigation

sponsored by the National Science Council of Taiwan.

REFERENCES

[1] Bureau of Soil and Water Conservation，Follow-up Investigation of Potential Debris Flow Torrents，*Report by National Taiwan University*. 2003

[2] Bureau of Soil and Water Conservation，Case History of Some Major Debris Flow Hazards，*Report by National Chung-Hsin University*. 2002

[3] Chen T. C, Wang, K.L. Hung, F.Y. Liu, T.C. Tsai, H.Y. and Lin, M.L.. Characteristics and causes analysis of debris flow caused by typhoon Toraji, *Journal of Chinese soil and water conservation*, Vol.32(4), pp. 281-291. 2001

[4] Hübl, J. and Steinwendtner, H., "Two-dimensional simulation of two viscous debris flows in Austria", *Physics and Chemistry of the Earth*, Vol. 26, No. 9, pp. 639-644 , 2001

[5] Lin, Meei-Ling, "Management of Debris Flow in Taiwan", Panelist report, *Proceeding, the 14th Southeast Asian Geotechnical Conference*, post conference volume. , 2001, 12

[6] Lin, M. L., et. al.. Potential analysis and scenario simulation of debris flow rivers of Chen-You-Lan river watershed", *NAPHM Annual Report*. 2001

[7] Lin, M. L., et. al. Potential analysis and scenario simulation of debris flow rivers of Fong-Chui, Ho-Ser No.1 river, and Chu-Shui river watershed, *NAPHM Annual Report*. 2000.

[8] Lin, M.L., Chen, C.H., Lin, M.L., Chen, H.Y., Lin, C. C., and Hsue, M.H., "Reconnaissance of the Hazard Induced by Typhoon Mindule in Ta-Chia River Watershed", *the magazine of the Chinese Institute of Civil and Hydraulic Engineering*, Vol. 31, No.4, pp19-25, 2004

[9] Lin, Meei-Ling, Chen, T. C., Lin, S.C., Hung, F. Y., and Chen, J.Y.,"Risk Assessment and Its Application in Debris Flow Hazard Mitigation", *Proceedings, The first International Conference on Debris-Flow Disaster Mitigation Strategy*, pp.210-223, 2002, 12.

[10] Lin, Meei-Ling, Ho, Ming-Hsien and Wang, Kuo-Long, "Methods for Mapping of Affected Zones of Potential Debris Flow", Proceedings, *International Workshop on Hazard Zone Mapping of Hillslope*, pp.3-1-3-25. ,2004, 06

[11] Lin, Meei-Ling, Hung, F. Y., Lu, Y.S., Lai, D.L., Wang, K.-L, Lin, S.H., Huang, G.-J., and Lu, B.H., " Potential Analysis of the Debris Flow Torrents" *NAPHM special Report*. 2000.

[12] Lin, M.-L. , Wang, K.-L. and Huang, G.-J., "Simulation and Analysis of Debris Flow of Chui-Sue River Watershed", *Proceedings of the Third International Conference on Watershed Management*, pp.69-79, 2001

[13] Lin, Meei-Ling, Wang, Kuo-Lung and Huang, Jih-Jen, 'Debris Flow Run-Off Simulation and Verification – Case Study Of Chen-You-Lan Watershed, TAIWAN', *Natural Hazards and Earth System Sciences*, 5, pp439-445, 2005

[14] Lin, Meei-Ling, Wen, Huei-Yu ands Jeng, Sue-Yia "Susceptibility Analysis of Potential Debris Flow Torrents", *Proceedings, International Symposium on Landslide and Debris Flow Hazard Assessment*, pp.10-1-10-10. , 2004,10

[15] Lin, M. L., Yu, F. C., Lin, P. S., Fan, J. C, and Wang, K. L.," Evaluation of Debris Flow as Potential Secondary Hazard Caused by Chi-Chi Earthquake", *sino-tech*, Vol 81, pp.97-104, 2000

[16] National Center for Research on Earthquake Engineering，Slope-type Debris Flow Hazard triggering Mechanism Following Chi-Chi Earthquake，*Report by National Taiwan University*. 2002

[17] NCREE, NAPHM, and Taiwan Geotechnical Society, , *Reconnaissance report of the geotechnical hazard caused by Chi-Chi earthquake*, National Center for Research on Earthquake Engineering, Taiwan, 111p, 1999

[18] O'Brien, J. S. and Julien, P. Y., "Physical process of hyperconcentrated sediment flows", *Proceedings of the ASCE Specialty Conference on the Delineation of Landslides*, Floods, and Debris Flow, 260-279, 1985

(1) Earthquake induced slope instability

台灣集集地震後大甲溪流域山區崩塌地與土石流潛勢預測之研究
Hazards Prediction and Assessment of the Landslides and Debris Flows in the Mountain Area of Ta-Chia River after Taiwan Chi-Chi Earthquake

摘要

After September 21, 1999, Chi-Chi Taiwan earthquake, the follow-up heavy rainfalls transported the sediment yields from the landslides into Ta-Chia main river. It caused the riverbed of Ta-Chia main river to deposit more than 30m, and debris flows occurred in almost all the branch rivers of Ta-Chia river main. There were a lot of damages in the watershed including dams, power plants, bridges, villages, amusement parks, and other infrastructure. In order to not only estimate the volume of the sediment yields from landslides and debris flows, but also to establish the relationships between the volumes of sediment yields, the rainfalls intensity, and the discharge, several satellite images after disasters, rainfall intensity, discharges were adopted in the study. The HEC-6 program was applied to simulate the flushing and deposit of Da-Chia river in the future. The results show the highest level of riverbed around the Chin-Shan area would raise 20m in addition. Among the branch rivers of Ta-Chia main river, Ji-Ler river and Pi-Ya-Sun river brought the most sediment yields from landslides in the sub-watershed. Dern-Shian river and Bi-Tarn river brought the most sediment yields from debris flows in the sub-watershed. In conclusion, there are at least 38% of the total sediment yields from landslides still remain in the watershed of Ta-Chia river. Therefore, the sediment will transported out in the near future, and monitoring should be conducted continually to mitigate the hazards.

Keywords 關鍵詞—*集集地震, 崩塌地, 土石流*

前言

集集地震之後台灣中部山區山崩面積劇烈增加，之後歷年的豪雨除再新增部分崩塌地外，更搬移邊坡下的崖錐堆積，造成各次集水區爆發土石流，大量土石匯入大甲溪主河道後造成河道淤積與洪水位增高，此威脅大甲溪兩岸的保全對象，尤其台電大甲溪水力發電相關設施、谷關風景區、松鶴部落災損慘重。本研究以大甲溪德基壩至谷關壩集水區區域為例，以各重要豪雨事件的航照與 DTM 資料進行差異分析，瞭解各事件新增之崩塌面積與崩塌厚度以及土石流量，並且進行各雨量之頻率年統計，擬完成各頻率年豪雨下的崩塌地暨土石流土砂產出量之率定。另外，根據目前觀測之輸砂量與流量之關係式，以及各支流河道之水理參數調查，以 HEC-6 結合日本關東大地震之研究經驗，完成河道長期之沖淤趨勢預測，該研究成果擬將提供後續水利工程與電廠復健之相關工程設計參考。

研究區域概況

本研究區位於台灣中部山區，大甲溪由東至西穿越德基水庫、青山壩與谷關壩，主河道平均坡度約 1.5-2.0 度，長度約 13.87km，集水區總面積 181.6km2，另包含五條支流，最長支流為 25.7km 的志樂溪，全區山勢高聳，海拔高程由 910m 至 3,500m 之間，溪谷兩岸間之山壁陡峭且狹窄，其間主要岩性屬於砂岩、板岩或砂頁岩互層。

距離研究區域 30-45km 之車籠埔斷層，於 1999/09/21 發生規模 M_L7.3 之集集地震，震源深度 8km，本區位於上盤已達 6 級震度以上。而本區於 921 集集大地震前少有大於規模 M_L5 地震發生，集集地震後餘震序列有多次 M_L6 以上者發生，主震與餘震序列已誘發大甲溪流域集水區內大量且嚴重之山崩。

依據研究區上游松茂水文站 1986-2004 年及下游白鹿橋水文站 1978-2003 年之實測懸浮載（suspended load）及流量資料，大甲溪上下游之流量與含砂量如圖

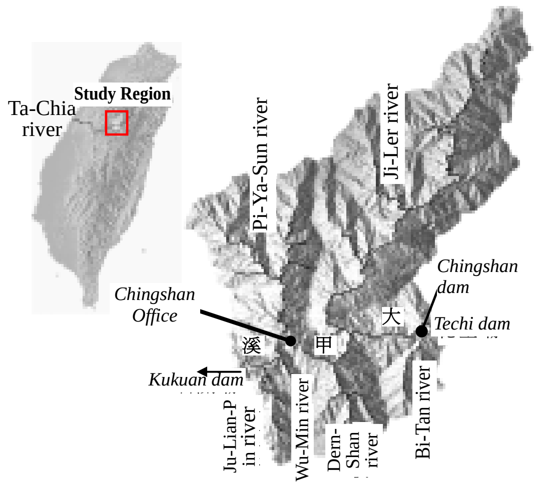

2 和圖 3 所示。從此二圖可比較集集地震前後大甲溪主要泥砂流量之變化，分析後發現，上游懸浮質濃度未因集集地震產生懸浮質濃度上升之趨勢，而下游白鹿橋站之率定曲線變化趨勢看出地震後懸浮載輸砂量濃度增加，由此可知，集集地震後崩塌土石因豪雨不斷將土砂帶往下游，輸砂行為正處於不安定期。

Fig.1 The watershed of study region.

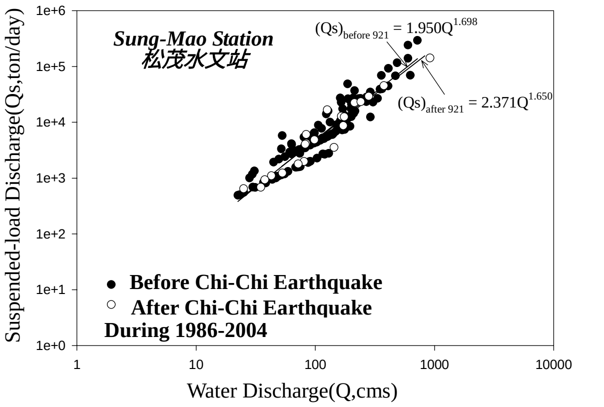

Fig.2 Upstream river regression analysis of suspended-load discharge as a function of water discharge, in logarithmic coordinates.

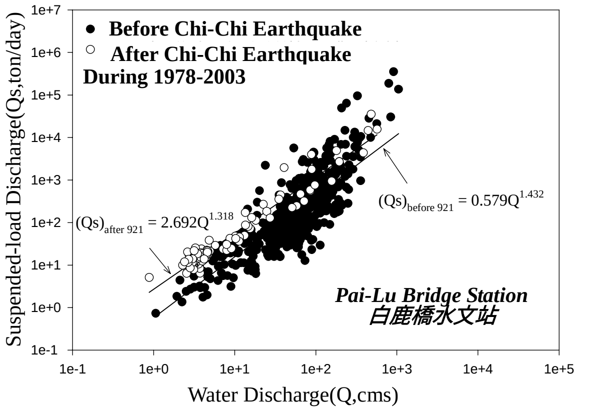

Fig.3 Downstream river regression analysis of suspended-load discharge as a function of water discharge, in logarithmic coordinates.

研究方法

本研究分別利用六期航照及五期衛星影像資料，涵蓋一次地震與四次颱風事件，如圖 4 所示，經由現勘與遙測判釋成果，完成崩塌地、土石流與其變遷研究，再利用航照製作之 DTM 分析各期崩塌厚度，分別推估大甲溪主支流崩塌以及支流殘餘之土石量，同時也分析歷次事件之河道斷面，瞭解各河段之沖淤變化。依據上述推估之崩塌與土石流土石量，結合水文分析方法推估出各再現期雨量下之崩塌與土石流土石量趨勢；另採用類神經網路方法，以過去事件之崩塌分布為訓練基礎，獲得研究區集水區內之山崩潛感圖，最後進行河道沖淤動床分析，以過去事件實際之沖淤情形進行校核，獲得大甲溪河道未來沖淤趨勢。

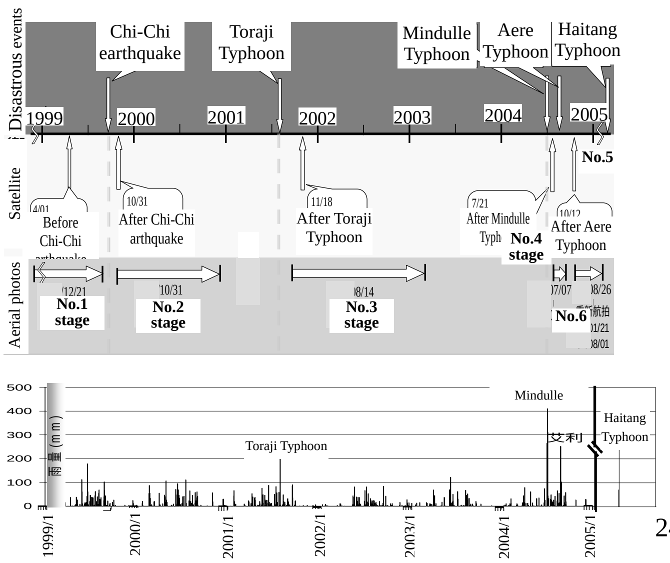

Fig.4 The dates of the remote sensing images took and the disastrous events occurred

三、災害評估

利用遙測影像判釋崩塌地可獲得各期崩塌面積與新增之崩塌面積，第一期至第六期分別代表集集地震前、集集地震後、桃芝颱風、敏督利、艾莉颱風及海棠颱風，如圖 5、圖 6 所示。

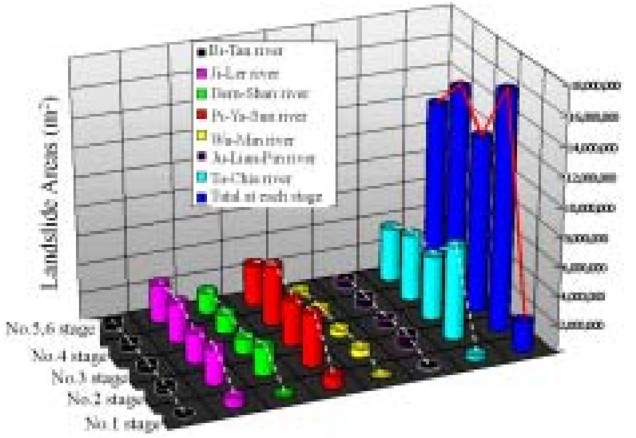

Fig.5 The summation of the whole landslide areas within each watershed.

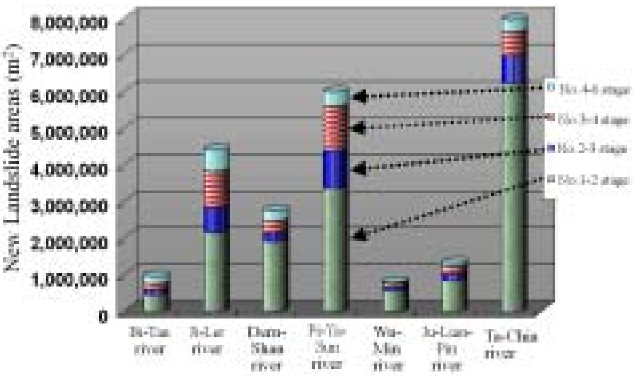

Fig.6 New generated landslide areas in each event.

再利用航照 DTM 之差異分析，各次集水區所產生的崩塌體積總量如表 1 所示，期統計圖如圖 7 所示，結合崩塌面積與崩塌體積則可推估各次事件誘發的崩塌厚度，如圖 8 所示。

Table 1 The volume of landslides in each event

Watershed	Chi-Chi earthquake	Toraji Typhoon	Mindulle Typhoon	Aere,Haitang Typhoon	Total
Bi-Tan river	150,556	237,357	144,819	143,769	676,501
Ji-Ler river	4,903,111	1,182,740	1,293,251	705,496	8,084,598
Dern-Shan river	2,807,337	502,134	432,960	327,138	4,069,569
Pi-Ya-Sun river	5,561,772	1,867,943	2,251,942	702,724	10,384,381
Wu-Min river	805,995	180,194	146,173	58,489	1,190,851
Ju-Lian-Pin river	1,415,744	344,620	344,839	178,782	2,283,985
Ta-Chia river	10,270,154	1,931,678	1,347,207	715,567	14,264,606
Study region	25,914,669	6,246,666	5,961,191	2,831,965	40,954,491

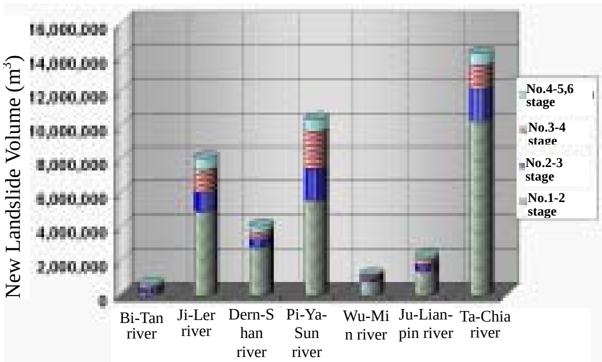

Fig.7 The volume of landslides in each stage (not include the inflated rate).

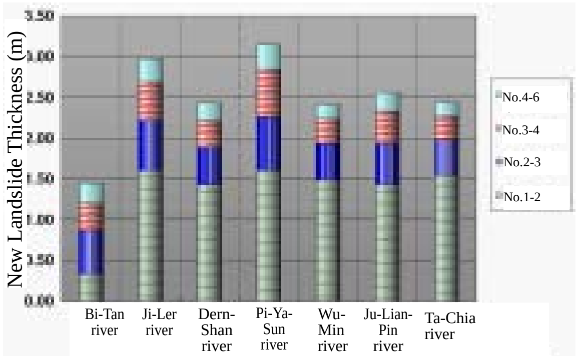

Fig.8 The thickness of landslides in each watershed.

由上述圖表可知，集集地震事件所誘發之崩塌面積、體積與崩塌厚度均為最大，由各期新增崩塌來看，因集集地震所誘發之新增崩塌面積最大，其後颱風豪雨事件之新增崩塌面積則漸漸趨緩，合計集集地震至海棠颱風後(約 6 年期間)新增之崩塌面積約 2,423 萬 m^2，而集集地震一次事件誘發崩塌就約佔了約 70%。就崩塌區域而言，谷關壩至德基壩間大甲溪主河道兩岸與匹亞桑溪流域崩塌最嚴重，此二處崩塌量合計就達到 60%，也是形成大甲溪河床淤積災害之主要因素。在崩塌體積變化上，原始崩塌體積差異約 4,095 萬 m^3，若考慮崩塌土石膨脹率 20%，則崩塌產生土石總量約 4,900 萬 mm^3，若再考慮膨脹率為 33%及 DTM 誤差 0.5m，則推估出崩塌產生土石量約 7,100 萬 m^3，可概估本研究範圍(德基壩至谷關壩)因崩塌後所產生之總土石量約於 5,000~7,000 萬 m^3 之間。

災害預測

新增崩塌面積預測

為推算本流域各子集水區於暴雨所造成之崩塌地泥砂流失量，本研究引用日本在集水區治理規劃時所採用之打荻氏公式，其示意圖如圖 9 所示，計算公式如下：

$$Y = \frac{C_a}{a} = K \times 10^{-6}(R-r)^2 \qquad \text{(公式 1)}$$

其中，Y：新增崩塌率，Ca：新增崩塌面積，a：集水區面積，K：係數，R：累積雨量，r：發生崩塌之臨界雨量。

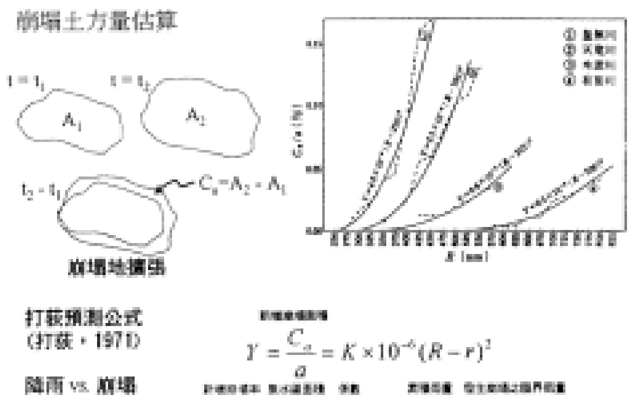

Fig.9 打荻's function of new landslide areas(1971).

K、r 為與現地地文條件之待定值，需透過研究區之崩塌地調查加以決定。另外，本研究區在不同重現期距之雨量分布如表 4 所示。

Table 2 The Return Periods for Rainfall in this study.

Return Periods	2 year	5 year	10 year	20 year	25 year	50 year	100 year	200 year
Rainfall (mm)	198	291	355	420	441	507	575	646

將上述六個集水區以打荻氏公式分別作推估運算，則可獲得不同重現期距下的新增崩塌面積，如表 5 所示，再依據新增崩塌率與日雨量繪圖則可分別獲得圖 10，圖中之分析結果所推估之集水區崩塌特性，可發現依崩塌發生之程度而言以匹亞桑溪集水區最易發生崩塌，之後為無名溪、久良屏溪、登仙溪、必坦溪與志樂溪集水區等。

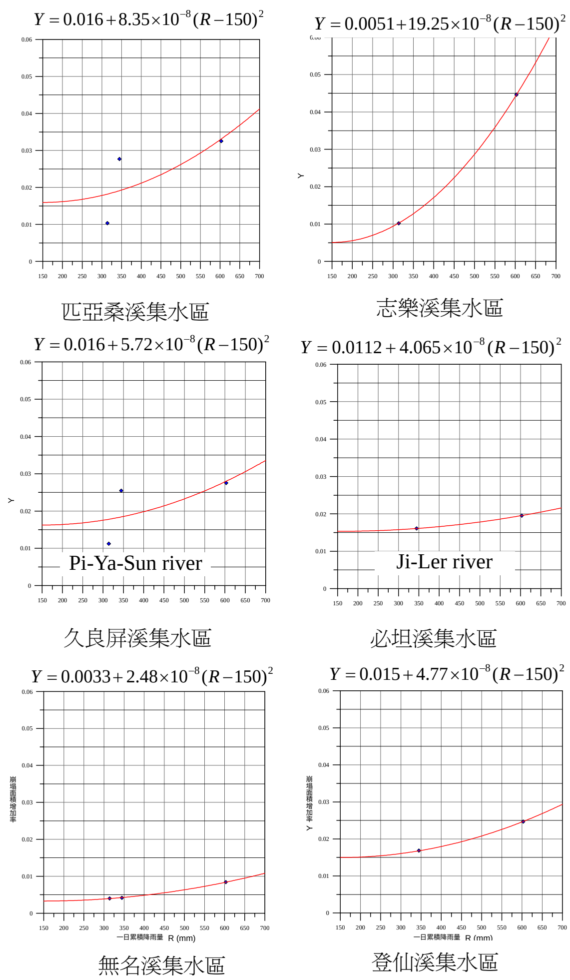

Fig.10 Regression analysis of New landslide areas for various return period rainfall on each watershed. (unit: m^2)

Table 3 New landslide areas for various return period rainfall.(unit: m^2)

Watershed	5year	10year	25 年	50 年	100 年	200 年
Bi-Tan river	7,209	15,238	30,705	46,213	65,494	89,205
Ji-Ler river	43,329	91,590	184,556	277,765	393,658	536,173
Dern-Shan river	12,926	27,323	55,055	82,861	117,434	159,948
Pi-Ya-Sun river	100,583	212,616	428,424	644,799	913,830	1,244,661
Wu-Min river	8,075	17,070	34,395	51,767	73,365	99,926
Ju-Lian-Pin river	8,495	17,957	36,183	54,457	77,178	105,119

土石流預測

台灣因溪谷陡峭，崩塌堆積河道之土石常發生土石流，為推估土石流之土石量，過去有學者謝正倫（2000）研究，建議土石流土砂產量的方式，以採用現場調查法為主，惟當現場調查法無法進行時，可藉由經驗公式法進行推算。根據現場調查資料分析，土石流土砂產量一般隨集水區面積大小變化，在各種土砂流出量不被超越機率下，台灣地區土石流土砂產量 *Vs* 與集水區面積 *A* 之公式如下：

$$Vs=K\times A^{0.61} \text{ (謝正倫，2000)} \qquad \text{(公式 2)}$$

然而，該推估公式僅用集水區面積計算，無法表現不同重現期距雨量下的差異，況且，大甲溪流域又經過集集大地震之影響，因此，本文將土石流土方量推估公式可改寫為：

$$Vs=K\times(R-r)\times A^{0.61} \qquad \text{(公式 3)}$$

其中，*Vs* 為土石流土方量，*A* 為集水區面積，r 為臨界日雨量，*R* 為土石流發生之日雨量，*K* 為係數。土石流發生之臨界日雨量係參考水保局土石流警戒基準值所公佈之有效累積雨量，即 r =200 公厘(台中縣和平鄉)。上述公式除 *K* 為反應現地土石流地文雨水文條件相關之待訂值，其餘係數均為已知。表 6 係以 DTM 比對與搭配不同重現期距雨量分析結果，再利用上述公式可推估各再現期雨量下之各次集水區土石流統計圖如圖 10 所示。

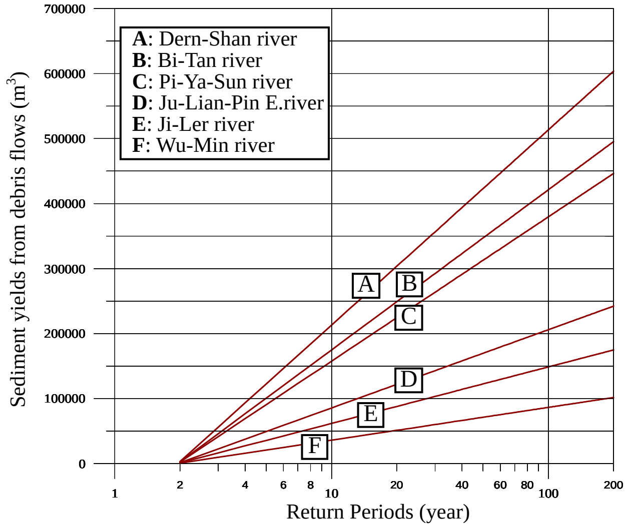

Fig.11 The sediment yields from debris flows for various return period rainfall.

經分析後可知，不同再現期下之土石流土石量以登仙溪為最多，其次依序分別為必坦溪、匹亞桑溪、久良屏溪、志樂溪與無名溪。以 200 年重現距雨量估算上述支流之土石流土石量分別依序達 61 萬 m^3、50 萬 m^3、45 萬 m^3、24 萬 m^3、18 萬 m^3 及 10 萬 m^3，本研究區 6 條支流合計約 210 萬 m^3。

Table 4 The sediment yields from debris flows between various return period rainfall and Mindulle typhoon.(unit: m^3)

Watershed \ return period	5 year	10 year	20 year	25 year	50 year	100 year	200 year	Min-dulle typhoon
Bi-Tan river	103,621	174,938	247,353	270,751	344,289	420,054	499,165	451,251
Ji-Ler river	36,549	61,708	87,245	95,498	121,436	148,160	176,062	159,164
Dern-Shan river	126,500	213,216	301,490	330,010	419,642	511,990	608,415	550,816
Pi-Ya-Sun river	93,369	157,623	222,881	243,964	310,226	378,496	449,778	406,607
Wu-Min river	21,230	35,841	50,678	55,473	70,540	86,063	102,272	92,455
Ju-Lian-Pin river	50,642	85,492	120,887	132,322	168,261	205,290	243,951	220,537

長期河道冲淤分析

美國陸軍工兵團所發展的 HEC-6 程式能模擬河川、水庫長時間的冲淤現象、水庫淤積現象、疏濬的影響及模擬支流與側流等功能。因此，爲預測本區主河道未來的冲淤趨勢，本研究採用該模式模擬一維河道冲淤。另外，爲模擬大地震後所產生長期冲淤趨勢，則須需給定長期之流量－泥砂入流量，唯現有資料並無類似大地震後流量－泥砂入流量隨時間遞減之研究資料。因此，本研究參考日本社團法人砂防學會、地震砂防研究會於關東大地震後之研究(中村浩之等人，2000)與經驗，將上述二者結合後作為推估集集大地震後之長期河道冲淤之預測。

如圖 12 所示，關東大地震後崩塌地自 1896 年至 1980 年間之變遷情形，大約可概分為發生期、不安定期、回復期及安定期等 4 個時期，其中不安定期約 15 年，而回復期約需 20 年以上，推估規模 M7.9 的關東

大地震對於該地區之崩塌影響年限約達 35-40 年。圖中曲線說明崩塌量隨時間遞減，再根據本研究分析集集地震後至今崩塌新增率及河道變遷資料發現，崩塌與泥砂入流量之遞減趨勢呈現某種程度相似。例如從敏督利颱風到海棠颱風期間，計畫區的崩塌新增量與河床淤積情況，兩者都隨時間遞減，因為河床淤積量隨泥砂來源變化，而泥砂供應來源亦隨崩塌遞減率變化。因此，本研究假設泥砂入流量隨時間遞減趨勢如圖 12，從圖 12 可轉換為圖 13 並作出崩塌遞減率隨時間之公式如下：

$$R(T) = \frac{0.9405}{1 + \exp\left[- \frac{(T - 21.2082)}{3.5204} \right]} \qquad \text{(公式 4)}$$

其中，R 為崩塌遞減率；T 為時間。

接著再建立特定區域泥砂入流量遞減率與河床平均年沖淤量公式如下(如圖 14)：

$$H(R) = 1.185 - 2.410R + 5.217R^2 - 4.476R^3 \qquad \text{(公式 5)}$$

其中，H 為平均年沖淤量；R 為泥砂入流量遞減率。上述之公式，係假設泥砂入流量遞減率與崩塌遞減率隨時間關係相同，將上述兩公式合併，得到特定區域平均沖淤量與時間之關係函數 H=f(R,T)，如圖 15 所示。此函數說明隨著時間增加，平均每年的淤積量會遞減，到三十年後會開始有沖刷現象。表 7 係經由模擬結果可分別獲得未來 50 年內於青山分廠出風口至青山分廠辦公室間、以及新的青山尾水出口可能河床淤積量。

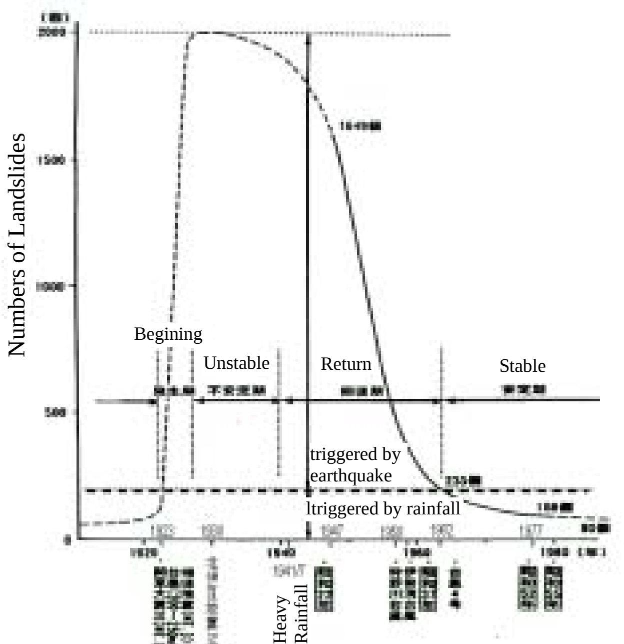

Fig.12 The change of landslides after great Kanto earthquake from 1896 to 1980 in Japan[2].

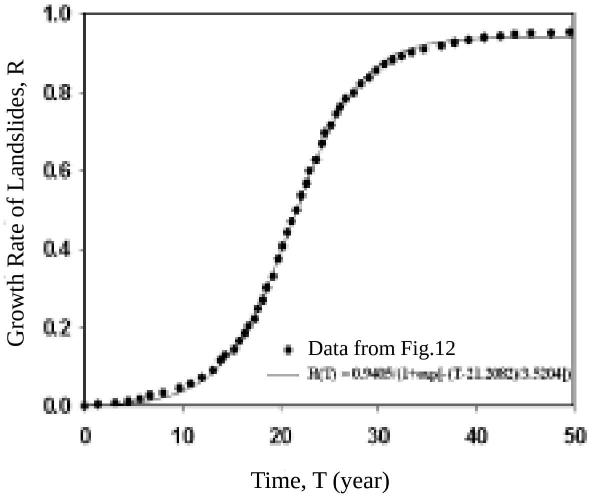

Fig.13 The relationship between the growth rate of landslides and time.

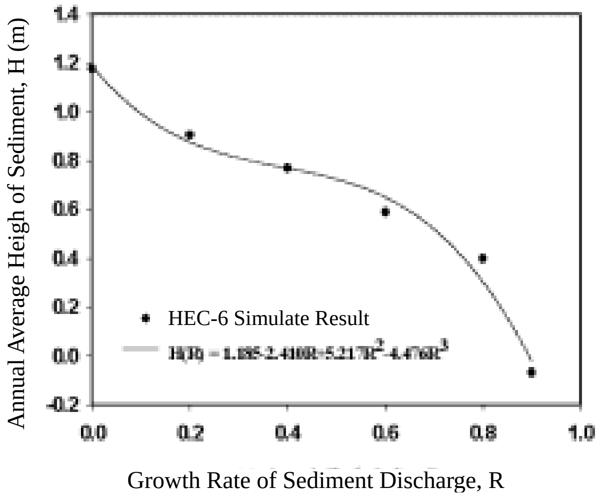

Fig.14 The relationship between annual average heigh of Sediment and growth rate of sediment discharge.

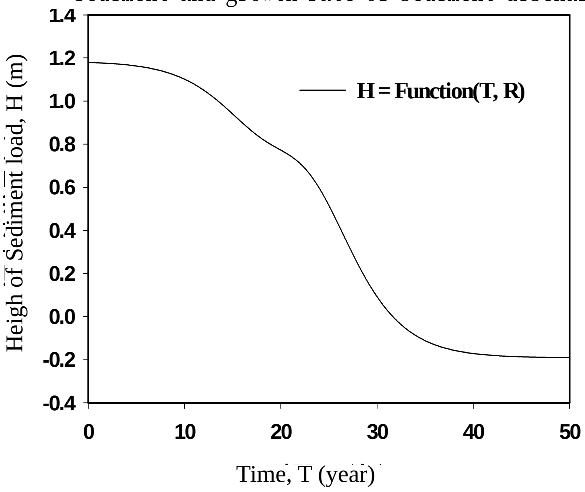

Fig.15 The relationship between heigh of Sediment and time.

Table 7 The valuation heigh Sediment of Ta-Chia riverbed nearby Chingshan plant in future 10-50 years.

Region	10 years	20 years	30 years	50 years

Between Outlet of Chingshan plant and Chingshan Office	11.6 m	20.9 m	25.7 m	23.1 m
400m upstream of Kukuan dam (New spillway gate of tailrace tunnel of Chingshan plant)	4.9 m	-2.0 m	-2.4 m	-2.7 m

地震誘發崩塌之潛感分析

本研究採用類神經網路方法，以 921 集集地震誘發山崩區域的之選用因子包括：坡度、坡度粗糙度、地形粗糙度、坡向、總曲率、全坡高、集集主震之 Ia (Arias Intensity)等七項因子，等因子作爲類神經網路的輸入層進行訓練。經訓練完成後，再以此網路架構進行回想，以獲得研究區發生類似集集地震誘發的山崩潛感。分析結果如圖 16 所示，大甲溪主河道山崩潛感高區位於谷關水庫庫區北側以及志樂溪至登仙溪西側。志樂溪高潛感位於溪流右岸，登仙溪幾乎整個集水區都是高潛感區域。匹亞桑溪崩塌地高潛感分布於上游右側支流。

豪雨誘發崩塌之潛感分析

藉由現地調查之結果，未來 50 年內邊坡岩體風化與再崩落大量土石的可能性不高，由集集地震後之歷次豪雨，尤其 2004 年敏督利與艾利風災發生後，集集大地震崩落的土石是提供土石流與河床堆積的主要材料來源。本研究採用類神經網路方法，以桃芝、敏督利、艾利等三個風災事件的山崩分布區域擷取地質、地形、水文、雨量因子，以及前述地震誘發山崩的潛感值作爲類神經網路的輸入層資訊進行訓練，完成類神經網路架構後，將依據各重現期下的日雨量而改變輸入層中雨量因子，再進行回想，圖 17 爲大甲溪德基至谷關段 200 年重現其距雨量下豪雨誘發山崩之潛感圖。比較地震誘發山崩潛感圖及豪雨誘發山崩潛感圖可發現，豪雨誘發山崩高潛感區域明顯較地震誘發山崩範圍要廣，大甲溪主河道兩岸分布皆高潛感區域，志樂溪高潛感位於溪流右岸，登仙溪及無名溪幾乎整個集水區都是高潛感區域，匹亞桑溪崩塌地高潛感分布於上游右側支流。

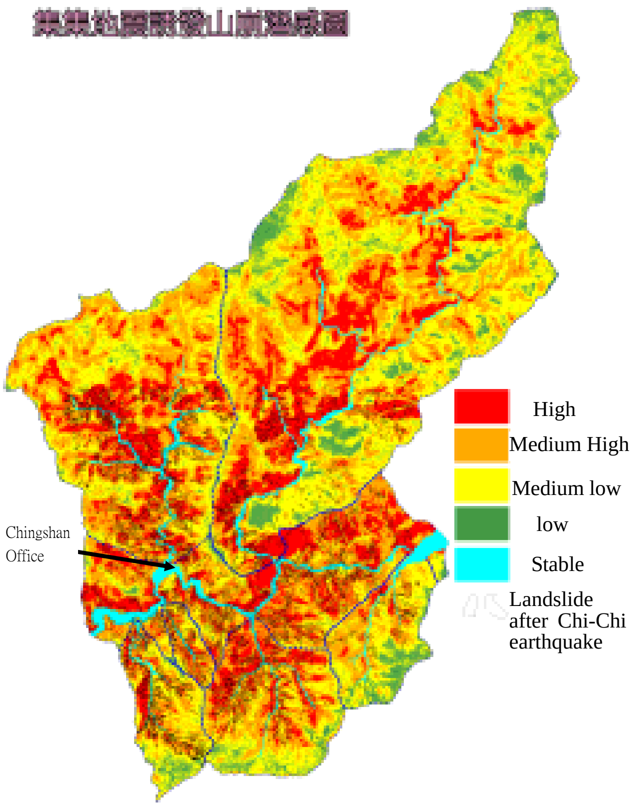

圖 16 Failure potential of landslides triggered by earthquake.

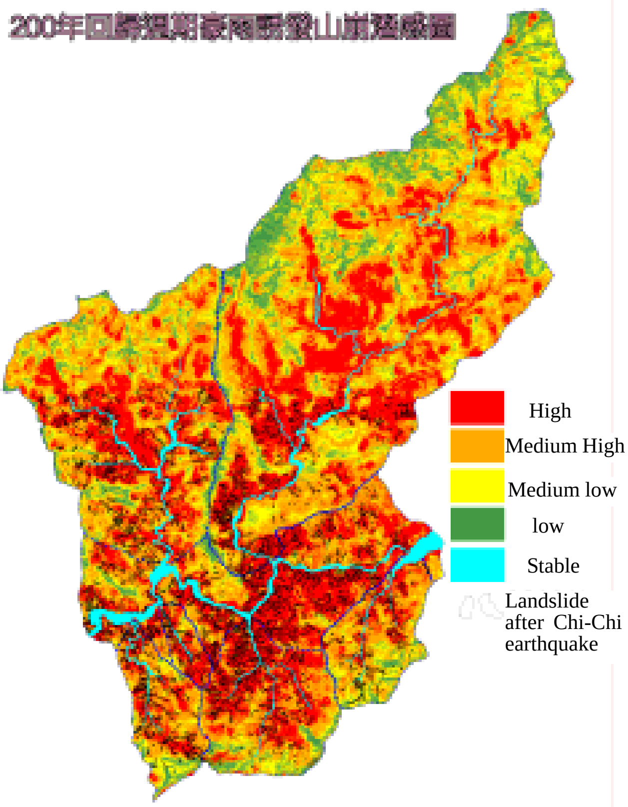

Fig.17 Failure potential of landslides triggered by heavy rainfall.

討論與建議

本研究區於集集地震後歷經多次颱風豪雨沖刷，

形成嚴重河道淤積，導致河道兩岸發電設施、建物與道路等重大災情，利用航照判釋、DTM 差異與不同預測模式分析結果，可知若未再發生類似集集大地震之情形下，大甲溪山區之山崩、土石流與輸砂量之趨勢未來將逐漸趨於平穩，但仍有若干問題值得深入討論：

1.崩塌衰減趨勢：目前僅有日本關東地震可作爲參考與應用，亦即在一次大地震後，大甲溪山區流域到底需歷經多少時間方能回復穩定，目前並無確定答案。但經由本文分析結果可大概估算，若將崩塌之土石全部持續沖淤至主河道，本區部分河道最大的淤積量將可能高達 25m，然後再逐漸下刷。因此，若能再後續一、二十年以上作持續性的監測與研究，相信對於台灣中部山區之地質災害研究，將有莫大貢獻，並可作爲未來本文研究結果的修正或提供其他研究之參考。

2.新增崩塌地與土石流土石量推估：採用打荻公式需要累積雨量、發生崩塌之臨界雨量等數據，對於台灣中部山區較缺乏雨量站與臨界雨量詳細資料，由於偏遠山區雨量站設置不易且容易沖毀等現象，在推估時將是常遇到的困難。在土石流方面，由於本區域所有支流在豪雨下均形成土石流，並直接流到大甲溪主河道陡峭溪谷堆積後，同時又遭遇到主流洪水大量掏刷至下游，整個主支流形成複雜的沖、淤循環過程，並非一般以土石流直接堆積在溪流沖積扇估算。另外，山區土石流的土石流發生之臨界雨量同樣長期缺乏現有資料，因此如何在各支流集水區取得各種地質災害臨界雨量，對於預測模式將有極大幫助。

結論

本研究完成山區集水區之崩塌量推估，以及崩塌地、土石流與雨量有關之預測模式推估，初步有以下結論：

1)集集地震是大量崩塌主因：依據航照及衛星影像資料經判釋後統計，本研究區域於集集地震後之崩塌數量急遽增加，若非集集地震促崩，即使發生極端豪雨仍無法有如此龐大之崩塌面積與土石量。自集集地震後迄今再經過數次颱風豪雨肆虐，加速土石崩落與流動，促使主支流邊坡之崖錐堆積或溪溝源頭崩落之土石，經由豪雨陸續將其帶入大甲溪河床中，造成河床劇烈抬昇。

2)崩塌面狀況：由各期航照影像判釋及野外現地調查成果，目前邊坡上鬆動之土石已大多於集集地震與豪雨後崩落，大甲溪主流與支流兩岸部分坡面已裸露出新鮮岩盤面，野外調查研判於短期間內不易形成破碎之風化坡面且持續崩落大量之土石。另外由各事件前後期之數值地形差異比較，可知歷次豪雨事件誘發崩塌地之厚度有趨緩的情形。

3)土石流溪流：堆積於大甲溪支流或溪溝中之崩塌岩屑，受豪雨溪水挾帶形成土石流匯入大甲溪主河道中，研究區域中之必坦溪、志樂溪、登仙溪、匹亞桑溪、無名溪及久良屏溪等，這六條溪流皆是土石流溪流。

4)潛感分析：由於集集地震之後地質條件改變，豪雨誘發山崩之問題必需考慮集集地震誘發山崩之情形，故本研究完成集集地震之後豪雨誘發山崩之潛感圖，圖中高潛感值之區位爲未來崩塌可能性極高之區位，值得後續復建計畫注意。潛感圖中豪雨誘發山崩高潛感區域較地震誘發山崩高潛感範圍要廣，志樂溪高潛感位於溪流右岸，登仙溪及無名溪幾乎整個集水區皆屬高潛感及中高潛感區域，匹亞桑溪崩塌地高潛感分布於上游右側支流。

5)各再現期雨量下土石流土石量：不同再現期下之土石流土石量以登仙溪爲最多，其次依序分別爲必坦溪、匹亞桑溪、久良屏溪、志樂溪與無名溪。以 200 年重現距雨量估算上述支流之土石流土石量分別依序達 61 萬 m^3、50 萬 m^3、45 萬 m^3、24 萬 m^3、18 萬 m^3及 10 萬 m^3，各支流產出合計約達 208 萬 m^3。

6)河道沖淤趨勢：依據河道沖淤趨勢分析成果，本範圍之青山壩至谷關壩大甲溪河道若一年內遭受類似敏督利颱風與艾利颱風相同規模下之降雨，於青山分廠辦公室至出風口間之河道將有持續淤積之趨勢，推估平均淤積高度約 3.2m。另外，依據較保守極端狀況下分析大甲溪河道長期沖淤結果顯示，在青山廠房通風口至青山辦公室間河段預估未來 30 年內仍將淤積，惟淤積趨勢將逐年減少；在 30 年後至 50 年間因淤砂入流量減少，該河段將反成沖刷趨勢。預估於未來 10 年、20 年、30 年及 50 年之平均淤積高度，分別爲 11.6m、21.0m、25.8m、23.1m。以相同方法推估谷關壩上游約 400m 處(新青山分廠尾水出口)，該處未來 10 年將淤高 5m，而未來 20 年、30 年及 50 年將分別下刷 2m 左右。

參考文獻

[1] 林美聆、林銘朗、陳宏宇、陳正興、許銘熙、林俊全，「大甲溪流域之初步堪災」，土木水利，第三十一卷第四期，2004年。

[2] 社團法人砂防學會、地震砂防研究會「地震砂防」，中村浩之、土屋 智、井上公夫、石川芳治編，古今書院，2000年。

[3] 謝正倫，「桃芝颱風災區土石流災害潛勢分析成果報告書」，行政院農委會水土保持局，2000年。

[4] 打荻珠男 (1971)，ひと雨による山腹崩壊について，新砂防，通巻79号。

Landslide Zonation of Hungtsaiping Area Based on Aerial photograph and PIV Technology

Chia-Ming Lo[1], Kuo-Chang Lee[1], Wei-Chu Lee[1], Ming-Lang Lin[1], Fu-Shu Jeng[1]
[1]*Department of Civil Engineering, National Taiwan University, Taipei, Taiwan*

Abstract

The Chi-Chi earthquake, triggered large scale landslide with sliding area about 100 hectares, occurred at Nantou country of central Taiwan in 1999. According to the research by Lee at 2004, they found the surface horizontal displacement vectors that moved to NW in this area after Chi-Chi earthquake. We infer that the mechanism of this landslide is very complex because of the irregular displacement vectors. Therefore, we collected five different times photo-base-maps (1977, 1984, 1991, 1998 and 1999) and three aerial photographs at 1966 to 1999 in order to identify the topography change and to analyze the surface displacement by PIV (Particle Image Velocimetry); Thus, we can differentiate landslide zonation and probability of sliding of Hungtsaiping. By means of identifying landform in topography, we can differentiate A, B and C three sliding areas in Hungtsaiping. The zone C located at western landslide has lower probability for activity, and the avalanches in the zone C most related to the river bank erosion. However, the probability sliding again of zone A and zone B are stronger than the zone C, and the avalanches in these two areas mainly belonged to the deep sliding and shallow sliding in the old colluvium. Besides, according to the result of analysis by PIV, we can differentiate three different zones (A1, A2, and B) in Hungtsaiping after Chi-Chi earthquake. We found that the displacement after Chi-Chi earthquake of zone A1, zone A2 and zone B was larger than other area, and then we found that the activity and the result by identifying topography of the zone A and zone B are identical to the zone A1, zone A2 and zone B. Let's sum up the results by field investigation, drilling, identifying topography and analyzing the displacement in Hungtsaiping, the sliding areas belong to the old colluvium and this area has higher probability for activity. Therefore, we will continue monitor the ground surface and the underground in Hungtsaiping area, and then we will to consider the influence of Hydro-geology. Finally, we hope the research can provide reference for landslide monitoring, drilling and land use management.

Keywords—*landslide, zonation, Hungtsaiping, topography, aerial photograph, PIV*

INTRODUCTION

Huangtsaiping, a famous scenery place of NanTou County, located at Jungliau Township. On the early morning 1:47 A.M. of September 21 in 1999, an earthquake with Richter magnitude of 7.3 and epicenter located at NanTou County has been recognized as a serious disaster event by the people in Central Taiwan. After Chi-Chi earthquake, the landslides were the most obvious phenomenon, such as Chiufengershan landslides and Tsaoling rockslides that are moving fast and catastrophic. However, many observation and reports told by researchers show that there are also slow slides taking place after Chi-Chi earthquake. Our study area of one of those slow slides is called Huangtsaiping landslide.

Topographically, the Huangtsaiping landslide is located in the valley of a small stream called Younglu. The Younglu creek belong to the basin of Jhangping creek that the upper reaches of the Wuhsi river, and the fountainhead of the Younglu is Kandoushan at an elevation of about 1,097 meters (Figure.1).

According to the geological map (Figure.2) edited by Central Geological Survey (CGS), the study area is underlain mainly by Miocene sedimentary rocks. The strata exposed in this area are, in ascending order, the Tanliaoti Shale (Tl), the Shihmen Formation (Sm), the Changhukeng Shale, and the Shenkeng Sandstone (Sk). The strata in this area are folded to form the Tsukeng anticline which axis trends nearly in the N–S direction and the azimuth of the left limb is (N135^{o}W, 19^{o}N), so we can infer that Huangtsaiping slide is a dip slope slide. The slide about is 1.2 km^2 (800 m x 1500 m) (Tsai and Hu, 2004), and the northern boundary is cut by a river and a fault. Along the river, we can find bending of slope foot and main scarp which can prove the sliding behavior of the formations in this area. Also, we can see the breaking of roads and bended stems of betel palms in this slide area.

According to researches by J.F. Lee and C.H. Tseng et al at 2004, they use photogramery and PIV technology to found the surface horizontal displacement vectors that moved to NW and infer large dip slope slide in Hungtsaiping area after Chi-Chi earthquake. But, we infer that the mechanism of this landslide is very complex because of the irregular displacement vectors and evidences of field investigation. Therefore, we will use aerial photograph and PIV technology to differentiate landslide zonation and probability of sliding in this study.

Nevertheless, we conjecture that the range of Huangtsaiping landslide was wider than 1.2km^2 from different times of the topographic maps and the aerial photographs, so we need more evidence to compare and check our results.

METHODOLOGY

The research mainly works on collecting the geo-environmental information, such as geology, faults, landform, topography etc. One of which we concert about is topography data included orthographic Photo-base-map, aerial photograph (Taiwan Grid 67, 1:5000, pixel size of 0.25*0.25m), and topographic maps (Taiwan Grid 67, 1/25000). In order to define the boundary and probability of sliding of Hungtsaiping landslide, we used topographic maps, and aerial photographs which were taken in 1966, 1977, 1984, 1991, 1998 and 1999. Besides, we use two gray orthographic Photo-base-maps from five different times through PIV analysis to evaluate the amount direction of the displacement which were differentiate landslide zonation and probability of sliding of Hungtsaiping area.

A. Topographic analysis and classes of slope stability

(a) Topographic maps: The topography or geometry of the ground surface is an overt clue to past landslide activity and potential instability. Furthermore, topographic maps show the size, shape, and depict of the landslide area. On some maps, the boundaries of the slide and arrows pointing toward the direction of movement are also shown. We used gray orthographic Photo-base-maps which acquired from Aerial Survey Office, Forestry Bureau (ASOFB) and were taken at a scale of 1:5000 of the same selected area in 1977, 1984, 1991, 1998 and 1999 to analyze the topography change (Table.1). However, the topography in Hungtsaiping area did not have a large scale change in recent forty years.

Table.1. The topography map of Hungtsaiping landslide under different time interval.

Image classification	Date	Pixel Size	Scale
Topographic map (Photo-base-map)	1977	0.25x0.25m	1:5000
	1984	0.25x0.25m	
	1991	0.25x0.25m	
	1998	0.25x0.25m	
	1999	0.25x0.25m	

(b) Aerial photographs: It is often possible to obtain aerial photographs taken for the same area 5, 10, or even 50 years earlier. We can get some evidence of past landslide movement at or near the study area from older aerial photographs. These photographs can provide valuable insight into conditions affecting slope stability in landslide area. For instance, landslide features, particular scarps and fissures, can be accentuated by low-angle illumination. Besides, whereas the value of photo-interpretation of aerial photographs for identifying slope instability has been reported by many investigators, we used aerial photographs which were taken at a scale of 1:5000 of the same selected area in 1966, 1998, and 1999 to extract landslide information (Table.2). Then, we used the stereoscope and these aerial photographs to depict in the stereo model the typical morphologic features of landslides, which often can provide diagnostic information concerning the type of movement.

(c) Landslide interpretation from aerial photographs: Landslide information extracted from aerial photographs is mainly related to the morphology, vegetation, and drainage of the slope. We use the stereoscopic model to study the slope morphology. Additionally, the study of variations in tone and texture or of pattern, shape, and lineament has to be related the expected ground conditions or landforms associated with slope instability process. The degree of landslide activity, as classified by aerial photointerpretation, is determined in this region by the freshness of the features related to the landslide. Nevertheless, the landform of older landslides, showing an erosion of their morphologic forms and usually overgrown by vegetation, is classified stable. The example of photographic characteristic of rock falls, Shallow slide, rotational slide…etc in Hungtsaiping area are listed in the Table.3 According to the type of movement, age (recent, old, very old) and activity and the depth of sliding, we make a geomorphological inventory map of Hungtsaiping area. (Figure.6 & Figure.7)

Table.2. The aerial photographs of Hungtsaiping landslide under different time interval.

Image classification	Date	Pixel Size	Scale	Event
Aerial photograph	1966	0.25x0.25m	1:5000	N/A
	1998	0.25x0.25m		HERB typhoon
	1999	0.25x0.25m		Chi-Chi earthquake

(d) Classes of slope stability: According to the result of interpretation from aerial photographs and topography analysis, we try to categorize the type of stability of slopes and landslides. A stability classification for slope developed on the basis of ideas by Crozier (1984) is presented in Table.4 This classification is based on recurrence of movement, analogy to stable or unstable slopes.

B. Image Process

In this study, we overlap two gray orthographic Photo-base-maps of four groups at 1977-1984, 1984-1991, 1991-1998, and 1998-1999 with all the same area. From the overlapped image at 1998-1999 (Figure.8), we can see clearly that the roads and other objects dislocated from its original position to another and trend of the dislocation are towards N and NW. But these results probably impropriety, because if the detailed objects of image are unapparent, we find authentic direction and displacement are very difficulty. Thus, we must use image process to spectral enhancement of gray image for several methods. First, the original RGB image must convert to three 8 bit gray level images and choose the clearly image. Second, the gray level image must adjust shading and sharp value to improve definition of image. Third, we can apply supervised or unsupervised classification to identify every objects of ground for original RGB image. Finally, we will compare and choose best procedure of image process base on correlation or difference between actual displacement and PIV results. According to results of comparing, we were chosen red-band transformed gray level image of image process to conducted PIV analysis in this study, because the correlated in this result was better than others and RMS was smaller than others of image process. So, the objects of image will become clear to obtain correct displacement at different time with all the same area. (Table.5)

C. Particle Image Velocimetry method

Particle Image Velocimetry(PIV) is a technique which enables instantaneous measurement of the flow velocity at several positions in a plane. The aim of the cross-correlation is the method for PIV to find the distance that the particle pattern has moved during the inter image time and translate this into a velocity measure. The cross-correlation function is not calculated on the whole images but on smaller parts of these called interrogations (I_p). The cross-correlation from one I_p results in one velocity vector. The cross-correlation can be seen as finding which relative displacement of the I_{ps} that gives the best pattern match. This displacement should be proportional to the average velocity in the I_{ps}. The direct procedure to compute an unbiased one dimensional sample cross-correlation function $C(\triangle x,\triangle y)$, for the m×n point samples I_{1p}(m,n) and I_{2p}(m,n), with $\triangle x$<m and $\triangle y$<n is defined by：

$$C(\Delta x,\Delta y)=\sum_{i=1}^{m}\sum_{i=1}^{n} I_{1p}(i,j)\, I_{2p}(i+\Delta x, j+\Delta y)$$

I_p：Interrogation (m×n pixels) ； $C(\triangle x,\triangle y)$：Correlation

$$C_n(\Delta x,\Delta y)=\frac{\sum_{i=1}^{m}\sum_{i=1}^{n} I_{1p}(i,j)\, I_{2p}(i,j)}{\left[\sum_{i=1}^{m}\sum_{i=1}^{n} I_{1p}^{2}(i,j)\right]^{\frac{1}{2}}\left[\sum_{i=1}^{m}\sum_{i=1}^{n} I_{2p}^{2}(i,j)\right]^{\frac{1}{2}}}$$

$C_n(\triangle x,\triangle y)$：Normalize Correlation ； $C_n \leq 1$

In this paper, we used the cross-correlation of PIV method to evaluate the displacement of picture objects including road, house, tree, and each has its own peak of gray levels of each pixel by PIVview2C program. By means of bilinear interpolation, we can find those peaks which are within the sub-pixels and then cross-correlate them to evaluate how they move or displace. Of course, we also have the deviation of cross-correlation, which is RMS error greater than 0.25m.

Besides, we could differentiate landslide zonation base on amount of displacement and direction of vectors by PIV analysis. Finally, we will sum up the results by different time displacement of PIV analysis with all the same slide zone to differentiate probability of sliding in Hungtsaiping area.

RESULTS

The results of landform interpretation and topographic analysis show that:

(1) We found that there are no large scale and obvious failure in this area according to the landform interpretation before and after Chi-Chi earthquake. However, there are several small scale and shallow rotational slide which existed before this earthquake in this area.

(2) According to the activity, morphology, vegetation and drainage of the failure zone in this area, we differentiate three main sliding areas in Hungtsaiping (Figure.6). First of all, there are four old sliding which are rotational sliding and two sliding triggered by Chi-Chi earthquake at head of the zone A. We determined the classification of zone A class Ⅰ$_b$ according Table.4, because this zone is a reactivated landslide; material is currently moving and represent renewed landslide activity; some landslide feature are fresh and well defined; others may appear older.

(3) The next, there are old rock fall slope about 500 meters and a fresh shallow rotational slide triggered by this earthquake located at south of the zone B. We determined the classification of zone B class Ⅰ$_b$ according Table.4, because the same reasons of zone A.

(4) The third one is located at east of the Hungtsaiping area, and there is only one very old sliding near the Younglu creek. Nevertheless, this C zone between two gullies which have the same fountainhead looks like an old sliding body. We determined the classification of zone C class □$_a$ according Table.4, because this features in this zone pointed that is a dormant-historic landslides; slopes with evidence of previous landslide activity that have undergone most recent movement during most recent movement within the preceding 100 years(approximately historic time).

The results of PIV analysis show that:

(1) At 1977~1991, the boundaries of the slide and arrows pointing toward the direction of movement has already existed (Figure.9).

(2) After Chi-Chi earthquake, the slide area, azimuth, and magnitudes of sliding are more than 1977~1998 (Table.6and Figure.10).

(3) According to the result of the output image at 1998-1999 by PIV (Figure.11), we can differentiate three different slides zones (A1, A2, and B) in Hungtsaiping area and the maximum amount of the displacement presented by red color vectors is about 28m.

(4) In this results of differentiate slides, we found that the displacement of zone A1, zone A2 and zone B at four different times was larger than other area, especially

Chi-Chi events (Table.7and Figure.11), and then we found that the activity and the result by identifying topography of the zone A and zone B are identical to the zone A1, zone A2 and zone B.

(5) In addition, according to the result of displacement analysis, there was a large scale sliding which triggered by Chi-Chi earthquake opposite to Hungtsaiping area (Figure.12). The fact possible influence the energy accumulated both sides of the Younglu creek, and then it will lead to a catastrophic avalanche like Chiufengershan landslide and Tsaoling rockslide.

DISCUSSION

(1) In this study, we also have field investigation including outcrop and cores of 8 bore holes. We find that the average thickness of colluvium is about 60m to 90m and the depth of boundary between colluvium and shale is about 82m. Nevertheless, these bore holes located near the eastern boundary, so the depth and thickness of the colluvium in Hungtsaiping may be more deeply. Therefore, the irregular horizontal displacement by PIV and the shallow landslide by field investigating and aerial photos in this area may be closely-related to the colluvium.

(2) In order to obtain quantitative and correct results from our deformation of landslide area, we observed the displacement field of two images by a commercial PIVview2C program. Nevertheless, the measurement errors in PIV analysis include human error, instrument error, evaluation error, and others etc. So, we must to assess the measurement uncertainty and systematic errors in PIV evaluation by variety of way. First, we use actual PIV recordings for which the displacement data is known reliably. Then, compare result of PIV with reliably displacement of object space, and we will know which is uncertainty. Besides, according the cross-correlation equation, which is demonstrates the strong dependence of image pixel permutation on displacement field, because the magnitude of correlation was determined from the image pixel permutation. From these results by PIV analysis (Table.6), it appears that the longer the times caused lower the magnitude of correlation (Cn). So, this result demonstrates that variations in objects of ground cause the decrease in magnitude of correlation.

(3) We used both PIV and identifying terrain features by aerial photos, because the PIV only can calculate the horizontal displacement of the object in gray aerial photos. Thus, we have to combine PIV with identifying terrain features by aerial photos in order to infer the type and the pattern of landslide.

CONCLUSIONS

In this study, we attempted to find a way about landslide zone identifying and analysis of the activity in Hungtsaiping, for talking about the transition in terrain features and inferring the history of landslide. It will be an example about boring in the field, site of monitoring and the engineering structures constructed for other case. Finally, combining some conclusions of this study with field investigation and boring core are summarized as follow： the zone A triggered by Chi-Chi earthquake belongs to a reactive old collvium existing a high risk of sliding again. Besides, the view of watershed area, landslide area continue enlarge may result in a great number of casualties in Neicheng.(Figure.13) The monitoring data shows that the evidence of the displacement and the change of terrain features triggered by typhoons and heavy rainfall in Hungtsaiping area already existed. The future work of this study will be continue ground and underground monitoring in landslide area, and further, we want to find the influence of the hydrogeological characteristics.

ACKNOWLEDGMENTS

The author wishes to express his appreciation to Central Geological Survey for financial support (project No: 5226902000-01-94-02) that make this work possible. Then, we want to thank Dr. Kuo-Liang Pan providing us suggestion about this research.

REFERENCES

[1] Chang, K.J., Alfredo, Taboada, Chan, Y.C., "Geological and morphological study of the Jiufengershan landslide triggered by the Chi-Chi Taiwan earthquake," Geomorphology 01685, 2005, pp. 17-30.

[2] Coupland, J. M., Halliwell, N. A., "Particle image velocimetry: rapid transparency analysis using optical correlation," 1988, Appl. Opt. 27, 1919–1921.

[3] Crozier, M.J., "Field Assessment of Slope Instability," In Slope Instability (D. Brunsen and D.B. Prior, eds.), John Wiley & Sons, New York, 1984,pp.103-142.

[4] Lee, J.F., Wei, C.Y., Huang, C.C., "The Study of Hungtsaiping Landslide Using Digital Aerial Photogrametric Technique," Proceedings International Symposium on Landslide and Debris Flow Hazard Assessment, 2004, pp. 5-1.

[5] Lee, K.C, Lo, C.M., Lin, M.L., "Topographic Change and Landslide in Hungtsaiping," Proceedings of The Eighteenth KKCNN Symposium on Civil Engineering, 2005, pp. 491-500.

[6] Raffel, M., Willert, C., kompenhans, J., "Particle Image Velocimetry - a practical guide," Springer Verlag, 1998, pp. 105–127.

[7] Wang, W.N., Masahiro, Chigira, Takahiko, Furuya, "Geological and geomorphological precursors of the Chiu-fen-erh-shan landslide triggered by the Chi-chi earthquake in central Taiwan," Engineering Geology 69, 2003, pp. 1–13.

[8] White, D.J., Take, W.A., Bolton, M.D., "Soil deformation measurement using particle image Velocimetry (PIV) and photo-grammetry," Geo-technique 53, No.7, 2003, pp. 619-631.

[9] Tseng ,Chia-Han, Hu Jyr-Ching, Chan Yu-Chang, Lee Jin-Fa, Wei Jheng-Yue., "A Slow Slide in central Taiwan Induced by Chi-Chi Earthquake revealed by PIV Analysis," American Geophysical Union journal-T11D-1307, 2004, pp. 1-4.

Table.3. Image characteristics of mass movement types (modified from Van Westen 1993)

Type	Characterization Based on morphological, vegetational, and drainage aspects visible on stereo images		Stereo image
Rock falls	Morphology	The slope mostly are steeper than 45 degrees, where the bedrock is directly exposed .Distinct rock wall or free face in association with scree slopes (20 to 30 degrees) and dejection cones.	Figure.3
	Vegetation	Linear scars in vegetation along frequent rock-fall paths; vegetation density low on active scree slopes.	
	Drainage	No specific characteristic	
Shallow slide	Morphology	Smooth planar slip surface; relatively shallow, certainly in surface material over bedrock; D/L ratio<0.1.	Figure.4
	Vegetation	Source area and transport-ational path denuded, often with lineations in tran-sportation direction.	
	Drainage	Disordered or absent surface drainage; stream deflected or blocked by frontal lobe.	
Rotational slide	Morphology	Abrupt changes in slope morphology characterized by concave and convex forms; semilunar crown and lobate frontal part; back-tilting slope facets, scarps, hummocky morphology on depositional part; D/L ratio 0.3 to 0.1; slope 20 to 40 degree.	Figure.5
	Vegetation	Clear vegetation contrast with surroundings.	
	Drainage	Contrast with nonfailed slopes, bad surface drainage or ponding in niches or back-tilting areas; seepage in frontal part of runout lobe.	

Table.4. Stability classification of slopes (modified from Crozier 1984)

CLASS	DESCRIPTION
Ⅰ Unstable Slopes	
Ⅰa	Active landslides; material is currently moving, and landslide features are fresh and well defined
Ⅰb	Reactivated landslide; material is currently moving and represents renewed landslide activity; some landslide features are fresh and well defined; others may appear older.
Ⅰc	Suspended landslides; slopes with evidence of landslide activity within the past year; landslide features are fresh and well defined.
Ⅱ Slopes With Inactive Landslides	
Ⅱa	Dormant-historic landslides; slopes with evidence of previous landslide activity that have undergone most recent movement within the preceding 100 years (approximately historic time)

Table.5. The different type of Gray Image Process that were compared correlation and RMS by PIV analysis.

Gray Image Process Type	Correlation (average)	RMS (average)
RGB Transform Gray image	0.72	1.17m
Blue-Band Transform Gray image	0.67	1.63 m
Green -Band Transform Gray image	0.76	0.74m
Red-Band Transform Gray image	*0.83	*0.32m
supervised Classification	0.82	0.47m
Unsupervised Classification	0.77	0.93m

Table.6. The results of landslide zonation with different years by PIV analysis that were appears that the longer the times caused lower the magnitude of correlation (Cn).

Years	Landslide Zonation	Landslide Area (km^2)	Displacement (m)	Cn (avg)
1977-1984	Zone A1	0.57	1.41	0.62
	Zone A2	0.28	2.22	0.57
	Zone B	0.08	1.13	0.54
1984-1991	Zone A1	0.64	1.37	0.65
	Zone A2	0.20	0.94	0.51
	Zone B	0.08	0.84	0.60
1991-1998	Zone A1	0.73	1.97	0.48
	Zone A2	0.20	0.75	0.51
	Zone B	0.14	1.82	0.56
1998-1999	Zone A1	0.81	9.08	0.74
	Zone A2	0.29	7.06	0.81
	Zone B	0.29	14.59	0.85

Table.7. The results of accumulating of displacement and landslide zonation in different times by PIV analysis.

Landslide Zonation	Accumulating of Displacement (m)			
	1977-1984	1984-1991	1991-1998	1998-1999
Zone A1	1.41	2.78	4.75	13.83
Zone A2	2.22	3.16	3.91	10.97
Zone B	1.13	1.97	3.79	18.38
Others	0.25	0.44	0.51	2.24

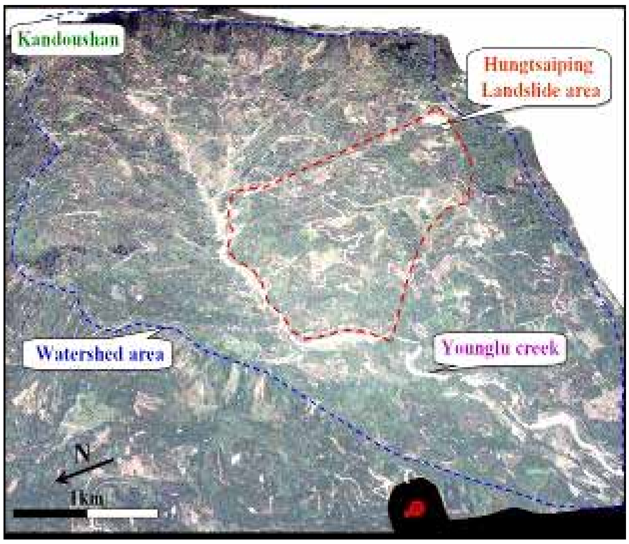

Figure.1. The 3D Aerial photograph of the Hungtsaiping area. The Huangtsaiping landslide is located in the valley of a small stream called Younglu creek.

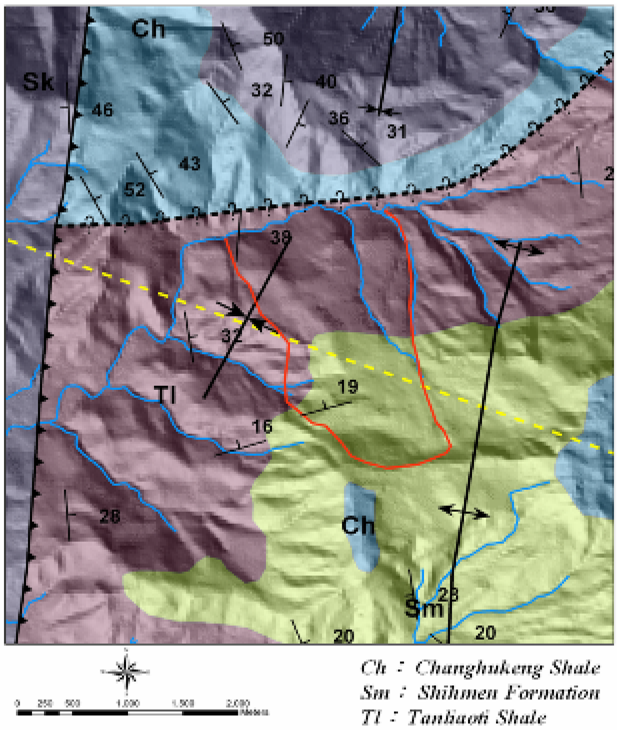

Figure.2. Geological map of the Hungtsaiping area.

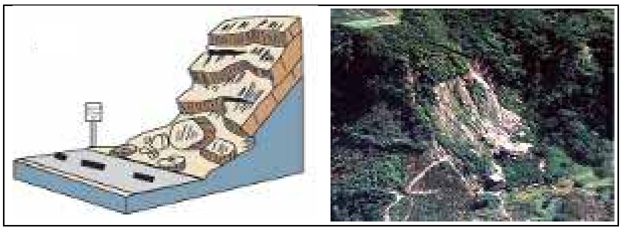
Figure.3. The left side sketch map is according to Varnes 1978, means the features of rock falls. The right side is the aerial photographs taken from Hungtsaiping.

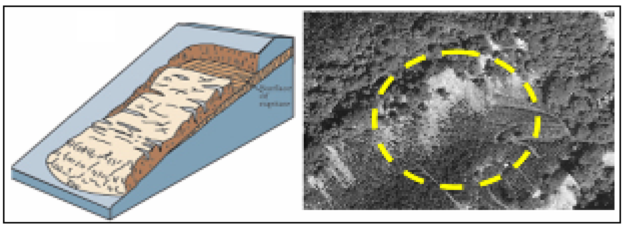
Figure.4. The left side sketch map is according to Lin 1988, means the features of shallow slide. The right side is the aerial photographs taken from Hungtsaiping.

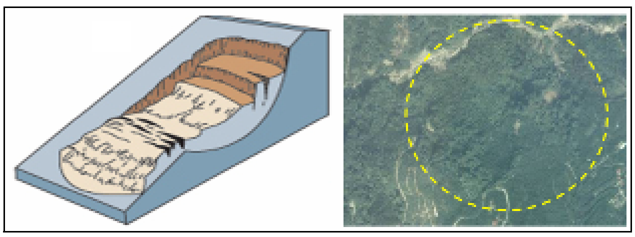
Figure.5. The left side sketch map is according to Varnes 1978, means the features of rotational slide. The right side is the aerial photographs taken from Hungtsaiping.

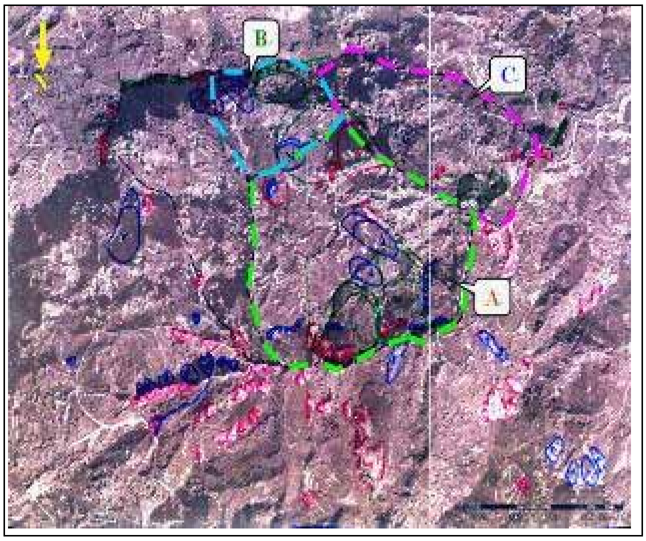

Figure.6. We determined the classification of zone A class I$_b$, zone B class I$_b$ and zone C class □$_a$.

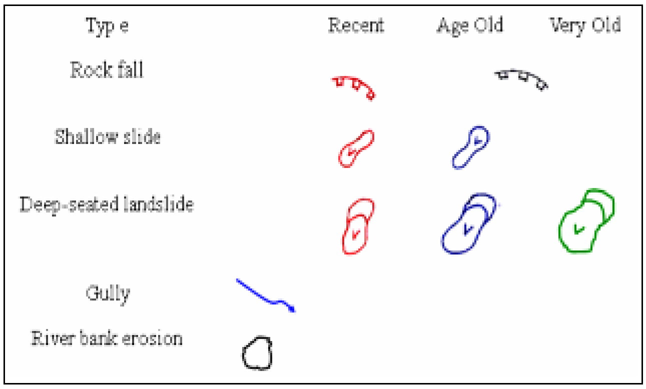

Figure.7. “Age old” means before Chi-Chi earthquake and “Very old” means never happened for a long time.

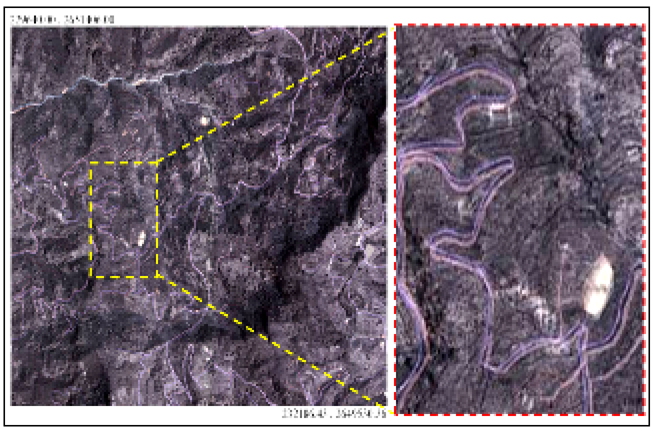
Figure.8. Overlapping of two Photo-base-maps at 1998~1999 of the Hungtsaiping area. From this picture we can see clearly that the roads and other objects dislocated from its original position to another and trend of the dislocation is towards N and NW. The scale is 1:5000, and the precision is 0.25m/pixel.

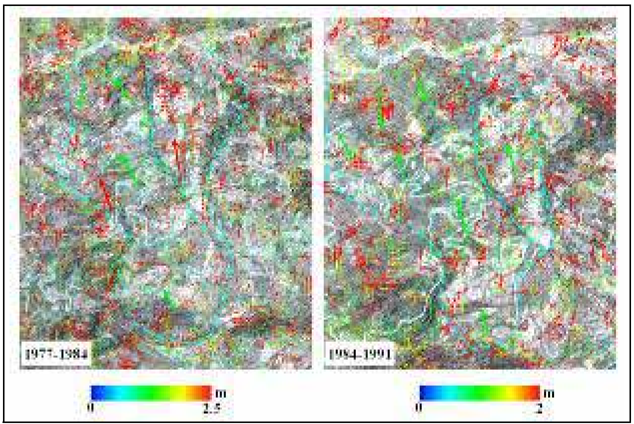

Figure.9. At 1977~1991, the boundaries of the slide and arrows pointing toward the direction of movement has already existed.

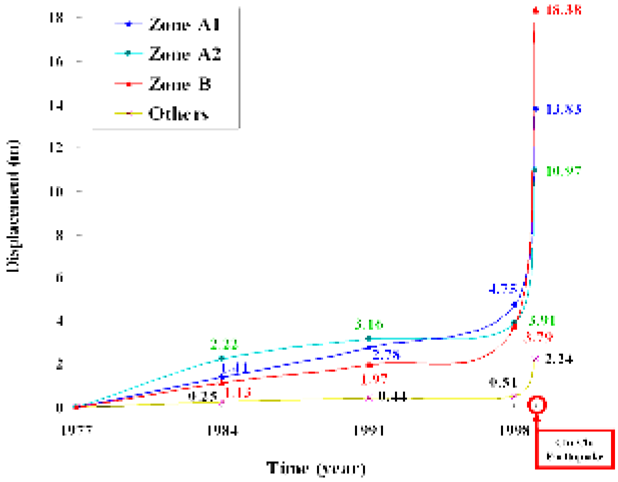

Figure.11. The results of landslide zonation and accumulating of displacement with different times by PIV analysis.

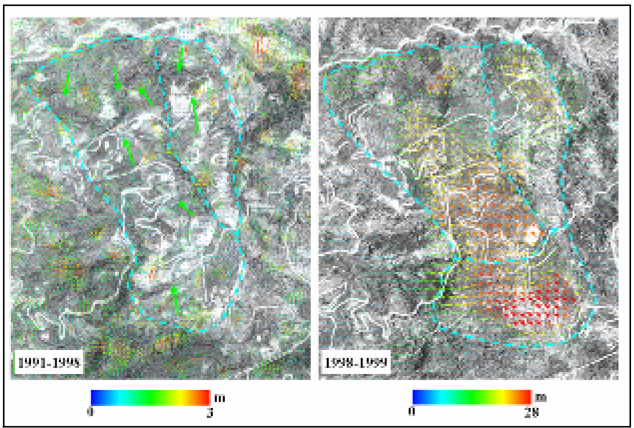

Figure.10. After Chi-Chi earthquake, the slide area, azimuth, and magnitudes of sliding are more than 1977~1998.

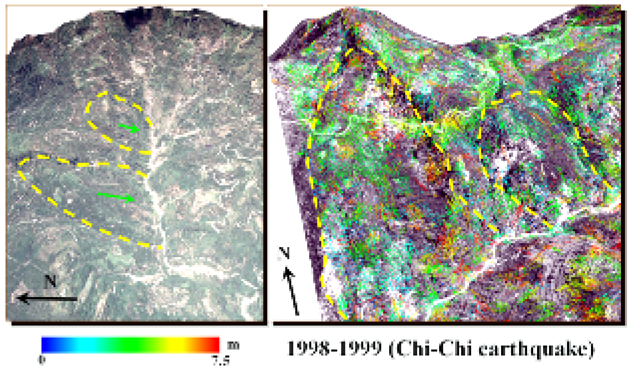

Figure.12. From the results at 1998-1999 by PIV, there was a large scale sliding which triggered by Chi-Chi earthquake opposite to Hungtsaiping area.

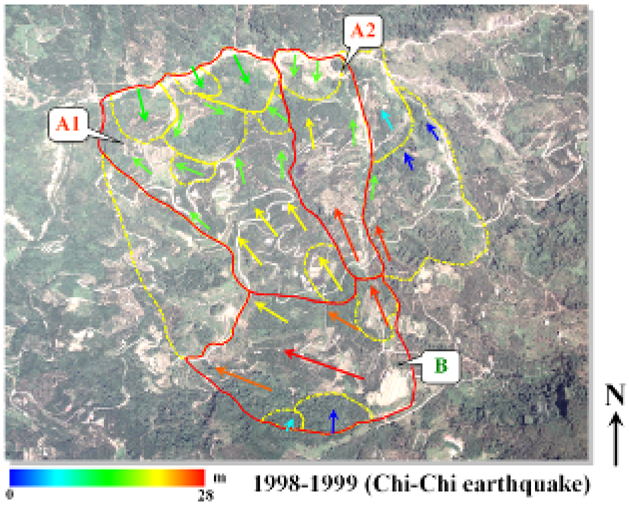

Figure.11. From the results at 1998-1999 by PIV, we can differentiate three slides for Hungtsaiping landslide and the maximum amount of the displacement presented by red color vectors is about 28m.

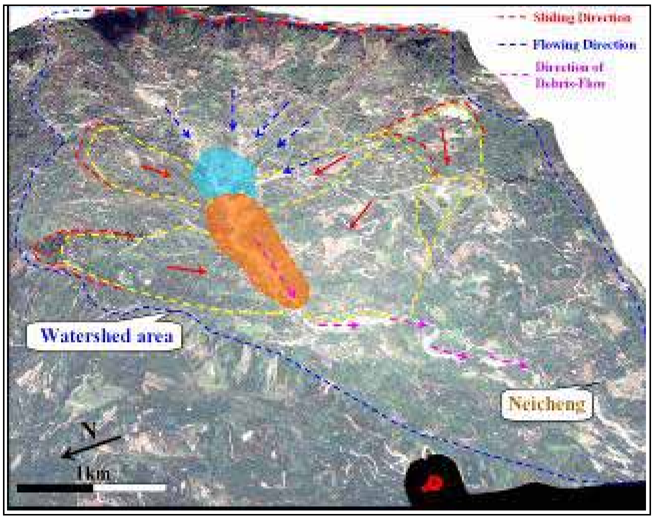

Figure.13. The view of watershed area, landslide area continue enlarge may result in a great number of casualties in Neicheng.

Characteristics of Damage of Road Embankment in the 2004 Mid Niigata Prefecture Earthquake

K. Tokida[1], Y. Egawa[1], A. Nakahira[2] and Y. Okajima[2]
[1]*Department of Civil Engineering, Osaka University, Osaka, Japan*
[2] *CTI Engineering Co., Ltd., Japan*

Abstract

The 2004 Mid Niigata Prefecture Earthquake was an inland epicentral earthquake characterized by damage focused in local and mountainous areas. The damage to road infrastructures is also marked by the characteristics of the local area. In order to prevent or reduce earthquake damage in the future, it is important to clarify the characteristics of the damage level and the road traffic performance in the local and mountainous area, and reflect them in future earthquake prevention measures. This study focuses on the level of damage to road embankments and the effects by road closures and road damage, and analyzes these factors based on data collected from related documents and in field investigations. The study also quantitatively estimates relationship between the seismic intensity and embankment type of damage. As the results, new knowledge on future earthquake prevention measures has been obtained.

Keywords, *The Mid Niigata Prefecture Earthquake of 2004, earthquake damage, road embankment, road traffic performance, factor analysis*

INTRODUCTION

Because not a few road embankments were damaged in the Mid Niigata Prefecture Earthquake of 2004, many road networks were blocked for some days. In this earthquake, the importance of road traffic performance against earthquakes relating to road embankments was emerged. Actually road-blocked points of trunk roads after this earthquake relating to road embankments were about 62% although relating to bridge damage were 6.5%. Through the earthquake, we have realized the importance of seismic reinforcement to reduce the earthquake induced damage of road embankment. For the effective and economical countermeasures to prevent and reduce the earthquake-induced damage, it is very important to discuss the relation between the damage level of structures and performance required structures [1), 2)].

In this paper, damage characteristic of road embankments, damage factors such as embankment structure, topographic features and the restoration process of road traffic performance are discussed based on detailed data of the earthquake damage and its restoration for national highways. As a result, the classification method of road embankment damage, the relationship between the seismic intensity and damage level of road embankment and so on are clarified.

LEVEL OF DAMAGE TO ROAD INFRASTRUCTURE

Types of Damage to Road Infrastructure

Seventy-seven road-blocked points were investigated; these were managed by the Ministry of Land, Infrastructure and Transport or Niigata prefecture, and the information about the road-blocked points was made available to the public via a website. Fig.1 shows the number of road-blocked points and ratio depending on the types of damage. The epicenter of the earthquake was in a local mountainous region, and therefore most of the damage types related to road-blocked points were settlement or bumps, which accounted for about 50% of the road-blocked points.

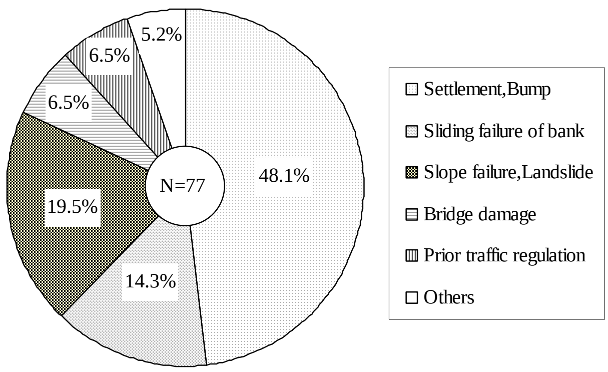

Fig.1: The number of road-blocked points and ratio, classified by type of damage

The next most frequently occurring types of damage were slope failure or mudslide and embankment failure. The number of road-blocked points caused by settlement or bumps or embankment failures accounted for 60% or more of the total. On the other hand, the number of road-blocked points caused by bridge damage accounted for only about 7% of the total. This difference can be explained by the advances made in seismic measures for bridges and the small number of bridges located in the regions where strong ground motion occurred.

Road-blocked point ratio and seismic intensity

Fig.2 shows the estimated relationship between a road-blocked point ratio and seismic intensity scale for each damage type. This shows the relative values of all road-blocked points on directly governed or prefecture managed national roads.

Regarding types of damage, the road-blocked point ratio caused by settlement or bumps is relatively light damaged, for areas with a seismic intensity of 6 Lower. The road-blocked point ratio caused by embankment failure or slope failure or landslide is relatively serious damaged, increase in areas with a seismic intensity of 6 Upper. On the other hand, the road-blocked point ratios due to bridge failure tend to occur in areas with a seismic intensity of 6 Lower or 6 Upper, but the ratios are small.

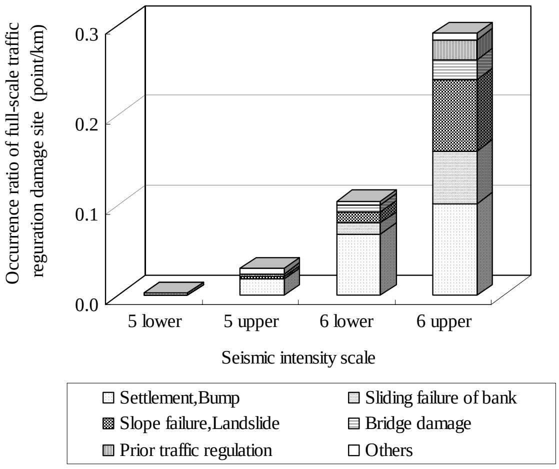

Fig.2 Relationship between road-blocked point ratio and types of damage

Restoration characteristics of roads that were blocked

a) Restoration characteristics for each type of damage

The time required from blocking to reopening blocked national and prefectural roads is summarized and classified by damage form. The change in the ratio of the number of roads reopened to that of roads blocked with the time elapsed is shown in Fig.3.

This figure shows that the blocked roads were reopened relatively soon and the number of points blocked caused by settlement or bumps was high. On the other hand, this figure also shows that it took time to reopen the roads that were blocked due to embankment failure, or slope failure or mudslide, and about 40% of the blocked roads had not been reopened even after 60 days had passed. The damage at many of the points was attributed to the slope failure or mudslide category, which, of all the types of damage found on the national and prefectural roads, was thought to be the most serious type of damage impacting road performance. The points where the roads were blocked due to bridge failure were few and were reopened soon, showing that the impact of bridge failure on road performance in this earthquake was minor.

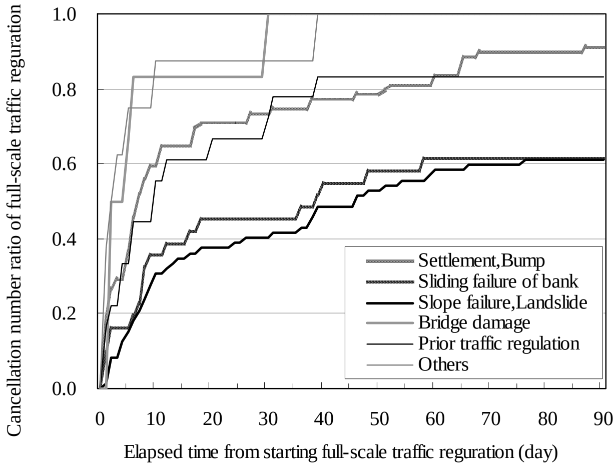

Fig.3 Cancellation number ratio of full-scale traffic regulation with time elapsed

b) Restoration characteristics for each type of road

For road-blocked points on directly governed national roads, prefecture managed national roads, main local roads, and general prefectural roads, the number of days required from blocking to reopening the roads has been summarized.

Fig.4 shows the reopening ratio with time elapsed. This figure shows that the road-blocked points on directly governed national roads, which were few in number, were reopened quickest, indicating that early-stage restoration was implemented. It took longer to reopen the prefectural roads than the national roads, but it is no surprise that emergency restoration was conducted first on roads with higher priority.

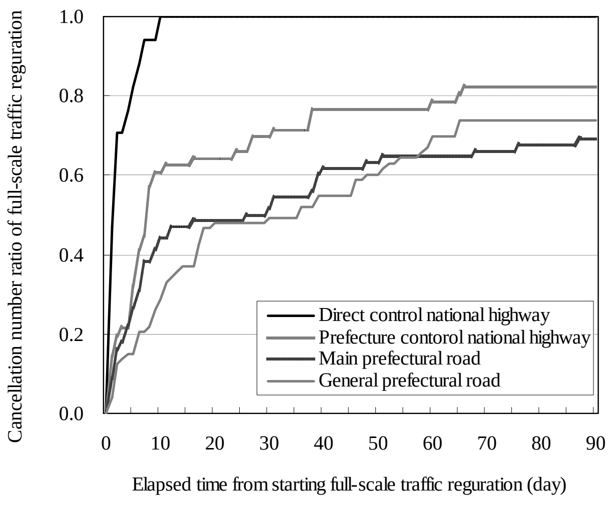

Fig.4 Change in ratio of reopening road-blocked points with time elapsed by road type

Damage Analysis of Embankment Failure

The Damage Data

The damage data used in this study were 42 points occurred at direct governed national highways: R8, R17 and R118. And the data were collected by Nagaoka National Highway Office, Hokuriku Regional Development Bureau of the Ministry of Land. These data are shown in Table 0.

For seismic intensity of damage sites, we use the seismic intensity scale of Japan Meteorological Agency and focused on 5 Upper, 6 Lower and 6 Upper.

Forms of damage to road embankments

We classified the damage of embankment by the method which has proposed by Tokida et al.[3)]

According to the field investigation, the various states of the damage to the road embankments are first classified into damage forms in either the transverse or longitudinal direction. Damage in the transverse direction is further classified into that on flat or sloping ground. Damage on sloping ground is further classified into two types of embankment structures: single or double side slope.

The f damage forms have been classified according to these types. In short, damage to embankments on TRF (TRansverse direction of Flat ground) is classified as shown in Fig.5(1). Damage forms to embankments on TRSD (TRansverse direction of Sloped ground with Double side slope embankment) and TRSS (TRansverse direction of Sloped ground with Single side slope embankment) are classified as shown in Fig.5(2) and (3), respectively. Damage forms are not limited to a single pattern and various patterns may be combined. The single-cut and single side-slope embankment is regarded here as the single side-slope embankment mentioned above. Furthermore, the forms of damage to road

Table 0: The damage data of direct governed national highways

(1) Damage index acoording to route number of direct contorol national highway

Route	Mnagement Length A (km)	Dmage site B (point)	Dmage site B/A (point/km)	Full-scale traffic reguration site C (point)	Full-scale traffic reguration site C/A (point/km)	Full-scale traffic reguration section D (section)	Full-scale traffic reguration section D/A (section/km)	Total damage length E (km)	Total damage length E/A (%)	Full-scale traffic reguration length F (km)	Full-scale traffic reguration length F/A (%)
R 8	35.0	10	0.286	8	0.229	7	0.200	8.475	24.2%	5.096	14.6%
R 17	102.5	30	0.293	24	0.234	9	0.088	24.925	24.3%	20.401	19.9%
R 117	34.8	2	0.057	2	0.057	1	0.029	0.038	0.1%	0.038	0.1%
Total	172.3	42	0.244	34	0.197	17	0.099	33.438	19.4%	25.535	14.8%

(2) Damage index acoording to scale of seismic intensity of direct contorol national highway

Scale of seismic intensity	Mnagement Length A (km)	Dmage site B (point)	Dmage site B/A (point/km)	Full-scale traffic reguration site C (point)	Full-scale traffic reguration site C/A (point/km)	Full-scale traffic reguration section D (section)	Full-scale traffic reguration section D/A (section/km)	Total damage length E (km)	Total damage length E/A (%)	Full-scale traffic reguration length F (km)	Full-scale traffic reguration length F/A (%)
5 lower	26.3	0	0.000	0	0.000	0	0.000	0	0.0%	0.000	0.0%
5 upper	92.0	5	0.054	4	0.043	4	0.043	5	5.4%	3.450	3.8%
6 lower	31.0	16	0.516	10	0.323	5	0.161	11.721	37.8%	5.888	19.0%
6 upper	23.0	21	0.913	20	0.870	8	0.348	16.717	72.7%	16.197	70.4%
Total	172.3	42	0.244	34	0.197	17	0.099	33.438	19.4%	25.535	14.8%

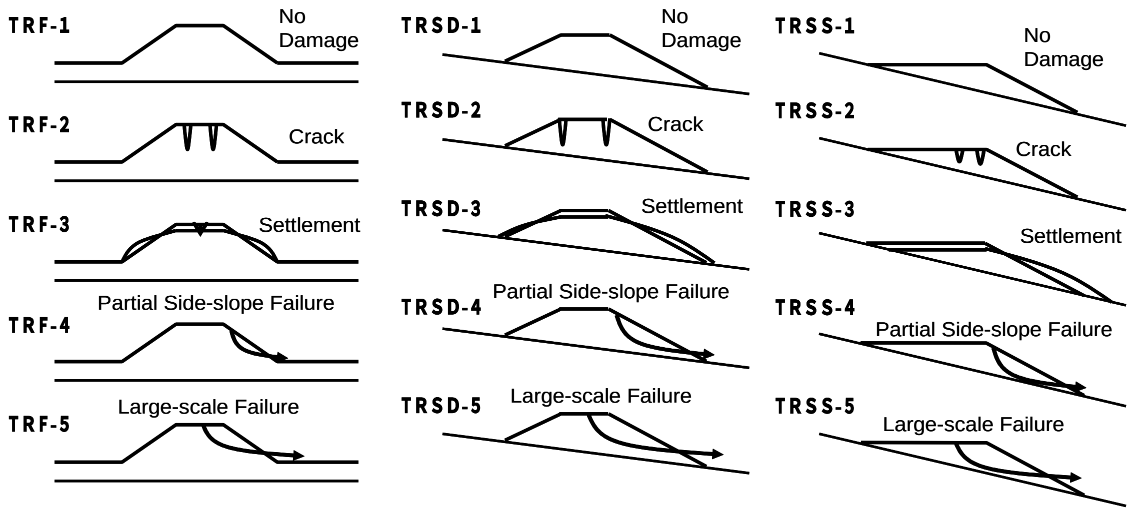

(1) Flat ground **(2)** Double side-slope embankment on sloping ground **(3)** Single side-slope embankment on sloping ground

Fig.5 Classification of damage to road embankment in the transverse direction embankments in the longitudinal direction are classified as shown in Fig.6, based on the relation to the ground formation or other structures such as bridges and transverse structures.

Table 1 shows the classification of road embankment damage types in transverse and longitudinal directions, in

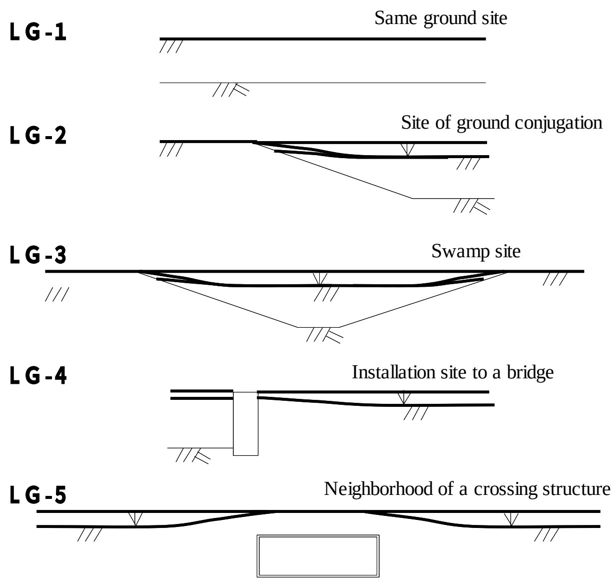

Fig.6 Classification of damage to road embankment in the longitudinal direction

Table 1 Classification of types of damage to road embankments

(1) Both sides bank on flat ground

Longitudinal / Transeverse	TRF1	TRF2	TRF3	TRF4	TRF5	Total
LG1		(4)	**3** (4)		**1** (1)	**4** (9)
LG2						
LG3						
LG4		(2)	**2** (3)	**1** (1)		**3** (6)
LG5		(1)	**5** (5)			**5** (6)
Total		(7)	**10** (12)	**1** (1)	**1** (1)	**12** (21)

(2) Both sides bank on sloping ground

Longitudinal / Transeverse	TRSD1	TRSD2	TRSD3	TRSD4	TRSD5	Total
LG1						
LG2						
LG3						
LG4		(1)	(1)	**1** (1)		**1** (3)
LG5						
Total		(1)	(1)	**1** (1)		**1** (3)

(3) One side bank on sloping ground

Longitudinal / Transeverse	TRSS1	TRSS2	TRSS3	TRSS4	TRSS5	Total
LG1		(2)	**1** (2)		**3** (3)	**4** (7)
LG2						
LG3		(1)	(1)		**1** (1)	**1** (3)
LG4		(2)	**1** (2)	(1)	**1** (1)	**2** (6)
LG5		(1)	(1)	(1)	**1** (1)	**1** (4)
Total		(6)	**2** (6)	(2)	**6** (6)	**8** (20)

*1) As for the number of a boldface type, only a greatest damage pattern of each 21 sites in damage section is counted.

*2) As for the number in ( ), all damage patterns occurring in damage sites are counted.

which damage was observed at national highway: R8, R17 and R118. Although there were 42 points of embankments damages at these direct governed national highways, we classified 21 damages because it was hard to clarify the damage form that any damage data was not existed.

In longitudinal direction, there are 9 damage points in LG-1, LG-2 and LG-3(general part of embankment), 6 damage points in LG-4(bridge part of embankment), and 6 damage points in LG-5(transverse structure part of embankment). All damages in LG-5 were related to box culvert.

LEVEL OF DAMAGE TO ROAD EMBANKMENT AND DAMAGE FACTOR

Relationship between seismic intensity and damage level

Fig.7 shows relationship between the seismic intensity scale and damage level of road embankment. In this figure, maximum amount of crack width, bump and settlement are plotted. The figure shows that crack width, bump and settlement tend to increase with seismic intensity. In any failure, the damage beyond 30cm in quantity reached to full-scale traffic regulation.

Relationship between seismic intensity scale and sliding type of failure

Fig.8 shows relationship between seismic intensity scale and sliding failure type. Sliding failure tend to increase with seismic intensity, and Large-scale sliding failure to both sides traffic lane and Large-scale sliding failure to one side traffic lane were mainly occurred in seismic intensity of 6 upper.

Fig.9 shows relationship between seismic intensity scale and elapsed time to cancellation of full-scale traffic regulation. The figure shows that the elapsed time to cancellation which is obtained Large-scale sliding failure to traffic lane has restored slower than other and the elapsed time to cancellation of full-scale traffic regulation tend to increase more with seismic intensity increase.

Relationship between embankment height and damage level of road embankment

Fig.10 shows relationship between embankment height and damage level.

In bump of bank top surface, the quantities of bump seem to increase with embankment height increase. As there is not strong relationship between the quantities of settlement and embankment height, so there is not strong relationship between the quantities of crack width and embankment height. In this figure, basically there is not strong relationship between damage level of road embankment and its height.

Fig.11 shows relationship between embankment height and damage form. This figure shows that if damage happen to the embankment whose height is more than 15m, the damage form is large–scale sliding failure to over one side traffic lane.

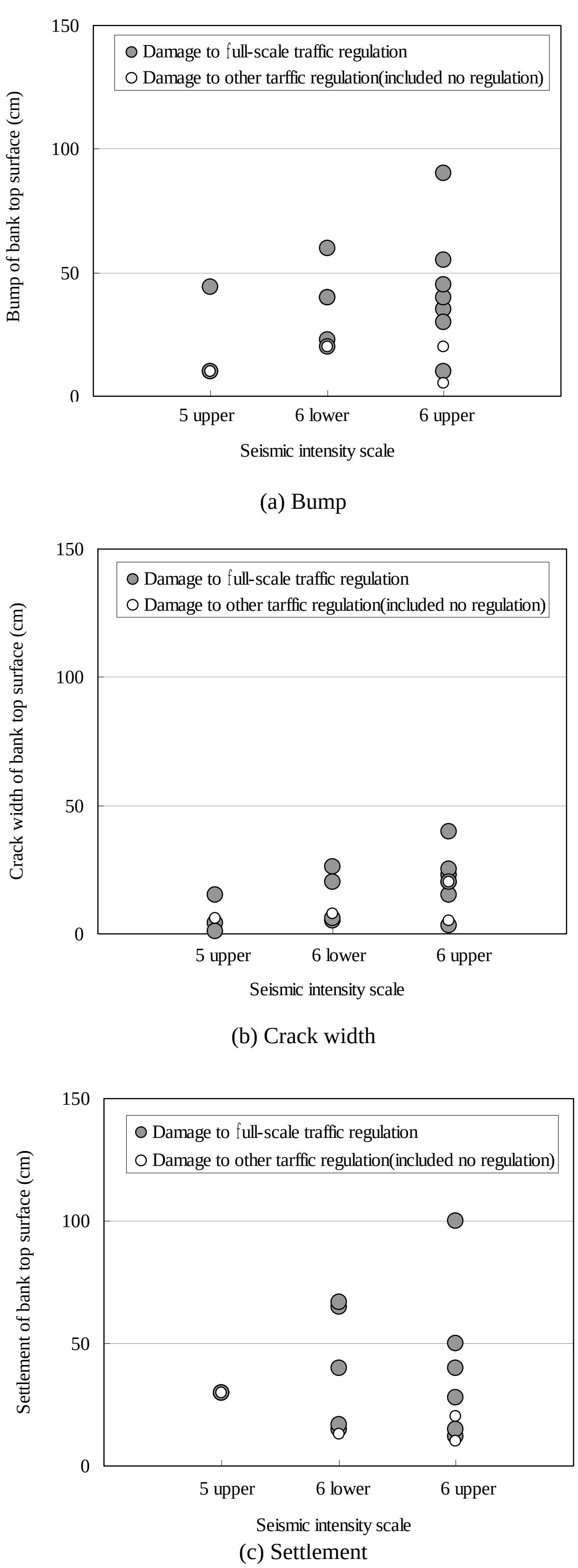

Fig.7 Relationship between the seismic intensity scale and damage level of road embankment

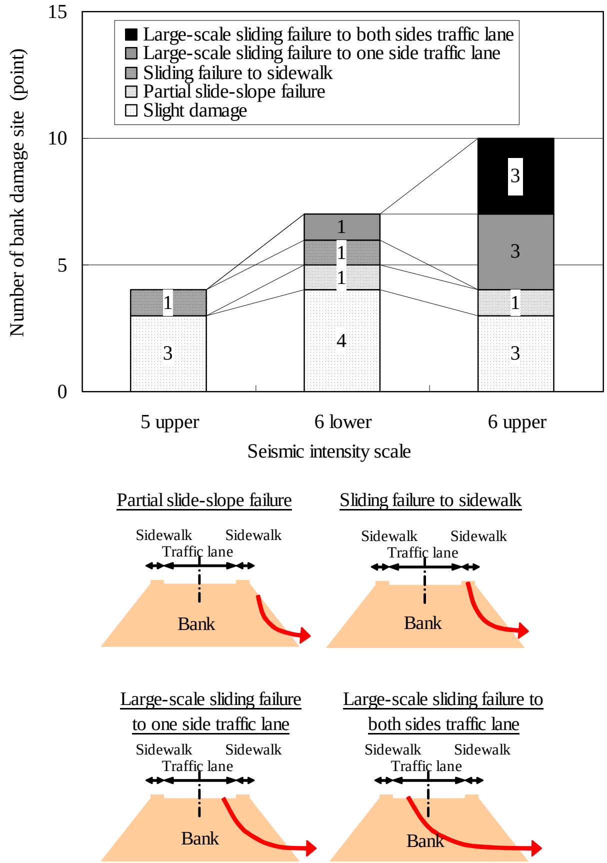

Fig.8 Relationship between seismic intensity scale and sliding type of failure

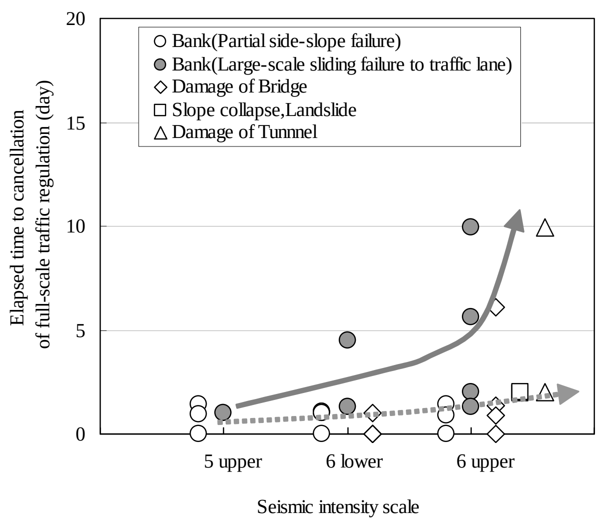

Fig.9 Relationship between seismic intensity scale and elapsed time to cancellation of full-scale traffic regulation

CONCLUSIONS

Main conclusions in this study are summarized as follows:

(1) Sixty percent or more of the damage leading to full-

scale traffic regulation was attributed to settlement or bumps or embankment failure. Less than 20% of damage was attributed to slope failure or mudslide, and less than 7% to bridge damage. Damaged embankments accounted for most of the devastation.

(2) Damage to road embankments was divided into damage in the transverse and longitudinal directions. Damage in the transverse direction was then divided into flat or sloped ground. Damage to sloping ground

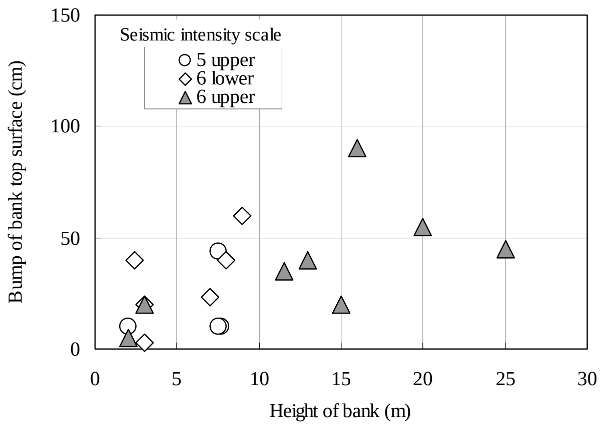

(a) Bump

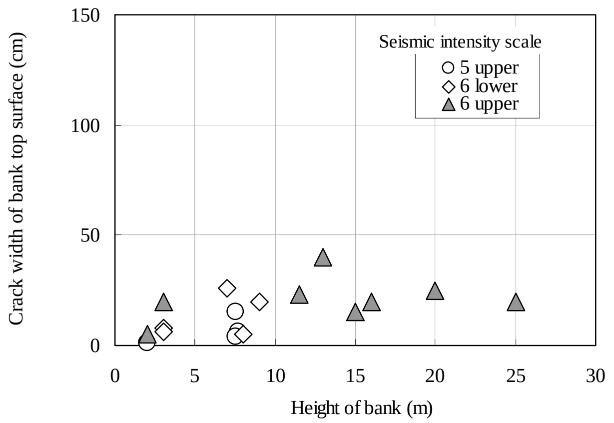

(b) Crack width

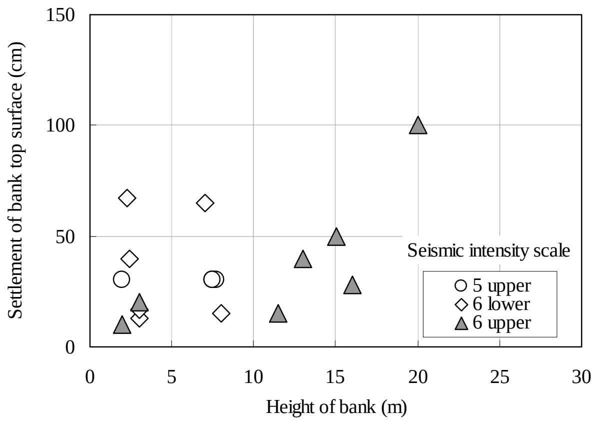

(c) Settlement

Fig.10 Relationship between embankment height and damage level

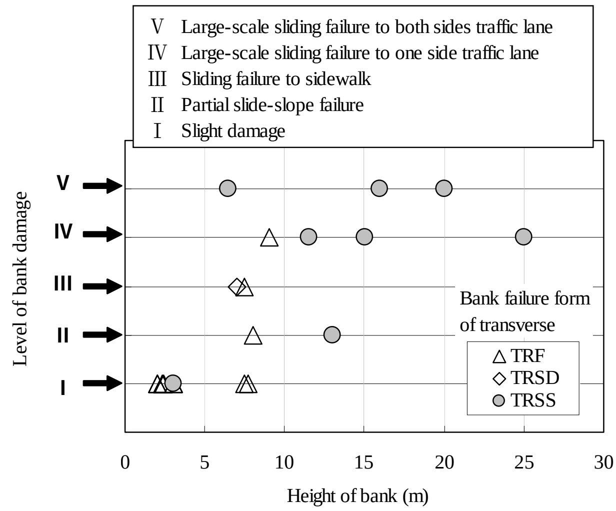

Fig.11 Relationship between embankment height and damage form

was further divided into single- or double-sided slopes. Damage forms are properly classified according to combinations of these types of damage.

(3) Large scale sliding failure occurred frequently to the damage form TRSS (TRansverse direction + Sloped ground + Single side-slope embankment).

(4) A relationship between seismic intensity and embankment damage level has been shown. Sliding failure tend to increase with seismic intensity, and large-scale sliding failure to both sides traffic lane and large-scale sliding failure to one side traffic lane were mainly occurred in seismic intensity of 6 upper. Relationship between embankment height and damage (crack, bump, settlement) is not strong.

(5) Once damage happen to the embankment whose height is more than 15m, the damage form is large-scale sliding failure.

REFERENCES

[1] Egawa, Y.,Tokida, K., Oda, K. and Nabeshima, Y.:Influence of Road Damage on Road performance in Mid Niigata Earthquake, Proc. of JSCE Kansai Branch Annual Meeting, May 2005 (in Japanese).

[2] Egawa, Y.,Tokida, K., Oda, K. and Nabeshima, Y.: Relationship between Seismic Intensity and Damage Characteristics of Highway during Mid Niigata Earthquake, Proc. of 60th JSCE Annual Meeting, September 2005 (in Japanese).

[3] Tokida, K., Oda, K. and Nabeshima, Y. and Egawa, Y.: Damage Level of Road Infrastructure and Road Traffic Performance in the Mid Niigata Prefecture Earthquake of 2004 .

Earthquake Induced Slope Failure
and Cyclic Shear Strength of Bedding Sandy Soil

A. Onoue[1], A. Wakai[2], K. Ugai[2], K. Higuchi[3], S. Kuroda[4]
[1]*Department of Civil Engineering, Nagaoka National College of Technology, Niigata, Japan*
[2]*Department of Civil Engineering, Gunma University, Gunma, Japan*
[3]*Kuroiwa Survey and Design Office, Gunma, Japan*
[4]*National Institute for Rural Engineering, Ibaraki, Japan*

Abstract
Numerous slope failures were caused by the 2004 Niigata-ken Chuetsu Earthquake. Characteristics of large scale natural slope failures that occurred at folding hills, river terraces, etc, were classified from a geometric structure view point. It was noted that surface failures occurred at steep cliffs and landslides occurred gently slanting dip slopes. The cause of a landslide in a dip slope structure was next examined through a series of cyclic shear tests and a stability analysis taking both horizontal and vertical seismic accelerations into consideration. This study reviled that the safety factor of the slope stability became momentarily smaller than 1.0 several times during the earthquake due to the small undrained shear strength of the tuff sand seam at the bedding plane. Furthermore, the landslide was simulated by an elasto-plastic dynamic finite element analysis where the shear strength decrease of the sand seam with increasing number of cycles was taken into consideration.

Keywords—*Slope failure, dip surface, bedding plane, shear strength, finite element analysis, earthquake*

INTRODUCTION

More than 40 thousands slope failures were induced by the 1848 Zenkoji earthquake （M7.4） [1] and over 10 thousand occurred following the 1891 Nobi earthquake （M8.0） [2], with numerous debris flows occurring just after the earthquakes [3]. Long faults with marked height difference and many lakes created by river blockade due to these earthquakes remain on site even to this day. Although 260 slope failures were noted on the Niigata-ken Chuetsu earthquake disaster map for a 20 km^2 basin of the Imo River at Old Yamakoshi village (Oct. 28, 2004, The Geological Survey Institute）, the actual number of failure sites including small landslides and slope failures of steep cliffs is considered to be at least several times this number with more than 500 failure sites occurring in the village. According to the emergency report (Nov. 11, 2004) announced by Ministry of Land, Infrastructure and Transportation, there were 1,665 landslides in natural slopes on the map including Old Yamakoshi village. It was, therefore, estimated that there occurred several thousand landslides occurred across the Chuetsu district. Since the numbers of landslide during the Zenkoji earthquake and the Nobi earthquake were greater than that occurring during the Niigata-ken Chuetsu earthquake, the damage caused by these earlier earthquakes is considered to be more severe. However, the total area ratio of landslides in the basin of the Imo River was, approximately 10.5%. This means an extremely high density in terms of the area ratio of landslide when compared with the significantly smaller area ratio which occurred during two earlier earthquakes [4]. Most of the past slope failures occurred due to earthquakes were of relatively minor consequence so far; however as far as the Niigata-ken chutes earthquake concerned, there was serious damage to many important secondary roads as well as destruction of residential areas and blockage of rivers due to landslides. In addition, several major transportation routes, such as the Joetsu line of East Japan Rail, Routes 17 and Root 117, were severely damaged due to the numerous large scale collapses of river terrace along the Sinano River beside which most of these transportation lines run.

In this paper, the types of many slope failures which occurred along the Shinano River during the 2004 Niigata-ken Chuetsu Earthquake were examined first in order to study the cause of each failure. The cause of a dip slope failure was next investigated to confirm the effectiveness of a stability analysis based on the limit equilibrium method. Furthermore, an erasto-plastic dynamic finite element analysis was applied to the slope failure for reproducing the long distance slide taking strain softening and decrease in strength due to cyclic shear loading into consideration.

GEOLOGICAL CONSIDERATION OF YOKOWATASHI SLOPE

As seen in the geological map shown in Fig. 1, the Shinano River joins the Uono River at Kawaguchi town near the epicenter of the earthquake and flows toward almost north from Shiroiwa, Nagaoka city after scraping the right coast at Yokowatashi, Ojiya city. The river encroaches on the attacking rock slopes ranging from Shiroiwa to Myoken, Nagaoka city along the right coast. Neogene deposits, such as Shiroiwa layer, and Uonuma layer sedimented by early Diluvium distribute as hills and terraces from Kawaguchi town to Nagaoka city along the

Shinano in this area. These layers fold several times forming the Higashiyama hill areas and the axis directions of these anticlines and synclines are almost South-North in direction. The Shinano locates to the west of the west end anticline axis.The slopes inclining toward west and facing to the river are dip slopes from geological structure view point. Geological characteristics of typical landslides which occurred during the earthquake in the vicinity of Ojiya city were tabulated as Table 1. According to this table, the landslide type failures occurred at dip slopes with relatively gentle slant. The Yokowatashi landslide is classified in this type as shown in Fig. 2(a). Surface failures occurred at steep cliffs having an inclination of about 50°which were classified into three categories, namely reverse dip slope (Fig. 2(b)), slopes perpendicular to the layer strike (Fig. 2(c)) and slopes with steep fissures (Fig. 3(c)). As seen in Fig.4, the cliff at Nishikura,

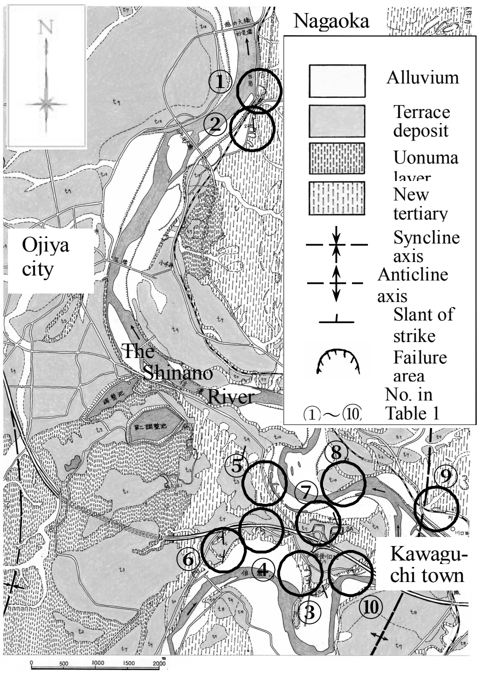

Fig. 1: Geologic map in the vicinity of Ojiya city

Table 1: Slope failure and geological structure along the Shinano

Failure type	Feature of slope	Geological structure	Location	Direction	№
Landslide	Slope of gentle slant	Dip slope	Shiroiwa*	West	1
			Yokowatashi**	West	2
			Unoki**	West	3
			Shiodono**	West	4
Surface failure	Steep cliff of about 50° slant	Reverse dip slope	Nishikura	East	5
			Shiodono**	East	6
		Slope perpendicular to layer strike	JH Echigo Kawaguchi SA	North	7
			Ushigashima***	South	8
			West to Echigo Kawaguchi RS	South	9
		Slope with steep fissures	Nishikura***	South	10

* Nagaoka city, ** Ojiya city, *** Kawaguchi town

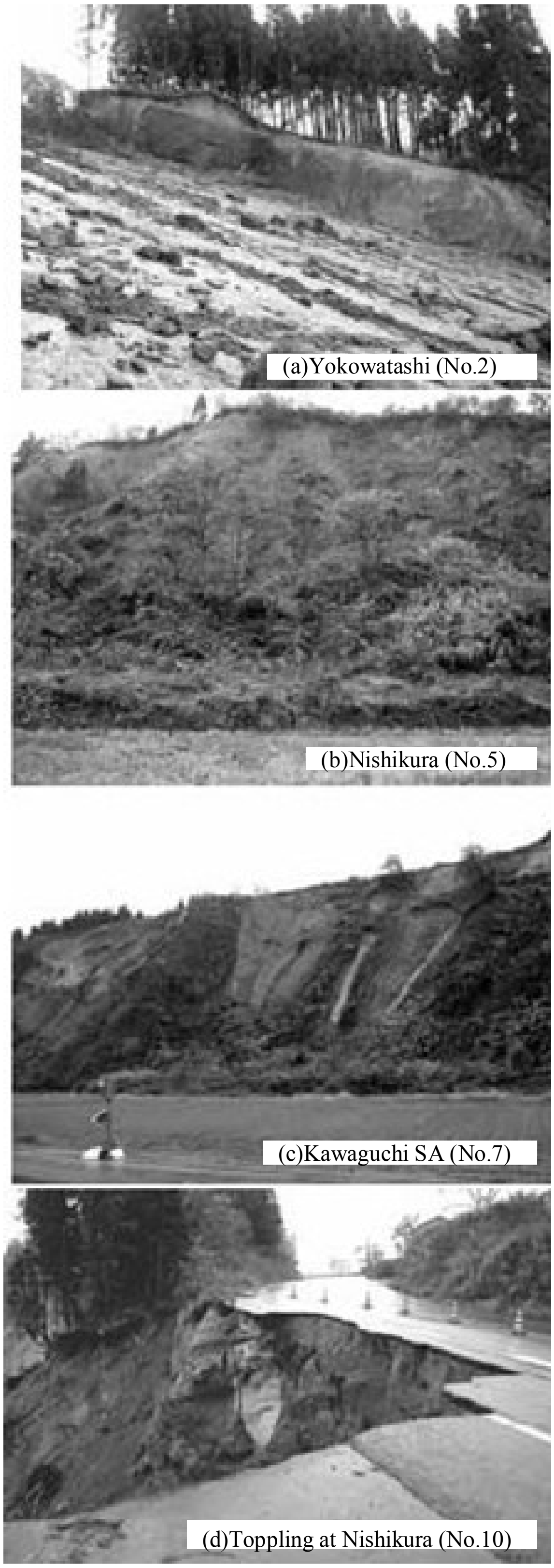

Fig. 2: Example of sliding and failures

Kawaguchi, has steep openings in fissures of about 80° inclination and failed because of toppling.

STABILITY OF YOKOWATASHI SLOPE DURING EARTHQUAKE

Seismic stability of infinite slopes

Fig. 3 shows a schematic cross section of an infinite slope with water flow in the soil. Now let us imagine the sliced element of width B and depth Z on the imaginary sliding plane having an inclination of β and parallel to the soil surface. The forces E_1, E_2 acting on the vertical sides of the element are assumed to exactly balance each other. When the depth of the water table is z and the horizontal and vertical seismic intensity act to the mass of the soil and water are, K_h , and K_v (downward; positive), respectively, the water pressure, u, on the sliding plane is, $u = \gamma_w h\{(1+K_v)\cos\beta - K_h \sin\beta\}/\cos\beta$. The total water force, U, perpendicular to the sliding plane between b and c is,

$$U = \gamma_w (Z-z) B\{(1+K_v)\cos\beta - K_h \sin\beta\} \cdots (1).$$

The weights of the soils above and under the water table are $W_1 = \gamma_t B z$ and $W = \gamma_{sat} B(Z-z)$, respectively. The horizontal inertias are $H_1 = K_h W_1$ and $H = K_h W$, and the vertical ones are $V_1 = K_v W_1$ and $V = K_v W$ due to seismic motions. The effective normal force N' and shear forth T on the sliding plane are indicated by Eqs. $(2)_1$ and $(2)_2$, respectively.

$$T = \{(1+K_v)\sin\beta + K_h\cos\beta\}(W_1 + W)B \qquad \cdots(2)_1,$$

$$N' = \{(1+K_v)\cos\beta - K_h\sin\beta\}\{\gamma_t z + \gamma'(Z-z)\}B \quad \cdots(2)_2$$

The effective normal stress, the shear stress and the factor of safety, F, are,

$$\sigma' = \frac{N'}{b}\cos\beta, \qquad \tau = \frac{T}{b}\cos\beta \quad \cdots(3)_1,(3)_2$$

$$F = \frac{c' + \sigma'\tan\phi'}{\tau} = \frac{c' + \{(1+K_v)\cos\beta - K_h\sin\beta\}\{\gamma_t z + \gamma'(Z-z)\}\cos\beta\tan\phi'}{\{(1+K_v)\sin\beta + K_h\cos\beta\}\{\gamma_t z + \gamma_{sat}(Z-z)\}\cos\beta} \cdots(4)$$

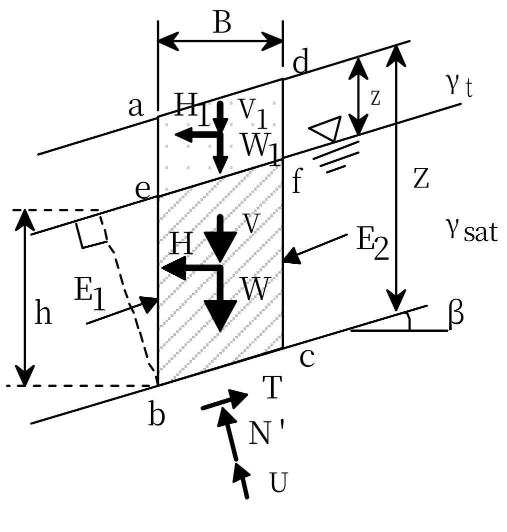

Fig. 3: Schematic picture of infinite slope.

Features of Yokowatashi landslide

Fig. 2(a) is a photograph taken from a northwest direction. As seen in the figure, a part of the upper Shiroiwa layer and the surface earth with high trees remain as they were on the bedding plane at far end of this picture. The remaining upper Shiroiwa layer of soft silt rock exposes its side face. The other part of the upper Shiroiwa layer which made up the opposite side of the slid area is visible on site. The portion of the upper Shiroiwa layer between them had covered the planer tectonic dip surface which is clearly seen in the picture, and it has slid more than 72m to the west toward the Shinano River. The inclination, β, of the bedding plane facing to almost west is slightly large, with a high of 22.4° at the relatively southern portion of the slid area and averaging approximately 22° overall. The thickness of the slid Shiroiwa block at the south end is about 4 m and those of earth on the block ranges from 20 cm to 1 m. The height of upper Shiroiwa layer remaining at the north side is about 2.5 m with earth cover of 60 cm thick near the ridge of the slope. Fig. 4 is a close picture showing a border between the bedding plane and an exposed face of the remaining Shiroiwa layer at the south end of the slid area. Both upper and lower Shiroiwa layers were excavated and scraped slightly for intact soil sampling just after the slide. A thin seam layer of 5-10 mm thick was sandwiched between the upper and lower Shiroiwa layers. The material of the sand seam is tuff sand. Both Shiroiwa layers were gray, weathered, and changed their color to brown up to about 8 cm inside from the boundary of the sand seam. As is evident from the discoloration belts with a thin crevice in the center of each belt, there were a lot of joints in the upper Shiroiwa layer. Plant roots expanded in the joints and the bedding plane to get water as seen in this figure.

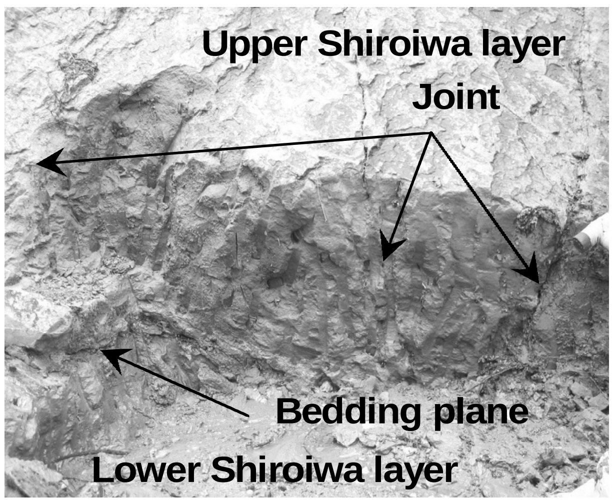

Fig. 4: Border of upper and lower Shiroiwa layers

Shear strength of the sand seam at the bedding plane

Fig. 5 shows an intact sample consisting of the upper and lower Shiroiwa soft rocks and the tuff sand seam in between. The sample was subjected to the cyclic direct shear test under the constant volume condition. The unconfined compression strength, q_u, of both Shiroiwa soft rock is 5.3 MN/m^2 and the unit weight is γ_t=18.0 kN/m^3. Fig. 9 shows examples of the shear stress vs. displacement of three samples during cyclic loading. As seen in the figure, the shear stress decreases with increasing number of loading-unloading cycles for the same shear displacement. Decrease in the shear stress at an arbitrary displacement is especially drastic in the second cycle and the latitudes of shear stress between loading and unloading processes become small and the hysteresis loops become flat gradually with increase in the number of cycles. The strength parameters were determined from the peak strengths of virgin loading process for different consolidation pressures. The average strength parameters concerning effective stress are that c'=35.3 (kN/m^2) and ϕ'=17.2 ° . Those concerning total stress are c=23.8 (kN/m^2) and ϕ=30.9 ° .

Safety factor of the slope during the earthquake

The average thicknesses of the slid Shiroiwa layer and the earth cover were assumed to be equal to 3.5 m and 50 cm in conversion to the unit weight of Shiroiwa rock, respectively. As aforementioned, the thin tuff sand seam is considered to be filled with water because of existence of plant's roots. Moreover, this district was suffered by heavy rain due to typhoon No. 23 three days before the earthquake. The sand was thus saturated and behaved under the undrained condition during the earthquake. Since the thickness of the sand layer is, however, slight as around 10 mm, the hydrostatic pressure was almost zero and the effective normal force on the bedding plane was nearly equal to the total one, in other words Z is almost equal to z, hence Eq.(4) yields Eq.(5) in this particular site.

$$F = \frac{c' + \sigma' \tan\phi'}{\tau} = \frac{c' + \{(1+K_v)\cos\beta - K_h \sin\beta\}\gamma_t z \cos\beta \tan\phi'}{\{(1+K_v)\sin\beta + K_h \cos\beta\}\gamma_t z \cos\beta} \quad \cdots(5)$$

Fig. 6 shows the time histories of acceleration in EW and NS directions observed by the Japan Meteorological Agency at Takezawa in Old Yamakoshi village. East and North directions are denoted by positive values. Fig. 7 shows the time history of F calculated by Eq. (5) using K_h and K_v values converted from Fig. 6. According to Fig. 7, the value of F before the event was considered to be 2.16. It had fallen below 1.0 first at 2.28 sec after the beginning of the event and several times by 10 sec.

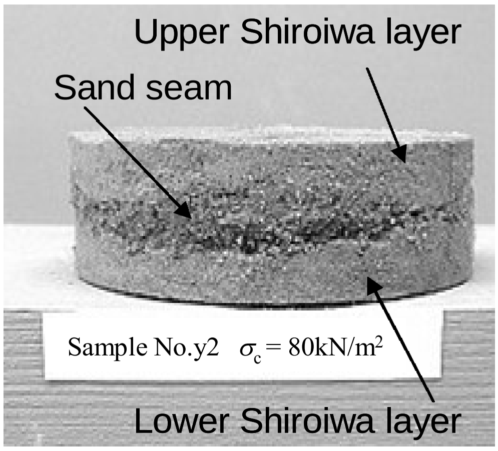

Fig. 5: Test specimen consisting of upper and lower Shiroiwa layers with sand seam in between

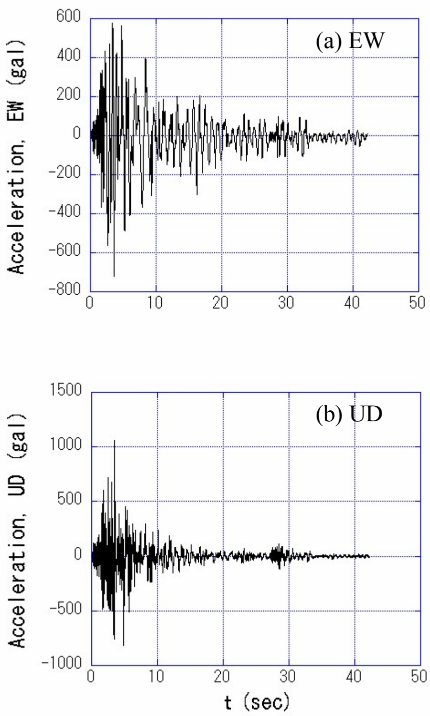

Fig. 6: Seismic wave observed at Takezawa.

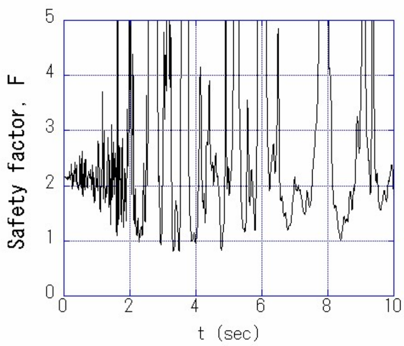

Fig. 7: Time history of stability.

EVALUATION OF THE SLIDE BY AN ELASTO-PLASTIC DYNAMIC FEM

Analysis model

As aforementioned, the thickness of the slid soft rock plus earth with trees was thin at the north end and it was thick at the south end. A two dimensional numerical analysis was focused on the cross section of the slid slope with its medium thickness. The finite element mesh consisting of eight nodes per each element were shown in Fig.8. The upper and lower soft rock layers were assumed to be elastic material and the sandwiched tuff sand layer was assumed to be elasto-plastic material having a thickness of 10 mm taking strain softening into consideration. The surface soil at the foot of the slope was assumed to be sand and gravel spreading down to the Shinano.

The basic concept of the elasto-plastic model used here is the same as the cyclic loading model originally proposed by Wakai and Ugai [5]. The undrained strength parameters, c and ϕ, which specify the upper asymptotic line of the hyperbolic skeleton curve of their model was modified as the decreasing functions of accumulated plastic strain to incorporate the strain softening characteristics [6] and used here. The shear stiffness ratio, *Go*, is also assumed to decrease in proportion to the decrease of shear strength. The cyclic loading model disregarding strain softening was used for the sand and gravel layer. The constants of Rayleigh damping were assumed to be basically α=0.171 and β=0.00174 which are equivalent to a damping ratio of about 3 % for a vibration period of 0.2 through 2.0 s. The material properties used in the analysis were summarized in Table 2.

Fig. 9 compares the simulated hysteresis loop and the tested loop of each specimen as mentioned before. The axis of abscissas is written in strain or displacement and 0.1 strains correspond 1.0 mm since the thickness of the sandwiched layer is 10 mm. Although they don't perfectly coincide, they are roughly similar to each other for the respective consolidation pressure.

Analyzed results and discussions

The acceleration record in EW direction observed at Takezawa was used in analyses. Two cases of analysis were conducted to examine the influence of seismic intensity on the inducement of sliding. One was the analysis for which the observed acceleration record was input as it was at the base of the analysis area, and the other was the one for which the acceleration amplitude was compressed to one half that of the observed wave was input. Fig. 10 shows the time histories of horizontal displacement at the foot of the slope, namely Point A, in Fig. 8. As seen in this figure, the slope does not fail in the case where the acceleration amplitude is compressed to one half that of the actual wave record. Contrarily

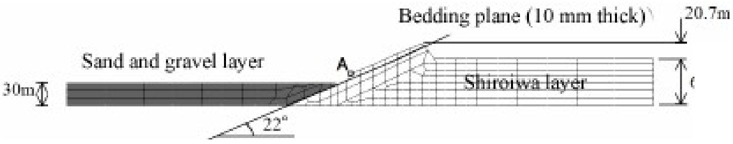

Fig. 8: Two dimensional finite element mesh

Table 2: Input parameters

	Layer	Shiroiwa	Sand seam	Sand & gravel
Basic para-meters	Young's modulus E (kN/m^2)	100000	30000	30000
	Poisson's ratio, ν	0.3	0.3	0.3
	Cohesion c (kN/m^2)	----	24	0
	Internal friction angle, ϕ (deg)	----	30.9	35
	Dilatancy angle ψ (deg)	----	0	0
	$b\,\gamma_{G0}$	----	5.0	0.85
	n	----	1.5	5.0
	Unit weight γ (kN/m^3)	20	18	18
Strain soften-ing para-meters	Residual strength ratio	----	0	----
	A B	----	2.0	----

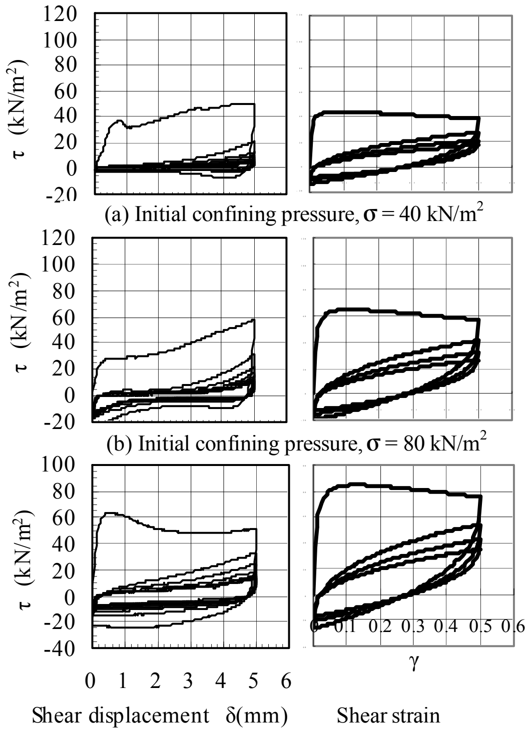

(c) Initial confining pressure, σ = 120 kN/m^2

Fig. 9: Examples of comparison between tested (left column) and simulated (right column) hysteresis loops

the large-scale slope failure occurs in the case of actual acceleration amplitude. The sliding amount in horizontal direction is 1.4 m at t=30 sec and almost 28 m at t=50 sec. Since the shear strength became smaller than the shear stress induced only by the self weight of upper Shiroiwa layer, continuous sliding on the bedding plane started at an elapsed time of about 11.5 s. Fig. 11 shows the relationship between the mean shear stress and the mean accumulated shear strain of the sand seam, both of which were averaged in all over the sandwiched layer. The accumulated plastic strain converged at γ=2.5 and τ = 38 kN/m^2 in the case of half acceleration amplitude. On the contrary, the shear stress decreases continuously with increasing γ for the actual wave case. The residual displacement at 50 seconds after the beginning of the seismic motion was shown in Fig. 12. The long distance sliding of the upper Shiroiwa layer along the bedding plane can be seen discontinuously at the sand seam in this cross section. The large-scale slide occurred on site was thus reproduced quantitatively through the present analysis.

CONCLUSIONS

The types of many slope failures occurred along the Shinano River during the 2004 Niigata-ken Chuetsu Earthquake were classified from a geometric structure view point. The cause of the slope failure at Yokowatashi, Ojiya city was examined based on the cyclic shear properties of the sandwiched material on the bedding plane and its long distance sliding was reproduced analytically. The following conclusions were obtained from the present work;

i) Surface failures occurred at steep cliffs and landslides occurred mainly at dip slopes of gentle slant.

ii) There exists a tuff sand seam at the bedding plane of Yokowatashi dip slope structure and the safety factor of the slope stability was confirmed to become smaller than 1.0 at the seam several times during the earthquake.

iii) The shear strength and stiffness of the sand decrease markedly with increasing number of cycles and the sand seam finally lose its shear strength enough to support just the self weight of soils above it.

iv) The long sliding distance of the slope failure was reproduced through the elasto-plastic dynamic finite element analysis taking the cyclic shear properties of the sand into consideration.

ACKNOWLEDGMENTS

The authors wish to thank Mr. Shintaro Wada, Mr. Hajime Hiroi and Mr. Tetsuo Hiroi for their willing approval of the soil sampling at Yokowatashi. This study was conducted in “Emergency research on the 2004 Niigata-ken Chuetsu Earthquake” based on the Special Coordination Funds for Promoting Science and Technology (MEXT).

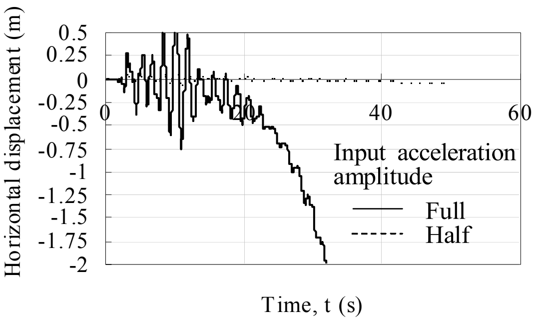

Fig. 10: Time history of horizontal displacement of upper Shiroiwa layer

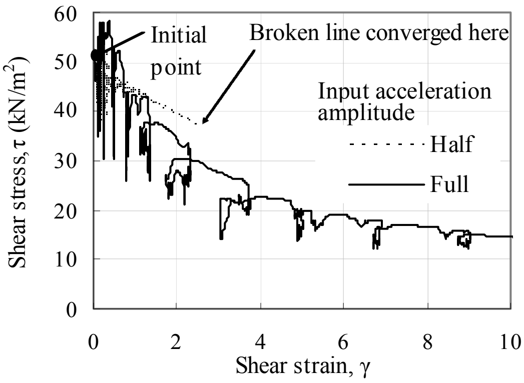

Fig. 11: Relationship between shear stress and shear strain of the sand layer during earthquake

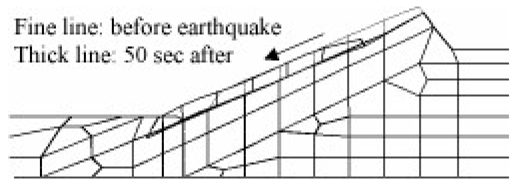

Fig. 12: Slide at 50 sec after the beginning of the event

REFERENCES

[1] Akabane, S., Kitahara, I., “Study from the Zenkoji earthquake” (in Japanese), Sinano Daily Newspaper co. Ltd., 2003.

[2] Muramatsu, I., Matsuda, T. and Okada, A., “The Nobi earthquake and Neodani belt of fault” (in Japanese), Kokin Shoin , 2002.

[3] Sorimachi, Y. “Actual condition of slope failure due to earthquake” (in Japanese), Civil Engineering Journal, No.20, 1978.

[4] Takahashi, H. and Oyagi, N., “Preperception and prevention of slope disasters” (in Japanese), Hakua Shobo, pp.259-268，1986.

[5] Wakai, A. and Ugai, K., ”A simple constitutive model for the seismic analysis of slopes and its applications”, Soils and Foundations, Vol.44, No.4, pp.83-97, 2004.

[6] Wakai, A., Kamai, T. and Ugai, K.,“Finite element simulation of a landfill collapse in Takamachi Housing complex” （in Japanese）, Proc. simpojium on Safeness and performance evaluation of ground for hausing, JGS, pp.25-30,2005.

Estimation of Natural Slope Failures Induced by the 2004 Niigata-ken Chuetsu Earthquake

H. Toyota[1]
[1]Department of Civil and Environmental Engineering, Nagaoka University of Technology, Niigata, Japan

Abstract

The Niigata-ken Chuetsu Earthquake caused a great deal of damage to hilly and mountain area. A great number of landslides occurred during the earthquake. It became a social problem where many villages were isolated because the landslides cut off traffic and lifelines. Earth of the landslides closed river channels and formed natural dams along rivers. The natural dams submerged the villages, and emergency measures to prevent debris flow caused by break of natural dams were performed promptly. It is necessary to clarify the endogenous and exogenous factors of those landslides because of small number of precedent. Therefore cyclic shear tests of saturated and unsaturated soils obtained form a slope failure site were conducted to examine dynamic strength properties of the soils.

Keywords—*cyclic shear, site investigation, triaxial test, undisturbed sample, unsaturated soil*

INTRODUCTION

At 17:56 on 23 October 2004, the Niigata-ken Chuetsu Earthquake whose main tremor was magnitude of 6.8 struck a mid part of Niigata-ken (Chuetsu area) and seriously damaged infrastructures of hilly and mountain area which are Kawaguchi town, Ojiya city, Nagaoka city, etc. (Fig. 1). This earthquake is an epicentral earthquake of thrust fault with hypocentre of about 10 km depth and characterised that frequent strong aftershocks led to increasing damage.

In Chuetsu area, thick alluvium distributes in plain parts, and hilly areas are composed mainly soft mudstone of quaternary and tertiary deposits. Quaternary deposit is relatively new stratum formed from two million years ago. Tertiary deposit is a geological structure formed between twenty-four million and two million years ago. This geomorphology formed by folding presents a prominent landslide area in this region. In addition, there was rainfall of more than 100 mm caused by Typhoon No. 23 two days before the earthquake in Chuetsu area. Daily rainfall of 21 October 2004 at Nagaoka city based on data of the Japan Meteorological Agency reached 115 mm (Fig. 2). Under those situations more than 3,000 landslides occurred in the hilly area close to the seismic centre during the earthquake. The individual damages were arranged in the report [1].

In present paper, topographical and geological characteristics of landslides caused by the earthquake are mentioned. In addition, monotonic and cyclic triaxial tests were conducted using undisturbed and reconstituted samples obtained from a slope failure point to elucidate dynamic properties of the saturated and unsaturated soil.

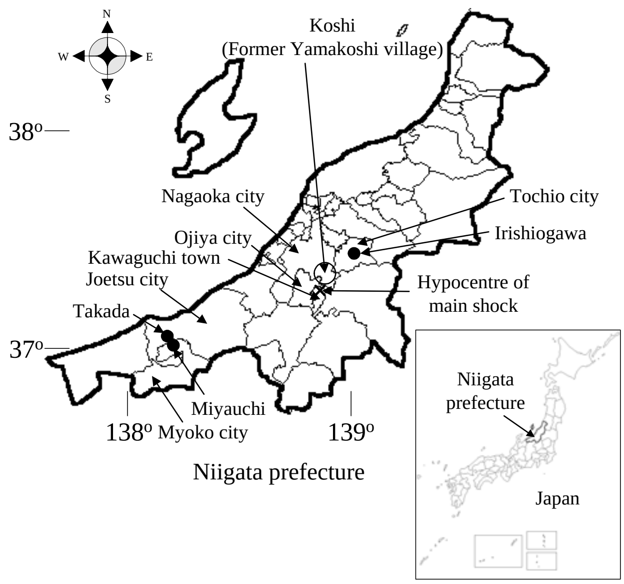

Fig. 1: Map of Niigata prefecture

CHARACTERISTICS OF NATURAL SLOPE FAILURE

Many river-clogging landslide occurred along

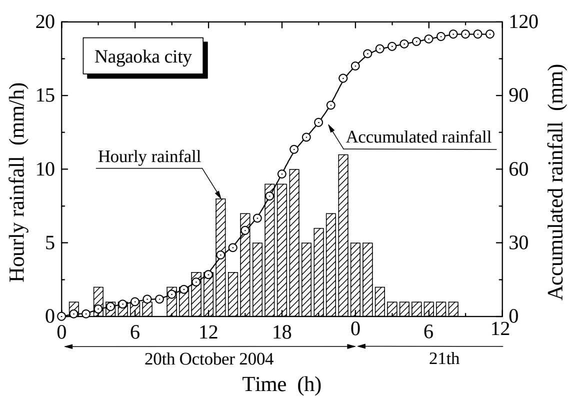

Fig. 2: Hourly and Accumulated rainfall in Nagaoka

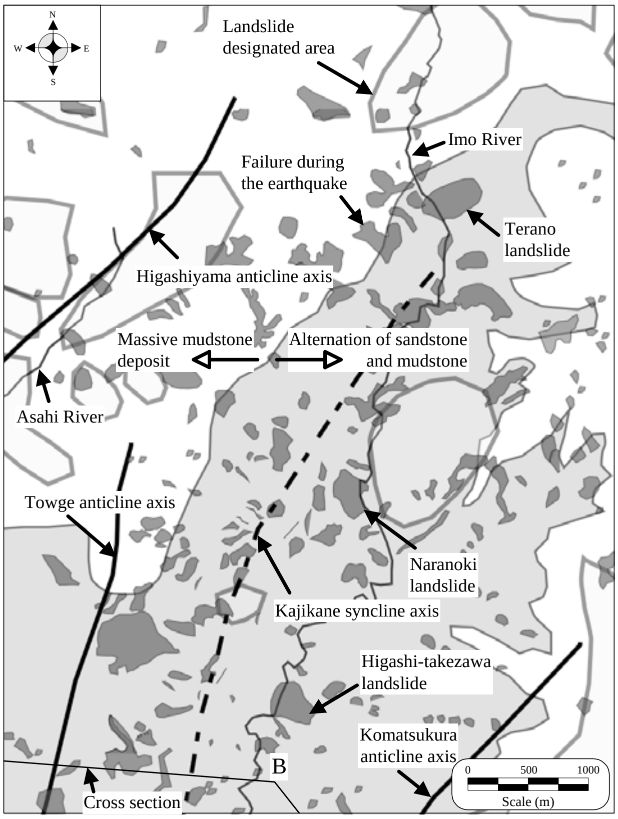

Fig. 3: Landslide distribution and geological map in Koshi

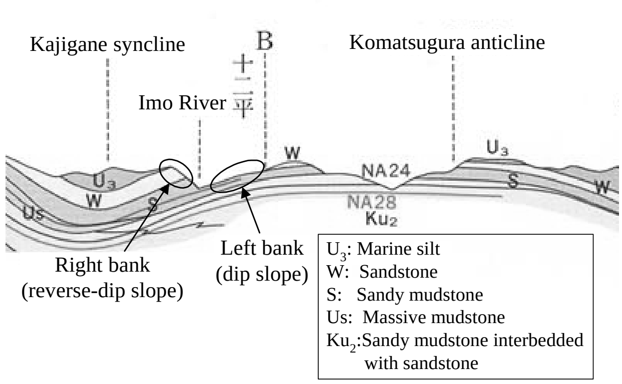

Fig. 4: Geological cross section of the south of former Ymamakoshi village [5]

Imo River during the earthquake. Figure 3 was prepared by laying the landslide locations induced by the earthquake [2] on the map simplified the geological map provided by [3]. Furthermore, landslide designated areas obtained from the conservation map of Niigata prefecture [4] are also indicated in the figure.

West side of the map including Mushigame, which is classified in Asahi River basin (Fig. 3), is geologically Araya deposit that is dark grey massive mudstone. Shifting toward east side of the map, which is classified in Imo River basin (Fig. 3), the deposit changes to alternation of sandstone and mudstone named Kawaguchi and Wanatsu deposits. The alternation of sandstone and mudstone is mainly distributed along Imo River except its upper course. A great number of landslides occurred during the earthquake in the alternation of sandstone and mudstone compared with massive mudstone deposit. This finding leads to a conclusion that sandy natural slope is more fragile than clayey natural slope during earthquake. On the other hand, the landslide-designated areas are mainly distributed in the massive mudstone deposit. This means that the failure mechanism of landslides induced by earthquakes is different from those induced by water such as melted snow.

Moreover the notable geological features of this region are syncline and anticline structures. Those are forming a complex topography where synclinal axes and anticlinal axes are ranging with a short interval. Then peculiarly cuesta topography appears in this region. Therefore fragile and week slopes are easily formed in that situation. In addition, the river scrapes away the surface of the ground and the toe of the slope becomes unstable.

Figure 4 shows the geological cross section of the south of former Ymamakoshi village (Jyunidaira) published by National Institute of Advanced Industrial Science and Technology (AIST) [5]. The location of the geological cross section sampled is shown in Fig. 3. Sandstone (W) and Sandy mudstone (S, Ku2) are widely distributed around Imo River. It is clear from the geological cross section that dip slope appears in left bank of Imo River and reverse-dip slope in right bank of the river. Peculiar slope failures occurred at each right and left bank of Imo River. That is, surface failures occurred frequently at right bank having reverse-dip slope strata, whereas problematical large landslides occurred occasionally at left bank, which is dip gentle slope.

SOIL PROPERTIES OBTAINED FROM A PLACE OF NATURAL SLOPE FAILURE

Monotonic Loading Tests

Soil properties obtained from the slope failure at Naranoki (Fig. 3) was examined in details. Block samples were extracted from the side of the failure (Fig. 5 (a)) and trimmed to make specimens for triaxial tests in the laboratory (Fig. 5 (b)). The soil is very soft and can be easily break the shape by hand. The grain size distribution of the soil is shown in Fig. 6. Specimen size was d=50 mm diameter and h=100 mm height. The specimens were saturated by the vacuum saturation procedure. Drained triaxial compression tests were performed under constant p' conditions with axial strain rates of 0.02 %/min. There were two type of density in nearby similar layers; one was very dense ($e \approx 0.69$) and the other was medium dense ($e \approx 0.85$). The maximum and minimum void ratios based on the Japanese industrial standards (JIS A 1224) were 1.207 and 0.676, respectively. However it must be cared that the soil is beyond the standard's application because the soil contains about 10% fines.

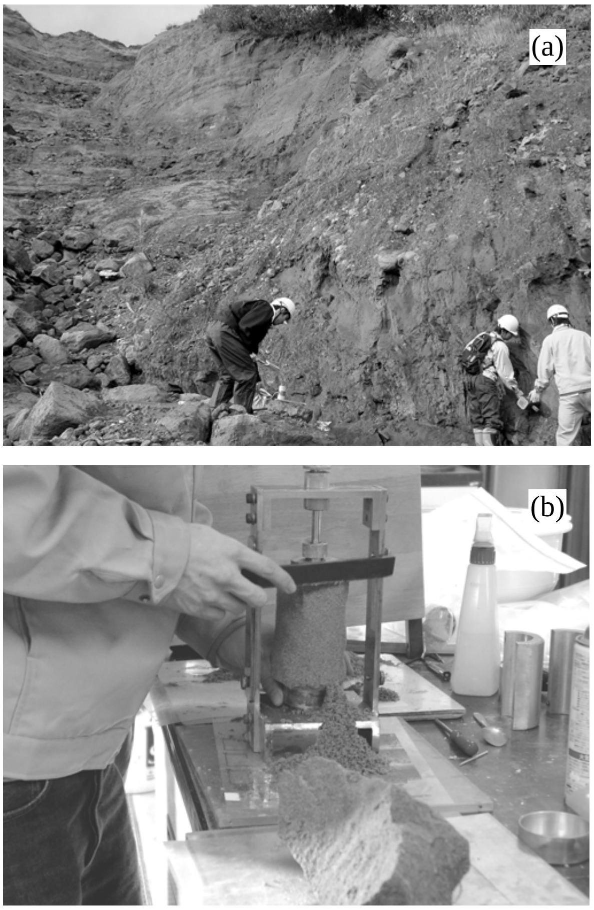

Fig. 5: Soil sampling at Naranoki failure area: (a) Sampling point, (b) trimming for triaxial tests

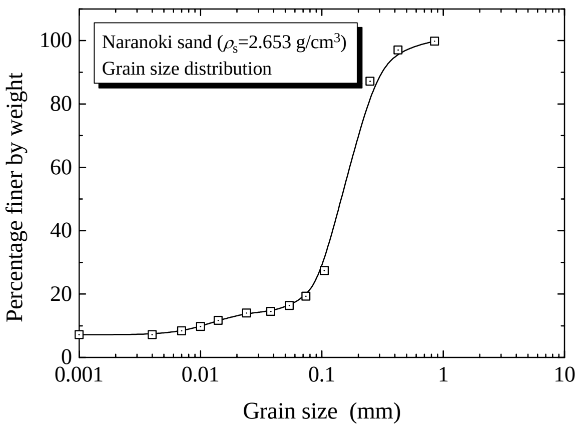

Fig. 6: Grain size distribution of Naranoki sand

Figures 7 and 8 show the comparison of shear behaviour between undisturbed and reconstituted specimens on dense and medium dense sand, respectively. The reconstituted dense specimens became denser than the undisturbed dense specimens. In the case of dense sand, peaks clearly appear in stress-strain relationships (Fig. 7 (a)) and dilative behaviours occur, as shown in Fig.

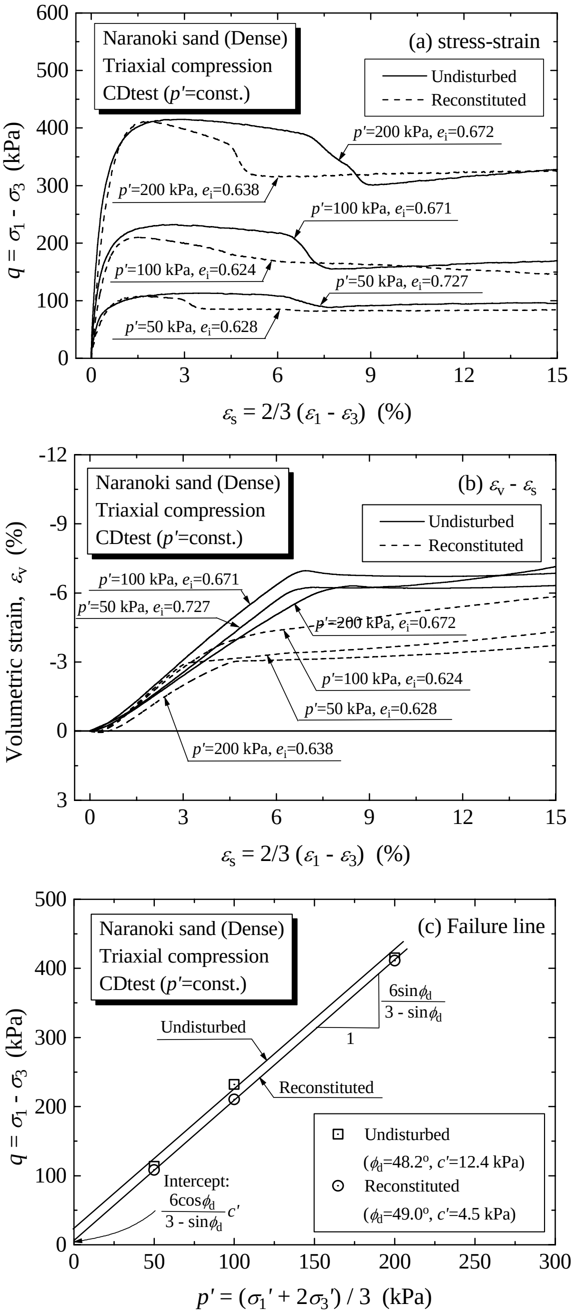

Fig. 7: Shear behaviour of dense Naranoki sand in triaxial compression tests

7 (b). In contrast, peaks of medium dense sand are indistinct (Fig. 8 (a)) and contractive behaviours appear at small shear strain region of large confining stress (p'=200 kPa) cases (Fig. 8 (b)). From the void ratios and shear behaviours, it can be seen that the dense Naranoki sand is extremely dense. At the ultimate state after the peak in the stress-strain relationships, the ultimate strengths of dense sands roughly agree with those of medium dense ones. This means that dense and medium dense sands possess similar physical properties each other.

It is a characteristic of the dense undisturbed sand that

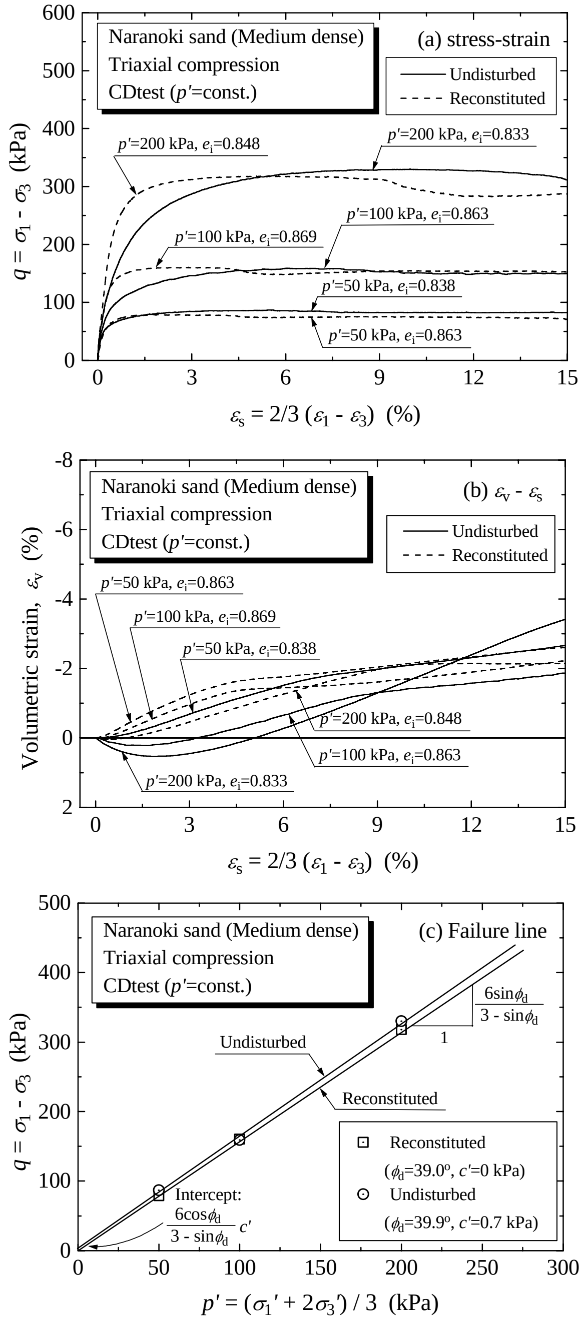

Fig. 8: Shear behaviour of medium dense Naranoki sand in triaxial compression tests

deviator stress suddenly drops at the shear stress of about 7% in the stress-strain relationship. The peaks of reconstituted specimens tend to appear at smaller shear strains than those of undisturbed specimens. The reason for this difference is the nature of fabric structure of specimens. The peaks of undisturbed specimens may have appeared at larger shear strain because the specimen was extracted laterally from the soil block.

Figures 7 (c) and 8 (c) show the failure lines obtained from triaxial compression tests in dense and medium

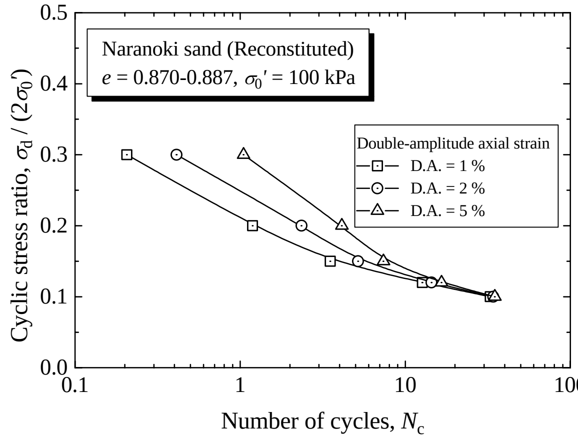

Fig. 9: Liquefaction resistance of medium dense Naranoki sand

dense specimens, respectively. The undisturbed dense sand has much larger angle of shear resistance, ϕ_d, and cohesion, c', than the undisturbed medium dense sand (Fig. 7 (c)). Although undisturbed specimens have similar angle of shear resistance, ϕ_d, with reconstituted specimens, there is larger cohesion, c', in undisturbed specimens because of aging effect. However, the cementation and ageing effects of Naranoki sand layer are small because the cohesions are very small, especially in medium dense specimens. It is understand that when cementation of natural sandy soil is small, reconstituted and undisturbed specimens, whose void ratios are approximately equal each other, have similar shear behaviour.

Cyclic Loading Tests

From the monotonic shear results, it is inferred that failure would occur in the medium dense sand layer because the dense Naranoki sand layer has much larger angle of shear resistance and cohesion than those of medium dense sand layer. Therefore reconstituted specimens were prepared in medium dense ($e \approx 0.85$) using the moist tamping (MT) method to examine other shear properties of the soil in detail. In MT method, the soil, which has water content of 10%, was placed in a 5cm-diameter mould and carefully tamped at each 1cm layers by a 2cm-diameter rod in order to control specimen density.

Cyclic undrained triaxial tests were conducted to investigate a dynamic strength of reconstituted medium dense Naranoki sand under saturated conditions. A specimen was first consolidated under an appropriate isotropic pressure. Uniform cyclic axial stress was applied to the specimen in both compression and extension directions under constant axial strain rate (0.1 %/min).

Cyclic shear loading under constant mean principal stress is considered to be suitable for the seismic problems because of importance of shear wave. When the specimen is completely saturated and under undrained conditions, the effective mean principal stress does not change

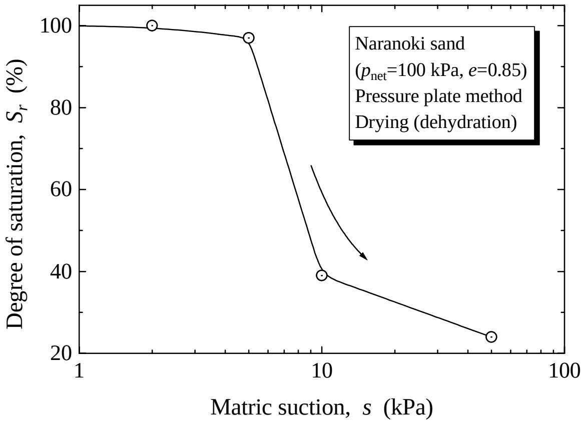

Fig. 10: Soil-water characteristic curve of Naranoki sand

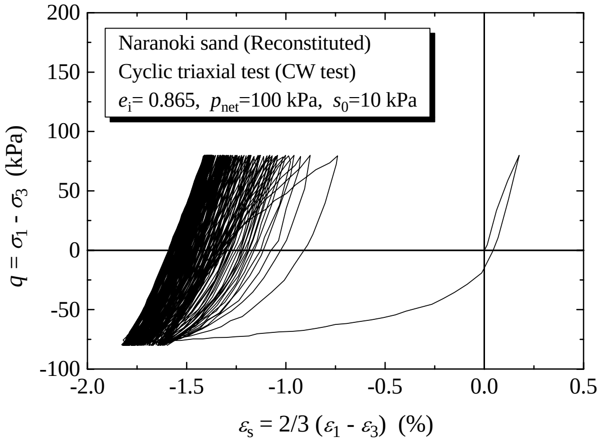

Fig. 12: Stress-strain relationship of unsaturated Naranoki sand in cyclic triaxial test

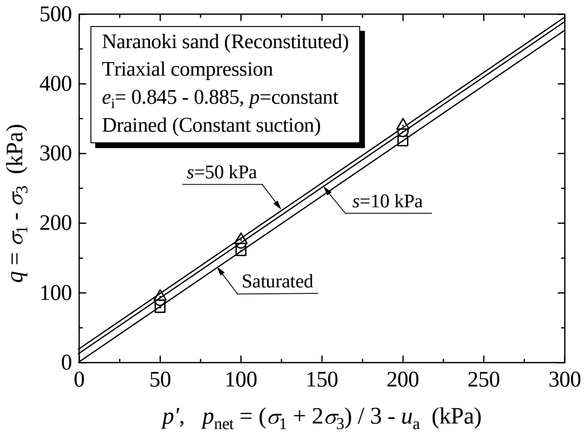

Fig. 11: Failure lines of unsaturated Naranoki sand (medium dense)

because pore water pressure varies as same as the change of mean principal stress. Therefore, cyclic triaxial tests of saturated specimens were carried out under constant cell pressure. The tests were terminated when the axial strain became more than 5%.

Figure 9 shows the liquefaction resistance where cyclic stress ratio plotted versus the number of cycles required to produce certain double-amplitude axial strain (D.A.). The inclination of the liquefaction resistance curve around the small number of cycles is gentle, and the estrangement of the liquefaction resistance curves to produce different D.A. is small. Therefore, the soil tested is week for dynamic loading where shear strain awfully increases when liquefaction occurs.

Next, shear properties under unsaturated state were also examined where suction was controlled by the pressure plate method using ceramic disc. The drying portion of the soil-water characteristic curve obtained from the pressure plate method is shown in Fig. 10. The experiment was carried out under p_{net}=100 kPa using triaxial apparatus. It took two days to settle water drainage during applying a certain matric suction. This result suggests that the air entry value of the soil is approximately between 5 and 10 kPa. The degree of saturation dramatically decreases at the air entry value because of sandy soil specimen. This derives that when the soil is under stable conditions, the soil is in either fully saturation or low degree of saturation.

Drained (constant suction, s) triaxial compression tests were performed under constant p' conditions with axial strain rates of 0.01 %/min. Figure 11 shows the failure lines of the unsaturated specimens. The failure lines of different suctions are approximately parallel to that of saturated soil. Cohesion is larger when the matric suction is larger. Although the cohesion changes to some degree between saturated and s=10 kPa, small differences exist between s=10 kPa and s=50 kPa. The reason for this is that the conditions tested (s=10 kPa and s=50 kPa) are in the part of the soil-water characteristic curve where there is small difference in degree of saturation with suction.

Cyclic triaxial tests were also conducted to investigate the effect of cyclic loading in reconstituted medium dense Naranoki sand under unsaturated conditions. A specimen was first consolidated under an appropriate isotropic pressure, and a certain matric suction was next applied to the specimen for two days. Then, uniform cyclic axial stress was applied to the specimen in both compression and extension directions under constant axial strain rate (0.1 %/min). Cyclic triaxial tests of unsaturated specimens were carried out under constant total mean principal stress to simulate the closer behaviour to real seismic loading than that under constant cell pressure. The tests were terminated when the number of cycles became 150.

Figure 12 is the representative result of stress-strain relationship in the unsaturated specimen. At first, the specimen considerably deforms to extension direction, and then the residual deformation to extension direction

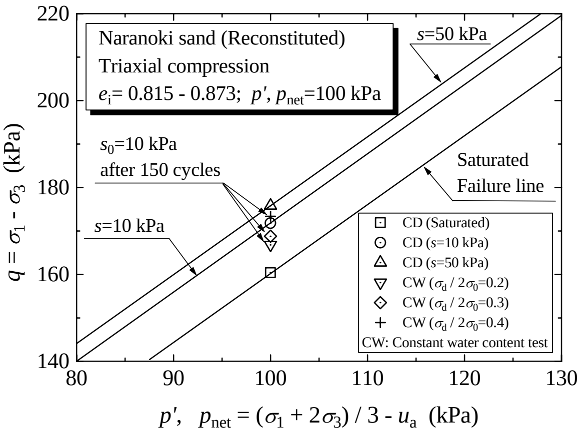

Fig. 13: Effect of cyclic stress ratio on shear strength of unsaturated Naranoki sand

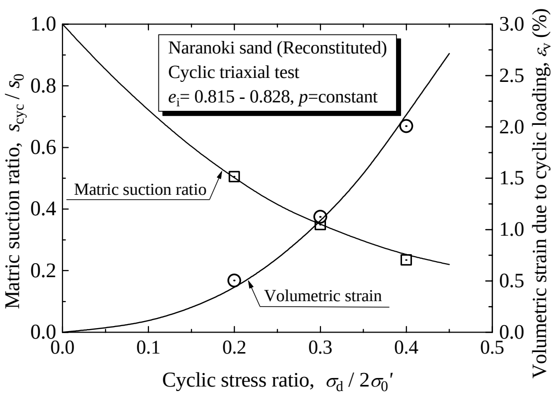

Fig. 14: Change of matric suction and volumetric strain during cyclic loading

tends to converge with the number of cycles. It can be understand that in unsaturated soil, whose degree of saturation is low, the stiffness against a cyclic loading is increased with the cyclic loading and the softening behaviour like liquefaction of saturated soils never occurs.

After applying the cyclic loading of 150 times, the specimen was monotonically compressed under net mean principal stress, p_{net}=constant conditions with axial strain rate of 0.02 %/min. The experiments were performed under drained conditions for the pore air phase and undrained conditions for the pore water phase (constant water content conditions). In Fig. 13, the static shear strengths after applying different cyclic stress ratio to the specimens are plotted. Each data comes close to a static failure line of s=10 kPa. This result indicates that there is no effect of cyclic loading on static shear strength of the unsaturated soil.

The change of matric suction during cyclic loading was examined as shown in Fig. 14. In this figure, "s_{res}" means the residual matric suction after applying cyclic loading, and "s_0" means the initial matric suction before applying cyclic loading. Residual matric suction after cyclic loading decreases as the cyclic stress ratio increases (Fig. 14). The static shear strength should more decrease by a larger cyclic loading because smaller matric suction remains after the cyclic loading. However, there is little difference in static shear strength after applying cyclic loading.

Furthermore, the volume change occurred during the cyclic loading was examined. The volumetric strain caused by cyclic loading is also shown in the same figure. The volumetric strain increases with an increase of cyclic stress ratio. The shear strength is inferred to be increase when the density of soil increases. Therefore the strength decreasing induced by a decrease of matric suction and the strength increasing induced by an increase of density may be cancelled each other.

CONCLUSIONS

The Niigata-ken Chuetsu Earthquake caused heavy damage to infrastructures in hilly and mountain area. Soil mass of the landslides clogged the river channels and formed natural dams. It brought out that there was effect of geographical and geological features such as folding. A detailed investigation was carried out on the landslides along Imo River of former Yamakoshi village to clarify the failure mechanisms. Moreover, monotonic and cyclic triaxial tests were conducted using soil sample obtained from the real failure point to find shear properties of the soil.

Main findings from the study are summarised as:

1. The greater part of slope failures during the earthquake broke out at alternation of sandstone and mudstone deposit, although landslides, which gradually move during snow melting season, usually occur at massive mudstone of quaternary and tertiary deposits.
2. During earthquake, surface failures occurred easily at steep reverse-dip slope, whereas large landslides occurred at gentle dip slope.
3. There were very dense and medium dense sand layers in Naranoki slope failure. From the results of triaxial tests, it can be inferred that failure would be triggered in the medium dense sand layer.
4. Reconstituted and undisturbed Naranoki sands, whose void ratios approximately equal each other, have similar shear behaviour because the cementation and ageing effects of them are small.
5. The medium dense Naranoki sand of saturated state is week for dynamic loading where shear strain awfully increases when liquefaction occurs.
6. In the unsaturated Naranoki sand, although the residual matric suction after cyclic loading decreases, the volumetric strain occurred during cyclic loading increases. Consequently, the shear strength is hardly affected by cyclic loading.

ACKNOWLEDGMENTS

We had an opportunity to investigate the stricken area with many researchers and could get useful information. Soil tests were conducted with the help of students who belong to the Geotechnical Engineering Laboratory, the Department of Civil and Environmental Engineering, Nagaoka University of Technology. The authors wish to express their sincere thanks to them for their contributions to this study.

REFERENCES

[1] Edited by Japan Society of Civil Engineers, "Report on the 2004 Niigata Chuetsu Earthquake," (in Japanese), JSCE, 2006, CD-ROM.

[2] Geographical Survey Institute, "Disaster map of Niigata-ken Chuetsu Earthquake," (in Japanese), 2004. Available: http://zgate.gsi.go.jp/niigatajishin/index.htm

[3] Takeuchi, K., Yanagisawa, Y., Miyazaki, J. and Ozaki, M., "1:50,000 Digital Geological Map of the Uonuma region," Niigata Prefecture (Ver. 1), GSJ Open-file Report, no. 412, 2004. Available: http://www.gsj.jp/GDB/openfile/files/no0412/index.html

[4] Edited by Niigata prefecture, "Conservation Map," (in Japanese), Niigata prefecture, 1982.

[5] Yanagisawa, Y., Kobayashi, I., Takeuchi, K., Tateishi, M., Chihara, K. and Kato, S., "1:50,000 Geological Map of the Ojiya region," National Institute of Advanced Industrial Science and Technology (AIST).

Run-out distances of landslides of reclaimed soil deposits at the residential hill in 2004 Niigata-ken Chuetsu Earthquake

Y. Tsukamoto[1], K. Ishihara[1], Y. Kobari[1]

[1]*Department of Civil Engineering, Tokyo University of Science, Chiba, Japan*

Abstract

During 2004 Niigata-ken Chuetsu Earthquake in Japan, a numerous number of landslides occurred on natural slopes, especially at the hillsides in the region of Yamakoshi. There have also been a couple of slope failures involving the backfills of reclaimed soil deposits behind retaining walls constructed for the development of residential districts in Nagaoka city. In the present study, case studies are made on such slope failures at Takamachi-Danchi. The slope failures are herein assumed to consist of two phases, “sliding” and “spreading”, as has been assumed for landslides on natural slopes in the previous study. The run-out distances of such slope failures are examined, and are compared with those calculated from a simple analysis based on the energy principle. From the comparisons between the run-out distances observed and thus calculated, the residual shear strength of soils involved in such slope failures is back calculated, and is compared with the laboratory triaxial test results.

Keywords—*Residual strength, run-out distance, landslides, earthquakes*

INTRODUCTION

A numerous number of landslides occurred on natural slopes in the Yamakoshi area during Niigata-ken Chuetsu Earthquake that struck the hilly region in Niigata at a local time of 17:56 on October 23, 2004, measuring the magnitude of M = 6.8 at the main shock followed by two huge aftershocks measuring M = 6.0 and 6.5 at 18:11 and 18:34. This was most probably because the tertiary deposits mainly prevailed in this area, which were known to be susceptible to landslides. The heavy rainfall passing three days before the earthquake was also suspected to be responsible for such a large number of landslides. In addition to the failures of natural slopes, there have been a couple of slope failures involving the backfills of reclaimed soil deposits behind retaining walls constructed for the development of residential districts in Nagaoka city. In the present study, case studies are made on such slope failures at Takamachi-Danchi. The location of the residential district of Takamachi-Danchi is indicated in Fig. 1, together with the epicentres of the main shock and the subsequent two aftershocks.

CASE STUDIES

The residential district of Takamachi-Danchi was located on the elevated hillside surrounded by the alluvial flat plain in Nagaoka city. This residential district contains several dozens of houses, and some portions of its circumferences were reinforced with retaining walls holding the backfills of reclaimed soil deposits. During the devastating 2004 Niigata-ken Chuetsu Earthquake, four portions of the hillsides at this residential district were collapsed and run down. At the three portions among them involved the collapse and run-down of the reclaimed soil deposits behind the retaining walls. These three sites were chosen for the reconnaissance investigation in the present study.

Figures 2(a) and 2(b) show the plan view and elevation view of the slope failure observed at the site No.2. In the previous study dealing with the landslides on natural slopes during earthquakes, the process of landslides was assumed to consist of two distinctive phases, “sliding” and “spreading”. Based on the same principle as above, the process of slope failures involving reclaimed soil deposits behind retaining walls is herein assumed to have the two phases of “sliding” and “spreading”. In case of landslides on natural slopes, the first phase was characterized by the “run-down distance”, for which the collapsed soils would run down on slopes, while the second phase was characterized by the “run-out distance”, for which the “run-down” mass of the collapsed soils would spread over almost plain fields. However, in case of slope failures involving reclaimed deposits behind retaining walls located on gentle slopes, the boundary between the two zones of “sliding and “spreading” is herein determined at the position of the toe of a retaining wall.

Figures 3 and 4 show the same set of the plan view and elevation view of the slope failures observed at the sites No.3 and 4, respectively. In Fig. 5, the “run-out” distances observed at Takamachi-Danchi are plotted against the “sliding” distances. It is apparently seen that the run-out distances are generally larger than the sliding distances. This feature was also observed on slope failures on natural slopes during this earthquake.

SIMPLE ANALYSIS BASED ON ENERGY PRINCIPLE

From the viewpoint of landslide hazard mitigations, the estimations of run-out distances of collapsed soils from expected sources of landslides are among the great

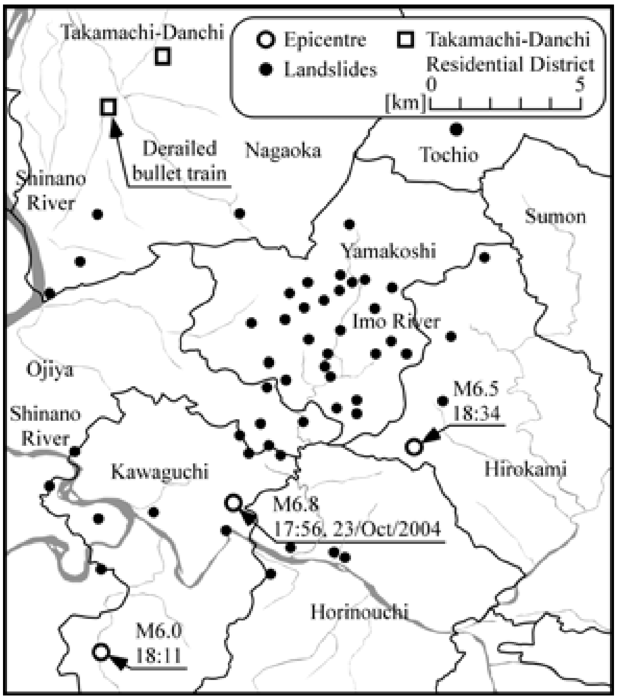

Fig. 1: Location of the residential district of Takamachi-Danchi in Nagaoka

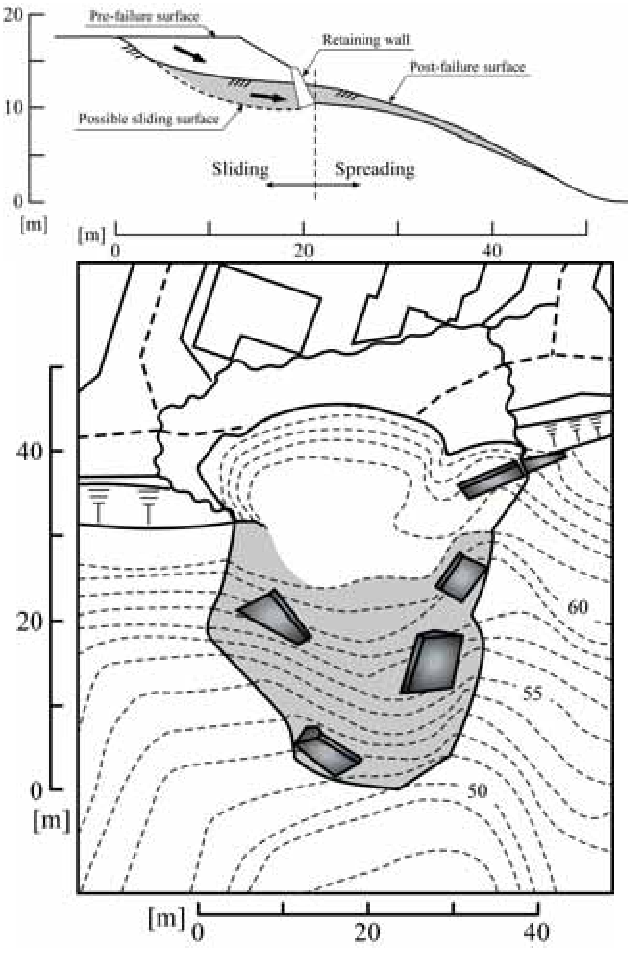

Fig. 2: Scaled features of slope failure at site No.2

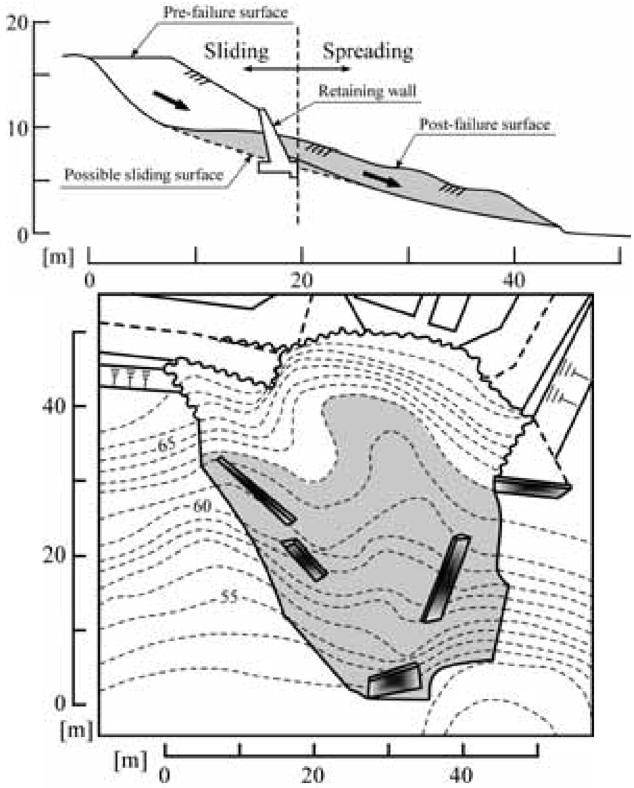

Fig. 3: Scaled features of slope failure at site No.3

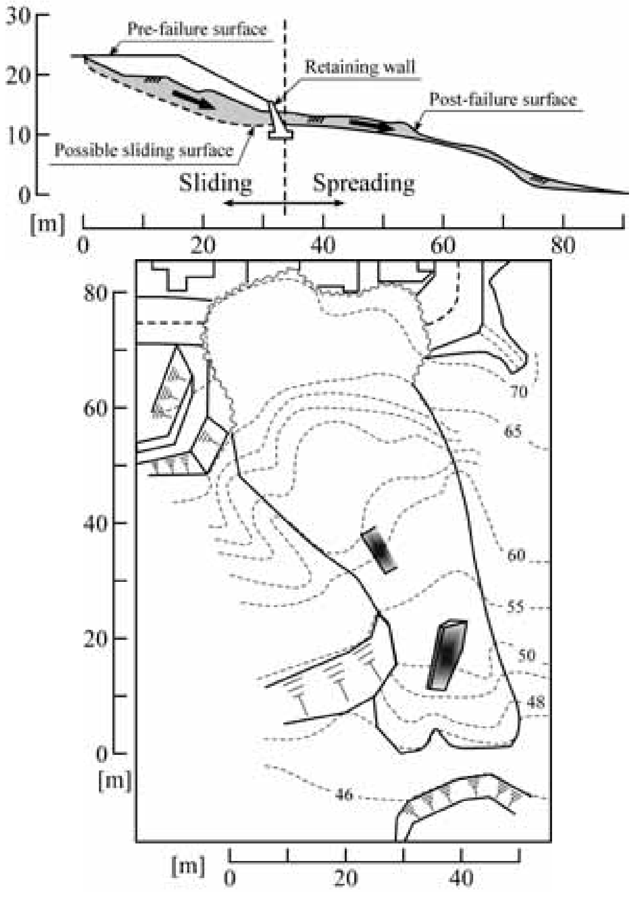

Fig. 4: Scaled features of slope failure at site No.4

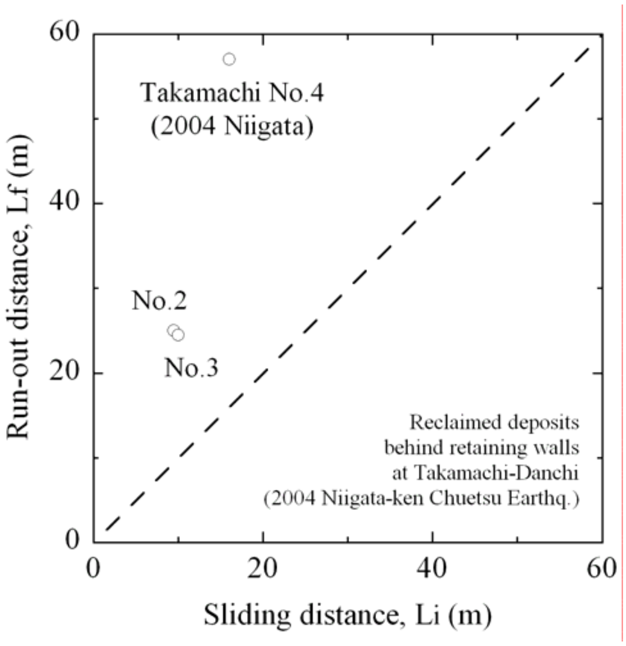

Fig. 5: Summary of “sliding” and “run-out” distances of slope failures at Takamachi-Danchi

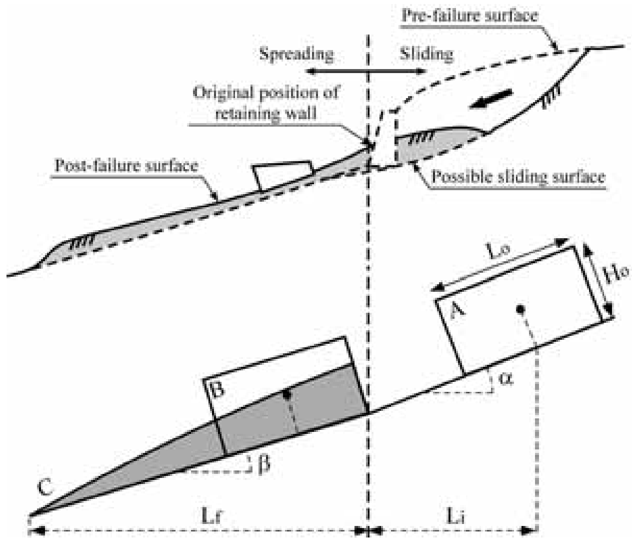

Fig. 6: Schematics illustrating the assumptions in the simple analysis

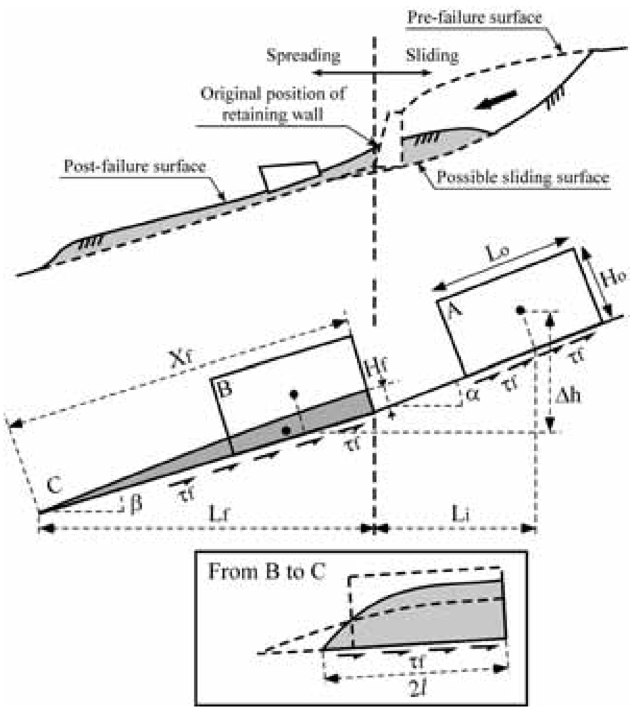

Fig. 7: Schematics illustrating the energy principle in the simple analysis

concerns. When it becomes possible to more accurately estimate the run-out distances, various types of landslide hazard maps would be improved.

In the present study, a simple method is developed to correlate the run-out distance with the residual strength of soils subjected to the run-down and run-out processes of slope failures. Fig. 6 shows the details of the simple analysis. In this analysis, the backfills of reclaimed deposits behind retaining walls are considered to collapse and run down on slopes.

Suppose the mass of soils expected to collapse is represented by the rectangular block located at the position “A”, which corresponds to the backfill of reclaimed deposits sitting behind a retaining wall, as indicated in Fig. 6. When the block of soils is subjected to perturbation during seismic shaking, the initiation of a soil failure is triggered, and the collapse state of soils propagates through the entire soil block in a progressive manner. Then, the soil block at “A” is assumed to move downwards until the right-hand side of the bottom surface of the block reaches the boundary between the regions of “sliding” and “spreading”, corresponding to the location of the toe of the retaining wall in the field condition, as indicated above in Fig. 6. This process is assumed to correspond to the “sliding” phase. It is then assumed that the block of soils at “B” is subjected to deformation, keeping the hyperbolic shape, while the length of the bottom surface becomes greater, and the block of soils eventually reaches the position “C”. This process is assumed to correspond to the “spreading” phase. Therefore, in the present study, the boundary between the two phases of “sliding” and “spreading” is assumed to lie at the initial position of the toe of a retaining wall prior to slope failure. These two phases are characterized by the initial distance, “L_i” and the run-out distance, “L_f”, as indicated in Fig. 6.

The appropriate consideration based on energy principles is described in Fig. 7. During the whole process from the positions “A” through “B” to “C”, the energy of position, E, available to the block of soils is given as follows,

$$E = \gamma H_o L_o \Delta h \ , \tag{1}$$

where γ is the unit weight of soils. During the first phase of "sliding" with the movement of the non-deformed block of soils from the positions "A" to "B", the work done by the residual shear strength exerted along the bottom surface of the block is expressed as follows,

$$W_1 = \tau_f L_o \times \frac{L_i}{\cos\beta} \ , \tag{2}$$

where τ_f is the residual shear strength acting at the bottom surface of the block. During the second phase of "spreading" with the block of soils changing its shape from the rectangular shape at the positions "B" to the hyperbolic shape at the position "C", it is assumed that the volume of the soil block is unchanged, and the following equation holds,

$$H_o L_o = \frac{2}{3} H_f L_f \ . \tag{3}$$

During the "spreading" phase, the work done by the residual shear strength exerted along the bottom surface of the block is expressed as follows,

$$W_2 = \int_{L_o/2}^{X_f/2} \tau_f \, l dl = \frac{\tau_f}{4}\{(L_f / \cos\beta)^2 - L_o^2\} \ . \tag{4}$$

It is to note here that the residual strength exerted along the bottom surface of the block during the two phases is assumed to be the same. By equating the energy of position available and the work done during the entire process, the following equation holds,

$$E = W_1 + W_2 \ . \tag{5}$$

By some manipulations of the equation, the ratio of the residual strength to the overburden stress is expressed as function of the following parameters,

$$\frac{\tau_f}{\gamma H_o} = f(\frac{L_i}{L_o}, \frac{L_f}{L_o}, \frac{H_o}{L_o}, \beta) \ . \tag{6}$$

Herein, it is to note that the residual strength ratio, $\tau_f/\gamma H_o$, which can be calculated from the above simple analysis, is equivalent to the ratio of the residual strength to the effective overburden stress, τ_f/σ'_v, which in turn can be obtained from laboratory triaxial tests, as follows,

$$\frac{\tau_f}{\gamma H_o} \cong \frac{\tau_f}{\sigma'_v} \ . \tag{7}$$

On the other hand, the above equation (6) implies that given the geometry of the problem, the run-out distance ratio, L_f/L_o, can be estimated from the initial distance, L_i/L_o, based on the residual strength ratio, $\tau_f/\gamma H_o$.

SIMPLE METHOD OF LABORATORY TRIAXIAL TESTING

Test apparatus and soil samples

The residual strength of soils plays an important role in estimating the run-out distance of collapsed soils during earthquakes. The collapse of soils during earthquakes might be triggered at an almost saturated zone. However, the soils subjected to run-down and run-out during earthquakes are not necessarily saturated. Therefore, the residual strength of soils in unsaturated states would serve as a key parameter determining the "sliding" and "spreading" phases of slope failures. These processes are known to occur rapidly, as have been observed during recent earthquakes, it would be reasonable to assume that there would be little time for soils to change their volume in the course of such rapid movement. In order for a potentially contractive soil to keep its volume unchanged during shearing, the overburden stress acting initially on the soil skeletons needs to be reduced, and instead, the portion of the initial overburden stress must be temporarily carried by other substances such as air-containing water or dust-containing air existing in the voids. Thus, it is assumed in the present study that the volume of even partly saturated soils is maintained almost unchanged during shearing and the initial overburden stress is reduced during shearing.

Based on the assumptions described above, a simple laboratory triaxial testing method is introduced in the previous study, (Tsukamoto and Ishihara 2005). The details of the test apparatus and test procedures can be found in the previous paper, (Tsukamoto and Ishihara 2005). The grain size distributions of soils from Takamachi-Danchi are shown in Fig. 8.

Test results

The soil samples prepared by the method of wet tamping with varying water contents were isotropically consolidated to an effective confining stress of σ'_o = 98 kPa. They were then subjected to axial compression while the effective confining stress was gradually reduced. The

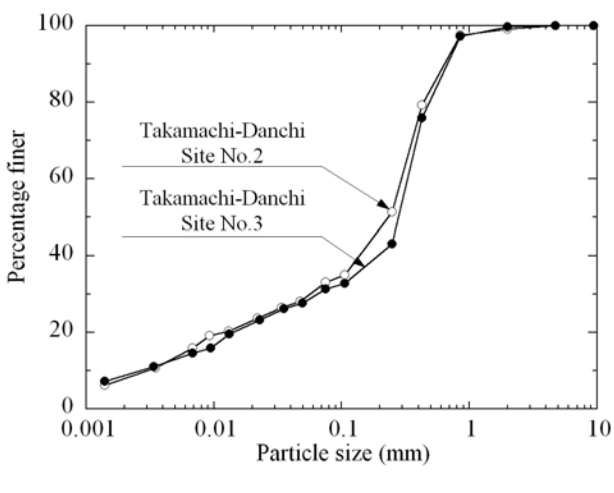

Fig. 8: Grain size distributions of soils used in the tests

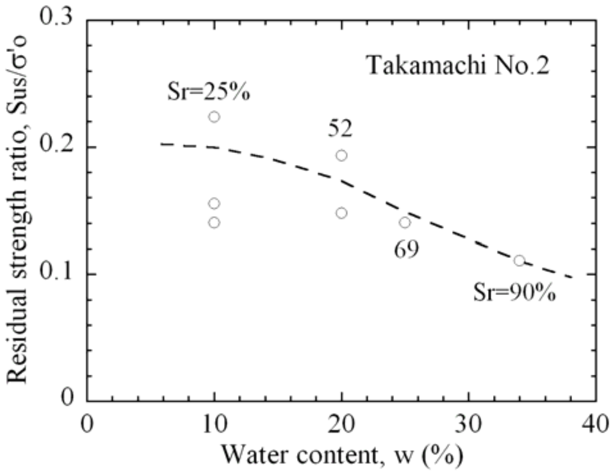

Fig. 9: Plots of residual strength ratio against water content, (Takamachi No.2)

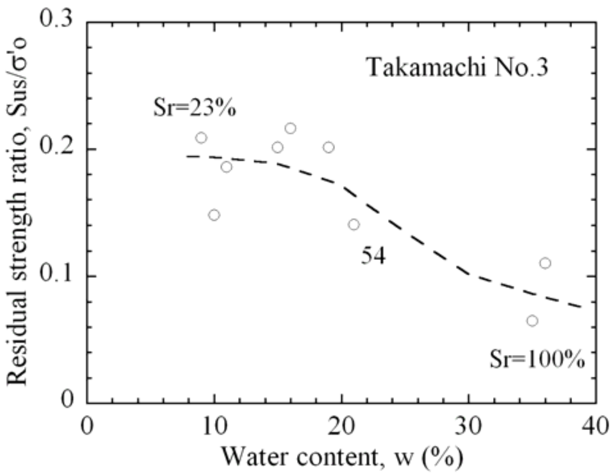

Fig. 10: Plots of residual strength ratio against water content, (Takamachi No.3)

residual strength was determined as $S_{us} = q/2 = (\sigma'_1 - \sigma'_3)/2$, at the time when the axial compression reached a state where the deviatoric stress tended to stay constant. The values of the residual strength ratio S_{us}/σ'_o thus obtained are plotted against the water content w in Figs. 9 and 10, for the samples of Takamachi No.2 and No.3.

RUN-OUT DISTANCE AND RESIDUAL STRENGTH

From the simple analysis described above, it is possible to calculate the "run-out" distance from the initial "sliding" distance based on the residual strength of collapsed soils, given the initial geometry of the problem, such as a slope angle, β, and an assumed length and height of a soil block, H_o and L_o. In other words, it is possible to produce a chart correlating the "run-out" distance ratio, L_f/L_o, with the initial "sliding" distance ratio, L_i/L_o, as function of the residual strength of soils at given values of β and H_o/L_o. Figures 11, 12 and 13 show such plots of the correlation for the cases of Takamachi-

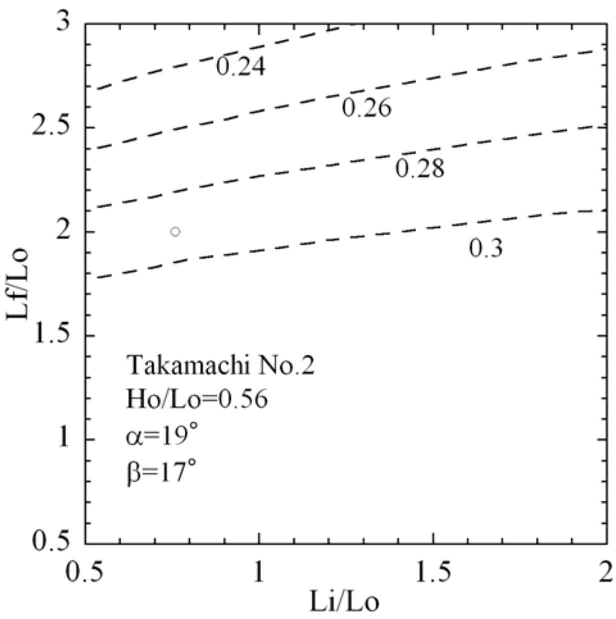

Fig. 11: Plots of L_i/L_o against L_f/L_o, (Takamachi-Danchi No.2)

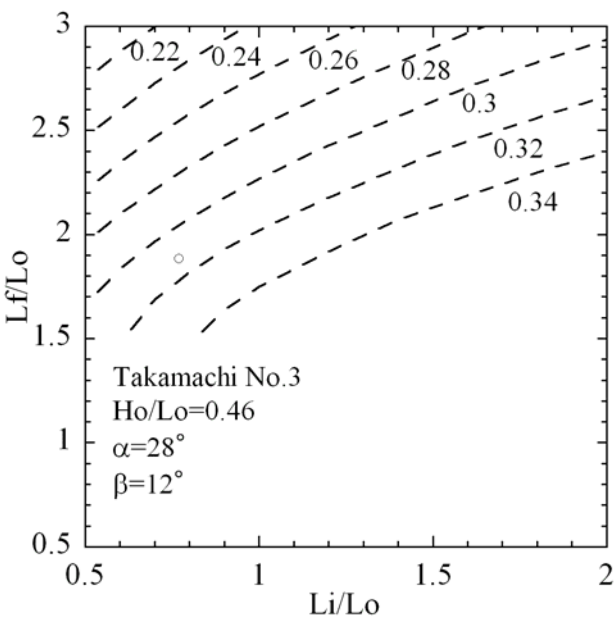

Fig. 12: Plots of L_i/L_o against L_f/L_o, (Takamachi-Danchi No.3)

Danchi. It is seen that a number of contours along which the residual strength is equal can be drawn. On these diagrams, the values of L_f/L_o and L_i/L_o inferred from the case studies shown in Figs. 2, 3 and 4 can also be plotted. Therefore, by comparing the analytically-obtained equal contours of the residual strength and the data plots of the field case studies as shown in Figs. 11, 12 and 13, it is possible to infer the values of the residual strength, which are supposed to develop in the case studies. It is found that the residual strength back-calculated from the simple analysis is greater than that obtained from the laboratory triaxial tests. This might be due to the fact that the

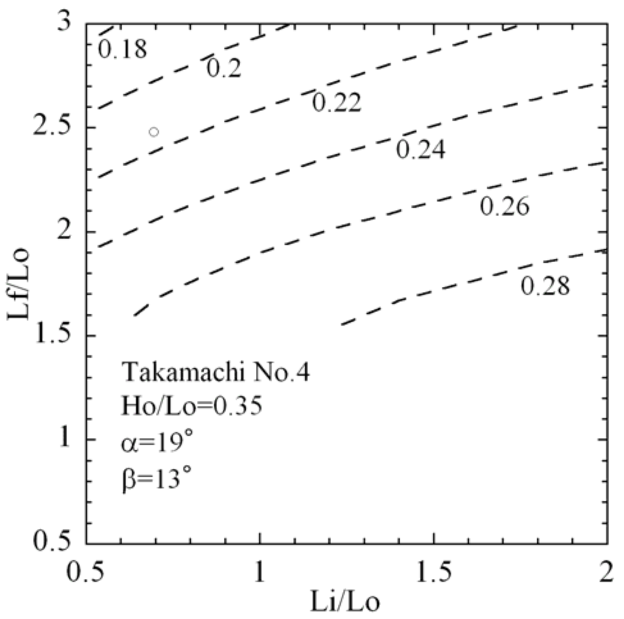

Fig. 13: Plots of L_i/L_o against L_f/L_o, (Takamachi-Danchi No.4)

reclaimed deposits have actually pushed away and run down the slopes in the field, which was not taken into account in the simple analysis.

CONCLUSIONS

The run-out distances of slope failures involving the backfills of reclaimed soil deposits behind retaining walls were examined, which occurred at the periphery of the residential districts, Takamachi-Danchi, in Nagaoka city during 2004 Niigata-ken Chuetsu Earthquake. The slope failures were assumed to consist of two phases, "sliding" and "spreading". The run-out distances of such slope failures were inferred from the field survey and were compared with those calculated from the simple analysis based on the energy principle. From the comparisons between the run-out distances observed and thus calculated, the residual shear strength of soils involved in such slope failures was back calculated and was compared with the laboratory triaxial test results.

ACKNOWLEDGEMENTS

The authors would like to thank the past students of Tokyo University of Science, M. Nakamura, S. Nakamura, R. Igarashi and S. Koh for their conduct of the laboratory tests reported in the present paper. Thanks are also extended to Dr. S. Otsuka and Dr. H. Toyota of Nagaoka University of Technology and Science, for their generous support in obtaining soil samples in Nagaoka.

REFERENCES

[1] Tsukamoto, Y. and Ishihara, K. (2005) "Residual strength of soil involved in earthquake-induced landslides", *Proceedings of Geotechnical Earthquake Engineering Satellite Conference*, Osaka, Japan, 10/September/2005, TC4-ISSMGE, pp.117 – 123.

Impact of Sediment Yields from Landslides and Debris Flows after Chi-Chi Earthquake on Hydropower Plants in Ta-Chia River and the Strategies of Geohazards Mitigation

S.H. Yu[1], S.D. Yang[1], C.F. Wang[1], C.H. Chiao[1], L.T. Hwang[1], J.C. Chern[2], C.T. Cheng[2], Y.L. Chang[2], C.Y. Ku[2], S.M. Shu[2], S.J. Chiu[2], Y.S. Lin[2]

[1]*Taipower Company, Taipei, Taiwan, R.O.C*

[2]*Sinotech engineering consultants, Inc., Taipei, Taiwan, R.O.C*

Abstract

The landslides and debris flows occurred in the Ta-Chia river watershed after Chi-Chi earthquake and the subsequent typhoons caused severe damages to the hydropower generation facilities of TPC (Taiwan Power Company). In order to assess the impact of sediment yields from landslides and debris flows on the hydropower generation system and to investigate the strategies of mitigating the geohazards, quantitative assessment was conducted by using aerial photos and satellite images obtained at 6 stages of major earthquake and typhoon events. Based on the result of this investigation, the total sediment yields are around 71 million m^3 in the catchment from Techi to Kukuan, with 60% of the total amount from Chi-Chi events and the rest from the subsequent typhoon events. Considering the sediment yields will be generated in the future heavy rainfall, the strategies of mitigating the geohazards, including slope protection, river channel stabilization, access road for reconstruction and long-term monitoring, are also discussed.

Keywords—*Chi-Chi earthquake, landslides, debris flows, hydropower*

INTRODUCTION

Water resource in Ta-Chia river basin in central Taiwan have most efficiently been used for power generation and water supply. Six reserviors , including Techi, Chingshan, Kukuan, Tienlun, Maan, Shihgang (as shown in Fig. 1) were constructed along the Ta-Chia river for power generation since 1960s by Taiwan Power Company (TPC). Seven hydropower platnts, including Techi, Chingshan, Kukuan, Tienlun (including New Tienlun), Maan, Houli and Sheliao (as shown in Fig. 1) and 21 generator which total installation capability of 1.1 million KW, and annual power generation of 26 Gwh, play a very important role in the hability of peek power supply of TPC.

After the catastrophic Chi-Chi earthquake, the subsequent typhoons, including Toraji typhoon in 2001, Mindulle typhoon and Aere typhoon in 2004, and Haitang typhoon in 2005, caused wide spread landslides. The huge volume of colluviums were flushed into riverbed. Debris flows were also occurred in the tributaries of Ta-Chia river and deposited as fan shapes in river junction which slited up the river channel and raised the flood level. these geohazards destroryed most of the infrustuctures, especially the hydropower generation facilities of TPC.

In order to assess the impact of the huge ammount of sediment yields from landslides and debris flows on hydropower system and to investigate the stratagy of mitigation, a comprehensive investigation program on landslides and transportation of sediment yields in the river channel was conducted. This paper presents the result of these studies.

METHODOLOGY

In order to evaluate the landslides and transportation of sediment yields in the riverbed, aerial photos and satellite images of 6 stages were used. They included NO.1 stage before Chi-Chi earthquake, NO.2 stage after Chi-Chi earthquake, NO.3 stage after Toraji Typhoon, NO.4 stage after Mindulle Typhoon, NO.5 stage after Aere Typhoon, and NO.6 stage after Haitang Typhoon. The steps of assessment are as follows:

(1) To search and collect the topography, geology, climate information and reference for the background understanding and field survey planning.

(2) To make the digital terrain model (DTM) and rectify aerial photos for each stage, and use these information to evaluate the landform changes and volume difference of sediment yields.

(3) To recognize and detect the hazard area of landslide and debris flows in the Ta-Chia watershed, and quantify the landslides area and the volume of sediment yields from landslides and debris flows.

(4) To evaluate the impact of great amount of sediment yields and to suggest the strategies for mitigating the hazards on the reservoirs, and power plants in Ta-Chia river.

The dates of the remote sensing images took and the disastrous events occurred are shown in Fig. 2.

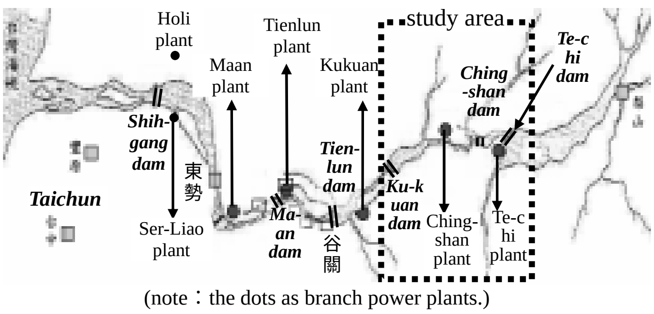

(note：the dots as branch power plants.)

Fig.1 The six reservoirs and seven branch power plant along Ta-Chia river

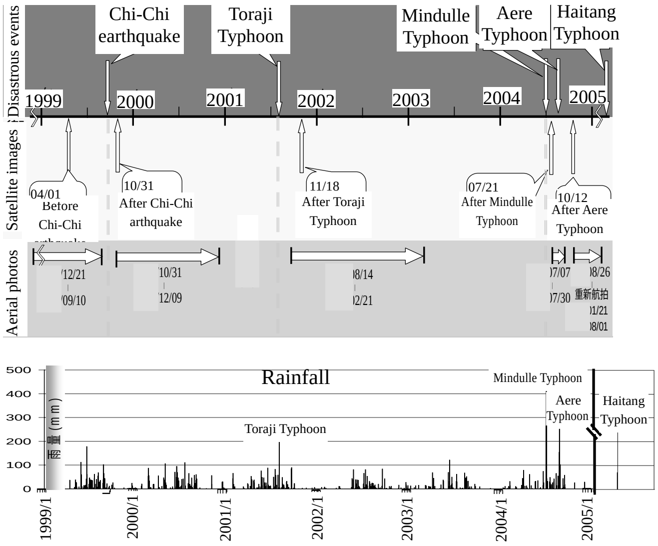

Fig.2 The dates of the remote sensing images took and the disastrous events occurred

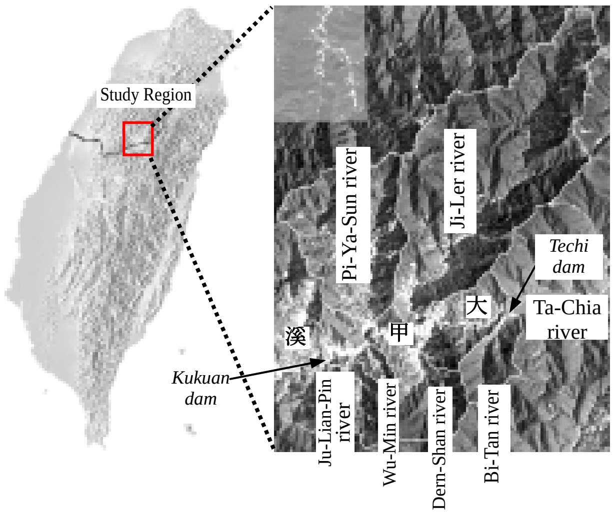

Fig.3 The study region

ENVIRONMENT AND BACKGROUND

A. Topography and Geology

1) ***Topography***: The study region is located at the Her-pin village of Taichung County, the watershed is between Techi dam and Kukuan dam as shown in Fig. 3. The main river channel length in the study region from upstream to downstream is 13.87km and the catchment area is 181.6km^2. The slope of the Ta-Chia river bank is very steep with average slope angle more than 40 degrees. The riverbed elevation range from 950 to 1,500m. Dasyueshan mountain (3,530m) in the northern, the Tajanshan mountain (3,594m) in the eastern, and Bikudashan mountain (3,341m) are the highest mountains in the study region. There are 6 tributories in the catchments of this study region, which are Ju-Lian-Pin river, Wu-Min river, Pi-Ya-Sun river, Dern-Shan river, Ji-Ler river, and Bi-Tan river.

2) ***Geology***: The rock formation of this study region belonged to the central portion of Syueshan Mountains. The strata of the study region are Tachien Sandstone layer in Eocene epoch age and Chiayang layer from Eocene epoch to Oligocene epoch age. The Tachien sandstone strikes in northeastern to southwestern direction, and the lithology of them is almost metamorphic sandstone with thick layer, granular texture and blocky failure type. But some portions are shown with slate and metamorphic shale alternately. Chiayang layer and Tachien sandstone layer always reveal alternately in the Eocene epoch age. The lithology of Chiayang layers is thick layered, black or dark gray slate. There are sometimes fine sandstone revealed between the layers, and the cleavage also well developed in Chiayang layers.

B. Hydrology and meteorology

1) ***Temperature***: This region is located at the northern part of Tropic of Cancer, and climate type is subtropical zone. The temperature decreases with the elevation, and the hottest season is in July and the coldest season is in January. The average of annual temperature is between 15.2 to 22.6 degrees centigrade.

2) ***Rainfall***: The annual rainfall is about 2,500 to 3,000mm in study region. The rainfall is almost concentrated in May to September, and it holds more than 75% of total annual rainfall. Most of the rainfalls are associated with typhoons. More than 500mm of rainfall per day is quite often during typhoon. The dry seasons begin in October till the next April, and just hold 25% of total annual rainfall.

3) ***Discharge***: Table 1 shows the measured discharges at the three major control points (Shihgan, Tianleng, Kukuan) of Ta-Chia river. The peak discharge is 3,752cms in 200 year return period in Kukuan.

Table 1 The discharges of the three major control points of Ta-Chia river

control points / return period	Shihgan	Tianleng	Kukuan
200 year	9,800cms	8,840cms	3,752cms
100 year	8,800cms	8,000cms	3,360cms
50 year	7,600cms	6,900cms	2,965cms
20 year	6,200cms	5,600cms	2,439cms
10 year	5,000cms	4,500cms	2,033cms
5 year	3,800cms	3,400cms	1,609cms
2 year	2,200cms	1,980cms	969cms

TRIGGERING FACTORS OF LANDSLIDE

A. Large Earthquakes

The largest earthquake within 50km of this study from the period of 1900 to 2005 is Chi-Chi earthquake, magnitude M_W7.6, and focal depth 8km. The magnitude of some after shock was also greater than M_W6.0. The study region is located on the hanging wall of Chelungpu fault rupture area. Therefore, in the whole study region, the intensity of ground motion was almost higher than 250gal. Chi-Chi earthquake triggered a lot of landslides. Fig. 4 is the spot image of the study region which shows the huge amount of landslides triggered by Chi-Chi earthquake, and most of the landslides occurred on the both sides of Ta-Chia river bank. Some loose rocks maybe not slide immediately during the Chi-Chi earthquake, but slides occurred during the subsequent heavy rainfalls.

B. Heavy Rainfalls

Huge amount of sediment yields were never occurred before the Chi-Chi earthquake, even during the heavy rainfall occurred in the study region. After Chi-Chi earthquake, the heavy rainfalls during Toraji typhoon in 2001, Mindulle typhoon in 2004, Aere typhoon in 2004 and Haitang typhoon in 2005, caused most severe sediment yields. The rainfall information observed at Shin-Po-Kon station of those typhoon events are described as follows:

(1) Toraji typhoon occurred during 2001/07/28-2001/07/31. The maximum daily rainfall is 234mm, and cumulated rainfall in three days 239mm.
(2) Mindulle typhoon occurred during 2004/06/28-2004/07/03, The maximum daily rainfall is 617.5mm, and cumulated rainfall in three days 1,000mm.
(3) Aere typhoon occurred during 2004/08/23-2004/08/26, the maximum daily rainfall is 314mm, and cumulated rainfall in three days 411mm.
(4) Haitang typhoon occurred during 2005/07/16-2004/07/20, and cumulated rainfall in three days 335mm.

After Chi-Chi earthquake the most disastrous typhoon was Mindulle typhoon, which triggered lots of new landslides and debris flows of tributories. The sediment yields silted up the channel of Ta-Chia river and made the riverbed become wider than before (as shown in Fig. 4). During Mindulle typhoon, the cumulative rainfall was more than 1,000mm, the maximum discharge was 2,104cms, but the maximum drainage of the Techi Dam was just 1,330cms, the water level of the Techi reservoir raised up from 1,397.62m to 1,407.16m. The capability of flood discharge was retained in Techi reservoir totally 3.886 hundred millions m^3. Therefore, hazard mitigation of the downstream is still an important issue in the near future.

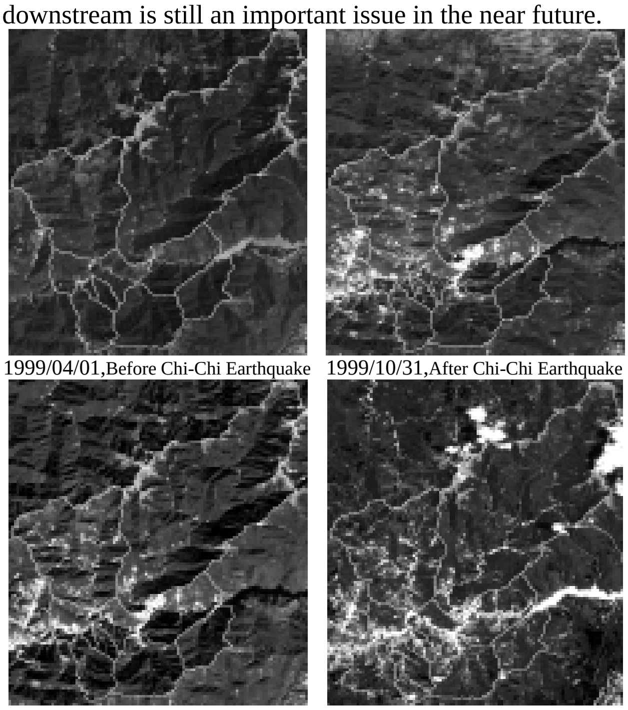

1999/04/01,Before Chi-Chi Earthquake 1999/10/31,After Chi-Chi Earthquake

2001/11/18,After Toraji Typhoon 2004/07/21,After Mindulle Typhoon

Figure 4 The SPOT images of the study region

INVESTIGATION OF GEOHAZARDS AND DAMAGES

In order to describe the damage of the hydraulic facilities between Techi dam and Maan dam during those disastrous events, some photos of damage to the facilities of different stages are shown in Fig. 5 to 8. The spillway gate of Techi reservoir was silted up by the sediment yield of debris flow of Bi-Tan river during Mindulle typhoon as shown in Fig. 6. After Mindulle typhoon and Aere typhoon, the sediment yields from the debris flows of Dern-Sang river and Ji-Ler river, and the talus of landslides on the both sides of Ta-Chia river were transported to the downstream area of the main channel. Hence, the riverbed in front of the Chingshan switchyard was raised by more than 15m and the switchyard was damaged by flood and mud-rock flow as shown in Fig. 7. The Chingshan underground powerhouse near the switchyard was still submerged under water. The riverbed adjacent to the Kukuan underground powerhouse had risen by more than 30m after those heavy rainfalls as shown in Fig. 8a~8d. After heavy rainfall in June, 2000, the riverbed raised by more than 10m and the riverbed was very close to the outlet of tailrace tunnel as shown in Fig. 8b. The heavy rainfall of Toraji typhoon also moved a lot of sediment, and it raised the riverbed by more than 9m further. It also filled up the outlet of tailrace tunnel completely, and the level of riverbed reached the access tunnel of Kukuan powerhouse as shown in Fig. 8c. After Mindulle typhoon in 2004, it also raised the riverbed by additional 12m, and it destroyed the conneting suspension bridge to the powerhose. The access tunnel of Kukuan underground powerhouse was totally filled by the sediment and the powerhouse was flooded. After a series of disastrous events, the riverbed adjacent to the Kukuan underground powerhouse was totally raised by more than 30m.

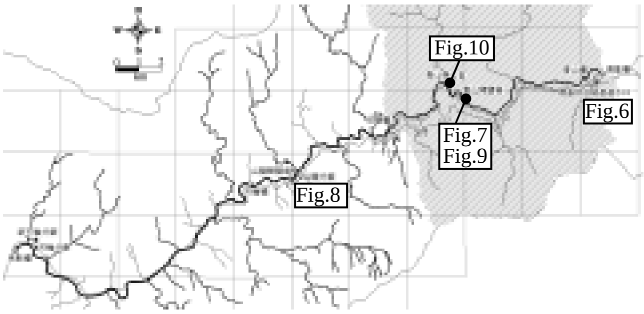

Fig. 5 Photo index of damage facilities.

Fig.6 Debris flow of Bi-Tan river in front of Techi dam.

Fig.7 The riverbed in front of the Chingshan Switchyard was raised up more than 15m.

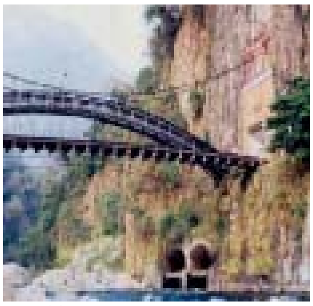

(a)Before Chi-Chi Earthquake

(b)After Chi-Chi Earthquake(1999)

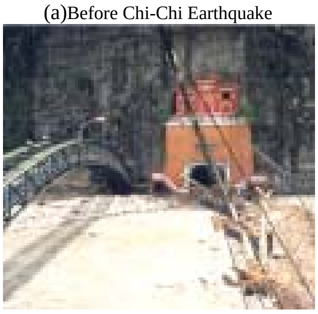

(c)After Toraji Typhoon(2001)

(d)After Mindulle Typhoon(2004)

Fig.8 The riverbed changed in front of Kukuan power house after the disastrous events.

RECOGNITION OF GEOHAZARDS DISTRIBUTION IN AERIAL PHOTOS

The aerial photos were adopted for recoganizing the geohazards at different stages. It is very useful to identify the topographic migration in wide area. Chingshan switchyard and Chingshan office of TPC were chosen as demonstration examples and the aerial photos, shown as Fig. 9 and Fig. 10, illustrate the increasing deposit condition of the riverbed in front of them.

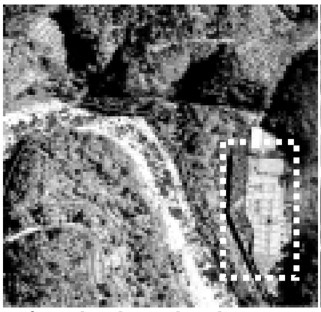

Before Chi-Chi Earthquake(1998)

After Chi-Chi Earthquak(2000)

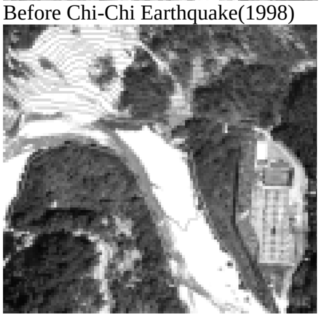

After Toraji Typhoon(2001)

After Mindulle Typhoon(2004)

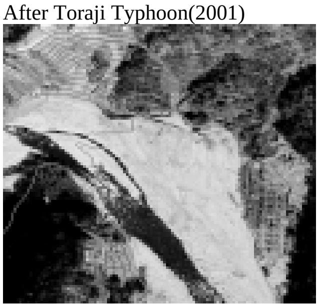

After Aere Typhoon(2005.01)

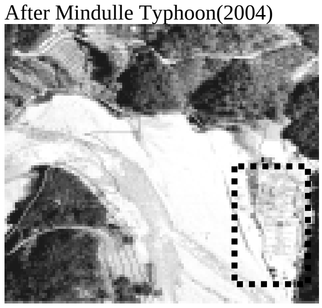

After Haitang Typhoon(2005.08)

Fig.9 The hazards of landslides and river channel silted nearby the Chingshan switchyard

Fig. 9 indicates the hazards of landslides and river channel silting up near the Chingshan switchyard. The width of channel was 50m and the height from riverbed to the terrace of Chingshan switchyard was more than 15m before 1999's Chi-Chi earthquake. But the width of channel became 160-200m and the level of riverbed raised to over the terrace of Chingshan switchyard after 2005's Haitang typhoon. The facilities in the Chingshan switchyard were also damaged by landslides triggered in heavy rainfalls. Fig. 10 reveals that the debris flows of Pi-Ya-Sun river striked the office of Chingshan power plant. The sediment yields from Pi-Ya-Sun river made an alluvium fan, which almost silted up the river channel. The riverbed of Ta-Chia river in front of the office was raised by more than 20m and the width of the channel increased from 40m to 150m. Additionally, the channel of Pi-Ya-Sun river was pretty small before Chi-Chi earthquake, the width of the channel became more than 200m through a series of heavy rainfalls. The geomorphology of the river changes quickly out of our imagination.

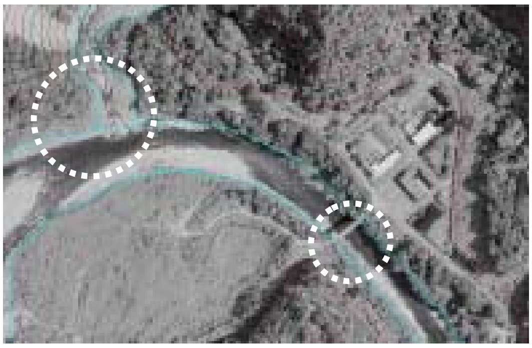

Before Chi-Chi Earthquake(1998)

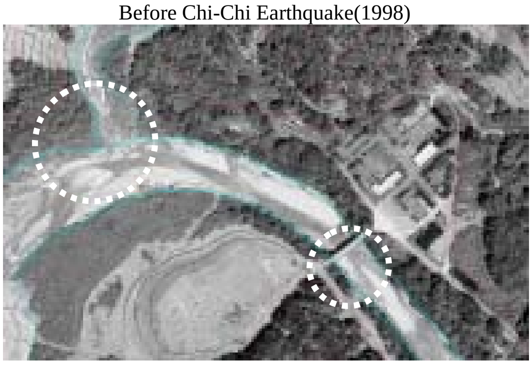

After Chi-Chi Earthquake(2000)

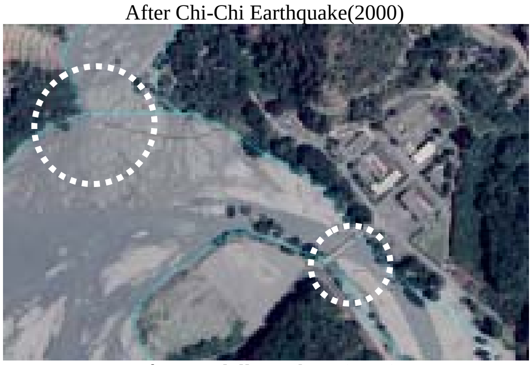

After Mindulle Typhoon(2004)

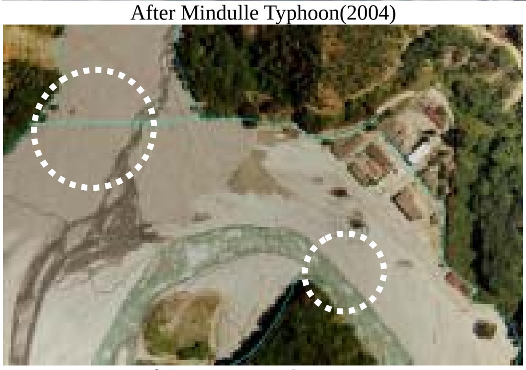

After Haitang Typhoon(2005)

Fig.10 The debris flows of Pi-Ya-Sun river striked the office of Chingshan power station.

ELEVATION CHANGES IN DTM FOR DIFFERENT STAGES

In order to quantify the volume of the geohazards, The DTMs of different stage were used for analyzing the elevation changes. We also took Chingshan switchyard and Chingshan office of TPC as examples. The results of the elevation change in DTM are shown in Fig. 11 to Fig. 13, the blue color means the deposited or silted area and the red color means the erosion or slide area.

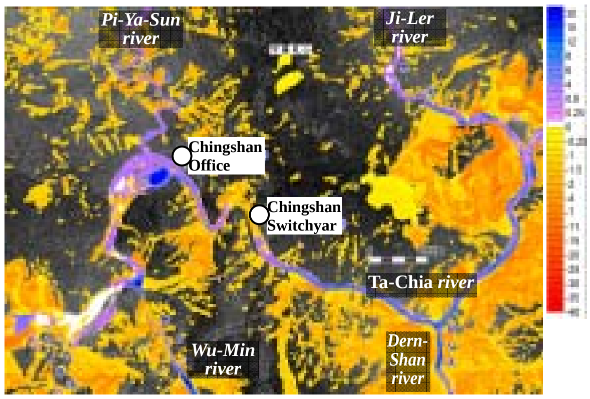

Fig.11 The elevation changes in the DTMs caused by Chi-Chi earthquake.

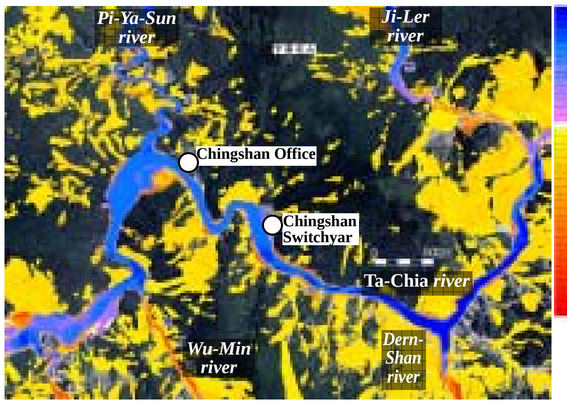

Fig.12 The elevation changes in the DTMs caused by Mindulle typhoon.

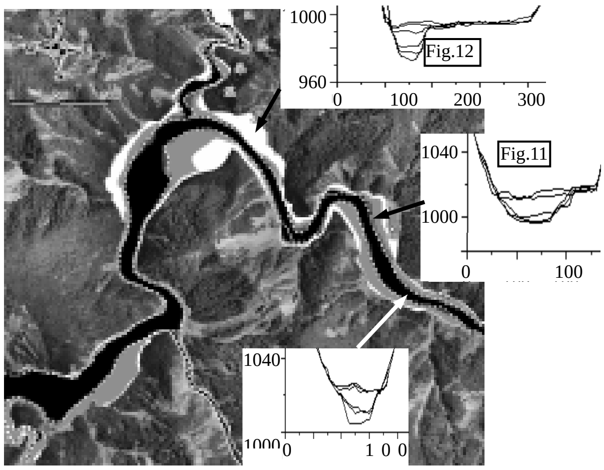

Fig.13 The river cross-sections in the front of Chingshan switchyard, and Chingshan office.

Fig. 11 shows the elevation changes in the DTMs from prior to Chi-Chi earthquake and afterward. The thickness of landslides is almost in the order of 1-2m. However, some areas of the thickness of landslides were over 10m. Debris and rock fall are the typical cases of mass movement in this study region because of the steeply slopes and the well developed joints of rocks. The debris and rock wedges almost directly fall into the riverbed of Ta-Chia river as well as in every distributary such as Dern-Shan river shown in the southeast part of Fig. 11. Hence, there were amount of talus on the toes of landslide slopes. The sediment yields transportation was not so severe in this stage. Fig. 12 shows the elevation changes in DTMs from Mindulle typhoon event. The taluses on the riverbed of tributaries were almost transported into the junctions. It made the riverbed of Ta-Chia river raising more than 10m on average in this region. The maximum deposit area was in the junction of Dern-Shan river and Chingshan switchyard. Extensive sliding aslo observed in the slopes on both sides of Ta-Chia riverbank near the Chingshan switchyard, because the raised riverbed and the flood eroded the toes of the slopes. Fig. 13 shows the change in river cross-sections in the front of the outlet of ventilation tunnel, Chingshan switchyard, and Chingshan office of TPC. Mindulle typhoon was the most adverse events which transported huge amount of sediment yields into Ta-Chia river.

Fig. 14 and Fig. 15 show the elevation changes along the riverbed, caused by Chi-Chi earthquake and Mindulle typhoon. After Chi-Chi earthquake, the elevation in the front of Chingshan office changed slightly, but the upstream of the switchyard increased by more than 5m. After Mindulle typhoon, maximum elevation change of the riverbed was situated at the front of outlet of ventilation tunnel. The change of elevation was more than 20m, and it seems that the huge sediment yields came from the debris flow of Dern-Shian river and the talus on the riverbank of Ta-Chia river.

Fig. 16 shows the cumulated elevation change from Chi-Chi earthquake to Hi-Tang typhoon, and the most significant changed area is situated at the vicinities of Chingshan switchyard. Furthermore, the elevation was changed slightly above the junction of Dern-Shian river.

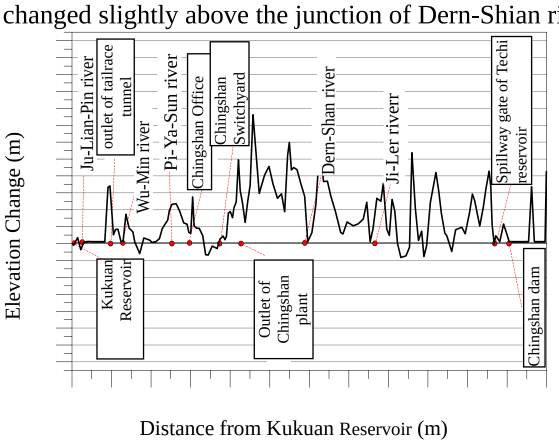

Fig.14 The elevation changes along the riverbed of Ta-Chia river caused by Chi-Chi earthquake.

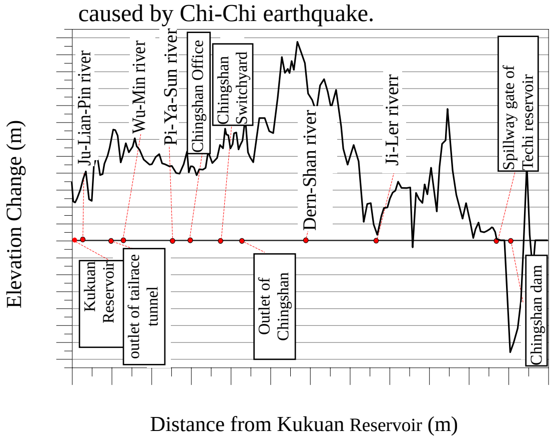

Fig.15 The elevation changes along the riverbed of Ta-Chia river caused by Mindulle typhoon.

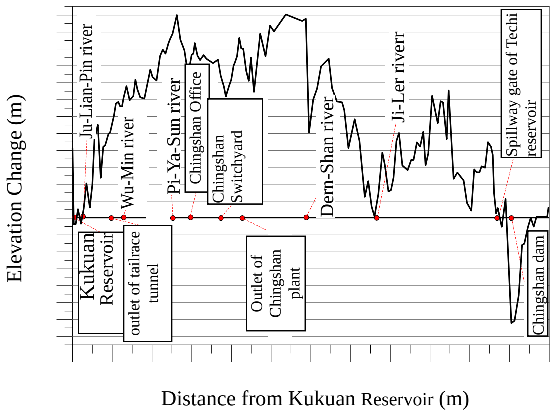

Fig.16 The totally elevation change from Chi-Chi earthquake to Hi-Tang typhoon.

LANDSLIDE RECOGNITION AND STATISTICS

A. Landslide Recognition

The aerial photos were used to identify the landslide hazard area, and the landslides at different stages were digitized in GIS for statistic purpose. The left hand side of Fig. 17 shows the landslides triggered by Chi-Chi earthquake with black color, the right hand side of Fig. 17 shows the increased landslides triggered by a series of heavy rainfalls with black color. However, it is obvious that Chi-Chi earthquake triggered the great majority of landslides.

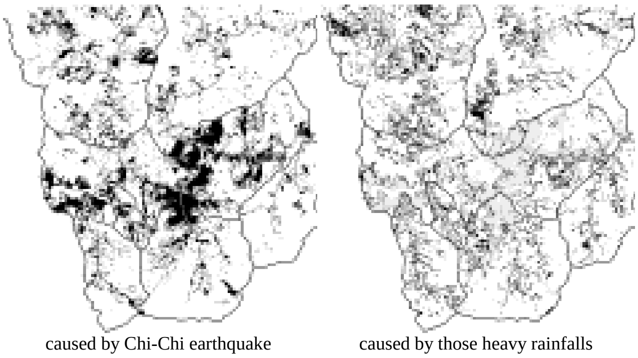

Fig.17 The left side shows the landslides triggered by Chi-Chi earthquake with black color, the right side shows the increased landslides triggered by a series of heavy rainfalls with black color.(The old landslides is gray.)

B. Landslides Statistics

*1)**Total landslide areas and newly added landslide areas**:* The summation of the whole landslide areas within each watershed are shown in Fig. 18. It reveals that on both sides of Ta-Chia river, and the Pi-Ya-Sun river generated the largest amount of landslides. Most landslides were triggered during Chi-Chi earthquake, even though Toraji typhoon caused some new landslides. But the total landslide areas were reduced by the recovery of vegetation. After Mindulle typhoon, the landslide areas of whole watersheds increased again, but the total areas are still less than that after Chi-Chi earthquake. The total landslide areas decreased after the last disastrous event, it seems to show a stabilizing trend. After Mindulle typhoon, the northern portion of the study region, there were the larger landslide areas on the both watersheds of Pi-Ya-Sun river and Ji-Ler river, but landslide areas of the other watersheds never expanded after Chi-Chi earthquake. Fig. 19 shows the increased landslide areas of each event, and the summation of the increased landslide areas triggered by difference events is around 24 million m^2. Furthermore, the total area of the increased landslides became smaller and smaller, it may indicated the geological condition would be more stable in the future.

***2)The thickness and volume of landslides*:** Fig. 20 and Fig. 21 show the volume and the thickness of landslides in each watershed, which were obtained by the calculation from DTMs. It reveals that the volume of landslide triggered by Chi-Chi earthquake is 5 times the volume of the landslide triggered by whole typhoon events. The average thickness of landslides of each event became smaller and smaller. When the rocks fall down and deposit as taluses, the sliding material would be inflated. If the inflated rate was suggested to be 20%, Ta-Chia main river and its tributaries had generated the volume of landslide are 17 millions m^3 and 32 millions m^3 individually (lower bound estimation), respectively. Furthermore, if we assumed the inflated rate to be 33% and consider the error of DTM, Ta-Chia main river and its branch rivers had generated the volume of landslide are 24.3 millions m^3 and 46.7millions m^3 individually (lower bound estimation), respectively. In conclusion, the total volume of landslides within the watershed between Techi dam and Kukuan dam was approximated from 50 milions m^3 to 72 millions m^3.

***3) The sediment yields remain in the tributaries*:** After Chi-Chi earthquake the sediment yields were continually transported to the tributary junction and the main riverbed of Ta-Chia river during the subsquent heavy rainfalls. Hence, the riverbed is still raised up because of the landslides triggered by those disastrous events still remained within the watershed of every branch rivers. However, those sediment yields would move into the riverbed of Ta-Chia river and damage the hydropower facilities in the near future. Therefore, the volume of sediment rested in the watershed of every tributaries were evaluated by using DTMs.

The total sediment yields in the main river channel are 11 millions m^3 based on DTMs. It was suggested to be bed load. If the ratio of suspend load and bed load is assumed 7 to 3, the suspend load moved out from Kukuan dam would be 26 millions m^3. The total load is 37 millions m^3. If the rock inflated rate is assumed as 20%, the sediment remained in the branch rivers are 12.2 millions m^3, and it is about 38% of total landslide volume. Furthermore, If the rock inflated rate is assumed as 33% and considers the elevation error of DTM to be 0.5m, the sediment remained in the branch rivers are 34.4 millions m^3, and it is about 74% of total landslides volume. In other word, there are 38-74% of the total landslide volume which remains in the tributaries, and the volume is approximately 12.2-34.4 millions m^3.

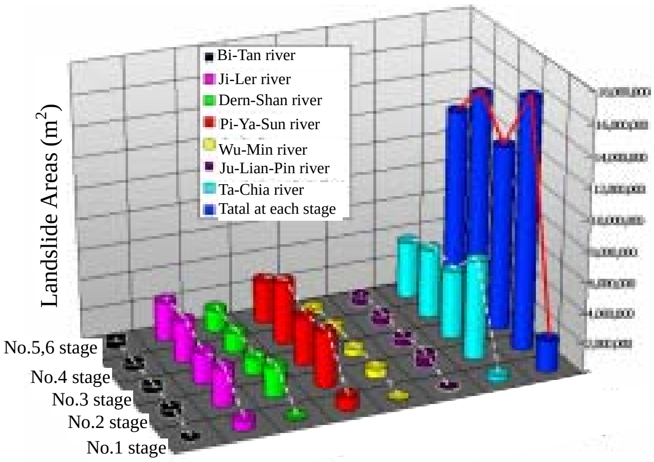

Fig.18 The summation of the whole landslide areas within each watershed.

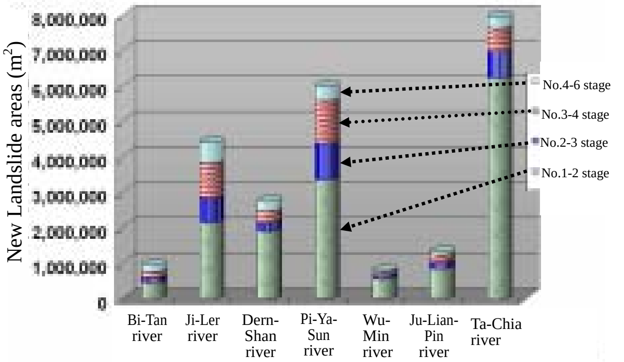

Fig.19 The new generated landslide areas of each event.

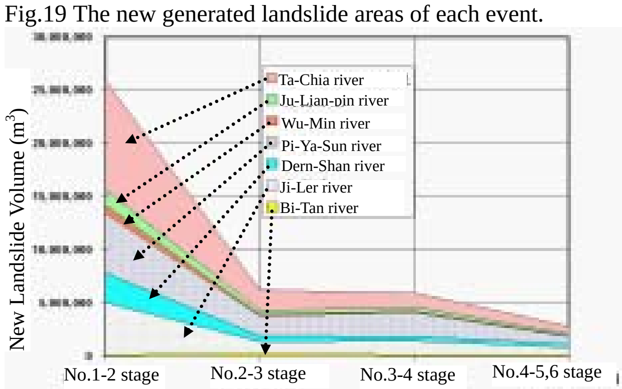

Fig.20 The volume of landslides in each watershed (not include the inflated rate).

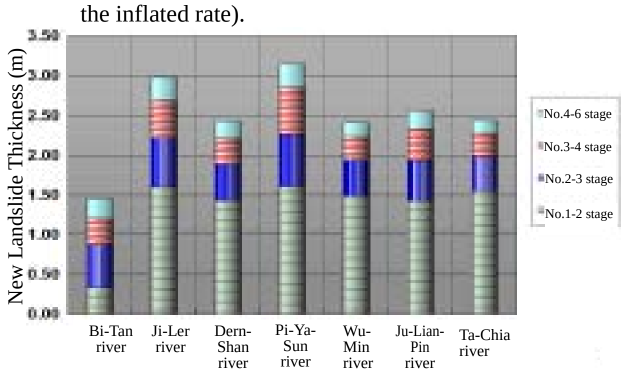

Fig.21 The thickness of landslides in each watershed.

THE CHARACTERISTIC OF GEOHAZARDS

A. Landslides

Joints and cleavages of rock slopes are well developed along the Ta-Chia river. The slope angle of Ta-Chia river in this study region are very steep, and the range of the inclination of the slopes are more than 45 degrees. It is a typical V shape river valley. Therefore, the landslide types of this study region are almost rock-falls, debris avalanches, wedge translational slides. The waste materials of road construction also contributed large amount of slide volume. There were some gravel layers on the higher terrace along Ta-Chia and its tributaries. Because of the topography of them were very steep and the gravel layers cemented poorly, therefore it caused serious landslides after Chi-Chi earthquake. The toes of the slopes always became unstable when the toes were eroded by high flood level. The total volume of landslides triggered by Chi-Chi earthquake and the subsequent rainfalls were esstimated to be arround 70millions m^3. Among them, 60% of total volume is delieved to be triggered by Chi-Chi earthquake and the rest by the typhoons events.

The rock-falls. The debris avalanches.

The waste materials. The gravel layer.

Joints and cleavages are well The wedge translational slide

Fig.22 The landslide types of this study region.

B. Debris Flows

Huge amount of sediments were produced by landslides after the strong shaking of Chi-Chi earthquake and subsequently transported from the sub-watersheds to Ta-Chia main river during heavy rainfalls. Almost all of the sediment yields were transported by debris flows, and most of debris flows caused by Mindulle typhoon. The alluvium fans of debris flows at the junctions were always silted up the Ta-Chia main riverbed. The height of the highest alluvium fans of debris flows in the watershed of Dern-Shan river is more than 25m. Bi-Tan river and Pi-Ya-Sun river are the second one and the third one. Pi-Ya-Sun river will be the river with highest risk of debris flows because of its location very closed to the Chingshan switchyard and office.

C. Riverbed deposited and silted

The width of the river channel of Ta-Chia main river and its branches became wider than that before Chi-Chi earthquake. From Techi dam to Kukuan dam, the riverbed of Ta-Chia river were raised up more than 10m in average. The highest portion of riverbed raised up with more than 22m was located at Chingshan switchyard.

THE STRATEGIES OF MITIGATING THE GEOHAZARDS

From the resluts obtained in the study, it is difficult to handle the huge amount of sediment yields remained in the main river channel. It would be impratical to remove the sediement materials considering large quantities of material will remain in the tributary watersheds, which would be transported to the main river channel in the near future heavy rainfall events. The stratergies of mitigating the geohazards for the power generation facilities are as follows:

(1) The landlides distributed widely in the watersheds, and most of them were not easily accessable for remediation. It is impossible to stabilize all of the sliding slopes. Hence stabilizing the slopes with direct threat to the major facilities would be a more rational approach.

(2) The debris flow of Pi-Ya-Sun river threatens the Chin-Shan office and switch yard. A series of sabo dam along the Pi-Ya-Sung river should be constructed and the sediment fan in the river junction removed.

(3) According to the policy of the central goverment, the highway No.8 will not be reconstructed in the foreseeable future due to the unstable slopes. construction of temporary road along the Ta-Chia riverbed appears to be the only viable alternative.

(4) It is expected that large quantity of sediment yields will be produced in the future heavy rainfall events. To preidict the gravity of sediment yields and the change of riverbed, which has direct impact on the rehabilitation of power generation facilities, it is necessary to rebuild the monitoring stations for collecting the information of rainfalls, discharges, suspend loads, etc. The slope stability and vegetation change with watershed should also be mornitoring by using satellite images for evaluating the change of landform in the future.

REFERENCES

[1] Turner, A. K. and Schuster, R. L., 1996, Landslides investigation and mitigation, special report 247, 1996, pp.42~43.

[2] 林美聆、林銘郎、陳宏宇、陳正興、許銘熙、林俊全，2004，「大甲溪流域之初步堪災」，土木水利，第三十一卷，第四期。

(2) Rainfall induced slop instability

Study on the Influence of Soaking Effects to the Shear Strength of the Colluviums on Mt. Da-Lum

S. Chen[1], P. S. Chen[1], H. C. Huang[2]
[1]*Department of Environmental and Hazards-Resistant Design, Huafan University, Taipei, Taiwan*
[2]*Department of Civil Engineering, Tankang University, Taipei, Taiwan*

Abstract

Landslide of colluviums often occurs during or after heavy rainfall because the huge quantity of precipitation induces the upsurge of groundwater table as well as the reduction of effective stress of soil stratum and the factor of safety from slope stability analysis. Moreover, the longer duration of heavy rainfall maintain the higher groundwater table, the shear strength parameters may be decline due to the soil being soaked for longer period of time. The campus of Huafan University is mostly covered by colluviums that located on Mt. Da-Lum, Shih-Tin Hsiang, Taipei County, Taiwan. Slope stability is one of the major concerned issues, for this reason, a slope monitoring test site has been established around the campus. According to the data collected, the magnitude of slope movement influenced by rainfall can be observed. In this study, the colluviums samples are collected from the campus of Huafan University and direct shear tests are performed to obtain the shear strength parameters of the remolded soil samples that soaked in the water for various periods of time, i.e. 0, 1, 2, 3, 5 and 7 days respectively. From these tests, the change of the shear strength and slope stability of colluviums with respect to the soaking time of soil has been further understood.

Keywords—*Landslide, soaking effects, shear strength, colluviums.*

INTRODUCTION

The upsurge of groundwater table that comes after Typhoon or/and heavy rainfall plays an important role to induce the landslide of colluviums slopes, especially when the extent of this heavy rainfall being long enough to keep the soil been soaked so that the shear strength of soil may drop to a critical situation. This kind of landslide of colluviums slopes mostly happens continuously and repeatedly. The basic idea to prevent this kind of hazards is to be aware of the material characteristics of colluviums regarding to this situation. Hung [1] indicates that the characteristics of loose fabric and high percentage of coarse grain causes the colluviums being permeable and easy to accumulate the groundwater. And, it is well known that soil stratum with high groundwater table has high potential to slide.

Chang [2] evaluated the correlation among landslides, soil properties, precipitation and vegetation by the data collected from the East-West Cross Island Highway that crosses the mountain area in the central part of Taiwan and found that most collapses of slopes happened on May (Mei-Yu Season) and August (Typhoon Season). It was also indicated that the risk of landslides exceeded 80% if the precipitation had been more than 120 mm that accumulated during the former 16 raining days. Fang [3] performed several sets of Large Direct Shear Test in situ on colluviums slopes where are located at 73K of New Central Cross Island Highway that also passes the mountain area in the central part of Taiwan. It is found from the outcomes of tests data that friction angle φ tends to decrease when the soil samples emerged in the water more than one day. Chien [4] studied the soaking effects on colluviums on Lishan by Tri-axial Test and found that cohesion c increased and friction angle φ decreased if soil samples have been emerged in the water elapsed 3 or 7 days. It was also pointed out that the factor of safety (FS) was about 1.33 if groundwater had no effect on potential slip surface of landslide while FS dropped to 1.30 with high groundwater, moreover, FS decreased 0.01 or more and became 1.29 when soil had been soaked for more than 3 days. It was also indicated that extra one third decrement of FS with respect to the influence of soaking effect. From previous studies stated above, it is obvious that the collapse of colluviums slope is very related to the upsurge of groundwater and being soaked for longer time. Chao [5] studied the displacement of colluviums slope on Mt. Da-Lum with respect to the heavy rainfall come with HAIYAN Typhoon in 2001. Regarding to Fig. 1, rainfall duration curve begins to be drawn from 10/15 and rainfall intensity hits the maximum value of 22 mm/hr at 10:00 a.m. 10/16, only slight movement can be read in the stratum at 15m in depth at this time. While obvious displacements of 3.5mm and 2mm are caught at noon 10/19 located at 10m and 15m in depth, respectively. According to the observed phenomenon, it is suspected that shear strength of soil declines after 4 days consistent heavy rainfall.

In order to study more details dealt with the upsurge of groundwater and the soaking effects with respect to the decrement of shear strength as well as factor of safety of slope in the colluvial deposit, series of experiments have been planned and performed on the remolded soil samples at lab in connection with the monitoring information observed at site. Moreover, the achievement of the mechanism of landslide in colluviums is also hoped.

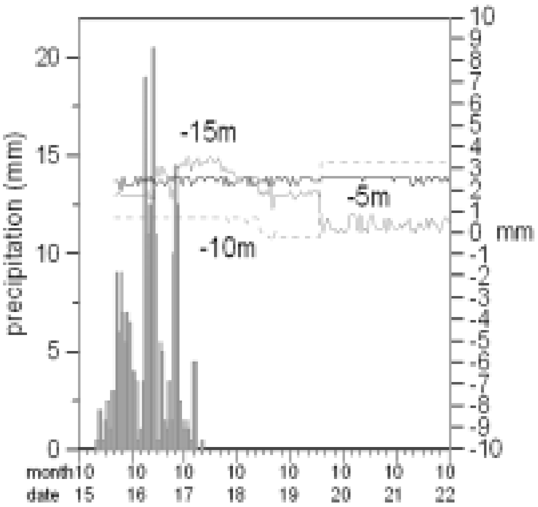

Fig.1 The precipitation mass curve versus the monitoring movements during HAIYAN Typhoon on Mt. Da-Lum in 2001.

METHODOLOGY

All soil samples are remolded at lab and collected from six sites in the campus of Huafan University that is shown in Fig. 2. The contours for equivalent thickness of colluviums are also plotted in Fig.2. Seven samples collected from these six sampling locations are determined in considering the different thickness of colluviums. Tests for physical properties and permeability are done after sampling, and the results are summarized as Table 1. The maximum particle grain size for remolded samples are restricted to be 4.75mm in preventing the scale effects that induces the diversity of test results. Therefore, the removal of the particles that is larger than 4.75mm are substituted by the particles with the grain size between 2.00mm (Sieve #10) and 4.75mm (Sieve #4) in terms of weight that is depicted in the Fig.3.

Table 1: Properties of soil samples

Soil Sample	w (%)	G_s	γ (kg/cm^3)	γ_d kg/cm^3)	w_l (%)	w_p (%)	e	k (cm/sec)
I	18	2.67	1.72	1.46	38	29	0.79	1.97×10^{-3}
II	22.8	2.65	1.93	1.58	27	15	0.64	1.08×10^{-3}
III	21	2.66	1.7	1.4	---	---	0.85	5.10×10^{-3}
IV	18	2.69	1.71	1.45	---	---	0.81	1.21×10^{-3}
V	18	2.65	1.85	1.56	---	---	0.66	1.10×10^{-3}
VI	13	2.65	2.09	1.85	39	23	0.41	2.80×10^{-6}
VII	13	2.66	2.09	1.85	33	26	0.41	1.87×10^{-6}

Remolded samples are produced by compaction with the same water content and unit weight that have been measured from site. The compactive effort used in the preparing the remolded samples with the same unit weight at site is decided by preliminary tests that some results are summarized in Fig. 4 through comparing the compactive effort with respect to the dry unit weight.

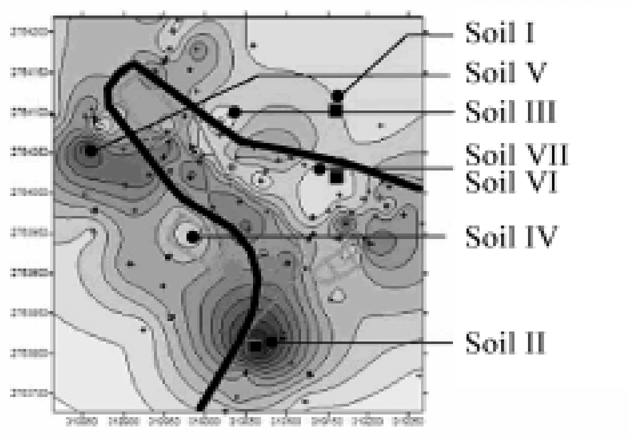

Fig. 2 Locations of soil samples versus thickness contours of colluviums.

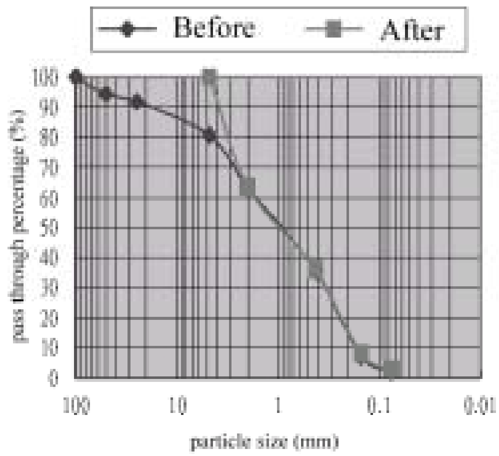

Fig 3 Grain-size distribution of sampled soil and remolded samples (Soil III)

The samples, which confined by sampling ring, are given a slightly pressure through putting the porous stones on both sides to prevent the over-swelling of the soil samples. The soaking time of emerged samples are arranged to be 1 hour, 8 hours, 1 day, 2 days, 3 days, 5 days and 7 days. The arrangement of soil samples in soaking is demonstrated as Fig. 5. Direct shear tests with shearing speed of 1.27 mm/min and the varied normal stresses of 1, 2, 4 kgf/cm^2 respectively, are carried on, and the shear strength parameters c and φ, cohesion and friction angle, are achieved. The influences of long-term torrential rain to the colluviums of the Da-Lum mountain can be studied by STABL program with the varied parameters, i.e. before and after soaking, obtained in previous mentioned experiment.

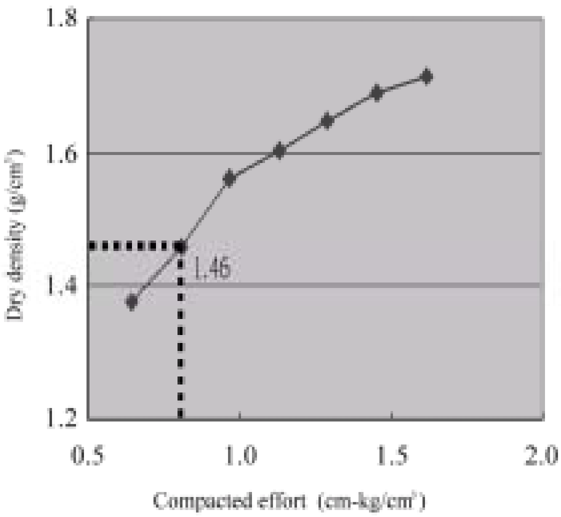

Fig 4 Relation between compactive effort and dry density (Soil I).

Fig. 5 Prepared arrangement of soil samples for soaking.

RESULTS AND DISCUSSION OF DIRECT SHEAR TEST

From previous studies, it can be noted that the colluviums have the characteristics of low clay content, high permeability and being easy to accumulate groundwater. The landslides are strongly influenced by these characteristics during the rainfall especially when the raining days or soaking days is greater than 3. Therefore, this study tries to find the influence of soaking effect during the rainfall to the slope stability of colluviums by investigating the variation of saturation and shear strength parameters, c and ϕ, with respect to the different soaking time. Many sets of direct shear tests on remolded colluvial samples with various soaking time are performed. The results and discussion are described as follows.

Saturation of soil versus soaking time

The degree of saturation of soil samples varies with respect to the soaking time. Refer to Fig. 6, soil samples labeled I ~ V reach saturated in 3 days, while indicated by dashed lines, the samples labeled VI and VII need more than 5 days. These 2 samples with larger unit weight and smaller void ratio may affect the permeability of water and evacuation of air so that the saturation needs longer time.

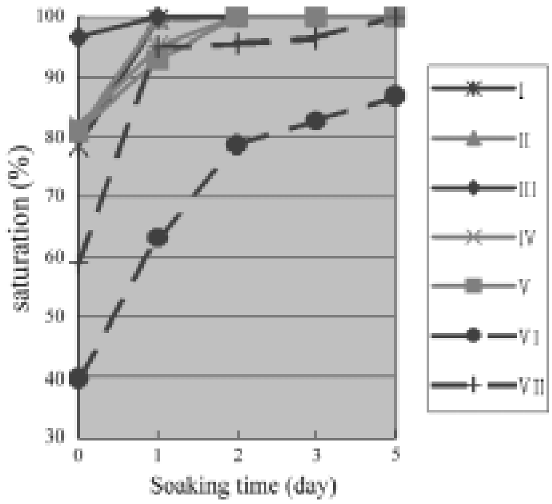

Fig 6. Saturation versus Soaking time.

Cohesion of soil versus soaking time

It can be observed at the curves of samples labeled I ~ V from Fig. 7 that the cohesion tends to decline at the first 2 days, then, goes up after day 3, but decline again at the day 5. As stated in the previous section that soil samples have not been saturated, or the soil fabric of samples are not settled, in the soaking condition at the first 2 days. The soil particles being in rearrangement should be the reason why cohesion decline. At day 3, soil samples are nearly saturated, the soil fabric is also nearly steady, and then, the cohesion of soil is recovered. But the lubrication of water among particles begins to function after the soil being saturated may be the reason why the cohesion of soil declines again at day 5. As for the soil samples labeled VI and VII, it is not saturated even at day 5, the cohesion of soil decline consistently.

Friction angle of soil versus soaking time

It can be observed at the curves of samples labeled I ~ V from Fig. 8 that the friction angle tends to develop and then decline at the first 2 days, the lowest value of friction angle happened at day 3, and develop again at the day 5. Concerning the soil samples labeled VI and VII, for the same reason of being not saturated in these 5 days, the friction angle of soil is smaller than that of soil samples being not soaked.

Shear strength of soil versus soaking time

The shear strength τ obtained in shear tests with respect to applied normal stress σ can be plotted failure envelope curve for samples that is summarized in Fig. 9. The accurate values of the shear strength obtained from soil sample III, as typical case, with varied soaking days versus normal stress σ are also listed in the Table 2 for more precise examination. From Fig. 9 and Table 2, the shear strength decreases obviously at the day 2 or day 3 and the risk of instable condition for slope failure is also higher. It is also worthy to pay more attention to is the decay tendency at day 7 in Table 2 that more investigations are needed for verification.

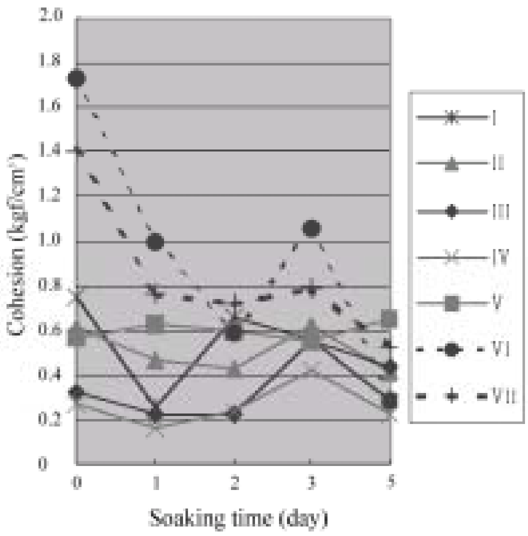

Fig 7 Cohesion versus soaking time.

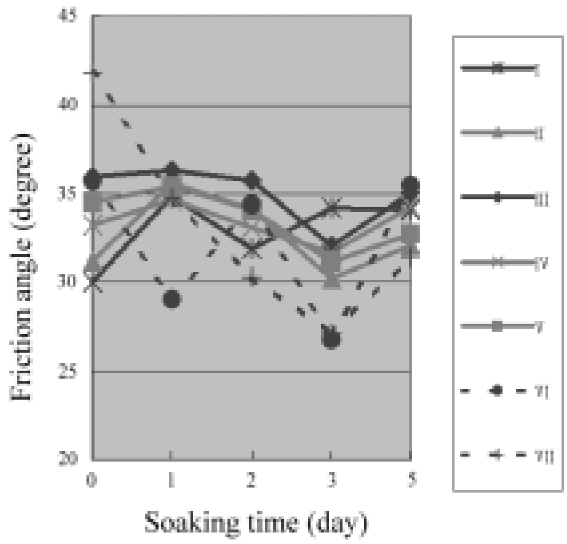

Fig 8. Friction angle versus soaking time.

Shear strength parameters versus degree of saturation

In order to verify how the shear strength of soil is affected by soaking, the inspection on the difference of shear strength parameters, c and ϕ, regarding to the degree of saturation of soil have been done that degree of saturation versus shear strength parameters are drawn, sample II as typical, in terms of cohesion and friction angle in Fig. 10 and 11 respectively. From the figures, it can be found that both parameters tend to decrease after saturated.

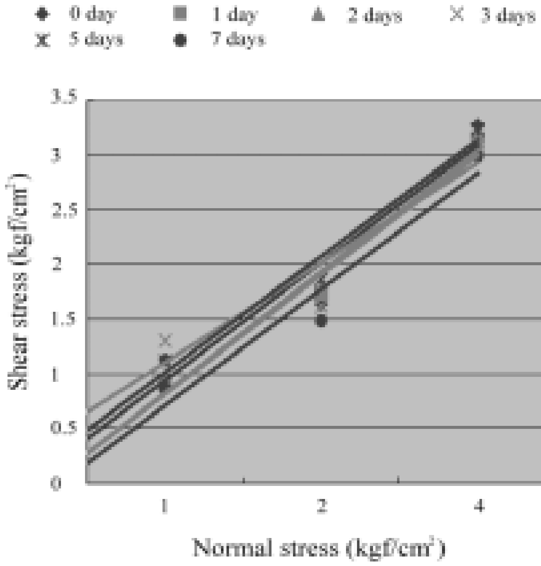

Fig 9. Shear stress versus Normal stress (Soil III)

Table 2: Shear strength obtained from soil sample III with varied soaking days vs. normal stress σ

σ kg/cm²	0 days	1 days	2 days	3 days	5 days	7 days
1	1.13	0.93	0.9	1.3	1.12	0.86
2	1.64	1.73	1.73	1.62	1.86	1.48
3	2.48	2.42	2.38	2.43	2.54	2.25
4	3.27	3.15	3.08	3.12	3.24	2.98

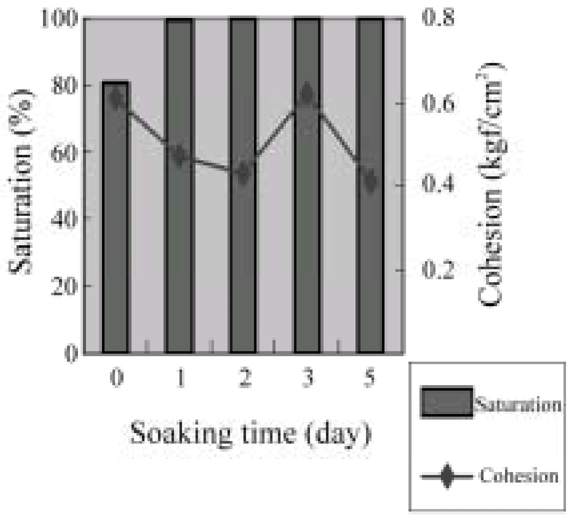

Fig 10. Saturation versus Cohesion (Soil II)

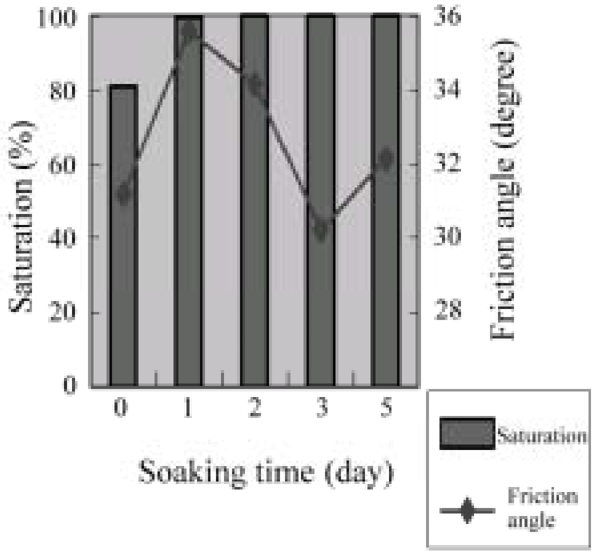

Fig 11. Saturation V.S. Friction angle (Soil II)

SLOPE STABILITY ANALYSIS

It is noted from previous section that shear strength parameters of colluviums will change with respect to the soaking time, but the tendency for c or φ are so different that the tendency of shear strength is not easy to be judged. On the other hand, the risk of slope failure in colluviums during heavy and durable rainfall is not easily predictable only by the various relations of shear strength parameters regarding to soaking time. In order to improve this situation, 2 typical sections, which have been observed in critical condition during heavy rainfall, in Mt. Da-Lum are selected for doing slope stability analysis by STABL program. The results of these analyses are summarized in Fig. 12~15 and Table 3.

Fig. 12 and 13 show the profiles of 2 selected sections and some most possible slip surfaces, the results used by the various shear strength parameters in connection with different soaking time from the analysis of STABL are summarized as Table 3. Observing Table 3, it is found that the factor of safety (FS) of all samples tend to change after soaking, the lowest FS happens at day 2 ~ day 5. It also indicates that the entering of water induces instable FS of slope before the saturation being reached because of the rearrangement of soil particles. When the saturation is fulfilled, soil fabric is changed by the influence of water that the lubrication of water causes the decrement of friction angle, and the cohesion of soil increases due to embrace of water.

The situation of saturation regarding to the distinction of FS is also studied by taking the degree of saturation vs. FS in term of soaking time in a same figure for a specific soil sample. Fig. 14 and 15 are plotted for soil samples V and VII, respectively, under this consideration. In Fig. 14, or soil sample V, the FS of 1.38 at day 3 is a drop in

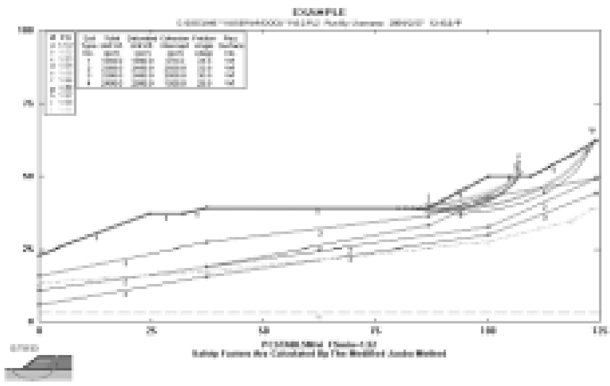

Fig 12. Analysis by STABL (section I)

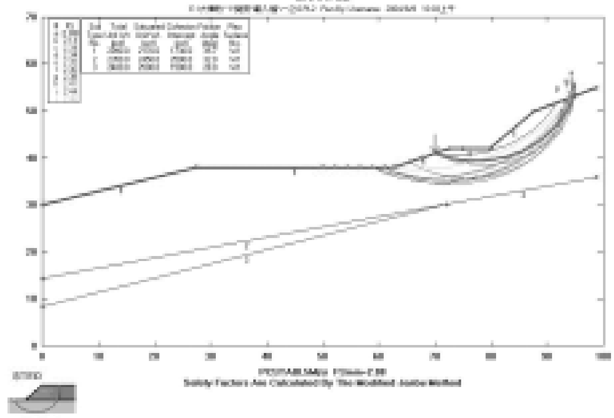

Fig. 13 Analysis by STABL (section II)

Table 3: Factor of Safety vs. soaking days for varied soil samples

	I	II	III	IV	V	VI	VII
0 day	1.49	2.05	0.97	1.16	1.52	0.97	2.39
1 day	1.32	2.3	0.97	1.18	1.54	0.97	1.72
2 days	1.5	2.17	$\boxed{0.96}$	$\boxed{1.14}$	1.52	$\boxed{0.96}$	1.48
3 days	1.52	$\boxed{1.77}$	0.99	1.16	$\boxed{1.38}$	0.99	$\boxed{1.36}$
5 days	$\boxed{1.31}$	2.02	1.03	1.18	1.49	1.46	1.45
7 days	--	--	0.9	--	1.44	0.9	--

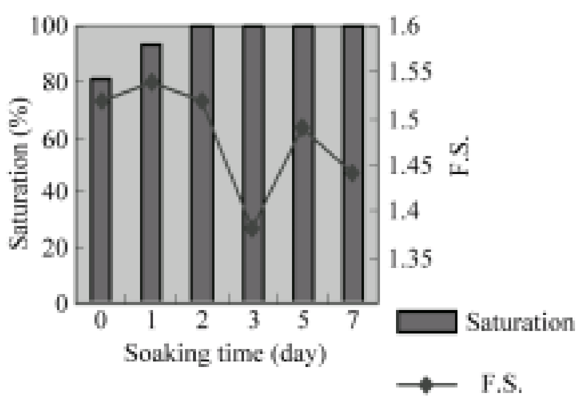

Fig. 14 Saturation versus F.S. (Sample V)

comparing with the FS of 1.52 at day 2. And, it is also commendable to note that day 3 is the second day when the soil sample has been saturated. And, it is concluded that the high risk of slope failure happens after 3 continuous days with heavy rainfall.

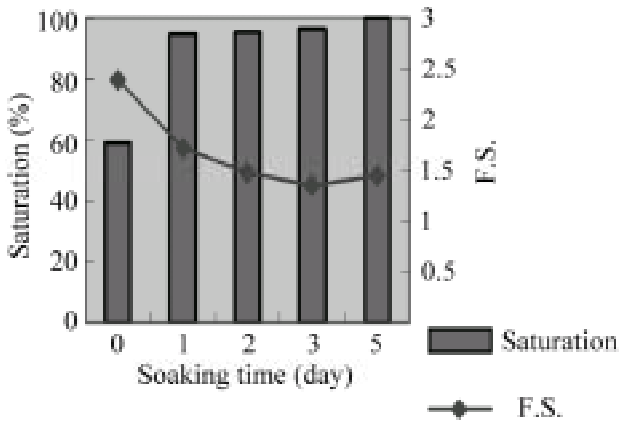

Fig. 15 Saturation vs. F.S. (Sample VII)

As for the soil sample VII, shown in Fig. 15, the saturation is completed at day 5, and the value of FS being steadily declined until the day 5. It is assumed that some existing weathered rock fragments dissolve become smaller pieces when soil sample has been soaking. The effect of rock fragment breaking down causes the falling of friction angle, then the decreasing of shear strength and the FS of soil. It is also interesting that the tendency will move up or down if the colluviums have been soaked for longer time.

CONCLUSIONS

From the outcomes of soil tests performed on colluviums regarding to soaking time, it is believed that the entering of water into partly saturated soil samples at day 1 induces the rearrangement of soil fabric as well as the variation of friction angle and cohesion of soil. When most soil samples are saturated at day 2, the cohesion of soil remains varying while the friction angle of soil begins to decline. The frictional resistance decreases to a critical situation at day 3 because of the lubrication of water that fully occupies the voids among the particles of soil.

One or two more days after soil being saturated, the factor of safety (FS) for slope stability arrives at a critical value that the slope has the higher risk to collapse. The achievements from direct shear tests and slope stability analyses show that the FS of the colluviums of Huafan campus drops to a comparatively low value when the soil has been soaked for more than 3 days. And this statement can also be verified by Chao's [5] finding that obvious displacements take place after 4 continuous days with heavy rainfall.

Under saturated condition, the longer the soil being soaked in the water, the FS of colluviums slope decreases more, Chien [4]. In this study, similar results are obtained from samples III and VI. But, experiments performed on more soil samples with longer soaking time are needed to support this statement in the future study.

REFERENCES

[1] Hung, J. J., "The Applications of Engineering Geology in Slope Stability (Except Mechanics)," Sino-Geotechincs, No.7, July 1984, pp. 35–42.

[2] Chang, C. C., "The study of landslides in Kukuan-Lishan section of the East-West Cross Island Highway," Master Thesis, Institute of Traffic and Transportation, National Chiao-Tung University, 1984.

[3] Fang, C. J., "A preliminary study on mechanical properties of the colluvial slopeland of Central Cross Island Highway," Master Thesis, Department of Civil Engineering, National Chung-Hsing University, 2001.

[4] Chien, L. K., Chen, E.Y., Hsiao, C. H., "The influence of the groundwater-seepage-soaking for the slope stability of colluviums," Proceedings of The 10th Conference on Current Researches in Geotechnical Engineering in Taiwan, 2003, pp. 655-658.

[5] Chao, C. P., "Study on the displacement of colluviums slope in Huafan University campus on Mt. Da-Lum," 2002 Taiwan Rock Engineering Symposium, Hsin-Chu, 2002, pp. 459-469.

Predicting Probabilities of Landslides along Mountain Roads in Taiwan Using Gaussian Process Model

Jianye Ching and Hung-Jiun Liao
Dept of Construction Engineering, National Taiwan University of Science and Technology, Taiwan

Abstract
This paper gives a brief introduction on the background and current status of landslides along mountain roads in Taiwan and presents a detailed analysis based on the Gaussian Process model for predicting locations and occurrence times of future landslides based on historical data. Based on inherent and man-made factors of failed and not-yet-failed slopes, locations of future landslides are predicted. Together with historical rainfall data, rainfall-sensitive fragility curves of slopes are established. The analysis results show that the Gaussian Process model is effective in predicting landslide potentials and probabilities. Comparisons of the Gaussian Process analysis and the discriminant function analysis are made, which show that the former outperforms the latter in many aspects. The results are valuable for predicting where and when landslides would occur in future heavy rainfalls.

Keywords—*landslide, slope stability, mountain road, probability, Gaussian Process, risk analysis*

INTRODUCTION

The island of Taiwan was formed by the collision action of Eurasia plate and Philippine sea plate. It is relatively young in geological age. For the total area of 36000 km^2, mountains cover more than two thirds of Taiwan. The area percentages of mountains are about 28.40% for elevation of 0~100m, 39.48% for 100~1000m, 20.22% for 1000~2000m, 10.73% for 2000~3000m, and 1.17% for 3000~4000m, respectively. To accommodate population of more than 23 million, a large portion of the lower mountain area has already been intensively developed for farming and tourism. To keep up with the development, an extensive mountain road network has been built over the past decades.

The total length of roads with elevation above 100m in Taiwan is more than 67,000 km. Some of them were built with high engineering standards, but a large number of them were built with low engineering standards. Even worse, some were built along river valley with cut-slope methods and suffered from both river scouring problems on the down-slope and stability problems on the up-slope. Therefore, landslides in different failure types are not unusual along mountain roads when the slopes are experiencing long period of rainfalls or torrential rain accompanied with typhoons.

When a landslide occurs, it may cause traffic interruption, damage vehicles and injure personnel. Therefore, it is desirable to predict where and when landslides may happen to provide a safe traffic condition for the public. Research on landslide prediction is not new. In forest science, prediction of landslides after fire in chaparral was investigated by Kojan et al. [1], logging-related landslides were analyzed using discriminant function analysis by Rice et al. [2], Pillsbury [3], and Furbish [4]. Landslides in grass and brush environment were studied by Waltz [5] and Rice and Foggin [6] using discriminant function analysis. The use of discriminant function analysis and logistic regression with geographic information system (GIS) for predicting landslides was also studied by Carrera et al. [7,8], Mark and Ellen [9], Gorsevski et al. [10], and Santacana et al. [11]. Chung and Fabbri [12] proposed the use of the Bayesian approach for landslide potential prediction. Wen et al. [13] and Liao et al. [14] employed the discriminant function analysis to predict landslide probabilities of slopes in hillside communities.

Although several research results on landslide prediction have been reported, those focusing on landslides along mountain roads are rare. Moreover, the Taiwan mountain road network is a critical infrastructure for the island, therefore, there is a special need in Taiwan to predict landslides along mountain roads. Landslides along mountain roads are somewhat different from other types of landslides: they are affected by numerous factors, especially manmade factors. Due to this difference, landslide prediction for slopes along mountain roads is by no means a straightforward matter and becomes an interesting topic to work with. In this study, Route T-18 in central Taiwan is chosen to demonstrate the suitability of landslide prediction. Two main research questions are of concerned: (a) Given the historical landslide data along the demonstrative mountain roads in Taiwan, where are the locations along the roads with high landslide potential in the future? (b) Given the historical landslide and rainfall data, what are the landslide probabilities of the slopes along the roads in a future heavy rainfall? The former mainly concerns with the locations of future landslides, while the latter concerns with the time of landslide occurrence in future rainfalls.

Note that the concept of probability is highlighted in this study due to the complexity of slope stability problems: it can never be certain where and when a slope will fail because there are numerous uncertainties involved. In this study, a full probabilistic analysis based on the Gaussian Process model [15-18] is presented to predict the landslide potentials and probabilities. This new model is versatile and flexible. Compared to discriminant function analysis [19], the Gaussian Process model possesses the desirable property that there is no need to assume the functional form for the discriminant function, which is highly nontrivial task for complicated problems. Moreover, the performance of the Gaussian Process analysis is comparable to neural network while the required computational cost is much less.

The structure of the paper is as follows: First the background information of mountain roads in Taiwan is introduced, including information for rainfalls and typhoons. Second, the landslide database adopted for the demonstrating mountain roads is discussed in details, including the definitions of the features used for the analysis. Then the analysis for predicting landslide locations and occurrence times is described, and the analysis results are presented and compared with those made by the discriminant function analysis. Finally, a brief discussion and a remark will be made.

BACKGROUND

Typhoons

Totally, 52 typhoons had attacked Taiwan between 1994 and 2004 with an average of 4.7 typhoons annually. Among them, Herb (year 1996), Toraji and Nari (year 2001), and Mindulle (year 2004) were the most devastating ones and caused a large amount of landslides in Taiwan. The accumulated rainfall ranges from 1994mm for Typhoon Herb to 414mm for Typhoon Nari. Landslides caused by these typhoons are classified into three major categories: rock fall & slips on the up-slope (Type I), road base failure (Type II), and washed-away of road base (Type III). Among them, rock fall & slip failure at the up-slope are the dominant failure type.

To deal with Type-I landslides, the road maintenance sector tends to implement various types of slope stabilization measures, such as tied-down RC grid structure and gravity retaining wall to protect the failed up-slopes. It is of interest to find that the number of Type-I damage decreases from 89 of Herb to 37 of Mindulle, although the accumulative rainfalls of Herb (1994mm) and Mindulle (1764mm) were not much different from each other. It indicates that the slope stabilization measures have significantly increased the stabilities of failed slopes. Once the failed slopes were properly protected, the reoccurrences of landslides can be effectively controlled for some period of time. Moreover, the cost spent to emergent repair (short-term stabilization) and to stabilize the failed slopes and road bases (long-term stabilization) decreases rapidly from Herb to Toraji and Nari although the rainfall of Mindulle is close to that of Herb.

However, the stabilization action cannot be done for all the slopes along the roads due to financial constraints, and new landslides may very likely occur in slopes that never failed, where stabilization measures are absent. Therefore, it is desirable to develop techniques to predict the locations and occurrence times of new landslides. This is achieved through analyzing historical data gathered from the slopes along the roads, which will be explained in details in the next section.

Geology

Route T-18 is nearby the Alishan mountain in central Taiwan. The geologic condition along the road mainly consists of sandstone and interlayered sandstone/shale strata with various bedding structures. The geologic strata can be classified into five main categories based on their geologic ages (from young to old): (a) Zuolan strata, (b) Jinswei shale, (c) Dawo sandstone and chalk, (d) Quandaushan sandstone, and (e) Nanzuan strata. Among them, Nanzuan strata is the most widely distributed strata. About 90% of outcrops found along the road belong to Nanzuan strata, which consists of thick sandstone layer, sandstone/shale interlayer, and shale layer. Zuolan strata consists of thick layers of silty sandstone with some sandstone/shale interlayers embedded. Route T-18 runs through five major faults. Dip slope outcrops are often found on the up-slope along the road.

LANDSLIDE DATABASE

Landslides along Route T-18 are documented. In total, 55 failed unprotected slopes along T-18 were extracted from the road maintenance records. Among them, 12 slopes failed during Typhoon Herb, 18 during Toraji, 9 during Nari, and 16 during Mindulle due to heavy rainfalls. To match the number of failed slopes, 54 not-yet-failed unprotected slopes were chosen. The not-yet-failed sites were checked on the field to assure that no evidence of previous slope failure is visible.

The locations of failed and not-yet-failed slopes in the database are shown in Figure **1**.

The data format is as follows: $D = \{(x_i, t_i)$: $i = 1, \ldots, p\}$, where x_i contains the values of the fifteen landslide factors of the i-th slope in the database; $t_i = 1$ if that slope failed, otherwise $t_i = 0$; p is the total number of slopes in the database. Totally, fifteen landslide factors are carefully chosen based on engineering judgments to reflect the status of a slope: these factors are believed to have significant influence on the stability of a slope. The landslide factors are obtained from the following sources:

(a) Digital maps and DTM information

Digital maps of various contents and scales are easily available through commercial organizations. In Taiwan, 1/5000 maps are available in populated areas and only 1/10000 maps are available in mountain areas. The DTM (Digital Terrain Model) employed in this study has resolution of 40m×40m. It provides digital horizontal and vertical coordinates of the terrain.

(b) Field reconnaissance

Although the method adopted here is to utilize the available geographic information and to minimize the field work, the field reconnaissance is still inevitable. For example, the items of block size and rock volume percentage on slope surface (Note: these two landslide factors will be explained later) are unable to determine from aerial photos nor satellite images.

Fifteen landslide factors (also called features later) are categorized into natural factors and man-made factors. Among them, thirteen are natural factors, and two are man-made factors. The natural factors cover the aspects of topography, geologic conditions, bed rock structure, weathering & fracturing, vegetation cover, catchment area of surface water, and peak ground acceleration (PGA) induced by a major earthquake. The man-made factors quantify the impacts induced by road construction. The detailed definition of each factor is described in the following:

Natural factors

Topography

Slope orientation angle is defined to be 0^o when slope is facing north and increases clockwise. Slope angle is the angle between slope face and road. Road curvature is the curvature of the road at a slope location (positive for convex slopes and negative for concave ones). Slope orientation angle, slope angle and height are determined from field reconnaissance, while road curvatures are determined with the aid of *ArcView* software.

Geology

Depending on the age of outcrop strata, the type of geologic strata at a slope location is quantified into five levels: integers 1 to 5. Integer 1 is given to Zuolan strata outcrops (the youngest) and integer 5 is given to Nanzuan strata outcrops (the oldest).

Bedrock orientation

The bedrock orientation is divided into two items: one is slope and dip orientation difference and the other is slope and dip angle difference. For a dip slope, its slope and dip orientation difference is less than 22.5^o. For an escarpment slope, its slope and dip orientation difference is larger than 157.5^o. The item of slope and dip angle difference is an indication of possible dip slope failure. If the slope angle is larger than the dip angle of bedding plane, the outcrop of bedding plane will be on the slope surface. In other words, there will be a high potential of dip slope failure if the bed rock structure is a dip slope.

Weathering and fracturing

The influence of weathering and fracturing on slope is divided into two factors: block size and rock volume percentage. The former is the nominal diameter of the predominant rock blocks on slope. Both factors are determined from visual inspection in field reconnaissance.

Vegetation coverage

Vegetation coverage is divided into two factors: area percentage of vegetation coverage and thickness of vegetation coverage. The former stands for the percentage of tree coverage on slope faces, while the latter is the thickness of tree crown. These are indices of tree protection against rainfall scouring on slope surface. Both factors need to be obtained from visual inspection in field reconnaissance.

Water condition

Surface water and groundwater are two major issues to the slope stability, and they are quantified in terms of the size of catchment area. The size of catchment area is estimated by DTM: First interpolate DTM into a smooth 3-D terrain, where the target slope is located. The catchment area of the slope is sketched manually with the visual aid from the terrain and elevation contours.

Seismicity

Many evidences have shown that since the Chi-Chi earthquake occurred in 1999, the number of landslides has increased. The peak ground acceleration (PGA) at the slope location is an indication of the effect of this earthquake. Totally, twenty one seismic monitoring stations were set up by the Central Weather Bureau of Taiwan around the roads. The PGA at a particular slope location is then interpolated from the PGA recorded at the stations in the Chi-Chi earthquake. Exceptions are the slopes failed in typhoon Herb, which arrived prior to the Chi-Chi earthquake. For simplicity, the PGA for these slopes are taken to be zeros since the impacts of earlier earthquakes is quite negligible compared to that of Chi-Chi earthquake.

Man-made factors

All slopes considered in this study are subjected to man-made hazards: road construction. Two factors are considered: excavation height at toe and change of slope grade due to toe excavation. The change of slope grade is defined as the difference in slope angle before and after toe excavation. If landslides occur above the toe excavation, then the change of slope grade is taken as zero. Both factors are obtained from field reconnaissance.

LANDSLIDE LOCATION ANALYSIS

Recall that one of the goals of this paper is to develop methods to predict the locations of future landslides. In this section, a methodology is proposed for the purpose. Predicting landslide occurrence times will the subject of a later section.

The key concept proposed here is "landslide potential". Since the slopes in the database have been classified into two groups (failed and not-yet-failed), it is sensible to study the similarity between the slope of interest and each of the two groups. If the slope of interest is more likely to be in the failed group, its landslide potential is higher, and vice versa. The terminology "failed" and "not-yet-failed" merits more explanations. In essence, many unprotected slopes will fail in future, so those are not yet failed may fail ultimately, so it is more plausible to use the term "not-yet-failed" than "stable" or "not-failed". Here a slope with high landslide potential means it is more likely to be a failed slope in the database rather than a not-yet-failed slope.

A single index is used to capture the similarity: $P(t=1|x,D)$, i.e. the probability that $t = 1$ given x and D, where x contains the fifteen features of the slope of interest; t denotes the membership of the slope, i.e. $t = 1$ if it belongs to the failed group and $t = 0$ for the not-yet-failed group; D is the historical data. Note that once $P(t=1|x,D)$ is known, $P(t=0|x,D)$ can be readily calculated. Therefore, $P(t=1|x,D)$ quantifies the landslide potential of the slope of interest.

In this paper, the Gaussian Process analysis [15-18] is implemented to estimate the landslide potential, i.e. to compute $P(t=1|x,D)$. A second purpose of the Gaussian Process analysis is to rank the importance of the fifteen features. The discriminant function analysis [19], which has been implemented by many previous researchers to predict landslide potentials and probabilities, is also implemented to compare with the Gaussian Process analysis. For the discriminant function analysis, the commercially available program SPSS is employed. Due to the limitation of paper length, the details for the discriminant function analysis are not presented here. Only the details for the Gaussian Process analysis are described in the following section.

A drawback of the discriminant function analysis is that one has to specify the functional form of the discriminant function, or equivalently, to specify the functional form of the separating boundary of the two membership groups in the feature space. In the absence of physical basis for the specification, a usual choice is to take the weighted sum of the features (weights are unknown and to be determined) as the discriminant function. However, it is dangerous to specify the functional form of the discriminant function if the problem at hand is highly complicated and not well understood such as the landslide problem. Doing so may lead to large bias.

For complicated problems, it is desirable to adopt an approach that is flexible in the sense that the discriminant function can be potentially arbitrary. The discriminant function analysis is not qualified for this purpose. Nonetheless, neural network fits in this purpose as long as the number of nodes in the network is sufficiently large. However, the required computational cost for neural network is quite high because when implementing neural network, a non-trivial high-dimensional non-convex optimization problem must be solved.

On the other hand, the Gaussian Process analysis is recently developed in the field of artificial intelligence for non-parametric regression and classification. It has the advantage of neural work: the discriminant function can be potentially arbitrary, but its required computational cost is much less than that required by neural network. In fact, Neal [20] showed that Gaussian Process models are equivalent to neural networks with an infinite number of nodes whose weights are Gaussian random variables. This result is essential: in order to implement infinite-node neural networks, an infinite number of parameters are needed, so the computational cost can be extremely high, but the same task can be achieved by considering Gaussian Process models with only a few parameters.

Gaussian Process model for discriminant function

A Gaussian process on $\mathbf{R}^\mathbf{n}$ is a stochastic process $Y(x)$ such that any finite combination of $\{Y(x_1), Y(x_2),\ldots, Y(x_m)\}$ is jointly Gaussian. Similar to multivariate Gaussian random variables, a Gaussian Process model is fully defined by the mean, variance, and covariance of the process.

Suppose the discriminant function Y is known (although in fact it is not), the landslide potential of a slope whose features are given as x is modeled as:

$$P(t=1|Y(.),x)=\frac{1}{1+e^{-Y(x)}}\equiv sig\left(Y(x)\right) \qquad (1)$$

where t indicates the group membership, i.e. $t = 1$ if the slope fails and = 0 otherwise; the discriminant function Y is, in fact, uncertain and is modeled as a Gaussian Process; $sig(.)$ denotes the sigmoid function. The uncertain discriminant function Y is to be determined, and our goal is to estimate this function by using the past data $D = \{(x_i,t_i): i = 1,\ldots,p\}$.

Instead of assuming the functional form of the Y function (as done in the discriminant function analysis), in the Gaussian Process analysis, it is only necessary to assume that the Y function is "smooth" in a certain sense. Note that this smoothness constraint is desirable for sensible prediction. In the context of Gaussian Processes, this smoothness requirement can be enforced by letting $Y(x_i)$ and $Y(x_j)$ be highly correlated when x_i and x_j are "similar". Physically, this smoothness constraint means that if the features of two slopes are similar, then the landslide potentials will be also similar, exemplified by the following covariance model:

$$Cov\left[Y(x_i),Y(x_j)\middle|H\right]=\theta_1\cdot e^{\frac{-1}{2}\sum_{k=1}^{n}\frac{\left(x_i^{(k)}-x_j^{(k)}\right)^2}{r_k^2}}+\theta_2 \quad (2)$$

where $x_i^{(k)}$ denotes the k-th feature in x_i; the exponent is the negative one-half of the square of the weighted Euclidean distance between x_i and x_j; Cov denotes covariance. One can verify that if the x_i-x_j distance is small (i.e. x_i and x_j are similar), the covariance (or correlation) between $Y(x_i)$ and $Y(x_j)$ will be large, and vice versa.

It is worthwhile to discuss the significance of the hyper-parameters. Among them, $\theta_1+\theta_2$ gives the variance of $Y(x)$: θ_2 gives the baseline variance of $Y(x)$ (the variance of the uncertain mean value of $Y(x)$) and θ_1 gives the variance of $Y(x)$ besides the baseline; r_k governs the importance of the k-th feature: if r_k is large, the k-th feature is influential, and vice versa.

The final goal of the analysis is to estimate the landslide potential $P(t=1|x,D)$. With the Theorem of Total Probability and the Law of Large Number, $P(t=1|x,D)$ can be estimated with the aid of stochastic simulation techniques, Gibbs sampler [21] and hybrid Monte Carlo [22].

Results of landslide location analysis

Comparison of prediction errors

Common practice of examining the performance of the adopted model/analysis is to quantify the so-called training errors, which are described as follows: Once the adopted model is trained by the data D, the trained model is used to predict the landslide potential for each slope in the database, i.e. compute $P(t_i=1|x_i,D)$ for i = 1, …, *109*. If this number is larger than 50%, the i-th slope is predicted as "failed", otherwise, it is predicted as "not-yet-failed". Compare the prediction with the actual status of the i-th slope, and the ratio of false prediction is the training error. Unfortunately, this calculation procedure of error is not fair. Because the i-th slope is already within the training data when its landslide potential is to be predicted, the resulting training error cannot effectively reflect the actual ***prediction errors*** on ***unseen slopes***.

For fair calculation of prediction errors, the so-called leave-one-out (LOO) prediction errors of the adopted model are adopted here. The LOO prediction error is an unbiased estimate of prediction error on unseen slopes of the trained model. The basic idea of LOO prediction error is to mimic the prediction process by removing one data point out of the training dataset and use the removed data point for prediction testing. The procedure of computing LOO prediction error is as follows: Remove the i-th data point $\{x_i,t_i\}$ from the dataset, call the remaining database $D_{\sim i}$. Estimate $P(t_i=1|x_i,D_{\sim i})$. If this number is larger than 50%, the i-th slope is predicted as "failed", otherwise, it is predicted as "not-yet-failed". Compare the prediction with the actual status of the i-th slope. Do so for i = 1, …, *109*, and the ratio of false prediction is exactly the LOO prediction error.

Table **1** shows the traditional training error rates and the LOO prediction error rates induced by the Gaussian Process analysis and the discriminant function analysis. Note that both training errors are quite small (one of them is zero), but these are not realistic estimates for the actual prediction errors on unseen slopes. The LOO prediction errors, which more realistically reflect the actual prediction error rates, are always larger than the training error rates. It is also clear that the Gaussian Process analysis results in smaller LOO prediction error rates than the discriminant function analysis, indicating that the performance of the former is superior.

Having shown that the Gaussian Process analysis results in consistent prediction of landslide potential, we are now more confident to draw the following conclusion: The landslide potential predicted by the Gaussian Process analysis is satisfactory (the prediction error rate is as low as 5.5%). Figure **2** shows the landslide potential map predicted by the analysis for the entire Route T-18, where dark regions are high landslide potential segments and light regions are low potential segments. This figure is beneficial for the road maintenance sector to predict the locations of potential landslides along the road.

It is worth highlighting that the result of the analysis in the landslide location analysis is the landslide potential, i.e. the probability that the slope of interest belongs to the failed group. The concept of probability is taken in the analysis to accommodate the intrinsic large uncertainties in the problem. With these uncertainties, it is not realistic to give a yes-or-no answer. Instead, a probabilistic approach will be more appropriate. To this aspect, although not shown, the landslide potential predicted by the discriminant function analysis is found to be either very close to 0 or very close to 1, implying that the associated uncertainty is little. This contradicts the reality of the problem at hand: there exist many uncertainties so it is expected that the estimated landslide potential should not be close 1 or 0.

Nevertheless, the landslide potentials calculated by the Gaussian Process analysis do not exhibit this undesirable behavior.

Relative importance among features

As discussed in a previous section, in the Gaussian Process model, r_k governs the relative importance of the k-th feature, hence the mean values of the r_k samples (obtained from Gibbs sampler and hybrid Monte Carlo) quantify the relative importance of the feature: the smaller the r_k mean value, the more important the k-th feature. It is found that slope height, catchment area, height of toe cutting, block size, and change of slope angle are the dominant features, among them are the two man-made factors. This result implies that the slope stability along mountain roads is noticeably affected by road construction. Also note that catchment area is among the dominant factors. This result is consistent with our intuition since slope stability should be sensitive to the amount of seepage and surface water, which is in general proportional to the size of catchment area.

It is of interest to verify if the removal of unimportant features will seriously degrade the performance of the proposed methodology. According to our analysis, the LOO prediction error rate of the T-18 data for the Gaussian Process analysis when only the most important five features are taken is only 1.83% (2 false LOO predictions out of 109). It is clear that the performance of the Gaussian Process analysis with only five features is exceptional, implying that five features are sufficient for accurate predictions.

LANDSLIDE OCCURRENCE TIME ANALYSIS

Besides predicting potential landslide locations, it is desirable to additionally predict "when" (i.e. during which typhoon) landslides may occur. In Taiwan, landslides are mostly triggered by heavy rainfalls during typhoons. As a consequence, we propose a second stage of analysis (landslide potential is the first stage) to predict the occurrence times of landslides, where rainfall amount is treated as the triggering factor of landslides. The goal here is to develop a methodology that determines the relationship between landslide probability and rainfall amount of a slope of interest given the past landslide and rainfall data. This relationship is called the rainfall-sensitive fragility curve. If rainfall amount can be effectively predicted *a priori*, it is then possible to predict the occurrence times of landslides with the fragility curve.

The database employed here is based on the database for the landslide location analysis. However, there are some changes in the database for the occurrence time analysis. First, one more feature, i.e. rainfall amount, is augmented into the database so that the total number of features is now sixteen. The actual rainfall data is obtained from 39 weather stations located around Route T-18. However, most of the weather stations are not nearby T-18. Therefore, the rainfall amount along Route T-18 are determined by interpolation with the inverse-distance-weighting method built in the *ArcGIS* program.

Second, the membership terminology in the database is changed from "failed" and "not-yet-failed" in the landslide location analysis into "failed" and "not-failed" in the occurrence time analysis. This subtle change is worth more explanation. Recall that in the landslide location analysis, the group names "failed" and "not-yet-failed" are taken because many unprotected slopes, even they are not yet failed for the time being, will fail in future. However, in the occurrence time analysis, we focus ourselves on the status (failed or not failed) of a slope right after a typhoon, so the group names "failed" and "not-failed" are more appropriate.

Third, the slope data for Typhoon Herb (year 1996) is removed from the database since the landslide behaviors of the slopes is believed to change significantly after the Chi-Chi earthquake (year 1999).

For the database in the occurrence time analysis, a failed slope is directly copied from the landslide location database, but the rainfall amount data is taken to be the accumulative rainfall (in mm) at the slope location during the landslide-causing typhoon. A not-failed slope in the landslide location analysis is duplicated into three not-failed data points in the occurrence time analysis, where the rainfall amount data is taken to be the accumulative rainfall amount at the slope location during each of the three typhoons (Herb is excluded). Let us call such not-failed cases as the actual not-failed cases.

Note that a failed slope was a not-failed slope before the landslide-causing typhoon, indicating that each failed slope in the database can be used to create not-failed data points. This is achieved by taking a failed slope in the database and replacing the rainfall amount by the accumulative rainfall during each of the typhoons prior to the landslide-causing typhoon. By doing so, each failed slope in the database is duplicated into several not-failed slopes. Let us call such not-failed cases as the temporary not-failed cases.

Instead of concerning with "landslide potential" in the landslide location analysis, here we are concerned with the probability of landslide occurrence right after a typhoon. Although the goal here is different from the one in the landslide location analysis, the same Gaussian Process analysis can be taken to compute the landslide occurrence probability $P(t=1|x,D)$, where x contains the sixteen features of the slope of interest; t denotes the status of the slope, i.e. $t = 1$ if it fails and $t = 0$ if it does not fail; D is the augmented data.

Table 2 shows the number of false LOO predictions and the LOO prediction error rates induced by the Gaussian Process analysis for the occurrence time analysis. The prediction error rates are significantly larger than the ones for the landslide location analysis. Furthermore, it is found that the discrimination between the actual not-failed cases and failed cases is easy, while the differentiation between the failed cases and the temporary not-failed cases is hard.

Recall that the only difference between the failed cases and temporarily not-failed cases is the rainfall data, so the results imply that the rainfall data is not sufficient to distinguish the failed cases from the temporary not-failed cases. There are several possibilities for this insufficiency: (a) although rainfall is indeed the only controlling factor, and the way that the rainfall amount is quantified is appropriate, the inverse-distance-weighting method performs poorly in interpolating the rainfall. (b) the way that the rainfall amount is quantified is not appropriate. (b) the rainfall is not the only controlling factor for discriminating the failed cases and the temporary not-failed cases, and there are some missing essential factors. (d) the union of the above possibilities. Understanding the possible causes and improving prediction results are left as future directions.

CONCLUSION

Evaluating landslide potentials and probabilities of slopes along mountain roads is a complicated matter due to large uncertainties. In this paper, a full probabilistic analysis based on the Gaussian Process model is proposed to predict landslide locations and occurrence times along mountain roads in Taiwan. The landslide database for the slopes along the Alishan mountain road, which contains the features of 55 failed and 54 not-yet-failed slope cases, is adopted to demonstrate the analysis. The analysis results show that the prediction error is around 5.5% for the landslide location analysis. The performance of the Gaussian Process analysis is superior to that of the discriminant function analysis, which is easier to operate than the former but less flexible. The relative importance of the chosen features is quantified. It is found that the Gaussian Process analysis based on the most importance five features performs exceptionally. For the landslide occurrence time analysis, the results from the Gaussian Process analysis are not satisfactory. The improvement is left as future research direction.

The research results of this paper include the landslide potential map and the rainfall-sensitive fragility curves. The former quantifies the landslide potentials of the slopes along the road, so it is valuable for predicting the locations of future landslides. The latter provides relationship between the landslide probability and the rainfall amount, hence it is valuable for predicting the occurrence times of future landslides. Note that the implementation of the latter requires accurate prediction of rainfall amount, which is a challenging research by itself and will be left as a future research topic.

ACKNOWLEDGEMENTS

The authors wish to thank the Second and the Fifth Road Maintenance Divisions of the Taiwan Highway Bureau for providing the case history records and all the necessary helps to carry out the field observations along Route T-18.

REFERENCES

[1] Kojan, E., Foggin III, G.T., and Rice, R.M. (1972). "Prediction and analysis of debris slide incidence by photogrammetry", *Proceedings of 24th International Geology Congress*, Section 13, 124-131.

[2] Rice, R.M., Pillsbury, N.H., and Schmidt, K.W. (1985). "A risk analysis approach for using discriminant functions to manage logging-related landslides on granitic terrain", *Forest Science*, **31**(3), 772-784.

[3] Pillsbury, N.H. (1976). "A system for landslide evaluation on igneous terrain", *Ph.D. Thesis*, Colorado State University, Fort Collins, Colorado, U.S.

[4] Furbish, D.J. (1981). "Debris slides related to logging of streamside hillslopes in northwestern California", *M.S. Thesis*, Humboldt State University, Arcata, California, U.S.

[5] Waltz, J.P. (1971). "Analysis of selected landslides in Alameda and Contra Costa counties, California", *Bull. Assoc. Eng. Geol.*, **8**(2), 153-163.

[6] Rice, R.M. and Foggin III, G.T. (1971). "Effect of high intensity storms on soil slippage on mountainous watersheds in southern California", *Water Resour. Res.*, **7**(6), 1485-1495.

[7] Carrera, A., Cardinali, M., Detti, R., Guzzetti, F., Pasqui, V., and Reichenbach, P. (1991). "GIS techniques and statistical models in evaluating landslide hazard", *Earth Surface Processes and Landforms*, **16**, 427-445.

[8] Carrera, A., Cardinali, M., Guzzetti, F., and Reichenbach, P. (1995). "GIS technology in mapping landslide hazard", in *Geographical Information Systems in Assessing Natural Hazards*.

[9] Mark, R.K. and Ellen, S.D. (1995). "Statistical and simulation models for mapping debris-flow hazard", in *Geographical Information Systems in Assessing Natural Hazards*.

[10] Gorsevski, P.V., Gessler, P.E., and Foltz, R.B.

(2000). “Spatial prediction of landslide hazard using logistic regression and GIS”, *Proceedings of 4th International Conference on Integrating GIS and Environmental Modeling*, Banff, Alberta, Canada.

[11] Santacana, N., Baeza, B., Corominas, J., Paz, A.D., and Marturia, J. (2003). “A GIS-based multivariate statistical analysis for shallow landslide susceptibility mapping in La Pobla de Lillet Area”, *Natural Hazards*, **30**, 281-295.

[12] Chung, C.F. and Fabbri, A.G. (1999). “Probabilistic prediction models for landslide hazard mapping”, *Photogrammetric Engineering and Remote Sensing*, **65**(12), 1389-1399.

[13] Wen, S.-L., Liao, H.-J., Lin, Y.-C., and Lan, Y.-S. (2001). “Evaluation study on probability of landslide in hillside community by discriminant analysis”, *Journal of Architecture*, **37**, 49-63, Architecture Institute of Republic of China (in Chinese).

[14] Liao, H.- J., Lin, Y.- C. & Liao, J.- T. (2001). “Evaluation of slope stability with discriminant analysis”, *Proc. of 14th Southeast Asian Geotechnical Conference*, Hong Kong, pp. 1131-1134, Balkema.

[15] MacKay, D.J. (1998). “Introduction to Gaussian Processes”, in *Neural Networks and Machine Learning*, vol. 168 of NATO Asi Series. Series F, Springer Verlag.

[16] Williams, C.K.I. and Rasmussen, C.E. (1996). “Gaussian Processes for regression”, in *Advances in Neural Information Processing Systems 8*, MIT Press.

[17] Neal, R. M. (1997). “Monte Carlo implementation of Gaussian Process models for Bayesian regression and classification.”, *Technical Report CRG-TR-97-2*, Dept. of Computer Science, University of Toronto.

[18] Gibbs, M. N. (1997). *Bayesian Gaussian Processes for Regression and Classification*, PhD thesis, University of Cambridge.

[19] Fisher, R.A. (1936). “The use of multiple measurements in taxonomic problems”, *Ann. Eugen.*, **7**, 179-188.

[20] Neal, R.M. (1996). “Bayesian learning for neural networks”, *Lecture Notes in Statistics 118*, Springer.

[21] Geman, S. and Geman, D. (1984). “Stochastic relaxation, Gibbs distribution and the Bayesian restoration of images.” *IEEE Trans. Pattern Anal. Machine Intell.*, **6**, 721-741.

[22] Duane, S., Kennedy, A. D., Pendleton, B.J., and Roweth, D. (1987). “Hybrid Monte Carlo.”, *Physics Letters B* 195: 216-222.

Table 1 Training and LOO errors on T-18 database

Methodology	Training errors	Number of False LOO Predictions (out of 109)	LOO Prediction Error Rate
Discriminant Function	7.3%	13	11.9%
Gaussian Process	0%	6	5.5%

Table 2 LOO errors for occurrence time analysis

	Failed cases (out of 43)	Temporary not-failed cases (out of 33)	Actual not-failed cases (out of 120)	All cases (out of 196)	Failed + temporary not-failed cases (out of 76)
Number of LOO errors	11	23	0	34	34
LOO error rate	25.6%	69.7%	0%	17.4%	44.7%

Fig. 1 Locations of 55 failed slope sites and 54 not-yet-failed slope sites along Route T-18

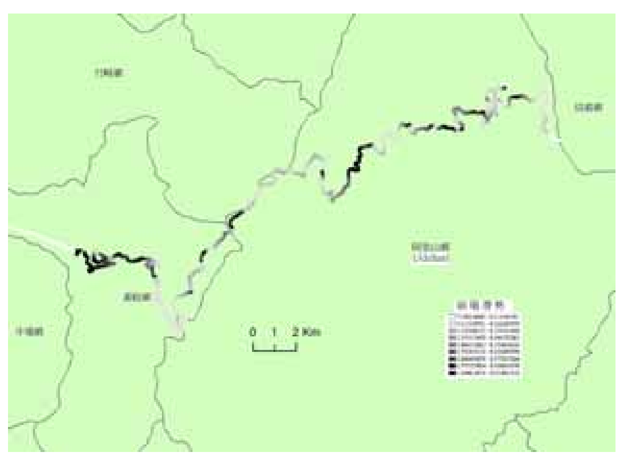

Fig. 2 Landslide potential map along Route T-18

Case study on the variation of water content and matrix suction of unsaturated colluvium slope

Jeng Ching-Jiang[1] Lin Tai-An[2]

[1]*Associate professor, Department of Environmental and Hazards-Resistant Design, Huafan University, Taiwan, R. O. C.* *(TPCE member)*

[2]Graduat student, Department of Environmental and Hazards-Resistant Design, Huafan University, Taiwan, R. O. C.

Abstract

Huafan University is located in northeastern Taiwan on a slope at an elevation of 500 to 550 meters. The surface of the slope consists of colluvium soil. In order to monitor potential landslides, an integrated monitoring system has been in continuous use for the last five years. This case study shows the results of observations of soil water content variation due to rainfall, and the corresponding matrix suction change, for a slope of unsaturated colluvium soil under different planting conditions. Those results will be used as reference data for research into the slope slide mechanism.

Keywords—matrix suction, unsaturated soil, colluvium slope, rainfall-induced, Soil-water Retention Curve

1. Introduction

Heavy rainfall frequently induces slope instability problems. Since the water content and matrix suction of unsaturated soil vary depending on weather conditions. The colluvium soil is being aware of the high permeability and usually low of ground water table. Field investigations have shown that sliding surfaces not only appear under saturated zone but may also be located above the ground water level. A thorough understanding of the sliding problem of an unsaturated colluvium slope, requires monitoring variations in soil water content and matrix suction. When it rains heavily, the matrix suction, extant largely in the unsaturated soil, will be more or less destroyed. Then a wet zone will be formed, in turn reducing the effective strength of the soil. Finally, sliding of the slope may result.

Huafan University is located in northeastern Taiwan on a slope at an elevation of 500 to 550 meters. The surface of the slope consists of a colluvium soil. In order to monitor potential landslides, an integrated monitoring system, including inclinometers, tiltmeters etc. has been continuously observing the slope for the last five years. This study shows the results of additional new inspection instruments, including devices to measure matrix suction, water content and ground water level, set up during different surface planting conditions, to obtain matrix suction and water content for each depth in real-time. These results can serve as a reference for the study of slope stability mechanisms.

2. Stratigraphy and Natural Environment of the Slope

The slope comprises an overburden of colluvium with a nonuniform particle size distribution, sitting atop Miocene sandstones and shales, above bedrock. The unified classification of this overburden is GW or SW. Maximum Particle size is between 152.4mm to 63.5mm. The annual mean temperature and precipitation exceed 20^{o}c and 5,227mm respectively. The monsoon, from northeast, usually causes the weather to become overcast and rainy in the winter. The daily temperature variation in the winter is not obvious, while large changes (more than 5 ^{o}c) between day and night are very common in the summer time. Typhoon-induced heavy rainfall occurs in summer due to the effects of the warm, wet current from the southwest.

The target slope has an average gradient of about 30 degrees, sloping more gently to 15 degrees at the top and foot. Three different planting areas may be found on the surface: a short grass zone on the top area, a broadleaf tree zone on the middle slope, and a 70 centimeter grassy zone at the foot of the slope. Figure 1 shows the geologic strata profile and the three distinct surface planting zones.

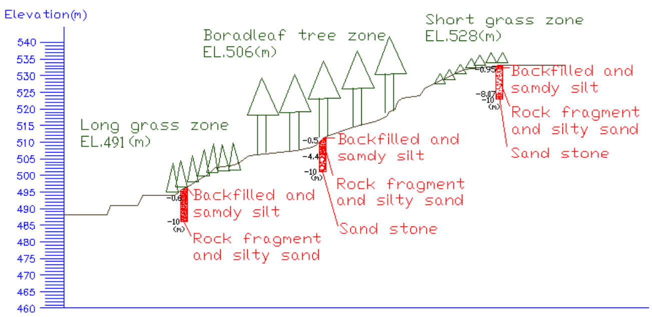

Fig1. Stratigraphy profile of the project site

3.Monitoring plan and measuring devices

3.1 Monitoring plan

A monitoring plan for the field matrix suction and water content variations of the three different planting zones was carried out. Ten sets of electrical tensilmeters, four sets of soil moisture meters and one set of water levelmeters were embedded in three boreholes located in each planting zone. Two tensilmeters were set in the short grass zone, one each at two and four meters depth, four sets placed in the broadleaf tree zone at 2, 3, 4 and 5 meters depth, respectively, while four more sets were embedded in the long grass zone at 2, 4, 6 and 8 meters depth, respectively. Four soil moisture meters were separately installed in each borehole at a depth of 2 meters, and additional one was installed at 8 meters depth in the long grass zone.

The installed measuring devices were numbered in sequence from the top of slope to the foot, as shown in Fig. 2 and described in Table 1. The soil matrix suction

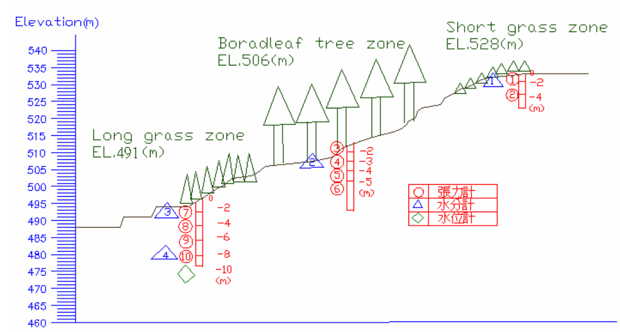

Fig2. Location of monitoring devices

Table 1 Detail of Measuring Devices

Short grass zone (EL.528m)							
No.	T-1	T-2	M-1				
EL. (m)	526	524	526				
Broadleaf Tree zone (EL.506m)							
No.	T-3	T-4	T-5	T-6	M-2		
EL. (m)	505	504	503	502	501		
Long grass zone (EL.491m)							
No.	T-7	T-8	T-9	T-10	M-3	M-4	W-1
EL. (m)	489	487	485	483	489	483	481

Note. : T means Tensilmemter; M means soil moisture meter; W means water level sensor.

and water content measured in the field were then correlated with the precipitation records obtained on campus. Through the relationship between those two data, the phenomenon of reduction in soil matrix suction caused by rainfall can be observed. This phenomenon is expected to further reduce soil strength and finally lead to sliding of the slope.

3.2 Measuring devices

Below is a description of the measuring devices used in this study, including tensilmeter, soil moisture meter and water level sensor, were described as follows:

(1) Tensilmeter： Campbell Scientific Co., Ltd, model-253, measuring range between zero to two bars, dimension in 3.25 inches long and 0.75 inches in diameter.

(2) Soil moisture meter： Decagon Devices Co., Ltd, model-ECH2O PROBES, measuring range between 0-100%, dimension in 10 inches long, 1.25inches width and 1.5mm thickness.

(3)Water level sensor：Campbell Scientific Co., Ltd, model-cs420, measuring range up to 100m, dimension in 9.5 cm long and 1.75 cm in diameter.

4. Monitoring Results and Analysis

Data recorded during continuous monitoring of the slope from March second to September 21st, 2005, will be discussed in this study. During this monitoring period, lacunae in the data occurred when lightning destroyed the data recorder. Figure 3 shows the precipitation records

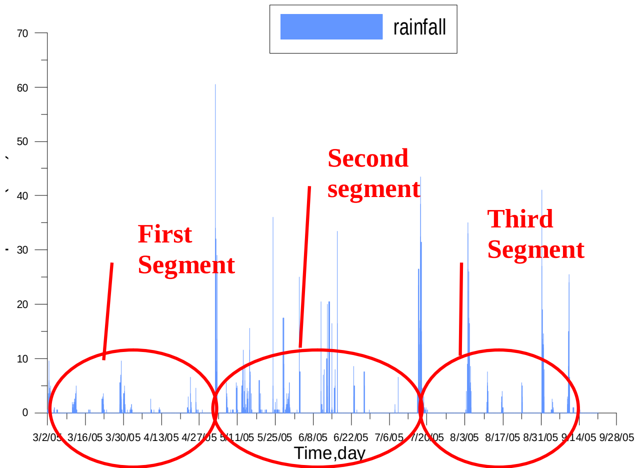

Fig3. Precipitation Record of project site

during this period. For convenience this period will be further divided into three time segments: March to April, when the weather is usually cloudy and wet due to frequent rain of low intensity (less than 10mm/hr); May to June, when continuous rain, due to thunderstorms, exceeds 20 mm/hr; and July to September, when average temperatures are the highest of the whole year, and rain is seldom continuous, but typhoons visit the island (four during the period under discussion).

4.1 Relationship between matrix suction and precipitation

Figure 4 to 6 shows the results of monitoring of matrix suction and precipitation. When compared with the results of Fig. 4 with Fig.5 and Fig.6, it indicates that for the short grass zone, regardless of the time period, it always possesses higher suction than the other planting zones. In the third time segment (i.e. July to September) of Fig. 4, the cumulative maximum suction value at two meters depth (No. 1) is highest, at 0.903 bars. The suction value for the same depth in the long grass zone shown in Fig. 6 is seconds. The broadleaf tree zone shown in Fig. 5 has lower levels of suction and preserves water the best. The matrix suction in the short grass zone will be destroyed during strong rains, such as those of a typhoon. The larger the variation in matrix suction caused by rainfall in the short grass zone, the lower the ability of slope protection there will be. During rainfall, a portion of

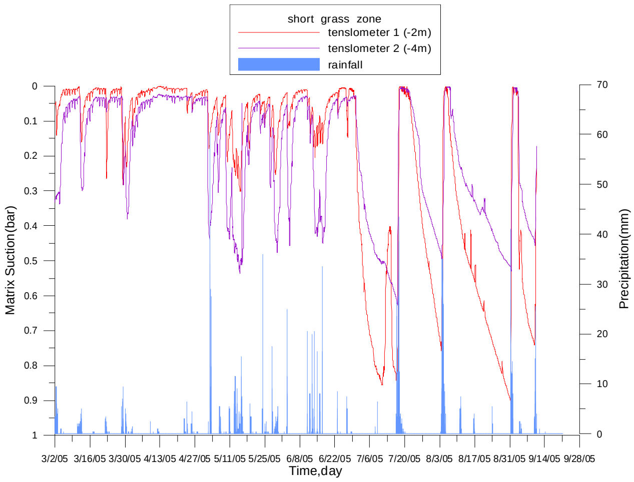

Fig4. Relationship between matrix suction and precipitation in short grass zone

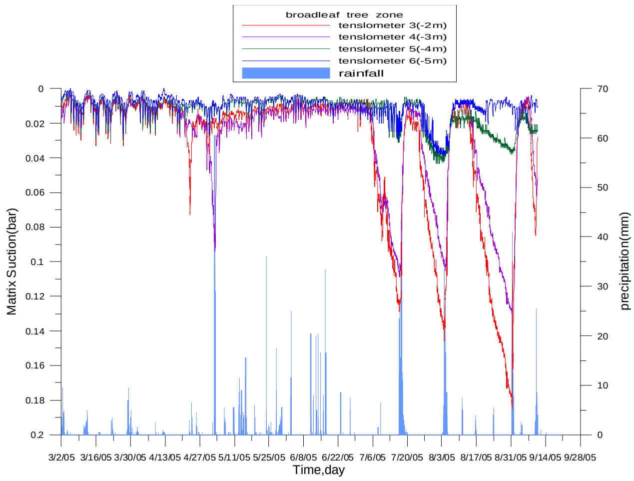

Fig5. Relationship between matrix suction and precipitation in broadleaf tree zone

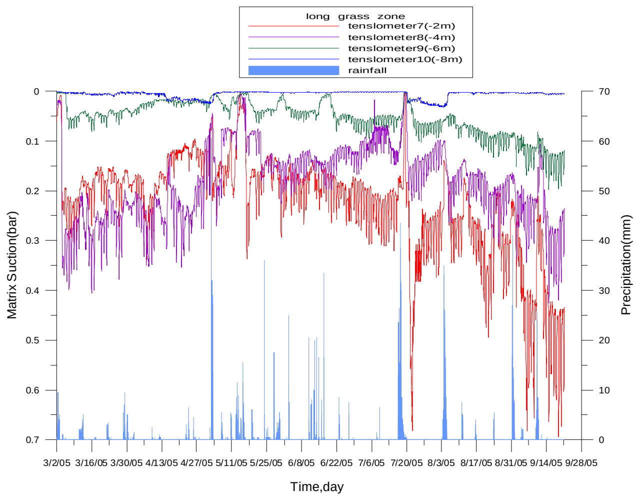

Fig6. Relationship between matrix suction and precipitation in long grass zone

the falling water is intercepted by the canopy, some of it passing through to the ground surface of the forest. If the intensity of precipitation is great, then most of the water will reach the ground surface and seep into the soil or be stored within voids in the soil (Chen, 1993). Figure 5 shows that the suction value in the broadleaf tree zone is the lowest, while the frequency of variation is the greatest. This can be attributed to the forest cover, which causes most of the runoff to be retained and seep into the soil. Moreover, the roots of the tree will increase the number of voids in the soil, thus improving the infiltration of the water.

A comparison of the shallow layer (2m and 3m) and deeper layer (lower than 4m) results in Fig. 4 and Fig. 6 shows that in the first and second time segment, the suction value in shallow layer is generally larger than in the deeper layer.

4.2 Time Lag in Suction Response to Rainfall

At the commencement of precipitation, the rainfall falling from the sky to ground passes through the canopy and is held by the plants. This lengthens the time required for a change in suction, leading to a time lag in the suction change response. Fig. 7 to 9 indicate precipitation began

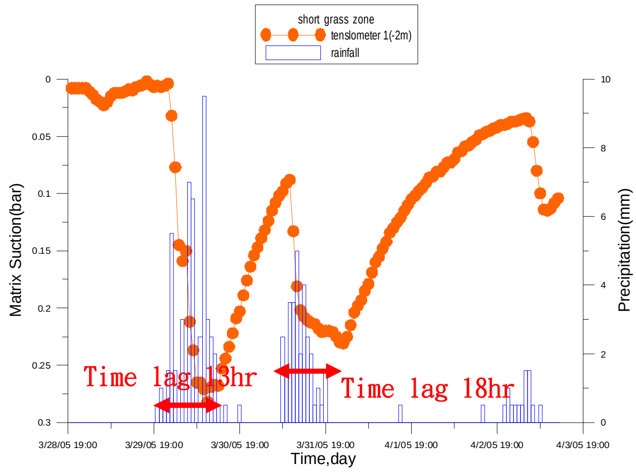

Fig7. Time lag in short grass zone

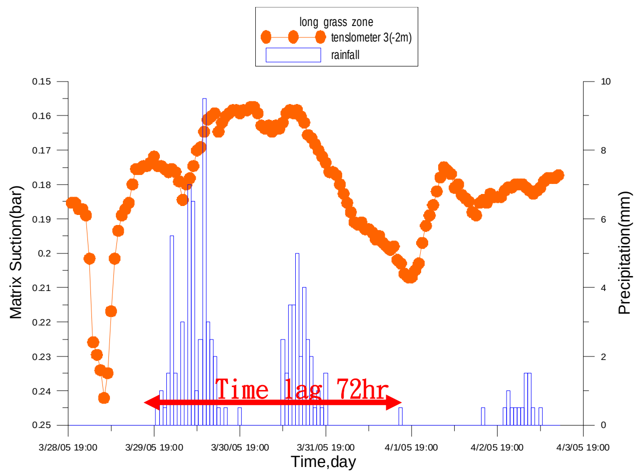

Fig8. Time lag in long grass zone

at 17:00 hours on March 29th and again at 16:00 hours on March 30th. The break time in the middle is about 10 hours. Maximum intensity reached 9.5 mm/hr and 4 mm/hr with duration of 25 hours and 12 hours,

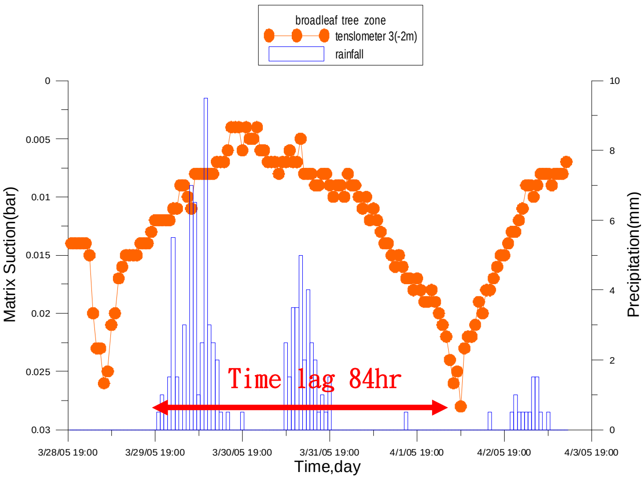

Fig9. Time lag in broadleaf tree zone

respectively. It was compared the time lag of suction response in three zones for the depth of 2 meters. The time lag in suction change response for the short grass zone in Fig. 7 is 13 hours and 18 hours, respectively. Figures 8 and 9 show that the first precipitation had no

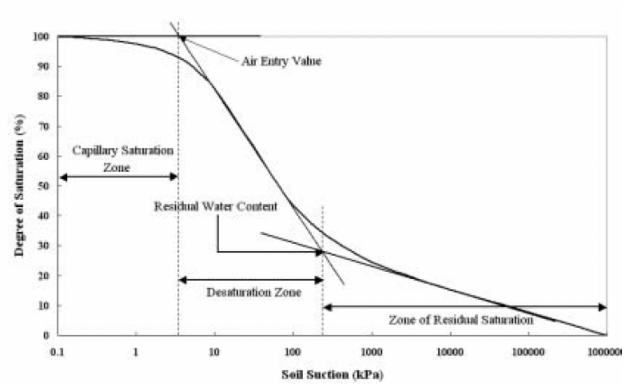

Fig10. Demonstration Soil-water Retention Curve

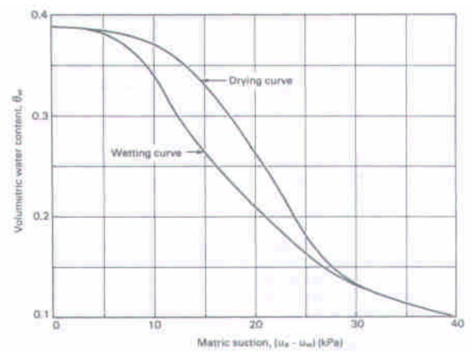

Fig11. Soil Drying and Wetting Course

effect on suction response in the long grass and broadleaf zones. The suction did not begin to reduce until the second rainfall commenced, leading to a time lag of 72 hours and 84 hours for each case. The forest cover area is most effective in ameliorating the effects of rainfall. In other words, the broadleaf zone protects the slope better than other plant cover.

4.3 Soil-water Retention Curve

The Soil-water Retention Curve (SWRC) in Fig.10 is the relationship between matrix suction and degree of saturation (or volume water content) reflecting soil strength, seepage and constitutive structure. In addition during the process of drainage and absorption, matrix suction will relate to different degrees of saturation (or volume content), as Fig. 11 depicts. That implies that the drain path is different from the absorption path. For this reason, the variation of SWRC due to the effects of different factors is a key to understanding water retention in unsaturated soil. Figures 12 to 14 show the SWRC of

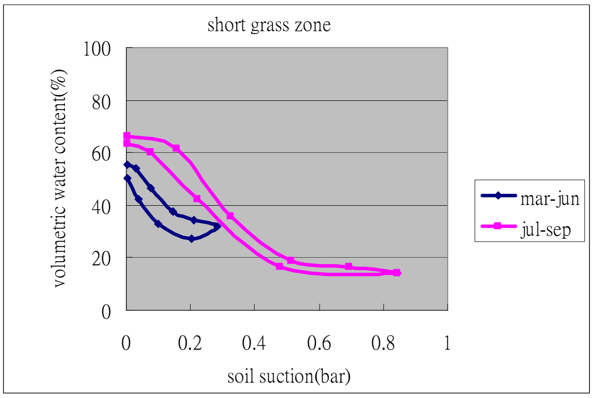

Fig12. SWRC for short grass zone

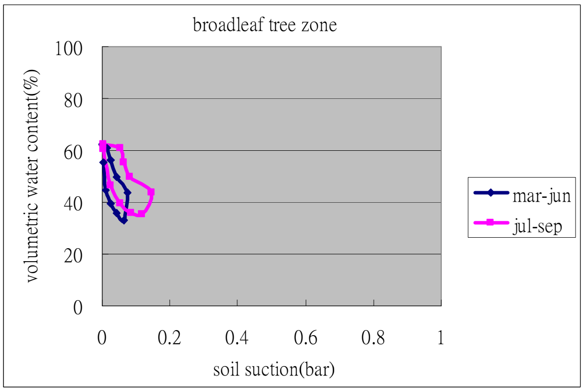

Fig13. SWRC for broadleaf tree zone

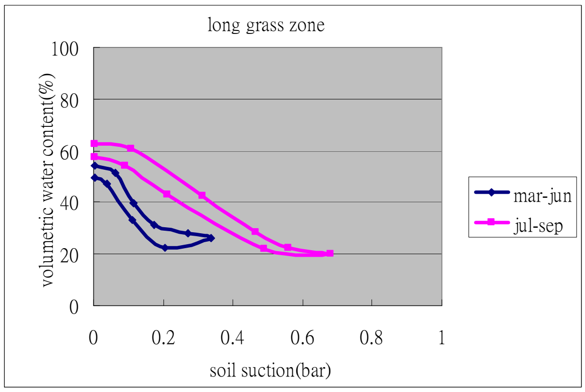

Fig14. SWRC for long grass zone

the shallow soil (2m depth) for different planting zones in the time segments of March to June, and July to September. According to these curves, the phenomena of absorption and drainage may be summarized as follows :

(a) Regardless of planting zone the SWRC curves in third time segment always have higher water content and air entry value than in the first and second time segment.

(b) The broadleaf tree zone has a more rounded SWRC than other zones. This shows that the forested area retains more water, and the difference in water content between the wet season and hot season is the least.

(c) The short grass zone has the highest matrix suction, 0.843 bars, in the third time segment. This is due to the higher temperatures and longer periods of sunshine in this time segment.

5. Conclusions

Based on the above results, several conclusions may be made.

(1) In the first and second time segment, due to more frequent instances of rain, soil water levels remained wet, leading to more frequent changes in matrix suction, though the change in value is not obvious. This implies that the figure for matrix suction is often low.

(2) In the short grass zone, because the lack of cover there is more sun, causing the matrix suction to be higher than the long grass and broadleaf zones.

(3) In the broadleaf tree zone, plant roots may increase the void ratio of the soil and thus facilitate infiltration. In this zone the water content is the highest, followed by the long grass zone and the short grass zone, respectively. The difference in water content between the three zones is more evident in the third time segment.

(4) Regardless of planting zone the change of matrix suction caused by rainfall is always clearer in the shallow layer than in the deeper layer.

(5) In case of the third time segment, because the higher mean temperature and the effect of evaporation caused by sunshine is stronger, the matrix suction in this time segment is higher. However, when heavy rains caused by typhoon fall on the area, matrix suction will drop quickly. This variation is obvious in short grass zone and less clear in the broadleaf tree zone.

(6) The ability to retain water is greatest in the broadleaf tree zone, followed by the long grass zone and the short grass zone, respectively.

References

[1]Ching-Jiang Jeng, Tai-An Lin, Jr-Kai Hsu, Shr-HungChen (2005), "Study on the Particle Size Simulation of Colluvium and its Shearing Characteristic," 2005 Culture and Design Conference, Fuafan University, pp.445-454.

[2]Ming-Chieh Chen (1993), "Research on the Characteristics of soil void distribution in different forest area of Lian-fua pool," Quarterly Jounal of Chinese Forestry, 26(2), pp. 63-77.

[3]Johnson Kung, Hung-Ta Lin (2005), "Influence of Vegetation on the slope stability of unsaturated soil slop," Proceeding of the 11th Conference on Current Researches in Geotechnical Engineering in Taiwan, pp.c17-1~c17-8.

[4]Zhou Jian(2005), "Main Influences on Soil Water Retention Curve," Proceeding of the Second Chinese National Symposium on Unsaturated Soils, pp.390-400.

Applicability of Rainfall Index *R'* for Recent Cases in 2004 - 2005

S. Nakai[1], M. Kaibori[2], Y. Sasaki[3], T. Moriwaki[4], S. Kano[5]

[1]*Disaster Prevention System Division, Fukken Co., Ltd., Hiroshima, Japan*

[2]*Graduate School of Integrated Arts and Sciences, Hiroshima University, Hiroshima Japan*

[3]*Japan Institute of Construction Engineering, Tokyo, Japan*

[4] *Kure College of Technology, Hiroshima Japan*

[5]*Graduate School of Engineering, Hiroshima University, Hiroshima, Japan*

Abstract

Proper warning and evacuation are essential for mitigating sediment-related disasters during heavy rainfall. For this purpose, a scientific and rational rainfall index should be established in accordance with regional geological and topographical characteristics. The authors proposed Rainfall index *R'* for warning against sediment-related disaster. It became possible to express influences of both preceding and present rainfall by a single value of *R'*. This rainfall index was developed by using the past disaster cases in Masado (decomposed granite soil) area in Hiroshima district. In this paper, several cases of slope failure and debris flow including non-granite zone in 2004-2005 were also examined to confirm the effectiveness of this newly-proposed rainfall index. It has been understood that the rainfall index *R'* will be able to use widely, if the coefficient and the reference value are chosen properly for each region considering its geological and topographical characteristics.

Keywords—*Rainfall index R', Sediment-related disaster, Geological and topographical characteristics*

INTRODUCTION

Sasaki et al. have introduced rainfall index *R'* for warning and evacuation from sediment-related disasters at "2004 Japan-Taiwan Workshop" [1]. There are also many sediment-related disasters occur in Japan after 2004 [2, 3]. During the year 2004-2005, numerous sediment-related disaster was triggered due to repeatedly occurred typhoon, heavy rain by seasonal rain front, and moreover the influence of the Niigata-ken Chuetsu Earthquake in 2004 and the Fukuoka-ken Seiho-oki Earthquake in 2005 (Fig. 1, Table 1). In some cases, the disaster prevention effect of SABO (erosion control) facilities are seen [4] but the numbers of these facilities are still not enough. Therefore, proper warning and evacuation is important in order to reduce the losses of human lives.

Table 1: The main sediment-related disaster that occurred in Japan in 2004 - 2005

Date	Cause	Numbers of Sediment-related Disasters	Mainly damaged region
2004			
07/12 - 07/18	Niigata Fukushima Rainfall	274	Niigata, etc.
07/18	Fukui Rainfall	138	Fukui, etc.
07/31 - 08/02	Typhoon 0410 (NAMTHEUN)	74	Tokushima, Kochi, etc.
08/17 - 08/20	Typhoon 0415 (MEGI)	71	Kagawa, Ehime, etc.
08/30 - 08/31	Typhoon 0416 (CHABA)	118	Tokushima, Ehime, etc.
09/07 - 09/08	Typhoon 0418 (SONGDA)	78	Oita, etc.
09/29 - 09/30	Typhoon 0421 (MEARI)	251	Mie, Ehime, etc.
10/09 - 10/10	Typhoon 0422 (MA-ON)	233	Shizuoka, Kanagawa, etc.
10/20	Typhoon 0423 (TOKAGE)	800	Okayama, Hyogo, etc.
10/23	Niigata Chuetsu Earthquake	225	Niigata
Others	Seasonal rain front, Snow melting, etc.	275	
Total of 2004		2,537	
2005			
03/20	Fukuoka Seiho-oki Earthquake	22	Fukuoka, etc.
04/01	Hakui Landslide	1	Ishikawa
06/27 - 06/30	Seasonal rain front	26	Niigata, Ishikawa
07/08 - 07/10	Seasonal rain front	11	Oita
07/26 - 07/27	Typhoon 0507 (BANYAN)	3	Shizuoka
08/25 - 08/26	Typhoon 0511 (MAWAR)	8	Kanagawa, Shizuoka, etc.
09/04 - 09/08	Typhoon 0514 (NABI()	363	Kyushu - Chugoku Regions
Others	Seasonal rain front, Snow melting, etc.	380	
Total of 2005		814	

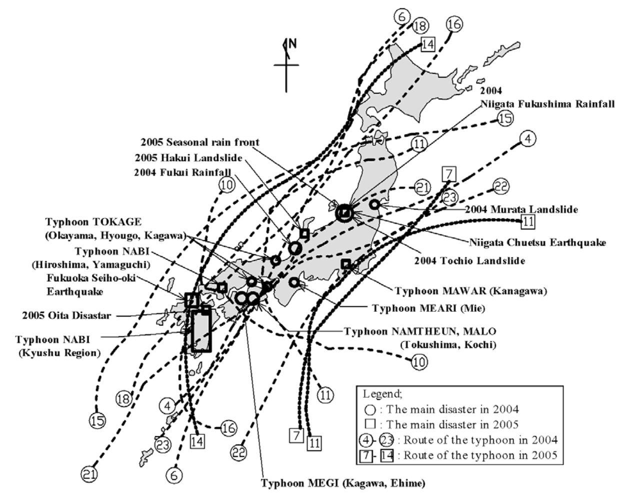

Fig: 1 Typhoon courses in 2004-2005 and the main disaster place

A proper prediction of disaster occurrence is needed for proper warning and evacuation; therefore, accurate "prediction of time" and "prediction of location" are essential. In past method, both rainfall intensity and preceding rainfall were directly used to express the rainfall situation. However, it is difficult to draw a map which indicates spatial distribution of dangerous area against sediment-related disaster in real-time manner. A new rainfall index *R'* which can express the precipitation situation by one number is appropriate to show the dangerous area that varies with time on the map [5].

R' has been proposed based on disasters that occurred in Masado area at several places in Hiroshima including the 6.29 rainfall disaster in 1999 (hereinafter "6.29-

disaster").

Especially, in Masado area where many people live on a steep slope or on a past debris flow deposit in Hiroshima Prefecture, sediment-related disaster often occurs due to heavy rainfall. However, the critical values of rainfall for disasters occurrence are not higher than those in metamorphic rocks area and/or those in frequently rained area in Shikoku district [6].

It is necessary for the accuracy improvement and the applicability expansion of the R' to verify further case. And it is also necessary to examine the applicability in the place other than Hiroshima region, where the geological and the geographical characteristics are different. Three heavy rainfalls that generate sediment-related disaster from 2004 to 2005 including regions other than Hiroshima are examined. In these cases, the distribution map of the R' was made from the on-going rainfall data, and places where sediment-related disaster will occur are forecasted.

Moreover, R' indicated the possibility of landslide occurrence due to preceding rainfall during the Niigata-ken Chuetsu Earthquake.

OUTLINE OF EXAMINED DISASTERS

The following three cases shown in Table 2 were examined:

a) Disaster on Oct. 21, 2004, at Tamano City in Okayama Prefecture by Typhoon 0423 (TOKAGE).

b) Disaster on Aug. 26, 2005, at Hakone Town in Kanagawa Prefecture by Typhoon 0511 (MAWER).

c) Disaster on Sep. 6, 2005, in the west part of Hiroshima Prefecture by Typhoon 0514 (NABI).

Table 2: Outline of Three Disasters Examined

Name and Date	Mainly damaged region	Total rainfall	Outline of the damage by sediment-related disasters
Typhoon 0423 (TOKAGE) 2004-10-20	Okayama, Kagawa, Hyogo , Kyoto, etc.	Tamano (Okayama): 245mm Higashi-kagawa: 395mm Muraoka (Hyogo): 298mm Maizuru (Kyoto): 326mm Total rainfall of 10/19 - 10/21	800 sediment-related disasters occurred, 27 persons were killed, 31 persons were injured, and 351 houses were destroyed.
Typhoon 0511 (MAWER) 2004-08-25	Kanagawa, Shizuoka, Yamanashi, Tokyo, etc.	Hakone (Kanagawa): 716mm Mt. Amagi (Shizuoka): 420mm Yamanaka (Yamanashi): 257mm Ohshima (Tokyo): 299mm Total rainfall of 08/21 - 08/26	8 sediment-related disasters occurred, 1 house was destroyed, and several facilities and structures were destroyed.
Typhoon 0514 (NABI) 2005-09-06	Miyazaki, Kagoshima, Kumamoto, Oita, Yamaguchi, Hiroshima, etc.	Nango (Miyazaki): 1321mm Kimotsuki (Kagoshima):995mm Shiragadake (Kumamoto)677mm Yufuin (Oita):726mm Mt. Rakan (Yamaguchi):540mm Otani (Hiroshima):496mm Total rainfall of 09/04 - 09/08	363 sediment-related disasters occurred, 19 persons were killed, 3 persons were missing, 3 persons were injured, 191 houses were destroyed, and many facilities and structures were destroyed.

Tamano City in Okayama Prefecture which adjoins Hiroshima Prefecture is covered with Masado while Hakone Town in Kanagawa Prefecture is in volcanic rock area. Two cases above were chosen due to the same geological characteristic and different geological characteristic, respectively.

As in the case where Typhoon 0514 hit the western part of Hiroshima Prefecture, sediment-related disasters occurred in both Masado area and paleozoic rock area.

The applicability of R' for different geological and topographical regional is examined using these three cases.

Besides these, the Niigata-ken Chuetsu Earthquake in 2004 is used to study the relation between landslide due to earthquake and residual condition of preceding rainfall.

In analysis of the R', the real time rainfall data from website of "Automated Meteorological Data Acquisition System of the Meteorological Agency (hereinafter "AMeDAS")" [7], "Water information system of the Ministry of Land, Infrastructure and Transport Government of Japan (hereinafter "MLIT-data")" [8], and "Disaster prevention information system of Hiroshima Prefecture (hereinafter "HIROSHIMA-data")" [9] were used.

Table 3 shows the number of analysis data and the maximum R'-value of the observatory near the disaster occurrence area.

Table 3: The number of analysis data and the maximum R'-value of the observatory near the disaster occurrence area.

	Number of rainfall data	Maximum R'-value near disaster area
Typhoon 0423 (TOKAGE)	Okayama Prefecture: 49 Otehr prefectures: 23	258.8mm (Tamano) 2004-10-20 15:00
Typhoon 0511 (MAWER)	Shizuoka and Kanagawa Prefecture: 18	688.5mm(Hakone) 2005-08-23 23:00
Typhoon 0514 (NABI)	Hiroshima Prefecture: 292	529.4mm(Otani) 288.4mm(Miyajima) 2005-09-06 22:00

METHODOLOGY OF RAINFALL INDEX R'

The method of R'-analysis reported in details during the "Workshop in 2004" is briefly explained here.

It is well known fact that the rain induced sediment-related disaster is strongly related to both accumulated precipitation and also the rainfall intensity. In the idea till then, the warning for sediment-related disaster was judged by drawing these two values in the X-Y graph as snake-line [10, 11]. Then, the critical line (CL) is drawn at the boundary between disastrous rainfalls and non-disastrous rainfalls. If snake-line exceeds CL, it is judged that this rainfall situation may cause sediment-related disaster.

Sasaki et al. had proposed to use single value of R_f instead of using two values for warning [12]. The concept of R_f is to express the critical value of the snake-line by using the radius of elliptical arc.

The rainfall index R_{fw} is proposed by improving the rainfall index R_f [5]. Fig. 2 shows the definition of rainfall index R_{fw}. Namely, the rainfall index R_{fw} is calculated from Equation (1) as well as the method of calculating R_f. Most important difference between them is that the concept of the effective rainfall using half-value period, that can take into account the discharging effect of infiltrated water from the ground in slope, is used for gaining R_{fw}. And the rainfall index R_{fw} is transformed into Rainfall Index R' as shown in Equation (2).

$$R_{fw} = \sqrt{(R_1 - R_w)^2 + a^2(r_1 - r_w)^2} \quad (1)$$

$$R' = R_{fw0} - R_{fw} \quad (2)$$

R_w and r_w are long-term and short-term effective rainfalls (in millimeters), respectively, R_1 and r_1 are reference points on the abscissa and the ordinate, respectively, a is a weighting factor, and R_{fw0} is the distance from the origin 0 to a reference point B (R_1, ar_1).

The half-value period is considered as an index to describe the water storage/discharge characteristics of the area. It is said that a short-term half-value period indicates the ground surface characteristics and a long-term half-value period indicates the underground characteristics. In Hiroshima Prefecture, the combination of 72 hours' and 1.5 hours' half-value periods was applied in the calculation of effective rainfall [13]. Hence, half-value periods of 72 hours and 1.5 hours respectively for R_w and r_w have been selected of R's calculation.

In several case analysis of Masado area around Hiroshima Prefecture including serious disaster during the "6.29-disaster", the coefficient R_1= 450, r_1= 150 and a= 3 are chosen and critical values of R' for debris flow/ hillside landslide/ slope failure are clarified as 250mm/ 175mm/ 150mm respectively.

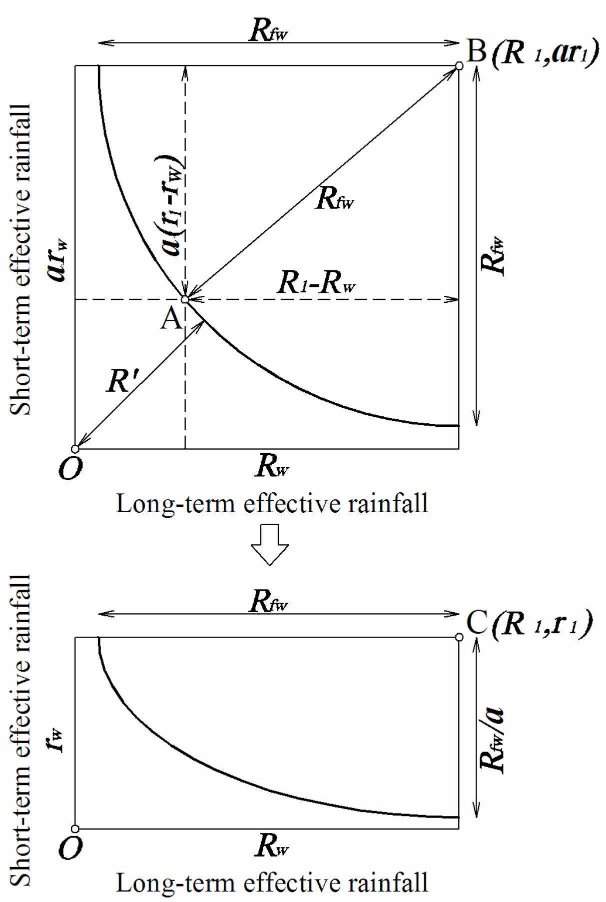

Fig. 2: Definition of the rainfall index R_{fw} and R'

THE CALCULATION RESULT OF R' IN THREE DISASTERS

Disaster on Oct. 21, 2004, in Okayama; Typhoon 0423 (TOKAGE)

Typhoon 0423 has caused heavy damage in western Japan. Some 800 sediment-related disasters occurred in Okayama, Kagawa, Hyogo, and Kyoto Prefecture, etc. [14].

On October 20, 2004, several sediment-related disasters occurred in Tamano City of Okayama Prefecture which adjoins Hiroshima Prefecture. Five human lives and a large number of properties were lost in one of the debris flows which occurred in this area (Figs. 3 - 4).

Fig. 3: Debris-flow in Tamano City (In Masado area). The shallow slide occurred in upstream. Debris-flow was extended and piled up at the exit of the valley.

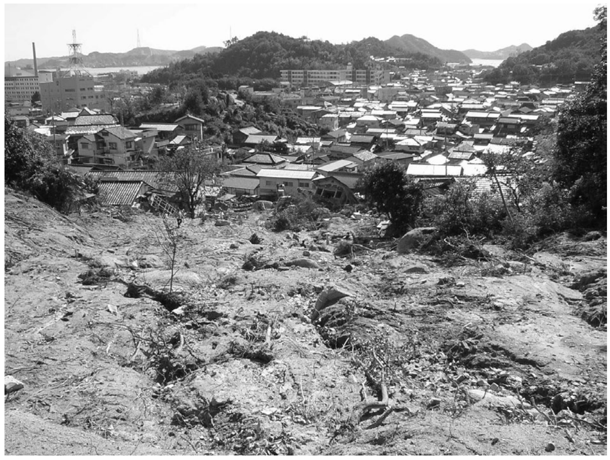

Fig. 4: Damage of debris-flow in Tamano City. A large amount of boulder and debris reached the residential quarter.

Debris flow occurred at shallow valley of Masado area in the vicinity of Tamano City. Rainfall data from Tamano station of AMeDAS shows that rainfall accumulation until disaster occurrence was 209mm (total rainfall was 245mm), and the maximum hourly rainfall was 27mm (recorded in 2005-10-20 15:00), which is comparatively a small value.

In Tamano City, 149mm of rainfall during Typhoon

0421 (MEARI) and 53mm of rainfall during Typhoon 0422 (MA-ON) occurred one month before the disaster. These were considered as very severe condition for this region where the usual rainfall is always light.

Fig. 5 shows the R'-distribution map of 2005-10-20 15:00. In this analysis, the coefficients R_I=450mm, r_I=150mm, and a=3 that Nakai et al. had used in the Hiroshima region [5].

Although the hourly rainfall was not that large in scale for a usual debris flow, it turns out that the value of R' at disaster occurrence time around Tamano City was 258.8mm, exceeded R'_c= 250mm due to the influence of preceding rainfall. This shows that debris flow occurrence can be well expressed by R'_c value.

The usefulness of application by this method was also confirmed in Masado area of Okayama Prefecture adjoining Hiroshima Prefecture.

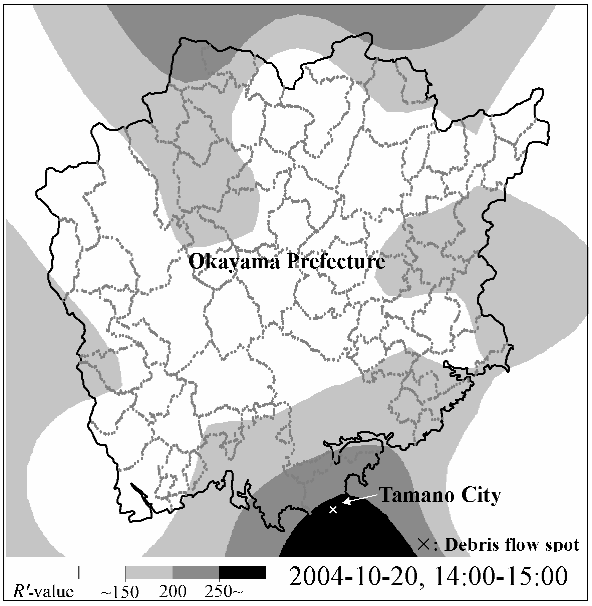

Fig. 5: R'-distribution map (Oct. 20, 2004 Okayama Prefecture)

Disaster on Aug. 26, 2005, in Kanagawa; Typhoon 0511 (MAWER)

Typhoon 0511 caused heavy rainfall in Kanto region, and brought heavy damage to Kanagawa, Shizuoka, Yamanashi Prefecture, and Tokyo. In Hakone Town of Kanagawa Prefecture, the rainfall was especially heavy from evening of August 25 to before-dawn of August 26, according to the rainfall data of Hakone station of AMeDAS, the total rainfall was 593.5mm, and the maximum hourly rainfall was 65mm (recorded in 2005-08-25 21:00 and 22:00).

A newspaper reported that a sediment-related disaster occurred in Yunohanazawa district of Hakone Town [15], hot spring facilities were destroyed as shown in Fig. 6, and 137 of the hot spring supply were stopped. The place where sediment-related disaster occurred was at hillside slope of volcanic rock area.

Fig. 6: Damage of debris-flow in Yunohanazawa district (Downloaded from Web site of Good Speed Tours Ltd. as in [16])

When the typhoon attacked Kanto Region, authors tried to trace the rainfall situation by using R' in a real-time manner. It was discovered from this case that R' value was far larger in scale than that which brought the sediment-related disaster in and around Hiroshima Prefecture up to now (Fig. 7). For this reason, R_I=750mm, r_I=250mm, and a=3 were used for the coefficient for calculation of R'.

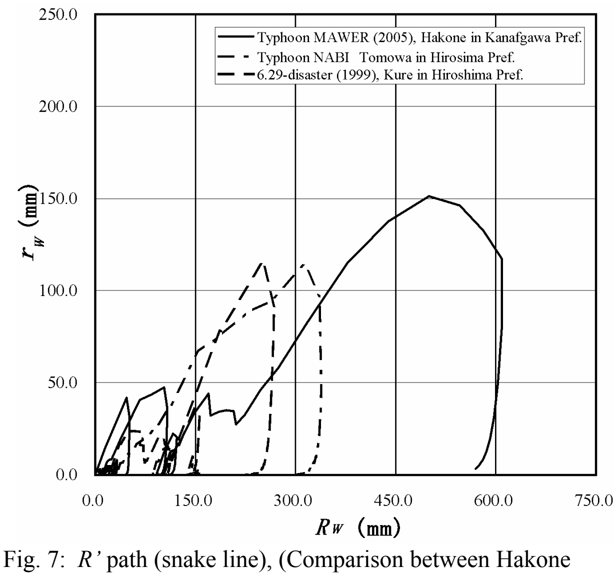

Fig. 7: R' path (snake line), (Comparison between Hakone region and Hiroshima region).

Fig. 8 shows R'-distribution maps in Kanto region during the Typhoon 0511 approach. It is understood that the R'-value around Hakone Town rose up remarkably from 19 o'clock of August 25. An extremely dangerous state of R'>600mm continued for five hours from 21 o'clock, and sediment-related disaster occurred in this period. The maximum value in Hakone observatory of AMeDAS reached R'=688.5mm (23 o'clock).

Though this rainfall were far larger-scale than that of "6.29-disaster" or Typhoon 0514 in Hiroshima Prefecture, the disaster scale seems to be smaller. It was noticed from this case that the rainfall condition that caused sediment-related disaster was different according to geological and geographical characteristics. However, by changing the coefficient, the rainfall index R' shows the movement of dangerous places due to heavy rainfall without contradiction. Also in this case, it was felt that the R'-distribution map displayed in real-time manner was very useful in understanding the change of a dangerous area with time.

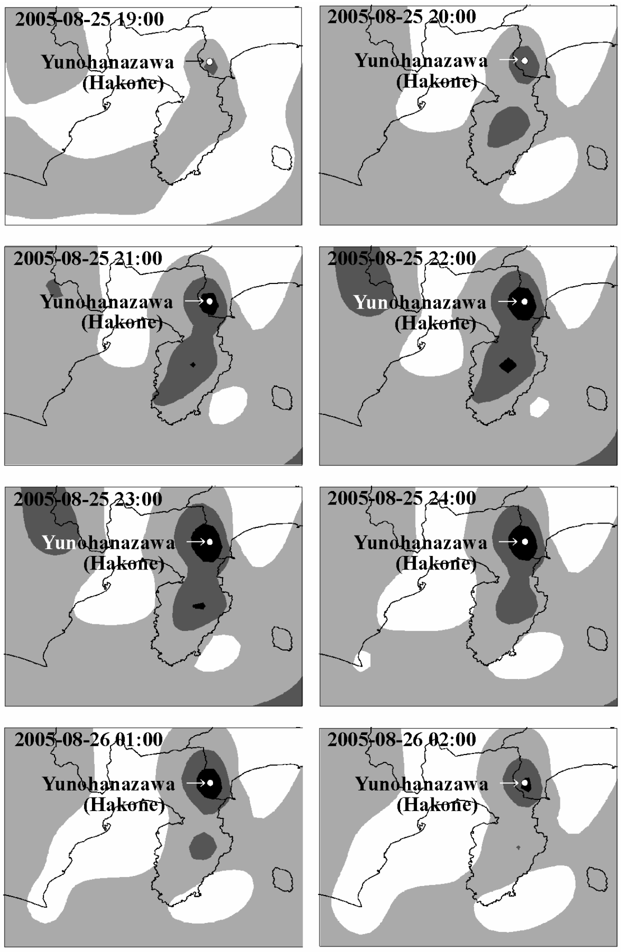

Fig. 8: R'-distribution map
(In Kanto region during the Typhoon MAWER)

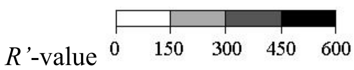

Disaster on Sep. 6, 2005, in Hiroshima; Typhoon 0514 (NABI)

Typhoon 0514 approached Kyusyu and Chugoku region from September 6 to 7 in 2005. In Miyazaki, Kagoshima, Kumamoto, Oita, Yamaguchi, and Hiroshima Prefecture, etc., 362 of sediment-related disasters occurred, 19 persons were killed, 3 persons were missing and 3 persons were injured during this disaster.

Heavy rainfall hit Nango District of Miyazaki Prefecture, and the total rainfall reached 1321mm in the Mikado station of AMeDAS.

Heavy rainfall also hit Chugoku region; total rainfall 540mm of Rakanzan station of AMeDAS in Yamaguchi Prefecture and total rainfall 496mm of Otani station of MLIT-data in Hiroshima Prefecture. Besides these, total rainfall records of more than 400mm were recorded in many rain-gauge stations of western part of Hiroshima Prefecture and eastern part of Yamaguchi Prefecture [4, 17].

As a result, several sediment-related disasters occurred in various places in this area. An embankment slope failure occurred between Iwakuni IC. and Kuga IC. of Sanyo Expressway in the Yamaguchi Prefecture, private house was destroyed, and three persons were killed by fluidized soil. Also, in the western part of Hiroshima Prefecture, 13 debris-flows, 1 landslide, and 7 slope-failures occurrences were reported by the Ministry of Land, Infrastructure and Transport. In this area, the debris-flows and the shallow-slides occurred both in Masado and paleozoic rock area, such as Shiraito River in Miyajima Town (present Hatsukaichi City), Kujima district in Hatsukaichi City, and Yoshiyama river-side in Hiroshima City, but the landslide occurred only in paleozoic rock area of Yuki district in Hiroshima City.

In this case, compared with the "6.29-disaster", the rainfall situation was heavier in the paleozoic rock area in the northwest of Hiroshima Prefecture, and was not so heavy in Masado area in the southwest of Hiroshima Prefecture.

Fig. 9 shows the R'-distribution during passing of the Typhoon 0514 across the Chugoku region. In this analysis, the coefficients of R_1=450mm, r_1=150mm and a=3 are used. Those coefficients are the same as used in past disaster case around Hiroshima area [5].

In this case where disaster occurred in western part of Hiroshima Prefecture, every R'-value that exceeded R'= 250mm is assumed to have reached enough condition as critical value for debris flow occurrence in Masado area. However, no disaster was induced even though some of the R'-value reached 350mm and disaster occurred only after R' reached 450mm.

Around Kujima district and Yuki district, the R'-value had exceeded 400-450mm, and the maximum R'-value of Otani station of MLIT-data recorded was 529.4mm. Although this rainfall was heavier than that of "6.29-disaster", the damage level of disaster seems smaller than that of "6.29-disaster". In this time, many regions where heaviest rainfall was recorded are not Masado area but paleozoic rock area. It seems that the critical value of rainfall against sediment-related disaster occurrence in paleozoic rock area was larger than that of Masado area from the geological characteristics.

At Shiraito River in Miyajima Town, a debris-flow occurred when the R'-value slightly exceeded 250mm, and the maximum R'-value in Miyajima station was recorded as 288.4mm. In Miyajima Town surrounding, although there was heavy rainfall that has equal or bigger level than that of "6.29-disaster", debris flow disaster did not occur at Shiraito River during that time. It is well known there could be lots of fallen woods damage on the slope caused by strong wind of several typhoons after 1999. However, causal relations of these are still not clear.

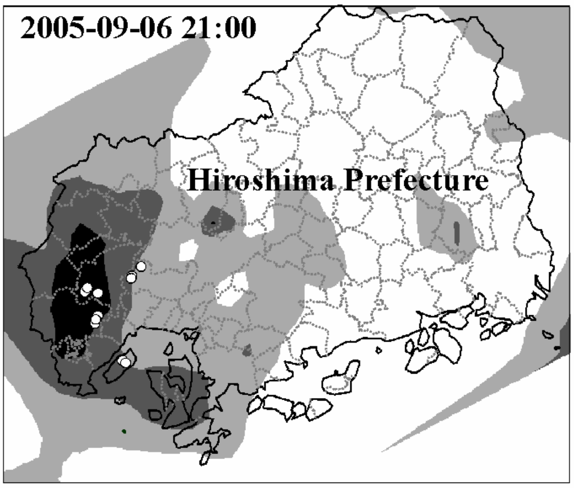

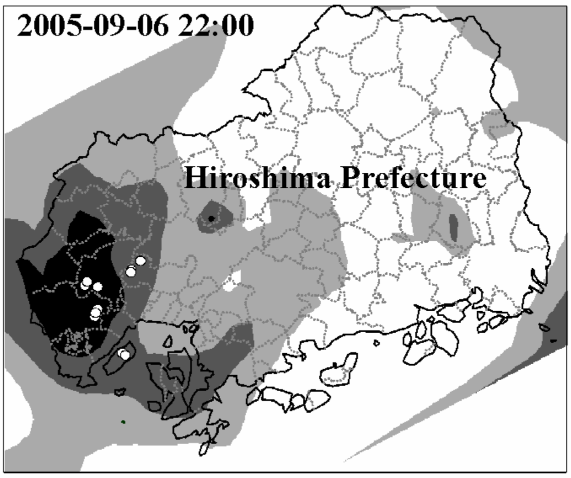

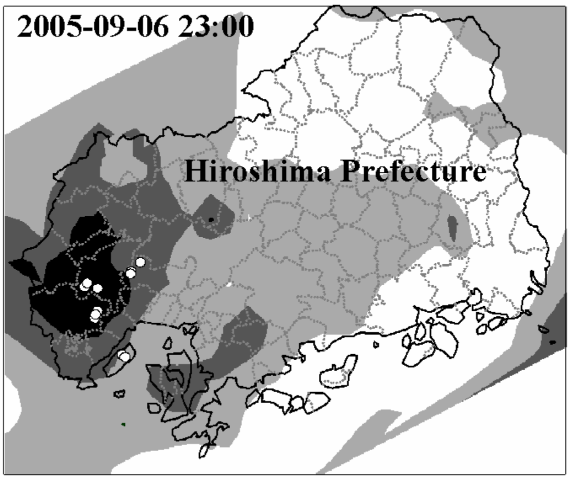

Fig. 9: *R'*-distribution map
(2005-09-06 21:00 - 23:00, Hiroshima Prefecture)

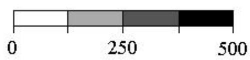

From these, it is known that natural hazards other than rainfall like strong wind or earthquake, etc might cause critical effect in triggering slope failure in addition to geological and topographical characteristics.

In this heavy rainfall case due to Typhoon 0514, although in Masado area there are mainly shallow slides or debris-flows (Figs. 10-11), in Paleozoic rock area there are some landslides (including large scale one) in addition to them (Figs. 12-13).

It has been understood that the type of disaster and the warning rainfall are different in each regional geological and topographical characteristics.

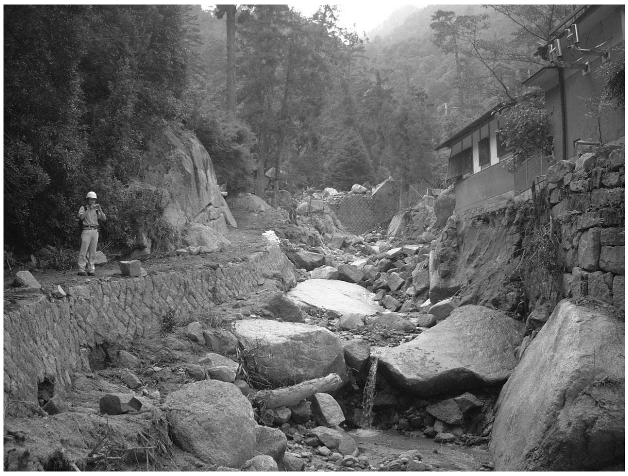

Fig. 10: Damage of debris-flow in Masado area (Shiraito River in Miyajima Town).
A large amount of boulder and debris reached the exit of valley, and the structure etc. were destroyed. However, houses in the downstream were defended as the effect of Sabo dams [4].

Fig. 11: Debris-flow in Masado area (Kujima district in Hatsukaichi City). The shallow slide occurred in upstream and grew up debris-flow.

Fig. 12: Debris-flow in Paleozoic rock area (Kujima district in Hatsukaichi City).The debris-flow carried with eroded soil, gravel, boulder, and trees of hillside and river bed.

Fig. 13: Landslide in Paleozoic rock area (Yuki district in Hiroshima City). Around the main scarp of landslide, the ground cracked and becomes uneven, and a house was destroyed.

CONSIDERATION OF *R′*-VALUE AT THE NIIGATA CHUETSU EARTHQUAKE

In the Niigata-ken Chuetsu Earthquake, 225 of sediment-related disasters occurred, 4 persons were killed and 2 persons were injured [19].

The relation between sediment-related disaster and earthquake is not clarified. However, it is pointed out in this earthquake that high moisture contents are found in the soil, as one of the reasons why a lot of sediment-related disasters occurred [20]. Especially, the rainfall during Typhoon 0423 peaked three days before (on around 2004-10-20 23:00) the earthquake. Using R_I=450mm, r_I=150mm, and a=3, the R'-value at Oguni station of AMeDAS reached the peak of 129mm.

While the influence of the preceding rainfall was gradually decreased after the peak, when the earthquake occurred, the R'-values at AMeDAS rain-gage stations of heavily damaged cities (Yamakoshi Village, Ojiya City, and Tokamachi City) were recorded as high as 50-60mm or more, and indicated as 61.9mm in the Koide station (Fig. 14).

Although neither the critical value nor the coefficient in the Tertiary rock area in Niigata Prefecture are verified, it can be pointed out from this case that one of the possible factors for the sediment-related disaster due to these earthquakes is a preceding rainfall, by confirming the residual condition of the preceding rainfall according to the value of the R'.

As reported about the case of Kure City after the Geiyo earthquake [1], failures were induced by ordinary level of rainfall on slopes that were affected by the earthquake. In the case of the Niigata-ken Chuetsu Earthquake, it can be shown that when there is preceding rainfall before earthquake, the possibility of sediment-related disaster to occur is higher than the situation of no rainfall condition.

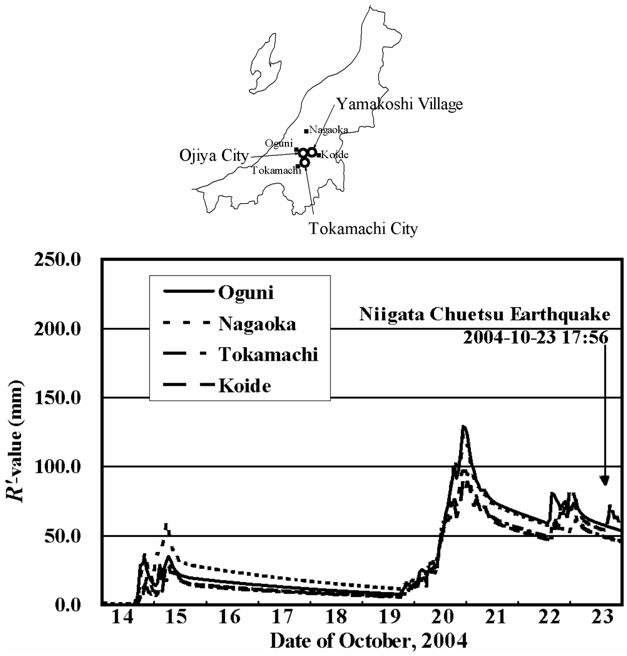

Fig. 14: R'-value around the Niigata Chuetsu Earthquake stricken area. Upper figure shows the location of rain-gage station.

CONCLUSIONS

In several recent disaster cases in 2004-2005, the authors calculated the rainfall index R' in real time based on the on-going rainfall data, with special attention to sediment-related disaster.

It was found from the case of Typhoon 0423 in Tamano City of Okayama Prefecture, that a serious disaster could occur when R' becomes larger beyond the critical value (250mm) even though the rainfall intensity is not so large.

During Typhoon 0511 case which affected the Kanto Region, authors kept watching on the rainfall situation through R' in a real-time manner. Disasters were caused by this typhoon at several places in volcanic rock area of

Hakone City in Kanagawa Prefecture. It was found from this case that R'-value was far larger than that for granite region around Hiroshima Prefecture. Also, it was felt that the R'-distribution monitored in real-time manner was very useful in understanding the movement of a dangerous area with time.

In case of Typhoon 0514 in Hiroshima, heavy rainfall that R' exceeded 250mm was caused in western part of Hiroshima Prefecture, and sediment-related disaster was triggered at a lot of places. In this case, it was found that debris flows and slope failures occurred more easily in weathering granite area than Paleozoic-rock area.

The rainfall index R' can be used widely and effectively, if the coefficient and the reference value are chosen properly for each region considering its geological and topographical characteristics.

In the case of Typhoon 0514, it can be shown that the possibility of disaster occurrence depends on severe condition (past typhoon or earthquake, etc) of slope, in addition to geological and topographical characteristics.

Moreover, in the example of the Niigata-ken Chuetsu Earthquake, it was pointed out that from R'-value, the possibility of sediment-related disaster to occur is higher due to the soil moisture situation caused by preceding rainfall.

ACKNOWLEDGMENTS

Authors express their gratitude for the assistance given by members of the "Hiroshima University Regional Disaster Prevention Network" and students of Hiroshima University during the site investigation and the analysis of Typhoon 0514.

REFERENCES

[1] Y. Sasaki, S. Kano, S. Nakai, T. Moriwaki and Thi Ha, "Rainfall index for warning against shallow slide on decomposed granite slopes", Reported in the "2004 Japan-Taiwan Workshop", 2004.

[2] Web site of the Ministry of Land, Infrastructure and Transport Government of Japan, "Occurrence of sediment-related disasters in 2004," (in Japanese). http://www.mlit.go.jp/river/sabo/h16dosya/h16dosya.pdf

[3] Web site of the Ministry of Land, Infrastructure and Transport Government of Japan, "Occurrence of sediment-related disasters in 2005," (in Japanese). http://www.mlit.go.jp/river/sabo/h17dosya/051231.pdf

[4] M. Kaibori, M. Ura, M. Yoshimura, E. Fujimoto, "Debris flow disaster on September 6, 2005 in Miyajima, Hiroshima Prefecture," Shin-Sabo, JSECE, Vol.58, No.5, pp. 18-21, 2006, (in Japanese).

[5] S. Nakai, Y. Sasaki, M. Kaibori, and T. Moriwaki, "Rainfall Index for Warning and Evacuation against Sediment-Related Disaster; Reexamination of the Rainfall Index R_f, and a Proposal of R'," Soils and Foundations, (in press).

[6] H. Hiura, M. Kaibori, A. Suemine, Y. Satofuka, D. Tsutsumi, "Sediment-related disasters in Kisawa-Village and Kaminaka-Town in Tokushima Prefecture, Japan, induced by the heavy rainfall of the Typhoon Namtheun in 2004 (prompt report)," Jour. Japan Soc. Erosion Control Eng., Vol. 57, No. 4, pp.39-47, 2004 (in Japanese).

[7] Web site of the Meteorological Agency, "Automated Meteorological Data Acquisition System," http://www.data.kishou.go.jp/

[8] Web site of the Ministry of Land, Infrastructure and Transport Government of Japan, "Water information system," http://www1.river.go.jp/

[9] Web site of Hiroshima Prefecture, "Hiroshima Prefecture disaster prevention information system," http://www.bousai.pref.hiroshima.jp/hdis/index.jsp

[10] H. Aboshi, and H. Sokobiki, "Slope failure occurring at the Masado natural slope," 7th Geotechnical Engineering Research Symposium, JGS, pp.507-510, 1972, (in Japanese).

[11] Ministry of Construction, "Results of the Conference of General Council for Measures against Sediment-Related Disaster," 1993, (in Japanese).

[12] Y. Sasaki, T. Moriwaki, S. Kano, and Y. Shiraishi, "Characteristics of precipitation induced slope failure disaster in Hiroshima Prefecture of June 29, 1999 and rainfall index for warning against slope failure disaster," Tsuchi-to-kiso, JGS, 49 (7), pp. 16-18, 2001, (in Japanese).

[13] M. Honke, and E. Ishiyama, "Provision of information about sediment-related disaster to residents," Shin-Sabo, JSECE, Vol. 54, No. 4: pp. 46-54, 2003, (in Japanese).

[14] K. Matsumura, M. Kaibori, K. Mizuhara, A. Suemine, N. Ebisu, T. Noro, T. Yamakoshi, "Sediment-related disaster caused by typhoon Tokage(T0423) in Tamano city, Okayama pref. and around Sanuki city, Kagawa pref.(prompt report)," Shin-Sabo, JSECE, Vol.57, No.6, pp. 40-46, 2005, (in Japanese).

[15] Web site of Kanagawa-newspaper, (in Japanese). http://www.kanaloco.jp

[16] Web site of Good Speed Tours Ltd., (in Japanese). http://www9.plala.or.jp/g-speed/sub34.html

[17] Research Committee of the Chugoku Branch , JGS, "Landslide disasters in Chugoku region by Typhoon No.14 in 2005," Tsuchi-to-kiso, JGS, 53 (12), pp. 125-130, 2005, (in Japanese).

[18] Y. Taniguchi, T. Uchida, H. Omura, H. Ochiai, M. Kaibori, T. Kubota, K. Sasahara, T. Jitousono, O. Shimizu, E. Shimokawa, H. Terada, Y. Teramoto, H. Hiura, S. Yoshida, "Sediment disasters caused by typhoon Nabi (T0514) in September, 2005," Shin-Sabo, JSECE, Vol.58, No.4, pp. 44-53, 2005, (in Japanese).

[19] Web site of the Ministry of Land, Infrastructure and Transport Government of Japan, "Occurrence of sediment-related disasters by the Niigata Chuetsu Earthquake," (in Japanese). http://www.mlit.go.jp/river/sabo/h16niigata/h16niigata.pdf

[20] M. Chigira, Committee for the investigation of the landslide hazards triggered by the Niigata-ken Chuetsu Earthquake (JSEG), "Landslide induced by the 2004 Niigata-ken Chuetsu Earthquake -Geology and Geomorphology-," Proc. of 44th Meeting for reading research papers of the Japan Landslide Society, pp.9-12, 2005, (in Japanese).

Stability of a model embankment subjected to artificial rainfalls

C.P.K. Gallage[1], E.F. Garcia[1] & T. Uchimura[1]
[1]Department of Civil Engineering, University of Tokyo, Tokyo, Japan

Abstract

This paper presents a method proposed to predict rainfall-induced instability of embankments in real-time. The method is based on a two-dimensional unsaturated flow analysis coupled with a slope stability evaluation using limit equilibrium analysis. Real-time "In-situ" measurements of pore-water pressures or water contents, rainfall, laboratory obtained soil-water characteristic curves (SWCCs), unsaturated permeability function, and unsaturated shear strength parameters are the necessary inputs for the method. First, the paper describes methods and results in the laboratory determination of SWCCs, Unsaturated permeability, and unsaturated shear strength measurements for a silty sand used in the model embankment The method is then applied to predict the stability of a model embankment subjected to artificial rainfall. The required inputs for the method were obtained in the laboratory. When the stability evaluations are compared with the displacement measurements of the model embankment, it can be seen that the failure of model embankment can be reasonably well predicted by the proposed method using laboratory obtained SWCCs, unsaturated permeability, and unsaturated shear strength parameters. Further, sensitive analyses have been carried out in order to observe the influence of SWCCs, initial conditions, and water permeability on the numerical seepage analysis.

Keywords— *Real-time "in-situ" measurements, Slope stability, Unsaturated flow,*

INTRODUCTION

Embankments are geo-structures that are mostly used to support rails and roads. The failure of such structures may lead to large numbers of human casualties. Rainfall has been identified as one of major causes to make embankments unstable and lead to subsequent failures.

A method was developed to predict rain-induced instability of embankments in real-time. It is basically based on a two-dimensional saturated-unsaturated seepage analysis (SEEP/W) coupled with a slope stability analysis (SLOPE/W)using limit equilibrium methods (Geostudion 2004). In addition to real-time in-situ measured pore water pressures (or water contents) and the rainfall intensity, SWCCs, unsaturated permeability functions, saturated-unsaturated shear strength parameters of embankment materials are the inputs for the proposed method. Real-time in-situ measured pore-water pressures or water contents (at the toe, the crest, and the mid of the slope) can be used to provide initial conditions for the seepage analysis as well as to back-calculate laboratory measured SWCCs and permeability functions (by comparing the results of seepage analysis and real-time in-situ measurements).

This paper first describes laboratory measurements of SWCCs, unsaturated permeability function, and unsaturated shear strength parameters of the testing material. Secondly, results of a test on a model embankment subjected to rainfall are presented. The results of sensitive analyses to investigate the effects of SWCCs, initial conditions, and water permeability on the numerical seepage analysis are then presented. Finally, the application of the proposed method to predict the failure of the model embankment is discussed.

TESTING MATERIAL

Tests were conducted on Edosaki silty sand which was excavated from a natural slope in Edosaki area, Chiba prefecture, in Japan. This sand contains 16.4 % of non-plastic fines (particles smaller than 75 microns). The physical properties of the sand which were determined by laboratory according to Japanese standards are D_{50}=0.228 mm, C_u=16.67, C_c=4.71, G_s=2.75, e_{max}=1.588, and e_{min}=1.011. The optimum gravimetric water content and the maximum dry density of the sand obtained from the standard proctor compaction test are 16.5% and 1.725 g/cm^3 respectively.

SOIL-WATER CHRACTERISTIC CURVES (SWCC) OF TESTING MATERIAL

Figure 1 shows the SWCCs of the testing material for the dry density of 1.22 g/cm^3 obtained using the Tempe pressure cell employing the axis-translational technique [1]. The details of the apparatus and the testing procedure are described in [2].

In order to fit experimental data of SWCCs, the equation proposed by Fredlund & Xing [3] was used and is given in Equation 1. This equation provides a better fitting for general soils over the entire suction range of 0 to 10^6 kPa.

$$\theta = C(\psi) * \theta_s / \{\ln[e+(\psi/a)^n]\}^m \quad (1)$$

Where $C(\psi)$ is a correction function defined as:

$$C(\psi) = \ln(1+ \psi/ \psi_r)/\ln[1+(1\,000\,000/ \psi_r)] \quad (2)$$

Where θ = volumetric water content; ψ = suction; ψ_r = suction corresponding to residual water content θ_r ; θ_s =

water content at zero suction; a, n, and m are fitting parameters that can be determined by a least-squares method using measured data for θ and ψ.

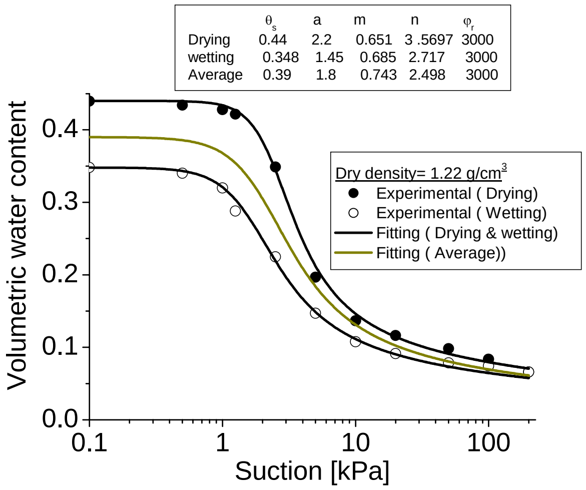

Figure 1. Laboratory obtained SWCCs of Edosaki sand

LABORATORY MEASUREMENT OF UNSATURATED PERMEABILITY FUNCTION

Permeability cell and testing procedure

Figure 2 depicts the schematic diagram of the apparatus used in the laboratory to measure the coefficient of permeability of unsaturated soil using the steady–state method [4]. The apparatus consists of a brass cylinder with the inner diameter of 7 cm and the height of 8 cm , two steel porous filters with the air entry value 15 kPa, Marriotte bottle to provide water with constant head, two tensiometers, h1 and h2, for the measurement of pore-water pressures. Small holes are made on the surface of brass cylinder in order to maintain uniform pore-air and atmospheric pressure inside the sample during the test. This apparatus has been designed to measure water permeability for low suction (0 ~ 10 kPa).

First, two steel porous plates were saturated and one was placed in the bottom cap. The brass cylined was then mounted on the bottom cap and the specimen was prepared inside the cylinder. Two tensiometers were installed during the sample preparation. After saturating the sample, the other steel porous plate and the top cam were positioned. Four tie-rods were used to tie both top and bottom caps together.

A water supply was applied to the top porous plate to develop a constant hydraulic gradient across the soil in the vertical direction. The water supply provides a constant hydraulic head by means of a Mariotte pipe. Water flows one-dimensionally through the top porous plate, the soil specimen, and the bottom porous plate. The outflow of water was maintained at a constant hydraulic head by controlling the outflow elevation, H_L. Increasing H_L , the suction inside the specimen can be increased. The drying curve is followed by the increase of H_L and wetting is simulated by the decrease of H_L. Once H_L is changed,

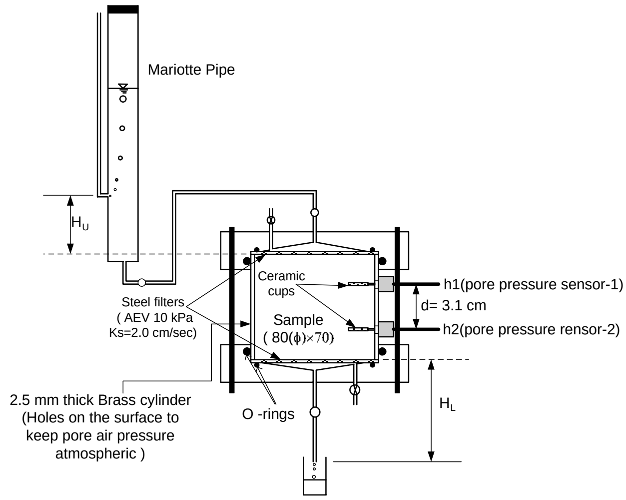

Figure 2. Apparatus for the measurement of coefficient of permeability using steady-state method

it is allowed to established constant readings in tensiometers, h_1 and h_2 . When the outflow rate is constant (steady-state), the volume of water, Q, in a period of time, t, is measured and used to calculate the coefficient of permeability at the maintained suction. Darcy's low is used to calculate the coefficient of permeability (k_w) as shown in Equation 3.

$$k_w = \left(\frac{Q}{At}\right)\left(\frac{d\rho_w g}{(h_2 - h_1) + d\rho_w g}\right) \quad (3)$$

The pore-air pressure (u_a) is assumed to be atmospheric inside the specimen.

$$(u_a - u_w)_{average} = -\left(\frac{h_1 + h_2}{2}\right) \quad (4)$$

Where, ρ_w = density of water; A = the cross sectional area of the soil; d = distance between two tesiometers; g = gravitational acceleration; h_1 and h_2 = pore-water pressures measured by tensiometers h_1 and h_2; $(u_a - u_w)_{average}$ = average matric suction.

Permeability function of the testing material

Figure 3 (a) shows the variation of measured coefficient of permeability with suction for both drying and wetting curves. The test was conducted on the dry density of 1.22 g/cm^3 of Edosaki sand. There is a hysteresis in the coefficient of permeability versus matric suction relationship. However, if the coefficient of permeability is plotted against volumetric water content, the resulting plot shows essentially no hysteresis, as demonstrated in Fig. 3 (b). There are some numerical models to predict the unsaturated permeability function using the saturated

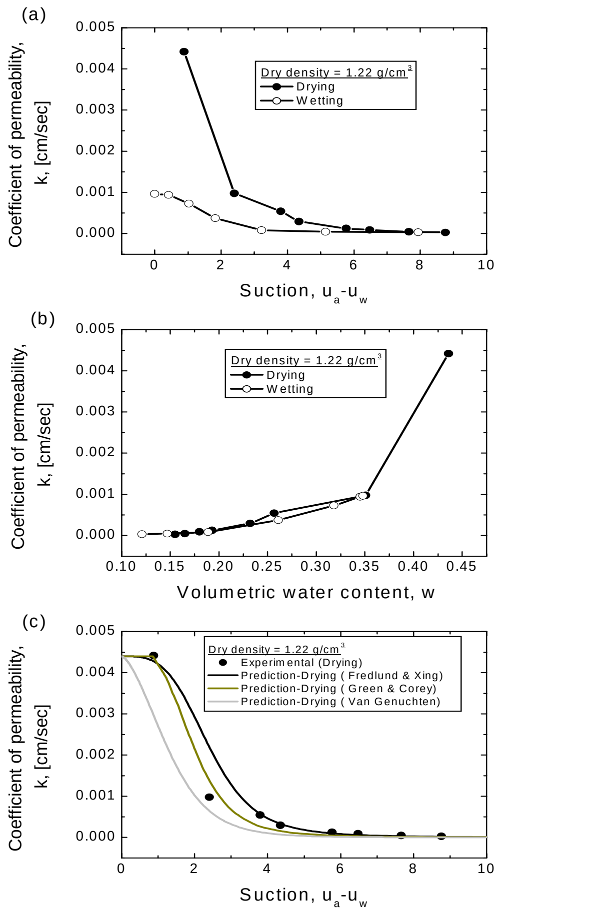

Figure 3. Laboratory measured permeability functions and their numerical prediction.

permeability coefficient and the SWCC. Fig. 3 (c) compares the laboratory measured permeability function for drying of Edosaki sand with the predictions using the methods proposed by Fredlund [3], Green & Corey [5], and Van Genuchten [6] (all three methods are included in SEEP/W). It can be observed that the methods proposed by Fredlund and Green & Corey can be used to predict the permeability function for the testing material. In this study the method proposed by Fredlund is used to predict the unsaturated permeability function.

LABORATORY MEASUREMENT OF UNSATURATED SHEAR STRENGTH PARAMETERS.

Fredlund [7] proposed an equation (Eq. 5) to interpret the shear strength of unsaturated soils in terms of two stress state variables,

$$\tau = (\sigma_n - u_a)\tan\phi' + c \qquad (5)$$

$$c = c' + (u_a - u_w)\tan\phi^b \qquad (6)$$

where τ = shear strength of unsaturated soil; c = apparent cohesion; c' = effective cohesion of saturated soil; ϕ' = the shearing resistance angle which is assumed to be constant for all values of matric suction and is equal to saturate condition; ϕ^b = the angle of shearing resistance with respect to suction; σ_n = the total normal stress on the plane of failure; u_a = air pressure in the soil mass; u_w = pore water pressure; (u_a-u_w) = the matric suction of the soil in the failure plane.

In this interpretation, the relationship between τ and (u_a-u_w) is assumed to be linear. However, [8] determined that this relationship is actually non-liear. Later several other researchers observed the non-linear relation between apparent cohesion and matric suction ([9]; [10]; [11]; [12]).

Unsaturated shear strength of the testing material

Figure 4 (a) depicts the variation of the ϕ' with the suction. The ϕ' was obtained from both saturated and unsaturated CD tests employing the modified direct shear device [13]. The results suggested that the effects of suction on the ϕ' is not significant . The same conclusion was drawn from the CD triaxial tests on unsaturated sand [14]. However, the ϕ' obtained from the direct shear is smaller than that of obtained from the triaxial tests for the same density.

As shown in Fig. 4 (b) , the apparent cohesion (c) increases with the suction in the decreasing rate. This is

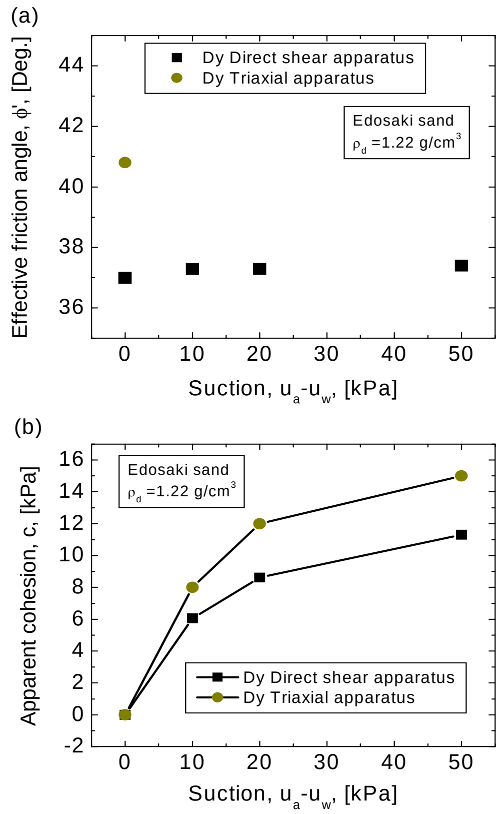

Figure 4. Effects of the suction on the internal friction angle and the apparent cohesion

consistent with the findings of other researchers ([9]; [10];

[11]; [12]). However, the apparent cohesion obtained from the direct shear is smaller than those obtained from the triaxial tests for the same suction and density.

For the stability analysis in this study, ϕ^b was obtained assuming linear relationship between the c and the suction for the range of small suction (0 ~ 20 kPa). This seems to be a reasonable assumption for the purpose of the prediction of rain-induced slop instability as slopes become unstable at low suction values. Furthermore, it can be suggested that the use of unsaturated shear strength parameters obtained from the direct shear device may give a conservative solution which is favorable in issuing warnings for the failure of slopes.

MODEL TESTS OF EMBANKMENTS SUBJECTED TO RAINFALL

In this study, a series of model tests of an embankment was performed with different materials, initial densities, boundary conditions, rainfall intensities and durations. However, the results of a test are discussed in this paper.

Equipments and procedures used in the model tests

The tank (Figure 5) used in model test has a length of 2.0 m, width of 0.8 m, and a height of 1.0 m. The walls of the tank are made up of steel plates, except for the front side which is made of acrylic glass for easy observation of deformation processes.

ADR (Amplitude Domain Reflectometry) and ECHO types soil moisture sensors were used in the model tests to measure soil moisture content during water infiltration. In order to measure both positive and negative water pressures, KYOWA 05 PMG pressure sensors were modified with a ceramic cup of 100 kPa air-entry value. Figure 6 shows the types of sensors used in the model tests. Two LVDTs (D1 and D2) were used to measure the local displacements in the slope. An Evaflow side spray irrigation tube (hole size, 0.1 mm) was used to simulate rainfall as shown in Fig. 5.

The soil slope shown in Figure 7 was constructed by compacting Edosaki sand with the initial gravimetric water content of 13 %. The compaction was performed in order to achieve the dry density of 1.22 g/cm^3. 18 pore-water pressure and 10 water content sensors were installed as shown in Figure 7. All the sensors were connected to a data acquisition system for continuous logging of data.

Approximately 20 hours after completing the slope, The model was first subjected to a rainfall with an approximate intensity of 30 mm/h for 2.5 hours and then allowed to dry for 23 hours, followed by the second rainfall with an approximate intensity of 25 mm/h. The complete failure of the embankment was observed approximately 2.5 hours after the start of the second rainfall.

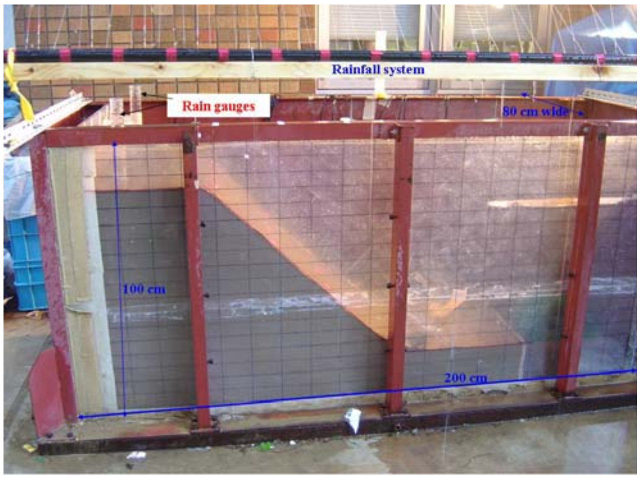

Figure 5. The tank used for model tests

The model test results and discussion

Figures 8 and 9 show the time history of measured water content (volumetric) and pore-water pressure at some selected points in the model slope during the entire test. It can be seen that both measurements clearly indicate the drying and the wetting of the slope. Figure 9 depicts the time history of displacement measurements. The failure of the slope occurred during the second rainfall and it was progressive. Figure 10 depicts the time histories of pore water pressure measurements at selected points and displacement measurements by D1 and D2 during the second rainfall. When steps of the progressive failure (Fig. 11) are compared with pore water pressure distributions in the model slope, it is clear that the progressive failure starts at the toe of the slope with the saturation and consequent building up of positive pore water pressures around the toe. It can be seen that local measurements of pore-water pressures (or water contents) displacements are not adequate for the successful prediction of the failure for a warning. Therefore, the authors suggested a method of warning of rain-induced embankment failure based on real-time evaluation of its stability. The proposed strategy and its application on a model slope are described in proceeding sections.

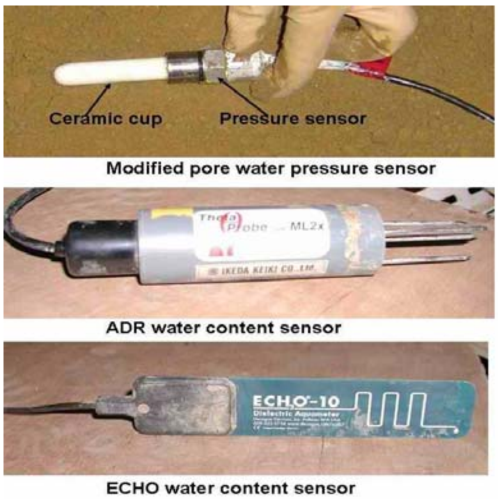

Figure 6. Type of sensors used in model tests

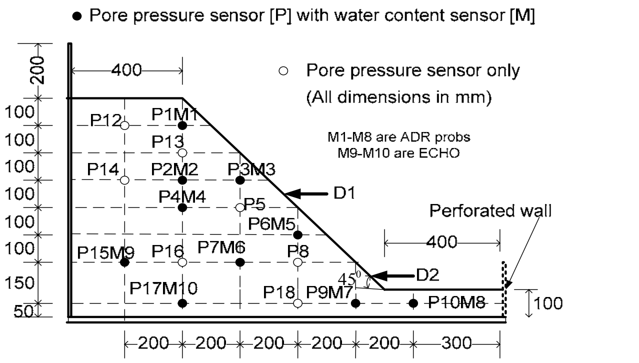

Figure 7. Dimensions of the model slopes and the embedded sensors

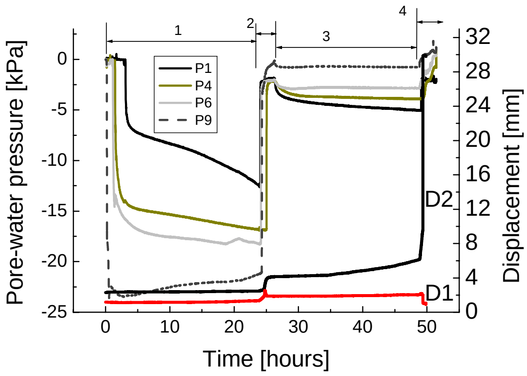

Figure 8. Time history of measured pore water pressures (at selected points) and displacements during the entire test

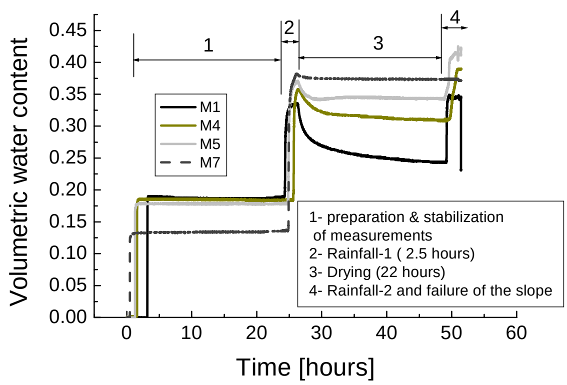

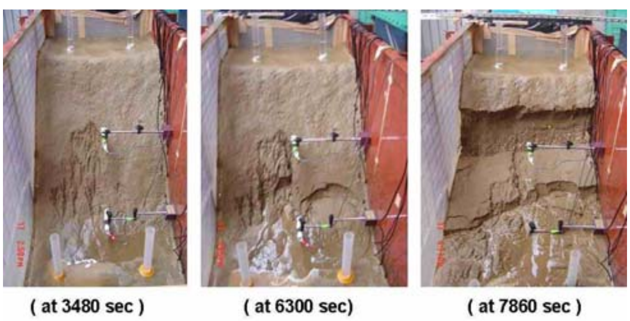

Figure 11. Appearance of the slope during the second rainfall event

Figure 9. . Time history of measured water contents (at selected points) during the entire test

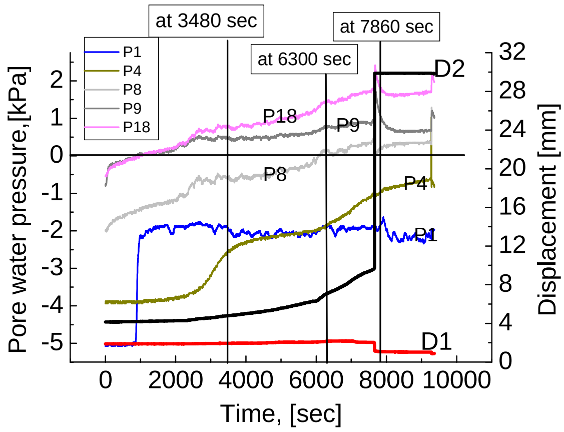

Figure 10. Time history of measured pore water pressures (at selected points) and displacements during the second rain fall event

PROPOSED METHOD FOR THE PREDICTION OF RAIN-INDUCED EMBANKMENT FAILURES IN REAL-TIME

Figure 12 depicts schematically the proposed method to predict the rain-induced instability of embankments in real-time. As shown in the figure, SWCCs and unsaturated permeability functions in addition to real-time in situ measurement of rainfall and pore-water pressures (or water contests) are necessary for the seepage analysis. The results of the seepage analysis are compared with the real-time measurements of pore-water pressures (or water

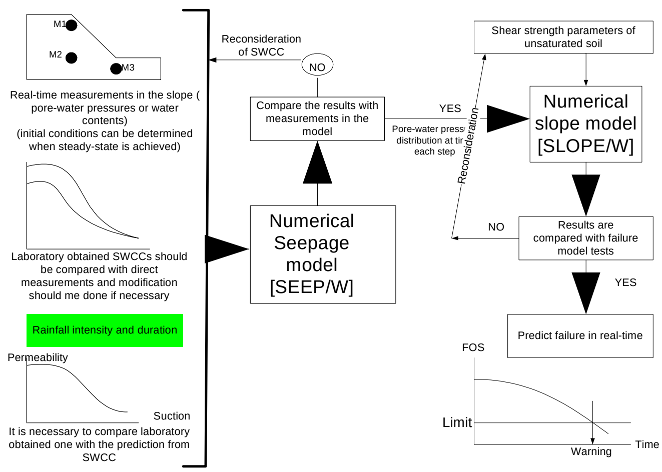

Figure 12. The proposed method for prediction of rain-induced embankment failures

contents). If necessary, SWCCs and unsaturated permeability function should be adjusted to have better agreement between real-time measurements and the results of numerical seepage analysis. This kind of adjustment can be considered as back-calculation of SWCCs and unsaturated permeability function using real-time in situ measurements. The adjustment of SWCCs and unsaturated permeability function can be done for some initial rainfalls after the installation until the better agreements are observed during the rainfall after the adjustments. It is assumed that the slope does not fail during initial rainfalls of the installation. Once the reasonable agreements are observed between measured and analytical values, real-time stability can be performed using laboratory measured unsaturated shear strength parameters. The warning against the failure of the embankment can be issued when the calculated factor of safety (FOS) reaches the limiting value.

Effects of SWCCs, saturated permeability coefficient, and initial condition on numerical seepage analysis

The described model test consists of two rainfall events and a drying process that was followed by the first rainfall event. The purpose of this parametric analysis on numerical seepage analysis of the first rainfall event is to back calculate the SWCCs and the unsaturated permeability function of the soil and check their validity by comparing measurements with the results of the numerical seepage analysis of the second rainfall event. Figure 13 depicts the 2D finite element mesh used in the numerical seepage analysis. Note that to evaluate the stability variation with time, the same mesh was used with the corresponding pore water pressure distribution.

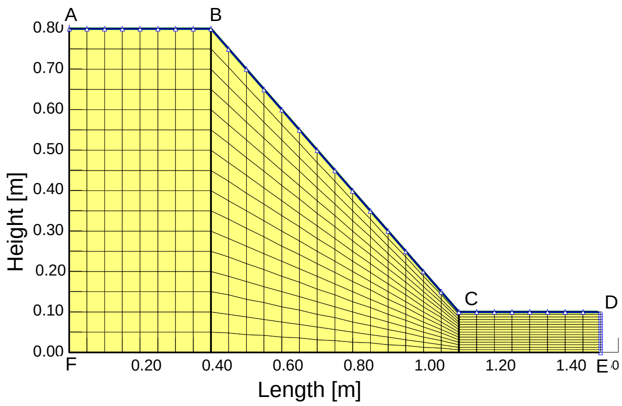

Figure 13. FE mesh used in the numerical simulations

For numerical seepage analysis, ABCD surface is defined as a unit flux boundary (q) (length/time), where the rainfall intensity is given, and as well as a potential seepage face. Furthermore water logging on the surface is not allowed. AF-FE and DE are defined as no flow boundaries and a potential seepage face respectively.

In order to investigate the effects of SWCC on unsaturated seepage analysis of wetting, the analysis was conducted using three SWCCs (see Fig. 1) namely , wetting , drying, average of wetting and drying curves. Constant rainfall of 25 mm/hr was given for the period of 9000 sec. (The first rainfall event of the model test). For each analysis, the unsaturated permeability function was predicted by saturated permeability coefficient of 0.0045 cm/sec (laboratory measured) and used SWCC employing Fredlund & Xing method. The initial condition (pore water pressure) was given by defining a water table and assuming a steady-state condition.

Figure 14 compares measured pore water pressures with the results of simulations at selected points in the model embankment during the first rainfall event. The results suggest that the results of numerical simulations conducted using wetting SWCCs exhibit better agreement with the measurements. This implies the possibility of obtaining the SWCC of the material by a trial and error method (back-calculation).

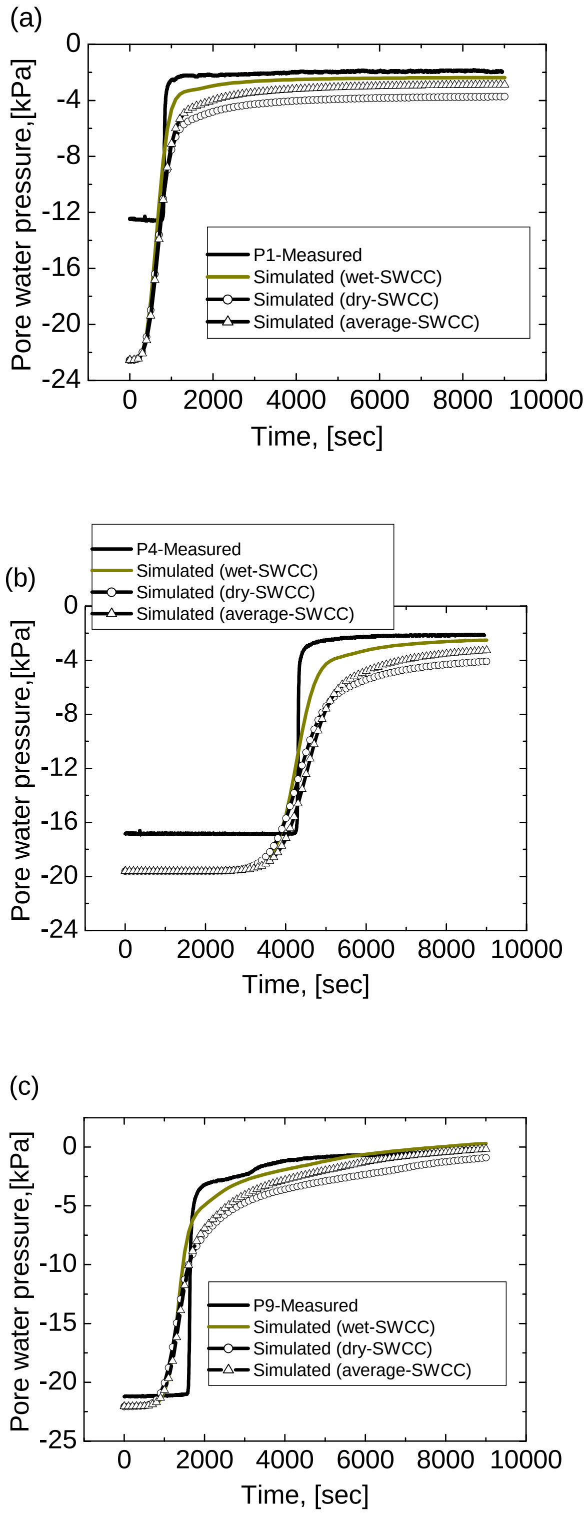

Figure 14. Effects of SWCCs on the unsaturated numerical seepage analysis (for the first rainfall event)

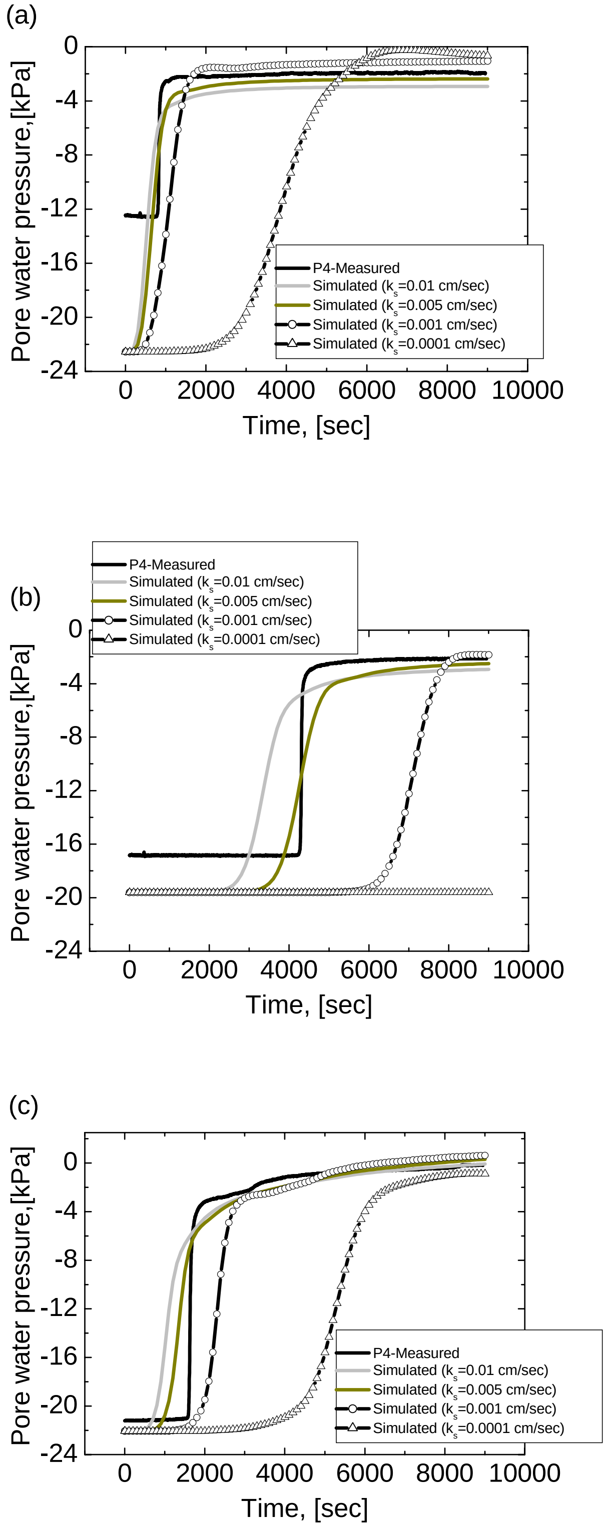

Figure 15. Effects of saturated permeability coefficient on the unsaturated numerical seepage analysis (for the first rainfall event)

The effects of saturated permeability coefficient (unsaturated permeability function) on the numerical seepage analysis of wetting were investigated performing the simulations for the saturated permeability coefficient of 0.01, 0.001, and 0.0001 cm/sec in addition to 0.0045 cm/sec. The wetting SWCC was used for all simulations. As depicted in Figure 15, saturated permeability coefficient has significant effects on the results of numerical simulations. The smaller the saturated permeability coefficient, the smaller the rate of increase of pore water pressure and the higher the final pore water pressure.

Referring to figure 14 and 15, it can be concluded that a trial and error method can be employed in numerical seepage analyses to determine the SWCC and the saturated permeability coefficient (unsaturated permeability function) which give better numerical simulation compared to measurements. In this model test, they are the wetting SWCC and 0.0045 cm/sec. However it is necessary check the validity of pre-determined SWCC and permeability coefficient by simulating the second rainfall on the model embankment. If it is necessary, further adjustment on pre-determined parameters should be done in the simulation of the second rainfall. In a real field application, this adjustment can be made during the simulations of several initial rainfalls until the most appropriate parameters of the soil are achieved.

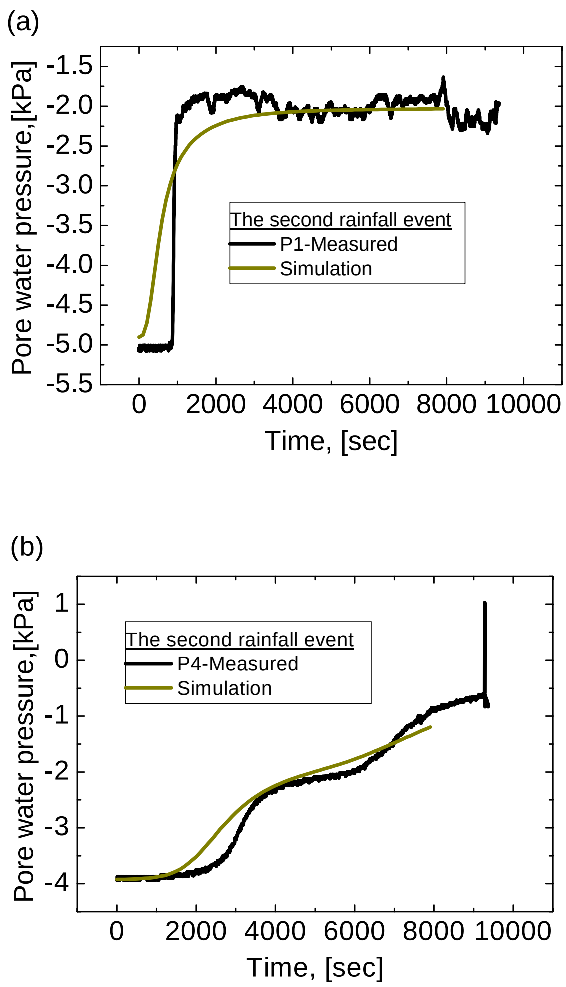

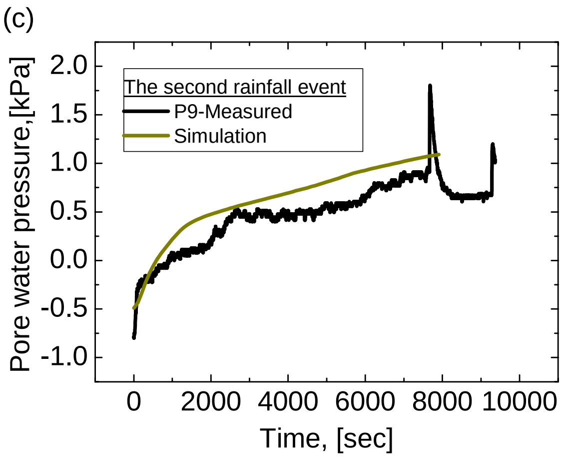

Figure 16. Comparison of measured and simulated time history of pore-water pressures (at selected points) for the second rainfall event on the model embankment

The second rainfall (20 mm/sec rainfall for the period of 8000 sec) of this model tests was simulated using pre-determined wetting SWCC and the saturated permeability coefficient of 0.0045 cm/sec. As shown in Figure 16, the results of the numerical seepage analysis of the second rainfall better describe the measurements. Therefore this model slope, the wetting SWCC and the saturated permeability coefficient of 0.0045 cm/sec are appropriate parameters for the numerical seepage analysis.

To study the effects of initial condition (pore-water pressure) on the numerical seepage analysis, the first rainfall event of the model test was simulated by giving initial pore water pressure higher and lower than the measured values. The wetting SWCC and the saturated permeability were used for numerical simulations. Note that it is not possible to give an exact value of measured initial pore water pressure at each point in the model. In SEEP/W (Geostudio 2004), the initial conditions are taken assuming a steady-state condition once the water table is defined. As shown in Figure 17, the effects of initial conditions are not significant as wetting proceeds. However, the given initial pore water pressures are much greater than the measured values, and the effects are considerably significant.

Stability analysis to predict the failure

The model embankment described in this paper failed during the second rainfall event (approximately 6000 sec after the start of the second rainfall). In order to predict the failure for early warning, the stability analysis of the slope was carried out at each 300 sec (5 min.) of the second rainfall event. The pore water pressure distributions at each time step was obtained by the numerical seepage analysis. The unsaturated shear strength properties obtained from both the direct shear and the triaxial apparatus were given for the stability analysis to investigate their effects on the analysis. Used unsaturated shear strength parameters in the stability analysis are summarized in table 01.

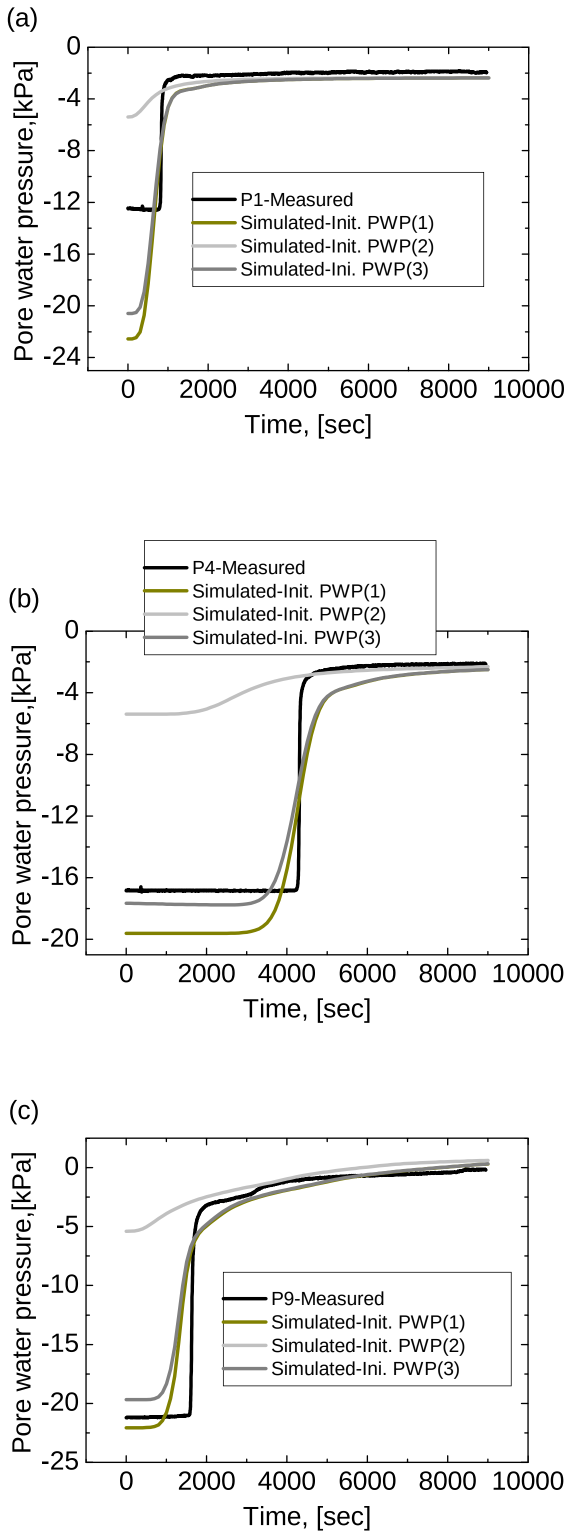

Figure 17. Effects of initial condition (pore water pressure) on the unsaturated numerical seepage analysis (for the first rainfall event)

Figure 18 and 19 compare the decrease of slope stability [FOS] with the displacement measurements (D1 & D2) and the pore water pressure measurements (selected points in the model) respectively during the second rainfall event. It can be seen that the factor of safety [FOS] calculated by shear strength parameters obtained from the direct shear apparatus reaches unity when the displacement starts. However, FOS calculated by the shear strength parameters obtained from triaxial apparatus may overestimate the stability. As shown in figure 19, it is difficult to compare the change of stability with each pore water pressure measurement; however, the increase of pore water pressures at points above the toe of the slope may bring FOS below unity. It can be seen from the results that there is a possibility to predict and warn about the failure of the slope by defining the limiting value of the FOS as 1.1. Finally, it can be said that the proposed method for prediction and warning of embankment failures due to rainfall can be successfully applied to the discussed model test.

Table 01: Shear strength parameters used in numerical slope stability

	c' [kPa]	ϕ' [deg.]	ϕ^b [deg.]
By direct shear	0	37.2	23
By triaixal	0	40.5	30

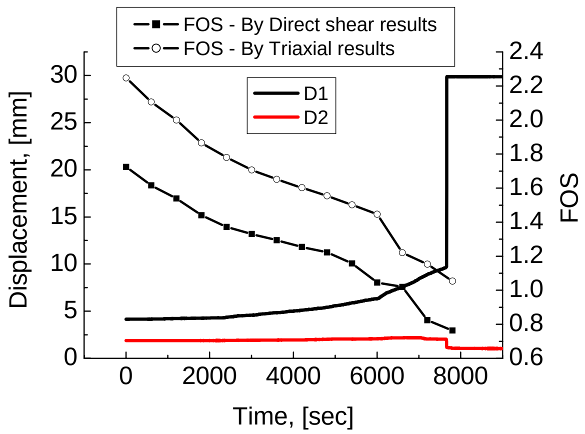

Figure 18. Time history of measured displacements and calculated FOS during the second rainfall event

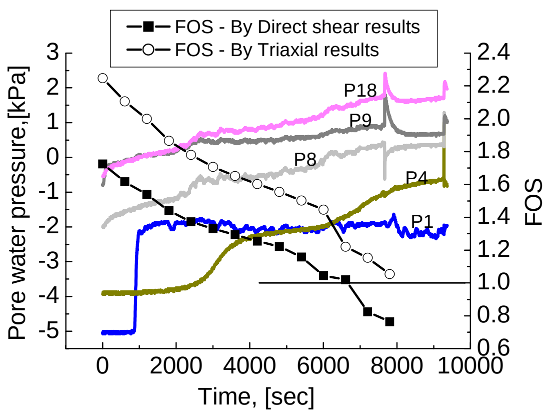

Figure 19. Time history of pore water pressures (at selected points) and calculated FOS during the second rainfall event

CONCLUSIONS

The following conclusions can be derived from the study described in this paper.

- Unsaturated permeability coefficient exhibits hysteresis in drying and wetting when it is plotted against suction. However, the unsaturated permeability shows a unique relationship with volumetric water content.
- Shear strength parameters obtained from Triaxial apparatus are greater than those obtained from the direct shear apparatus. The effective friction angle may not depend on suction. However,the apparent cohesion increases at a decreasing rate as the suction increases.
- The failure of the model embankment may occur with the saturation of the area near the toe of the slope.
- The effects of saturated permeability coefficient on unsaturated seepage analysis are more significant than the effects of SWCCs. However, a trial and error technique can be successfully employed to obtain better SWCC and saturated permeability coefficient. Their accuracies can be checked during the next rainfall event comparing real-time measurements with the results of numerical seepage analysis.
- The effects of initial pore water pressures on numerical seepage analysis seem insignificant as rainfall proceeds. However, there is a significant effect if the given initial pore water pressures are much higher than the measured (actual) values.
- According to the results presented in this paper, the proposed method can successfully be employed to predict and warn the failure of the model embankment using shear strength parameters obtained from the direct shear apparatus. The stability of the slope is overestimated by the shear strength parameters obtained from the triaxial apparatus.

ACKNOWLEDGMENTS

The authors gratefully acknowledge the Promotion Fundamental Transport Research from Japan Railway Construction, Transport and Technology Agency (JRTT) for the financial support for this study.

REFERENCES

[1] Hilf, J. W., " An investigation of pore pressure in compacted cohesive soils,"Technical Memorandum 654, Unite States Department of the Interior, Bureau of Reclamation, Denver, CO, 1956.

[2] Gallage, C. P. K., Garcia, E. F., Peiris, A., and Uchimura, T., "Use of soil-water characteristic curve in determination of stability of embankments during drying and wetting processes," *Proceedings of Advanced Experimental Unsaturated soil mechanics***,** Trento, Italy, pp. 351-357, 2005.

[3] Fredlund, D. G., and Xing, A., "Equation for the soil-water characteristic curve," *Canadian geotechnical Journal,* Vol. 31, pp. 521-532, 1994.
[4] Klute, A., " Laboratory measurement of hydraulic conductivity of Unsaturated soil," *in methods of soil analysis,*Mono. 9, Part 1, Amer. Soc. Of Agronomy, Madison, WI, pp. 253-261, 1965.
[5] Green, R. E., and Corey, J. C., "Calculation of hydraulic conductivity: A further evaluation of some predictive methods," *Soil Science Society of America Proceedings*, Vol. 35, pp. 3-8, 1971.
[6] Van Genuchten, M. Th., " A closed-form equation for predicting the hydraulic conductivity of unsaturated soils," *Soil Science Society of American Journal*, Vol. 44, pp. 892-898, 1980.
[7] Fredlund, D. G., Morgenstern, N. R., and Widger, R. A., "The shear strength of unsaturated soils," *Canadian Geotechnical Journal*, Vol. 15, pp. 313-321, 1978.
[8] Escario, V., and Saez, J., " The shear strength of party saturated soils," *Geotechnique,* Vol. 36, pp. 453-456, 1986.
[9] Fredlund, D. G., Rahardjo, H., and Gan, J. K. M., " Non linearity of strength envelope for unsaturated soils," *Proceedings of the 6th International Conference on Expansive Soils*, New Delhi, India, pp. 49-54, 1987.
[10] Wheeler, S. J., " An alternative framework for unsaturated soil behavior," Technical note Geotechnique, Vol. 45(2), pp. 257-261, 1991.
[11] Ridley, A. M., Burland, J. B., and Monroe, A. S., "Unconfined compression tests with pore pressure measurements," *Proc. 11th African Regional Conference*, SMFE, Cairo, 1995.
[12] Ridley, A. M., "Strength-suction-moisture content relationships for Kaolin under normal atmospheric conditions," UNSAT, Paris, Vol.2, pp. 645-651, 1995.
[13] Chaminda P. K. Gallage, and Taro Uchimura, " Direct shear testing on unsaturated silty sand under low suction," *Proc. 134th annual conference of Japanese Geotechnical Engineering Society*, Kagoshima, Japan, 2006. (to be appeared).
[14] Chaminda Pathma Kumara Gallage, and Taro Uchimura, "Effects of wetting and drying on the unsaturated shear strength of a silty sand under low suction," *The Fourth International Conference on Unsaturated Soils*, April 2-6, 2006, Carefree, Arizona, USA

GIS-Based Nationwide Evaluation of Erosion Rate Potential in Japan

K. Hasegawa[1], K. Wakamatsu[2] and M. Matsuoka[3]

[1] Researcher, Kawasaki Laboratory, Earthquake Disaster Mitigation Research Center, NIED, Kawasaki, JAPAN

[2] Team Leader, Kawasaki Laboratory, Earthquake Disaster Mitigation Research Center, NIED, Kawasaki, JAPAN

[3] Team Leader, Earthquake Disaster Mitigation Research Center, NIED, Kobe, JAPAN

Abstract

In order to estimate regional erosion rates in Japan we developed a simple method to estimate local specific sedimentation rate, which shows the reservoir sedimentation per year and by area in a river basin, using a topographic index and surface geology contained in the GIS database "Japan Engineering Geomorphologic Classification Map (JEGM)". For a basic analysis, several topographic indices were compared with specific sedimentation rates for 72 reservoirs in Japan. After the analysis it was found that the average grid slope in a river basin based on the 1 km^2-grid slope data contained in the JEGM was the best index to estimate specific sedimentation rate. Based on a regression analysis, we obtained equations to estimate specific sedimentation rate using simple parameters: average grid slope and surface geology. The estimation error of specific sedimentations for the proposed model is smaller than those for previous models. Finally, the potentials of specific sedimentation rate in every drainage basin all over Japan were mapped. From this potential map it is also found that the areas where the erosion rates are high correspond to the areas where amounts of Quaternary uplift are large.

Keywords—*erosion rate, reservoir sedimentation, specific sedimentation rate, grid slope, Japan Engineering Geomorphologic Classification Map (JEGM), GIS*

INTRODUCTION

The major cause of erosion of mountainous areas in Japan is considered to be mass movements like landslides and debris avalanches [1]. The amount of erosion over a long time span has often been assumed to be nearly equal to the amount of reservoir sedimentation gathered from an upper river basin. In other words, specific sedimentation rate, which is the reservoir sedimentation per year in a given area, roughly represents average erosion rate in the river basin, in a case where the reservoir has certain dimensions and where there are no reservoirs in the upper reaches of the river. In addition, in mountainous areas with highly dense vegetation, in such a country as Japan, the effect of precipitation on erosion rate is not prominent, although from the global viewpoint erosion rate is influenced by both vegetation density and precipitation [2].

For the purpose of assessing regional erosion in Japan, evaluating local specific sedimentation rate distribution is important; however, it is impractical to measure all the regional erosion rates all over Japan. Thus an estimation method of regional erosion rates using a simple topographic index calculated from a GIS database such as the Digital Elevation Model should be proposed.

In previous studies several topographic indices to estimate specific sedimentation rate have been proposed individually in Japan. But they have not been compared with one another yet. So we examined the relationships between specific sedimentation rates for 72 reservoirs across the country and several topographic indices proposed by previous studies.

This paper proposes a simple method to estimate specific sedimentation rate using single topographic index, based on the comparison of the relationships between the topographic indices and specific sedimentation rate. Finally, potential rates of regional erosion rate all over Japan are mapped using the new method.

METHODOLOGY

This study consists of several steps: 1) building a reservoir sedimentation database; 2) constructing topographic indices and geologic age databases; 3) examining the relationship between data in 1) and 2) for each river basin; and 4) proposing estimation equations and map potentials of regional erosion in Japan.

Reservoir Sedimentation Data

We built a database of sedimentation for a total of 391 reservoirs across the country during the period from 1962 to 2001 based on annual reports on each reservoir in the Journal of the Japan Electric Power Civil Engineering Association. Based on this database, we measured slope value as an average sedimentation (unit: m^3/yr.) from a curve profile mapping the sedimentation amount relative to its duration for each reservoir. Then specific sedimentation rate (unit: m^3/km^2/yr.) was calculated by dividing the average sedimentation by the area of its river basin. Here, the number of reservoirs for which we were able to measure the average sedimentation from curve profile was 72 among a total of 391 reservoirs in the

Table 1 Chief topographic indices for estimating specific sedimentation proposed by previous studies

ID	Topographic Index Name	Explanation	Literature
A	Relief ratio	A value of relief divided by river length in a river basin.	Yoshimatsu [3]
B	Catchment area	A measured valued of area of upper river basin to a dam.	Ashida and Okumura [4]
C	Relief times altitude	An average of grid based relief times average altitude in a river basin to a dam.	Tanaka and Ishigai [5]
D	Dispersion of altitude	An average of grid based standard deviations in a river basin to a dam.	Fujiwara et al. [2]
E	Relief larger than median times altitude	A value of grid based relief sum larger than median times average altitude in a river basin to a dam.	Okano et al. [6]
F	Grid slope	An average value of grid based slope in a river basin to a dam. The database JEGM adopted this index as 1-km grid cell slope.	Okimura et al. [8]

database. Fig.1 shows the distribution of the 72 reservoirs, which are used in the analysis hereinafter.

Topographic indices used to estimate specific sedimentation rate

The major topographic indices previously proposed to estimate specific sedimentation rate in Japan are shown in Table 1. Indices A and B are measured by drainage basin, and the other indices are measured by grid cell. In these indices, the F "grid slope" is included in the database "Japan Engineering Geomorphologic Classification Map (JEGM)", which was created by the present authors and released as a digital database in November 2005 [9].

The grid slope contained in the JEGM is defined as the average gradient within each 1-km grid cell, which is calculated using a 250-m grid Digital Elevation Model [7]. Fig. 2 shows the procedure used to calculate the grid slope. First, slopes for each 250-m grid cell were calculated based on the method proposed by Okimura et al. [8]: 3x3 grid cells in the DEM were picked up as shown in step 1 of Fig. 2; using least squares method, the appropriate surface, which presented the greatest distribution of elevations for 3x3 grid cells, was then calculated; the slope of the surface was defined as that for the center cell of 3x3 grid cells (cell "e" in Fig. 2). In this order, each slope of the surface was calculated for all 250-m grid cells covering Japan. A slope for each 1-km grid cell was finally obtained as an average value of the slopes for 4x4 250-m grid cells within a 1-km grid cell as illustrated in step 2 in Fig. 2.

Relationship between specific sedimentation rates and topographic indices

The relationships between specific sedimentation rates for every river basin and the topographic indices in Table 1 are shown in X-Y graphs in Fig. 3; the plots are varied with respect to the geologic age of each river basin categorized based on geologic age data contained in the JEGM.

We examine the correlation between specific sedimentation rates and various topographic indices shown in Fig.3; the average grid slope (index F) of a river

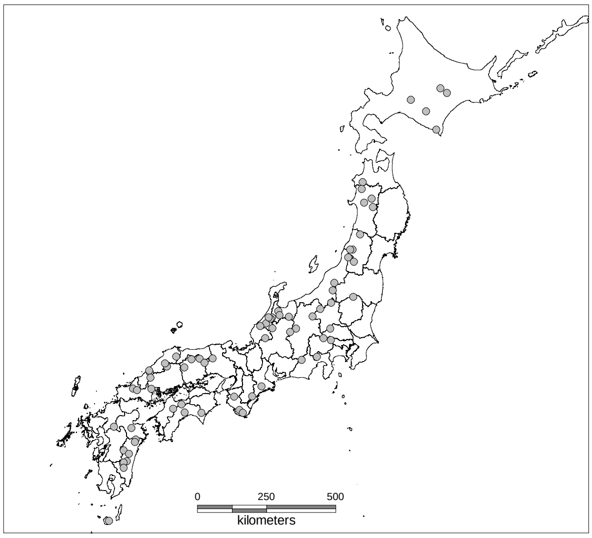

Fig. 1: Distribution of 72 dams used in this study

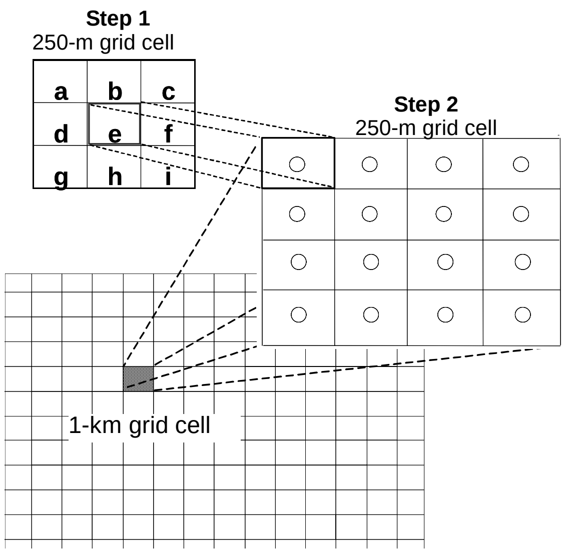

Fig. 2: Procedure for calculation of grid slope per 1-km grid cell

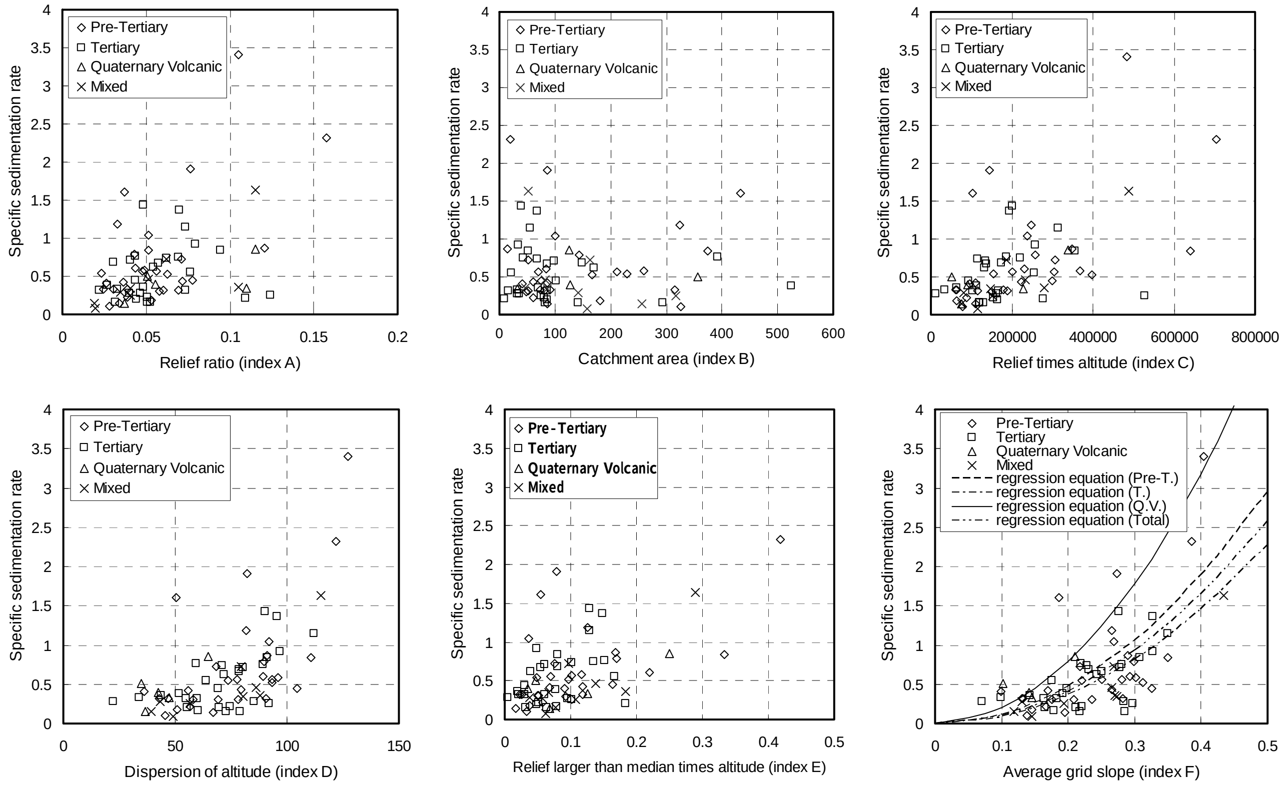

Fig. 3: Relationship between specific sedimentation rate and topographic indices by geologic age

Table 2 Correlation coefficient between topographic indices and specific sedimentation rates to geologic age

Geologic age	Number of dam	A	B	C	D	E	F	D’	F’
Pre-Tertiary	30	0.60	-0.03	0.56	0.58	0.41	0.61	0.65	0.68
Tertiary	28	0.14	-0.10	0.26	0.58	0.44	0.59	0.63	0.63
Quaternary Volcanic	5	0.49	0.14	0.68	0.83	0.73	0.80	0.84	0.83
Mixed	9	0.77	-0.46	0.90	0.81	0.84	0.89	0.88	0.95
Total	72	0.46	-0.06	0.55	0.60	0.46	0.61	0.66	0.67

* D’ and F’: the square of respective indices D and F

basin contained in the database JEGM has the highest correlation among the indices A to F. The correlation coefficient for the square of indices D and F are also shown in Table 2. The square of the grid slope (index F’) was found to be more applicable than the single grid square (index F) to estimate specific sedimentation rate.

A linear regression analysis was performed to estimate the specific sedimentation rate using the average grid slope as an explanatory variable. As the result of analysis by each geologic age unit, the following regression equation was obtained:

$$y = ax^2 \pm \sigma \qquad (1)$$

where y is specific sedimentation rate in $10^3 m^3/km^2/yr.$, x is average grid slope in tangent, a is coefficient by geologic age and σ is standard deviation. Table 3 shows the coefficient and standard deviation in equation (1). Regression curves for each geologic age unit derived by equation (1) are shown in the graph labeled index F in Fig. 3. The "coefficient a" for the Quaternary volcanic is the largest, followed by those of the Pre-Tertiary and the Tertiary, which implies that susceptibility to erosion is greater in the same order. This tendency is consistent with the number of occurrences of large landslides by geologic

Table 3 Coefficient and standard deviation in equation (1)

Geologic age	a (coefficient)	σ (standard deviation)
Pre- Tertiary	11.8	0.53
Tertiary	9.1	0.29
Quaternary volcanic	19.8	0.16
Whole data	10.3	0.41

age in Japan (Nakamura [10]).

Evaluation of Erosion Rate

Fig. 4 shows the relationship between estimated and actual specific sedimentation rates by geologic age for the 63 basins whose geologic age was clearly distinguished among the 78 reservoirs. Estimation by regression equation improved the estimation accuracy by approximately ±52m^3/km^2/yr., which shows that specific sedimentation rate can be estimated much accurately by this calculation than using the empirical formula previously proposed by Okano et al. [6].

Fig. 5 shows the relationship between estimated and actual sedimentation amount for the 63 basins. The logarithmic standard deviation is 0.29, which indicates that the estimated specific sedimentation rate shows good agreement with the actual one.

Thus, estimation of specific sedimentation rate was possible using simple parameters: grid slope and geologic age, both contained in the JEGM. Fig. 6 presents erosion rate potentials for drainage basins all over Japan using equation (1) and the JEGM, and drainage basins included in the “Digital National Land Information” [11]. In Fig. 6 the low-lying areas composed of Holocene or Pleistocene deposits are represented by blanks. The areas with higher erosion rates include the central part of the main island, Honshu, the southern part of Hokkaido, and Shikoku. Fig. 7 shows the distribution of the amounts of Quaternary uplift [12]. Comparing Figs. 6 and 7, it is found that the areas with higher erosion rates in Fig. 6 corresponded to the districts where the amounts of uplift during the Quaternary Era were larger as shown in Fig.7. This is consistent with the result of a previous study, which showed that erosion rates in mountainous areas are correlated with uplift during the Quaternary Era [12].

The relationship between specific sedimentation rates and the percentage of area degraded by drainage basins was also examined. As a result, it was found that the average specific sedimentation rate and the average grid slope were also larger in the basins with high percentages of degraded mountain areas.

Conclusions

After examining the relationship between some topographic indices and specific sedimentation rates for 72 reservoirs in Japan, we found that the topographic index “grid slope” was the best index to estimate regional erosion rates. Then we proposed a new empirical formula to estimate specific sedimentation rate using the “grid slope” data contained in the database “Japan Engineering Geomorphologic Classification Map (JEGM)”.

The proposed method was applied to JEGM and drainage basins to map the regional potential erosion in Japan. It was also confirmed that larger sedimentation rate areas are consistent with the area where the amounts of Quaternary uplift are large.

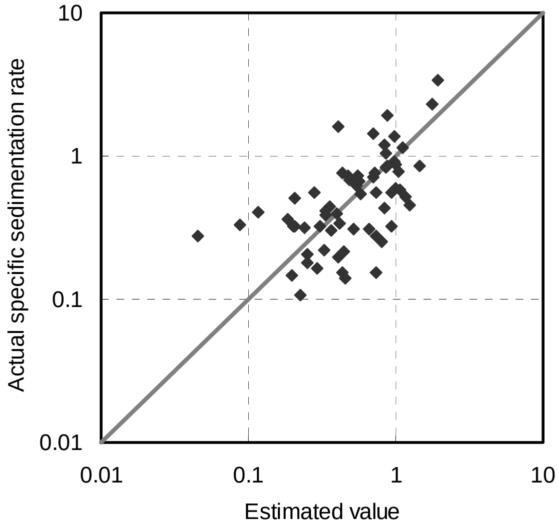

Fig. 4: Relationship between estimated specific sedimentation rate and actual specific sedimentation rate (Unit: $10^3m^3/km^2/yr.$)

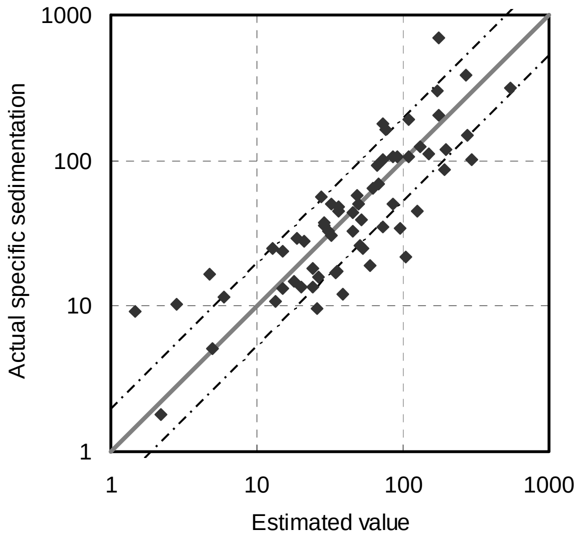

Fig. 5: Relationship between estimated reservoir sedimentation and actual reservoir sedimentation (Unit: $10^3m^3/yr.$)

Acknowledgments

The work presented in this paper was supported by the Grant-in-Aid for Scientific Research sponsored by the Japan Society for the Promotion of Science, under task numbers 15510155. The authors gratefully acknowledge this support. They also are grateful for financial support provided by the Hyogoken Research Organization for Human Care and the Fukutake Science and Culture Foundation.

REFERENCES

[1] Yoshikawa, T., Sugimura, A., Kaizuka, S., Ohta, Y., and Sakaguchi, Y., *Geomorphology in Japan* (in Japanese). University of Tokyo Press, 1973.

[2] Fujiwara, O., Sanga, T. and Ohmori, H., "Regional Distribution of Erosion Rates Over the Japanese Islands" (in Japanese with English abstract), *JNC Technical Report*, No.5, 1999, pp. 85–93.

[3] Yoshimatsu, H., "The estimation of expression on landslides," (in Japanese with English abstract), *Journal of the Japan Society of Erosion-Control Engineering*, 102, pp. 1–9, 1977.

[4] Ashida, K. and Okumura, T., "Study on sedimentation in reservoirs," (in Japanese with English abstract), *Annuals of Disaster Prevention Research Institute*, Kyoto Univ., 17-B, pp. 1–16, 1974.

[5] Tanaka, H. and Ishigai, H., "On the relation of sedimentation of reservoirs to configuration and nature of rocks of catchment area (1st. report)," (in Japanese with English abstract), *Journal of the Civil Engineering Society*, Vol.36, No.4, pp. 173–177, 1951.

[6] Okano, M., Takayanagi, J. and Fujii, T., "Considerations about setting the design sediment capacity and a rough estimate method for reservoir sedimentation based on sediment inflow," (in Japanese with English abstract), *Annual Report of Water Resources Environment Research Institute*, pp. 31–37, 2002.

[7] Geographical Survey Institute, Digital Elevation Map 250 m Grid, CD-ROM, 1997.

[8] Okimura T., Yoshinaga S. and Torii R., "Distribution of the local value calculated from geometry of landform at each divided landform and some relations between the value and depth of a surface soil layer - A case in a small mountainous area, Irisugaya, Rifu-cho, Miyagi-gun, Miyagi Prefecture, Japan -," (in Japanese), *Report of Reclamation Engineering Research Institute*, Kobe University, vol.9, pp.19-39, 1991.

[9] Wakamatsu, K., Kubo S., Matsuoka M., Hasegawa K., and Sugiura M., *Japan Engineering Geomorphologic Classification Map* (in Japanese with English abstract, GIS data in CD-ROM), University of Tokyo Press, Tokyo, 2005.

[10] Nakamura, S. and Mochizuki, K., *Shamen-saigai* (in Japanese). Daimei-do Press, 1984.

[11] National Land Agency of Japan, *Digital National Information (Revised version)* (in Japanese), Ministry of Finance, Japan, 1992.

[12] Yoshikawa, T., "Prof. N. Yamasaki's contribution to tectonic geomorphology", *Geographical review of Japan*, 44–8, pp.552–564, 1971.

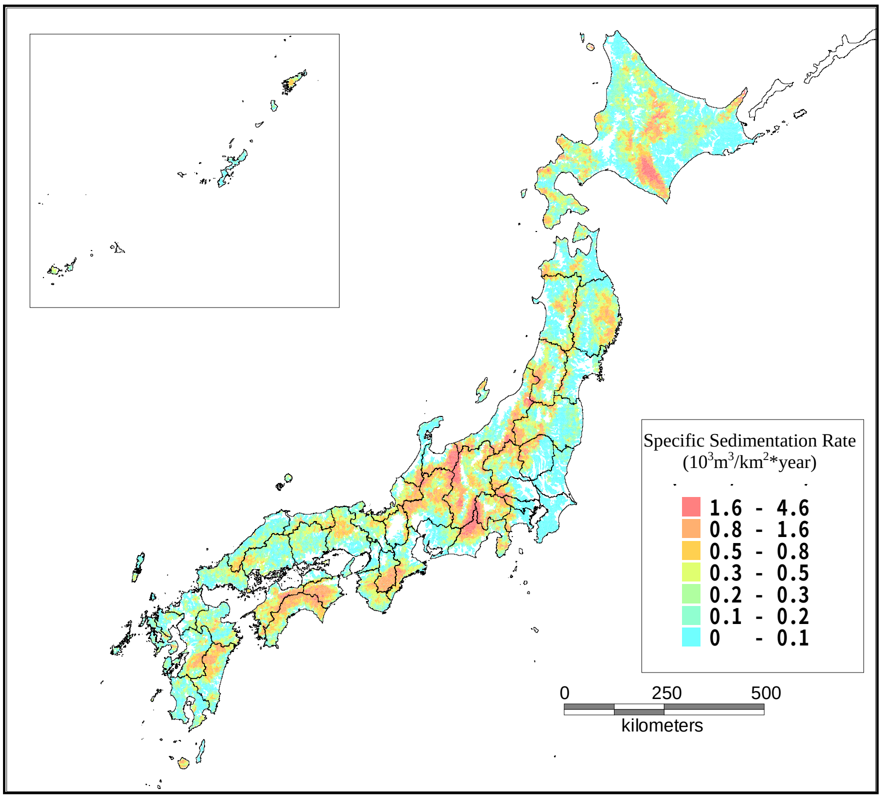

Fig. 6: Map showing erosion rate potential of each drainage basin in Japan (this study)

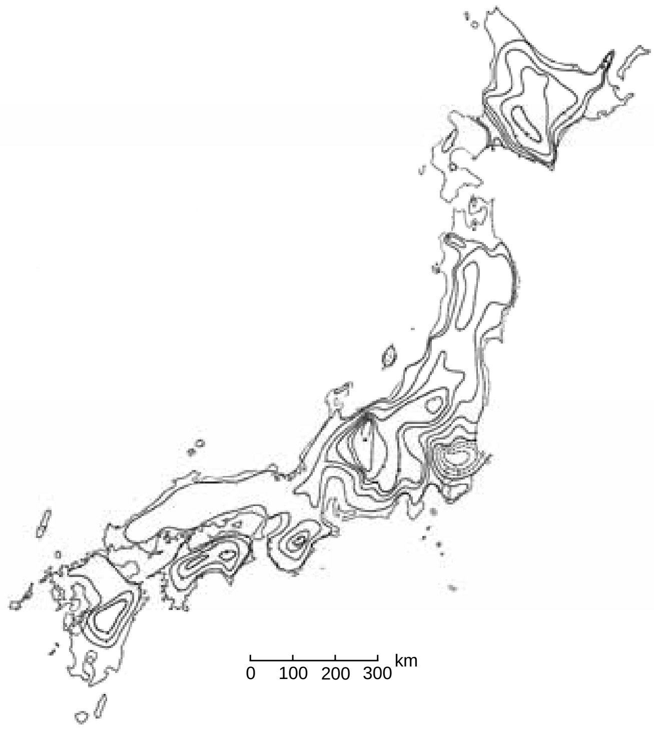

Fig. 7: Distribution of amounts of Quaternary uplift [12]

Improvement of slope hazard assessment by using physical properties of local soil

M. Mizuhashi[1], J. Sato[1], I. Towhata[1], T. Tsujimura[2]
[1]*Department of Civil Engineering, University of Tokyo, Tokyo, Japan*
[2]*Fudo Construction Company, Tokyo Japan*

Abstract

This paper concerns with the physical properties of soils in slopes which failed recently during the 2004 Niigata Chuetsu earthquake. Since the size of the landslide soil mass has a significant effect on the extent of seismic risk, it was attempted to find a correlation between the soil mass and the properties of local soil. A special attention was paid to rain water or ground water which may deteriorate the mechanical properties of soil. Tests were run on ground soil powder in order to accelerate the process of water absorption. Test results show that the landslide soil mass is correlated with plasticity index or swelling strain together with the topography. Finally, an improvement of risk assessment method is proposed.

Keywords—*landslide, earthquake, rainfall, field investigation, plasticity index*

INTRODUCTION

The Chuetsu earthquake in Niigata on October 23rd, 2004, caused many slope failures in the epicentral area. The extent of the failure was so vast in both numbers and size of affected areas that the restoration of the area became difficult. From the viewpoint of disaster management, it is important to detect potentially unstable slopes precisely. For safety of local community, missing unstable slopes is worse than judging stable slopes as being unstable. The state of art in risk assessment prior to the quake did not meet this requirement and the present study attempts to improve the identification of slopes which are prone to seismic failure.

The landslides during the 2004 Niigata Chuetsu earthquake were characterized by the possible effects of rainfall which occurred three days before the quake. Filtration of rain water into slopes saturates the slope materials, and thereby increases the degree of saturation and the weight of the slope, while decreasing the factor of safety. Thus, one of the motivations to initiate the present study was the concern on the possible effects of this rainfall immediately prior to the quake. Another aim was the improvement of hazard mapping methodology in which an attention is paid to rainfall effects.

SLOPE FAILURES DURING NIIGATATA-CHUETSU EARTHQUAKE IN 2004

The scale of landslides during this earthquake was significantly variable. Figure 1 demonstrates a mountain slope which was covered totally by failures. Although this picture gives an impression that the extent of mountain failure was substantial, which is particular the case in interpretation of air and satellite photographs, actually the depth of failed soil mass was shallow and the volume of soil mass was limited. This lesson suggests that hazard management should consider not only the area of instability but also the volume (depth) of unstable soil

Figure 1: Mountain slope in (former) Yamakoshi Village which was covered by failures.

Figure 2 : Failure of slope on west entrance of Haguro Tunnel (total volume of soil = 100,000 m^3).

This paragraph is going to introduce failures of large size. Figure 2 indicates the one which occurred upon an entrance of Haguro Tunnel (HGR site). From the length, size and depth of the failure, it was inferred that the total volume of failed mass was around 100,000 cubic meters. The second example is the one in Figure 3 which shows another slope failure in Naraki site (NRK) which had a soil volume of 100,000 m^3 as well. This failure is considered to be "big" because the failed soil mass stopped river flow and formed a natural dam.

Figure 3 : Failure of slope at Naraki which formed natural dam (total volume of soil = 100,000 m^3).

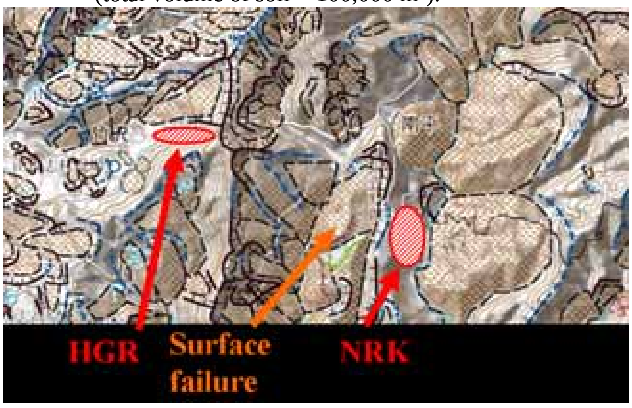

Figure 4 : Landslide-induced topography and locations of big slope failure (original map by National Research Institute for Earth Science and Disaster Prevention).

Three failed slopes as mentioned above are located in a map in Figure 4 that was originally drawn prior to the 2004 quake by NIED in order to show locations of landslide-induced topographies. Since such maps are widely used to identify potentially hazardous slopes, its capability to identify hazardous slopes has to be discussed. It is interesting in Figure 4 that the surface failure in Figure 1 is correctly identified. It seems that this particular slope is composed of materials which are prone to weathering and the surface soil produced by mechanical weathering process has fallen down repeatedly upon either heavy rainfalls or earthquakes. It is however important that sites of two bigger landslides (HGR: Haguro Tunnel, and NRK: Naraki natural dam) were not recognized as a landslide-induced topography. It is thus possible that big and hazardous landslides are overlooked by risk management based on topography.

METHOD OF LABORATORY TESTS

The ongoing risk assessment often relies on topography. Since recent experiences in Niigata-Chuetsu earthquake suggests that this idea is doubtful, the present study attempts to improve the methodology from the view point of risk assessment and hazard mapping. Note that such a goal of study does not fully acknowledge the use of triaxial tests on undisturbed samples because, although being precise, the substantial size of the target area and the budget limitation make it impractical to run shear tests.

The authors started this study by collecting soils from landslide sites, crushing them to particle size finer than 75 microns, and running tests on liquid and plastic limits. The idea behind was that the effects of water on mechanical properties may be related with those Atterberg limits. Furthermore, swelling tests were conducted on the same powder of soil in order to measure the absorption of water by constituting minerals. Collected soil was crushed to powders in order to facilitate water-mineral interaction. Note that the tests aimed to measure the water-mineral interaction and it was not intended to reproduce the behavior of in-situ soil during rainfall.

Figure 5 : Failure of slope at Dainichi Mountain near Shiotani village (total volume of soil > 1,000,000 m^3).

Figure 6 : Falling of surface clayey material in Nigorisawa valley (total volume of soil = 20 m^3).

TEST RESULTS

A variety of soil was collected from different landslide sites which were made unstable during the 2004 earthquake. The biggest landslide was the one at Shiotani Dainichi Mountain. The sliding mass measured approximately 900 meters in width, 300 meters in length, and 50 meter at maximum in thickness, making the total volume more than 10,000,000 m^3 (Figure 5). Sandy and clayey samples were collected from the exposed slip surface here. On the other hand, one of the smallest slope failures to be studied was the one in Nigorisawa Valley in Nagaoka City (Figure 6). Weathered clayey material fell down at this site and the size of the unstable soil mass was 20 m^3 in volume.

The aim of laboratory tests was to examine the possibility that water absorption by constituting minerals affects the significance of landslide. More clearly, it was studied whether or not the size of landslide was made greater by water absorbing minerals. In this respect, the collected specimens, whether being a piece of soft rock or clayey, were ground to particle size finer than 75 microns in order to accelerate the process of water absorption. The ground dry soil/rock powder was placed in a conventional oedometer which measured 20 mm in sample height. All the specimens were compacted by the same energy of 20 impacts by a hammer. Hence, the dry density was variable to a certain extent among different kinds of materials.

Dry specimens thus prepared were loaded under 20 kPa of overburden pressure, and, after elapsing 24 hours while allowing for possible creep deformation, the specimen was submerged in water quickly. This introduction of water caused compaction due to lubrication of grain-to-grain friction etc. Thereinafter, some specimens exhibited swelling due to water absorption, while others did not. It was supposed that water absorption would thus reduce the density and shear strength, and, in the field, cause slope failure of a greater scale more easily during earthquakes.

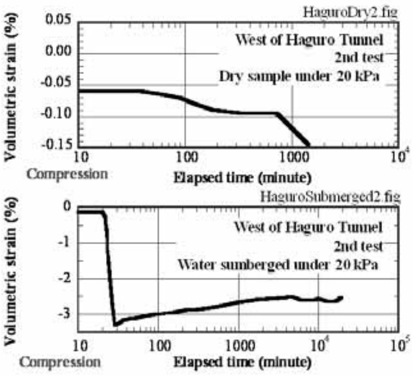

Figure 7 : Swelling test on powder from Haguro-Tunnel slope.

Figure 7 illustrates the test results obtained from the soil in the Haguro Tunnel slope (Figure 2). Atterberg limits of this specimen was Liquid limit (LL)=48.5%, Plastic Limit (PL)=28.4%, and Plasticity Index (I_P=LL-PL)=20.1%. The upper diagram indicates the volume change when 20 kPa of stress was loaded in a dry state. Some creep deformation was observed. Then, the lower diagram shows the behavior after water submergence. Following the initial contraction, swelling of 0.75% occurred. Note that this material exhibited the maximum magnitude of swelling and the plasticity index.

Figure 8 illustrates another example in which clayey specimen from Dainichi Mountain slope (Figure 5) was tested. This material exhibited LL=37.6%, PL=33.6%, and Ip=4%. The measured swelling strain was 0.34%.

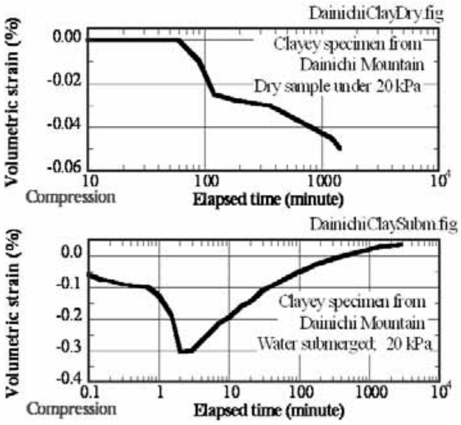

Figure 8 : Swelling test on powder from clayey specimen of Dainichi Mountain slope.

All the test results were assembled. Firstly, the correlation between swelling strain and the volume of landslide mass is presented in Figure 9. As expected, there is some positive relationship, suggesting that greater water absorption affects slope stability. Note in this figure that the said correlation becomes more evident by removing two data groups which are from sandy soil of Dainichi Mountain (○) and from the soil mass of Higashi Takezawa sliding (△). The former was eliminated because the clayey material at the same site appears to be more responsible for the instability. The latter was removed as well because the Higashi Takezawa slide was of a reactivated type which was probably caused by sliding along a preexisting slip plane; thus the soil behavior was not responsible.

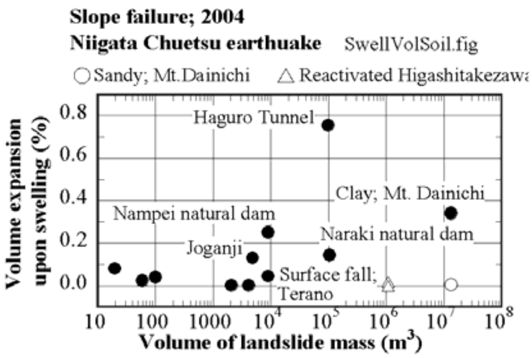

Figure 9 : Correlation between landslide mass and swelling strain.

Figure 10 plots swelling strain against plasticity index. Since there is a positive correlation to a certain extent, it is expected to find a similar correlation as in Figure 9. Thus, Figure 11 was drawn. By removing the data from the reactivated Higashi Takezawa site (△), it is possible to find a positive correlation. However, the significance of this correlation is less evident than that in Figure 9. Hence, the swelling of constituting minerals seems to be the best parameter to account for the effects of rain water filtration on the slope instability.

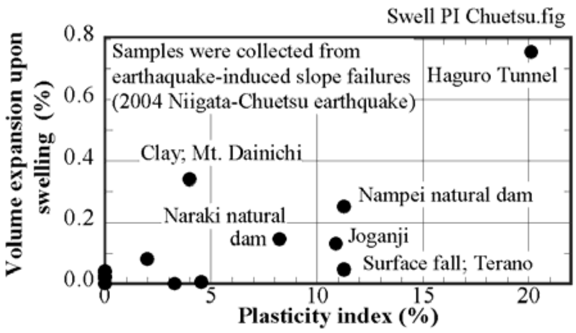

Figure 10 : Correlation between plasticity index and swelling strain.

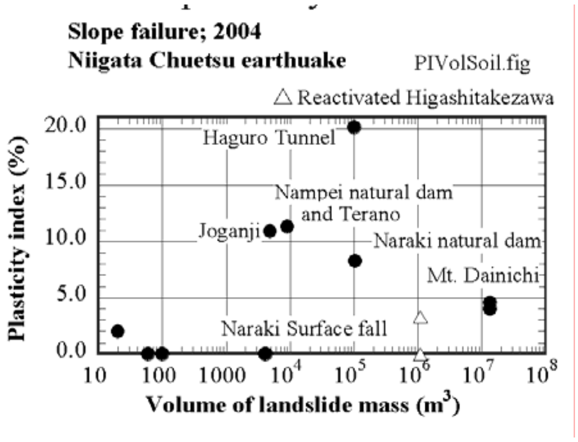

Figure 11 : Correlation between plasticity index and sliding soil mass

TRIAXIAL SHEAR TESTS

More studies were conducted on the effects of water filtration on shear strength. For this purpose, triaxial compression tests were performed in drained (CD) manner on laboratory reconstituted samples in dry or water-submerged conditions. Medium dense samples were prepared by using dry ground powder and consolidated isotropically under 20 kPa. When a water submerged specimen was desired, distilled water was introduced from the bottom. This procedure could not achieve high extent of saturation as is shown by Skempton's B value being 0.8 or less. The present study aimed to reproduce the wetting procedure upon filtration of rain water and drained shear tests did not need high degree of saturation. Triaxial compression was run slowly, spending six hours to failure.

Figure 12 compares the test results obtained from Toyoura sand which had no water-absorbing mineral and hence was "not" ground to powder. Since the water-submerged specimen was slightly denser, the peak strength became greater. Thus, when a tested material does not absorb water, water submergence does not significantly affect the measured shear strength.

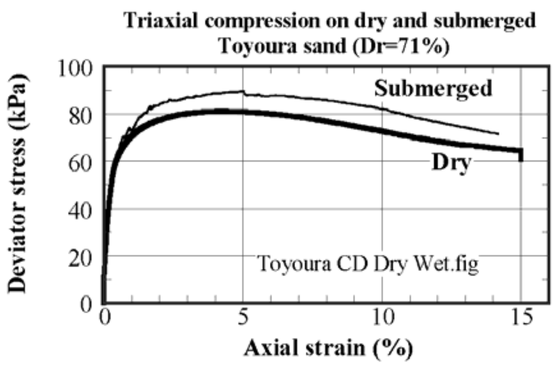

Figure 12 : Drained triaxial compression tests on submerged and dry specimens of compacted Toyoura sand.

Figure 13 : Sakashidani slope in Niigata Chuetsu.

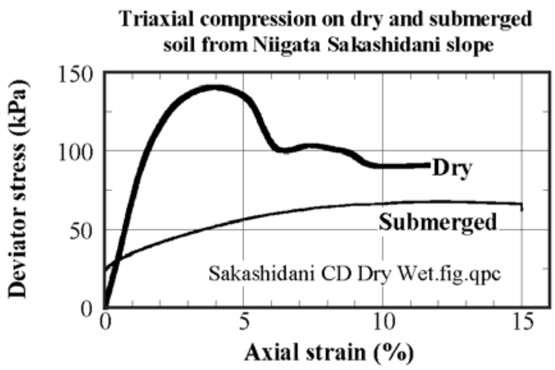

Figure 14 : Drained triaxial compression tests on submerged and dry specimens of compacted powder of soil collected from rainfall-induced slope failure site in Sakashidani..

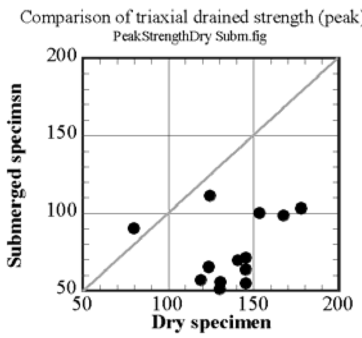

Figure 15 : Comparison of peak strength measured in triaxial drained compression tests on dry and water-submerged specimens.

The next test employed a material which was collected from Sakashidani slope in Niigata where a rainfall-induced landslide occurred in July 2004 (Figure 13). The test results are presented in Figure 14. The water submerged specimen developed much lower peak strength. All the measured peak strength is summarized in Figure 15. These tests were conducted on samples collected from sites of rainfall induced landslides. Strength on submerged specimens was significantly lower despite that shear was conducted in a drained manner. Consequently, triaxial test data was assembled to draw Figure 16 which shows that the submerged strength decreases with the increasing plasticity index. One of the reasons for this is probably the absorption of water and swelling of clay minerals.

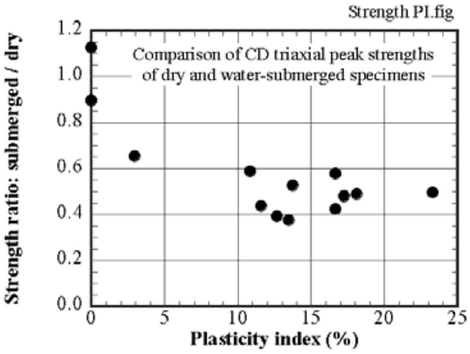

Figure 16 : Variation of strength ratio (submerged / dry strength) with plasticity index of soil..

RISK ASSESSMENT ON SLOPES UNDERGOING SEISMIC EFFECTS

The present study attempts to improve the current risk assessment of slope failure caused by seismic loading. It is therein focused to take into account the size of failed soil mass because the greater soil mass affects a bigger adjacent area. Although Figures 9 and 11 paid attention to the volume of soil mass, the extent of accuracy was not satisfactory. The reason is that the size of failed soil mass depends not only the nature of soil but also the local topography. The bigger slope may cause a greater size of landslide, for example. Thus, the findings in the foregoing sections have to be improved by paying attention to topography.

The present study makes use of the method which was developed by Kanagawa Prefectural Government (Table 1). This method assigns points to each slope in accordance with the topography in a 500m*500m square mesh. The proposed points were obtained by regression analyses of previous landslides. By adding points from different factors, the total point suggests the extent of risk (Rank of Risk); the higher points imply greater risk. Although soil type is somehow considered as shown in Table 1, hard rock is therein assigned higher point than soil; making rock slope more vulnerable to failure than soil slope. This strange nature of the points comes from regression analyses; most probably the studied cases included more rocky slopes than soil slopes. Therefore, it is attempted in the present study to improve the points and, if possible, make it possible to assess the size of failed soil mass as well.

Firslty, the original Kanagawa Prefectural method was applied to the slope failures during the Niigata-Chuetsu earthquake. Since the surface acceleration in the study was uniformly made greater than 400 Gal, based on the observation, all the slopes received high points automatically. The results are shown in Figure 17. Large landsides at Dainichi Mountain and Higashi Takezawa were classified as Rank D (highest risk), followed by another big slide at Haguro Tunnel in Rank C. These cases were accompanied by deep slip planes and were of more hazardous nature. Thus, there is a certain consistency between assessment and reality. However, the risk of Joganji case, for example, is overestimated, although this case was accompanied by a deep slip plane as well. The reason for this is the lack of proper consideration of soil nature.

Table 1 : Seismic risk assessment of slopes practiced by Kanagawa Prefectural Government (topography in 500m*500m mesh is employed for evaluation of the points)

Factors	Classification	Point
Surface acceleration (Gal)	0 – 200	0.000
	200 – 300	1.004
	300 – 400	2.306
	400 -	2.754
Horizontal length of slope (meter)	0 – 1000	0.000
	1000 – 1500	0.071
	1500 – 2000	0.320
	2000 –	0.696
Elevation difference (meter)	0 – 50	0.000
	50 – 100	0.550
	100 – 200	0.591
	200 – 300	0.814
	300 -	1.431
Ground type	Soil	0.000
	Soft rock	0.169
	Hard rock	0.191
Length of fault (meter)	No fault	0.000
	0 – 200	0.238
	200 -	0.710
Length of artificial fill (meter)	0 – 100	0.000
	100 – 200	0.539
	200 -	0.845
Vertical cross section of slope	Convex upwards	0.000
	Planar	0.151
	Concave	0.184
	Combined	0.207

Total point	**Rank of risk**
0 – 2.39	A: least risk
2.39 – 3.53	B
3.53 – 3.68	C
3.68 -	D: highest risk

The risk assessment was improved by correcting the Kanagawa-method point by one of the following formula;

$$\text{Point} = \text{Kanagawa Method} + 0.01 \times Ip(\%) \quad (1)$$

$$\text{Point} = \text{Kanagawa Method} + 0.1 \times \text{Swelling strain}(\%) \quad (2)$$

The new calculated points are plotted in Figures 18 and 19.

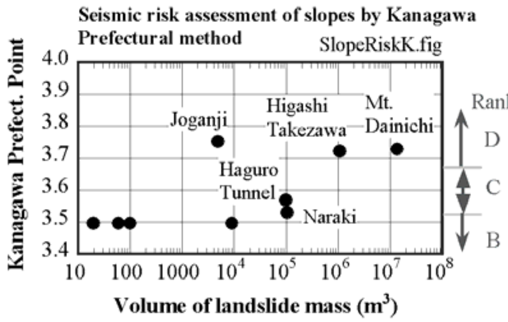

Figure 17 : Risk assessment of slope failures during Niigata Chuetsu earthquake by using original Kanagawa method...

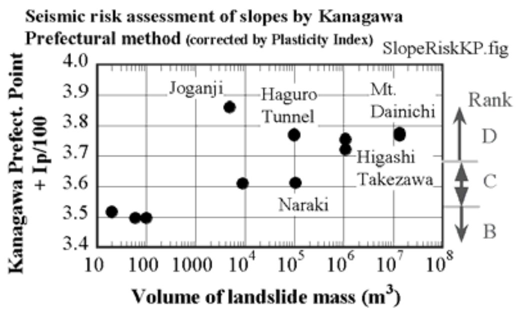

Figure 18 : Risk assessment of slope failures during Niigata Chuetsu earthquake by improving Kanagawa method by plasticity index.

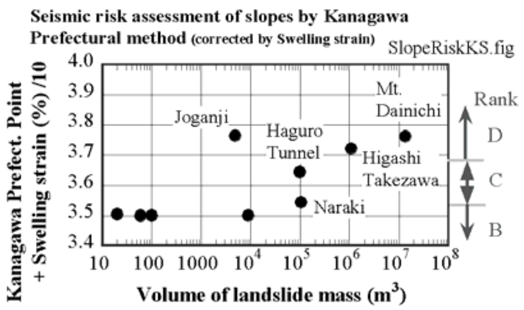

Figure 19 : Risk assessment of slope failures during Niigata Chuetsu earthquake by improving Kanagawa method by swelling strain.

Secondly, Figure 18 illustrates the correlation between the volume of landslide mass and the point calculated by Eq.1. Although there is a good correlation, the overestimation of Joganji case looks to be a problem. As illustrated in Figure 20, the size of the Joganji slide is not so significant as Dainichi Mountain, Higashi Takezawa, and Haguro Tunnel cases. This problem was solved to some extent in Figure 19 for which Eq.2 was employed. Therefore, the correction of risk points in terms of swelling strain appears to be the most recommendable.

Figure 20 : Upper and bigger slope failure at Joganji site in Nagaoka City.

For practice, the labor which is needed to measure the swelling strain of ground powder may be significant. It is however less substantial than collecting undisturbed soil specimens from the site and running shear tests. This issue needs to be considered carefully.

CONCLUSIONS

Soil samples were collected from slopes which failed during the 2004 Niigata-Chuetsu earthquake in order to examine the effects of rain and ground water on the extent of slope instability. It was aimed to improve the present method of risk assessment so that the size of landslide mass can be assessed more appropriately. The conclusions as what follows were drawn.

1) To avoid the difficulty in practice, collecting undisturbed samples and running laboratory tests are not planned.
2) Plasticity and swelling strain were measured on ground powder of soil. This enables to measure quantitatively the extent of water absorption and possible weakening of soil under the effects of water.
3) There is a correlation between swelling extent and plasticity.
4) The volume of slope failure should be assessed by using not only the soil nature but also the topography.
5) This aim is satisfied to a certain extent by combining the Kanagawa Prefectural method with correction by means of plasticity index of swelling. The latter seems more promising.

ACKNOWLEDGEMENT

The present study was conducted by the aid of Dr. H. Toyota of Nagaoka University of Technology. His collaboration is deeply appreciated by the authors.

Field measurement for natural disasters due to slope failures caused by heavy rainfall

K. Sako[1], R. Fukagawa[2], R. Kitamura[3], Ikuo Yasukawa[1]
[1]Organization of 21st century COE Program Promotion, Ritsumeikan University, Shiga, Japan
[2]Department of Environmental System Engineering, Ritsumeikan University, Shiga, Japan
[3]Department of Ocean Civil Engineering, Kagoshima University, Kagoshima, Japan

Abstract

The green house effect has brought change in climate all over the world. In Japan, many slope failures due to rainfall have been frequently happened in the rainy season. A lot of lives, infrastructures and heritages have been lost due to slope disaster. Therefore, it is necessary to construct a slope disaster prevention system in order to predict the slope failure during heavy rainfall. The prevention system used in this research mainly consists of the field measurement data, the numerical modeling and the laboratory soil tests. In this paper, outline of the slope disaster prevention system is described in which we focus on the field measuring system. The field measurement data are obtained by using the tensiometers, rain gage and thermometers. These data are then transmitted to our laboratory through the cellular phone and used for analyzing the seepage behavior of the slope. In addition, the effectiveness of the field measuring system for natural disasters due to slope failures caused by heavy rainfall is also examined in this study.

Keywords—*Field measurement, Pore water pressure, precipitation*

INTRODUCTION

Changes in climate all over the world have caused various disasters such as flood, drought and so on. Ten typhoons hit Japan in 2004, and slope failures due to heavy rainfall often occurred. A lot of lives, infrastructures and heritages have been lost due to slope disaster. Therefore, it is necessary to construct a slope disaster prevention system in order to predict the slope failure during heavy rainfall.

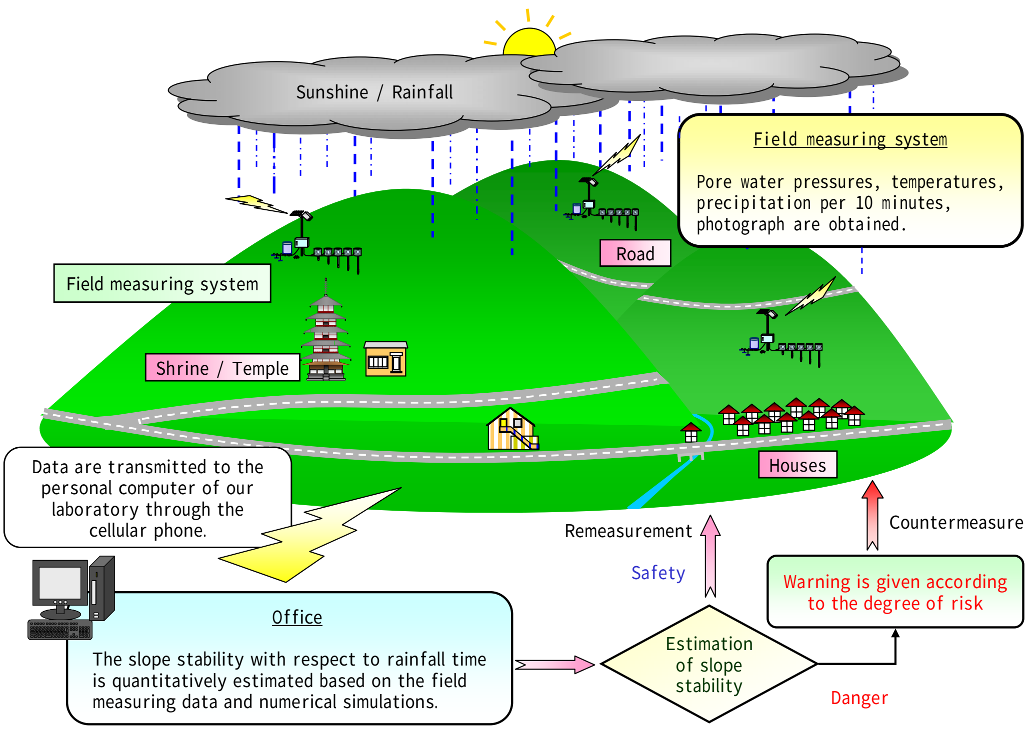

Fig.1: Schematic of a slope disaster prevention system.

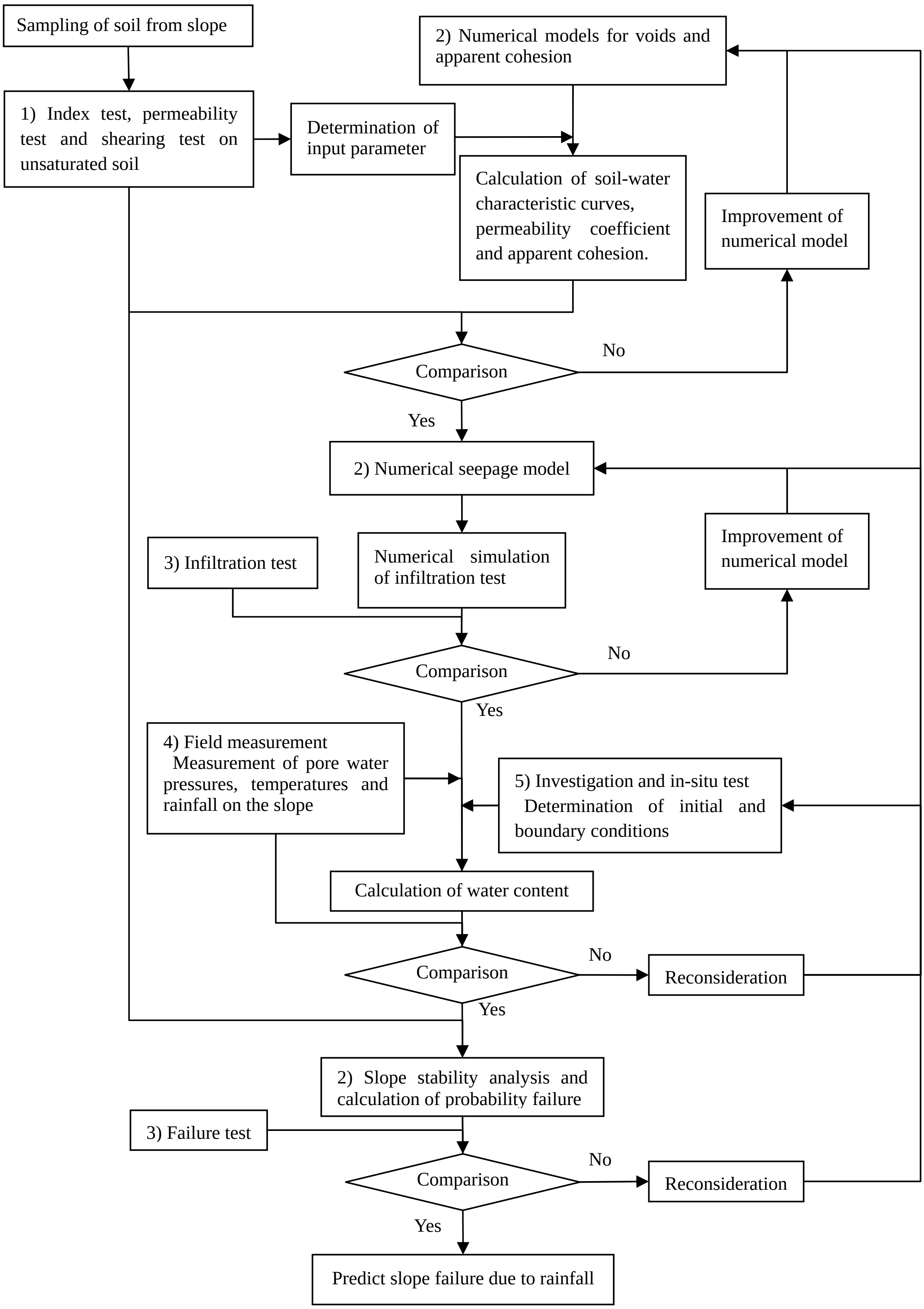

Fig.2: Research strategy of the prevention system of slope failures due to heavy rainfall.

It is qualitatively said that the slope failures with rainfall are mainly caused by the increase in weight of soil mass, the decrease in suction of unsaturated soil with the increase in water content and the rise in groundwater level. So, it is important to measure the suction, rainfall, temperature etc., in order to predict the slope failure caused by heavy rainfall.

In this paper, the outline of the slope disaster prevention system is explained. The filed measuring system, which is used to measure the suction, rainfall, and temperature, is also presented. Moreover, our observation about the measurement result is described.

SLOPE DISASTER PREVENTION SYSTEM

Fig.1 shows the schematic of the slope disaster prevention system. First, a measuring point is determined by ground surveys and in-situ tests. And then, the field measuring system (i.e. tensiometers, rain gage, thermometers and camera) are set up at that point. Using this measuring system, the suction (negative pore water pressure), precipitation, temperature and photograph in the field can be obtained; these data are then transmitted to our laboratory through the cellular phone. On the other hand, in the laboratory, the slope stability with respect to rainfall time is quantitatively estimated based on the field measuring data and numerical simulations (i.e. slope stability analysis and 2-D unsaturated saturated seepage analysis). Finally, the warning is given according to the degree of risk obtained in our analysis.

Fig. 2 shows a research strategy of the prevention system of slope failures due to heavy rainfall proposed by Kitamura et al. [1]. The strategy is mainly composed of five items as shown in Fig.2. There are 1) laboratory soil tests on disturbed and undisturbed samples, 2) numerical simulations, 3) soil tank tests of seepage and failure, 4) Field measurement of suction, temperature and precipitation and 5) some in-situ tests for identification of geological and geotechnical characteristics of slope.

The purposes of each item will be explained as follows:

1) The results of laboratory soil tests are used as the input parameters for the numerical models and also used to validate the simulation.

2) The numerical simulations are important items for the prevention system. These items consist of a numerical model for voids, a numerical model for apparent cohesion, a 2-D unsaturated saturated seepage analysis and a slope stability analysis. The use of numerical model for voids [2] computed the unsaturated seepage characteristics of soil, i.e. the soil-water characteristic curve and the relationship between degree of saturation and unsaturated saturated permeability coefficient. The use of numerical model for apparent cohesion [3] computed the change in apparent cohesion with the change in water content. This change is one of the main causes of the slope failures due to rainfall. The Finite Element Method is used as the numerical seepage model. The results of numerical model for voids are applied to the above numerical seepage model. The Janbu method is used as the slope stability analysis. A probability of failure [4] is introduced as the new estimation method of slope stability in the rainfall.

3) The soil tank tests of seepage and failure are carried out to prove the validity of numerical scheme by means of the above-mentioned models in the soil tank where the initial and boundary conditions can be easily controlled.

4) The data of the field measurement, which are the pore water pressure, rainfall and temperature, are used to determine the initial and boundary conditions of 2-D unsaturated-saturated seepage analysis and to discuss the validity of numerical models.

5) Some in-situ tests such as CPT and boring are

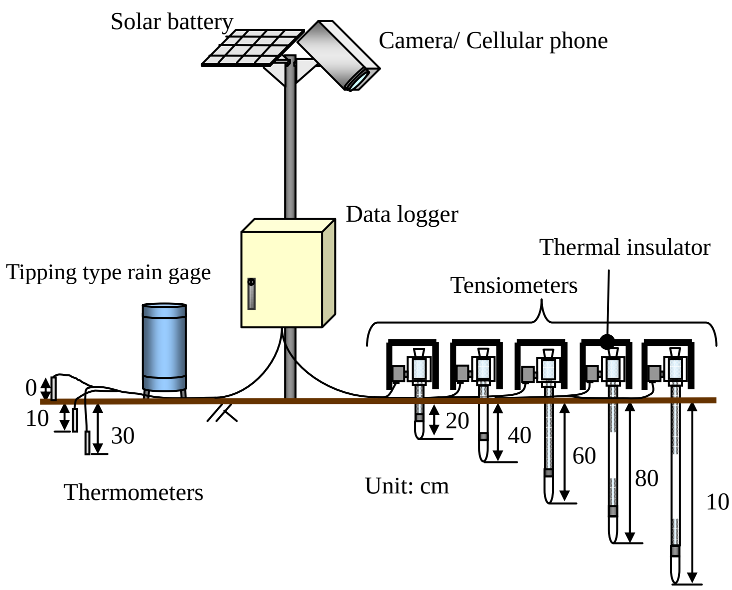

Fig.3: Schematic of the field measuring system.

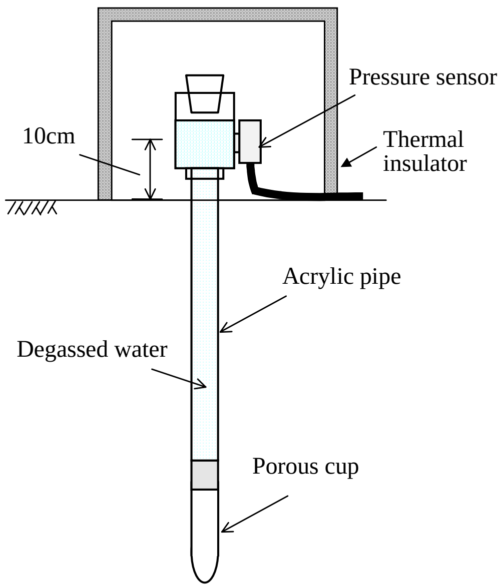

Fig.4: Tensiometer

carried out to identify the geological and geotechnical characteristics of the slope. The calculation domain, the structure of layers and the potential slip plane are determined based on the data obtained from some in-situ tests.

FIELD MEASURING SYSTEM

Fig. 3 shows the schematic of the field measuring system. This system is made up of tensiometers, tipping bucket type rain gage, thermometers, camera and data logger. Photo. 1 shows the field measuring system, which has already set up in the field.

Five tensiometers are laid to the depth of 20, 40, 60, 80 and 100cm, respectively. The pore water pressure at each depth is obtained by tensiometers. Fig. 4 shows a schematic of tensiometer, which is composed of a porous cup, a semiconductor type pressure sensor and an acrylic pipe filled with degassed water. The porous cup is made of ceramic that is saturated and the air cannot pass through under a pressure smaller than its air entry value. The upper part of the tensiometer from the ground surface is covered by a box, which is surrounded by a thermal insulator, in order to avoid the influence of change in atmospheric temperature [5]. The tipping type rain gage is used to measure the rainfall. The thermometers are laid to the depth of 0, 10 and 30cm. And, the data are used for a numerical simulation of evaporation. The photographs of 350,000 pixels of the measuring point are taken in order to check the condition of the slope. The actual photograph of the measuring point is shown in Photo. 2.

The pore water pressure, rainfall, temperature and photograph are measured by the data logger after every 10 minutes. All of the measuring data are the transmitted to our laboratory through the cellular phone after every 2 hours.

FIELD MEASURING RESULTS

Fig. 5 shows the cross-section of the slope and the measuring point of the field measuring system. In July 2004, the measuring system has been set up on this slope behind a concerning building, which was one of the important cultural assets in Japan. The penetration tests were carried on this slope by using the simplified dynamic penetrometer before setting up the field measuring system. From these tests, a potential slip plane from ground surface was found from 80cm to 200cm depth. The measuring point in our research was set at the depth of 120cm.

Fig. 6 shows the field measuring data in which we presented the change in pore water pressures, rainfall and temperatures with respect to the time. Fig.6 (a) and (b)

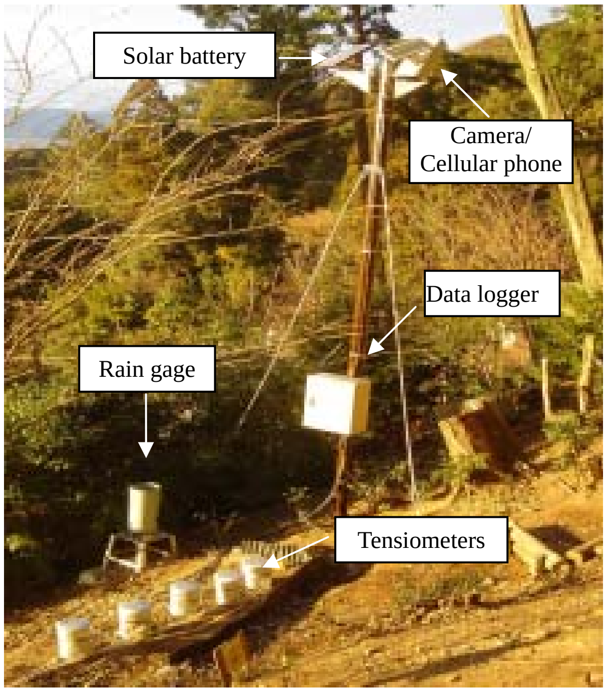

Photo.1: Field monitoring system

Photo.2: The actual picture of the measuring point

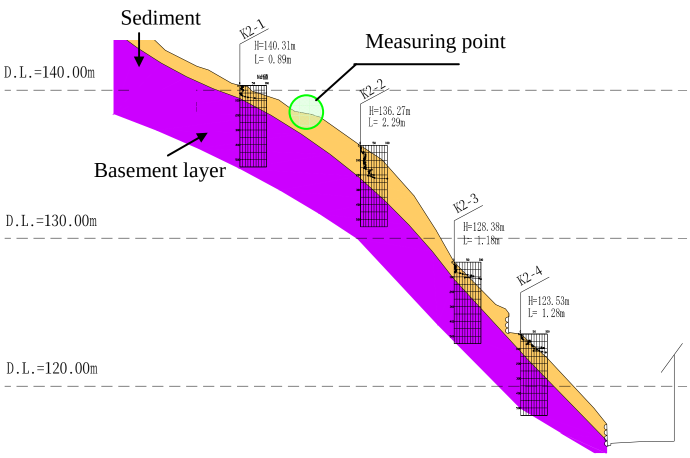

Fig.5: Cross-section of the slope and measuring point of the field monitoring system

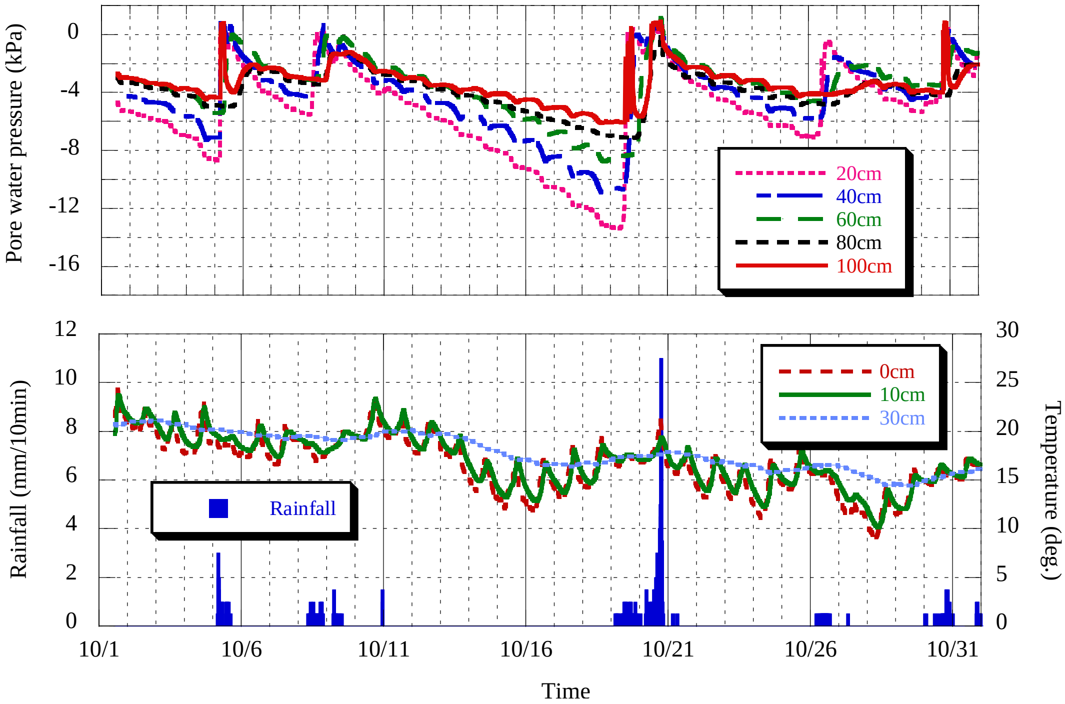

(a): The data in October 2004.

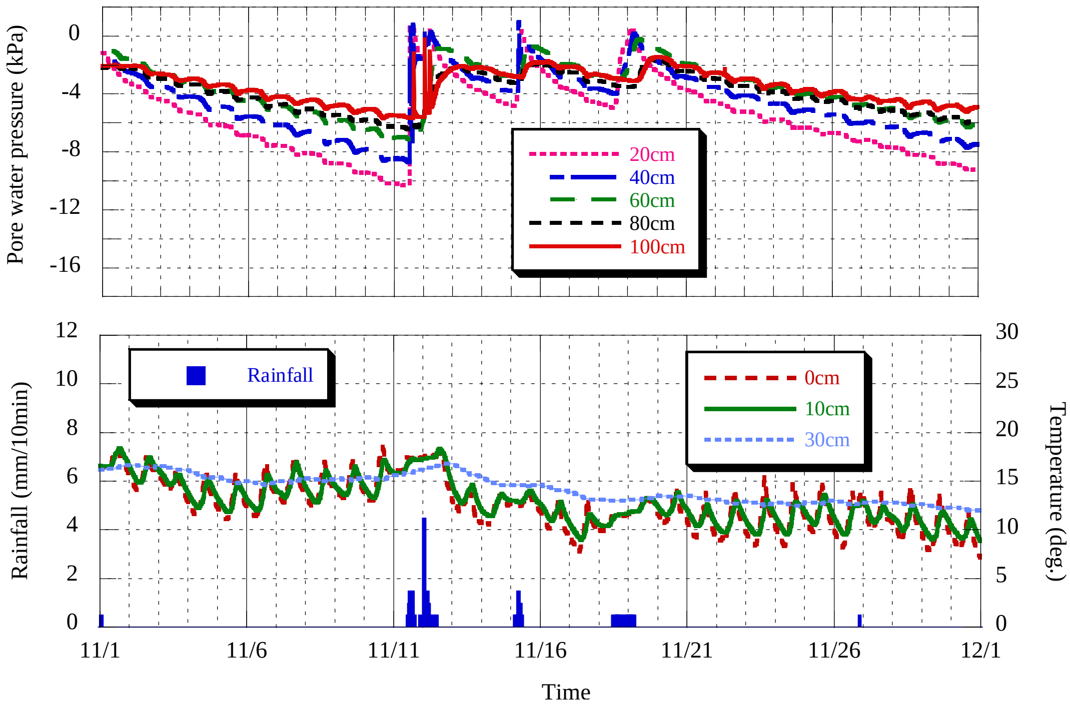

(b): The data in November 2004.

Fig.6: Field measuring data (Pore water pressure, temperature and precipitation per 10 minutes)

show the data in October and November 2004, respectively. From these figures, it is seen that the pore water pressures increase during rainfall, and decrease at the fine weather. The daily variation of temperature appears clearly at the depth of 0cm and 10cm, except at the depth of 30cm. Furthermore, it is also seen that a little influence of the temperature on the pore water pressure can be perceived from the measuring results. It is also seen that the heavy rainfall has been occurred due to the typhoon No.23 on October 20, 2004 and following by many natural disasters in the Kansai Region.

In addition, it has been understood from the measuring data that the difference in tendency of the rainfall influences the change in pore water pressure. Fig.7

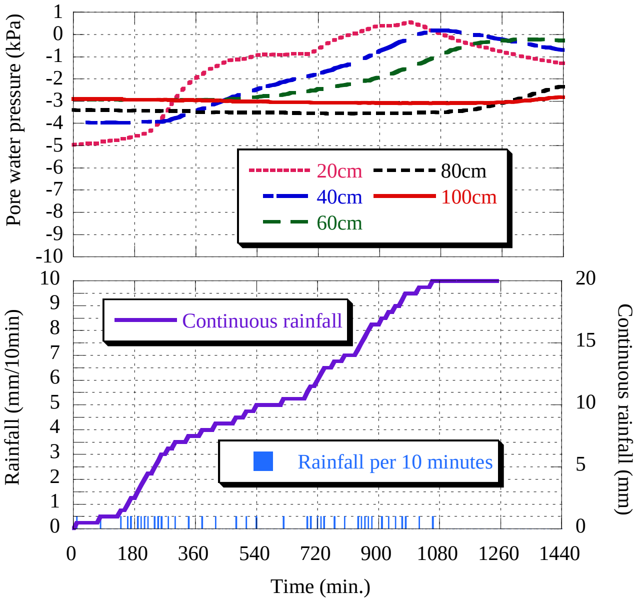

(a): November 18, 2004 (Small precipitation)

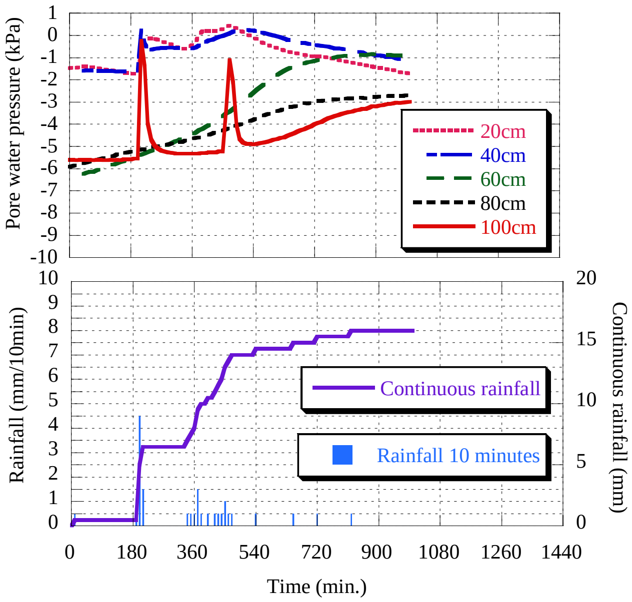

(b): November 12, 2004 (Large precipitation)

Fig.7: The tendency of the change in the pore water pressure due to the difference in precipitation per 10minutes.

shows the change in pore water pressure due to the difference in rainfall. Fig.7 (a) and (b) show the results on November 18 and November 12, 2004, respectively.

When the rainfall per 10 minutes is small as shown in Fig.7 (a), the pore water pressure sequentially increases from the shallow part. On the other hand, when the large rainfall per 10 minutes occurred as shown in Fig.7 (b), the pore water pressure at the depth of 100cm increased after the increasing of the pore water pressure at the depth of 20 and 40 cm.

The early change in the pore water pressure at the depth of 100cm when the large rainfall occurred can be explained due to the rainwater flow on the potential slip plane from the upper part of the measuring point.

In general, the increase in pore water pressure, especially in the deep area, causes a considerable decrease in slope stability. Therefore, monitoring the change in pore water pressure due to rainfall is important in order to predict the slope failure.

Fig. 8 shows the relationship between the change in pore water pressure and rainfall. The horizontal axis is continuous rainfall while the vertical axis indicates the maximum rainfall per hour. A total of 65 measuring data, which were obtained from August 2004 to January 2005, are used in Fig.8. The tendencies of the change in pore water pressure are divided as follows: 1) ▲: The pore water pressure only increased at the shallow depth which was less than 40cm, 2) ■: The pore water pressure sequentially increases from the shallow part (Fig.7 (a)), 3) ●: The pore water pressure at the depth of 100cm increased after the increasing of the pore water pressure at the depth of 20 and 40 cm (Fig.7 (b)).

It is found from this figure that the pore water pressure from the depth of 20 to 100cm increased when the continuous rainfall is lager than 7.0mm. Moreover, the pore water pressure at the depth of 100cm was found considerable change when the maximum rainfall per hour is larger than 4.0mm as shown in Fig.7 (b).

On June 27, 1999, the slope failure due to heavy rainfall occurred at the slope near the field measuring point. The weather data of the slope failure in 1999 was shown in Fig. 9 [6]. These data was also shown in Fig.8 (◆). The time of the slope failure was 8:45a.m., the rainfall per hour from 7:00a.m to 8:00a.m was 28mm/hour and from 8:00a.m to 9:00a.m was 47mm/hour. The continuous rainfall by 9:00a.m was 123.5mm.

In Fig.8, the measuring data were compared with the data of the slope failure in 1999. It is found that the measuring result of rainfall on October 20, 2004 is close to the rainfall of the slope failure in 1999. The measuring result was obtained at the typhoon No.23 on October 20, 2004 and following by many natural disasters in the Kansai Region. Therefore, it is seen that the degree of risk of the slope failure at the measuring slope was probably high.

CONCLUSIONS

In this paper, the outline of the slope disaster prevention system was explained. The filed measuring system was introduced and the seepage behavior of the slope was considered based on the measuring data. Comparison between the current measuring data and the data of slope failure in 1999 has been made. From this research it is concluded that the field measuring system plays an important role in predicting the slope failure due to rainfall. In the near future, 2-D seepage analysis and

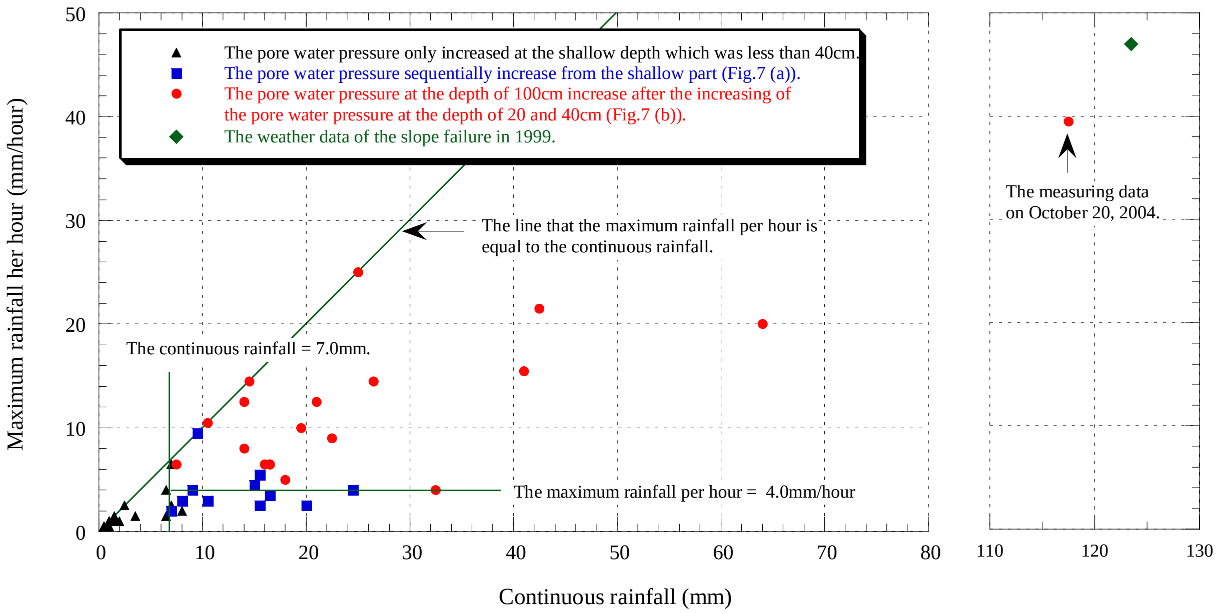

Fig.8: The relationship between the change in pore water pressure and rainfall.

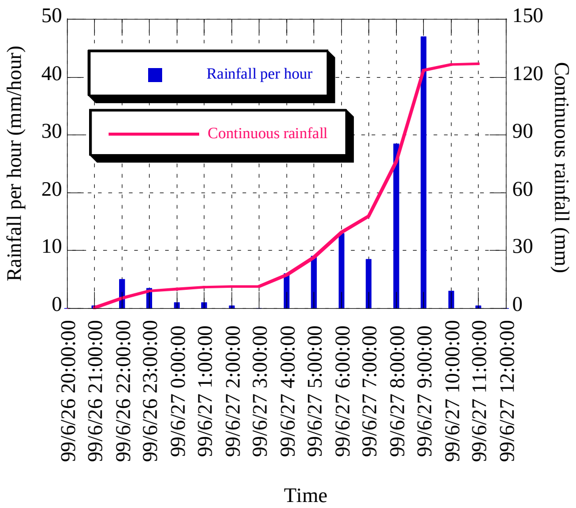

Fig.9: The weather data of the slope failure on June 26-27, 1999 [6].

slope stability analysis will be performed in order to quantitatively estimate the change in slope stability due to rainfall. Finally, the prevention system of the slope failures due to rainfall is established by combining the field monitoring system with numerical simulations.

REFERENCES

[1] Kitamura, R., Sako, K. and Matsuo, K., "Research strategy on unsaturated soil for prediction of slope failure due to heavy rainfall," Proc. 2nd World Engineering Congress, Engineering Innovation and Sustainability: Global Challenges and Issues, pp.196-202, 2002.

[2] Kitamura, R., Fukuhara, S., Uemura, K. Kisanuki, G. and Seyama, M., "A numerical model for seepage through unsaturated soil." Soils and Foundations, Vol.38, No.4, 261-265, 1998.

[3] Sako, K., Kitamura, R. and Yamada, M., " A consideration on effective cohesion of unsaturated sandy soil. Proc. of the Fourth International Conference on Micromechanics of Granular Media." Powders and Grains 2001, pp.39-42, 2001.

[4] Sako, K, Araki, K. and Kitamura, R., "Research on probabilistic estimation of shear strength parameters for slope stability analysis", Proc. of The Shio-Japanese symposium on geotechnical engineering, Geotechnical engineering in urban construction, pp.320-325, 2003.

[5] R. Kitamura, M. Kawaida, H. Abe, K. Jomoto and T. Terachi, "Development of field measuring system for suction in unsaturated soil with rainfall," (In Japanese) J. of Geotechnical Engineering, JSCE, No.652/III-51, pp.287-292, 2000.

[6] Japan meteorological agency：http://www.data.kishou.go.jp/etrn/index.html.

(3) Liquefaction associated phenomena

Influence factors on damage to pile foundation by liquefaction ground flow

Yuji ADACHI[1], Kinya MIURA[2] , Shingo MORIMASA[2] , Masaya MIHARA[1], Kazuhiko URANO[1]

[1] *Technical Research Institute, HAZAMA Corporation, Ibaraki, Japan*

[2]*Department of Architecture and Civil Engineering, Toyohashi University of Technology, Aichi, Japan*

Abstract

Several types of structures have been suffered from structural damage induced by liquefaction in destructive earthquakes. Since the flow slide of liquefied ground sometimes induces extraordinary thrust to underground structures, pile foundations for bridges and buildings, pipeline networks, and etc are severely damaged. The aim of this study is to investigate the mechanism of the damage to structural pile foundation induced by the flow slide of liquefied ground, and a series of shaking table tests on the model pile foundation were conducted. Basically three types of model sloping grounds with the pile foundation were shook on the shaking table; the test cases were selected for the examination of the thrust to pile foundation. In the standard case the sloping ground with a surface non-liquefaction layer was shook; the flat ground with surface non-liquefaction layer and the sloping ground without non-liquefaction layer were also shook with the same base vibration. The vibration behaviors of the ground and pile foundation were observed, and the thrust on the pile foundation from the liquefied ground were monitored through the measurement of bending moment along a pile. Furthermore the influence factors on the thrust to pile foundation during the liquefaction and ground flow were examined with additional tests with different surface non-liquefaction layer thicknesses, ground inclinations, or input base shakings. As a result of the comparative examination of the observed behaviors, the important roles of the influence factors on the thrust to pile foundation induced by the flow slide of liquefied ground was clarified.

Keywords— *Pile, Shaking table test, Liquefaction, Ground flow*

INTRODUCTION

In destructive earthquakes, many structures are severely damaged due to the liquefaction of ground. On riverside, seaside or port and harbor area, liquefied ground often flows toward river or sea; the lateral displacement of the ground sometimes exceeds a few meters and rarely reaches ten meters, as in [1]. The sloping liquefied ground with low shear stiffness is driven laterally by the gravity force. In port and harbor area the lateral flow is usually induced by the failure of retaining structures at water edge, as in [2]. Since the 1964 Niigata Earthquake, the damages to pile foundations for bridges and buildings by the flow of liquefied ground have been reported in many large earthquakes in Japan, as in [1]. And the mechanism and the countermeasure to this type of damage have been investigated, as in [3] and [4].

In this study a series of shaking table tests were conducted on the model sloping ground with surface non-liquefaction layer under 1g-gravitation field. We are aiming to reveal the mechanism of the damage to pile foundation induced by the ground flow of liquefied sloping ground, with special attention to the interaction between the pile foundation and the ground through the surface non-liquefaction layer. Furthermore, the influence factors on the thrust on pile foundation were examined based on the test results; slope of ground surface, thickness of surface non-liquefaction layer, direction and intensity of base shaking, and density of ground, were parametrically changed in the series of model shaking

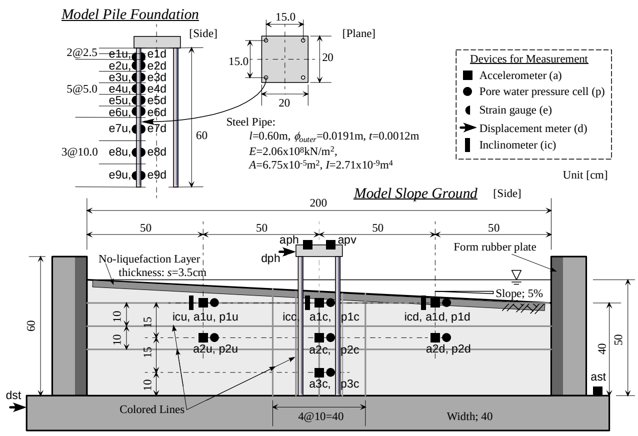

Fig. 1: Pile foundation model and instrumentation inside the soil of sloping ground mode

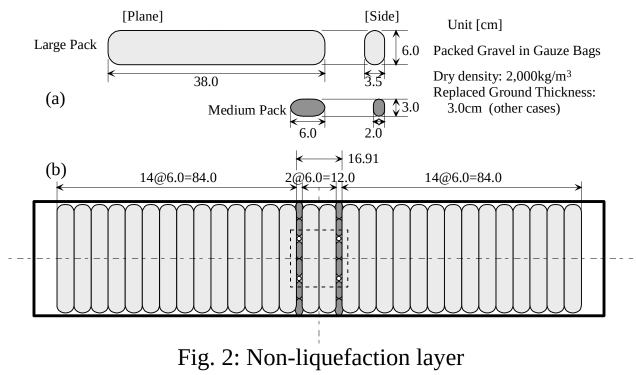

Fig. 2: Non-liquefaction layer

a) Densely packed gravel bags

b) Arrangement of the gravel bags on ground surface.

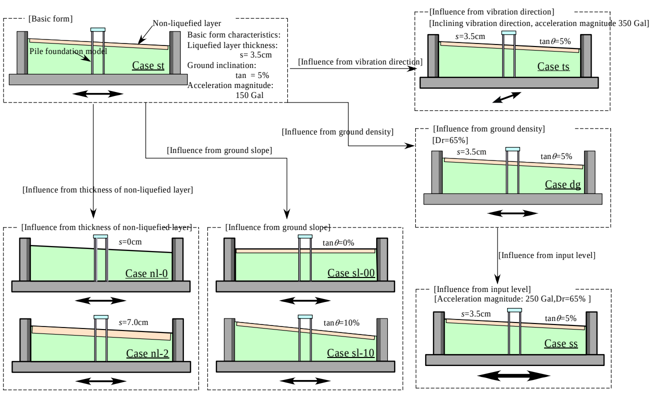

Fig. 3: Test cases for the influence of ground condition

Table 1: Test cases for the influence of base shaking duration time

Case	Non-liquefaction layer	Duration time (s)
Case st_d02		2
Case st_d03	with	3
Case st_d12		12 (Case st)
Case nl-0_d02		2
Case nl-0_d03	without	3
Case nl-0_d12		12 (Case nl-0)

table tests. The significance of some influence factor was qualitatively examined, rearranging and compeering observed behaviors.

MODEL SHAKING TABLE TEST

Model sloping grounds with the pile foundation of standard case and the non-liquefaction layer used in the test are shown in Figs. 1 and 2. A soil container of 200cm, 60cm and 40cm in length, depth and width, respectively, was made of steel plates and tempered glass plates on front and back. The model pile foundation consists of four steel pipes and a rigid footing box made of steel plates of 10.13kg in mass. The accelerations in horizontal and vertical directions, and horizontal displacement of the footing were monitored during shaking. One of the pipes on upstream side, that is the left hand side in the figure, has nine pairs of strain gauges for monitoring the bending moment along the pile. The sand material for liquefiable sloping ground is siliceous sand with a mean diameter D_{50} of 0.54mm, a uniformity coefficient U_c of 2.11, a maximum dry density ρ_{dmax} of 1.745g/cm^3, and a minimum dry density ρ_{dmin} of 1.475g/cm^3. The sand material was dried in an oven, and pluviated through the slit of sand hopper which moved cyclically back and forth. The sand was deposited under water uniformly, so as to create a saturated medium dense ground with a relative density Dr of 50%. Its liquefaction strength was 0.17 in a series of undrained cyclic tri-axial tests; i.e., the shear-

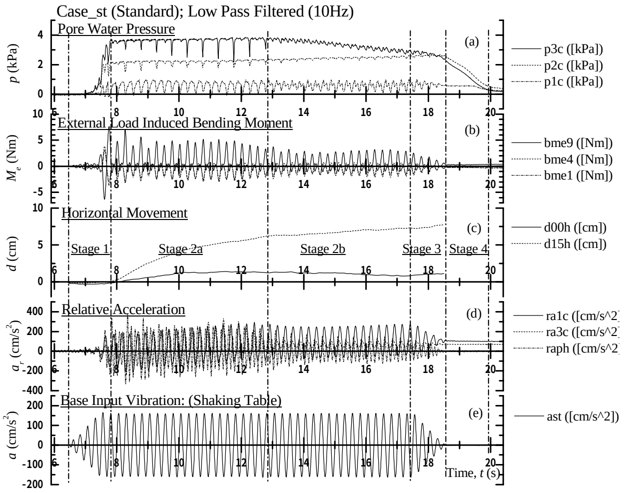

Fig.4. Behavior of ground and pile foundation during shaking observed in Case st.

normal stress ratio of 0.17 was required to increase the excess pore water pressure up to 95% of initial effective stress in 20 cycles of loading. During the preparation of the ground, accelerometers and pore water pressure meters were arranged as shown in Fig. 1. Surface non-liquefaction layer consists of subangular gravel which was 6.3mm in D_{50} and 3.55 in U_c; the gravel was densely packed into thirty narrow gauze bags and twelve small gauze bags. The gravel bags were not connected one another and arranged on the surface of ground as shown in Fig. 2. Standard base shaking was sinusoidal wave with tapers both at beginning and end, the acceleration was 150Gal in single amplitude and was 4Hz in frequency, and the duration time was 12s. Details of the model test including materials, setting, model conditions and measurement method can be found in reference [5].

The test cases prepared are shown in Fig 3. Test conditions were arranged so as to examine the influence factors: sand ground density, slope angle, surface non-liquefaction layer, and input base shaking. Especially the behavior of the surface non-liquefaction layer was discussed with paid special attention. The surface non liquefaction layer was prepared to model the solidified surface layer in the in-situ ground condition. The condition of the ground surface must play an important role in the interaction between pile foundation and liquefied ground. Several test cases were additionally prepared to examine the effect of the base shaking duration time on the residual thrust to pile foundation; see Table 1.

TEST RESULTS

Fig. 4 shows the overall vibration behavior of the ground and pile foundation during shaking in the standard condition, Case st. Top figure is the time history of excess pore water pressure beneath the footing. In standard test condition (Case st), liquefaction was initiated at 1.3s after shaking was started, and the liquefaction was retained for about 5s. And the excess pore water pressure began to

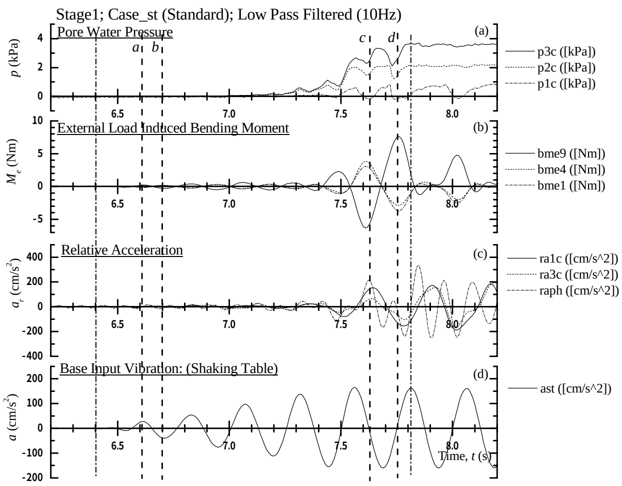

Fig.5. Behaviors of ground and pile foundation in Stage 1 of Case st

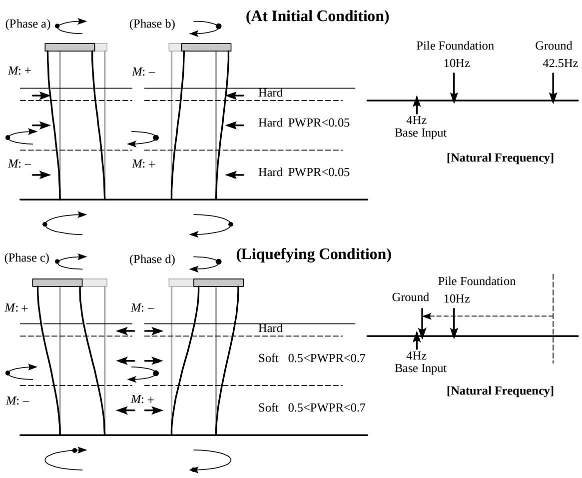

Fig.6. Illustration of deformation and external force in Stage 1 of Case st

reduce first at the deep part of the ground (p3c). After the end of shaking, the excess pore water pressure reduced back to a hydrostatic state. This overall tendency was common and independent of the ground slope and the existence of the surface non-liquefaction layer.

Top second figure is the time history of bending moments *M*e due only to external force from ground. While total bending moment *M*t tells the displacement of the footing and the deformation behavior of pile foundation, the bending moment due to external force *M*e tells the behavior of external force which is resulted from the interaction between ground and pile foundation. *M*e was calculated by subtracting *M*i(due to inertial force on pile foundation) from observed measured total bending moment Mt.

Top third figure shows the lateral displacements of the liquefied ground at surface and depth of 15cm. This obstruction of the ground by the pile foundation causes the thrust on the pile foundation from the ground. In standard test condition (Case st), the horizontal

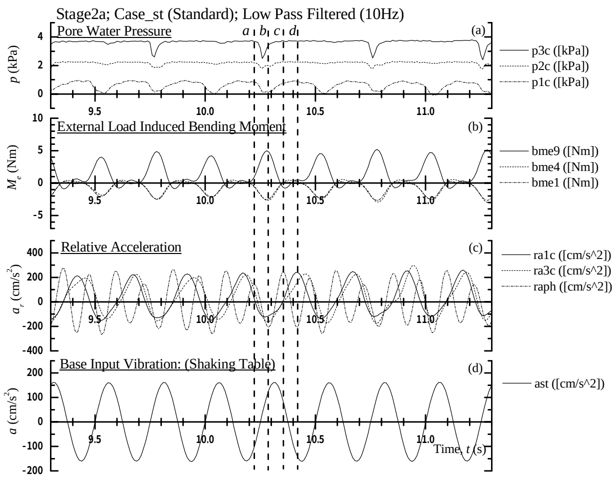

Fig.7. Behavior of ground and pile foundation in Stage 2a of Case st.

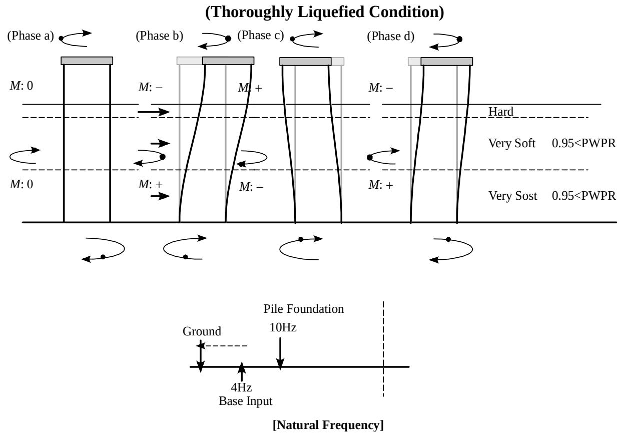

Fig.8. Illustration of deformation and external force in Stage 2a of Case st

displacement didn't become maximal at ground surface but at intermediate depth, because the displacement of the surface layer was obstructed by the pile foundation. From the examination of the video image of the deformation of the ground, it was also suggested that a notable shear deformation and associated shear force was generated at the interface between the surface non-liquefaction layer and the ground.

The top fourth graphs show the time history of relative horizontal accelerations at the ground and the footing of pile foundation with respect to the shaking table; the relative acceleration tells the deformation behavior of ground and pile foundation as a result of not only base input vibration but also the interaction between ground and pile foundation.

The figure at bottom are for absolute horizontal accelerations of shaking table as input base vibration.

For the detailed examination of the interaction between ground and pile foundation, we divided the shaking process into five stages according to the behaviors of base input vibration and pore water pressure as shown in Fig. 4.

-Stage 1: in the process to liquefaction.

-Stage 2a: until the start of reduction in pore water pressure.
-Stage 2b: until the end of shaking with uniform amplitude.
-Stage 3: until the end of shaking.
-Stage 4: until the reach to hydrostatic condition.

DISCUSSION

In this section, first the behavior observed in standard test condition (Case st) is examined in detail. Then, the interaction between ground and pile foundation is analyzed by the comparative examination of the behaviors of the three test cases, Case st, Case nl-0 and Case sl-00, with an attention to the influence of surface non-liquefaction layer and lateral flow of the ground. And furthermore, the influence factors to increase the thrust to pile foundation are considered on the basis of the result of all the test cases.

Detailed Examination of Vibration Behavior (Case st)

In the Process to Liquefaction (Stage 1: Figs. 5 and 6)

At the early part of this stage, since the ground still maintains certain amount of stiffness with some excess pore water pressure of a fraction of initial effective stress, the ground vibration was rather small and the phase of vibration of the ground and pile foundation was almost same as that of the input base vibration (Phase a and b in Figs. 5and 6). Here, due to the support by the ground, the vibration of pile foundation was fairly small compared with the case of the pile foundation standing alone.

With a continuous reduction in effective stress and associated stiffness of ground corresponding to a further increase in excess pore water pressure, the natural frequency of ground would have reduced more. Then the resonance condition was met just before the initiation of liquefaction, where the phase difference angle in vibration between shaking table and ground was about a half of π. At the resonance the bending moment Me along the pile was fluctuated with notable amplitude in a few cycles (Phase c and d in Figs. 5 and 6). In this condition, the ground stiffness was small but the integrity of the ground was still maintained, so that the interaction between ground and pile foundation and the interactive force must have been enhanced instantaneously. The variation of relative acceleration of pile foundation (raph) indicates that the pile foundation vibrated twice in a cycle of input base vibration as a result of the interaction. The occurrence of the resonance was common feature in all the test cases conducted in this study, except for Case dg with dense ground.

In the Full Liquefaction Stage (Stage 2a: Figs. 7 and 8)

In this stage the interaction between ground and pile foundation was emphasized by the fairly large vibration and flow of liquefied ground. The characteristic variation of the bending moment *M*e tells that the external force was intermittently applied to the pile foundation only in downhill direction in every cycle of shaking. That is, the external force became maximal when the pile foundation and ground both deflected in downhill direction at the same time; see Phase b in Figs. 7 and 8. This characteristic behavior of the external force suggests the significance of surface non-liquefaction layer in the interaction. It seems that due to the combined effect of vibration and flow, the surface non-liquefaction layer would contact with the pile foundation only when the ground deflected in downhill direction; only compressive force but not tension would be expected between them.

In this process the cyclic mobility of ground stiffness was perceived clearly in the sloping ground as shown in Figs. 7 and 8; the instantaneous reduction in the pore water pressure is the evidence of the cyclic mobility, and is followed by the increase in effective stress and mobilization of stiffness. This characteristic mechanical behavior is related to the dilatancy in granular materials like sand. The dilatancy causes an increase in volume in drained condition or a reduction in pore water pressure in undrained condition. The careful examination of the time history of excess pore water pressure indicated that the cyclic mobility occurred not only in the vicinity of the pile foundation but also near the interface with the surface non-liquefaction layer. Thus the pile foundation would have been subjected to two kinds of external forces: one directly from liquefied ground and the other from the surface non-liquefaction layer. The cyclic mobility occurs when ground moves in downhill direction, but it did not occur every cycles of shaking regularly. It was interesting that the intensity of external force on the pile foundation was related to the amount of the instantaneous decrease in pore water pressure.

Effects of Surface Non-Liquefaction Layer and Flow of Ground

Shown in Fig. 9 are the time histories of excess pore water pressure *p* at (p1c) and external force induced bending moment *M*e at (e9u and e9d) in the three test cases, Case st, Case nl-0 and Case sl-00, conducted in this study. From the comparative examination of the behaviors observed in the three test cases, the following characteristic effects of the surface non-liquefaction layer and the flow of liquefied ground on the interaction between the ground and the pile foundation could be found.

Resonant vibration just before Initial Liquefaction

The resonant response of the ground and the associated large external force on the pile foundation were recognized just before liquefaction was attained in Stage 1, commonly in the three test cases, as shown in Fig. 9. In this stage the application of the large external force was only in a few cycles but the intensity was comparable with those in full liquefaction stage (Stage 2a). The maximum bending moment *M*e was 7.6, 6.2, and 5.6 Nm in Case st, Case nl-0 and Case sl-00, respectively. The

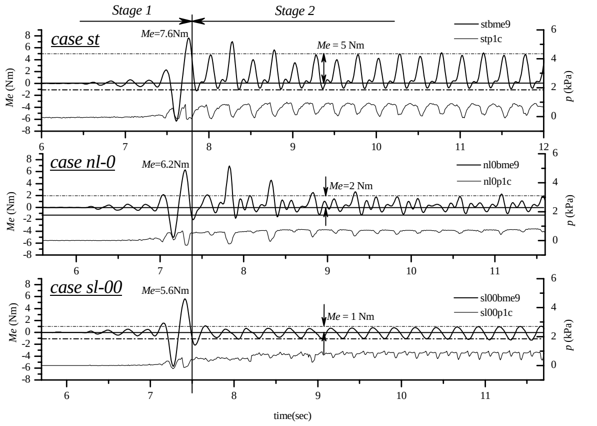

Fig.9. Comparison of behaviors of ground and pile foundation observed in Case st, Case nl-0 and Case sl-00.

influence of surface non-liquefaction layer and lateral flow was rather small, and it seems, however, that the external force was enhanced by the surface non-liquefaction layer and the lateral flow.

Flow of Liquefied Ground

In the cases of sloping ground (Case st and Case nl-0) the flow of liquefaction ground began at the initiation of liquefaction; however, in the case of flat ground (Case sl-00) the horizontal flow displacement was negligibly small, and the ground was just vibrated responding to the base input vibration. Without surface non-liquefaction layer (Case nl-0) the horizontal displacement was maximal at the surface and exceeded 10cm. By contrast, with the surface non-liquefaction layer (Case st) the displacement was not more than 2cm at surface and became maximal at intermediate depth, because the displacement of the surface layer was obstructed by the pile foundation.

Cyclic Mobility

The cyclic mobility of the stiffness of liquefied ground, which was induced by a decrease in pore water pressure and associated regain in effective stress, was recognized in the three test cases. However, the intensity of the instantaneous decrease in excess pore water pressure was larger in sloping ground; and also enhanced by the surface non-liquefaction layer.

Influence of ground condition and base shaking

The time history of bending moment *M*e (=bme9) induced by ground external force occurred at the bottom part of the pile is shown in Fig. 10 for each of the cases. The maximum amplitudes of the bending moment *M*e (bme9) in the process to liquefaction (Stage 1) and the averaged value of peak bending moment during liquefaction (Stage 2), which was measured in all the test cases, are listed in Table 2.

In the process to liquefaction (Stage 1)

The maximum amplitudes of *M*e was almost independent on slope of ground surface and existence of

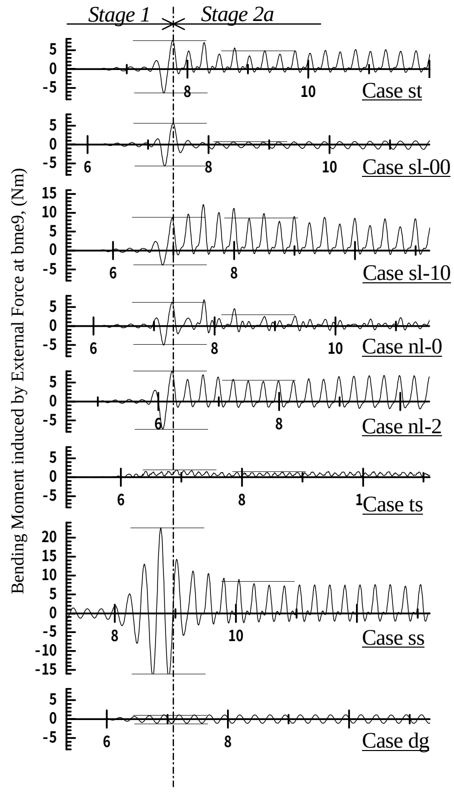

Fig. 10: Deformation sketch of color sand after termination of vibration

Table 2: Amplitude and averaged peak bending moment

Case	Amp. of Me Stage1 (Nm)	Ave. peak Me Stage2 (Nm)
Case st	13.5	4.1
Case sl-00	11.1	0.6
Case sl-10	12.1	8.6
Case nl-0	12.4	2.8
Case nl-2	12.9	6.0
Case ts	1.5	1.0
Case ss	38.1	8.5
Case dg	0.7	---

Note: The values in the table are all representing the inclination direction.

surface non-liquefaction layer, but dependent on the intensity of base shaking and density of ground. In Case ss with strong base shaking, the amplitude of *M*e was more than twice as large as that in Case st. In Case ts with shaking in the transversal horizontal direction, the amplitude of *M*e was extremely small; base shaking did not contributed to the deformation of pile foundation in the direction of slope, since the direction of base shaking was perpendicular to that of slope and liquefaction flow. Also in Case dg with dense ground, the amplitude of *M*e was extremely small; the resonance condition in the process to liquefaction was not met due to the insufficient generation of pore water pressure in dense ground during shaking.

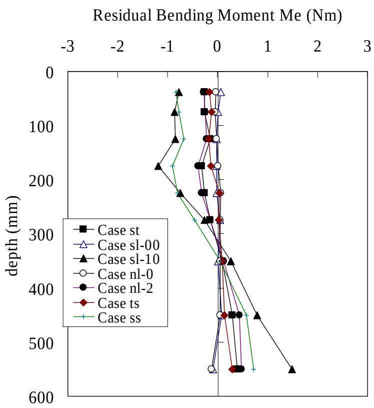

Fig. 11: Comparison of residual bending moment

During liquefaction and ground flow (Stage 2a)

The averaged values of peak bending moment strongly depended on the degree of slope of ground surface, thickness of surface non-liquefaction layer and the intensity of base shaking. In Case nl-2 with thick surface non-liquefaction layer, the obstruction of displacement of the surface layer and cyclic mobility of stiffness were enhanced. In Case sl-10 with steep slope, liquefaction flow was increased especially at the intermediate of ground and shear deformation and associated shear force at the interface between the surface non-liquefaction layer and the ground were enhanced. In both Case nl-2 and Case sl-10 the peak bending moments were almost twice as great as that of Case st. In Case ss with strong base shaking, the averaged peak bending moment became almost three times as great as that in Case st. In Case ts, where base shaking was in transversal direction, the external force was not cyclic, but monotonic in the direction of slope and liquefaction flow. The intensity of external force induced only by liquefaction flow was negligibly small compared with Case st. In Case dg, where liquefaction flow did not occur because of the dense ground. Accordingly the external force was extremely small.

Residual external force on pile foundation

Comparison of residual bending moment *M*e after terminating vibration for various test cases is shown in Fig.11. From Case sl-10 (twice higher ground inclination) and Case ss (twice higher input acceleration magnitude), the generated residual bending moments are twice greater than that from other cases. However, those values are as small as about 1/10 to 1/20 of the peak values obtained during vibration. This is considered related to the ground state after vibration, in which the ground inclination had been lessened and ground flow was almost terminated.

Influence factors for the external force on the pile foundation

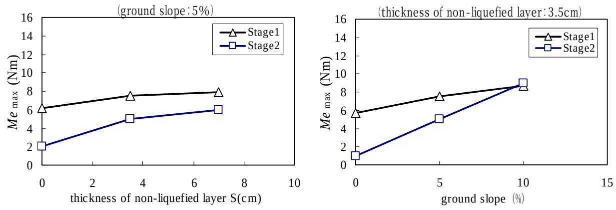

(a) Thickness of non-liquefaction layer (b) Ground inclination
Fig. 12: Comparison of maximum bending moment

Relationships of the bending moment Me with the thickness of non-liquefaction layer and with the ground inclination are plotted in Fig. 12.

From these figures, maximum bending moment appeared to be less influenced by variation of the thickness of non-liquefaction layer, while the effect from the ground inclination tends to be essential. Such influences become remarkably visible in Stage 2. However, it is clear from the time history of bending moment *M*e in Fig.10 that for the case with high thickness of non-liquefaction layer, the amplitudes of external force during liquefaction becomes large, therefore from the point of view of accumulated load, a tendency of increasing damage to the pile foundation can be expected.

Among the considered factors, the level of ground density exerts the most fundamental influence on what the liquefaction may or may not occur. At high density, if liquefaction is not generated, the resonance phenomenon during the process to liquefaction does not take place, either. Furthermore, the accompanied ground flow would not occur. Consequently, the external force would be suppressed to small in accordance to ground rigidity. During process to liquefaction (Stage 1), influences from vibration direction and input acceleration magnitude are extremely big, the external force intensity is almost proportional to the acceleration magnitude.

On the other hand, during liquefaction flow (Stage 2a), in addition to the input acceleration magnitude, the ground inclination controlling the level of ground flow has become dominant. The existence of non-liquefaction layer as well as the rigidity and the unity are also big influence factors.

Influence of base shaking duration time

Figs. 13 and 14 show the ground and pile behaviors for conducted cases with different base shaking duration. The graphs in these figures include: a) Time history of excess pore water pressure, b) Time history of bending moment Me induced by ground external force, c) Time history of lateral displacement of liquefied ground (d00h: at ground surface; d15h: at the depth of 15cm), and d) Input acceleration wave profile. Also, distribution of residual bending moment along the pile depth after base shaking is plotted in Fig. 15.

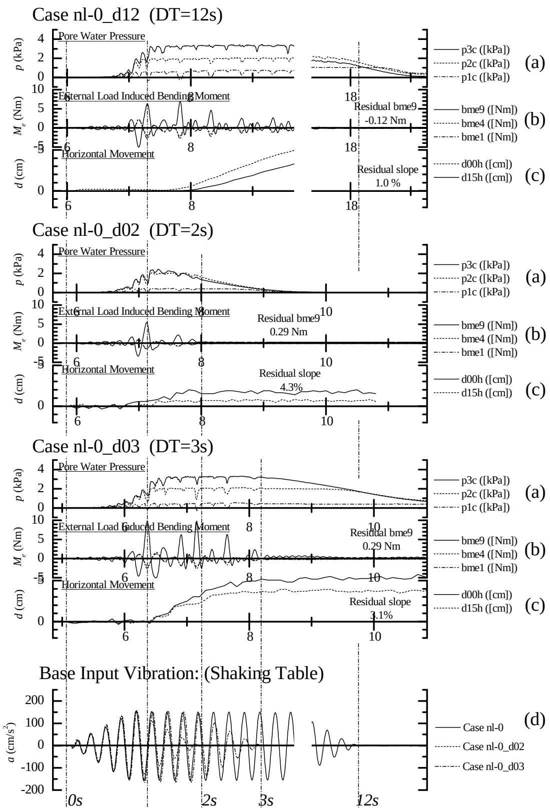

Fig. 13: Comparison of different continuation duration of vibration (Ground without non-liquefaction layer)

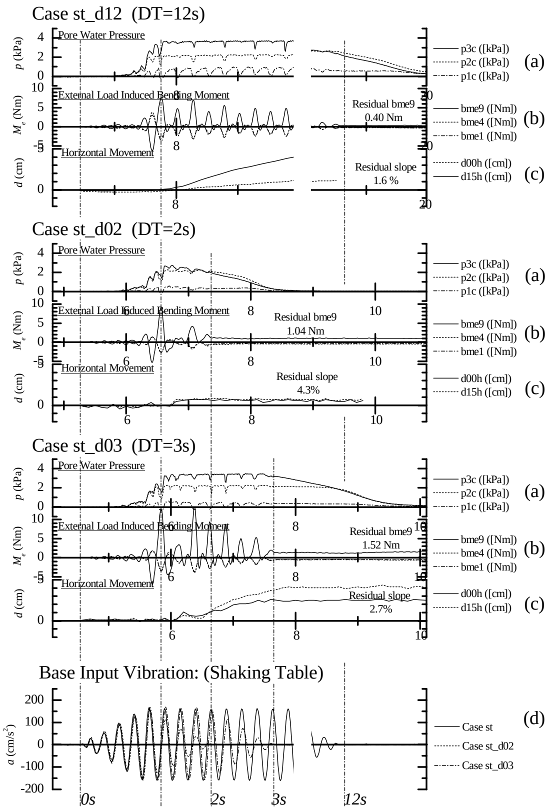

Fig. 14: Comparison of different continuation duration of vibration (Ground with non-liquefaction layer)

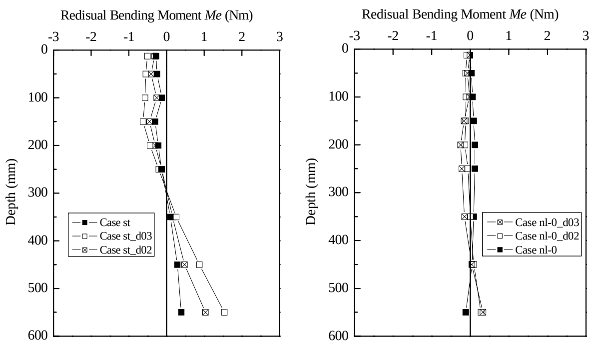

a) with non-liquefaction layer b) without non-liquefaction layer
Fig. 15: Comparison of residual bending moment

In the cases with short input shaking duration time (Cases st_d02, st_d03, nl-0_d02 and nl-0_d03), the fundamental behaviors during shaking were similar to those with long base shaking duration time (Cases st_d12, and nl-0_d12). The interaction of ground external force under resonance which attained just before the ground liquefaction could be seen in all the cases, irrespective of existence of non-liquefaction layer. For the cases with base shaking duration time of 2s (Case st_d02 and Case nl-0_d02), because the vibration is terminated just after the ground liquefaction was attained, the external force application to the pile foundation during the ground flow could not be perceived.

In the test cases with the surface non-liquefaction layer, the comparison of the residual bending moments after shaking showed large difference depending on the input shaking duration time. In Cases st_d02 and st_d03, the residual external force after base shaking was rather large compared with that in the test case with longer base shaking duration time (Case st). If the base shaking duration time is not sufficient long, the liquefaction ground flow was terminated by the termination of the base shaking. Then the final ground slope after base shaking in Case st_d02 and Case st_d03 was larger than that in Case st; in Case st the final ground surface was almost flat. The magnitude of the residual bending moment was different depending on the final ground slope.

On the other hand, in the cases without surface non-liquefaction layer (Cases nl-0, nl-0_d02 and nl-0_d03), the residual bending moment was rather small compared with those in the test cases with the surface non-liquefaction layer. Even in Cases nl-0_d02 and nl-0_d03 where the final ground surface after base shaking was not flat with insufficient base shaking duration time, the residual bending moment was small. From these test results, it can be said that the existence of the surface non-liquefaction layer is effective to induce the residual thrust to the pile foundation.

Comparative examination of the influence factors on the thrust

Table3: Influence factor analysis on external force to pile foundation

Factors increasing the external force	In process to liquefaction	During liquefaction and ground flow	After vibration
Ground inclination	+C	+A	+A
Non-liquefaction layer thickness	+C	+A	+A
Stiffness of surface layer, combination degree	+C	+B	+B
Input acceleration level	+A	+A	+A
Vibration direction	-A	-A	-B
Ground density (liquefaction strength)	-A	-A	-A
Residual ground inclination	-	-	+A

A, B, C : big, medium and small influence degree, respectively
" + " : indicating the external force increased with increasing degree of influence factor
" – " indicating the external force decreased with increasing degree of influence factor

Based on the comparative examination of the behaviors observed in all the test cases conducted in this study, we tried to indicate the intensity of the influence factors on the thrust to the pile foundation in Table 3 in the three stages

Ground density would be the most significant factor to the thrust on pile foundation in all the stages. Since the occurrence of liquefaction is suppressed by increasing ground density, the dense ground did not show the resonance with the base shaking, and the flow of the ground during shaking was not susceptible. The thrust on pile foundation was generally fairly small in dense ground.

In the stage of the process to liquefaction, intensity and direction of base shaking are the major influencing factors to the thrust on pile foundation. The external force is in proportion to the intensity of base shaking. The other factors are not related directly to the thrust on pile foundation in this stage. In the stage during liquefaction, in addition to the factors above mentioned, the base shaking motion, the ground surface slope and the existence of surface non-liquefaction layer are the most effective factors.

CONCLUSIONS

From the observed interactive vibration behavior of ground and pile foundation in a series of model shaking table tests, the mechanism of the thrust on pile foundation was examined. And influence factors on thrust on pile foundation were discussed. The significant effects of liquefied ground flow, surface non-liquefaction layer and the other factors can be summarized as follows:

- In the process to liquefaction, resonant vibration behavior of ground was recognized just before the initiation of liquefaction in all the test cases except for the case with dense ground. In this condition, notable thrust was applied to the pile foundation in a few cycles. In this stage, the effect of surface non-liquefaction layer on the thrust was rather small.

- The thrust to the pile foundation during liquefaction was strongly related to the cyclic mobility of ground stiffness; the thrust was synchronized with the instantaneous decrease in excess pore water pressure and the associated regain of effective stress. The cyclic mobility was observed clearly in the cases of sloping ground; the stiffness of ground was mobilized only when the liquefied ground displaces in downhill direction. The intensity of the thrust was strongly related to the amount of a decrease in excess pore water pressure.

- After base shaking, the final slope of the ground and the surface non-liquefaction layer affects considerably the residual external force on pile foundation.

REFERENCES

[1] Hamada, M., Yasuda, S., Isoyama, R., Emoto, K., (1986). "Measurement and consideration of permanent displacement of ground by liquefaction" Journals of the Japan Society of Civil Engineers," Journal of JSCE, No.376, III-6, pp.211-220, in Japanese.

[2] Inagaki, H., Iai, S., Sugano, T., Yamazaki, H. and Inatomi, T. (1996), "Performance of caisson type quay wall at Kobe port, Special Issue on Geothechnical Aspects of the January 17 1995 Hyogoken-Nambu Earthquake," Soils and Foundations, p.119-136.

[3] Hyogo-ken Nambu Earthquake road bridge earthquake counter measures committee (1995), Investigation Report for damage of road bridge of Hyogo-Ken Nambu Earthquake, in Japanese.

[4] Hamada, M., Ohtomo, K., Sato, H., and Iwatate, T. (1992), "Experimental Study of Effects of Liquefaction – induced Ground Displacement on In-ground Structures," Proc., 4th Japan-US Workshop on Earthquake Resistant Design of Lifeline Facilities and Countermeasures for Soil Liquefaction, Technical Report NCEER-92-0019, Vol.1,pp.481-492.

[5] Miura, K., Adachi, Y., Mihara, M., Urano, K., and Morimasa, S., (2004), "Thrust on Pile Foundation from The Flow of Liquefied Ground with Surface Non-Liquefaction Layer" Proceedings of the 13th World Conference on Earthquake Engineering.

Study of Ground Treatment on Improvement of Pile Foundation Response in Liquefiable Soils

Sung-Ju Chan[1], Ting-Chiun Su[2]
[1] *Geotechnical Engineering Department, Moh and Associates, Inc., Taipei, Taiwan*
[2] *Geotechnical Engineering Department, Moh and Associates, Inc., Taipei, Taiwan*

Abstract

In light of the disastrous Chi-Chi Earthquake in 1999, the government of Taiwan has conducted studies to revise the seismic design code, and elevated peak ground accelerations have been adopted. Consequently, revisions on existing design to comply with the updated code are required for public projects that are still undergoing. The design safety needs to be reassessed, and implementation of strengthening measures is required if deemed necessary. For liquefaction countermeasures, ground treatment techniques that could increase the density of soils are often the preferable alternatives. The treatment usually increases the in-situ SPT-N or CPT-q_c values, which in turn would increase the resistance of soil against liquefaction. For many public infrastructures in Taiwan supported by bored piles embedded partly or entirely in sandy soils, reevaluation of design safety against soil liquefaction would be required. In an assessment of possible retrofitting countermeasures for an infrastructure foundation, ground treatment has been considered. In this case study, effect of ground treatment on response of piles in liquefiable soils was investigated with numerical analyses using FLAC. Results provide insights into this ground treatment effect and useful information for consideration in future design or decision making.

Keywords－*liquefaction, pile, ground treatment, retrofitting countermeasures*

INTRODUCTION

In the early morning of September 21 in 1999, a devastating earthquake struck middle Taiwan. The epicenter was located in Ghi-Ghi, Nantau County, close to the geographic center of the island. With the magnitude of 7.3 on Richter Scale, on both sides along the nearby Chelungpu Fault, almost all the roadways, bridges, electricity poles, buildings, schools, check-dams collapsed or were destroyed. Power outage hit the rest part of island and caused severe interruption to the livelihood function and social activities. This catastrophic incidence was known as the Ghi-Ghi earthquake.

Disastrous damages extended to the mid-west area of Taiwan. The affected places included Wufeng and Taiping of Taichung County, Yuanlin and Sheto of Changhua County, Caotun and Nanton of Nanton County, and Taichung Harbor District where liquefaction induced settlement, tilt, heave or collapse of buildings, roadways, bridges, embankments and retaining facilities, lateral movements of riverbanks, and sand piping on ground surface occurred. The most severe damages occurred near Nanton, Wufeng, and Yuanlin. According to [1], liquefaction induced damages in Yuanlin such as sand piping on ground surfaces and significant ground subsidence resulting in buildings settlement, tilt, and lateral movement from 3cm to 45cm, 2^o to 3^o, and 1cm to 20cm, respectively, were recorded.

Most of the foundations of major infrastructures located on western Taiwan are composed of pile foundations. Because the surface soils in this area are primarily alluvial with characteristics of composition, dense/loose extents and ground water levels prone to liquefaction during earthquake, it is obvious that a pile foundation situated in this area is subject to high risk of failure when liquefaction occurs. The consequences may cause collapse of the superstructure. To avoid the damage of pile foundation and associated superstructure situated at the liquefaction-prone soil layers, prevention measure should be implemented in planning, design and construction, while one of the methods that has been widely applied in practice is ground treatment.

This paper presents a potential to approach determine and evaluate the range of ground treatment in practice and the verification of the effectiveness of ground treatment with the behavior of the pile foundation.

METHODOLOGY

The causes of liquefaction in sandy soils can be grouped into two categories: internal and external. The internal factors include soil density, fine contents, permeability, etc., while the external factors are related to the scales and durations of earthquakes. Liquefaction countermeasures can be developed in accordance with these two aspects and specific characteristics of local ground condition. Most of the current practices use SPT-N value (i.e. [2], [3], [4]) or CPT-q_c value (i.e. [5], [6]) as baselines for evaluating the liquefaction potential. These baselines reflect the loose or dense extent and fine content of the ground soils of interest in which the denser the subsoil, the greater the values of these baseline factors and the lower the liquefaction potential. In gravel soils, liquefaction is in essence a function of void size and the properties of material filled-in rather than the above baseline factors. Thus, the direct use of the SPT-N value or the CPT-q_c value in evaluating the liquefaction potential of gravelly soils is inappropriate.

During liquefaction, the lateral resistance of the pile decreases and may result in significant lateral deformation. In some cases, buckling failure may also occur. To minimize the lateral resistance reduction and lateral deformation of pile foundations in such a way that the risk of buckling failure can be controlled or avoided, the ground treatment methods, such as low pressure grouting, high pressure grouting, compaction grouting and dynamic compaction, are usually adopted in practice. The liquefaction potential can be reduced by increasing the densification extent or shear strength of the soils.

While the liquefaction of sandy soils occurs during an earthquake, the lateral earth pressure acting on the pile foundation decreases significantly as the effective stress reduces to zero, and the pile foundation will reach the maximum lateral deformation. With the dissipation of the excess pore pressure, the effective stress will recover and the soil will regain its shear strength. Nevertheless, this strength will not be the same as the one before the liquefaction. This recovered strength is generally termed the residual strength and can be estimated by using the reduction factor published in some codes ([4], [7]). Results of centrifuge tests indicated that the liquefied fine sand has a residual strength of about 10 percent of the initial p-y curve resistance, and other soil types with less liquefaction potentials are expected to have higher residual strength values [8].

Reference [9] used centrifuge tests to develop a dimensionless degradation parameter Cu, which was a multiplier to reduce the load p on p-y curves developed for piles in sand under static conditions to account for excess pore water pressure effects. As can be seen in [9] , Cu can be lower than 0.1 for high values of excess pore water pressure ratio. This implies that the residual p-y resistance can be less than 10 percent of the initial resistance during liquefaction.

Reference [10] applied centrifuge model tests to develop the multiplier used for reducing the load p of static p-y curves for a single pile and to account for the effect of relative density on liquefaction potential. It shows that the valves of the multiplier are generally between 0.1 and 0.2 for fine sand at a relative density of about 35 percent, and between 0.25 and 0.35 for a relative density of about 55 percent, respectively.

To estimate the lateral deformation of the pile foundation during liquefaction, the strength parameters of the liquefied soil are subject to reduction because of the residual strength of the liquefied soil. The extent of the ground improvement can also be determined in such a manner. Assuming that the soils do not liquefy after appropriate ground improvement, the lateral deformation of the pile subject to the same magnitude of earthquake should also be reduced. The amount of reduction depends on the strength of the improved soils.

Researches on the effects of ground treatment types, sizes, and locations showed that there were associated results for embankment. Reference [11] studied and reported the effects of improved ground sizes and locations on the performance of a section of the Highway I-57 bridge abutment. As shown from the results, the effect of the treatment size and location of an embankment underlain by a liquefiable soil layer indicate that a 24-m-wide treatment zone was most effective when it was located beneath the sloping portion of the embankment, as the treated zone location moves outward from beneath the sloping portion, predicted lateral displacement become progressively larger.

The impact of different treatment types on the performance of an embankment is illustrated by centrifuge test results from [12] and summarized in [13]. Reference [13] made several observations on the effectiveness of the various ground treatment methods on improving the performance of the embankment. If the intent of the ground improvement is to minimize lateral displacement and vertical settlement of the embankment, Reference [13] suggests that the available methods in order of decreasing effectiveness are: (1) sheet piles with tie rods, (2) densification or gravel buttresses, and (3) cement-treated blocks, the latter the less effective. Reference [14] showed that the reduction of liquefaction-induced ground deformations to acceptable levels may require more than one improvement type, and a particular type of improvement may be effective for only one target reduction (i.e. acceleration, deformation, or pore water pressure) but less effective in improving others.

The effect of the width of a densified sand zone on settlement of a supported shallow foundation structure was investigated using shaking table tests [15]. Results showed that for a given structure width, the increment of ratio of treatment zone width to structure width resulted in a decrease in the structure settlement ratio (measured settlement of structure divided by the liquefiable sand layer thickness).

The effect of treatment depth on response of a footing supported on a densified sand zone within a liquefiable sand deposit was investigated using centrifuge tests [16]. The results showed that the magnitude of footing settlement could be reduced by increasing depth of treatment beneath the footing, however with the adverse effect of increasing the peak footing acceleration.

Centrifuge model and field case history information were not available on the performance of deep foundations situated in improved ground zones during earthquake loading and liquefaction. Further research was needed on the performance of deep foundations in liquefiable soil deposits and the benefits of using ground improvement to reduce the risk of damage on deep foundations, particularly in areas prone to lateral spreading [14].

The objective of this paper is to determine the range and effect of ground treatment for existing pile foundations situated in treated soils with liquefaction potential for retrofitting countermeasure. Results of the study can be used as a reference for decision-making or design practice. The computation software used for this study is the FLAC© 2D (version 4.0), developed by Itasca Inc., USA. Because the behavior of pile foundation studied herein is in essence a result of a complicated soil-structure interaction and the deformation of interest depends on applied earthquake force and ground condition, the following assumptions were made for that the physical realities can be described with appropriate simplification:

1) During the earthquake, the pile foundation is subject to the same applied force before and after the soil liquefaction.
2) The residual strength of the liquefied soil is a constant and independent of time.
3) The displacements of the pile and the surrounding soils are continuous and compatible.
4) The soils are homogeneous and isotropic, linear elastic, and perfectly plastic before and after liquefaction, and after ground treatment.

RESULTS

A realistic pile foundation located in western Taiwan was studied in this paper. The on-site soils consist primarily of silty sand (SM) and silty clay (CL). The simplified soil profile and parameters are listed in Table 1. The peak ground acceleration (PGA) is 0.34g, and the groundwater table is about 0.1m below the ground surface.

Table 1: Summary of soil parameters used for the case study

Depth (m)	Thick (m)	USCS Classification	SPT-N	γ_t (kg/m^3)	s_u (kg/m^2)	ϕ' (deg)	Young 's modulus, E (Gpa)	Poisson's ratio ν	Reduction factor D_E
10.1	10.1	SM	10	2020		31.0	17.10	0.3	1/3
20.6	10.5	SM	19	1970		31.5	33.66	0.3	2/3
23.6	3.0	CL	15	1900	7300		14.60	0.495	1
29.6	6.0	CL	11	1920	8600		17.20	0.495	1
49.1	19.5	CL	18	1880	10600		21.20	0.495	1
56.6	7.5	SM	27	2000		30.5	48.96	0.3	1
61.1	4.5	SM	64	2180		32.5	114.66	0.3	1
72.6	11.5	SM	49	2050		31.0	88.02	0.3	1

The results of liquefaction hazard assessment using "Assessment of Liquefaction Potential" [4] and "Evaluation of Liquefaction Index" [17] showed that the sandy soil layers within 20.6m from ground surface had low to medium liquefaction potential, and the associated reduction factors were respectively 0.33 and 0.67, referred to [4]. During liquefaction, the maximum lateral displacement of 2.2cm at top of foundation piles is expected, and the shearing stresses exceed the shearing resistance of pile.

In the analysis, high pressure jet grouting is assumed as the retrofitting measure of ground treatment, and the allowable lateral displacement of foundation piles is 1.66cm in the original design requirement of pile to avoid shearing failure during liquefaction in the surrounding soils of improved ground.

The original analysis and design for the pile group were performed using the Group software (version 3.0), developed by Ensoft Inc., USA. For the case study, we used the FLAC software in stead to estimate range of ground treatment, and the displacement compatible principle was used in the analysis to bridge over the commercial softwares, FLAC and Group, for the analysis of pile foundation and effectiveness of ground improvement. Using FLAC, we simulate and determine the range of treated zone by changing the soil parameters in local treated region while satisfying the same displacement between pile head and pile cap analyzed by Group and FLAC, respectively.

The analysis procedure is illustrated as follows:

1) Using maximum lateral displacement as the control factor, the simulation was completed when the displacements of pile cap and pile head obtained from FLAC and Group, respectively, are identical.
2) The activity forces applied to soil layers came from parts of pile cap and pile. The pile cap was assumed as a rigid body, so its lateral displacement was same as the pile head. By using the lateral displacement of soils before ground treatment, in the seismic situation, analyzed by Group for checking, the distribution of applied forces on pile foundation used as an initial condition in FLAC was calibrated with the displacement compatible principle of which the associated displacement field of pile foundation must be identical to that obtained from Group analysis.
3) By conducting a parametric study for a treated zone based on the consideration of post ground treatment and seismic state, and numerically simulating soil displacements with input forces as indicated above. Until the simulated lateral displacement is identical to the results obtained from Group, the improvement zone (i.e. zone with soil parameters changed) can be identified.

According to the statements mentioned above, the analytical scheme and the results are described as below:

1) Set up the semi-infinite numerical mesh (X68×Y58), according to soil profiles and characteristics as shown on Table 1, and assign corresponding soil parameters to corresponding soil region, respectively. Mohr-Column model as the failure criterion is considered, and the scale unit is in KMS system (fig.1).
2) The maximum lateral displacement of pile group obtained from the analysis of Group, prior to ground improvement in seismic conditions, is simplified as the control soil displacement curve (fig.2).
3) Assuming that the displacement of pile cap (s_{cap}) is equal to the displacement of pile head (s_{pile}) gained from Group, and then the applied forces can be obtained with iteration until the s_{cap} is identical to s_{pile} for this particular case (fig.3 and fig.4).
4) With the applied forces mentioned above, the

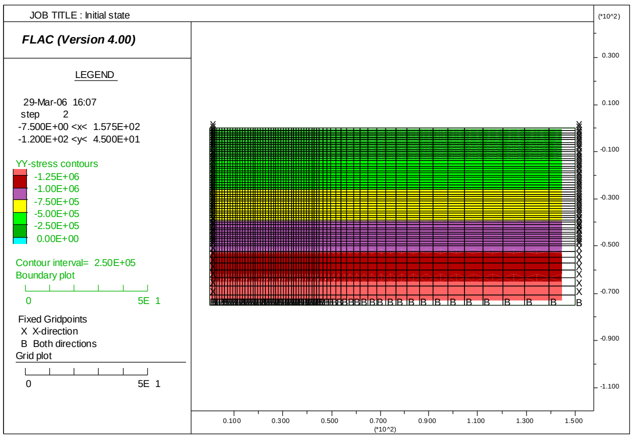

Figure 1: The initial state of the finite difference mesh generated with FLAC grid

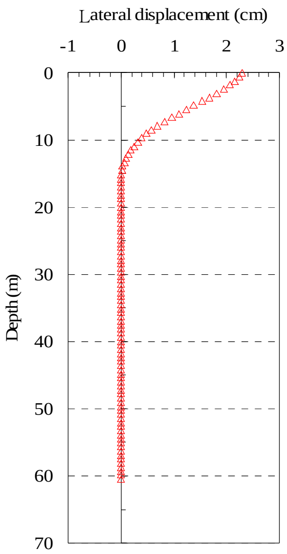

Figure 2: The maximum lateral displacement of pile group computed by Group

liquefaction conditions with treated ground, and the treated strength shown as undrained shear strength,s_u, the improvement zone can be obtained by iteration until the maximum lateral displacement is almost identical to that obtained from Group (fig.5 and fig.6).

The strength reduction from liquefaction generally causes increased lateral displacements. The less allowable lateral displacements of piles are, the larger the range of improvement zone is.

Results of analysis in this case study showed that the treated range was considerably large when the treated strength was equal to 12500 kg/m^2 in improvement zone, with width, W=15.7m, and depth, D=7m.

DISCUSSION

The following statements can be concluded from the analysis results stated above:

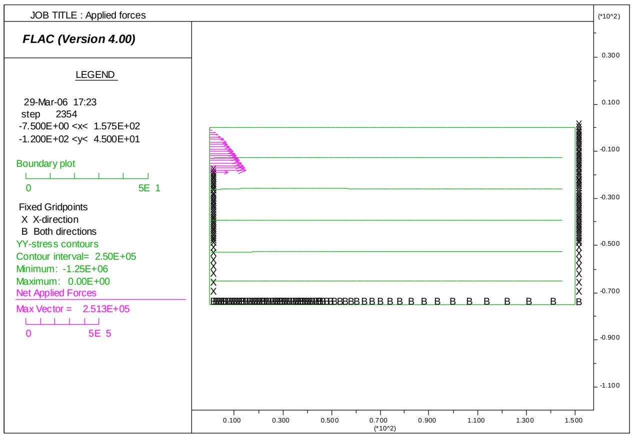

Figure 3: The applied forces gained to analyze the case being studied (Liquefaction without ground treatment)

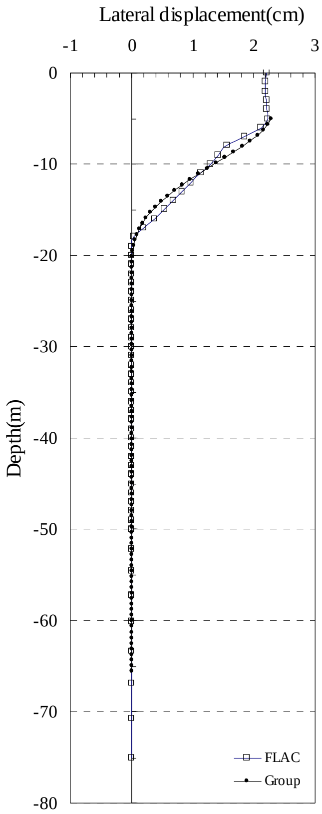

Figure 4: Results of the computed maximum displacement for pile group (with pile cap) subjected to simulated lateral forces are in agreement with each other between Group and FLAC in the liquefaction without ground treatment state

1) When soils were liquefied, the displacement vectors of soils around the pile group exhibited downward movement (fig.7), which was in agreement with liquefaction phenomenon in practice, where the ground settlements were observed in liquefied soils.
2) When soils were subject to lateral forces, the displacements in vertical direction could be developed. With the same treated strength and

constant treated width, the vertical displacements of soils around the pile group would change from settlement into dilation with the increasing treated depth gradually, which agreed with real soil behavior in the same situation. In other words, only horizontal displacement would be developed when the treated depth increased to some critical value (fig. 8). When the treated depth was insufficient, the improvement zone would sink, i.e. the treated effect would not be suitable.

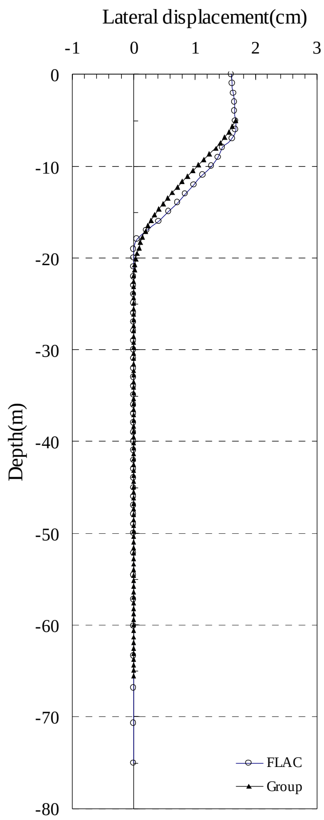

Figure 5: Results of the computed maximum lateral displacements of pile group (with pile cap) subjected to simulated lateral forces are in agreement with each other between Group and FLAC in the liquefaction with ground treatment state

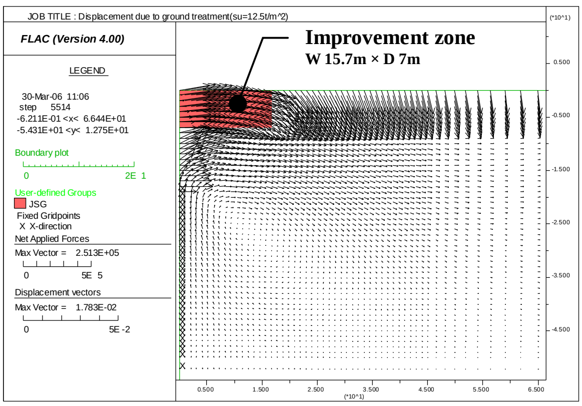

Figure 6: The improvement zone is identified and the displacement vectors of improved zone has upward potential after ground treatment

3) With the same treated strength and constant treated depth, the horizontal displacement and vertical displacement decrease with the increasing treated width gradually (fig.9). However, because the strength of soil in the improvement zone was higher than the unimproved liquefied soil underneath, the soils around the improvement zone still settle and the treated effect would be limited.

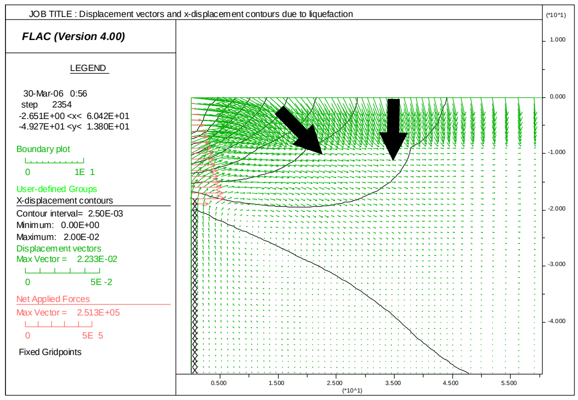

Figure 7: Liquefaction induced soil settlements associated with downward potential as implied by the displacement vectors

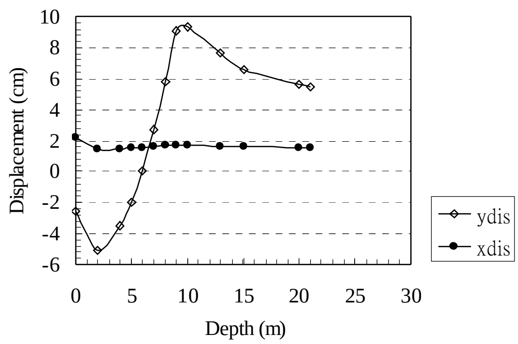

Figure 8:The computed displacements verse the depth of the improvement zone at a constant treated width of 15.7m

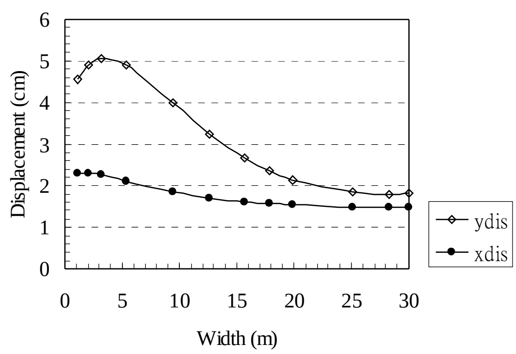

Figure 9: The computed displacements verse the width of the improvement zone at a constant treated depth of 7m

CONCLUSIONS

According to the study above, if simply consideration of effect of ground treatment, the suggestion to determine the range of improvement zone is that to assume the treated depth, which not more than depth of liquefiable soils, and then to decide the smallest treated width satisfied with design treated strength and vertical displacement, which not less than zero in the bottom of improvement zone.

If consideration of adopting ground treatment to increase soil shear resistance in order to avoid shear failure of existing piles, the suggestion is that to determine design demands in terms of treated depth and treated strength, then to decide treated width of the improvement zone incorporating with the control of allowable lateral displacement of pile. Besides, it is need to recheck vertical displacement such that it is no less than zero.

Although the effect of ground treatment in resistance of displacement is effective, but the corresponding cost is significant, most of the time the ground treatment countermeasure is not agreed by the client. Unless the other retrofitting measures are not working, the ground treatment would be limited to unformed countermeasure, and it is an inevitable problem in construction practice.

ACKNOWLEDGMENTS

The study was supported and assisted by Moh and Associates Inc., and the authors wish to thank Dr. C. T. Chin, who encouraged this research, Manager C. H. Wang for valuable suggestion, Dr. T. C. Yao, Dr. H. C. Chao and Dr. J. R. Chen for proofreading.

REFERENCES

[1] Su, T. C., Chiang, K. W., Lin, S. J., Wang, F. G. and Duann, S. W., "Field Reconnaissance and Preliminary Assessment of Liquefaction in Yuan-Lin Area," (in Chinese), Sino-Geotechnics, No.77, pp.29-38, Feb., 2000.

[2] Seed, H.B., Tokimatsu, K., Harder, L. F. and Chung, R. M., "The Influence of SPT Procedures in Soil Liquefaction Resistance Evaluation," Journal of Geotechnical Engineering, ASCE, Vol. 111, No.12, pp.1425-1445, 1985.

[3] Tokimatsu, K. and Yoshimi, Y., "Empirical Correlation of Soil Liquefaction Based on SPT-N Value and Fines Content," Soils and Foundations, Vol.23, No.4, pp.56-74, 1983.

[4] Japan Road Association, *Code of Bridge Design (methodology and explanation), Section 5, Earthquake Resistance Design*, (in Japanese), Japan, 1996.

[5] Robertson, P.K. and Wride, C.E., "Cyclic Liquefaction and its Evaluation Based on SPT and CPT," Proceedings of the NCEER Workshop on Evaluation of Liquefaction Resistance of Soil, Edited by Youd T. L. and Idriss I.M., NCEER-97-0022, pp.41-88, 1998.

[6] Olsen, R. S., "Cyclic Liquefaction Based on the Cone Penetrometer Test," Proceeding of the NCEER Workshop on Evaluation Liquefaction Resistance of Soils, NCEER-97-0022, pp.225-276, 1997.

[7] Japan Architecture Institute, *Guide to Architecture Foundation Construction Design*, (in Japanese), Japan, 1988.

[8] Applied Technology Council, "ATC-32: Improved Seismic Design Criteria for California Bridges: Provisional Recommendations," Applied Technology Council, Redwood City, CA, pp.215, 1996.

[9] Liu, L. and Dobry, R., "Effect of Liquefaction on Lateral Response of Piles," Year 1 Research Tasks – Technical Research Papers, Seismic Vulnerability of New and Existing Highway Construction, National Center for Earthquake Engineering Research, Buffalo, New York, 1994.

[10] Wilson, D. W., Boulanger, R. W., and Kutter, B. L., "Lateral Resistance of Piles in Liquefying Sand," Analysis, Design, Construction, and Testing of Deep Foundations, Proceedings, Offshore Technology Research Center '99 Conference, Geotechnical Special Publication No. 88, ASCE, Reston, VA, pp.165-179, 1999.

[11] Riemer, M. F., Lok, T. M. and Mitchell, J. K., "Evaluating Effectiveness of Liquefaction Remediation Measures for Bridges," Proceedings of the 6th Japan-U.S. Workshop on Earthquake Resistant Design of Lifeline Facilities and Countermeasures for Soil Liquefaction, Technical Report NCEER-96-0006, NCEER, Buffalo, New York, 1996.

[12] Adalier, K., " Mitigation of Earthquake Induced Liquefaction Hazards," Ph. D. Dissertation, Rensselaer Polytechnic Institute, Troy, New York, 1996.

[13] Adalier, K., Elgamal, A.-W., and Martin, G. R., "Foundation Liquefaction Countermeasures for Earth Embankment," Journal of the Geotechnical and Geoenvironmental Engineering, ASCE, Vol.124, No.6, pp.500-517, June, 1998.

[14] Cooke, H. G. and Mitchell, J. K., "Guide to Remedial Measures for Liquefaction Mitigation at Existing Highway Bridge Sites," Technical Report MCEER-99-0015, MCEER, Buffalo, New York, 1999.

[15] Hatanaka, M., Suzuki, Y., Miyaki, M. and Tsukuni, S., "Some Factors Affecting the Settlement of Structures Due to Sand Liquefaction in Shaking Table Test1," Soils and Foundations, JSSMFE, Vol. 27, No. 1, pp.94-101, 1987.

[16] Liu, L. and Dobry, R., "Seismic Response of Shallow Foundation on Liquefiable Sand," Journal of the Geotechnical and Geoenvironmental Engineering, ASCE, Vol. 123, No. 6, pp.557-567, June, 1997.

[17] Iwasaki, T., Arakawa, T., and Tokida, K., "Simplified Procedures for Assessing Soil Liquefaction During Earthquakes," Soil Dynamics and Earthquake Engineering Conference Southampton, pp.925-939, 1982.

Uncoupled Numerical Analyses for Ground Lateral Spread Effects on Single Pile

Lin, San-Shyan[1], Tseng, Y.J.[1], Wang, C.H.[2], and Lee, W.F.[2]
[1]Dept. of Harbor and River Eng., National Taiwan Ocean University, Keelung, Taiwan 20224
[2]Taiwan Construction Research Institute, Taipei County, Taiwan.

Abstract

It's known that the effects of liquefaction on piles are often damaging. Permanent ground deformation or ground lateral spreading is observed to be the main cause for the distress of piles. The purpose of this paper is to use uncoupled method for analysis of ground lateral spread effect on piles. The computer code, CYCLIC-1D developed at University of California at San Diego and accessible from the web, is used for lateral ground deformation estimation. Subsequently, the pile performance is studied considering the effect of ground deformation obtained from Cyclic-1D. Two centrifuge tested examples were studied by the aforementioned method. Reasonable agreement was obtained between the predicted and the measured results.

Keywords—*soil liquefaction, pile, lateral displacement*

INTRODUCTION

In the history of soil liquefaction-induced hazards, pile foundation damaged by the lateral spreading is one of the main concerns for the geotechnical engineers. The lateral spreading usually is triggered at the slight inclined slope with liquefiable soils are embedded among the soil layers. When the soil liquefaction was initiated, the liquefied soils tend to slide downward along the inclined surface. While the pile is embedded among these moving liquefied soils, the pile can sustain lateral force caused by the liquefied soils. Serious structural damages can be produced especially when only the upper part of the soils is liquefied. In this case, the tremendous and concentrate bending moment of pile can be induced along the interface between the liquefied layer and the stable non-liquefied soils. Subsequently, the concentrate bending moment may fracture the pile that reduces the pile capacity. Furthermore, the lateral movement of the pile may cause the entire structure to lose its desired performance requirement.

In order to understand this condition with the numerical analyses approach, the paper uses the uncoupled numerical analysis to resolve this problem. First, the Winkler model is used to simulate the soil-structure interaction with the lateral forces. The Bouc-Wen model is used to illustrate the lateral force caused by the lateral spreading. At the same time, the Bouce-Wen model is also used to calculate the pile structure integrity while the pile fracture is triggered. Second, while considering the soil-structure interaction during the soil liquefaction event, another important factor is the changing of the excessive pore water pressure. To obtain this solution, the CYCLIC-1D (developed at the University of California at San Diego) is used to generate the acceleration and excessive pore water pressure values within soils under the corresponded input earthquake motion. Then the values of excessive pore water pressures at various depths can be combined with the Winkler model.

In order to verify this uncoupled approach, this paper also simulates the results of a centrifuge test by the aforementioned method. Reasonable agreement was obtained between the predicted and the measured results.

MATERIALS MODELING

This study uses the Winkler model to simulate the soil-structure interaction caused by the earthquake motion. Considering the force equilibrium between the surrounding soil and the pile itself, the equation is described as Eq. (1).

$$E_P I_P \frac{\partial^4}{\partial x^4} w(x,t) + m \frac{\partial^2}{\partial t^2} w(x,t) = F_S(x,t) + F_d(x,t) \quad (1)$$

where $w(x,t)$ = the lateral pile displacement in various time step t ; x = depth to the ground surface; m = mass of pile; E_P = Young's Modulus of pile; I_P = moment of inertia of pile; $F_S(x,t)$ = non-linear soil reaction force; $F_d(x,t)$= radiating damping force of pile. Two major components of Eq. (1) are the $F_S(x,t)$ and $F_d(x,t)$. In the following, these two parts are defined based on the soil modeling.

After the initiation of soil liquefaction, the lateral force produced by the soil movement may cause the increasing the bending moment. Furthermore, when the bending moment increases to a certain level, this may cause the material fracture that leads to the strength reduction. This study involves the pile fracture phenomenon that is described in the following section of moment-curvature relation of pile.

Soil Modeling

Based on the Bouc-Wen model, the force resulting from the nonlinear spring alone can be give as

$$F_S(x) = \alpha \cdot K \cdot w + (1-\alpha) \cdot K \cdot w_0 \cdot \varsigma(x) \tag{2}$$

where α = a parameter controls the post yielding stiffness; K = a reference stiffness; w = the pile deflection at the location of the spring; w_0 = the value of pile deflection that initiates yielding in the spring; and ς = a hysteretic dimensionless quantity that is governed by the following Eq. (3)

$$w_0\dot{\varsigma} + \gamma \cdot |\dot{w}| \cdot \dot{\varsigma} \cdot |\varsigma|^{n-1} + \beta \cdot \dot{w} \cdot |\varsigma|^n - A \cdot \dot{w} = 0 \tag{3}$$

where A, β, γ and n are parameters that control the shape of the hysteretic loop and are chosen such that the shape of the loop are reasonable for the type of material considered. The maximum value of ς is given as

$$\varsigma = \left(\frac{A}{\beta+\gamma}\right)^{1/n}, \text{ when } d\varsigma / dw = 0 \tag{4}$$

The spring reactions of the pile for cohesion-less soils were given by Badoni and Makris (1996) [1] as

$$F_s(x) = \mu \cdot \gamma_s \cdot d \cdot \frac{1+\sin\phi_s}{1-\sin\phi_s} \cdot x \cdot \zeta(x) \tag{5}$$

where d = the pile diameter; ϕ_s = the angle of the soil internal friction; μ = a parameter; γ_s = the specific weight of the soil.

Another major concern of the soil liquefaction event is the initiation of the excessive pore water pressure. Kagawa et al. (1992) [2] used a reduction factor F to describe the reducing the soil strength as followed.

$$F = (\sigma' / \sigma_0')^{\alpha} = (1-u)^{\alpha} \tag{6}$$

By combining Eq. (6) with Eq. (5), Eq. (7) shows the non-linear soil reaction force F_S with the effect of the reduction form the pore water pressure generation.

$$F_S = (1-u)^{\alpha} \ \mu\gamma_s d \frac{1+\sin\phi_s}{1-\sin\phi_s} x \cdot \zeta \tag{7}$$

When the soil-structure interaction is subjected to the seismic force, the radiation damping should be considered. According to Badoni and Makris (1996) [1], it can be described as Eq. (8) and Eq. (9).

$$F_d = Q a_0^{-0.25} \rho_S V_S d \omega \langle \Delta w \rangle \tag{8}$$

$$Q = 2\left[1 + \frac{3.4}{\pi(1-\nu_s)}\right]^{1.25} \cdot \left(\frac{\pi}{4}\right)^{0.75} \tag{9}$$

where ν_s = Poison's ratio of soil; a_0 = non-dimensional frequency dependent parameter ($a_0 = \frac{\omega d}{V_s}$) ; ω = frequency; d = diameter of pile; V_s = shear velocity of soil; ρ_s = soil density; $\langle \Delta w \rangle = w_0 (\Delta w > w_0)$ for the non-linear case; $\langle \Delta w \rangle = \Delta w (\Delta w \le w_0)$ for the linear case.

Under the effect of the excessive pore water pressure, Eq. (9) can be re-written as Eq. (10).

$$F_d = \left[(1-u)^{1/4} + \frac{V_L u}{(V_s + V_p)}\right] Q a_0^{-0.25} \rho_S V_S d \omega \langle \Delta w \rangle \tag{10}$$

where V_p = velocity of pressure; V_L = viscous velocity of liquefied soil.

Moment-Curvature Relation of Pile

The Bouc-Wen model is also used to model moment-curvature relationship of the pile and is expressed as (Lin et al., 2001) [3]

$$M = \alpha(E_P I_P)\phi + (1-\alpha) M_y z \tag{11}$$

where M = the moment; M_y = the yield moment; ϕ = the curvature; α_M = a parameter controlling the rigidity of the pile after yielding; and z = the hysteretic parameter, which can be expressed as (Lin et al., 2001) [3]

$$\dot{z} = \left\{ A_M I_P - \left[B \cdot z^2 \left\{ Sgn(\dot{\phi} \cdot z) + 1 \right\} \frac{1}{\phi_y} \right] \right\} \dot{\phi} \tag{12}$$

in which $Sgn(\dot{\phi} \cdot z) = 1$ if $\dot{\phi} \cdot z > 0$; $Sgn(\dot{\phi} \cdot z) = -1$ if $\dot{\phi} \cdot z < 0$; ϕ_y = the yielding curvature; and A_M and B = the parameters controlling the shape of the hysteretic loop.

For concrete piles, once the moment induced on the pile exceeds a certain magnitude, the moment of inertia of the pile may be reduced due to concrete cracking. A semi-empirical moment versus moment of inertia relationship is used in this paper (Lin et al., 2001) [3]. The semi-empirical form is expressed as

$$I_{ef} = I^I, \ (M < M_{cr}) \tag{13}$$

$$I_{ef} = I^{II} + \left(I^I - I^{II}\right)\left(\frac{M_{cr}}{M}\right)^3, (M_{cr} < M < M_u) \tag{14}$$

where I_{ef} = the effective moment of inertia; $I^{I} = I_{p}$, the moment of inertia of the non-cracked section; I^{II} = the moment of inertia of the completely cracked section where the reinforcement has reached the yield strength; M_{cr} = the bending moment corresponding to the beginning of cracking; and M_{u} = the bending moment corresponding to I^{II}.

In order to take into account the effects of finite size of plastic regions, the model chosen for this study is based on the global frame member model proposed by Roufaiel and Meyer (1987) [4], in which the model was also successfully used for concrete pile analyses (Badoni, 1997) [5].

CENTRIFUG TESTINGS

For the purpose to verify the accuracy of the materials modeling proposed in this paper, the analytical results will be compared with the measured data from the centrifuge testing results. Abdoun et al. (2003) [6] presented the results of the centrifuge testing that simulates a single pile sustained the lateral spreading force from the soil liquefaction. In this study, two centrifuge tests are compared.

Case 1

As shown in Fig. 1, the dimension of the box is 45.72m╳25.4m╳26.39m. The embedded model pile is 20cm long with diameter of 0.95cm. This entire assemble is tested under the gravity value of 50g. Under such gravity, it can simulate a full-sized pile of 10m in length with 60cm in diameter. To test the soil liquefaction-induced lateral spreading effect, the layout of the model including three layers of soils:

1. Top layer: 2m cemented sand with 34.5° of friction angle and 5.1kN of cohesion.
2. Middle layer: 6m liquefiable sand (Nevada sand) with relative density of 40%, dry unit weight of 17.33kN/m^3~13.87 kN/m$^{3.}$
3. Bottom layer: 2m cemented sand with the same properties of the top layer.

(Note: the dimension shown above is the prototype model.)

During the testing, the bottom of the box is applied with an excitation to simulate the earthquake motion. The excitation has frequency of 20Hz, maximum magnitude of 0.3g, and 40 cycles. In order to simulate the effect of lateral spreading, the entire box is tilted by 4.8° .

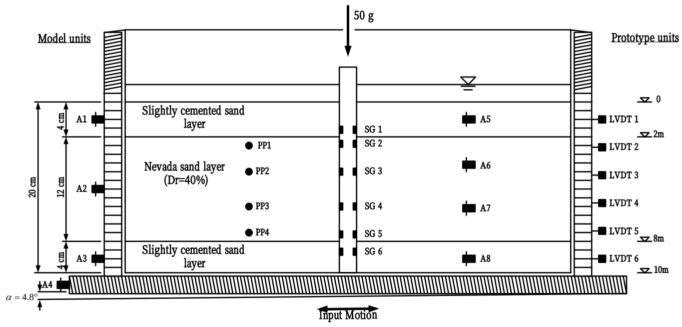

Fig. 1 Centrifuge Testing Model, Case 1 (after Abdoun et al., 2003) [6]

Case 2

As shown in Fig. 2, the layout and the input motion of the Case 2 are the same as those of Case 1. The major difference is the prototype dimension of pile is 8m, in which the bottom of the pile does not extend into the bottom non-liquefiable layer.

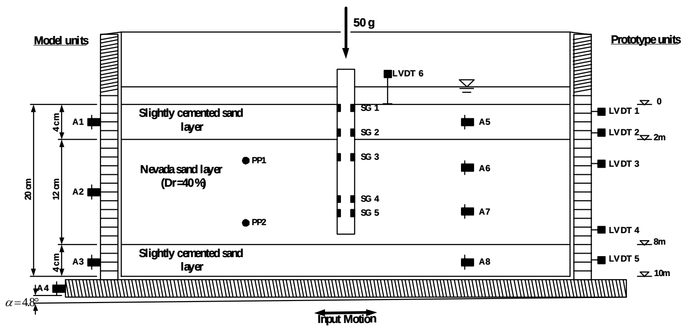

Fig. 2 Centrifuge Testing Model, Case 2 (after Abdoun et al., 2003) [6]

MODEL VERIFICATION

To verify the accuracy of the materials model proposed in this paper, the verification procedure includes two steps, including CYCLIC-1D simulation and the materials modeling calculation.

CYCLIC-1D Simulation

CYCLIC-1D was developed in the University of California at San Diego, by Prof. A. Elgamal and other coworkers. This program aims to solve soil liquefaction-induced lateral spreading problems. By providing the soil properties and soil profiles, it can estimate several soil responses (e.g. acceleration, spectrum, excessive pore water pressure, etc.) under the effect of the base motion. For further information, please access http://cyclic.ucsd.edu/index.html for details.

In this step, this study uses CYCLIC-1D to simulate the acceleration and pore water pressure time histories within various depths of the prototype test, including depth of 1m, 4m, 6m, and 9m. Fig. 3 and Fig. 4 show the results of Case 1 while Fig. 5 shows the results of Case 2. Note that the acceleration time histories in various depths of Case 1 and Case 2 are the same.

The data generated in this step will be implemented with the materials modeling to estimate the lateral displacement and bending moment at the corresponded depth of pile.

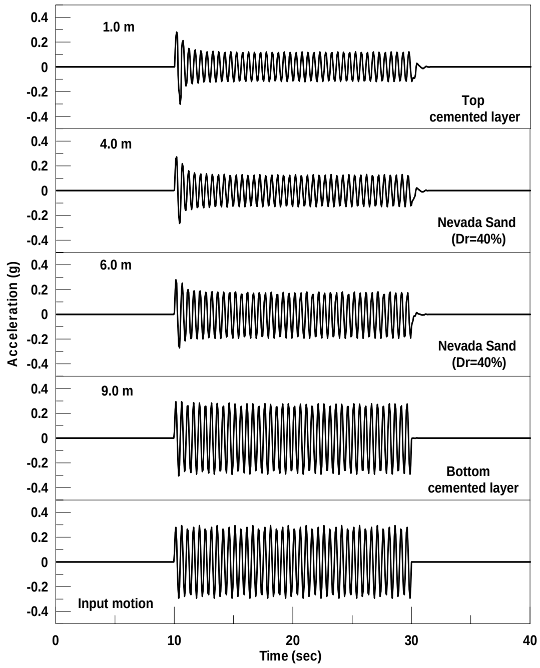

Fig. 3 CYCLIC-1D simulation of acceleration time histories at various depths of Case 1.

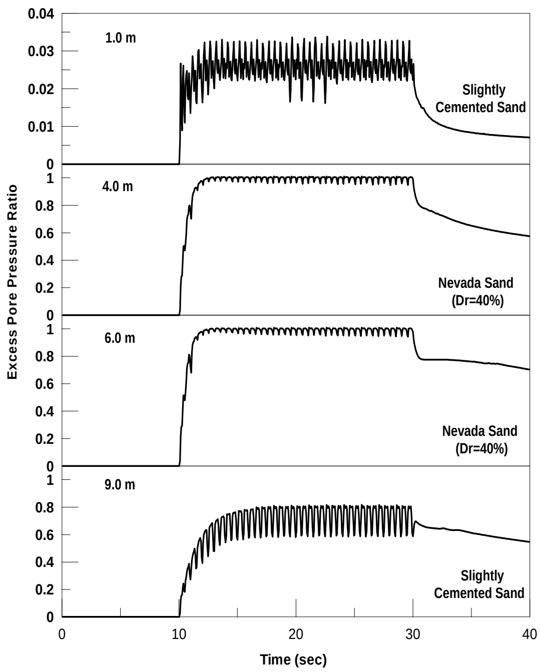

Fig. 4 CYCLIC-1D simulation of pore water pressure time histories at various depths of Case 1.

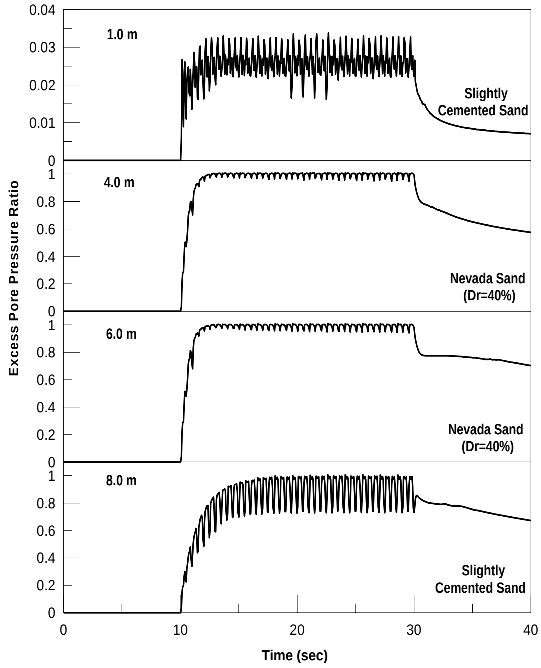

Fig. 5 CYCLIC-1D simulation of pore water pressure time histories at various depths of Case 2.

Materials Modeling Calculation

Combined with the results from the CYCLIC-1D, the materials model estimates the lateral displacement and the bending moment of the pile. In the calculation procedure, it also considers the possible concrete cracking when the bending moment exceeding the maximum value.

For the Case 1 study, Fig. 6 and Fig. 7 shows the calculation results of pile lateral displacement and bending moment, respectively. In general, due to the soil liquefaction effect at the middle layer, it produces the lateral movement among the top and middle layer. However, the bottom layer with non-liquefiable soils that remain relatively intact. This action of lateral movement that produces force to apply on the pile, which also carry the upper part of pile to move with soil. The lower part of pile, on the other hand, remain relatively unmovable. This phenomenon produces large bending moment concentrate at the boundary between the middle liquefied layer and the bottom non-liquefied layer.

Compared with the Case 1 study, Fig. 8 shows the bending moment of pile in Case 2. Even though the pile does not extend in to the bottom non-liquefiable layer, it still shows a concentration of bending moment between the top non-liquefiable layer and the middle liquefied layer.

By compared with the actual measured data collected from the centrifuge data, both of cases show a good agreement between the calculations results and the actual measured data.

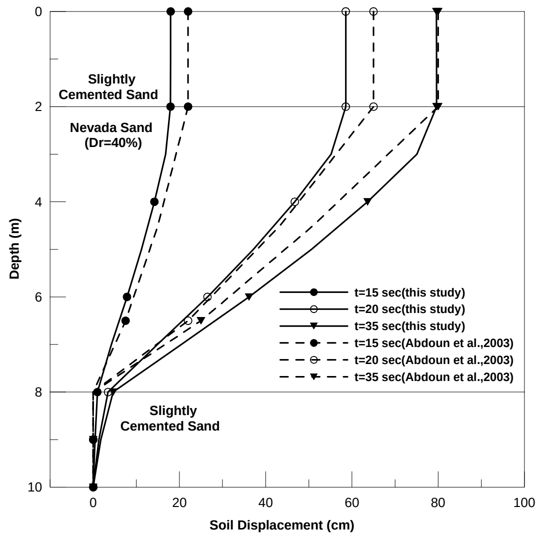

Fig. 6 Calculation of lateral displacement of prototype pile at various time steps of Case 1.

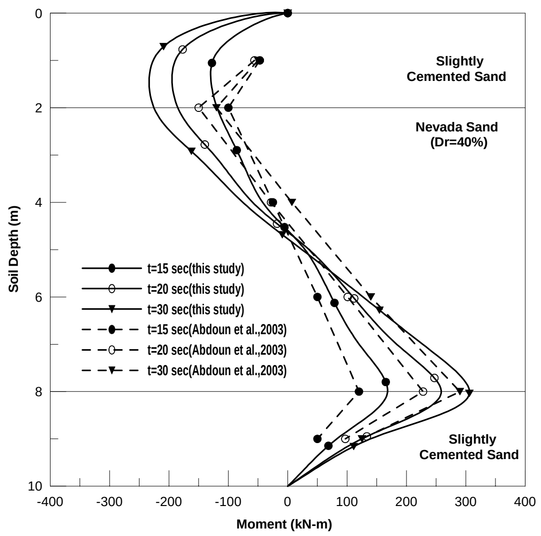

Fig. 7 Calculation of bending moment of prototype pile at various time steps of Case 1.

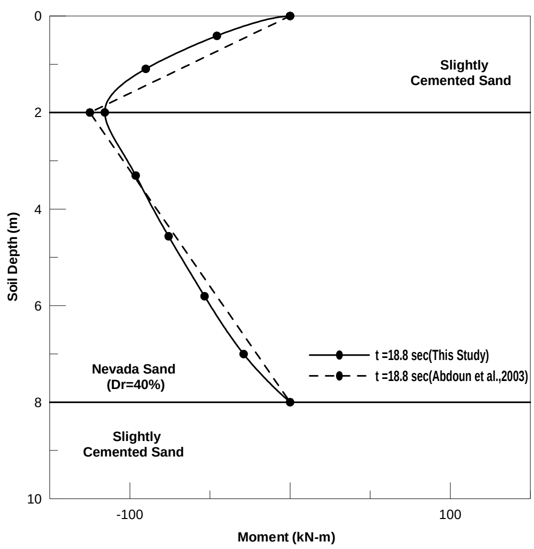

Fig. 8 Calculation of bending moment of prototype pile at various time steps of Case 2.

CONCLUSIONS

This paper presents an uncoupled numerical analyses approach to simulate the single pile response under the effect of the soil liquefaction ground lateral spreading. This first part of the uncoupled analyses is to simulate a proper soil-structure interaction between the pile and the surrounding liquefied and non-liquefied soils. This study uses the Winkler model to simulate the interaction with the lateral force. Besides, this interaction is represented by the Bouce-Wen model to simulate the reaction of pile with the external force generated by the lateral spreading action. Furthermore, during the lateral spreading event, when the bending moment of pile exceeds a certain level, it usually causes the concrete cracking that reduces the integrality of pile. This study also involves this phenomenon into the Winkler model. The second part of the uncoupled analyses is to use the CYCLIC-1D (developed at the University of California at San Diego) to generate the acceleration and excessive pore water pressure time histories during the soil liquefaction-induced lateral spreading event. Finally, the entire uncoupled numerical analyses approach combines the results of the CYCLIC-1D and the Winkler model to estimate the lateral displacement and bending moment of the single pile under the effect of lateral spreading force.

In order to verify the accuracy of the proposed approach, this study examines two centrifuge tests produced by Abdoun et al. (2003) [6]. The results show a good agreement between the measured and calculated lateral displacement and bending moment of pile.

REFERENCES

[1] Badoni, D. and Makris, N. “Nonlinear response of single piles under lateral inertial and seismic loads.” *Soil Dynamics and Earthquake Engineering*, 1996, Vol. 15, pp 29-43.

[2] Kagawa, T., Taji, Y., Sato, M., and, Minowa, C., “Soil-Pile-Structure Interaction in Liquefying Sand from Large-Scale Shaking-Table Tests and Centrifuge Tests” *Analysis and Design For Soil-Pile-Structure Inter Actions*, 1992, pp 69-84.

[3] Lin, S.S., Liao, J.C., Yang, T.S., and Juang, C.H. “Nonlinear response of single concrete piles” *Geotechnical Engineering Journal*, 2001, 32(3), pp 165-175.

[4] Roufaiel, M.S.L. and Meyer, C. “Analytical modeling of hysteretic behavior of R/C frames” *Journal of Structural Engineering*, ASCE, 1987, 113(3), pp.429-444.

[5] Badoni, D. *Nonlinear response of pile foundation-superstructure systems*, P.h. D Dissertation Department of Civil Engineering, University of Notre Dame, Indiana, USA, 1997.

[6] Abdoun, T., Dobry, R., O'Rourke, T. D., and Goh, S. H. “ Pile response to lateral spreads: centrifuge modeling,” *Journal of Geotechnical and Geoenvironmental Engineering*, ASCE, 2003, 129(10), pp 869-878.

Uplift of Buried Manholes and Pipes due to Liquefaction of Replaced Soils

Susumu Yasuda[1], Hiroyoshi Kiku[2]
[1]*Department of Civil Engineering, Tokyo Denki University, Saitama,Japan*
[2]*Department of Civil Engineering, Kanto Gakuin University, Yokohama, Japan*

Abstract

About 1400 sewage manholes were uplifted during the 2004 Niigataken-chuetsu earthquake in Japan. Many buried sewage pipes were also uplifted. The authors conducted field investigation at damaged area after the earthquake. Based on the investigation, it was clarified that the uplift occurred in mainly clayey grounds. No sand boils were observed on the clayey ground. However, boiled sands were observed just beside the uplifted manholes and on the buried pipes. Soil investigation of the replaced soils after the earthquake revealed that replace sands were very loose and easy to liquefy. Then, it was concluded that the uplift of the manholes and pipes occurred due to the liquefaction of the replaced soils.

Keywords— *liquefaction, sandy soil, earthquake damage, sewage manhole, sewage pipes*

INTRODUCTION

The 2004 Niigataken-chuetsu earthquake struck to the middle part of Niigata prefecture and brought severe damage to sewage facilities. About 1400 manholes and many sewage pipes were uplifted. Maximum value of the uplift of manholes was about 1.5 m. Road on the buried pipes caved in several ten cm. Detailed soil investigation conducted after the earthquake revealed that the uplift of manholes and pipes occurred due to liquefaction of replaced sandy soil.

This was not the first experience that sewage manholes and pipes are uplift during earthquake. Several big earthquakes occurred in Hokkaido area in Japan, have already brought similar damage to sewage manholes and pipes.

In 1993, Kushiro-oki earthquake occurred near Kushiro City caused severe damage to sewage pipes, manholes, disposal plants and pump stations in and around Kushiro City.(JGS, 1994) In geomorphological point of view, damage was concentrated in peaty ground. The main patterns of the damage were uplift, meander, bends and joint failure. The maximum amount of the uplift was 1.3 m. According to the soil investigation after the earthquake, an artificially filled layer with a thickness of about 2 m and a peat layer with a thickness of 1 to 2 m were deposited from the ground surface.

In 2003, Tokachi-oki earthquake occurred in southern part of Hokkaido. Sewage facilities were severely damaged in 14 towns (JGS,

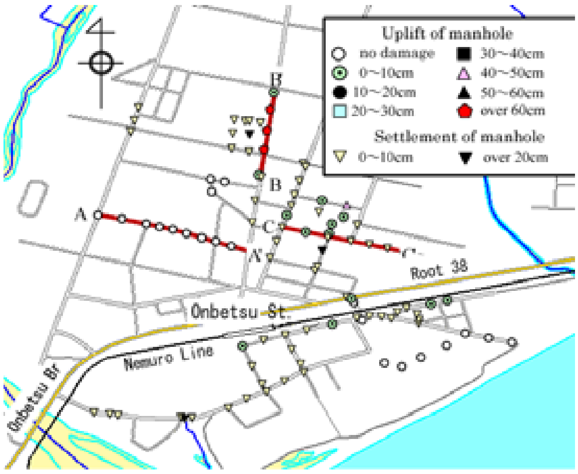

Figure 1: Distribution map of damaged and not-damaged manhole in Onbetsu Town (Tokachi-oki Earthquake,2003)

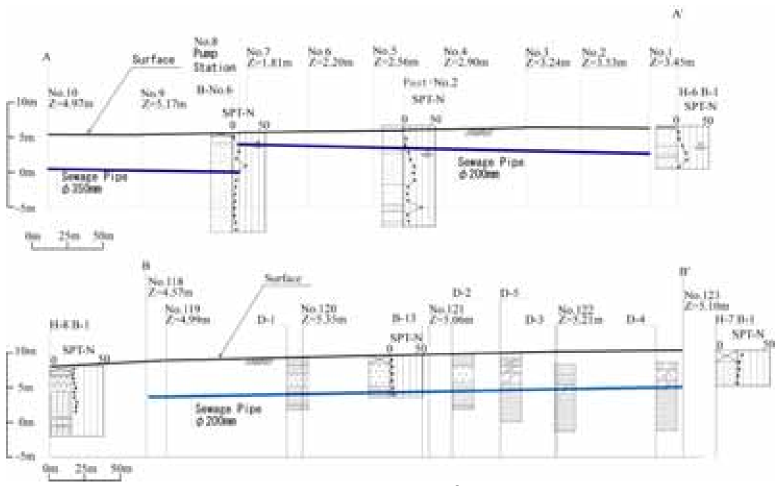

Figure 2: Depositional cross sections and depth of sewage pipe along A-A' and B-B' line

2005). The similar type of uplift of sewage manholes occurred in Toyokoro Town, Onbetsu Town and other towns. The maximum value of the uplift of manholes was about 1.9 m. Figure 1 shows locations of damaged and not-damaged sewage manholes. The manholes along B-B' line uplifted more than 60cm. On the contrary, the manholes along A-A' line were not uplifted.

Figure 2 shows soil cross sections and depth of sewage pipes along A-A' line and B-B' line. Along B-B' line, peat and soft clay layers are deposited from the ground surface to the depth of the pipe. However, soil at the depth of pipe was mainly gravelly soil along A-A'. Construction method along both lines was same. Ground was excavated first, placed pipes and manholes in the dug ditch, then replaced the ditch by sands. Therefore, it is estimated that the replaced soil in peaty or clayey ground liquefied, and the replaced soil in gravelly ground did not liquefy. In restore work, excavated the ground, place a new sewage pipe and replaced the ditch again. As a countermeasure against liquefaction of replaced soil, cement was mixed in the replaced soil.

As shown in these experiences, damage to sewage pipes and manholes due to liquefaction of replaced soil has already known before the 2004 Niigataken-chuetsu earthquake. However, the damage during the Niigataken-chuetsu earthquake was much severer than those during previous earthquakes.

DAMAGE OF SEWAGE MANHOLES AND PIPES DURING THE NIIGATAKEN-CHUETSU

On October 23 in 2004, the Niigataken-chuetsu earthquake, of Magnitude 6.8, occurred in Japan. The maximum surface acceleration recorded at Kawaguchi Town was 1722 Gals. Many railways including Shinkansen, roads, houses, pipelines and other structures were severely damaged. Moreover, huge number of landslides, more than 1700, occurred and hit many towns and villages, including Yamakoshi village. The slid soils dammed up rivers and made natural dams. Sewage facilities were damaged at 22 cities and towns. Maximum distance from epicenter to the damaged towns was about 30 km. Total loss of sewage facilities was 20.5 billion Yen. Length of damaged pipes reached 152.1 km. Number of uplifted manholes as shown in photo 1, was 1453. Many buried sewage pipes were uplifted also. The maximum value of the uplifted manholes was about 1.5 m. Moreover, 6 water treatment plants and 6 pumping stations were injured.

Road cave-in occurred at 5,908 sites. Settlement of the surface of the road reached up to several ten cm. Therefore, damage of sewage manholes and pipes affected not only the function of waste water but also the obstacles to traffic and restoration activities. The road cave-in became worth after the earthquake. At some sites, road cave-ins were newly found a half year after the earthquake, when covered snow was melt.

Photo 1: Uplifted manhole at Wakaba district in Ojiya city

Most severely damaged area was located in Ojiya City and Nagaoka City. The authors carried out a field reconnaissance at damaged area. Large number of manholes were uplifted. Sand boil was observed beside the manholes and along the sewage pipelines with road cave-ins. Figure 3 shows height of uplifted manholes measured by the authors at Wakaba district in Ojiya City. The maximum value of uplift of manhole in this area was 1.20 m. Road cave-in was 14 cm around the manhole. Actual value of uplift of that manhole was 1.06 m. Other manholes uplifted 10 to 100 cm and road cave-in at these sites were 10 to 40 cm as indicated in Figure 3.

Severely damaged districts around Wakaba district are shown in Figure 4 together with average uplift of

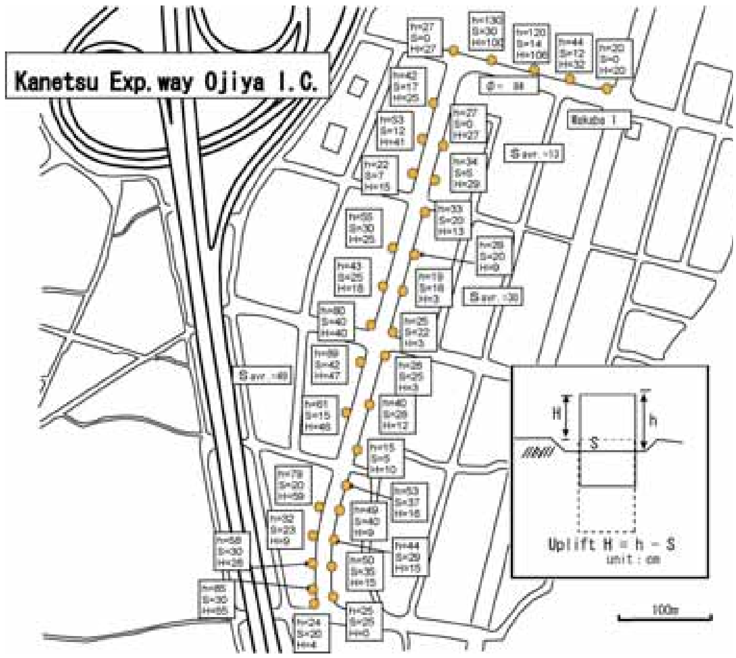

Figure 3: Height of uplifted manholes and value of cave-in measured at Wakaba district in Ojiya City.

manholes in 250 m grid. Zones along Kanetsu Express Way were seriously damaged. In geomorphological condition, this zone belongs to river terraces formed by Shinano River. Comparatively lowland formed by small rivers are existed as shown in Figure 4. Figure 5 shows the columnar section and boring log near the Wakaba district. Subsoil is mainly silt, silty clay and peat with SPT N-value of 0 to 5.

Figure 6 shows the grain size distribution curve of replaced soil used in Ojiya city. Replaced soil contained sand and gravely sand for the most part. However, the replaced soil was comparatively uniform with uniformity coefficient of 6.16. It indicates that the replaced soil has possibility of soil liquefaction.

Sand boils which indicate the occurrence of liquefaction were not observed on natural grounds in this zone. However, boiled sands were observed on the damaged sewage pipes. Therefore, it was estimated that replaced soil liquefied and brought the uplift of manholes, same as the damage during previous earthquakes.

Damage pattern in other district in Ojiya City and Nagaka City was similar. It is difficult to see the damage of sewage pipes just after the earthquake.

MECHNISM OF DAMAGE OF UPLIFT OF MANHOLE

After the Earthquake, detailed soil investigation at damaged and not damaged sites in Nagaoka City, Ojiya City and Kawaguchi Town were carried out by a technical committee was organized by the Ministry of Land Infrastructures and Transport.

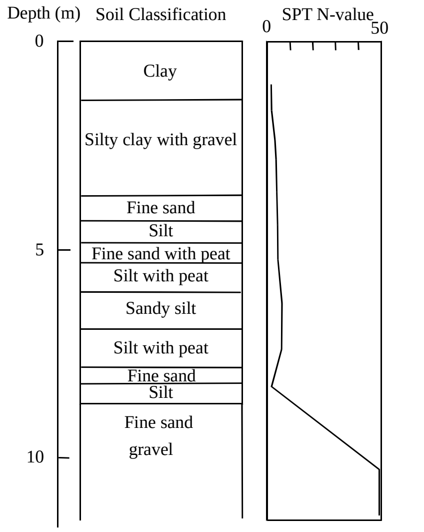

Figure 5: Columnar section and boring log near the Wakaba district.

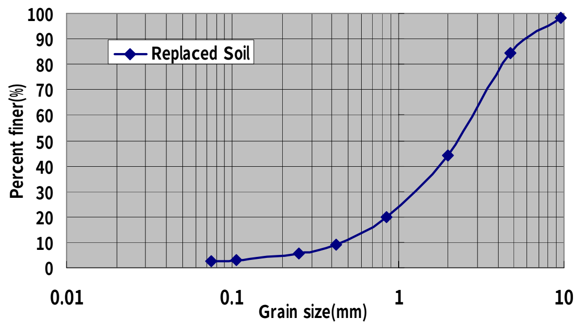

Figure 6: Grain size distribution of replaced soil

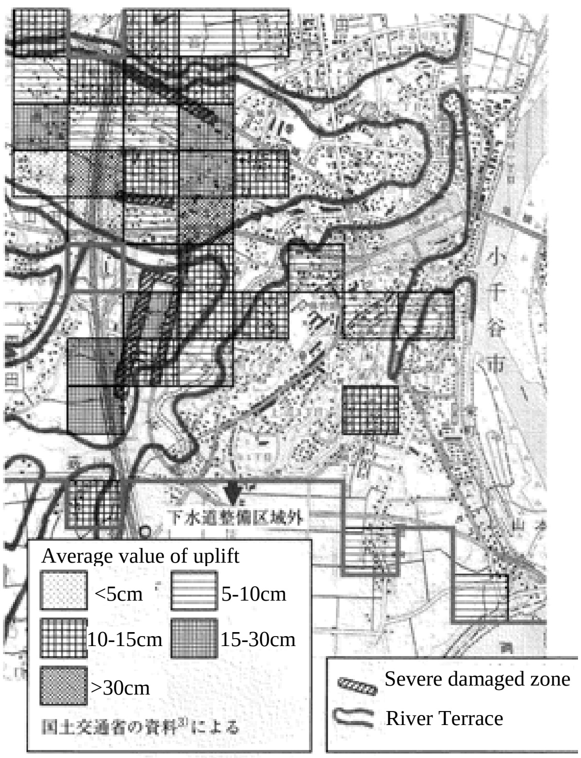

Figure 4: Zoning meshes on average uplift of manholes

Soil conditions at damaged and not damaged sites are compared in Table 1. Replaced soils in the damaged sites were sand with fines to sand with gravel. Water levels in the replaced soils at the damaged sites were extremely shallow as 0.2 m to 1.1 m. Density of the replaced soils at the damaged sites were very low as degree of compaction D_C=74% to 81% or relative density Dr=38 % to 41%. Therefore, it can be convinced that the replaced soils liquefied and caused uplift of manholes due to the earthquake. Water tables at the not damaged sites were slightly deeper than those at the damaged sites. This may be the reason why manholes were not uplifted at these not damaged sites. In Table 1, one more interesting point is the natural soils surrounding the replaced soils were clayey soils, which are hardly to liquefy.

In the other study, Nagaoka City and Ojiya City were divided into 250 m meshes and relationships between the damage to manholes and several factors in each mesh were investigated. Following relationships were found:

a) Rate of damage increased with the decrease of the depth of water table in clayey ground as shown in Figure 7.

Table 1: Soil conditions at damaged and not damaged sites

	Parameter	Nagaoka (Nakazawa)		Ojiya (Sakuramachi)		Kawaguchi	
	Zone	damaged	no damaged	damaged	not damaged	damaged	not damaged
Surrounding Ground	*Soil Classification*	Silt Silty sand	Silt	Sandy silt	Sand with Silt Sandy silt	Clayey soil	Sandy soil Clayey soil
	SPT N-value	2-4	2	0-5	1	-	-
Replaced Area	*Soil Classification*	Sand with gravel	Sandy Gravel	Gravelly sand with fines	Gravelly sand with fines	Gravelly sand with fines	Sand with fines
	Water Table	GL -0.65m	below the pipe	GL -1.1m	GL -1.38m	GL -0.2m	GL -0.9m
	SPT N-value	11-14	-	-	-	-	-
	D_c	-	-	74%	78-82%	81%	-
	D_r	38-41%	-	-	-	-	-
Uplift of manhole		40cm uplift 30cm cave-in	no damage	8-20cm uplift 20cm cave-in	not uplift meandering	24cm uplift 23cm cave-in	no damage

b) Rate of damage at newly constructed meshes was high. This means liquefaction strength of replaced soils may increase with age due to aging effect.
c) Rate of damage of the manholes buried under sidewalk was higher than that of the manholes buried under roadway. Density of replaced soils under roadway must be higher than that under sidewalk.

One of the authors conducted shaking table tests on uplift of manhole due to soil liquefaction. Two series of test were carried out under different geotechnical condition of the surrounding ground. Series 1 simulates a manhole buried in the peat deposit. Series 2 simulates a manhole buried in the sand deposit. Liquefaction of the surrounding ground is not occur in the former case whereas it will occur in the latter. The manhole ,in the peat ground, was uplifted with excess pore water pressure increases. The uplift reached up to 16 mm during liquefaction. On the contrary, the uplift of the manhole installed in the sandy ground, was a little. There were significant difference between the uplift of the manhole installed in the peat ground and that in the sandy ground.

Figure 8 shows the schematic drawing on a mechanism of uplift of manhole due to liquefaction in the replaced soil with surrounding soft ground.

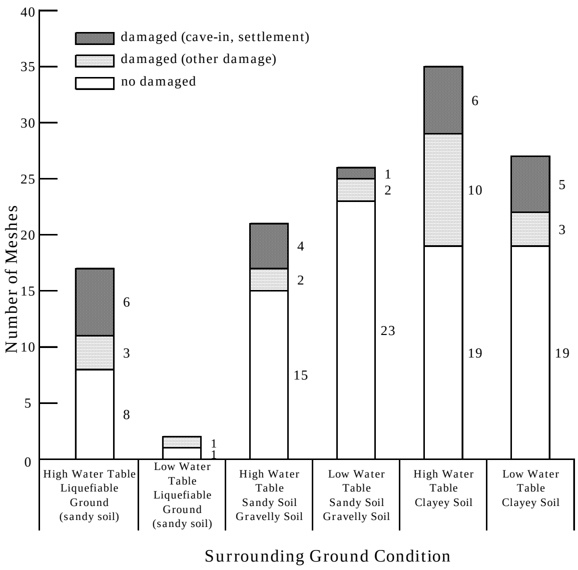

Figure 7: Comparison between damage rate and surrounding ground condition

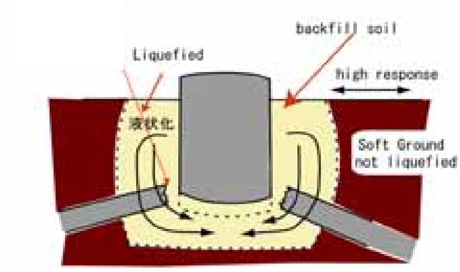

Figure 8: Schematic drawing on a mechanism of uplift of manhole

CONCLUSIONS

Based on these investigations, appropriate restoration methods were proposed not to have damage during future earthquake by a Technical committee on the sewer earthquake countermeasures organized by the Ministry of Land Infrastructures and Transport. The proposed methods are as follow:

(1) compact the replacing sands more than about 90 % of degree of compaction (Dc>90 %) or,
(2) replace the dug ditch with gravel,
(3) mix the replacing sands with cement and fill.

In Nagaoka City, the manholes uplift more than about 5 cm and the pipes uplifted more than height of 3/4 of the diameter of the pipe had to be restored. In the restoration work, third method was selected and mixing plants were constructed. Blast furnace cement were mixed to the sand excavated from damaged sites with the rate of 20 kg/m^3.

REFERENCES

[1] Japanese Geotechnical Society: Reconnaissance report on the 1993 Kushiro-oki earthquake and the 1993 Notohaoto-oki earthquake. (in Japanese), 1994
[2] Japanese Geotechnical Society: Reconnaissance report on the 2003 Tokachi-oki earthquake. (in Japanese), 2004.
[3] Technical committee on the sewer earthquake countermeasures: Report of the technical committee on the sewer earthquake countermeasures, Ministry of Land Infrastructure and Transport, 2005.

Pile-soil interaction in liquefied soil ground of Kazakhstan

A. Zh. Zhusupbekov[1] & A. A. Zhusupbekov[1] & A. S. Zhakulin[2]
[1]Geotechnical Institute, L. N. Gumilev Eurasian National University, Astana, KAZAKHSTAN,
[2]Karaganda State Technical University, Karaganda, KAZAKHSTAN

Abstract

The paper highlights the soil characteristics on the territory of the Republic of Kazakhstan along with the basic theses of the elastic and plastic soil models elaborated by the authors through solving the physical non-linear mixed problem of the elasticity and plasticity theory to describe the initial stressed and deformed condition of water saturated grounds with consideration of the pore pressure.

The elastic and plastic model was taken as a base for the axle-symmetrical problem solution to estimate the stressed and deformed condition in the areas around driven piles sectioned in 30x30 cm and 40x40 cm for the Atyrau soils liquefied condition.

Keywords – *Pile, soil, interaction, liquefied, stress, load, settlement*

INTRODUCTION

Taking into consideration of the emission and stratification properties of the grounds which will consequently serve as the base for buildings and constructions is obligatory both in industrious and public construction.

According to the principles of zone segregation concerning the engineering and hydrogeological conditions the territory of Kazakhstan is divided into the following zones:

- Central Kazakhstan (Central Kazakhstan Low Hills, Betpak-Dala Plateau, intermountain, foothill lowlands and plains of theTengiz, Zhezkazgan, Balkhash as well as estuary valleys of the Ishim, Nura and Irtysh);
- The Corrugational formations of South Kazakhstan (the Thyan-Shyan, the Zaisan, intermountain, foothill lowlands and valleys of the Alykol and Ili);
- The Russian Platform and Skiff Plate (Pre-Caspian lowlands and the region of West Kazakhstan);
- The Turan Plate (eolithic sandy deserts of the Muyunkum, Kyzylkum, Pre-Aral; eluvial and eluvial-deluvial plains of the Torgay and Kostanay Plateau, foothill plains of the Chu Cavity and valleys of Shimkent and Caratay; valleys and deltas of rivers, sea and lake-alluvial lowlands of the Chu and Syrdarya).

DESCRIPTION OF GEOLOGICAL CONDITIONS

The complex zonal geoengineering surveys of the territories and eventual estimation have revealed that the bases of buildings are originally continental sedimentary non-cemented rocks of the Quatenary System.

To evaluate the properties of the Quatenary system sedimentary rocks as those of the buildings base, the conditions of their genesis have been defined. Genetically the grounds of the Quatenary system are divided into marine, eolithic, eluvial, deluvial, lake, alluvial and etc.

Eluvial grounds of the Quatenary system are more frequently used as the base for buildings on the territory of Kazakhstan. CNiP 2.02.01-83 (CIS Republics Standard) stipulates the specifics of the building base designing in the eluvial grounds. Eluvial argillaceous soil is composed of weak loam and rarely of clay, both characterized by comparatively low resistance. The base structured in eluvial grounds should be designed with consideration of their particularities:

- compositional non-homogeneity and wide-ranged resistance and deformation terms;
- sandy loam and sand may get quick while water-saturated;
- sandy loam and fine sand may easily settle down while soaked;
- high mutability of physical and mechanical properties of clay and loamy grounds while water-saturated (Ter-Martirosyan, 1990; Zaretskyi, 1988).

The analysis reveals that most of buildings and constructions in the Kazakhstan industrious regions are erected mainly on the grounds of the Quaternary period. The soil of the Quaternary period is distinguished by its physical mutability, complexity and variability of mechanical properties. Therefore, within the scientific object (geotechnical system) the Quaternary water-saturated loam and sandy loam of West and Central Kazakhstan were taken as a research subject.

The major factors leading to water saturation of the base are considered to be technogenic (technical and technological) and climatic (atmosphere precipitation infiltration).

Water-saturated grounds could be met in all towns of Kazakhstan without exceptions, as well as in the oil fields region along the Caspian coastline. Water-saturated grounds of the bases possessing low deforming and resistance features require further investigation to prevent accidents and structural defects of buildings and constructions.

The pore pressure is an excessive pressure of the pore water in the water-saturated ground, exceeding the hydrostatic one and found as a component of the base stressed and deformed condition. The pore pressure as a component of the stressed condition determines the character of the filtrational consolidation process and influences the stability and resistance of the water-saturated bases as buildings and constructions are being erected and exploited.

The pore pressure being one of the components of the stressed condition in the water-saturated ground principally determines the process of consolidation and influences the stability and resistance of the building and construction base. Therefore, spreading and change of the pore pressure in the ground is one of the significant geomechanical problems as to reliably design the foundations on the water-saturated base of the Quartery system.

The prognosis for the ground deformation process in the water-saturated base depends primarily on the formation of the stressed condition subsequent to the interaction with the building. At that, the sought for stressed condition is induced in the water-saturated base which considerably differs from the initial one.

We suggest exploring the pre-marginal stressed condition of the water-saturated base at its four stages: initial, primary, intermediate, final.

The primary stressed (momentary) condition in the water-saturated base forms quickly enough and is, as a rule, followed by the intermediate stage. At the given stage, the interaction between the pore water and the ground carcass does not lead to significant change in their qualitative correlation. It is not necessary to apply the equation of the consolidation theory to describe the primary stressed condition.

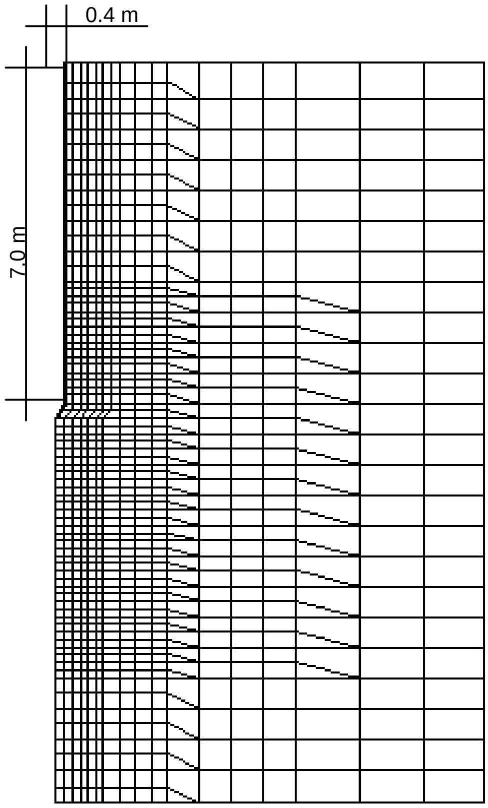

Fig. 1: The calculation mesh by FEM

THE ANALYSIS OF RESULTS OF NUMERICAL CALCULATION BY FEM

To make a complete description of the problem it is necessary to define border and primary conditions. Apparently, the equation system is self-starting, as by the time moment $t = 0$ of the loading application, the primary conditions are automatically realized on the account of the fact that the joint displacements and pore pressure components for the previous moment are equal to zero (Fig. 1).

To estimate the primary stress condition with consideration of the pore pressure in the water-saturated base around a single pile and to determine its bearing capacity the axle-symmetrical problem within the elastic-plastic set was solved on the basis of the non-linear deformational model applying the principle of the effective stress of the “water-saturated base - pile” system by the FEM according to the program “NONSOLAN” (Japan). The theoretical solutions were compared with the data of the static pile test of the vertically pressing loading carried out on the test field in Atyrau (Fig. 2).

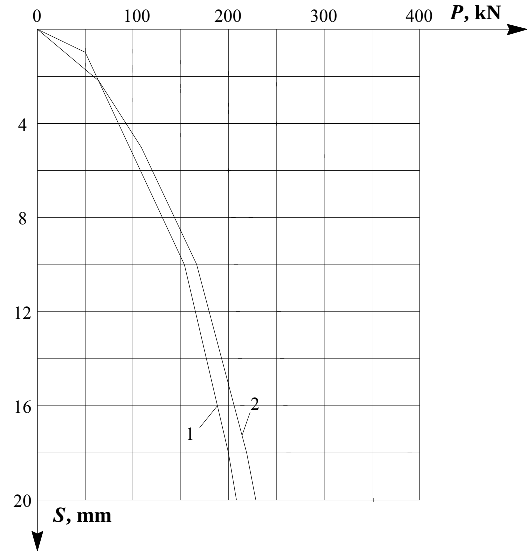

1 – experimental dates; 2 – theoretical dates

Fig. 2: The diagram of load-settlement of single pile

The ground base properties determined through the test results on the triaxile compression device of the construction by Tokyo University, Japan (Tatsuoka, S.Shibuya & R.Kuwano, 2001) are represented in the table 1 below.

Table 1: The ground properties accepted while calculating

Name of strata	E, MPa	ν	γ, kN/m^3	α_{cs}	e_0	λ	k	γ_{wH}, MPa
Loam	5.0	0.3	17.5	20	0.7	0.312	0.1	0.49

Certainly, the element scheme for the single pile calculation takes only a half of the calculated zone due to the pile section symmetry. The scheme of the pile cast in the water-saturated base clarifies that relatively to axle, Z is an absolute symmetry.

The calculated area is conditionally divided in 13 zones, the joint points are marked and placed in the proper locations. To provide the complete fading of the local disturbance the boundaries of the area in question are expanded for the distance not shorter than the piles length from each side.

In the calculation scheme during the pile cast in the water-saturated base the modeling was carried out in the form of the non-linear problem within the axle-symmetrical set generated as a result of a pace-out shearing of the field 3-4 between the joint points 4, 5 and 6 corresponding to the contact surface "water-saturated base – pile" up to the position 4', 5' and 6' as a rigid integer. The fluidity condition of the water-saturated ground is reflected through the deformation model equation. The calculation of the proper weight at the different depth levels was made in the form of the basic stress s.

The mesh zone in the horizontal direction has been divided in 4 zones. zones 5 and 13 have been divided in six equal parts of 15cm, zones 6 and 12 in four equal parts of 40cm, zones 7 and 11 in three equal parts of 75cm, zones 8 and 10 in three equal parts of 150cm.

In the vertical direction the division was made in 5 character zone, zone 1 in 8 equal parts of 31.8cm, zone 2 in 36 equal parts of 16cm, zone 3 in 16 equal parts of 16cm, zone 4 in 14 equal parts of 31.8cm, and zone 9 in 24 equal parts of 63.6cm.

The problem was solved through the numeric method of the final elements under the following primary boundary conditions:

1 ÷ 3 joints – $\varepsilon_r = \varepsilon_2 = 0$; 4÷6 joints – $\varepsilon_r = \varepsilon_2 = 15$cm or 20cm;

7 ÷ 10 joints – $\varepsilon_r = \varepsilon_2 = 0$; 10 ÷ 11 joints – $\varepsilon_2 = 0$; 11÷14 joints – $\varepsilon_r = \varepsilon_2 = 0$.

Thus, the upper area is free. The right side along the axle r and z is fixed. The left side along the axle z is fixed, and along the axle r it is fixed for the pile. The boundary conditions of the pile surface on the left side are denoted by the displacement $\varepsilon_r=\varepsilon_2=0{,}15$cm or $\varepsilon_r=\varepsilon_2=20$cm. The capacity of the studied water-saturated ground block is as follows: the depth H=15m, the breadth L=20m. The piles cross section is 30×30 cm and 40×40 cm, their length is 7.0m. It is supposed that there is complete adhesion along the contact line of the lateral surface "pile - ground". The physical nature of FEM permits to consider the system "Water-saturated base - pile" together (Fadeev, 1987). The rigidity is defined through its geometrical characteristics specification, the ground specific gravity is replaced by the all-sided hydrostatic stress tensor which is summed with the factual stress magnitude.

As a result of the numeric analysis of the given problem the following epures and contour lines of the stress , deformation and pore pressure around a single pile in the water-saturated base for the standard and propagated cross sizes of 0.3×0.3m and 0.4×0.4m:

contour lines of the zero deformations radial – ε_r,, the axle– ε_z,, tangential - ε_θ;

contour lines of the maximal deformations tangent (shearing) -γ_{rz};

spreading of the stresses radial - σ_r, axle - σ_z, tangential - σ_θ,;

contour lines of the stress tangent (shearing) - τ_{rz} (Fig. 3);

zero contour lines of the pore pressure – P_w (Fig. 4).

The contour lines of the zero radial – ε_r,, axle - ε_z, and tangential - ε_θ for the piles of 30×30cm and 40×40cm are similar both in form and character.

The largest interest is attracted by the contour lines of the maximal tangent deformations around the piles, conditioned by the shearing deformations. The spreading zone of the shearing deformations for the piles of 40×40cm encompasses more base ground than the pile of 30×30cm.

Spreading of the radial - σ_r,, axle - σ_z, and tangential - σ_θ stress s around the pile discovers that the stress zone generates under the tip and their spreading is similar. No the ground surface rise is observed from outside (from the upper ground surface) which is proper to the water-saturated base. The contour lines of the tangent (shearing) stress (Fig. 3) indicate distinctly that two compressed zones are forming around and under the pile tip with the nucleus with the stress value of 0.1MPa and 0.05MPa which in their turn spread around up to 2.0m from the pile edges. Altogether with this, the stress spreading zone for the piles of 40×40cm is wider than that for the piles of 30×30cm.

The contour lines of the pore water pressure – P_w (Fig. 4) indicate at the pore pressure spreading around the piles. Three zones of the pore pressure spreading are forming around the piles: by the bottom., along the lateral surface, under the bottom. The zone by the tip is up to 1.0m and takes a circle form. The second zone along the lateral surface is 2.2m in breadth and 4.3m in height. The third zone under the tip reaches 4.0m in depth for the piles of 30×30cm and 7-8m for the piles of 40×40cm.

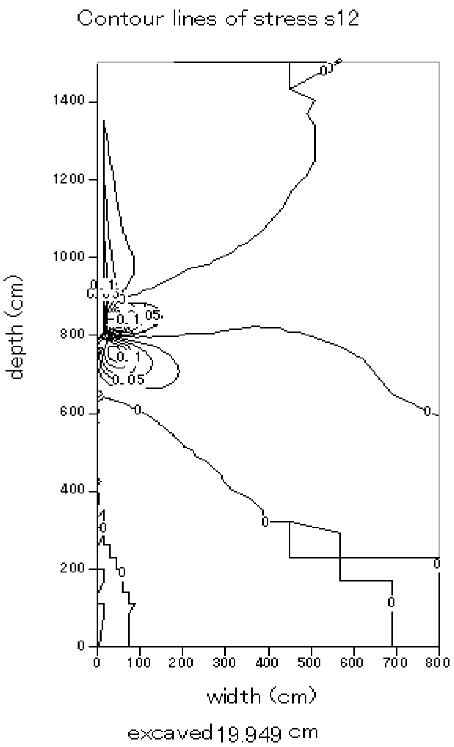

Fig. 3: Contour lines of shearing stresses – τ_{rz} around the pile of 40×40 cm

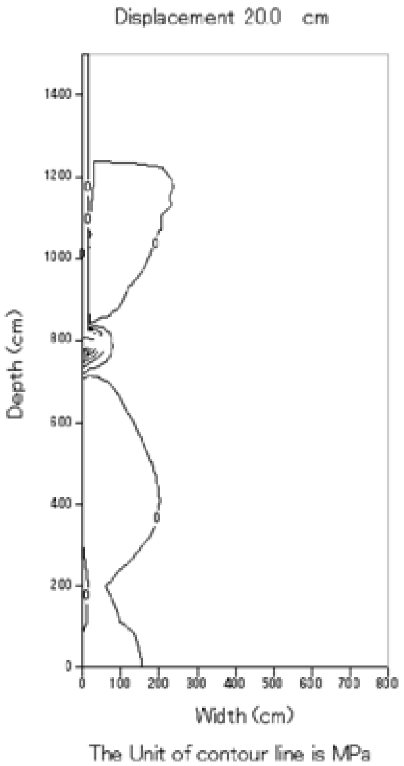

Fig. 4: Zero contour lines of the pore pressure - P_w around the pile of 40×40cm

CONCLUSIONS

Spreading of the contour lines of the pore pressure reveals that the determination of the stressed and deformed condition of the water-saturated liquefied ground around the pile should necessarily be fulfilled with consideration of the pore pressure as it, in its turn, determines the pile bearing capacity.

The process of the pore pressure spreading around the pile clarifies the mechanism of the interaction between a single pile and the water-saturated liquefied ground base and allows to estimate its primary stressed condition.

ACKNOWLEDGMENTS

The authors whish to thank to Professor Tadatsugu TANAKA and Dr. Kenji OKAJIMA (Tokyo University, Japan) for discussion about results of numerical analysis by FEM of pile –soil interaction.

REFERENCE

[1] Z.G.Ter-Martirosyan. Reologic Parameters of the Grounds and Calculations of the Construction Foundations, Moscow, Stroyizdat, 1990, 200 p.
[2] Yu.K.Zaretskyi. The Ground Ductility and Plasticity and Calculations of the Construction, Moscow, Stroyizdat, 1988, 352 p.
[3] F. Tatsuoka, S.Shibuya & R.Kuwano. Advanced laboratory stress-strain testing of goematerials, Tokyo, A.A.Balkema, 2001, 329p.
[4] A.B.Fadeev. Finite Elements Method of in Geomechanics, Moscow, Nedra, 1987, 221 p.

(4) Soil liquefaction and remediation

EQWEAP ~ a simplified procedure to analyze dynamic pile-soil interaction with soil liquefaction concerns

D. W. Chang and B. S. Lin
Department of Civil Engineering, Tamkang University, Tamsui, Taiwan

Abstract

The effects of soil liquefaction and lateral spread are significantly important to pile foundations under large earthquakes. Practicing the design work of pile foundations needs to take them into account in order to prevent structural failures due the foundation damages. This paper suggests a simplified but effective procedure called *EQWEAP* to analyze the dynamic pile-soil interaction under the earthquake. In the analysis, the pile deformations are obtained solving the discrete wave equations of the pile, where the seismic ground motions are pre-calculated from one-dimensional lumped mass model and superimposed onto the pile assuming a free-field condition. For soil liquefaction, various models could be incorporated in the analysis. For instance, soil parameter reduction factor along with the factor of safety against the liquefaction potential is often adopted. On the other hand, one can use the empirical excess pore pressure model to monitor more details of the liquefaction. In that case, the amount of pore pressure ratio coefficients were suggested to modify for soils underneath the liquefied layer, in which the empirical relationship between the pore pressure ratio coefficient and the factor of safety against liquefaction is followed. In both cases, liquefaction potential of the site needs to be evaluated prior to the analyses. Validation of this procedure has been made by a number of case studies on foundation failure reports in 1964 Niigata earthquake. Rational results can be found to support the field observations with the time history details of the occurrence of foundation failures.

Keywords—*pile foundations, EQWEAP, damages, liquefaction.*

INTRODUCTION

For saturated sand deposit subjected to earthquake excitations, if the pore pressure were instantly generated and equal to the effective stress of soil, the liquefaction would occur. Liquefied soils can cause considerable loss of the ground strengths to yield large settlement via to result in lateral spreading. For superstructures supported on pile foundations at that site, these effects are significantly important. Recent studies have focused on the mechanism of soil-pile interactions in a liquefied layered soil (Hamada, 1992; Meyersohn, 1994; Tokimatsu, 2003). Excavations surveys by Hamada (1992) had clearly showed that the bending failure of piles could occur at the interface between liquefied and non-liquefied layers. This observation has been verified by Meyersohn (1994) and Lin *et al*. (2005) with static numerical techniques. They both confirmed that it is indeed a dangerous zone for piles under the liquefaction.

To depict this phenomenon through the dynamic analysis, this study suggests a numerical procedure termed *EQWEAP* (Earthquake Wave Equation Analysis for Pile). Free-field seismic motions of a site were obtained first from a 1-D lumped mass analysis. The ground motions were then mounted to the piles, and the 1-D wave equation analysis was subsequently conducted to obtain the corresponding pile responses. Two methods were used to simulate the weakness of soil under liquefaction. One is to incorporate with the empirical model of excess pore water pressure (Finn et al, 1977). The other is to reduce the soil modulus, in which the soil parameter's reduction factors of the site could be used such as those suggested in the Japanese Codes. For validation of the procedure, a couple of studies based on reports of 1964 Niigata earthquake was conducted. With the suggested analysis, one can obtain effectively the time-history details of the pile responses under the soil liquefactions. Feasible computation time would be valuable for such analysis in the routine design practice.

NUMERICAL PROCEDURE

Seismic responses of the grouped piles can be analyzed effectively by decomposing the whole structural system. Solving the seismic horizontal/vertical motions of the free field from the one-dimensional lumped mass analysis, the ground displacements are superimposed onto the foundation. The pile deflections are then obtained from the discrete time-domain wave equations of the piles. Figure 1 depicts the discrete structural systems and the procedures for the analysis. The authors (Chang *et al*., 2000; Chang and Lin, 2003) have used these procedures to model the horizontal and vertical responses of the pile foundation under the Kobe and Chi-Chi earthquakes, and the solutions were found compatible to the FEM ones from ABAQUS analysis. Figure 2 presents the compatible solutions of a 2×2 pile foundation assuming that the foundation is subjected to Kobe earthquake record. Notice that the ground has no liquefaction to occur. Representative equations for the Lumped Mass (LM) analysis and the Wave Equation (WE) analysis of the cases under horizontal earthquake excitations are again summarized as follows.

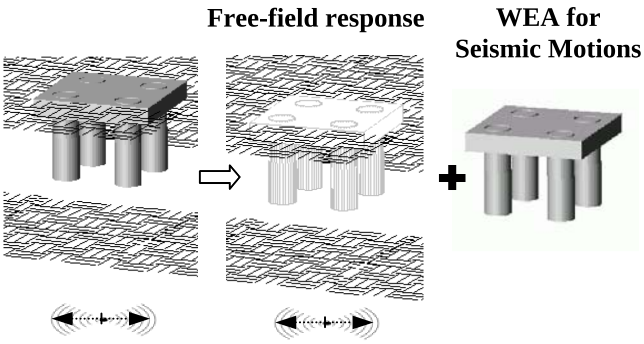

Fig. 1: Superposition of the free-field analysis and WEA

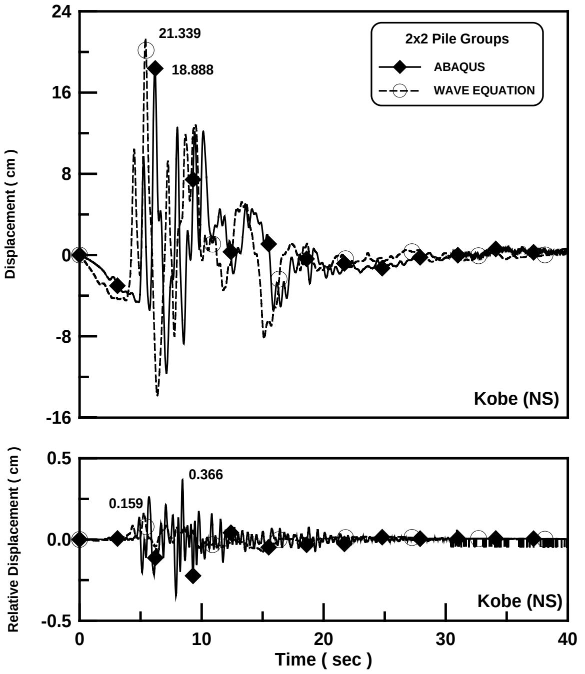

Fig. 2: Comparison of numerical results from WEA and FEM

Free-field Responses

For horizontal ground response due to the earthquake excitations, the governing equation of the structural system for a multi degree-of-freedom lumped mass system would be written as

$$M\ddot{U} + C\dot{U} + KU = -MU_g \tag{1}$$

where U , $\dot{U}$, $\ddot{U}$ and U_g denotes respectively for the vectors of relative displacement, the corresponding velocity and the corresponding acceleration, and acceleration of the ground; the matrices of the mass, M and the viscous coefficient, C as well as the stiffness, K, of the level ground can be expressed as follows,

$$M = \begin{bmatrix} m_n & 0 & \cdots & 0 & \cdots & 0 & 0 \\ 0 & m_{n-1} & 0 & \cdots & 0 & 0 & 0 \\ \vdots & 0 & \ddots & 0 & 0 & 0 & \vdots \\ 0 & \vdots & 0 & m_i & 0 & \vdots & 0 \\ \vdots & 0 & 0 & 0 & \ddots & 0 & \vdots \\ 0 & 0 & 0 & \cdots & 0 & m_2 & 0 \\ 0 & 0 & \cdots & 0 & \cdots & 0 & m_1 \end{bmatrix} \tag{2}$$

$$K = \begin{bmatrix} K_s & -K_s & 0 & 0 & \cdots & 0 & 0 \\ -K_s & 2K_s & -K_s & 0 & 0 & 0 & 0 \\ 0 & -K_s & 2K_s & -K_s & 0 & 0 & \vdots \\ 0 & 0 & \ddots & \ddots & \ddots & \vdots & 0 \\ 0 & \vdots & 0 & -K_s & 2K_s & -K_s & 0 \\ \vdots & 0 & 0 & 0 & -K_s & 2K_s & -K_s \\ 0 & 0 & \cdots & 0 & 0 & -K_s & K_s \end{bmatrix} \tag{3}$$

$$C = \alpha M + \beta K \tag{4}$$

where $m_i = \rho AL$, $K_s = GA_s / L$, m_i is the ith mass, K_s is the stiffness in ith layer, G is the shear modulus of the soil, A_s is the cross sectional area of the soil mass, L is the thickness of the horizontal soil layers, ρ is the mass density of the soil, α and β are the parameters of Rayleigh damping model. One can easily obtain the ground responses by solving the governing equations with proper numerical procedures.

Induced Pile Responses

To make the wave equation analysis more accessible at the time-domain, the author (Chang and Yeh, 1999; Chang *et al*., 2000; Chang and Lin, 2003) has suggested a finite difference solution for the deformations of single piles. A time-dependent soil damper based on Novak’s impedance functions was proposed. The solutions were found agreeable with the analytical predictions and the field experimental data (Chang *et al*., 2000). For lateral response of the pile during seismic shaking, the governing differential equations of the pile segment can be written as:

$$E_p I_p \frac{\partial^4 y_p(x,t)}{\partial x^4} + \rho_p A_p \frac{\partial^2 y_p(x,t)}{\partial t^2} + P_x \frac{\partial^2 y_p(x,t)}{\partial x^2} + C_s \frac{\partial y(x,t)}{\partial t} + K_s y(x,t) = 0 \tag{5}$$

where $y(= y_p - y_s)$ is the relative pile displacements, y_p is the absolute pile displacements, y_s is the absolute soil displacements, E_p is Young's modulus of the pile; I_p is moment of inertia of the pile, ρ_p is the uniform density of the pile, A_p is cross-section area of the pile; P_x is the superstructure loads, C_s and K_s are damping coefficient and stiffness of the soils along the pile. Considering earthquake loading transiting from the soils, Eq. (5) can be written in the difference form such that:

$$y_p(i,j+1)=\frac{1}{A+C}\begin{bmatrix}-y_p(i+2,j)+(4-B)y_p(i+1,j)\\-(6-2A-2B+D)y_p(i,j)\\+(4-B)y_p(i-1,j)-y_p(i-2,j)\\-(A-C)y_p(i,j-1)\\+C[y_s(i,j+1)-y_s(i,j-1)]+Dy_s(i,j)\end{bmatrix} \quad (6)$$

where $A=\frac{A_p\rho_p\Delta x^4}{E_pI_p\Delta t^2}$; $B=\frac{P_x\Delta x^2}{E_pI_p}$; $C=\frac{C_s\Delta x^4}{2\Delta tE_pI_p}$; $D=\frac{K_s\Delta x^4}{E_pI_p}$

Eq. (6) indicates that the absolute pile displacements under the earthquake excitations can be solved directly from the absolute displacements of the adjacent soils. One could simply use a free-field analysis to obtain the liquefied soil displacements, and then substitute them into Eq. (6) for the desired solutions. This is similar to those suggested in the multiple-step analysis of the soil-structure interaction problems. In addition, the equations of the highest and lowest elements of the pile should be modified with proper boundary conditions listed as follows.

At the top of the pile:

(a) Free head: $\frac{\partial^3 y_p(x,t)}{\partial x^3}=\frac{P_t}{E_pI_p}$; $\frac{\partial^2 y_p(x,t)}{\partial x^2}=\frac{M_t}{E_pI_p}$ (7)

(b) Fixed head: $\frac{\partial^3 y_p(x,t)}{\partial x^3}=\frac{P_t}{E_pI_p}$; $\frac{\partial y(x,t)}{\partial x}=0$ (8)

At the tip of the pile:

$$\frac{\partial^2 y_p(x,t)}{\partial x^2}=0;\ E_pI_p\frac{\partial^3 y_p(x,t)}{\partial x^3}+P_X\frac{\partial y_p(x,t)}{\partial x}=0 \quad (9)$$

where M_t and P_t are the external moment and load applied at the pile head. The discrete forms of these equations can be derived with the central difference schemes It can be obtained by a separate analysis, for example, from a dynamic structural analysis for a bridge system. Their solutions are dependent of the soil displacements too. The detailed derivations can be found in Wu (2005).

SOIL LIQUEFACTION

Reduction Factors

In this matter, the liquefaction potential of a ground can be analyzed using the methods suggested by Tokimatsu and Yoshimi (1983) and those from Japanese Road Association (1990, 1996). One may use the in-situ geological data and the corresponding SPT-N values to predict the liquefaction zone, in which the safety factors of the soils F_L at arbitrary depth against liquefaction are defined by the ratios between the cyclic strengths and stresses. The factor of safety of the soil can be used to obtain the soil parameter reduction factor D_E accordingly with the tabularized relationships such as those by Japanese Road Association (1996) in Table 1. The parameter reduction factor would be used to reduce the stiffness of the soils in the liquefied zone along the piles. For the lumped mass and the wave equation analyses, the reduction factors would be both applied to the modulus of the soil in liquefaction zone, in which the Equations (3) and (4) would be affected by the reduced modulus of the liquefied soil**.**

Table 1: The soil reduction factors D_E (from JRA, 1996)

Safety Factor F_L	Depth Z (m)	Reduction factor D_E	
		$R \le 0.3$	$0.3 < R$
$F_L \le 1/3$	$0 \le Z \le 10$	0	1/6
	$10 < Z \le 20$	1/3	1/3
$1/3 < F_L \le 2/3$	$0 \le Z \le 10$	1/3	2/3
	$10 < Z \le 20$	2/3	2/3
$2/3 < F_L \le 1.0$	$0 \le Z \le 10$	2/3	1
	$10 < Z \le 20$	1	1

Note: R = cyclic resistance ratios

With these reduction factors on hand, the seismic free-field response of that site, where the liquefaction would occur, could be obtained conducting the lumped mass analysis. For simplicity of the analysis, an equivalent homogeneous soil profile is assumed. The Young's modulus of that profile is calculated as follows,

$$\frac{\sum_{i=1}^{n} L_i}{\sum_{i=1}^{n}\frac{L_i}{V_i}}=V_{eq} \quad (10)$$

where V_{eq} is the equivalent propagation velocity of soil, L_i is the thickness of each soil layer and V_i is the propagation velocity of each soil layer.

Pore-pressure Model

The soils affected by build-up pore-water pressure would reduce the lateral resistance of piles. This study employed the empirical model of excess pore water model as an effective stress analysis (Finn et al, 1977) and to obtain the free-field motions under liquefaction. Kim (2003) has successfully predicted the excess pore-water pressure subjected to earthquake shaking for a physical model test utilizing this model and verified with laboratory results. This model can be divided into undrained condition and drained condition as follows:

(a) Undrained condition:

$$\Delta u=\frac{\Delta\varepsilon_{vd}}{\frac{1}{\bar{E}_r}+\frac{n_p}{K_w}} \quad (11)$$

where Δu = an increase in pore water pressure; $\Delta\varepsilon_{vd}$ = an increment in volumetric strain; $\overline{E}_r$ = one dimensional rebound modulus at an effective stress σ'_v; n_p = porosity, and K_w is the bulk modulus of water.

For saturated sand $K_w >> \overline{E}_r$ and therefore

$$\Delta u = \overline{E}_r \Delta\varepsilon_{vd} \tag{12}$$

According to simple shear test, the volumetric strain increment ($\Delta\varepsilon_{vd}$) is a function of the total accumulated volumetric strain (ε_{vd}) and the shear strain (γ). The relationship has the form given by

$$\Delta\varepsilon_{vd[i]} = C_1(\gamma - C_2\varepsilon_{vd[i-1]}) + \frac{C_3\varepsilon^2_{vd[i-1]}}{\gamma + C_4\varepsilon_{vd[i-1]}} \tag{13}$$

$$\varepsilon_{vd[n]} = \sum_{i=1}^{n}\Delta\varepsilon_{vd[i]} \tag{14}$$

where [i] = ith time step or cycle; and C_1, C_2, C_3, and C_4 are constants depending on the soil type and relative density. An analytical expression for rebound modulus ($\overline{E}_r$) at any effective stress level (σ'_v) is given by

$$\overline{E}_r = \frac{(\sigma'_v)^{1-m}}{mk_2}(\sigma'_{v0})^{m-n} \tag{15}$$

where σ'_{v0} is initial value of the effective stress; and k_2, m and n are experimental constants for the given sand.

(b) Drained condition:

If the saturated sand layer can drain during liquefaction, there will be simultaneous generation and dissipation of pore water pressure (Finn *et al*. 1977). Thus, the distribution of pore-water pressure at time (t) is given by

$$\frac{\partial u}{\partial t} = \overline{E}_r \frac{\partial}{\partial z}\left(\frac{k}{r_w}\frac{\partial u}{\partial z}\right) + \overline{E}_r \frac{\partial\varepsilon_{vd}}{\partial t} \tag{16}$$

where u = the pore-water pressure; z = the corresponding depth; and k = the permeability ; and r_w is the unit weight of water. Before proceeding the free-field analysis, the adequate shear modulus (Seed and Idriss, 1970) may be determined from the equation and given by

$$G = 1000K_2(\sigma'_m)^{0.5} \tag{17}$$

where K_2 is a parameter that varies with shear strain and σ'_m is the mean effective stress. The pore water pressure increases during shaking and then leads to the decrease of the effective stress. In some situation, the pore-water pressure equals to the overburden stress in sand deposit and it may liquefy. The initial shear modulus can be calculated from the initial effective stress. Then, G is modified due to shear strain and pore water pressure under liquefaction. The modified value is to substitute for the former value and should ensure the convergence and equilibrium of the system in an iterative manner.

In addition, to avoid over-predicting the excess pore water pressure for the soils at deep depths, and be more compatible with the field observations. It is suggested to use the pore water pressure ratio (r_u) to control properly the level of soil liquefaction (Tokimatsu and Yoshimi, 1983). The available equation is given by

$$r_u = \frac{1}{2} + \frac{1}{\pi}\sin^{-1}(2F_L^{\frac{1}{\alpha_1\beta_1}} - 1) \tag{18}$$

where α_1, β_1 are the experienced constants, and F_L is the safety factor of liquefaction. In order to use the above formulas, the liquefaction potential analysis of the site need to be conducted prior to the analysis. The pore pressure ratio obtained from Eq. (18) can be used as a maximum value for the ratio of computed pore pressure and initial effective stress in the above analysis.

PILE MOMENT AND SHEARS

In a design process, engineers need the limit states to define the serviceability of members according to the safety of performances to structures (Priestley *et al*., 1996). Figure 3 indicates the typical moment-curvature relationship. This moment-curvature relationship implies various principles in use, which include the cracking limit state, yielding limit state, spalling limit state and ultimate limit state. Besides, the above relationship can be obtained based on the assumption that the bending characteristic in a neutral plan and concrete is nonlinear material. In the JRA codes (1996), the nonlinear behavior of pile material is represented by the tri-linear model and the bilinear model as shown in Figures 4~5. The tri-linear model can be applied in the precast pile, prestressed high strength concrete pile, and reinforced concrete pile. The bilinear model only can be applied in the steel pile. Figures 4~5 indicate the typical relations between bending moments and curvatures where M_c is the cracking bending moment that make the concrete crack initially, M_y is the yielding bending moment when steels yield, and M_u is the ultimate bending moment that pile body reaches the ultimate strain and generates a plastic hinge herein. Thus, predicting the reliable relation between moments and curvatures needs to incorporate with the adequate model of stress and strain.

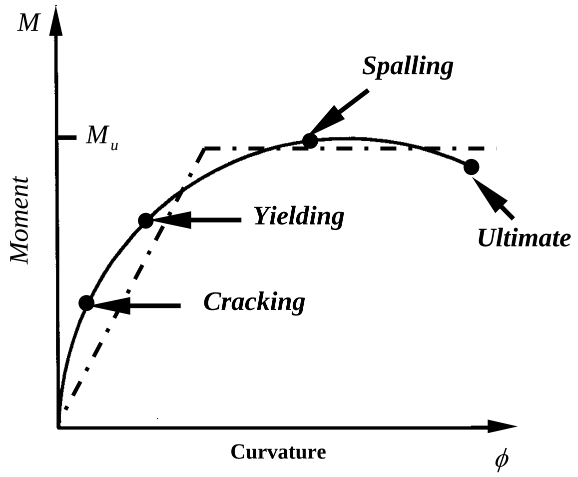

Fig. 3: Typical moment-curvature relationship

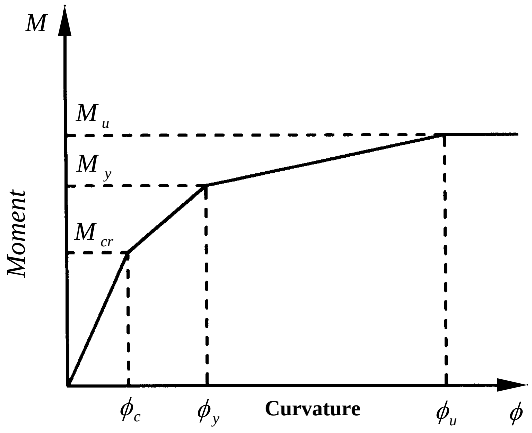

Fig. 4: Tri-linear model of Moment-curvature relationship

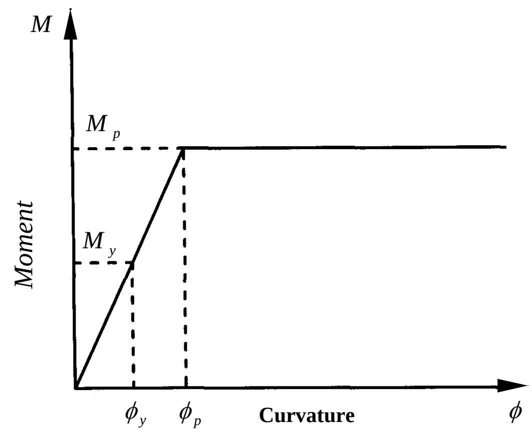

Fig. 5: Bilinear model of Moment-curvature relationship

When the shear stress applied on concrete exceeds the ultimate shear strength, the concrete are supposed to be sheared off (ACI, 1988). The equation of the ultimate shear strength is determined by

$$V_u = 0.53\sqrt{f_c'} \cdot b_w \cdot d \tag{19}$$

where f_c' is the compression strength, b_w is the diameter of pile, and d is the effective depth of cross section.

VALIDATIONS

Following studies are focusing on the damages of the pile foundations during Niigata earthquake in Japan (Hamada, 1992). The investigation conducted in situ had showed that the permanent ground displacement caused the failure of pile due to liquefaction. In this paper, the free-field analysis and the wave equation are both performed to calculate the dynamic responses of piles under liquefaction. Therefore, the mechanism behind the failures of the piles can be interpreted.

Niigata Family Court House

The Niigata Family Court House was a four-story building located on the left bank of the Shinano River. The building was supported on concrete pile foundation (see Figure 6) each with a diameter of 35 cm and a length of 6 to 9 m. During the earthquake, the pile foundations were damaged by liquefaction-induced ground displacement. Excavation surveys had showed that two piles (No.1 pile and No.2 pile) of them had severe cracks (see Figure 7). They were conjecturally crushed by excessive bending moments at the interface between liquefied and non-liquefied layer as shown in Figure 7. According to the aerial photograph (Figure 8) of the area, the permanent ground displacement in the vicinity of building moved approximately by 1.1m and the maximum displacement of No.1 pile and No.2 pile were respectively 50 cm and 70cm. For a simplification, the entire soil system could be assumed as the upper layer and lower layer. The upper layer from the ground surface to the depth of 8m is classified as medium-dense sand. The lower layer from the depth of 8 to 11m is classified as dense sand. All the soil and pile properties are listed in Table 1. The time history of earthquake record adopted the NS-component of Niigata Earthquake in 1964 as illustrated in Figure 9.

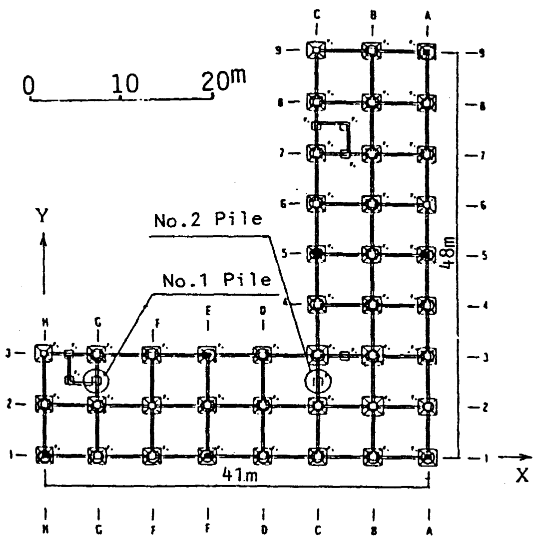

Fig. 6: Footing and foundation beams of Niigata Family Court House (from Hamada, 1992)

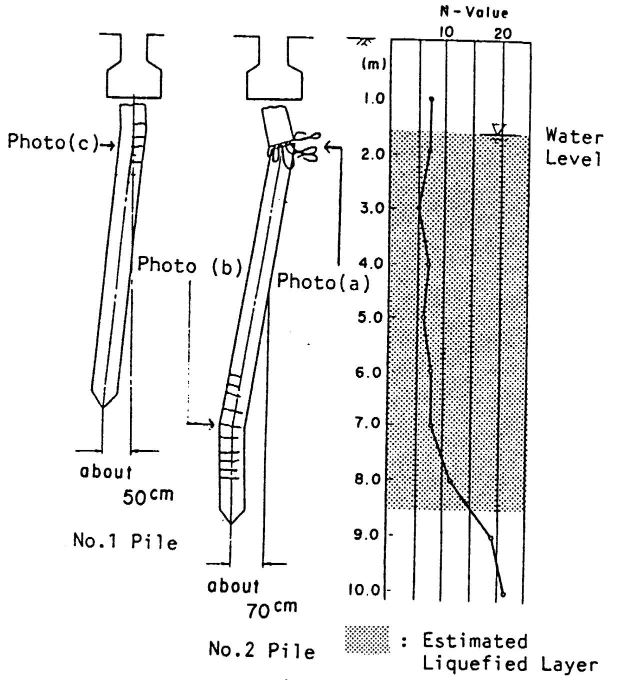

Fig. 7: Damage to piles and SPT-N values in situ (from Hamada, 1992)

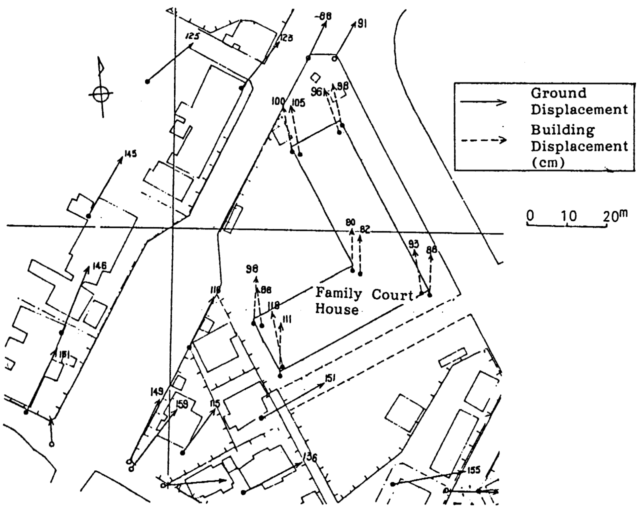

Fig. 8: Permanent ground displacement of the area from aerial photograph (from Hamada, 1992)

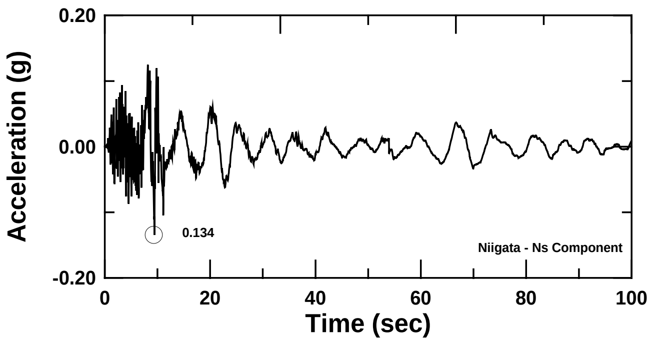

Fig. 9: Time history of Niigata Earthquake (NS Component)

Table 1. Material properties for piles and soils

Case study	Niigata Family Court House	
Pile properties	**No.1**	**No.2**
$E_P I_P (kN-m^2)$	**5625**	**7500**
$M_{cr} (kN-m)$	**2.65**	**18.19**
$M_y (kN-m)$	**45**	**75**
$M_u (kN-m)$	**56.61**	**86.17**
$V_u (kN)$	**12.06**	**59.57**
Soil profile		
Upper layer Depth (m)	**0.0-8.0**	
$\gamma_s (kN/m^3)$	**16.5**	
$\phi_s (degree)$	**32**	
Lower layer Depth (m)	**8.0-11.0**	
$\gamma_s (kN/m^3)$	**18.5**	
$\phi_s (degree)$	**34**	

Numerical results

The determination of pore water ratio pressure (r_u) and reduction factors (D_E) versus the depths can be estimated by liquefaction potential method suggested by Tokimatsu and Yoshimi (1983) with Eq. (18) to govern the level of liquefaction as shown in Figure 10. One can input the soil properties to lumped-mass system and obtain the liquefied free-field responses respectively with the uses of the reduction factors and the empirical model of pore water pressure.

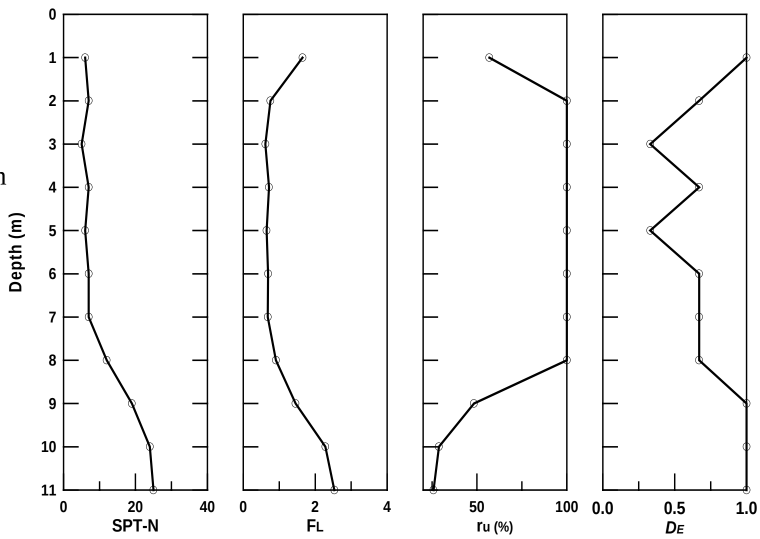

Fig. 10: Pore water pressure ratios and reduction factor versus various depths

Figures 11~12 indicate the maximum displacements of piles at various depths from *EQWEAP* analysis. The maximum pile displacement would occur at the interface between liquefied and non-liquefied layers by reduction factor method. On the other hand, the maximum pile displacement from using the pore-pressure model is found at the ground surface. Deviations of these numerical results were caused by the modeling. In the second solutions, the relative displacements between the pile head and the pile tip are about 46 cm and 69 cm, which is similar to the field observations. The maximum bending moments of piles are shown in Figures 13~14 where those peak values would also occur approximately at interface between liquefied and non-liquefied layers. Comparing the numerical results by Meryersohn (1994) as shown in Figure 17, the computed values are nearly consistent with the ones reported. In the meantime, the peak shear forces of piles almost occur at this zone shown in Figures 15~16. Therefore, the dangerous zone that makes excessive bending moment and shear on pile is again revealed in this study with the suggested procedures.

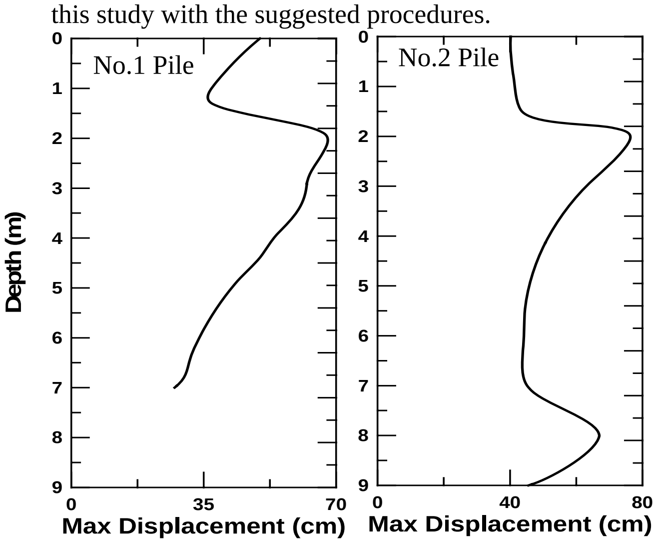

Fig. 11: Maximum pile displacements for No.1 Pile and No.2 Pile (Reduction factor method)

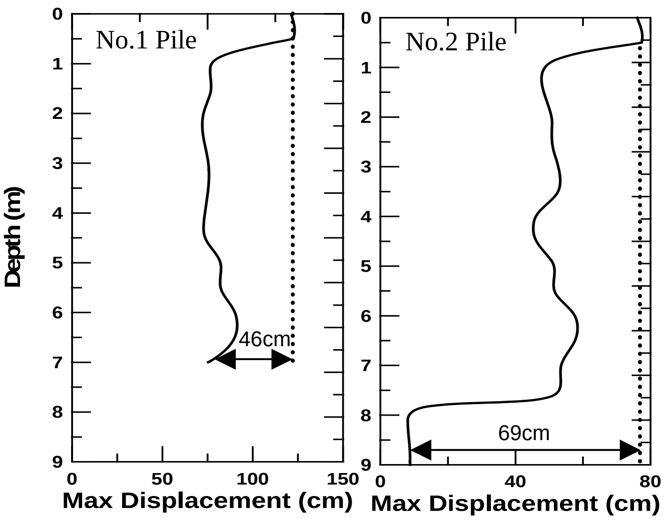

Fig. 12: Maximum pile displacements for No.1 Pile and No.2 Pile (Pore-pressure model method).

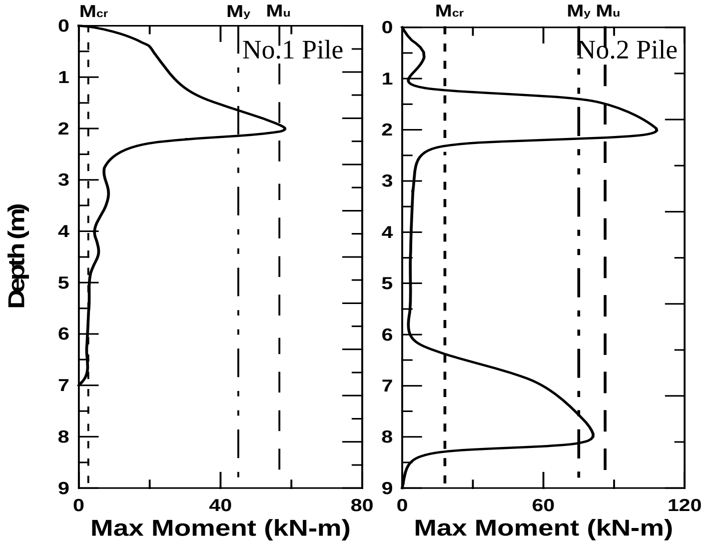

Fig. 13: Maximum pile bending moments for No.1 Pile and No.2 Pile (Reduction factor method)

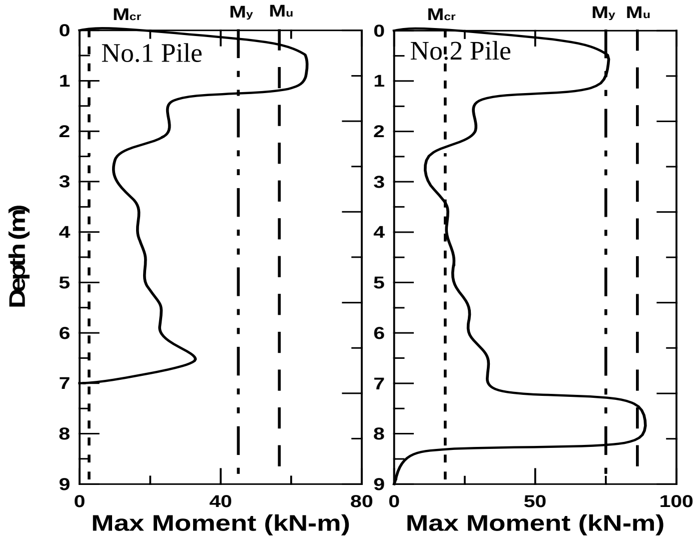

Fig. 14: Maximum pile bending moments for No.1 Pile and No.2 Pile (Pore-pressure model method)

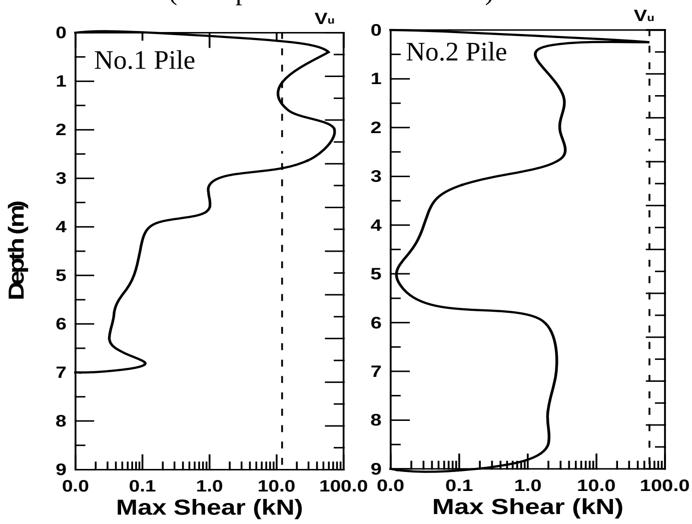

Fig. 15: Maximum pile shears for No.1 Pile and No.2 Pile (Reduction factor method)

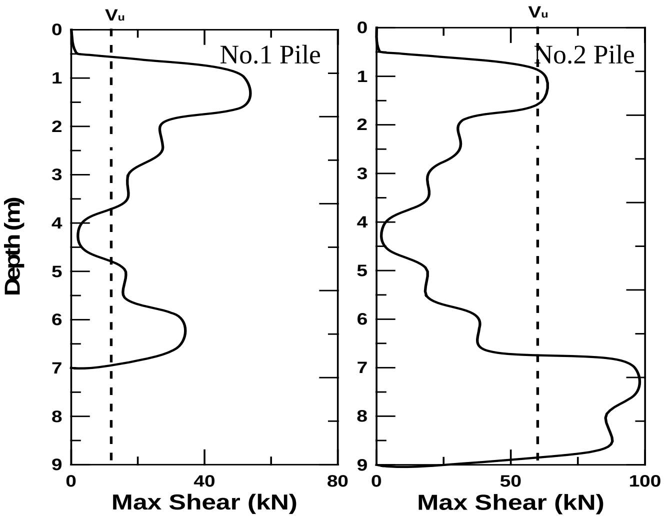

Fig. 16: Maximum pile shears for No.1 Pile and No.2 Pile (Pore-pressure model method)

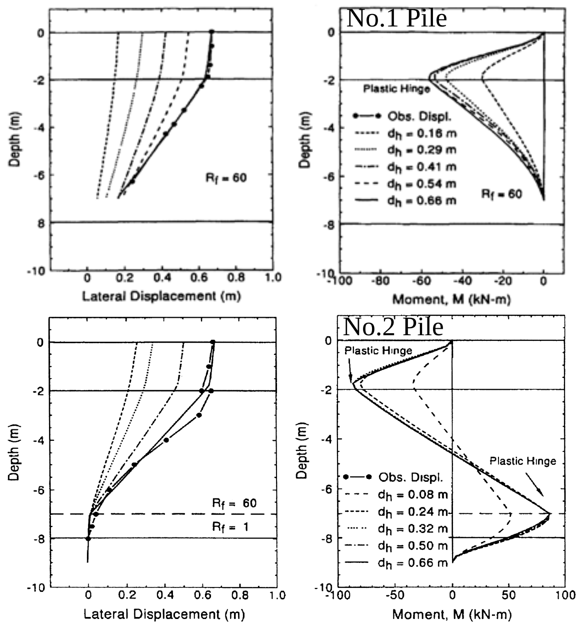

Fig. 16: Numerical results for piles of Niigata Family Court House (from Meyersohn, 1994)

SUMMARY

Based on the suggested numerical procedure *EQWEAP*, one can monitor the simultaneous motions of the soil stratum and the pile foundations at various depths to prevent the occurrence of pile damages and estimating the patterns of failure. Not only the interfaces between the liquefied and non-liquefied layers could exert excessive bending moments and shears, but also the layer contrast of the soils would yield similar ones.

ACKNOWLEDGMENTS

This work is a partial result of the studies through research contrasts NSC94-2211-E032-010 from National Science Council in ROC. The authors express their sincere gratitude for the supports.

REFERENCES

[1] Hamada M., “Large Ground Deformations and Their Effects on Lifelines：1964 Niigata Earthquake,” in Case Studies of Liquefaction and Lifeline Performance During Past Earthquakes, Vol. 1, Japanese Case Studies, Technical Report NCEER-92-0001, NCEER, Buffalo, NY, USA, 1992.

[2] Meyersohn, W.D., “Pile Response to Liquefaction-induced Lateral Spread ,” Doctor’s Dissertation, University of Cornell, USA, 1994.

[3] Tokimatsu, K., “Behavior and Design of Pile Foundations Subjected to Earthquakes”, *Procds.*, 12th Asian Regional Conf. on Soil Mechanics and Geotechnical Engineering, Singapore, August, 2003.[4]

[4] Lin, S.S., Tseng Y.J., Chiang C.C. and Hung C.L., “Damage of Piles Caused by Laterally Spreading – Back Study of Three Cases”, Workshop on Simulation and Seismic Performance of Pile Foundation in Liquefied and Laterally Spreading Ground, University of California, Davis, March, 2005.

[5] Finn, W.D.L., Lee, K.W., and Martin, G.R., “An Effective Stress Model for Liquefaction”, Journal of the Geotechnical Engineering Division, ASCE, Vol. 103, No. SM7, 1977, pp. 657-692.

[6] Chang, D.W. and Lin, B.S., “Wave Equation Analyses on Seismic Responses of Grouped Piles”, Procds., 12th Asian Regional Conf. on Soil Mechanics and Geotechnical Engineering, Singapore, August, pp.581-586, 2003**.**

[7] Chang, D.W., Roesset, J.M. and Wen, C.H., “A Time-domain Viscous Damping Model Based on Frequency-dependent Damping Ratios”, Soil Dynamics and Earthquake Engineering, Vol. 19, pp. 551-558, 2000.

[8] Chang, D.W. and Yeh, S.H., “Time-domain Wave Equation Analyses of Single Piles Utilizing Transformed Radiation Damping”, Soils and Foundations, JGS, Vol. 39, No. 2, 1999, pp. 31-44, 1999

[9] Wu, S.S., Analyses for Dynamic Responses of Pile Foundations Affected by Modulus Reduction of Liquefied Soils, M.S. Thesis, Dept. of Civil Engineering, University of Tamkang, Tamsui, Taiwan, 190 p, 2005.

[10] Japanese Road Association (JRA), Specification for Highway Bridges, Part V, Seismic Design, 1990.

[11] Japanese Road Association (JRA), Specification for Highway Bridges, Part V, Seismic Design, 1996.

[12] Tokimatsu, K. and Yoshimi, Y., “Empirical Correlation of Soil Liquefaction Based on SPT N-Value and Fines Content”, Soil and Foundations, JSSMFE, Vol. 23, No.4, pp. 56-74, 1983.

[13] Kim, S. I., “Liquefaction Potential in Moderate Earthquake Regions”, *Procds.*, 12th Asian Regional Conf. on Soil Mechanics and Geotechnical Engineering, Singapore, August, pp.1109-1138, 2003**.**

[14] Seed, H.B., and Idriss, I.M. (1970), “Soil Moduli and Damping Factors for Dynamic Response Analysis”, Report No. EERC 75-29, Earthquake Engineering Research Center, University of California, Berkeley, California

[15] Priestley, M.J. N., Seible F. and Calvi, G.M., “Seismic Design and Retrofit of Bridges”, John Wiley & Sons, Inc, 1996.

[16] American Concrete Institute (ACI), “Building Code Requirements for Structural Concrete”, ASCE, USA, 1995.

Experimental Study of Liquefaction Resistance of Clayed Sands by Cyclic Direct Simple Shear

W. J. Chang[1], B. Y. Chou[2], P. S. Lin[2], C. C. Huang[1], and M. L. Hong[1]
[1]*Department of Civil Engineering, National Chi Nan University, Nantou, Taiwan*
[2]*Department of Civil Engineering, National Chung-Hsing University, Taichung, Taiwan*

Abstract

Fines content of sandy soil is one of the major factors affecting the liquefaction resistance of granular soils. Generally, nonplastic or low plasticity index silts are more common in land stratum and gain more interest in liquefaction research. However, Liquefaction of clayed sands was reported in offshore locations, near-shore reclaimed sites, and natural deposits. The binary packing model used in study the engineering properties of silty sands is implemented to study sands with kaolinite. Series stress-controlled, undrained cyclic direct simple shear tests were performed on reconstituted specimens with various clay contents and void ratios to systematically study the effect of clay content on liquefaction resistance. The results show that the minimum liquefaction resistance was observed for specimens with fine content around the transitional fines content (TFC) and the undrained cyclic behavior of clay-sand mixtures should be described as sand-controlled or fine-controlled soils for fines content less and greater than TFC, respectively. For soils with clay content less than TFC, the soil behaves similarly to clean sands and the liquefaction resistance decreases with increasing intergranular void ratio. Current results show that the concepts used in silty fines are valid for reconstituted clayed fines.

Keywords—*Clayed sands, Cyclic simple shear, Fines Content, Intergranular void ratio, Liquefaction resistance, Transitional fines content*

INTRODUCTION

The fines content, defined as the soil portion finer than No. 200 sieve (0.075 mm), of sandy soils has been recognized as one of the major factors affecting the liquefaction resistance of granular soils. According to [1], soils with fines are the most common soil type in observed liquefied sites. Natural liquefiable granular soils often contain certain amount of silty and clay fines. Generally, nonplastic or low plasticity silts are more common in land stratum and gain more interest in liquefaction research. However, sands mixed with 5 % to 15 % of clay particles (smaller than 0.002 mm), termed as clayed sands [2], are widespread in estuaries, tailings dam, and sometimes occur in offshore foundations. The USCS classifications of these soils are SC or double symbol soils (e.g., SP-ML, SP-CL). Liquefaction of clayed sands due to cyclic loading are reported in offshore sites [3] and near-shore reclaimed sites [4]. The liquefied site in Maoluo river during Chi-Chi earthquake contains significant portions of clay [5]. To properly evaluate the liquefaction resistance of clayed sands, the understanding of undrained behavior under cyclic loading is warranted.

From the point of liquefaction mechanism, the characteristics of volume change during shearing will directly affect the initiation of liquefaction. In undrained conditions, the changed volume will result in generation of excess pore water pressure. The generated excess pore pressure is the key factor in triggering the liquefaction and the subsequent phenomena. Significant volume change only occurs at intermediate to large strain levels, which is mainly governed by global void ratio and mean effective stress level. Therefore, void ratio has been considered as the major factor contributed to the normalized liquefaction resistance [6], represented as cyclic resistance ratio ($CSR = \tau / \sigma_v^{'}$, where τ is the cyclic shear stress induced by the earthquake and $\sigma_v^{'}$ is the vertical effective stress of the soil). In a clean granular soil consisted with coarse-grained particles only, the global void ratio could well represent the packing conditions of the coarse particles. However, in a coarse-fine mixture, the presence of fine grains can significantly influence the microstructure of the mixture and the shearing behavior.

The effect of the fines in a mixed soil depends on the grading of the coarse particles, the amount of fines, the mineralogy of the fines, and the distributions of fines with the mixture. Binary packing models have been implemented to describe the engineering properties of mixed soils consisted of coarse and fine particles [7] [8]. In these models, intergranular void ratio (e_s) and interfine void ratio (e_f) are used to describe coarse-grained dominated and fine-grained dominated soils, respectively. For coarse-fine mixtures with fines distributed within the voids formed by coarse grains, the mixture packing could be described by the intergranular void ratio defined as [7]:

$$e_s = (e + FC)/(1 - FC) \quad (1)$$

where e is the global void ratio, FC is soil portion finer than 0.075 mm by weight and expressed as decimal. For coarse-fine mixtures with high fines content and the coarse particles are dispersed without contact, the mixture packing is better described by interfine void ratio defined as:

$$e_f = e / FC \tag{2}$$

Reference [9] extended the ideal binary packing and proposed the contact density indices, which represent the intergranular contact conditions between coarse and fine particles, and developed a mixed-soil classification system based on the contact density indices as shown in Fig. 1. The specific fines content that translates the coarse-grained dominated to fine-grained dominated behavior is called transitional fines content (TFC) [1]. These void parameters have been implemented to depict the effect of silts on undrained shear strength [10] and cyclic resistance [9] of silty sands.

If clay fines are filled within the voids formed by sand particles instead of silt fines, as cases i to iii of Fig. 1, the mixed soil behavior is expected to change. The clay fines not only increase the plasticity index but also act as lubricator at sand contact [11]. The effect of PI on liquefaction resistance had been addressed by researchers (e.g. [12]). Reference [13] reviewed test data on undisturbed and reconstituted specimens of silt-clay mixtures and concluded that the clay fines increase the rate of pore pressure generation in low plasticity range due to reducing in hydraulic conductivity, resulting in reducing of cyclic resistance. However, the cyclic resistance increases for high plasticity mixtures because of the imparting of cohesion. Nevertheless, systematic study of clay-sand or clay-silt mixture is needed to clarify these confusions.

An experimental study was conducted to systematically study the cyclic liquefaction resistance of clayed sands. Clean sand is mixed with kaolinite to prepare reconstituted, clayed-sand specimens at various void ratios and clay contents. Series of stress-controlled, undrained, cyclic direct simple shear tests (CDSS) were performed to determine the cyclic liquefaction resistance under K_0 condition. Cyclic simple shear tests have been recognized as a better testing technique than cyclic triaxial tests in liquefaction study due to more close to the field conditions. The effect of clay contents on liquefaction resistance is study in view of various void parameters and pore pressure generation characteristics.

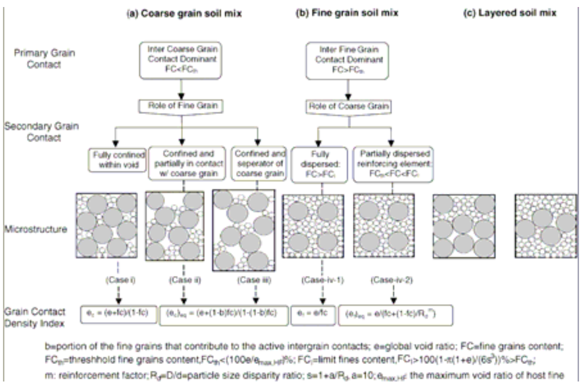

Fig. 1: Hypothesized coarse-fine mixtures packing structure [9]

Preliminary results are presented and compared with previous published results. The concept of interpreting liquefaction resistance of silty sands is adopted in clayed sands and is verified based on testing results. In addition, variation of stress-strain relationship and pore pressure generation characteristics due to the clay content is discussed.

TESTING PROGRAM

Cyclic Direct Simple Shear Apparatus

A NGI-type cyclic direct simple shear testing system manufactured by GCTS is used in this study, as shown in Fig. 2. The servo-controlled system includes two hydraulic actuators for the normal and shear loading and a pneumatic actuator for cell pressure applying. The three actuators are close-looped controlled by a Window-Based digital controller, which enables the system to be able to perform cyclic tests under various loading conditions, such as stress-controlled, strain-controlled, and specimen volume-controlled. The specimen and the normal and shear loading mechanisms are sealed in a pressure chamber, which allows applying the cell and back-pressure for saturation and consolidation. Similar system had been used to study pore pressure generation characteristics of silty sands [14]. To minimize the rocking error of the top plate due to lack of the complementary shear stresses on the vertical side of the specimen, the axial loading structure has been improved with highly reinforced supporting system. High-position, prestressed rollers slider are used in both normal and shear loading mechanisms to ensure constant frictions.

To ensure the accuracy of the system, crucial calibrations of all instrumental components have been performed. All the electronic sensors, including the normal and shear LVDTs and load cells, the volume change transducer, and the pressure transducer, are calibrated with standard sensors. To account for the friction of the roller sliders connected to the normal and shear loading mechanisms, both frictions have been measured under various displacement ranges and normal forces. The results show that a constant friction of 14 N and 5 N are observed in shear and normal loading

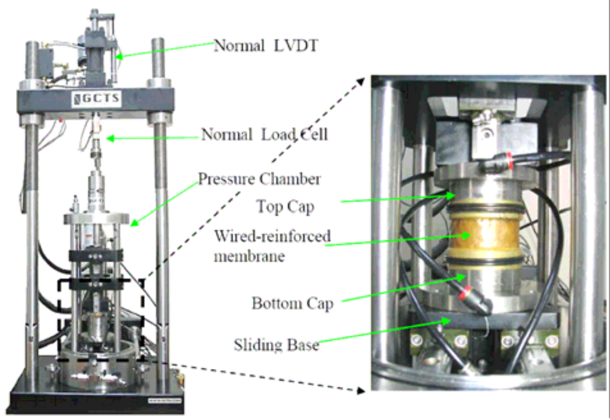

Fig. 2: Cyclic direct simple shear apparatus

mechanism, respectively. These values are used in the corrections of shear stress calculations and compensation of applied normal stress.

Both 100 mm and 71 mm diameter specimens are applicable for the GCTS CDSS. In this study, all specimens are 71 mm in outer diameter and approximate 30 mm in height. A NGI-type wire-reinforced latex membrane is used to confine the lateral deformation to mimic K_0 condition. The top and bottom surfaces contacted with the specimen are roughed to reduce sliding between the specimen and the contact surfaces. Circular porous stones are embedded in the center of the contact surfaces to provide drain paths for pore pressure measurement and back saturation.

Sample Preparation and Testing Conditions

Undrained cyclic behavior of clayed sands had been studied by researchers [2] [12]. In those studies, cyclic testing was conducted on reconstituted specimens with kaolinite added to clean sands. In this study, fine silica sand retained on #200-sieve is used as coarse grains and mixed with commercially available kaolinite. The sand is from Vietnam and has been used in liquefaction study in Taiwan for its consistent gradation control and easy purchasing [5]. The Vietnam sand is white in color and has a specific gravity of 2.65, maximum void ratio of 0.92, and minimum void ratio of 0.61. The USCS classification of the Vietnam sand is poor-graded sand (SP). The kaolinite is also white in color and has a specific gravity of 2.61, liquid limit of 49 %, and plasticity index of 19 %. The USCS classification of the kaolinite is clayed silts with slight plasticity (ML). The grain size distributions of the Vietnam sand and kaolinite are shown in Fig. 3. The USCS classifications for fines content of 5, 15, and 35 % are SP, SM, and SM-SC, respectively.

Different specimen preparation procedures will produce different soil fabric resulting in different cyclic resistance [15] [16]. To prepare specimens with homogeneously-distributed fines at specific void ratios, various specimen preparation procedures have been considered. Although water sedimentation procedure [16] and the slurry deposition method [7] are generally considered to be more close to natural deposition mode, wet tamping procedure was selected to avoid particle segregation, which should be more significant in clay-sand mixtures.

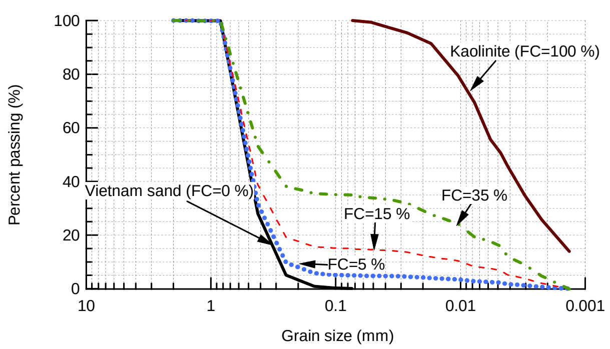

Fig. 3: Grain size distributions of all specimens for CDSS

Weighted oven-dried sands and kaolinites are mixed with 5 % water then they are divided into two equally weighted portions. The first half is placed into the wired-reinforced membrane fixed on the bottom cap and tamped to half of the specimen height (15 mm) then the second half is placed and tamped to full height of the specimen (30 mm). Because the height and diameter of all specimens are the same, the void ratio and fines content of specimens can be controlled by varying the weights of the sand and kaolinite portions.

The tamped specimens are fixed on the sliding base with the top cap tightened with the membrane, as shown in Fig. 2. De-aired water is flushed into the specimen from the bottom with 10 kPa vacuum pressure applied at top cap. Then, a back pressure of 95 kPa and cell pressure of 100 kPa is applied in 20 kPa increments and maintained for at least 30 minutes. The saturation is verified by the B-value test and a specimen with B-value greater then 0.95 is considered saturated. The saturated specimens are consolidated by applying 150 kPa vertical effective stress ($\sigma_v^{'}$). Because the wired-reinforced membrane will constrain the lateral deformation of the specimen, a K_0-consolidation is achieved. During the consolidation, the volume change and the height of the specimen are monitored. The consolidation is finished if no volume change is observed in 30 minutes and the height of the specimen is recorded to compute the consolidated void ratio.

To determine the undrained cyclic resistance of the specimens under K_0 conditions, which represent the undrained behavior of a soil element subjected to upward propagating shear waves, consolidated specimens are subjected to constant-amplitude, sinusoidal shear stress with a constant vertical stress and loading frequency of 0.1 Hz. The combination of wired-reinforced membrane, constant vertical stress, and constant volume condition will somewhat maintain the K_0 conditions during cyclic loading [17]. The cyclic shearing was terminated when initial liquefaction was achieved. The initial liquefaction is defined as excess pore pressure ratio ($r_u = \Delta u / \sigma_v^{'}$, Δu = excess pore pressure) exceeding 0.9 [14] or the double strain amplitude (DA) greater than 6 % [16].

Testing Program

The testing program consists of 4 testing series with 0, 5, 15, and 35 % of kaolinite by weight. The fine content values are selected to compare with empirical correlation of cyclic resistance with corrected SPT-N values [18]. In each testing series, specimens are prepared to void ratios of 0.8, 0.75, and 0.7 to study the variations of void parameters. For a specific fine content at the same void ratio, at least 3 specimens were prepared and tested under different stress amplitudes. The sampling rate for all sensors is 20 Hz per channel. There are 11 specimens for clean sand and 9 specimens for other three series.

RESULTS AND DISCUSSIONS

Testing Results

The time histories of the shear stress, shear strain, excess pore pressure ratio are calculated from recorded shear forces, shear strains and pore pressure, respectively. Typical time history results for a clean sand specimen are shown in Fig. 4. The cyclic stress ratios and the corresponding number of cycles to liquefaction are used to construct the cyclic resistance curve as shown in Fig. 5. The cyclic stress ratio corresponding to liquefaction at 15 loading cycles is defined as cyclic resistance ratio (CRR) for earthquakes with magnitude of 7.5 [18].

In Fig. 5, all the testing results are grouped by same global void ratio. The global void ratio, intergranular void ratio, and interfine void ratio of each consolidated specimen are computed according to the consolidated specimen height and equation (1) and (2). The applied cyclic stress ratios and the number of cycles to induce excess pore pressure of 0.9 and double strain amplitude of 6 % are determined separately. The results show that the sample preparation procedure produced consistent specimens to designated void ratios and the testing system performed very well in stress control and data recording.

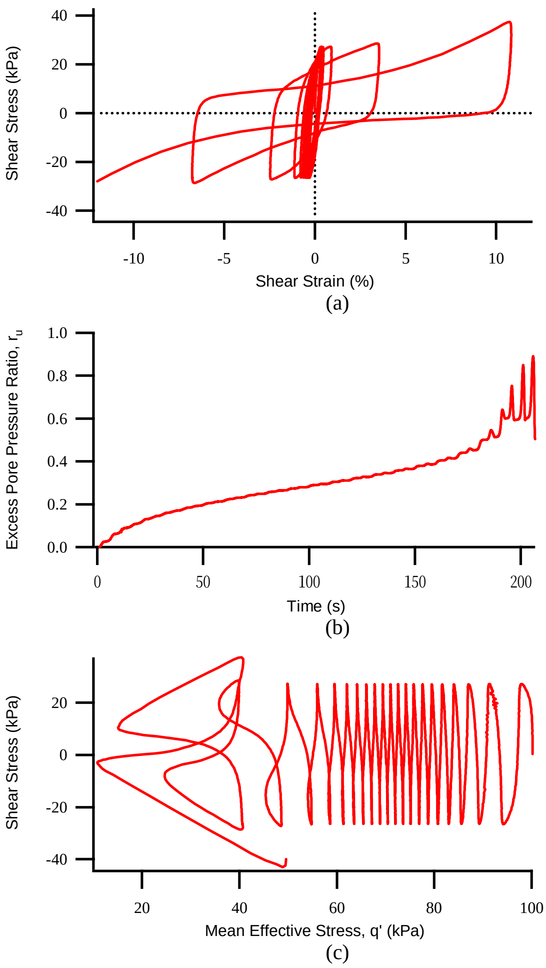

Fig. 4: Typical testing results for clean sands: (a) Hysteretic loops, (b) Time histories, and (c) Stress path

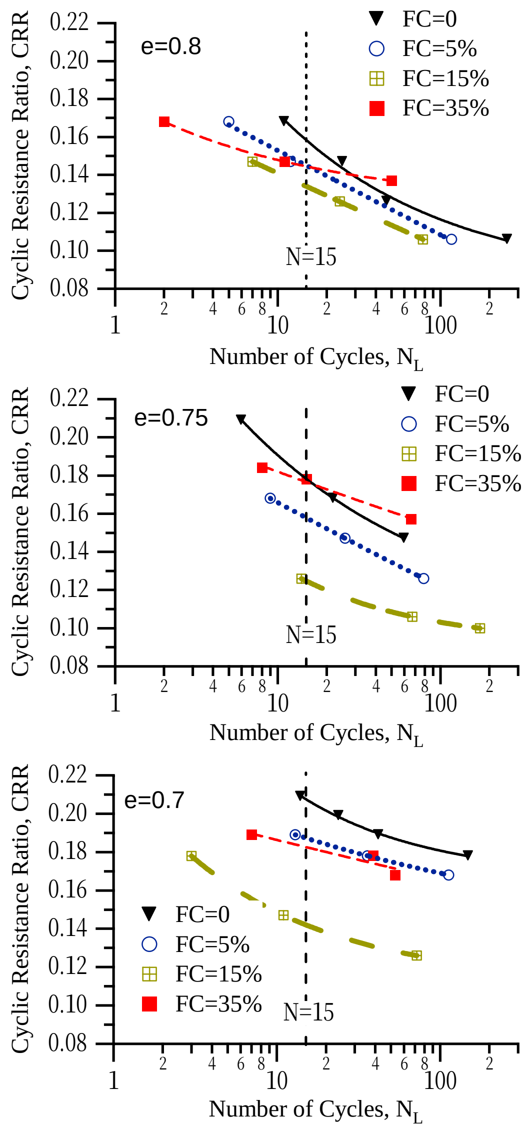

Fig. 5: Cyclic resistance curves from CDSS

Effect of Liquefaction Criteria

The definitions of liquefaction for clean sands under undrained cyclic shearing have been customary considered as the state that the excess pore pressure ratio reaches 100 % or sizeable amount of induced strain [16]. In sands with fines, the buildup of excess pore pressure ratio is only up to 90 to 95% [16] when significant strain is induced. In this study, both the 90 % of excess pore pressure ratio and 6 % of shear strain amplitude are used as termination criteria in undrained CDSS testing. The cyclic stress ratios and loading cycles to reach the two criteria at void ratio of 0.8 but different clay contents are shown in Fig. 6. For specimens with clay contents of 0, 5, and 15%, both criteria can be reached, however, for specimens with clay content of 35 %, only double amplitude of 6 % is developed. The variations of CRRs defined by both criteria for clayed sands with clay content less than 15 % are less than 3 % at N=15, which agree

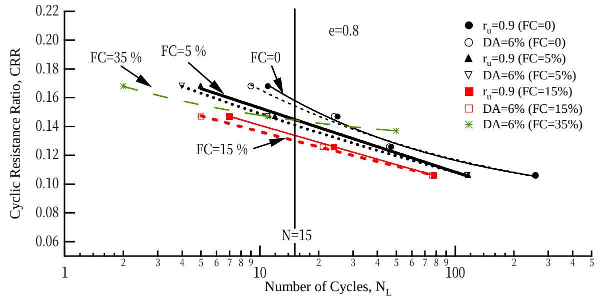

Fig. 6: Comparisons of different liquefaction criteria (e=0.8)

with the results form clean sands. In addition, the fail of generating high excess pore pressure ratios for clay contents of 35 % implies a different failure mechanism between specimens with different clay contents. The following discussions will support this point.

Hysteretic Loops and Pore Pressure Generation

To demonstrate the effects of clay contents on stress-strain relationship and pore pressure generation, hysteretic loops and the time histories of pore pressure generation of clean sand and sands with 35 % kaolinite are shown in Fig. 7(a) and 7(b), respectively. For clean sand specimens, constantly fixed shear strain amplitude without accumulation of strain is observed for excess pore pressure ratio less than 0.5. After that, the shear strain amplitude and excess pore pressure ratio rapidly increase and both criteria for initiation of liquefaction occur in the next couple cycles. Similar behaviors had been observed for clay contents of 5 and 15%. Collapsed failure mechanism is dominating for sands with clay content less than 15 %.

For the specimen with 35 % kaolinite, constant strain amplitude was observed for excess pore pressure less than 0.5, whereas different characteristics of strain development and excess pore pressure generation were shown after that point. The excess pore pressure continually increases in a constant rate accompanied with progressive accumulation of shear strain. The excess pore pressure ratio corresponding to double strain amplitude of 6 % is only 0.7 instead of 0.9. In other words, for clayed sands with high clay contents, stiffness softening due to generation of excess pore pressure is more dominating than in clean sands. The observations of the stress-strain relationships and pore pressure generation patterns for sands with various fine contents reveal that the clayed fines not only affect the cyclic resistance but also affect the shearing characteristics and the subsequent failure mechanism.

Cyclic Resistance of Various Void Parameters

The relationships between the cyclic resistance ratio, void parameters, and fine contents are shown in Fig. 8. The results show that the CRR decreases as the global void ratio increases for sands with same fines content except for FC=15 %. The trend also exists for both intergranular and interfine void ratios. The inconsistence

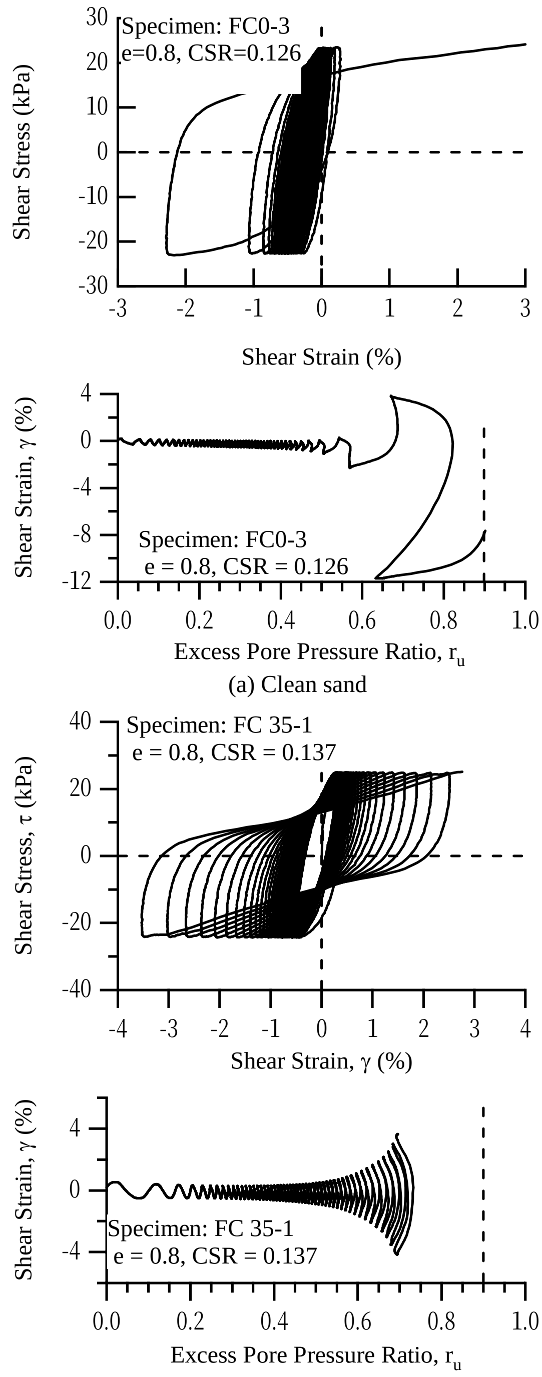

Fig. 7: Hysteretic loops and pore pressure variation for same void ratio specimen (a) clean sand and (b) FC=35 %

at FC=15 % is due to transition from coarse grain soil mix to fine grain soil mix as shown in Fig. 1. At the proximity of this fines content, the overall contact of coarse grains is the smallest resulting in the smallest cyclic resistance. Greater than this fines content, the fine grains start to dominate the shearing behavior. The fines content corresponding to the smallest CRR is call transitional fines content (TFC) [9]. Descriptions of the cyclic resistance of mixed soils should be separated as two distinct groups, sands-controlled and fines-controlled soils,

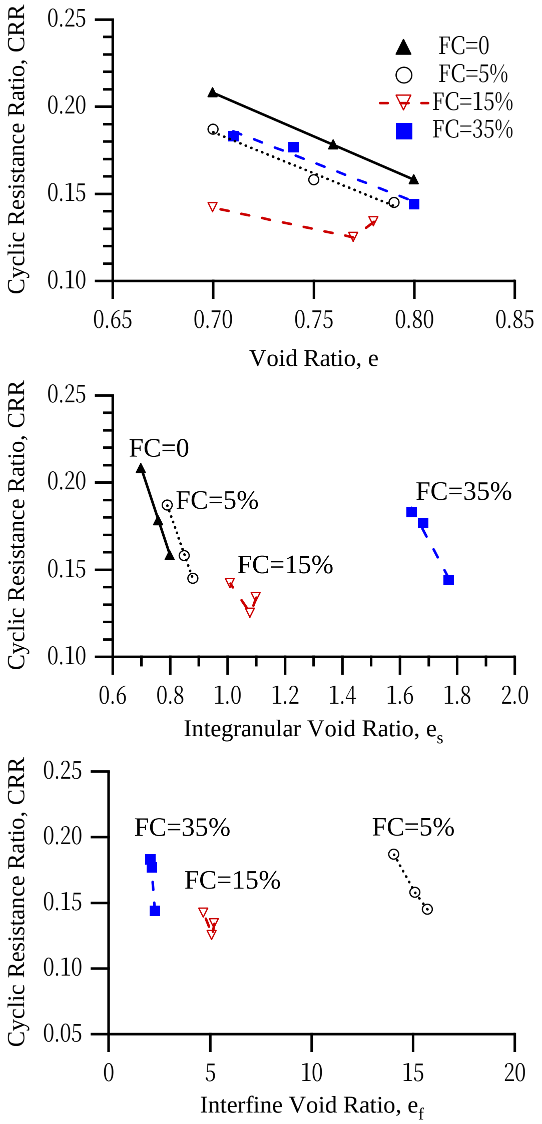

Fig. 8: Cyclic resistance of different void parameters: (a) void ratio (b) intergranular void ratio, and (c) interfine void ratio

according to the fines content and the TFC of the mixtures. For a sand-controlled mixture (i.e., FC<TFC), void parameters that describes the packing conditions of the coarse grains will be more appropriate. In contrast, for a fines-controlled mixture (i.e, FC>TFC), void parameters that describe the packing of fine grains should be used. The different shearing behaviors described in Fig. 7 also reflect this point.

The variations of cyclic resistance ratio with fines content at same void ratio are shown in Fig. 9, along with data by Polito and Martin [19] for comparison. For a specific void ratio, no monotonic relationship exists between the cyclic resistance and fines content in clay-sand mixtures, which occurs in silty sands as well. For specimens with fines content less than TFC (i.e., FC=15 % in current study), the cyclic resistance ratio decreases with increasing of fines content. The trend reverses as the fines content greater than 15 %. This tend

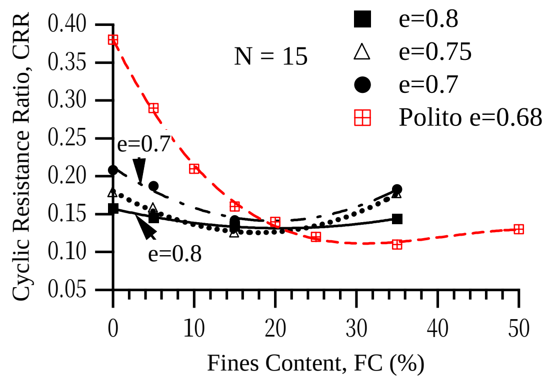

Fig. 9: Variations of cyclic resistance with fines content for same void ratio

agrees with data by Polito and Martin but the fines content corresponding to the minimum CRR is different. The discrepancy could be possibly due to the difference in particle characteristics of the coarse grains and fines.

Alternatively, intergranular void ratio is used as the constant property to correlate the CRR and fines content and the result is shown in Fig. 10. Again, data from silty sand by Polito and Martin are shown for comparisons. Although only limited data are available in current study, the increasing of CRR with increasing of fines for sands with FC less than TFC is observed and the result agrees with data from silty sands. The linearly proportional relationship implies that the CRR increment contributed by the fines can be determined and the rate of increment should be related with the shearing resistance of fines. Comparisons of the rate of increment between the clayed sands and silty sands show that the clayed fines provide smaller cyclic resistance increment than the silty fines at same fines content. Ongoing research focusing on the comparisons of rate of CRR increment between silty and clayed fines will provide more evidences.

SUMMARY AND CONCLUSIONS

Series of undrained, cyclic direct simple shear tests were performed to systematically study the effects of clayed fines upon cyclic resistance of clayed sands. All tests were conducted on reconstituted specimens prepared

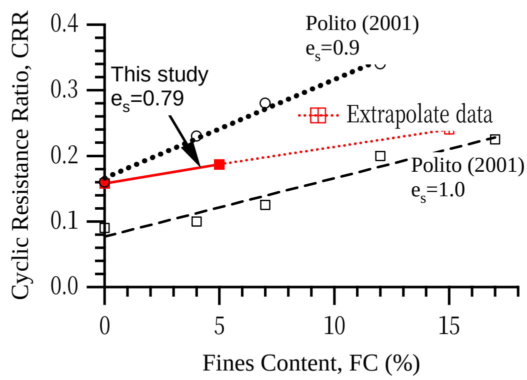

Fig. 10: Variation of cyclic resistance with fines content for same intergranular void ratio

by wet tamping method and consisting with a clean sand mixed with different percentage of kaolinite. Stress-controlled, CDSS testes were performed under K_0 conditions. Different void parameters were used to correlate with the cyclic resistance and the fines content. The testing results and findings are summarized as following:

1) The minimum cyclic resistance exits at the transitional fines content (TFC). Depending on the FC and TFC, clay-sand mixtures can be divided into sands-controlled soils and fines-controlled soils. For fines content less than the TFC, the pore pressure generation pattern and mechanism of liquefaction initiation of the mixed soil are similar to the clean sand. For fines content greater than the TFC, stiffness softening due to generation of the excess pore pressure and progressive accumulation of shear strain is the major failure mechanism during undrained cyclic shearing process.

2) The difference between the cyclic resistances defined by excess pore pressure ratio of 0.9 and double shear strain amplitude of 6 % is less than 3 % for sands-controlled clay-sand mixtures, which agrees with results from clean sands. However, for fines-controlled mixtures, only shear strain criteria can be reached.

3) Similar to data from silty sands, no monotonic relationship exists between the cyclic resistance and fines content in clayed sands at same void ratio. However, a monotonic decreasing relationship exists between CRR and fines content for clayed sands with fine content less than TFC.

4) A linearly proportional relationship exists between cyclic resistance ratio and fines content at same intergranular void ratio. The CRR increment contributed by fine grains can be determined based on the linear proportionality by subtracting the CRR corresponding to the fines content with CRR of the clean sand. From this point of view, using the intergranular void ratio as the packing parameters is in favor for clayed sands.

5) The rate of CRR increment contributed by fine grains should be related to the shear resistance of fines filled within the intergranular voids. Comparisons of the rate of increment between the clayed sands and silty sands show that the clayed fines provide smaller cyclic resistance than the silty fines.

ACKNOWLEDGMENTS

Financial support was provided by the National Science Council of ROC under grants NSC 92-2211-E-260-005 and NSC 93-2211-E-260-006. These supports are gratefully acknowledged.

REFERENCES

[1] Lade, P. V. and Yamamuro, J. A., "Effects of non-plastic fines on static liquefaction of sands," Can. Geotech. Journal, Vol. 34, No. 6, pp. 918–28, 1997.

[2] Georgiannou, V. N., Hight, D. W., and Burland, J. B., "Behaviour of clayed sands under undrained cyclic triaxial loading," *Geotechnique*, Vol. 41, No. 3, pp. 383-393, 1991.

[3] Tjelta, T. I., Skotheim, A. A., and Svano, G., "Foundation design for deepwater gravity base structure with long skirt on soft soils," *Proc. Int. Conf. Behaviour of Offshore Structures, Trondheim*. Vol. 1, pp. 173-192, 1988.

[4] Ishihara, K., Shimizu, K., and Yamada, Y., "Pore water pressure measured in sand deposits during an earthquake," Soils and Foundations, No. 4, pp. 85-100, 1981.

[5] Ueng, T.-S., Sun, C. –W., and Chen, C. –W., "Definition of fines and liquefaction resistance of Maoluo River soil," *Soil Dynamics and Earthquake Engineering*, Vol. 24, No. 9-10, pp. 745-750, 2004.

[6] Seed, H. B., "Soil liquefaction and cyclic mobility evaluation for level ground during earthquakes," *Journal of the Geotechnical Engineering Division*, ASCE, Vol. 105, No. GT2, pp. 201-255, 1979.

[7] Kuerbis, R. H., Negussey, D., and Vaid, Y. P. "Effect of gradation and fines content on the undrained response of sand," *Geotechnical Special Publication No. 21*, ASCE, pp. 330-345, 1988.

[8] Yang, S., Lacasse, S., and Forsberg, C.F., "Application of packing models on geophysical property of sediments," *Proc. ICSMGE'16*, Osaka, Japan, pp. 869-874, 2005.

[9] Thevanayagam, S. and Martin, G.R., "Liquefaction in silty soils screening and remediation issues," *Soil Dynamics and Earthquake Engineering*, Vol. 22, No. 9-12, pp.1035-1042, 2002.

[10] Thevanayagam, S., "Effect of fines and confining stress on undrained shear strength of silty sands," *J. of Geotech. and Geoenviron.l Eng.,* ASCE, Vol. 124, No. 6, pp. 479-491, 1998.

[11] Mitchell, J.K. and Soga, K., *Fundamentals of Soil Behavior*, 3rd ed., NJ: John Wiley & Sons, 2003, 577 pp.

[12] Ishihara, K. and Koseki, J., ''Cyclic shear strength of fines-containing sands,'' *Earthquake and Geotech. Engrg.*, Japanese Society of Soil Mechanics and Foundation Engineering, Tokyo, pp. 101–106, 1989.

[13] Guo, T. and Prakash, S., "Liquefaction of silts and silt-clay mixtures," *Journal of Geotechnical and Geoenvironmental Engineering*, ASCE, Vol. 125, No. 8, pp. 706-710, 1999.

[14] Hazirbaba, K., "Pore pressure generation characteristics of sands and silty sands：A strain approach," Ph.D. Dissertation, The University of Texas at Austin, 2005.

[15] Mulilis, J. P., Seed, H. B., Chan, C. K., Mitchell, J K., and Arulanadan, K., "Effects of sample preparation on sand liquefaction," *Journal of the Geotechnical Engineering Division*, ASCE, Vol. 103, No. GT2, pp. 91-108, 1977.

[16] Ishihara, K. *Soil Behaviour in Earthquake Geotechnics*, Clarendon Press: Oxford, 1996, 350 pp

[17] Kammerer, A. M., "Undrained response of Monterey 0/30 sand under multidirectional cyclic simple shear loading conditions," Ph.D. Dissertation, The University of California, Berkeley, 2002.

[18] Seed, H. B., Tokimatsu, K., Hader, L. F., and Chung, R. M., "Influence of SPT procedures in soil liquefaction resistance evaluations," *Journal of Geotechnical Engineering*, ASCE, Vol. 111, No. 12, pp. 1425-1444, 1985.

[19] Polito, C. P., and Martin, J. R., "Effects of non-plastic fines on the liquefaction resistance of sands," *Journal of Geotechnical and Geoenvironmental Engineering*, ASCE, Vol. 127, No. 5, pp. 408-415, 2001.

Liquefaction Strength Of Sands Containing Fines Compared With Cone Resistance In Triaxial Specimens

Takaji Kokusho, Tadashi Hara, Keita Murahata
Department of Faculty of Science and Engineering, University of Chuo, Tokyo, Japan

Abstract
Innovative miniature cone penetration tests and subsequent cyclic triaxial tests were carried out on sand specimens containing fines both in the undrained conditions. It has been found that one unique curve relating cone resistance and liquefaction strength can be established, irrespective of relative density and fines content. This indicates that liquefaction strength corresponding to a given cone resistance is constant despite the difference in fines content, which differs from the current liquefaction evaluation practice. In order to examine the effect of sustained consolidation on the relationship between penetration resistance and liquefaction strength, samples were consolidated for variable lengths of time up to a week. The results from the tests on the sustained consolidation specimens plotted a little shifted above the unique curve obtained from thetests on the normal consolidation specimens. This may indicate that, if in situ consolidation effect is considered, liquefaction strength for the same cone resistance tends to increase with increasing fines content.

Keywords—*Liquefaction, Fine contents, Cone Resistance, Cyclic triaxial tests*

INTRODUCTION

Liquefaction strength is evaluated using penetration resistance of Standard Penetration Tests (SPT) or cone penetration tests (CPT) in engineering practice. If sand contains a measurable amount of fines, liquefaction strength is normally raised in accordance to fines content in most of liquefaction evaluation methods, such as the road bridge design code using SPT *N*-values [1]. In the case of CPT, Suzuki et al. (1995) carried out in situ penetration tests and soil samplings by in situ freezing technique from the same soil deposits and compared the tip resistance q_t-value and liquefaction strength from lab tests [2]. The comparison showed that the higher fines content tends to increase the liquefaction strength for the same penetration resistance. In contrast to their finding, however, quite a few laboratory tests show that liquefaction strength clearly decreases with increasing content of low plasticity fines having the same relative density (e.g. [3], [4], [5], [6]). Thus, a wide gap seems to remain between the current practice for liquefaction potential evaluation and the laboratory experiment on the modification of the liquefaction strength in sands containing fines despite its importance in engineering design.

In establishing empirical correlations between penetration resistance and liquefaction strength, calibration chamber tests are sometimes carried out to develop relationships between the penetration resistance and relative density at first and then, liquefaction tests are separately conducted for the same sand reconstituted in the same way as in the chamber tests (e.g. [7]). On the other hand, in situ penetration tests are combined with laboratory liquefaction tests on intact samples recovered from the same ground [2]. In both experimental methods, the soils tested in the penetration test and in the liquefaction test are not exactly the same and may change due to heterogeneity of in situ soils or other reasons.

In order to establish more direct correlations between cone resistance and liquefaction strength considering the effect of fines, a systematic experimental study was undertaken, in which a miniature cone penetration test and subsequent cyclic loading test were carried out on the same triaxial test specimen. An innovative simple mechanism was introduced in a normal cyclic triaxial apparatus enabling a miniature cone to penetrate the sand specimen at a constant speed. Results from the two serial tests on the same specimen are compared to develop direct correlations between penetration resistance and liquefaction strength for sands containing various amount of fines.

TEST APPARUTUS AND TEST PROCEDURES

In a triaxial apparatus used in this research, the specimen size is 100 mm diameter and 200 mm height. In liquefaction tests, the soil specimen can be loaded cyclically by a pneumatic actuator from above as a stress-controlled test. In order to carry out a cone penetration test in the same specimen prior to undrained cyclic loading, a metal pedestal below the soil specimen was modified as shown in Fig.1, so that a miniature cone can penetrate into the specimen from below. For that goal, the pedestal consists of two parts, a fixed circular base to which the cone rod is fixed and a movable metal cap, through the center of which the cone rod penetrates in the upward direction into the overlying specimen. The annulus between the two parts is sealed by O-rings, enabling the cap to slide up and down by water pressure supplied into a water reservoir in between the two parts.

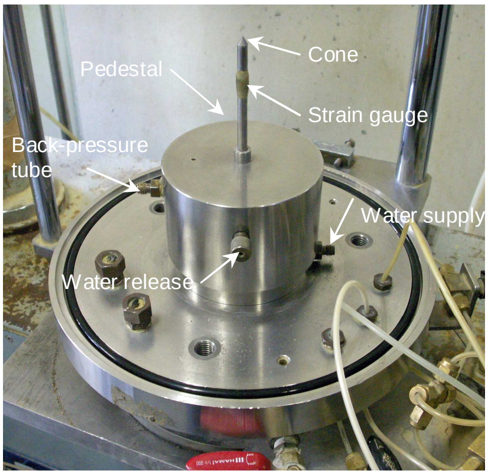

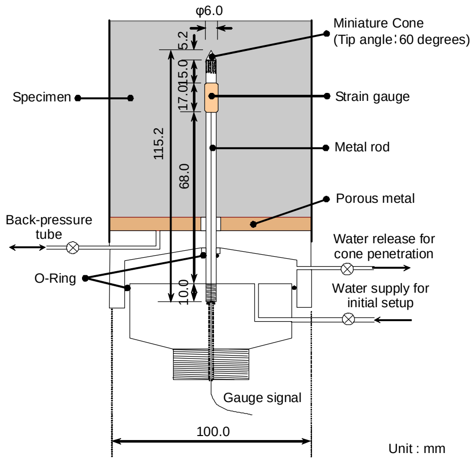

Fig. 1: Photograph (left) and cross-section (right) of the modified pedestal (in the lower part of the triaxial apparatus)

During the test, the pedestal cap is initially set up at the highest level by supplying water inside, and specimen is constructed on it. In this stage, the cone already projects into soil specimen by 47 mm. By opening a valve at the start of the cone penetration, the water in the reservoir is drained by the chamber pressure, resulting in settlement of a total body of the specimen together with the disc and piston at the top and realizing the relative upward penetration of the cone by 25 mm. The penetration rate is almost constant, though it is much slower than prototype CPT tests.

The miniature cone is 6 mm diameter, 6 mm height and 60 degrees tip angle, about1/35 smaller in the cross-sectional area than the 10 cm^2 prototype cone normally used in engineering practice. The strain gauges are glued at the top part of the rod, 20 mm lower than the foot of the cone, meaning that the measured vertical load includes not only the tip resistance but also the skin friction at the top portion of the rod. Though the separation of the tip load is actually needed, the total load is considered as the cone resistance (denoted here by q_c) in the present study because the contribution of the skin friction seems to be considerably smaller than the tip load.

In the test sequence, the penetration test was first carried out after consolidating the specimen. Then, after releasing pore pressure and reconsolidating it under the same confining pressure, the same specimen was cyclically loaded in undrained condition. The cone penetration was basically carried out under the undained condition in the triaxial specimen, though a few drained penetration tests was also conducted to be compared as will be explained later. In undrained conditions, the pore pressure of the specimen was also measured by the electric piezometer in the same way as in normal undrained triaxial tests.

In Fig.2, relationships between penetration lengths versus elapsed time obtained during preliminary tests by Toyoura sands of different densities are shown. The penetration rate is about 1 mm per second, much slower than prototype CPT, and is almost constant despite the difference in relative density of the sand specimen D_r =20 to 49%.

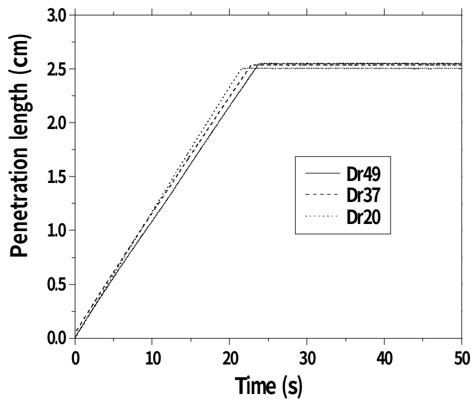

Fig.2: Penetration length versus time relationships for the miniature CPT in triaxial specimens under undrained condition

The cyclic axial load of a sinusoidal wave was applied with the frequency of 0.1 Hz. The cell pressure and the pore-water pressure were measured with electric piezometers with the maximum capacity of 490 kPa and the axial deformation is measured with LVDT of 100 mm maximum capacity outside the pressure chamber.

It may well be suspected that, in such a test sequence, the liquefaction strength is possibly influenced by the preceding cone test and subsequent reconsolidation. In order to examine the influence of the test sequences, preliminary comparative tests were conducted in which results by normal liquefaction tests in the same triaxial apparatus without the cone rod were compared with those in this test sequence. Specimens of Toyoura sand with the relative density of around 40-50% were prepared by wet tamping and tested. Fig.3 shows the comparison of the results with or without the cone, indicating no clear difference between the two corresponding best-fit curves (the solid curve with cone and the dashed curve without

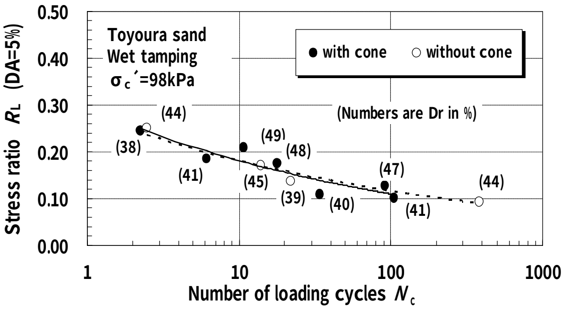

Fig.3: Comparison of liquefaction strength (R_L versus N_c curve) between specimens with or without cone rod

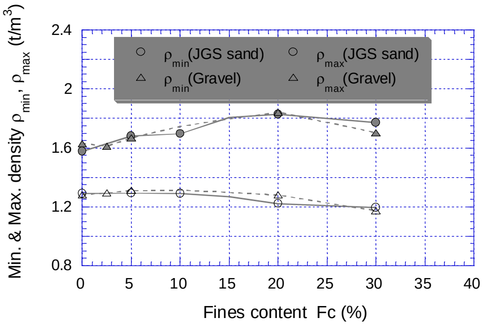

Fig.4: Minimum and maximum density of the sand with different fines content

cone) correlating stress ratios R_L and number of loading cycles N_c reaching 5% double amplitude strain.

The same river sand consisting of sub-round particles of hard quality as used in another research by the same authors [6] was used in this test. Fines mixed with the sand is silty and clayey soils with low plasticity index of $I_p \simeq 6$ sieved from decomposed granite in reclaimed ground of the Kobe city, Japan. Soil specimens of 100 mm diameter and 200 mm height were prepared by wet tamping method to meet prescribed relative densities as close as possible. The specimen was fully saturated by using CO_2-gas and de-aired water so that the Skempton's B-value larger than 0.95 was measured, and isotropically consolidated to an effective stress of 98 kPa with the back-pressure of 196 kPa.

In the test, relative density D_r and fines content F_c of the specimens were parametrically changed to investigate their effects on penetration resistance and undrained cyclic strength. The minimum and maximum densities, ρ_{dmin} and ρ_{dmax}, of the sands containing fines necessary for evaluating relative densities were determined by a method standardized by the Japanese Geotechnical Society [8] and also by a method for gravelly soils currently under standardization in JGS [9]. In Fig.4, the variations of ρ_{dmin} and ρ_{dmax} are plotted versus the fines content. Note that the densities both increase and then decrease with increasing Fc. A threshold fines content may be estimated as around F_c =20~30%, at which the voids of sands are completely filled with fines and the soil structure changes from a sand skeleton supporting type to a fines matrix supporting type. The density change in

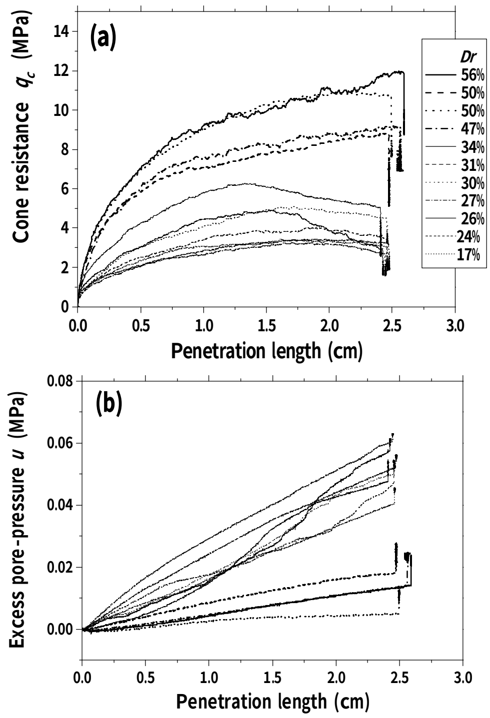

Fig.5: Cone resistance (a) or excess pore-pressure (b) versus penetration length for river sand specimens with different densities

Fig.4 is likely to reflect such a change of soil structure with increasing F_c.

PENETRATION TESTS

Clean River Sand with different densities

First, a series of miniature cone penetration tests were conducted on the clean river sand under undrained conditions having loose or medium density. Figs.5 (a) and (b) show variations in cone resistance q_c and excess pore-pressure u , respectively, along with the penetration length. As maybe observed higher q_c-values and lower positive pore-pressures are measured for the denser sands. The cone resistance tends to monotonically increase and asymptotically converges to an ultimate value, but in some cases, starts to decrease after the peak values. In contrast, the pore-pressure tends to increase in the positive direction, almost linearly with the penetration length in all cases. The pore pressure increases up to 60 to 5% of the initial effective confining stress for D_r ≈20 to 50%, respectively, presumably resulting in slightly lower penetration resistance than a completely drained condition.

River Sand with Different Fines Content

In Figs.6 (a) and (b), variations in cone resistance q_c and excess pore-pressure u are shown as a function of the penetration length for specimens of D_r ≈50% with different fines content of F_c.=0~30%. The increase in fines content tends to develop larger pore-pressure increase and reduce penetration resistance during penetration. The effect of fines content is pronounced

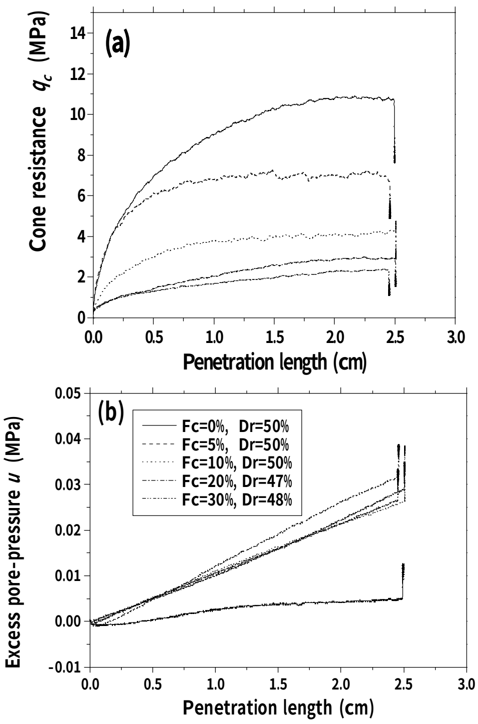

Fig.6: Cone resistance (a) or excess pore-pressure (b) versus penetration length for river sand specimens of D_r≈50% with different fines content

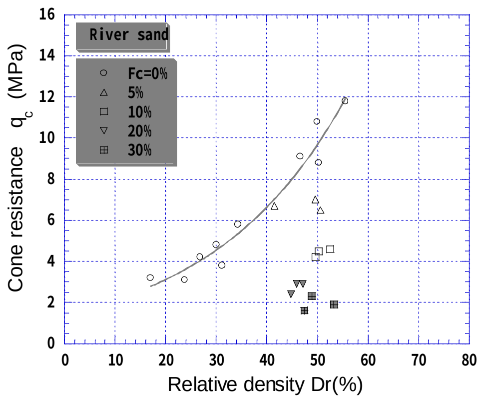

Fig.7: Cone resistance versus relative density for river sand with different fines content

even at a small value of F_c =5% particularly on the pore-pressure build-up and tends to asymptotically converges as it approaches to F_c =30%. The sand behavior due to cone penetration probably reflects the change of the soil structure due to increasing fines content as explained before on the Fc-dependent variations of the minimum and maximum densities.

Penetration Resistance versus Relative density

The cone penetration resistance q_c to be correlated with relative density or other design parameters such as liquefaction strength should be represented by the value attained after the cone has penetrated a sufficient length at a constant rate. As shown in Fig.5 (a) or Fig.6 (a), the penetration resistance tends to asymptotically converge to an ultimate value in the majority of the cases. However, in some other cases, it still increases during 25 mm penetration, or starts to decrease after a peak value. In the former case, the maximum value during 25 mm penetration was taken, while, in the latter case, the average in the last part of the resistance versus penetration length curve was taken as a representative q_c-value.

In Fig.7, q_c-values evaluated in this manner are plotted versus corresponding relative densities D_r of the specimens. For the clean sand without fines, the plots concentrate along a solid curve on the chart, while the q_c-values of fines-containing sand are obviously lower and decrease with increasing fines content for the same relative density of D_r ≈50%, indicating the dominant effect of fines on cone resistance.

PENETRATION RESISTANCE VERSUS LIQUEFACTION STRENGTH

Figs.8 (a) ~ (e) show relationships on log-log charts between stress ratios R_L and number of loading cycles N_c for 5% double amplitude axial strain obtained by the series of undrained cyclic loading tests on sand specimens having D_r ≈ 50% with fines content, F_c = 0, 5, 10, 20 and 30%, respectively. The filled circles on the charts are the results from undrained cyclic loading tests conducted on the same test specimens after the cone penetration tests, while the open circles are those without preceding cone tests, demonstrating again that the history of prior cone penetration is unlikely to significantly affect the liquefaction strength subsequently tested (The relative density actually increased only by 2% on average between the initial consolidation and the reconsolidation). The plotted data points can be approximated by the straight lines on the log-log charts with relatively high regression coefficients *rc* as indicated in the charts. By comparing the stress ratios R_L for double amplitude strain, ε_{DA}, equal to 5%, the R_L -value evidently decreases with increasing fines content.

In order to correlate penetration resistances to corresponding liquefaction strengths
for the soil specimens with different F_c, the stress ratio R_L for ε_{DA}=5% in N_c=20 are estimated from the line regressed through the filled circles. In Fig.9 (a), the liquefaction strengths R_L thus obtained are plotted on the vertical axis versus cone resistances q_c on the horizontal axis. The data points concentrate in a narrow area which may be represented by a single straight line drawn in the chart (the regression coefficient =0.95). As maybe observed, a unique relationship between R and q_c exists despite the large differences in relative density or fines content. This finding seems quite contradictory to the present state of practice in which liquefaction strength corresponding to a given CPT resistance is increased by a certain amount according to increasing fines content.

In Fig.9 (b) the same test results are plotted again to compare with field investigation data obtained by Suzuki et al. (1995) combining prototype cone tests in situ and undrained cyclic triaxial tests on intact samples recovered

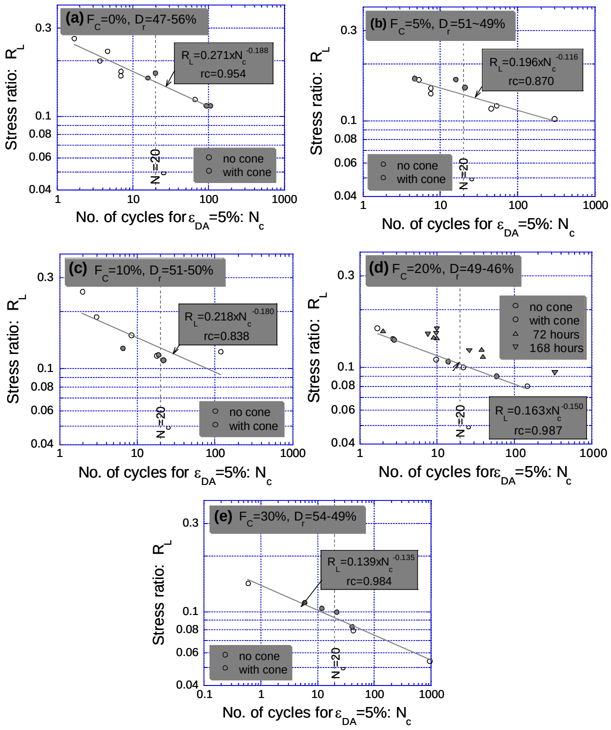

Fig.8: Liquefaction strengths for sands of $D_r \approx 50\%$ with fines content, F_c, (a) 0%, (b) 5%, (c) 10%, (d) 20% and (e) 30%.

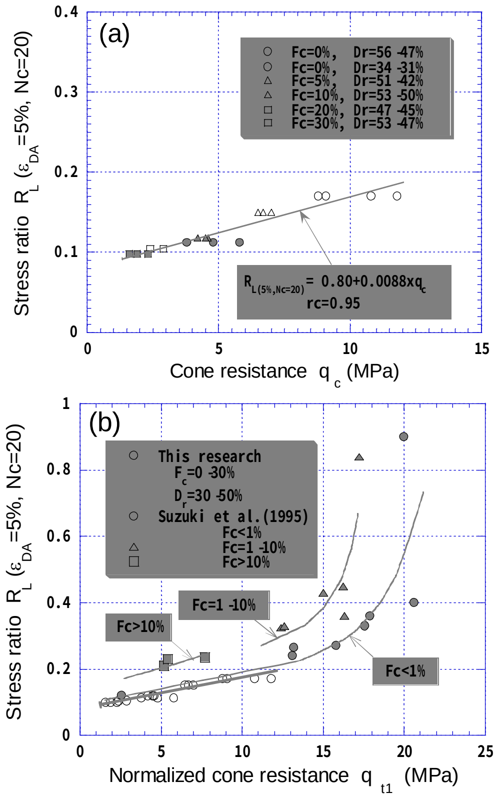

Fig.9: Direct relationship between stress ratios for liquefaction (DA 5%, N_c=20) and cone resistances for sands of $D_r \approx 50\sim30\%$ with fines content, F_c=0~30%

from the same soil deposits by in situ freezing technique. On the horizontal axis, q_{t1} is taken in place of q_c, to normalize in situ cone tip resistance q_t as, where the vertical overburden stress and $q_{t1} = q_c$ is assumed for the present study. Needless to say, considerable differences exist between the miniature cone tests conducted here and prototype tests in terms of cone size, penetration rate, drainage condition, consolidation effects, etc. Nevertheless, the correlation by the present research is in surprisingly good agreement both qualitatively and quantitatively with in situ data for F_c <1% in the interval of $q_{t1} \approx 0\sim12$. It should be noted however that the cone resistance looks quite insensitive to fines content in the present study whereas the in situ data indicate its clear influence. In order to examine the contradiction between the two experimental studies more closely, the effects of long-time consolidation and drainage during cone penetration were further investigated in the present test series.

EFFECT OF SUSTAINED CONSOLIDATION

In the test series, the consolidation sustained about 1 hour before the cone test and also before the undrained cyclic loading test. In order to investigate the effect of longer consolidation time in the both tests, specimens of F_c =20% were chosen, because higher fines content is likely to accelerate the long time consolidation effect in comparison with clean sands. Specimens with the relative density around D_r =50% were consolidated for three different durations; 1 hour, 72 hours (3 days) or 168 hours (7 days).

Figs.10 (a) and (b) compare the typical results of cone resistance q_c and excess pore-pressure u, respectively, plotted versus the penetration length. It is obvious that even several days of sustained consolidation makes measurable difference in the cone resistance. Also, undrained cyclic triaxial tests performed after the penetration tests give the data points plotted with filled triangles on the log-log charts in Fig.8 (d). Though the data are somewhat scattered, it is doubtless that the sustained consolidation tends to raise the $R_L \sim N_c$ fitting line, too. In order to correlate penetration resistances to corresponding liquefaction strengths for the individual test specimens, the stress ratio R_L of 5% DA axial strain for N_c =20 were estimated by drawing straight lines through the filled triangles in parallel to the line statistically determined as explained before. In Fig.11, data points thus obtained for the sustained consolidation are plotted for F_c =20% with filled symbols encircled as a group to compare with all the other data for 1 hour consolidation. It may well be judged that, despite some data dispersion, the sustained consolidation tends to shift the R_L versus q_c correlation, leading higher liquefaction strength for the same q_c-value. Consequently, even the correlation for very young test specimens looks to be insensitive to fines content and uniquely determined; it is

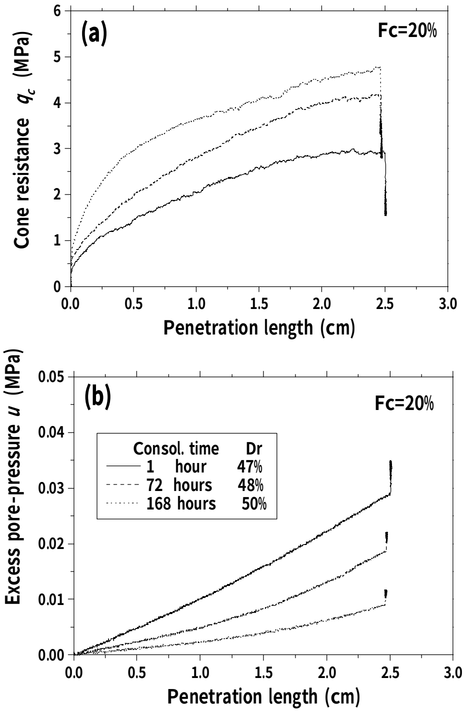

Fig.10: Cone resistance (a) or excess pore-pressure (b) versus penetration length for river sand specimens of D_r≈50% with different consolidation time

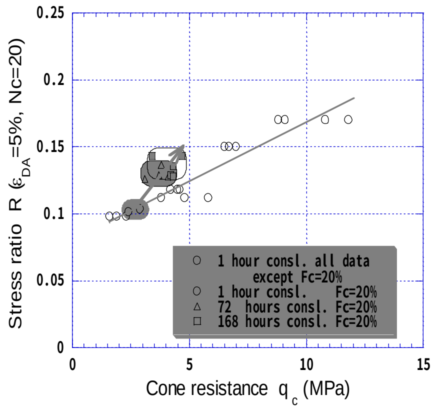

Fig.11: Relationship between stress ratios for liquefaction (DA 5%, N_c=20) and cone resistances for sands of F_c=20% with different consolidation time

likely that long time consolidation in situ makes the difference. However, much more systematic research is certainly needed to draw more general conclusions considering much longer period and different history of consolidation, different plasticity of fines, etc.

EFFECT OF DRAINAGE ON CONE PENETRATION TEST

The drainage condition during cone penetration tests does not seem so simple and depends on several

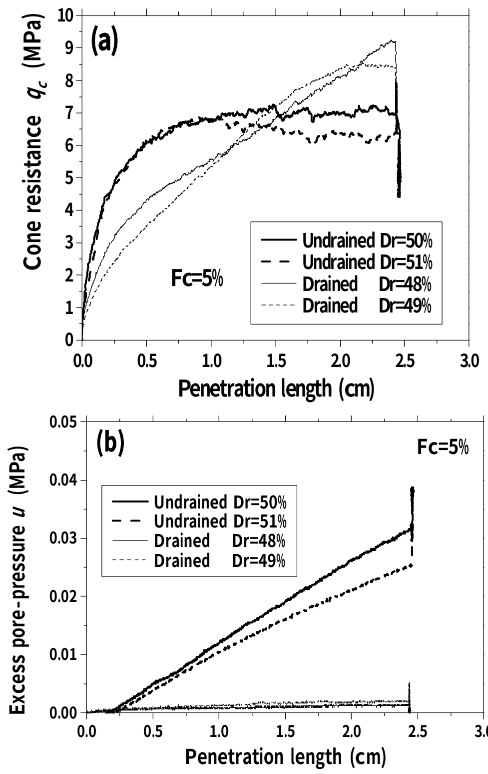

Fig.12: Cone resistance (a) or excess pore-pressure (b) versus penetration length for river sand specimens of D_r≈50% and F_c=5% under drained and undrained conditions.

influencing factors, such as the penetration rate, the cone size, the fines content, etc. In this test series, completely undrained condition was chosen basically for the sake of simplicity of test conditions and data interpretation. However, the reality may be in between the undrained and drained conditions. Consequently, it is worth carrying out the other extreme, drained penetration tests.

Figs.12 (a) and (b) compare typical results of undrained and drained tests in terms of cone resistance q_c and excess pore-pressure u, respectively, plotted as a function of the penetration length for specimens of D_r ≈50% and F_c =5%. While undrained q_c-value tends to asymptotically converge to an ultimate value, drained one keeps increasing even at the maximum penetration length of 25 mm. The difference is also remarkable in the pore pressure u. Although the pressure even in the drained penetration is not actually zero, its contribution on the cone resistance seems minimal. The drained q_c-values at the maximum penetration length were taken and directly correlated to corresponding stress ratio, R_L for ε_{DA} =5%, N_c =20. In Fig.13, data points of the drained condition are compared with the undrained data. Although the number of data is not enough to make a final judgment, the two extreme drainage condition seems to shift the R_L ~q_c fitting line approximately by 1 MPa, which is not large compared to the data scatter involved in the test series. Considering this fact and also that the cone resistance measured in the present study is in good coincidence with in situ prototype test results, it may be said that the miniature cone test under the undrained condition shares important mechanisms for liquefaction potential evaluation of sands containing fines as in situ cone tests.

CONCLUSIONS

The major findings of this study are;

- Cone penetration tests performed prior to cyclic undrained tests have little effect on liquefaction strength of specimens, demonstrating that direct and reliable comparison between penetration resistance and liquefaction strength is possible.
- For river sand with or without low plasticity fines, a good correlation between relative density and cone resistance has been found, which is basically consistent with previous research using a prototype cone. With increasing fines content, both cone resistance q_c and liquefaction strength R_L decrease, resulting in a unique curve on the q_c~R_L chart despite the difference in the fines content and relative density. This indicates that liquefaction strength for a given cone resistance is constant despite the difference in fines content, which is contrary to the current liquefaction evaluation practice.
- In order to examine long term consolidation effect on the R_L ~q_c relation, samples with certain fines content were consolidated for variable durations up to a week. The sustained consolidation of such a short time increases both cone resistance and liquefaction strength by measurable amounts. If the results are plotted on the R_L ~q_c chart, they seem to be located slightly above the unique curve obtained by the normal consolidation tests. This may indicate that, if in situ consolidation effect is considered, liquefaction strength will increase with increasing fines content.
- Cone penetration test under the undrained condition in this research seems to shift the R_L ~q_c line along the q_c axis approximately by 1 MPa in comparison with the drained condition, which is not large compared to the scatter in the data involved in the test series. Thus, the present research has been able to provide valuable insights into the liquefaction strength evaluation based on cone penetration. However, more test results on long term consolidation effect and drainage effect for different fines contents are certainly needed before reaching general quantitative conclusions on this important issue.

REFERENCES

[1] Japan Road Association "Liquefaction potential evaluation in sandy ground" (in Japanese), *Road Bridge Design Code*, Chap.7.5, 91-94, 1996.

[2] Suzuki, Y., Tokimatsu, K., Taya, Y. and Kubota, Y. "Correlation between CPT data and dynamic properties of in situ frozen samples", *Proc. 3rd Int. Conf. on Recent Advances in Geotechnical Earthquake Engineering and Soil Dynamic*s, St. Louis, Vol.1 249-252, 1995.

[3] Sato, M., Oda, M., Kazama, H. and Ozeki, K. "Fundamental study on the effect of fines on liquefaction characteristics of reclaimed ground" (in Japanese), *Journal of Japan Society for Civil Engineers*, No.561/III-38, 271-282, 1997.

[4] Kokusho, T. and Komiyama, Y. "Undrained shearing characteristics of gravelly soils containing non-plastic fines", (in Japananese), *Proc. Symposium on Mechanical Properties of Gravelly Soils*, Japanese Geotechnical Society, 233-238, 2001.

[5] Hara, T., Kokusho, T. and Komiyama, Y. "Undrained shear characteristics of sandy gravel containing non-plastic fines" (in Japanese), *Journal of Japan Society for Civil Engineers*, NO.785/III-70, 123-132, 2005.

[6] Hara, T. and Kokusho, T. "Effect of non-plastic fines on undrained strength characteristics of sand and sandy-gravel" (in Japanese), *Journal of Earthquake Engineering*, Vol.28, Paper No.93, 2005.

[7] Kokusho, T. and Yoshida, Y.: SPT N-value and S-wave velocity for gravelly soils with different grain size distribution, *Soils and Foundations*, Vol.37, No.4, 105-113, 1997.

[8] Kokusho, T., Hara, T. and Hiraoka, R. "Undrained shear strength of granular soils with different particle gradations", *Journal of GGE*, Vol.130, No.6, 621-629, ASCE, 2004.

[9] Japanese Geotechnical Society "Minimum and maximum density tests for sands" (in Japanese), *Soil Testing Methods and Their Backgrounds*, Chap.8, 136-145, 2001.

[10] Hara, T., and Kokusho, T. "Experiments on Influencing factors on minimum and maximum density for sandy gravel" (in Japanese), *Journal of Japan Society for Civil Engineers*, NO.778/III-69, 151-162, 2004.

Dynamic Centrifuge Model Test of Road Embankment

Y. Nabeshima[1], K. Tokida[2], A. Nakahira[3], A. Ohtsuki[4], Y. Nakayama[5]
[1]*Department of Civil Engineering, Akashi National College of Technology, Hyogo, Japan*
[2]*Department of Civil Engineering, Osaka University, Osaka, Japan*
[3]*Division of Road Construction, CTI Engineering, Osaka, Japan*
[4]*Institute of Technology, Shimizu Corporation, Tokyo, Japan*
[5]*Geotechnical Laboratory, Kansai Geo-Environment Research Center, Osaka, Japan*

Abstract

In the 2004 Mid Niigata Prefecture Earthquake, many road infrastructures, especially road embankments, were suffered sever damages. Seismic countermeasures for road embankments had not been considered up to now, however, this earthquake emphasized the necessity of seismic countermeasures for road embankments. The seismic failure of embankments was not fully elucidated yet. The dynamic centrifuge model test was performed to simulate the dynamic slope failure of road embankment. The slope failure with deep slip surfaces was observed in the centrifuge model test. The time when the slope started to slide during shaking was tried to determine by using the wavelet transformation for the dynamic response wave recorded in the model.

Keywords—*Centrifuge model test, road embankment, dynamic failure, wavelet transformation*

INTRODUCTION

In the 2004 Mid Niigata Prefecture Earthquake, many road infrastructures were suffered sever damage, especially settlement, slide failure and slope failure of road embankments occurred in many sites. Seismic countermeasures for road embankments had not been considered up to now, however, this earthquake emphasized the necessity of seismic countermeasures for road embankments. Accordingly, efficient seismic countermeasure and seismic performance of road embankment are urgently required to insure the road traffic performance.

In this paper, the authors classified major damages and features of road embankments in the Mid Niigata Earthquake on the basis of field investigations. A dynamic centrifuge model test was carried out to investigate dynamic failure mechanism of road embankment during shaking. The time when the slope started to slide during shaking was tried to determine by using the wavelet transformation for the dynamic response wave recorded in the model.

MAJOR DAMAGES AND FEATURES IN THE 2004 MID NIIGATA PREFECTURE EARTHQUAKE

On the basis of the minute field investigations, the authors summarized the following reports regarding the damage level and features to road infrastructure and road performance resulting from the 2004 Mid Niigata Earthquake as referred to [1].

(1) Sixty percent or more of the damage leading to road closures was attributed to settlement or bumps or embankment failure. Less than 20% of damage was attributed to slope failure or mudslide, and less than 7% to bridge damage. Damaged embankments accounted for most of the devastation.

(2) Damage to road embankments was divided into damage in the transverse and longitudinal directions. Damage in the transverse direction was then divided into flat or sloped ground. Damage to sloping ground was further divided into single- or double-sided slope. Damage forms are properly classified according to combinations of these types of damage.

(3) Concerning the restoration of transportation, road traffic tended to be restored sooner than rail traffic. Therefore, traffic at an early stage of restoration is highly dependent on road traffic.

(4) In order to prevent the deterioration of the entire road network just after an earthquake, it is necessary to set an adequate and well balanced earthquake-resistant level for each of the road infrastructure components.

(5) In the local mountainous regions, seismic countermeasures are required for road embankments and slopes to meet requirements for road performance. Therefore, it is necessary to apply existing construction methods suitably and develop new effective and economical construction methods.

(6) A clear correlation between seismic intensity and road-blocked point ratio has been shown. The three parts are proposed to estimate the change of road-blocked point ratios with time elapsed for each seismic intensity for the entire damage form, embankment damage and slope damage, respectively.

(7) To assess damage to road infrastructure based on seismic intensity information just after an earthquake, damage to road infrastructure and road performance for each seismic intensity scale is proposed.

In this paper, the slope failure which was the typical damage in the transverse direction of road embankments in the 2004 Mid Niigata Earthquake is investigated by using a dynamic centrifuge model tests.

CENTRIFUGE MODEL TEST PROCEDURE

Centrifuge Facility

Centrifuge facility in the institute of technology, Shimizu Corporation was used in this research. The view of the centrifuge facility is shown in Fig.1 and its specifications of key items are summarized in Table 1. Some kinds of soil box are available in the centrifuge facility with requests of the test. This is comparable size to the biggest centrifuge facility. Details on this dynamic centrifuge facility were summarized in the reference [2].

Fig. 2 shows the soil box used in the dynamic centrifuge test. A rigid soil box was used in this test because a main scope in the test is to simulate slope failure of road embankment on the stiff ground. The soil box has 50 cm in width, 80 cm in width and 40 cm in depth, in which the model slope of road embankment.

Fig. 1: Dynamic centrifuge facility in Shimizu Company.

Table 1: Specifications of the centrifuge facility.

Key items	Specifications
Rotary drive system	Rotary servo system using oil motor
Effective radius	3.11m (using shaking table)
Maximum acceleration	5 – 50 g (using shaking table)
Platform dimension	950 mm X 650 mm
Maximum payload	350 kg
Maximum shaking acceleration	15 g (sine wave and seismic wave)
Shaking frequency range	50 – 350 Hz
Shaking system	Electromagnetic system
Wave types	Sine wave, Seismic wave (earthquake wave), Sine wave sweep

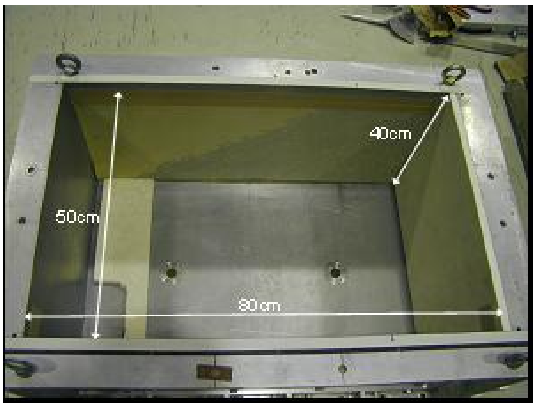

Fig. 2: Soil box in the dynamic centrifuge facility.

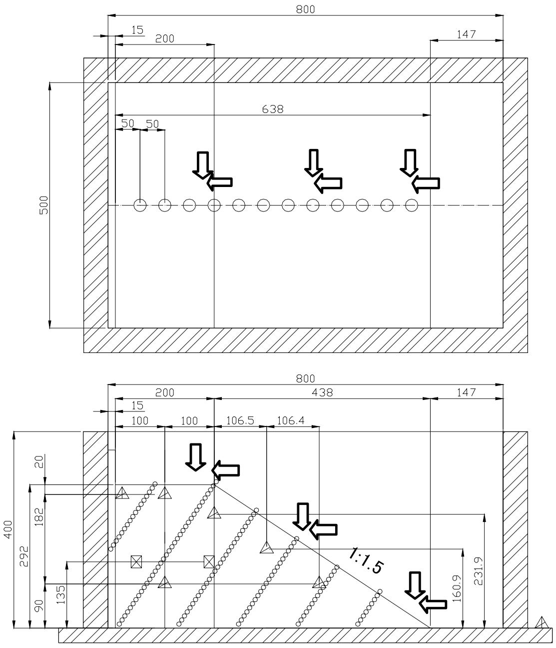

Fig. 3: Plane and front views of model ground in the dynamic centrifuge test.

Model slope and Characteristics of Test Soil

Many slope failures of road embankments occurred in the 2004 Mid Niigata Earthquake, therefore the dynamic centrifuge model test of road embankments was carried out. In the test, half bank model slope was used to simplify the road embankment. Fig. 3 shows the model slope used in the centrifuge test and model slope was built on the horizontal flat basement.

DL clay was used as test soil in the centrifuge test. Table 2 shows soil properties of DL clay. To use it in the centrifuge model test under 30 times gravitation, DL clay was mixed with silicon oil at 5 % of oil content instead of water. Model ground was made at every 3 cm thickness until about 30 cm by a wet tamping method using a rammer. The wet density of model ground was 1.548 g/cm^3. The model ground was applied 30 times gravitation by centrifuge facility to stabilize the ground and then the ground was formed to the slope. Slope gradient of model slope was decided at 1 : 1.5. Because rigid soil box was used in the dynamic centrifuge model test, to absorb the vibration shock from rigid soil box wall to model ground, an expanded polystyrene board with 1.5 cm thickness was set between rigid soil box wall and model ground. Silicon grease and rubber membrane were used to lubricate the friction between side wall and model ground.

In the centrifuge model test, the shear wave velocity of model ground was measured by bender element equipments to discuss the stiffness of model ground. The shear wave velocity of model ground was 182 m/sec under normal gravitation, and 192 m/sec under 30 times gravitation.

Table 2: Soil properties of DL clay.

Key items		Specifications
Gradation	Sand	0.0 %
	Silt	90.4 %
	Clay	9.6 %
	Maximum grain size	0.075 mm
	Uniformity coefficient	4.26
Density of soil particle		2.653 g/cm^3
Plasticity index		No point
Silicon oil content		5 %
Void ratio		0.8
Degree of saturation		16.6 %
Dry density		1.474 g/cm^3
Wet density		1.548 g/cm^3
Cohesion		22 kN/m^2
Internal angle		36.3 º

Dynamic Loading

Dynamic loading was applied by sine waves with three steps. At first step, 30 sine waves of about 30 gal and 2 Hz were applied for 15 seconds. In case which the failure of model slope did not occur, the dynamic loading proceeded to next step until the slope failure occurs. The maximum acceleration increased to about 350 gal at second stage. At third stage, the maximum acceleration increased to about 520 gal. Because the dynamic slope failure was observed during the third stage, the dynamic loading was stopped at third stage in this test.

Before the dynamic loading, to investigate the primary eigen frequency of model slope, the sweep vibration was applied. The primary eigen frequency of model slope was around 6.2 Hz judging from the transfer function between basement and top of embankment.

Measuring System

The slope surface deformation was measured by laser displacement gages and colored ball marks. Vertical and horizontal displacements were measured by long span laser displacement gauges at 3 points which were top, middle and toe of slope as shown in Fig.3. The colored ball marks were set on a center line of the slope and the deformation of slope surface was calculated by measuring their positions before and after the centrifuge test.

The deformation in the slope was investigated by colored sand as shown in Fig. 3. Six lines of colored sand were embedded in the slope at right angle to the slope. The dept of slip surface was measured from the break point of the colored sand after the centrifuge test.

The accelerations in and on the slope were measured by accelerometers. Seven accelerometers were installed as shown in Fig. 3 with triangle marks.

The shear wave velocity of model ground was measured by embedded bender elements as referred to above. Bender elements were embedded in the model ground and were used to measure the shear wave velocity.

TEST RESULTS AND DISCUSSION

Dynamic Failure Surface

Although the slope failure was not observed at first and second dynamic loadings, the slope failure occurred during third dynamic loading of 520 gal. Figs. 4 to 6 show the overall view of slope failure, close view of top of slope and close view of toe of slope, respectively. Fig. 7 also shows the schematic drawing of slope failure before and after dynamic centrifuge test.

Clear slip surfaces, at least two lines, from the top of embankment to the toe of slope can be observed in Fig. 4. The depth of slip surface was about 10 cm at top of slope and about 7 cm at middle part of slope, which were equivalent to 3.0 m and 2.1 m in the full scale slope. It was confirmed that the deep slope failure was simulated in the dynamic centrifuge model test. The deep slope failure of the embankments was often observed in the Mid Niigata Earthquake.

The settlement and bump due to the slope failure of embankment in the transverse direction can be observed in Fig. 5. The horizontal movement of soil mass was also observed in Fig. 6. Horizontal displacement of model slope was found about 4 cm from Fig. 7, which was equivalent to 1.2 m in the full scale slope.

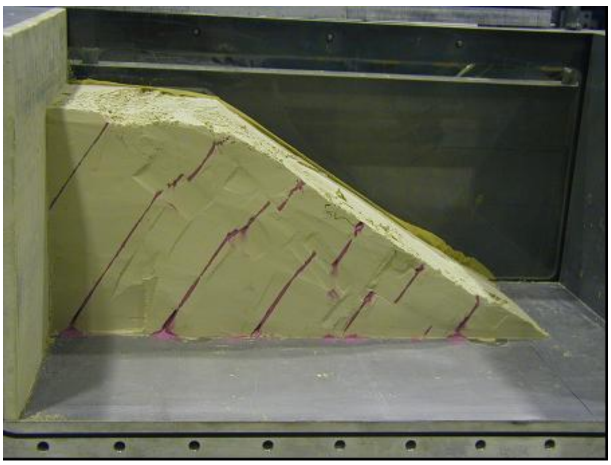

Fig. 4: Overall view of slope failure.

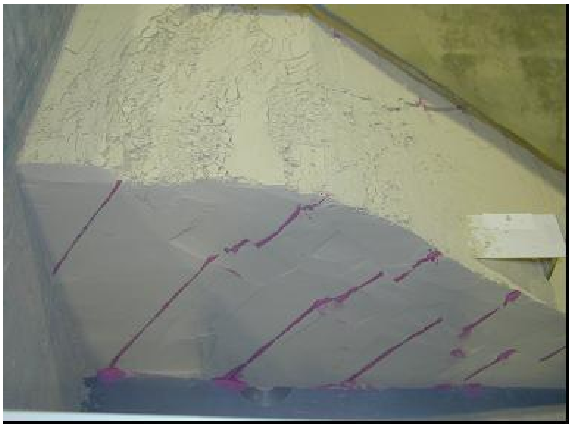

Fig. 5: Close view of top of slope.

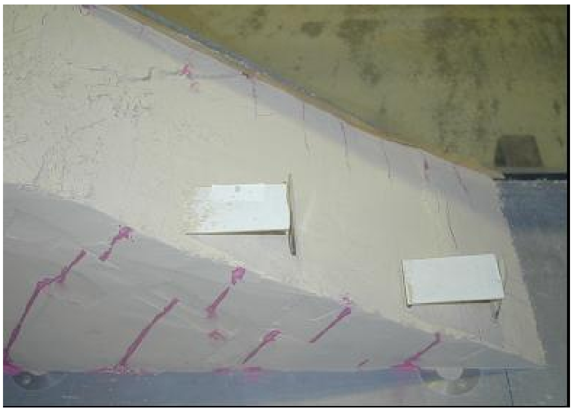

Fig. 6: Close view of toe of slope.

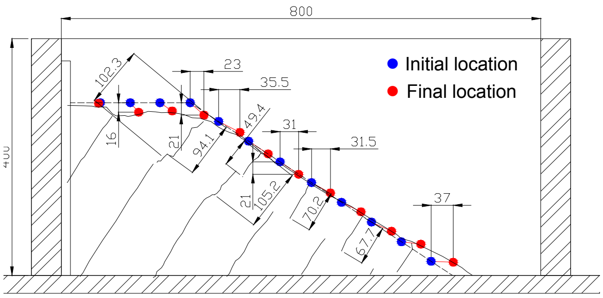

Fig. 7: Schematic drawing of slope failure before and after dynamic centrifuge test.

Dynamic response wave

Fig. 8 shows the dynamic accelerations recorded during third dynamic loading of 520 gal. In Fig. 8, "Base" means the acceleration recorded at the basement and from AG-1 to AG-6 means the accelerations recorded at every point in the model embankment as shown at upper right in Fig. 8. The acceleration behaviors recorded at AG-2 and AG-5 which were located around top of the embankment disorderly changed after about 8 seconds, because the slope failure might occur around 8 seconds.

The maximum acceleration at AG-6 was about 1500 gal, at AG-2 and AG-5 about 1000 gal, at AG-4 about 850 gal, at AG-3 about 760 gal and at AG-1 about 520 gal, respectively. From the maximum acceleration records, the acceleration record at the top of slope was quite different from that at the toe of slope.

Vertical and Lateral Deformation

Fig. 9 shows the vertical and horizontal deformation at three points on the slope during the third dynamic loading. Measured three points were shown in Fig.8. Although horizontal deformation increases with dynamic cycles until dynamic slope failure occurred, some of vertical and horizontal deformation could not be measured after the failure occurred as show in Fig. 9.

Estimation of Starting Time of Slope Failure

To estimate the starting time of slope failure during shaking, the wavelet transformation was applied to the dynamic response wave recorded in the model ground. In the wavelet transformation, since time period of the window function can be approximately varied with frequency, the time period is long in the low frequency, while it is short in the high frequency. Thus, the wavelet transformation can capture the change of trend. The original wave is divided into high and low frequency components, then the divided high frequency component is divided into high and low frequency components again. By repeating this process, the trend and the discontinuity point can be easily captured in the wavelet transformation.

Fig. 10 shows the location of accelerometers in the centrifuge model slope. The dynamic response wave recorded during shaking at AG-5 in the third step of 520 gal was shown at upper left in Fig. 11. The reconstitute acceleration wave and accelerations divided by the wavelet transformation were shown at right side in Fig. 11. By transforming the dynamic response wave, the abnormal wave can be observed around eight seconds as shown in Fig. 11, it means something, probably slope failure, occurred at this moment. Similar abnormal waves were observed at four accelerometers around top of embankment as shown in Fig. 10. Thus, the starting time of slope failure during shaking can be estimated from the dynamic response wave transformed by the wavelet transformation.

CONCLUSIONS

The authors carried out the dynamic centrifuge model test of the road embankment to elucidate and simulate dynamic slope failure during earthquake. Main conclusions in this paper can be summarized as follows:

(1) The slope failure of road embankment can be simulated in the dynamic centrifuge model test. The deep slip surfaces can be observed and the acceleration record at the top of slope was quite different from that at the toe of slope.

(2) The starting time of slope failure during shaking can be estimated from the dynamic response wave transformed by the wavelet transformation. In this dynamic centrifuge model test, the slope failure

might occur around eight seconds.

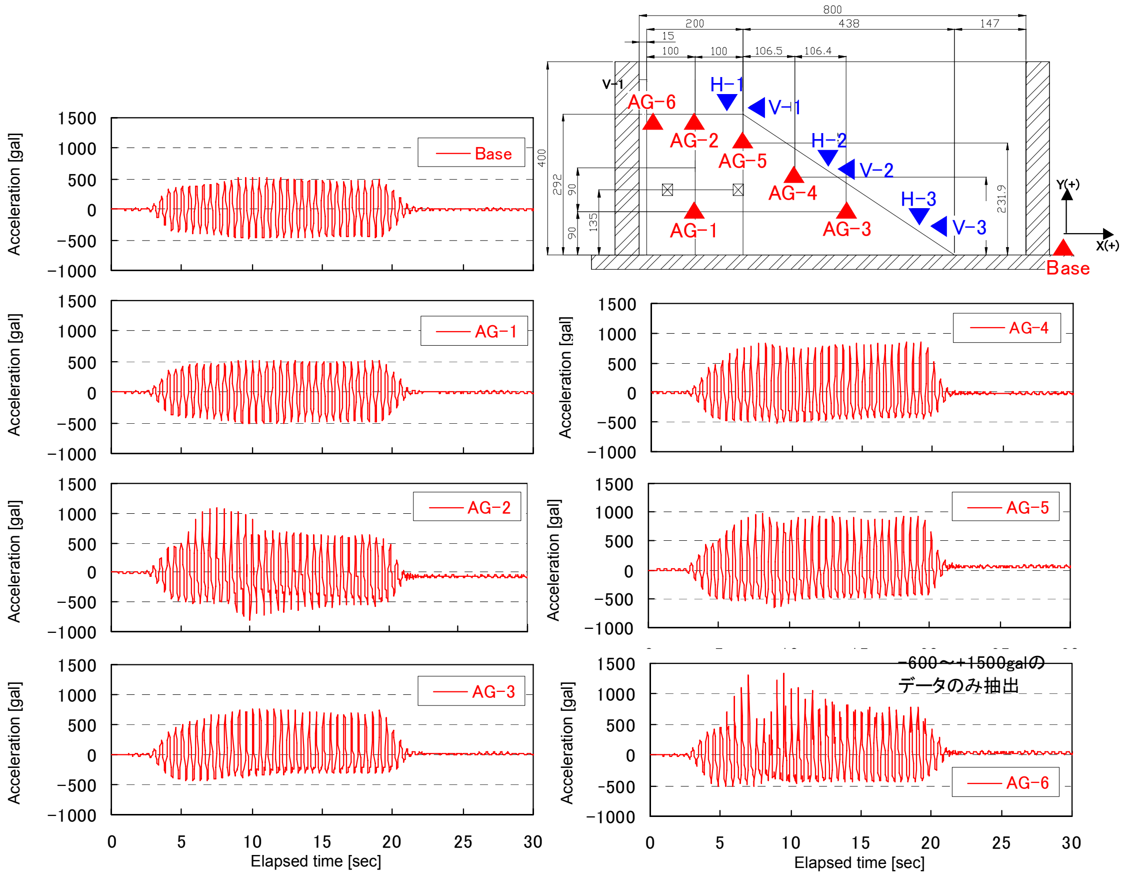

Fig. 8: Dynamic accelerations recorded during third dynamic loading.

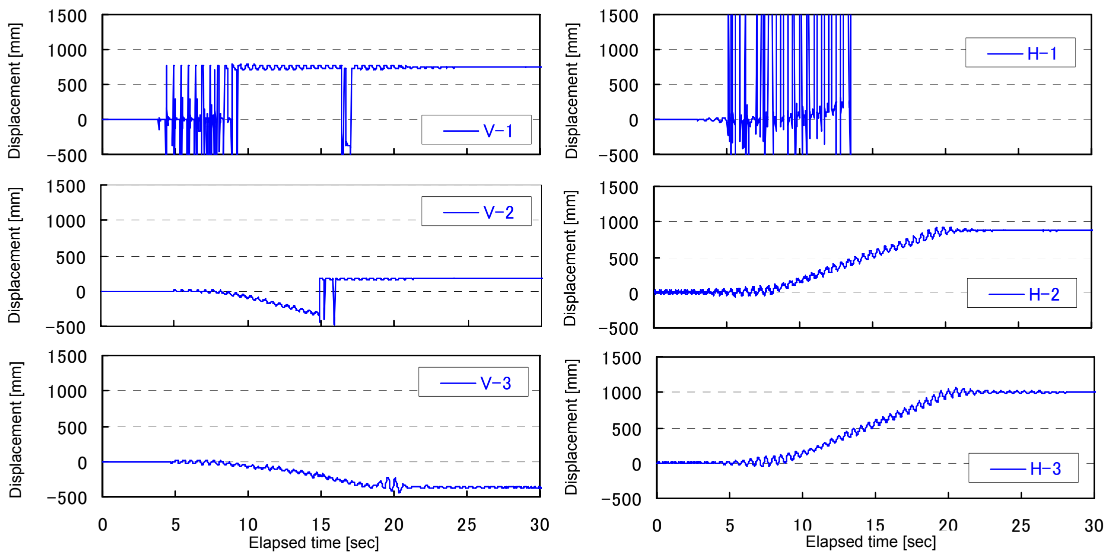

Fig. 9: Vertical and horizontal deformation during the third dynamic loading.

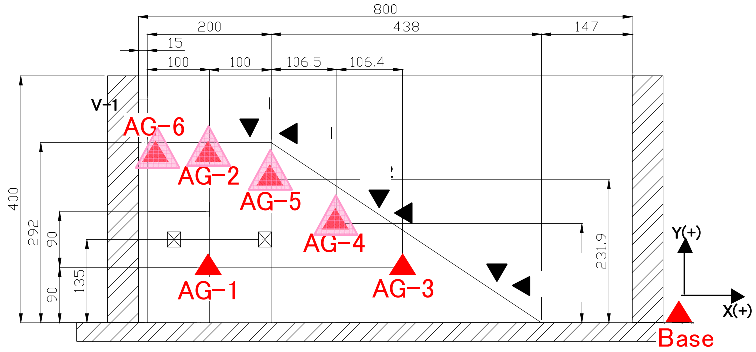

Fig. 10: Locations of accelerometers in the centrifuge model slope.

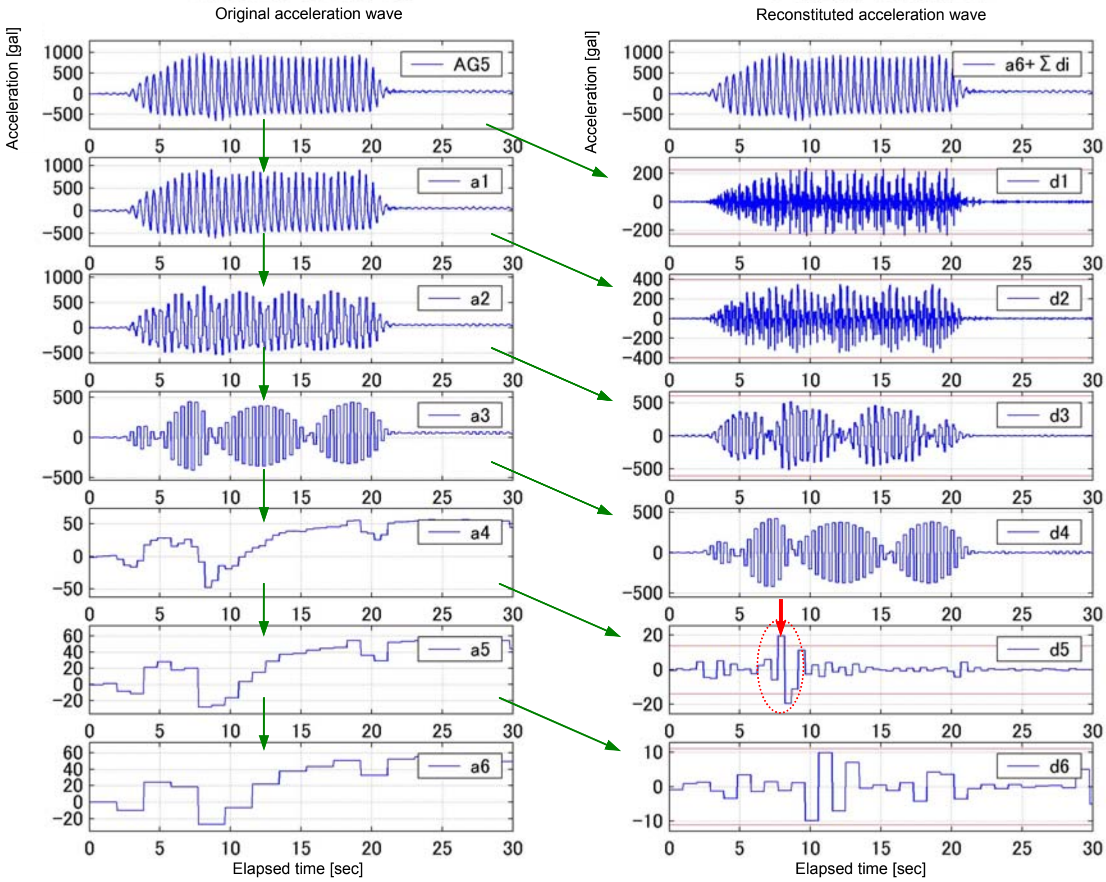

Fig. 11: Accelerations transformed by the wavelet transformation.

ACKNOWLEDGMENTS

The research in this paper is subsidized by the Bureau of Road of The Ministry of Land, Infrastructure and Transport. The authors wish to gratefully acknowledge the financial support.

REFERENCES

[1] Sato, M., "A new dynamic geotechnical centrifuge and performance of shaking table test," *Centrifuge '94*, pp.157-162, 1994.

[2] Tokida, K., Oda, K., Nabeshima, Y. and Egawa, Y., "Damage level of road infrastructure and road traffic performance in the Mid Niigata Prefecture Earthquake of 2004," (in press).

Evaluation of Liquefaction Resistance of Gravel Drain Improved Loose Sandy Ground considering the Partially Drained Cyclic Behaviour

N. H. Priyankara, M. Kazama, N. Sento, R. Uzuoka
Department of Civil Engineering, University of Tohoku, Sendai, Japan

Abstract

The installation of drainage system offers an attractive and economical procedure for stabilizing potentially liquefiable sand deposit. The design procedures for gravel drains recommended by the Japanese Geotechnical Society and the Japanese Port and Airport Research Institute are based on the conventional method proposed by Seed and Booker and it is therefore useful to consider modifications to this approach using laboratory facilities. In the research reported here examines the liquefaction resistance of gravel drain improved ground based on the concept of partially drained condition. The process of partially drained condition under the cyclic loading in the field was simulated in the laboratory by considering the seepage analysis based on the Darcy's law in a hollow cylindrical tortional shear apparatus. The liquefaction resistance under partially drained condition has been represented using the non-dimensional parameter named as coefficient of drainage (α). The test results indicated that minimum liquefaction resistance under partially drained condition $R_{d(min)}$ can be used as a tool to predict the liquefaction resistance of gravel drain improved ground. Finally, a simplified method for designing gravel drains based on the safety factor (F_L) method has been proposed with a detailed flow chart.

Keywords— *Coefficient of drainage, gravel drains, liquefaction resistance, partially drained condition*

INTRODUCTION

In recent years substantial gains have been made in understanding the phenomenon of liquefaction of saturated granular materials. Conventional types of liquefaction tests usually performed under undrained condition. Much of the work performed under conventional type of liquefaction test finds its application in situations in which the redistribution and dissipation of pore water pressure do not have any significant influence on the liquefaction potential of the soil mass. It has been recognized, however, that such mechanisms may be of considerable importance and may have some beneficial effects [1]. In the real ground, excess pore water pressure generated by cyclic loading may be dissipated to some extent as they are created, then the danger of liquefaction can be averted.

However, the liquefaction test method which could be able to simulate the in-situ real drainage condition is not yet been well established. There are some limited information available about the use of partially drained condition under cyclic loading in the literature. Reference [2] shows the effect of drainage on the pore water pressure response in an approximate way, in order to evaluate the wave induced liquefaction potentials of sandy soils beneath an oil storage tank. Reference [3] illustrates a new evaluation method for liquefaction resistance under partially drained condition using modified cyclic shear triaxial apparatus.

In order to evaluate the partially drained condition on gravel drain improved ground, multiple series of laboratory tests were conducted using hollow cylindrical tortional shear apparatus. Using this method, series of dynamic tests were conducted under different conditions of drainage, with closed drainage system as well as retarded drainage system. Both effects of drainage and the influence of frequency on liquefaction resistance were quantitatively evaluated. On the basis of these results, the prediction method of liquefaction potential is proposed in this paper.

BASIC CONCEPT OF PATIALLY DRAINED CONDITION UNDER CYCLIC LOADING

Gravel drains are one of the most widely used pore water pressure dissipation methods and which could be enable the prevention of liquefaction during an earthquake [4]. The real drainage system during an earthquake is governed by the length of the drainage path *l*, and the permeability of the seismically endangered layer *k*, as shown Fig. 1, and further influenced by the rate of cyclic loading frequency, *f*. It was assumed that the

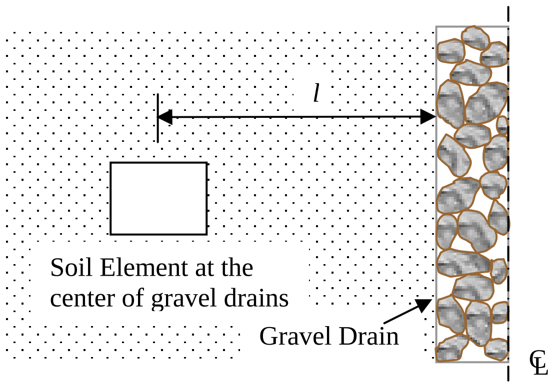

Fig. 1: Pore water migration towards gravel drain

excess pore water pressure developed in the sand layer by the shear stress reversals during an earthquake may be partially dissipated at the same time. For saturated soils, even a minor drainage during cyclic loading leads to visible reduction in pore water pressure.

In order to evaluate the drainage effects on liquefaction potential, consider a situation in which the pore water flow towards gravel drain dominates as a result of total head difference between center of gravel drains and boundary of the gravel drain. It can be assumed that pore water pressure in the gravel drain is always equal to atmospheric pressure as permeability of the gravel drain was considered as infinite (no well resistance), thus the excess pore water pressure in the gravel drain is equal to zero. Based on this sense, it can be considered that the loss of head, Δh between these two points is governed only by the excess pore water pressure at the center of gavel drains at surrounding ground, as shown in Fig. 1.

$$\Delta h = \frac{u}{\gamma_w} \tag{1}$$

where u and γ_w represent the excess pore water pressure at the center of gravel drains and unit weight of water respectively. In addition, it was assumed that the flow velocity varies linearly between these two points. It is noted that flow velocity at mid point of gravel grains is very small and can be neglected. Therefore flow velocity is a function of flow velocity at gravel drain, v_1 and drainage length, l.

$$\frac{\partial v}{\partial x} = \frac{v_1}{l} \tag{2}$$

Further, it was assumed that the dissipation of excess pore water pressure induced by an earthquake will occur according to the Darcy's law [1];

$$v = ki = k\left(\frac{u}{\gamma_w l}\right) \tag{3}$$

where v, k, i represent the flow velocity, coefficient of permeability and hydraulic gradient respectively. By differentiating Eq. (3) with respect to flow direction x,

$$\frac{\partial v}{\partial x} = k\left(\frac{u}{\gamma_w}\right)\frac{1}{l^2} \tag{4}$$

By considering the continuity of flow and unit cross sectional area normal to the flow direction, flow volume discharge rate towards gravel drain, dQ can be expressed as,

$$dQ = k\left(\frac{u}{\gamma_w}\right)\frac{1}{l} \tag{5}$$

Based on Eq. (5), change of volumetric strain, $d\varepsilon_v$ per small time increment, Δt is expressed as follows.

$$d\varepsilon_v = k\left(\frac{u}{\gamma_w}\right)\frac{1}{l^2}\Delta t \tag{6}$$

Then, the volume change ΔV due to pore water pressure dissipation during Δt time is represented in Eq. (7);

$$dV = k\left(\frac{u}{\gamma_w}\right)\frac{1}{l^2}\Delta t V_0 \tag{7}$$

where V_0 is the initial volume of the soil specimen. For laboratory experiments, soil sample volume after consolidation was considered as the initial volume.

The Eq. (7) was used as the basic equation for governing the pore water pressure dissipation. The actual drainage condition was simulated in the elementary tests by automatically controlling the drainage system in the hollow cylindrical tortional shear apparatus.

EXPERIMENTAL PROGRAM

Test equipment and specimen preparation

In order to study the pore water pressure dissipation during cyclic loading, multiple series of elementary tests were conducted in the laboratory using hollow cylindrical tortional shear apparatus. The details of the hollow cylindrical tortional shear apparatus used in this research study are given in [5][6]. Toyoura sand, having mean grain size of 0.16 mm, coefficient of uniformity U_c=1.46, specific gravity G_s=2.64, maximum void ratio e_{max}=0.977 and minimum void ratio e_{min}=0.605, was used as the testing material. All specimens were prepared by dry tamping method (lightly in a circular pattern). The details of the dry tamping method used for the sample preparation are given in [7]. It was make sure to maintain the relative density, D_r of all specimens as 50%, in order to consider the medium dense sand. Soil specimens were prepared in 3 layers, in order to achieve a more uniform density. Reconstituted specimens were compacted in a hollow cylindrical mold 7 cm in outer diameter, 3 cm in inner diameter and 10 cm in height.

Samples were isotropically preconsolidated under 20 kPa and were saturated by circulating carbon dioxide, de-aired water and applying back pressure of 100 kPa. When the Skempton's B parameter larger than 0.95 was achieved, the specimens were accepted as fully saturated for this study. Saturated samples were isotropically consolidated to the confining pressure of 100 kPa before apply the cyclic loading.

Test Procedure

Liquefaction tests under undrained conditions were conducted in the conventional way with close drainage system. Previous studies have shown that the influence of cyclic loading frequency, f on dynamic behaviour of soil under the undrained condition is negligible within the frequency range of 1/6 Hz to 4 Hz [8][9]. Therefore, the frequency of 3 Hz was adopted in the undrained tests. On the other hand, liquefaction tests with partially drained condition were conducted under different drainage conditions as well as different cycling loading frequencies.

Fig. 2 illustrates the summary of the experimental procedure for partially drained condition. The cyclic shear strain was applied to the specimen, such a way similar to the undrained condition and keeping the confining pressure constant. As a result, excess pore water pressure increases. Based on this resultant excess pore water pressure, generated due to undrained cyclic loading, calculate the volume change, ΔV, of the sample which is equal to the drained volume of pore water as stated in Eq. (7). Then, the calculated volume change, ΔV, was applied to the volume controller by keeping the confining pressure constant and it behaves similar to the drained condition. As a result, pore water pressure induced during undrained cyclic loading decreases. It can be seen that pore water pressure has been generated under undrained condition and it has been dissipated under drained condition in the same cyclic loading step, thus this process is named as "Partially drained condition". In this method, a computer analysis cyclic loading and pore water pressure dissipation were combined with the online data processing system. It was assumed that the initial liquefaction was occurred when the pore water pressure ratio, $\left(r_u = u_{\max}/\sigma_c^{'}\right)$ reaches to 1.0, where u_{max} and $\sigma_c^{'}$ are maximum excess pore water pressure and initial effective confining pressure respectively [10].

Test Cases

Test cases are shown in Table 1. Previous studies have shown that the difference in the frequency of cyclic loading does not have a highly significant effect on the pore water pressure rise and liquefaction potential of sand [9][10]. However, under partially drained condition, it was found that coefficient of permeability, k, drainage length, l as well as cyclic loading frequency, f are important factors to be considered, thus k, l and f were selected as control parameters in this research study. It is noted that cyclic loading frequency, f is not the actual frequency of elementary test. Further, k, l and f are assumed values and drainage process was controlled according to these assumed values. Test case displayed in the table implies the combination of drainage condition and shear stress amplitude. For example T11P25 indicates the test number of T11, drainage condition (P for partially drained and U for undrained) with shear stress amplitude of 25 kPa. D_{rc} in the table 1 depicts the relative density of the soil specimen after consolidation.

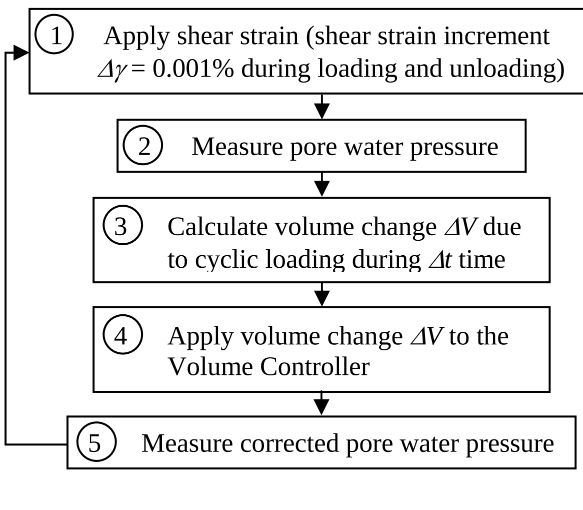

Fig. 2: Partially drainage system test procedure

It was found that liquefaction resistance under partially drained condition can be well represented by non-dimensional parameter, defined as follow.

$$\alpha = \frac{k}{lf} \tag{8}$$

This non-dimensional parameter is named as "Coefficient of Drainage" in this paper. It was noted that partially drained condition converges to undrained condition when k/l becomes smaller or cyclic loading frequency, f becomes larger. In other words, $\alpha = 0$ represent the undrained condition where as $\alpha > 0$ indicates the partially drained condition.

RESULTS AND DISCUSSION

Comparison of Undrained and Partially Drained Cyclic behaviour

A series of liquefaction tests on saturated sand were conducted under various drainage conditions. Fig. 3 depicts the typical examples of test results under both undrained (T03U25) and partially drained (T12P25) conditions. These two cases illustrate the same stress ratio under different drainage condition. The typical excess pore water pressure generation and dissipation curves indicate the effect of drainage in reduction of excess pore water pressure as shown in Fig. 3(c). The excess pore water pressure curve with the partially drained condition, initially increases with the increasing stress cycles, but gradually decreases without becoming equal to the

Table 1: Test cases

Test Case	f (Hz)	k(m/s)	α	D_{rc}(%)
T01U10	3.0	0	0	56.01
T02U20	3.0	0	0	58.61
T03U25	3.0	0	0	55.47
T04P25	0.1	5.78×10^{-5}	5.78×10^{-4}	57.60
T05P30	0.1	5.78×10^{-5}	5.78×10^{-4}	51.18
T06P30	0.1	5.78×10^{-4}	5.78×10^{-3}	56.61
T07P35	0.1	5.78×10^{-4}	5.78×10^{-3}	59.20
T08P20	0.3	5.78×10^{-6}	1.93×10^{-5}	50.66
T09P25	0.3	5.78×10^{-6}	1.93×10^{-5}	47.92
T10P30	0.3	5.78×10^{-6}	1.93×10^{-5}	52.60
T11P25	1.0	5.78×10^{-6}	5.78×10^{-6}	58.66
T12P25	1.0	5.78×10^{-5}	5.78×10^{-5}	49.95
T13P30	1.0	5.78×10^{-5}	5.78×10^{-5}	54.60
T14P30	1.0	5.78×10^{-4}	5.78×10^{-4}	57.51
T15P35	1.0	5.78×10^{-4}	5.78×10^{-4}	44.67

confining pressure. It was noted that no noticeable increase in shear strain under partially drained condition (Fig. 3(a)). In some cases under partially drained condition, liquefaction occurs as similar to the undrained condition; however initial liquefaction may be delayed when compared with undrained condition, where as in other cases, the generated excess pore water pressure dissipates rapidly before liquefaction. In the partially drained cyclic loading test, the volumetric strain curve response is associated with the dissipation of excess pore water pressure, as shown in Fig. 3(e).

The axial strain ε_a curves (Fig. 3(d)), both under undrained and partially drained condition increase gradually with the number of loading cycles. However, curve corresponding to the undrained condition has been increased significantly at near liquefaction. Due to the dissipation of excess pore water pressure during cyclic loading, the increment of ε_a under partially drained condition was small.

The cyclic stress path and cyclic stress-strain relationship of typical test results (corresponding to the above test cases) under undrained and partially drained condition are presented in Fig. 4. The Critical Stress Ratio Line (CSRL) and Phase Transformation Line (PTL) were determined from Compression Undrained tests (CU)[11]. It can be seen that the effective stress path does not reach CSRL under partially drained condition (Fig. 4(b)), where as under undrained condition, effective stress path not only moves until upper end touches the CSRL and PTL, but also finally reaches to the zero mean effective stress state (Fig. 4(a)). The reason for this behaviour under partially drained condition is that the excess pore water pressure peak for each cycle will not be as high as it is under undrained condition, even though applied cyclic loading is same for both cases. The characteristic of cyclic stress-strain relationship shows that no noticeable increase in shear strain under partially drained condition (Fig. 4(d)) when compared with that of undrained condition (Fig. 4(c)).

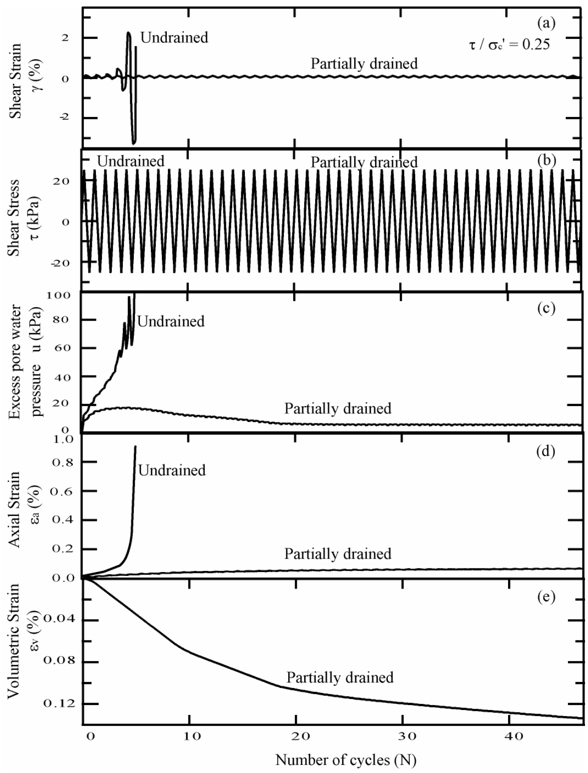

Fig. 3: Typical test results of undrained (T03U25) and partially drained condition (T12P25)

Liquefaction Resistance under partially drained condition

The relationship between stress ratio both under undrained and partially drained condition and number of loading cycles (N) required to cause excess pore water pressure equal to confining pressure is shown in Fig. 5. Shear stress ratio was obtained by normalizing the shear stress amplitude with respect to initial effective confining stress, σ_c' of 100 kPa. Solid line depicts the stress ratio corresponding to undrained condition where as dotted line represents that of partially drained condition. It is clearly seen that larger the coefficient of drainage α, the greater the resistance to liquefaction. In spite of this fact, it may be seen that, the minimum liquefaction resistance, defined as $R_{d(min)}\left(=\tau_{(\min)}/\sigma_c'\right)$, for each drainage condition is represented with parallel lines to the x-axis, where $\tau_{(min)}$ is the minimum shear stress ratio. It can be seen that minimum liquefaction resistance, $R_{d(min)}$ increases with the increasing coefficient of drainage, α.

In order to clarify this relationship, minimum liquefaction resistance, $R_{d(min)}$ was plotted against the coefficient of drainage, α as shown in Fig. 6. Even though, cyclic loading frequency, f, length of drainage path, l and coefficient of permeability, k are different for each case, $R_{d(min)}$ for different α values can be observed on an identical straight line. Therefore, it can be concluded that $R_{d(min)}$ can be used as an index property to evaluate the effect of drainage.

The improvement of liquefaction resistance due to partially drained condition, R_d can be explained using the schematic diagram shown in Fig. 7. In addition, comparison between undrained liquefaction resistance, R_u

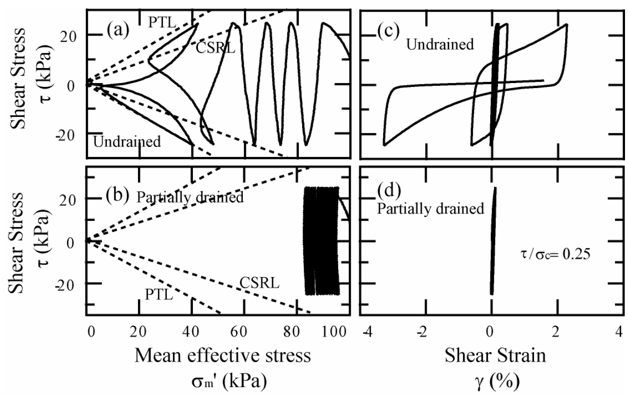

Fig. 4: Mean effective stress path and stress-strain relationship under undrained and partially drained condition

and partially drained liquefaction resistance,R_d are clearly illustrated in this figure with the possible trends which could occur. Fig. 7(a) is corresponding to the high drainage condition where as Fig. 7(b) represents the low drainage condition. It can be noted that for a particular cyclic number, the partially drained liquefaction resistance, R_d under high drainage condition (Fig. 7(a)) is always greater than that of undrained liquefaction resistance, R_u. Another notable feature is that, cyclic stress ratio under partially drained condition, R_d decreases with the increasing number of loading cycles similar to the undrained condition (R_u), however, it reaches to a constant value while further increasing the number of loading cycles. On the other hand, under low drainage condition, R_d behaves same as R_u up to a particular cyclic number and then R_d remains constant while R_u decreases with the increasing number of loading cycles (Fig. 7(b)).

Many authors have found that coefficient of volume compressibility, m_v is approximately constant if the pore water pressure ratio of the soil sample remains below 0.5 – 0.6 [1][12] and significant distortion may be occurred when the pore water pressure ratio exceeds this value. However, in this research study, it was observed that significant axial strain occurred under partial drained condition when the excess pore water pressure ratio exceeds 0.3 - 0.4 and it depends mainly on the cyclic loading frequency, f and coefficient of permeability, k (Fig. 8). It can be seen that magnitude of m_v is small when compared with previous literature [1][12][13]. In the conventional method, m_v is obtained during the reconsolidation process after liquefaction. However, in this research study, m_v was obtained during the partially drainage process and it takes the change of stress state (dilatancy) of soil into account, thus leads to reduction in m_v value.

Further, even if the value of 0.5 is taken as the upper

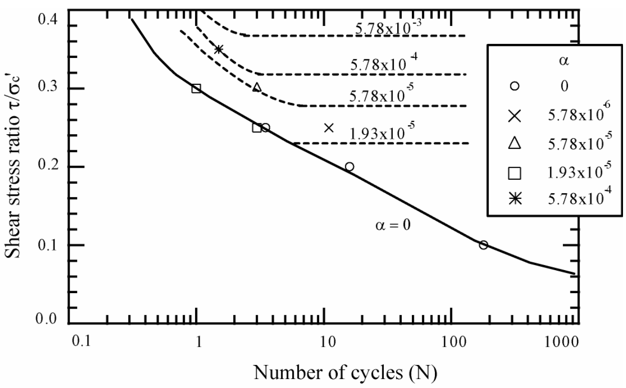

Fig. 5: Shear stress ratio versus number of loading cycles

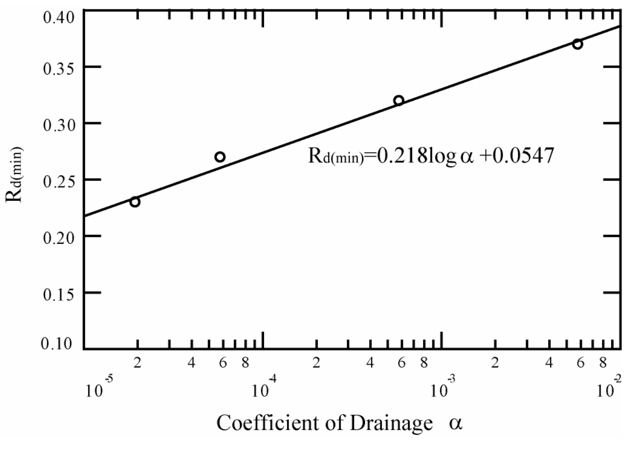

Fig. 6: Variation of minimum liquefaction resistance under partially drained condition

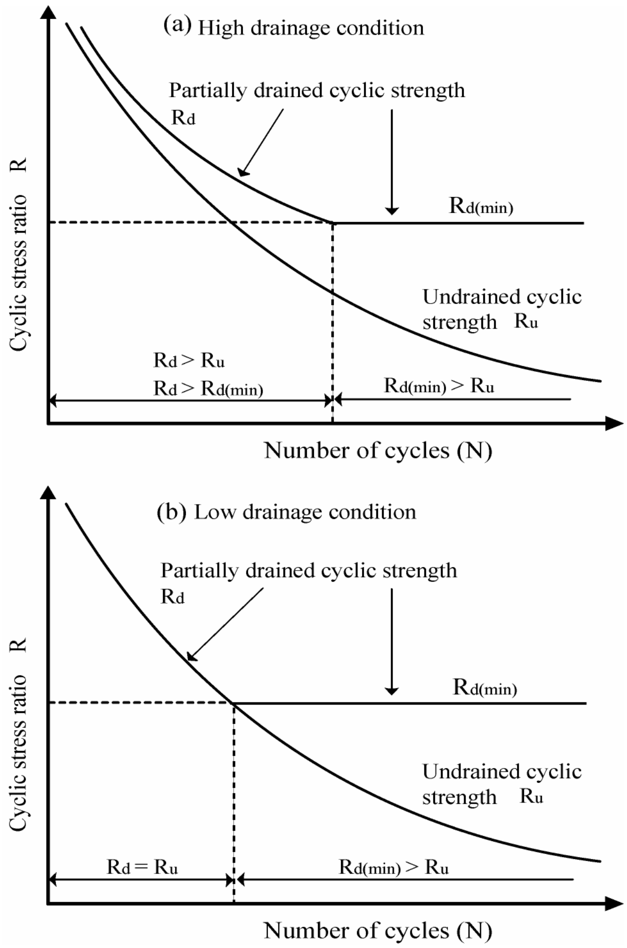

Fig. 7: Definition of partially drained liquefaction resistance

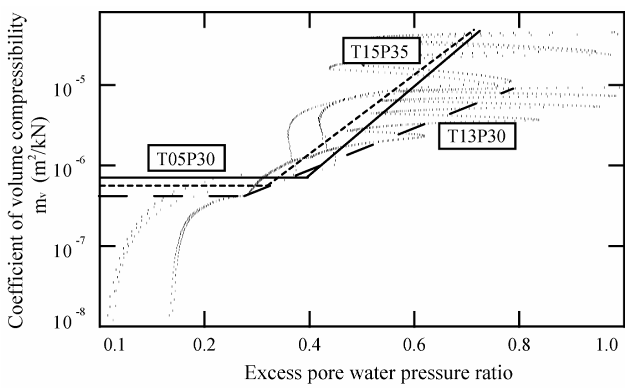

Fig. 8: Variation of m_v with excess pore water pressure ratio

limit for excess pore water pressure ratio, sometimes mean effective stress path can touch the CSRL and PTL, thus it implies the instability of the soil [11]. Therefore, shortcomings in this conventional design method can be overcome by defining the liquefaction resistance under partially drained condition, R_d and make use of R_d in the design process.

Development of partially drained condition for gravel drain design

As explained in the above section, $R_{d(min)}$ can be used as a tool to predict the liquefaction resistance of gravel drain improved ground. It is seen from the Fig. 6 that $R_{d(min)}$ has a linear relationship with coefficient of drainage, α and can be expressed as follows.

$$R_{d\,(\min)} = 0.218 \log \alpha + 0.0547 \tag{9}$$

In order to compare the effectiveness of partially drained condition on gravel drain design, R_d/R_u was obtained from the Fig. 5 and plotted against the coefficient of drainage, α for different N values such as N=2, 5 and 10, as shown in Fig. 9. R_d/R_u=1.0 indicates the lower boundary and there is no effect of drainage at this level and which is equivalent to $\alpha = 0$. It can be noted that curves corresponding to different N values intersect the R_d/R_u=1.0 at different α values and those α values indicate the minimum coefficient of drainage required to achieve the effectiveness of partially drainage, which can be denoted as α*. In order to understand this phenomenon, consider the schematic diagram shown in Fig. 10, which indicates the relationship between R_d/R_u and *log* α. It is conservative to assume that R_d/R_u over *log* α is varying lineally for a particular N value when $\alpha > \alpha$* as expressed in Eq. (10), where m and β are cyclic loading dependent constants. In addition, when $0 \le \alpha \le \alpha^*$, R_d varies almost same as R_u and it implies the behaviour of undrained condition (Eq. (11)).

$$\alpha > \alpha^* \qquad \frac{R_d}{R_u} = m \log \alpha + \beta \tag{10}$$

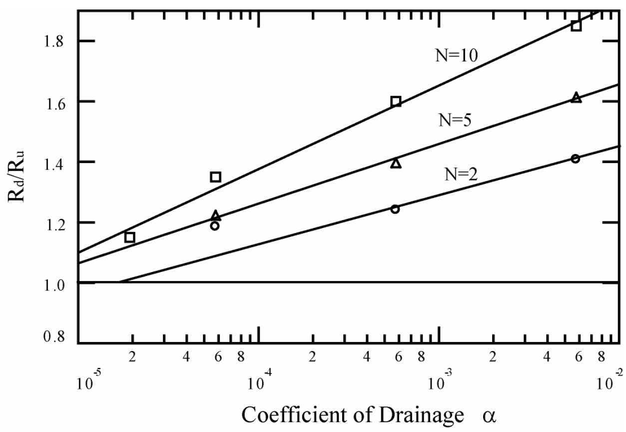

Fig. 9: Variation of R_d/R_u with Coefficient of drainage α

$$0 \le \alpha \le \alpha^* \qquad \frac{R_d}{R_u} = 1.0 \tag{11}$$

It can be noted that, in order to function gravel drain properly, α should be grater than α*. This is a clear indication that the partially drainage will cause significant increment in liquefaction resistance characteristics. The α* can be expressed by substituting R_d/R_u=1.0 in Eq. (10) as follows.

$$\alpha^* = 10^{\frac{(1-\beta)}{m}} \tag{12}$$

The cyclic loading dependent constants m and β can be graphically represented with respect to cyclic loading number as illustrated in Fig. 10 and Fig. 11 respectively. In addition, the relationships between these parameters with the cyclic loading number are expressed as follows.

$$m = 0.1043 N^{0.4288} \tag{13}$$

$$\beta = 0.5524 N^{0.4280} + 1.0 \tag{14}$$

With these definitions and graphical representations, it is

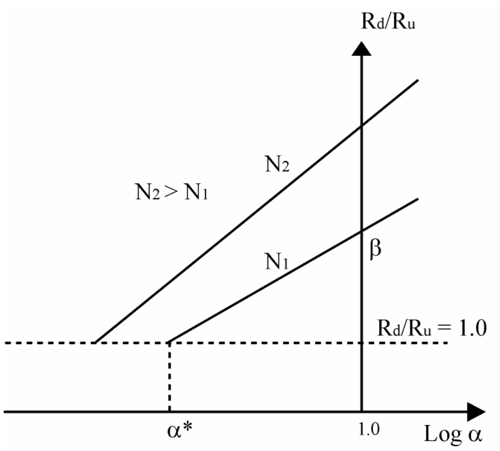

Fig. 10: Typical diagram of R_d/R_u versus *Log* α

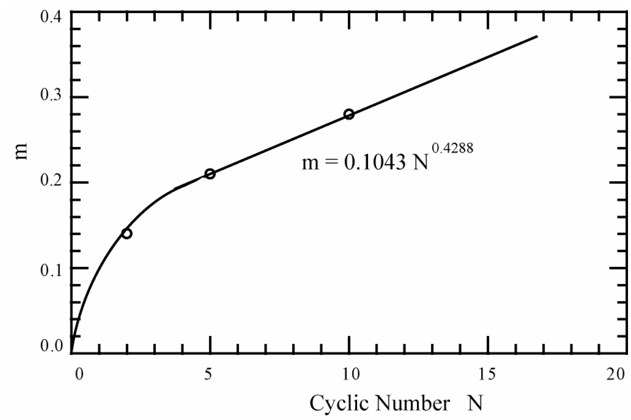

Fig. 11: Relationship between m versus cyclic number N

possible to fine partially drained liquefaction resistance, R_d with respect to coefficient of permeability, cyclic loading number and drainage length, in other words with respect to coefficient of drainage.

The data presented in this paper is related with clean sand (Toyoura sand). Therefore, in order to develop more generalized design method, it is necessary conduct more experiments with different percentages of fine content. Further, it is realized that gravel drain improvement is economical if the liquefiable ground is medium dense (D_r=40-60%).

Simplified design procedure

The simplified design procedure proposed by the authors is presented in Fig. 13. In this analysis, irregular shear stresses due to earthquake shaking are converted to equivalent uniform shear stresses [1]. The equivalent number of cycles, N_{eq} is corresponding to the equivalent uniform shear stress, τ_e defined as $\tau_e = 0.65\tau_{\max}$, where $\tau_{\max}$ is the maximum shear stress amplitude [14]. Based on this concept, N_{eq} corresponding to magnitude of earthquake, M can be obtained [14]. It is clear that larger the magnitude of earthquake, greater the equivalent number of cycles, N_{eq}. In addition, effective duration of earthquake, t_d can be obtained from the relationship proposed based on the field evidences [15].

The relative density, D_r of the liquefiable soil is determined based on the empirical correlation related with the *SPT-N* value [16]. The assessment of the liquefaction potential, F_L can be carried out based on the soil liquefaction resistance, R_u and equivalent dynamic shear stress, L [16]. In this proposed design method, the well resistance in the gravel drain is neglected for simplicity. The complete details of the design procedure are illustrated in the flow chart.

CONCLUSIONS

On the basis of partially drained condition under cyclic loading, the following conclusions may be drawn.

1. No noticeable increase in shear strain under cyclic loading in the partially drained condition. Even soil liquefied under partially drained condition, initial Liquefaction may be delayed when compared with that of undrained condition.
2. Liquefaction resistance under partially drained condition, R_d is relatively high when compared with that of undrained condition. Further, larger the coefficient of drainage α, greater the resistance to liquefaction.
3. The minimum liquefaction resistance $R_{d(min)}$ can be observed on an identical straight line irrespective of the cyclic loading frequency, length of drainage path and coefficient of permeability. Therefore, $R_{d(min)}$ can be used as an index property to evaluate the effect of drainage.
4. In order to function gravel drain properly, α should be greater than α*, where α* is the minimum coefficient of drainage.
5. Simplified design procedure is proposed for gravel drain design based on the test results of partially drained condition under cyclic loading.

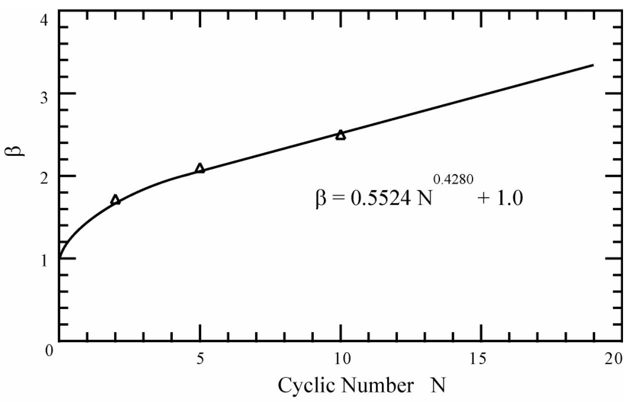

Fig. 12: Relationship between β versus cyclic number N

REFERENCES

[1] Seed, H. B. and Booker, J. R., "Stabilization of potentially liquefiable sand deposits using Gravel drains," *Journal of the Geotechnical Engineering Division*, ASCE, Vol. 103, No. GT7, pp. 757–768, 1977.

[2] Lee, K. L. and Focht, J. A., "Liquefaction potential at Ekofisk tank in North Sea," *Journal of the Geotechnical Engineering Division*, ASCE, Vol. 101, No. GT1, pp. 1–18, 1975.

[3] Umehara, Y., Zen, K. and Hamada, K., "Evaluation of soil liquefaction potentials in partially drained conditions," *Soils and Foundations*, Vol. 25, No. 2, pp. 57–72, 1985.

[4] The Japanese Geotechnical Society, "Remedial Measures against Soil Liquefaction," *A.A. Balkema*, pp. 297–338, 1998.

[5] Tatsuoka, F., Sonoda, S., Hara, K., Fukushima, S. and Pradhan, T. B. S., "Failure and deformation of sand in Torsional shear," *Soils and Foundations*, Vol. 26, No. 4, pp. 79–97, 1986.

[6] Pradhan, T. B. S., Tatsuoka, F., and Horii, N., "Simple shear testing on sand in a Torsional shear apparatus," *Soils and Foundations*, Vol. 28, No. 2, pp. 95–112, 1988.

[7] Mulilis, J. P., Seed, H. B., Chan, C. K., Mitchell, J. B. and Arulanandan, K., "Effect of sample preparation on sand liquefaction," *Journal of the Geotechnical Engineering Division*, ASCE, Vol. 103, No. GT2, pp. 91–108, 1977.

[8] Peacock, W. H. and Seed, H. B., "Sand liquefaction under cyclic loading simple shear condition," *Journal of the Soil Mechanics and Foundations Division*, ASCE, Vol. 94, No. SM3, pp. 689–708, 1968.

[9] Yoshimi, Y. and Oh-oka, H., "Influence of degree of shear stress reversals on the liquefaction potential of saturated sands," *Soils and Foundations*, Vol. 15, No. 3, pp. 27–40, 1975.

[10] Tokimatsu, K. and Seed, H. B., "Simplified procedures for the Evaluation of settlements in sands due to earthquake shaking," *Journal of Geotechnical Engineering Division*, ASCE, Vol. 113, No. GT8, pp. 861–878, 1987.

[11] Vaid, Y. P. and Eliadorani, A., "Instability and liquefaction of granular soils under undrained and

partially drained states," *Canadian Geotechnical Journal*, Vol. 35, pp. 1053–1062, 1998.

[12] Baez, J. I. and Martin, G. R., "Quantitative evaluation of stone column techniques for liquefaction mitigation," *Proceedings of the 10th World Conference on Earthquake Engineering*, A. A. Balkema, pp. 1477–1483, 1992.

[13] Blewett, J. and Woodward, P. K., "The dissipation of excess pore pressures in contractive vibro-column at small strains," *Ground Improvement*, Vol. 5, No. 2, pp. 85–93, 2001.

[14] Seed, H. B., Idriss, I. M. and Arango, I., "Evaluation of liquefaction potential using field performance data," *Journal of the Geotechnical Engineering Division*, ASCE, Vol. 109, No. GT3, pp. 458–482, 1983.

[15] Tokimatsu, K. and Yoshimi, Y., "Effects of vertical drains on bearing capacity of saturated sand during earthquakes," *Proceedings of International Conference on Engineering for Protection from Natural Disasters*, pp. 643–655, 1980.

[16] Tokimatsu, K. and Yoshimi, Y., "Empirical correlation of soil liquefaction based on N-value and fines content," *Soils and Foundations*, Vol. 23, No. 4, pp. 79–97, 1983.

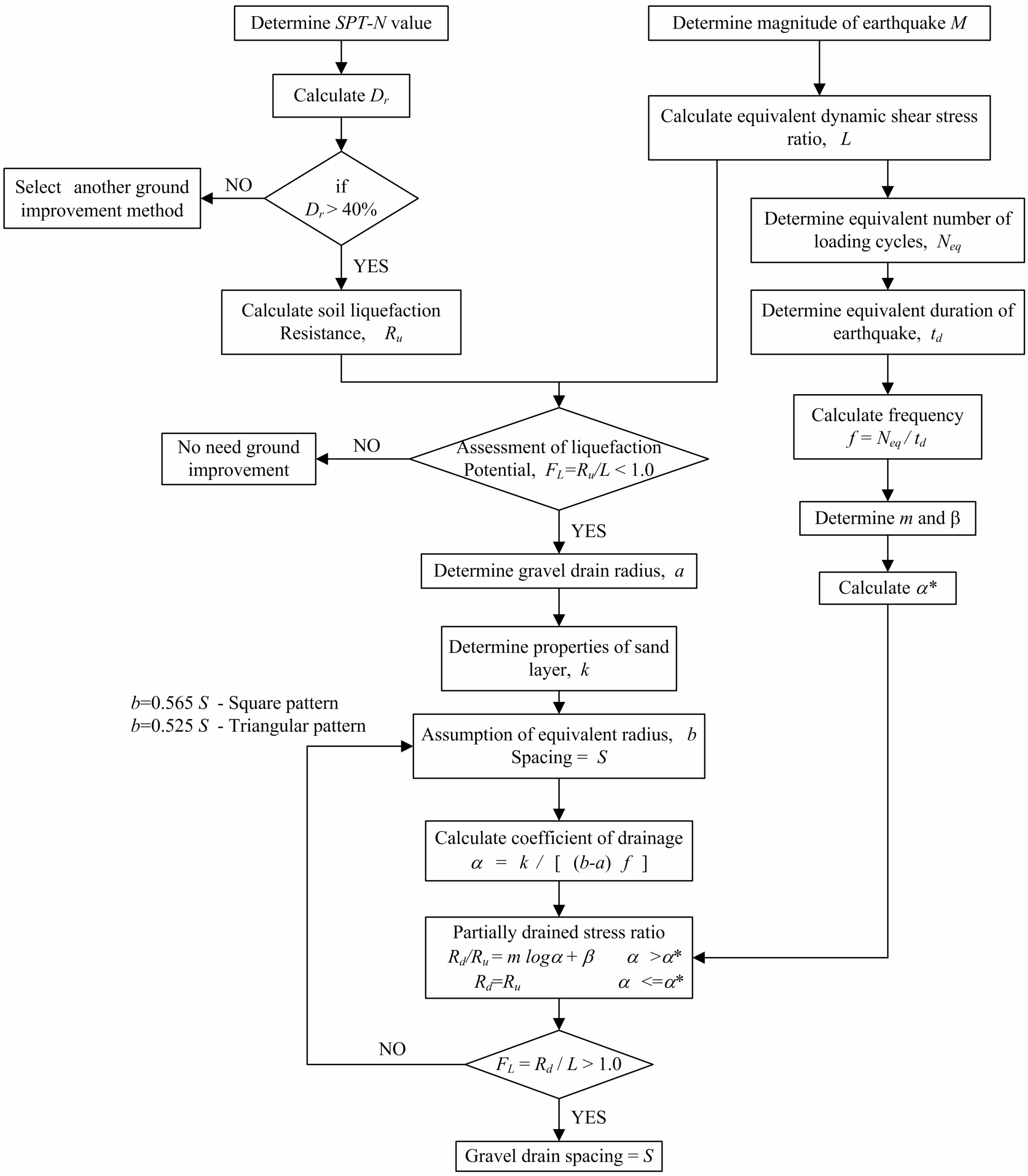

Fig. 13: Flow chart of simplified gravel drain design procedure

Pore Pressure Measurements in Cyclic Triaxial Tests of Sand with High Fines Contents

T. S. Ueng[1], C. L. Yeh[1], S. H. Wu[1]
[1]*Department of Civil Engineering, National Taiwan University, Taipei, Taiwan*

Abstract

Cyclic triaxial tests on sand with various fines contents were conducted. The pore water pressures at different locations (both ends, 1/4 height, mid height, and 3/4 height) in the test specimen were measured. It is found that for a clean sand with a high permeability, the pore water pressure measurement system in an ordinary triaxial test system can obtain a single value of pore water pressure changes within the specimen regardless of the position of measurement. However, because of compliance of the pressure measurement system and a lower permeability of sand with higher fines contents, the measurements of water pressure changes at different locations within the specimen could be quite different from those measured at the ends of the specimen during a cyclic triaxial test. This could affect the assessment of the pore pressure ratio and liquefaction resistance of the sand specimen. The effect increases with increasing fines content of sand. The non-uniformity of the triaxial specimen and the uncertainty of the measured data should be evaluated for sand with high fines contents especially when the soil reaches liquefaction.

Keywords—*sand, fines content, water pressure measurement, cyclic triaxial test*

INTRODUCTION

Previous studies on the soil liquefaction characteristics and evaluation of liquefaction potential are mostly based on the laboratory test results of clean sands with little fines (< 0.075 mm). It was considered that soils with higher fines content should have a higher liquefaction resistance. In many recent earthquakes, soils containing high fines contents were found liquefied in many cases, for example, soil liquefaction in Nantou City during the 1999 Chi-Chi Earthquake. Therefore, the liquefaction resistance of sand with fines was studied extensively in the recent year, e.g., [1], [2], [3].

Cyclic triaxial test apparatus, e.g., [4], is one of the most used testing devices in the soil liquefaction studies. In the typical cyclic triaxial tests, the researchers often use small and stiff tubes to connect the cap and bottom of the specimens to the pore water pressure sensors. They assume that there is no change in the volume of specimens and measuring systems in the undrained test. As a result, the values of water pressure changes measured by the sensors should be the pore pressure changes throughout the soil specimen.

In fact, there exists volume changes in the triaxial measurement systems, such as tubing, when water pressure changes. Therefore, when the pore water pressure changes in a certain location of the specimen, the soil in other locations or at another end of the water pressure measurement of the pipeline senses the pressure changes with a water flow according to the compliance of testing system. Flowing of water can occur and reflect the pore water pressure change rapidly for sand of a high permeability. However, for sand with high fines contents, the pressure measurements at the ends of specimen cannot immediately reflect the pore water pressure changes within the specimen due to the low permeability of the soil.

In order to evaluate the effect of the permeability on the results of liquefaction tests on sand with various fines contents, the water pressures at different heights of the triaxial specimen with various fines contents were measured and compared with those obtained at the specimen ends during the cyclic triaxial tests.

TESTING SETUP

The cyclic triaxial test apparatus was modified, as shown in Fig. 1, to provide three holes at the base platen of the triaxial cell for installing three 3-mm rigid stainless steel tubes with filters at the tips [5]. The heights of these tubes are 40 mm, 80 mm, and 120 mm. They are corresponding respectively to approximately 1/4, 1/2, and 3/4 of the specimen height of about 160 mm. The pore water pressure changes at the tip of each stainless steel tubes can be measured with the miniature pressure sensors (6.4 mm in diameter and 11.4 mm in length) directly beneath the metal pipe. Due to the limitation of the measuring system, only two metal tubes were used at the same time in each test. The water pressure changes at both ends of the specimen are measured as in the ordinary triaxial test with an external differential pressure transducer connected by stiff Teflon tubes with a total length of approximately 1000 mm for the cyclic testing apparatus at Department of Civil Engineering, National Taiwan University.

Thus, the pore water pressure changes at both ends, mid height, and 1/4- or 3/4-height of the specimen can be measured simultaneously during a cyclic triaxial test.

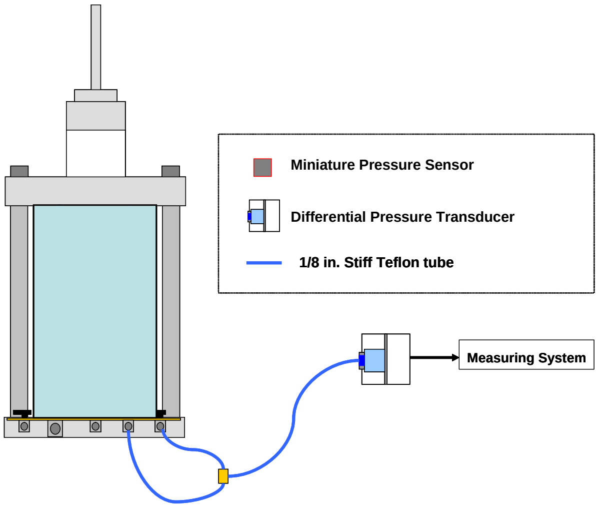

Fig. 1: Modified cyclic triaxial testing apparatus

The soils used in this study were obtained from Maoluo River bank in Nantou City where extensive soil liquefaction occurred in the 1999 Chi-Chi Earthquake. Fig. 2 shows the grain size distribution curves for the Maoluo River soils obtained from two near-by locations on the river bank. The soils varies from ML (NP) to CL (PI = 8) containing low-plastic fines (PI = 7-14).

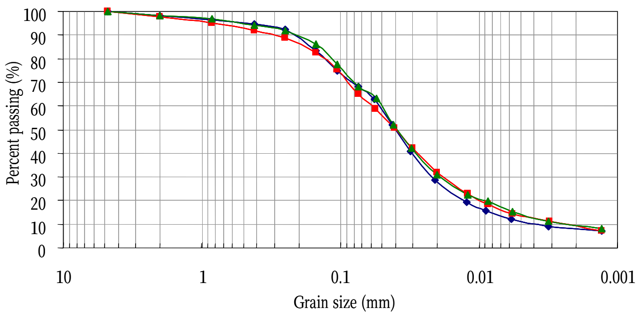

(a) Soil 1

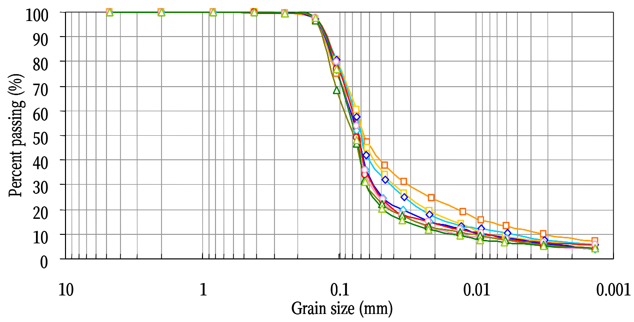

(b) Soil 2

Fig. 2: Grain size distribution curves for the Maoluo River soils

The sand (> 0.075 mm) and fines (< 0.075 mm) of these soils were separated using wet sieving method. Soils with various fines contents were obtained by remixing different proportions of sand and fines. The triaxial specimen was prepared using the moist tamping method to obtain a dry unit weight of 14.0 kN/m^3. Three holes were also provided for the compaction foot to facilitate the sample preparation.

Cyclic Triaxial Test Results

Liquefaction Resistances of Specimens with and without Metal Tubes

Cyclic triaxial tests on specimens with and without metal tubes were conducted to evaluate the effect of the metal tubes within the specimen on the liquefaction resistance. Fig. 3 indicates that there is little difference of liquefaction resistance between specimens with and without the inner metal tubes.

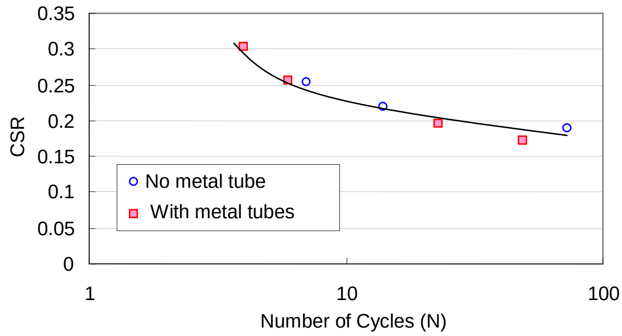

(a) FC = 0

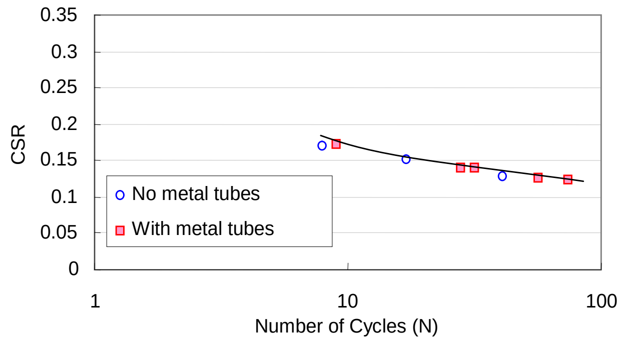

(b) FC = 60 %

Fig. 3: Comparison of liquefaction resistance between triaxial specimens with and without inner metal tubes

Pore Pressure Changes at Different Locations within the Specimen

Cyclic triaxial tests on soils with different fines contents were conducted and the pore water pressure changes at different locations were measured [6], [7]. Fig. 4 shows the comparison of water pressure measurements at various locations. It can be seen that for the clean sand (FC = 0), the pore water pressure changes during the cyclic triaxial test are essentially the same at different locations within the specimen. For the sandy silts (FC = 60% and 65%), the measured pore pressure changes are the highest at 3/4 height of the specimen, followed by those obtained at mid height, 1/4 height, and the ends of the specimen. This indicates a earlier liquefaction of the soil at 3/4 height where the necking of specimen usually occurs. A correction for the number of cycles to liquefaction can be assessed comparing the number of cycles to reach pore water pressure ratio, r_u = 1.0 at the ends and the 3/4 height or mid height of the specimen. A correction of number of cycles (Cn) to reach liquefaction can be expressed by:

$$Cn = N_i/N_o \tag{1}$$

where N_o = Number of cycles to liquefaction based on pressure measurements at specimen ends

N_i = Number of cycles to liquefaction based on pressure measurements within specimen

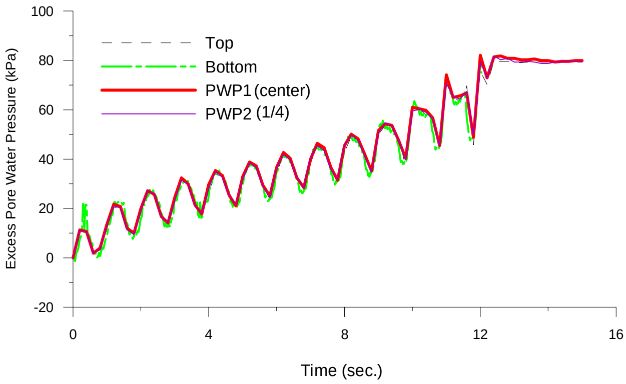

(a) Soil 1, FC = 0

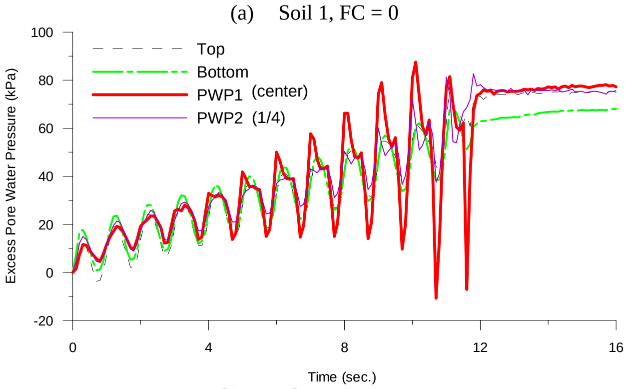

(b) Soil 1, FC = 65%

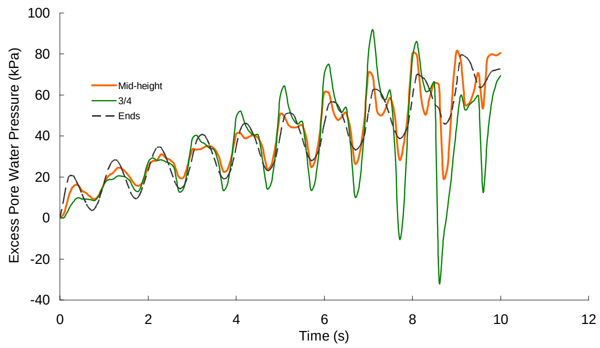

(c) Soil 2, FC = 60%

Fig. 4: Comparison of pore water pressure changes at various locations in the triaxial specimen

Permeability and Correction of Liquefaction Resistance

Permeability of the soil with different fines contents were measured as shown in Table 1.

Table 1: Permeability of soils with different fines contents

Soil 1		Soil 2	
FC (%)	Permeability (cm/s)	FC (%)	Permeability (cm/s)
0	2.98E-03	0	3.07E-03
15	1.87E-03	20	1.09E-03
48	3.57E-04	40	1.40E-04
65	4.44E-05	60	3.62E-05
100	1.32E-05	100	1.10E-05

The effect soil permeability on Cn is shown in Fig. 5, based on ratio between the pressure measurements at the mid height and the ends of the specimen. It can be seen that, according to the test results in this study, no correction is needed for soil permeability higher than about 10^{-4} cm/s.

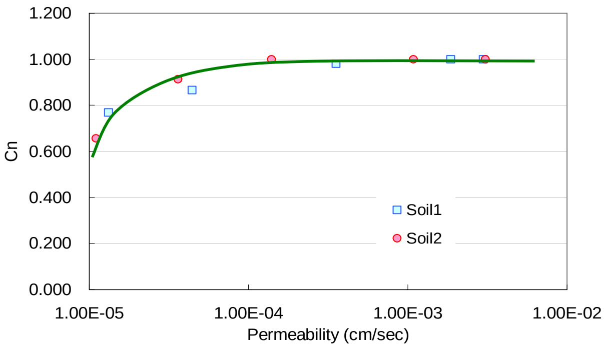

Fig. 5: Cn versus soil permeability

Concluding Remarks

This study points out the following major affecting factors of pore water pressure measurements for high fines content soil in dynamic triaxial tests:

1) The higher the fines contents, the lower the permeability of a soil. The true pore water pressure changes within the specimen of permeability less than about 10^{-4} cm/s cannot be obtained correctly by the pore pressure measurements at the specimen ends.

2) There is a longer duration of loading during tests of lower frequency, and pore water pressure measurement can obtain better pore water pressure within the samples.

3) Higher pore water pressure changes usually occur in the triaxial tests with larger CSR, and result in more volume change in the pipeline section.

It should be noted that the quantitative results in this study were obtained using the cyclic triaxial test apparatus at Department of Civil Engineering, National Taiwan University. Different triaxial test devices with different system compliances at other laboratories can give different values of deviations in measurements at different locations in the specimen. However, the qualitative trend obtained in this study should be applicable.

REFERENCES

[1] Chan, C. K. and Mulilis, J. P., "Pneumatic Sinusoidal Loading System," *J. Geotechnical Eng. Division*, ASCE, Vol. 102, GT3, pp. 277-282, 1976.

[2] Prakash, S., Guo T. and Kumar, S., "Liquefaction of silts and silt-clay mixtures," *Geotechnical Earthquake Engineering and Soil Dynamics III.* ASCE Geotechnical Special Publication No. 75, Vol. 1, pp. 337-348, 1998.

[3] Thevanayagam, S., Fiorillo, M. and Liang, J., "Effect of non-plastic fines on undrained cyclic strength of silty sands," *Soil Dynamics and Liquefaction 2000. ASCE Geotechnical Special Publication No. 107*, pp. 77-91, 2000.

[4] Yamamura, J. A. and Kelly M., "Monotonic and cyclic liquefaction of very loose sands with high silt content," *J .Geotechnical and Geoenvironmental Engineering*, ASCE, Vol. 127, No. 4, pp. 314-323, 2001;.

[5] Chan, S. R., "The study of liquefaction characteristics for Taipei silty sands under different drainage conditions," (in Chinese), Ph.D. dissertation, Department of Civil Engineering, National Taiwan University, Taipei, Taiwan, 2000.

[6] Yeh, C. L., " Pore water pressure generation in specimens with high fines content in dynamic triaxial tests," (in Chinese), M.S. thesis, Department of Civil Engineering, National Taiwan University, Taipei, Taiwan, 2005.

[7] Wu, S. H., "Effect of fines content on pore water pressure measurements for Maoluo River soil," (in Chinese), M.S. thesis, Department of Civil Engineering, National Taiwan University, Taipei, Taiwan, 2006.

Liquefaction of Silty Sand with Micro-layered Structure due to Segregation

M. Yoshimine[1], R. Koike[2]
[1]*Department of Civil and Environmental Engineering, Tokyo Metropolitan University, Tokyo, Japan*
[2] *Government of Kawasaki City, Kanagawa Prefecture, Japan*

Abstract

Previous case studies on liquefaction of ground suggest that silty sand deposits are more resistant to liquefaction than clean sand deposits. However, it is often observed that the liquefaction strength of silty materials is very low in laboratory testing. It is also reported that the resistance of undisturbed samples are stiffer than disturbed samples. In general, silty sand deposits in-situ are not uniform but the sands and fines are segregated with beddings of millimeters to centimeters in thickness. This micro-layered structure may cause the differences of the liquefaction resistances of the in-situ soils and the disturbed samples tested in laboratory. In this study, we examined the liquefaction resistances of uniform sand-silt mixture and alternatively layered deposit of the same materials by means of undrained cyclic triaxial tests. The test results showed that the layered samples exhibited much higher strength compared with the uniformly deposited samples.

Keywords—*Liquefaction, segregation, silty sand, stratification, triaxial test, undrained shear strength*

INTRODUCTION

We often observe laminar structure generated by segregation of particles on cross sections of ground in the field. However, we usually employ homogeneously reconstituted specimens of the soil in laboratory tasting to evaluate the strength and deformation characteristics of the ground. This difference in structure of in-situ soil and reconstituted specimen could resulted in some misreading in the evaluation of the behavior of the natural deposit.

Yoshimine and Koike [1] inspected the effects of graded bedding structure of clean sand without fines on its strength against liquefaction. They sieved and separated the clean sand into four components with different ranges of particle size, and then deposited alternatively to create stratified structure in specimens. Undrained triaxial compression tests in monotonic loading and cyclic triaxial loading tests were performed on these stratified samples as well as the uniformly mixed samples of the same sand. It was observed that the liquefaction resistance of the stratified specimens was larger than the uniform specimens. Although only clean sand was examined in this previous study, silty sands that have wider range of particle size should have higher potential of segregation and creating stratified structure in natural deposits, which may exhibit more serious effects on their liquefaction characteristics.

Based on the anticipation mentioned above, undrained triaxial tests were conducted on homogeneous samples consisted with well-mixed sand and silt contents, and heterogeneous samples created by alternative deposition of the same sand and silt contents which are completely separated in layered structure. One of the difficult problems is the selection of appropriate index for density of sand with fines contents. The comparison of the behaviors of samples with different fines contents and different structure was assessed on the basis of void ratio, skeleton void ratio and relative density, in this study.

TESTED MATERIALS AND TEST PROCEDURE

Tested Materials

Toyoura sand has mean particle diameter of D_{50} = 0.2mm, particle density of ρ_s = 2.650g/cm^3, maximum and minimum void ratios of e_{max} = 0.977 and e_{min} = 0.597. The kaolin silt has particle sizes of D_{10} = 0.002mm, D_{30} = 0.02mm, D_{50} = 0.035mm and D_{60} = 0.045mm, and particle density of ρ_s = 2.733g/cm^3. Though the GJS method for evaluating maximum and minimum density of soil is recommended not to apply on fine materials, we apply the method to the kaolin silt and found maximum and minimum void ratios of e_{max} = 6.613 and e_{min} = 3.889. The particle size distribution curves for Toyoura sand and the kaolin silt are shown in Fig. 1. Maximum and minimum void ratios of uniform mixture of the sand and the silt (fines contents of *FC*=5% and 10%) were also examined by JGS method, and e_{max} = 1.106 and e_{min} = 0.589 for the mixture of *FC*=5%, and e_{max} = 1.119 and e_{min} = 0.598 for the mixture of *FC*=10% were obtained. These values are nearly the same as reported by Zlatovic and Ishihara [2] for Toyoura sand – kaolin silt mixture.

Sample Preparation Methods

The triaxial samples had diameter of about 50mm and height of about 100mm. Wet tamping method was adopted for constructing the samples of uniformly mixed materials in five layers. Firstly the 1/5 of the total amount of dry Toyoura sand and kaolin silt were weighed and uniformly mixed, then distilled water was added to the mixture to make the water content about 5%. The material was well mixed again to have completely homogeneous distribution of sand, silt and water contents. After that the

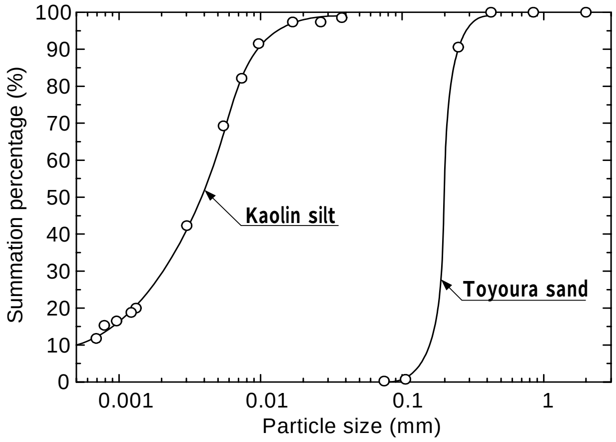

Fig. 1: Particle size distributions of the tested materials

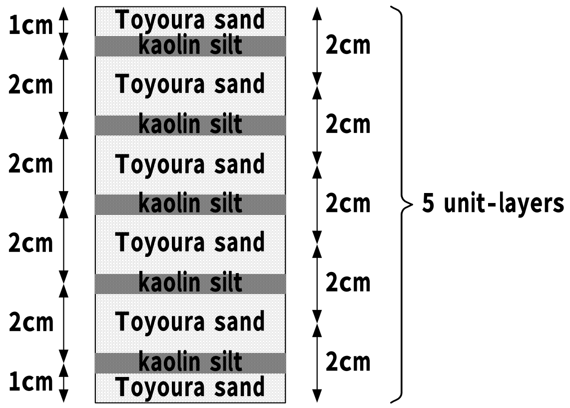

Fig. 2: Segregated and layered structure of specimen of 10cm height with five unit-layers

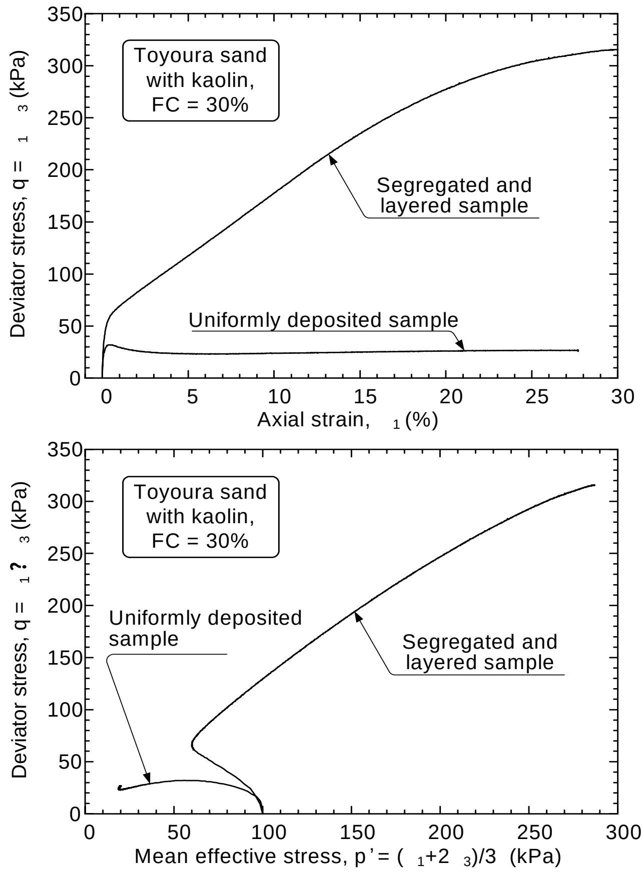

Fig. 3: Undrained monotonic loading tests on segregated and uniform silty sand with *FC*=30%

mixed material was poured into the mold and compacted by a metallic tamper which has a diameter of 24mm. This procedure was repeated 5 times and a uniform specimen was completed.

Most of the segregated and layered specimens were deposited in 5 unit-layers and 11 sub-layers as schematically shown in Fig. 2. Firstly the 1/10 of the total dry weight of Toyoura sand was mixed with water to make the water content 5%, and the moist Toyoura sand was poured into the mold and compacted by the tamper. Then the 1/5 of the total weight of kaolin silt was placed on the sand surface, and gently compacted by the tamper. Next, the 1/5 of the total dry weight of Toyoura sand was moistured, deposited and compacted in the same manner, then the first unit-layer and the lower half of the second unit-layer were constituted. These processes were alternatively repeated and a sand-silt layered specimen was completed. Some specimens were deposited in larger numbers of layers to examine the effects of the thickness of the sub-layers.

Saturation, Consolidation and Shear tests

After constituting a specimen, CO_2 and then de-aired water were circulated through the specimen from the bottom to the top to saturate the material. It was confirmed that all of the specimens had Skempton's B-value higher than 0.96. The saturated samples were consolidated under isotropic effective confining stress of $\sigma_c'=p_{ini}'$=100kPa. The kaolin silt layers were only slightly compacted, thus it is expected that the layers had the same density for all of the specimens in normally consolidated states after consolidation regardless to the thickness of the layers. After completion of consolidation, the specimens were sheared undrained in monotonic compression or cyclic loading conditions. The axial strain rate in the monotonic triaxial compression tests was about 1%/min. and the frequency in the triaxial cyclic tests was 0.1Hz. We can assume uniform distribution of pore water pressure throughout the samples during the monotonic and cyclic loading schemes, because the thickness of the sub-layers of the kaolin silt was small enough. After the completion of the undrained monotonic or cyclic shear test, the pore water was drained as much as possible by application of drained cyclic loading and then the water content of the specimen was measured. The void ratio of the specimen was calculated in the accuracy of 0.001 based on the amount of the drainage, the water content after testing and the density of the soil particle.

To minimize the end friction of the samples, small porous stones of diameter 10mm were embedded at the center of top and bottom platens. The platens had an enlarged diameter of 60mm, and they were lubricated by layers of grease and rubber membranes. Membrane force was corrected in the data processing. However the effects of membrane penetration were not corrected during the testing and data processing in this study.

RESULTS OF MONOTONIC LOADING TESTS

Effects of Fines Content and Layered Structure

Undrained triaxial compression tests in monotonic loading condition were performed on the uniform specimens and stratified specimens with fines content of *FC*=0%, *FC*=5%, *FC*=10%, *FC*=15% and *FC*=30%. Figure 3 shows representative test results on uniform and stratified specimen with *FC*=30%. One may see a great effect of stratified structure due to segregation of silt and sand materials. The segregated and stratified sample behaved much stiffer than the uniformly deposited sample, even though the void ratio of the segregated specimen (e = 0.865) was greatly higher than the void ratio of the uniform specimen (e = 0.587).

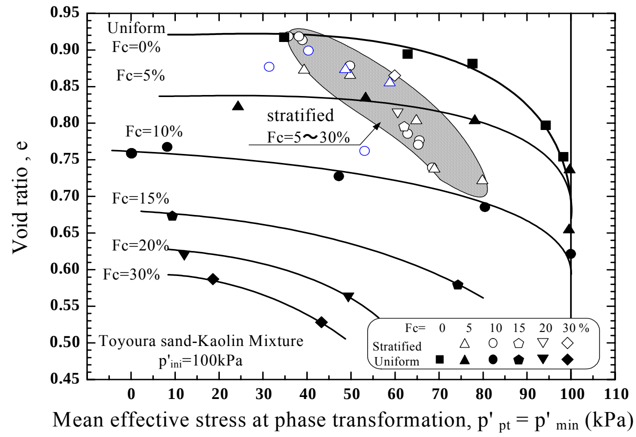

Fig. 4: State of phase transformation during undrained monotonic loading ($e - p'_{min}$ plot)

All of the test results of uniform specimens and stratified specimens with 5 unit-layers were summarized and plotted in Fig. 4 on $e - p'_{min}$ plane, where e is the entire void ratio of the specimen and p'_{min} is the minimum mean effective stress at phase transformation during the monotonic undrained shear process. The lower positioned phase transformation points indicate that the specimens behaved softer and higher pore water pressure developments. Figure 4 confirms that, if the silty sand was uniformly and homogeneously deposited, the phase transformation lines positioned lower when the fines contents were increased. This indicates that the undrained behavior was softer and more contractive for the sand with higher fines contents if it is compared on the basis of void ratio. On the other hand, the phase transformation points of the stratified specimen with *FC*=5% to 30% positioned in a narrow band irrespective to the amount of fines contents. The band exists above the phase transformation line for the uniform specimen with *FC*=10%, thus we can conclude that the segregation and stratification of the silt makes the undrained behavior of the entire deposits stiffer if the fines contents are more than 10% and if the comparison was made on the basis of void ratio.

Figure 5 is the plots of phase transformation lines based on relative density on $D_r - p'_{min}$ plane. Only the test results of specimens with *FC*≤10% are shown in this figure, because of the limitation of the maximum and minimum density tests. The general trend is the same as the one observed in the $e - p'_{min}$ plots, whereas the line for stratified samples with *FC*=10% positioned slightly lower than that of stratified samples with *FC*=5%. Note that the maximum and minimum densities were evaluated from uniformly mixed material even for calculation of relative density of segregated and stratified specimens.

Kuwano et al [3] reported that undrained behaviors of silty sands were similar regardless of their amount of fines contents if their skeleton void ratios were the same.

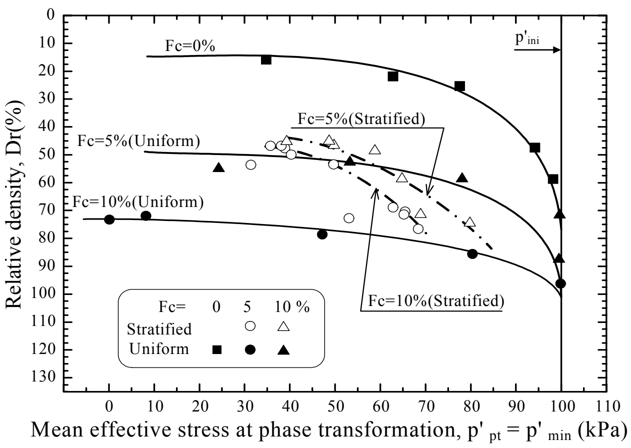

Fig. 5: State of phase transformation during undrained monotonic loading ($D_r - p'_{min}$ plot)

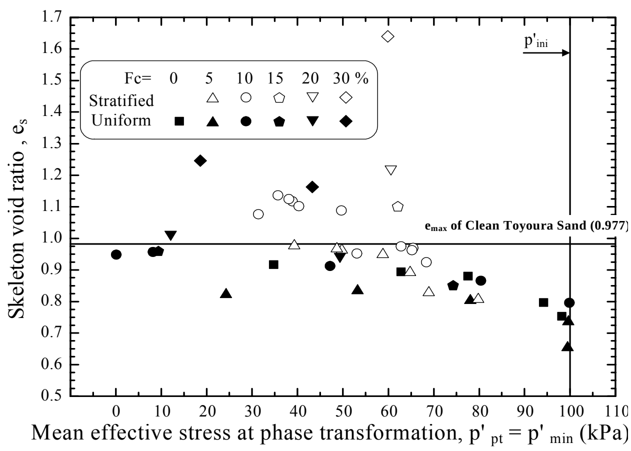

Fig. 6: State of phase transformation during undrained monotonic loading ($e_{skeleton} - p'_{min}$ plot)

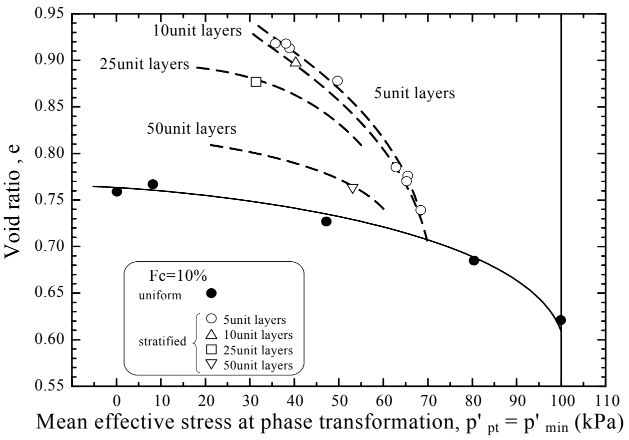

Fig. 7: Effect of the number (thickness) of layers on the undrained behavior in monotonic loading

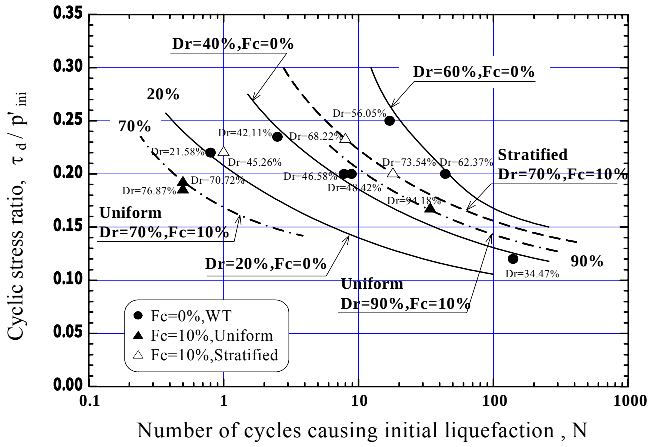

Fig. 8: Results of undrained cyclic loading tests

Skeleton void ratio ($e_{skeleton}$) of saturated material is the ratio of the volume of water plus fines to the volume of sand particles, which is calculated by $e_{skeleton} = e + FC (\rho_{silt}/\rho_{sand})$ where e is the void ratio of the entire specimen, FC is the fines content, ρ_{silt} and ρ_{sand} are the density of silt particles and the density of sand particles, respectively. Figure 6 is the $e_{skeleton} - p'_{min}$ plots from the test results of this study. This figure indicates that the undrained behavior is more less similar regardless of fines contents and segregation of fines, if $e_{skeleton}$ is the same and if the $e_{skeleton}$ is smaller than the maximum void ratio of the sand particles (e_{max} = 0.977), especially for the uniform mixture. This fact suggests that, when $e_{skeleton}$ is smaller than the e_{max} of the sand particles, the interlocking of the sand particles was maintained and the fine particles in the inter-voids of the sand particles took minor role in shear behavior. When $e_{skeleton}$ is larger than the e_{max} of the sand particles, the undrained behavior became stiffer and more dilative in the comparison on $e_{skeleton}$ basis, and the plots of phase transformation positioned higher for specimens with larger fines content. This tendency is more prominent in the case of segregated and stratified specimens, and thus it can be concluded that the segregation of fines contents makes the undrained behavior stiffer also in the comparison on $e_{skeleton}$ basis.

Effects of the thickness of the layer

It is reasonable to assume that thinner thickness of the graded layer results in more similar behavior with the uniform deposit, because the layered structure of the specimen is essentially identical to the uniform structure if the thickness is reduced to the order of the particle size of the sand. To examine this issue, segregated specimens deposited in 10, 25 and 50 unit-layers with fines content of 10% were tested in addition to the uniformly deposited specimens and the 5 unit-layered specimens. The thickness of a unit-layer was 20mm, 10mm, 4mm and 2mm in the 5, 10, 25 and 50 unit-layered specimens.

The results of undrained monotonic loading tests are plotted on $e - p'_{min}$ plane in Fig. 7. This figure shows that the phase transformation points positions lower and nearer to the phase transformation line for the uniform specimens when the number of the layers were increased and the thickness of one unit-layer was decreased. This fact ensures the rightness of the assumption about the effects of thickness on the behavior of stratified deposits.

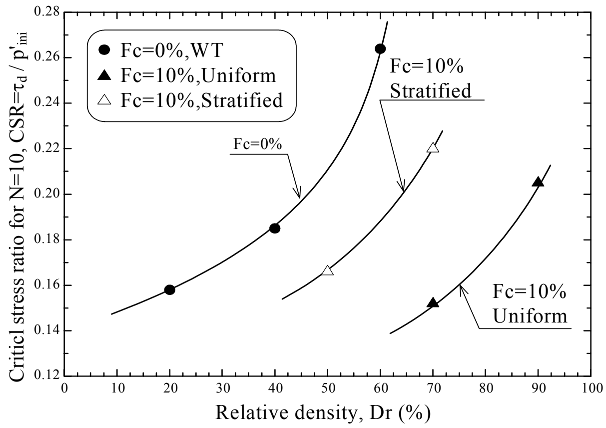

Fig. 9: Cyclic liquefaction strength versus relative density

RESULTS OF CYCLIC LOADING TESTS

Triaxial cyclic loading tests in undrained condition were performed on uniformly deposited specimens and segregated and layered specimens with fines content of FC=10%, as well as the clean sand deposit with FC=0%. The number of the unit-layers in the segregated samples was fixed to five. The initial liquefaction during cyclic loading was identified by the development of double amplitude of axial strain equal to 5%, and the relation between the cyclic stress ratio (τ_d/p_{ini}') and the number of cycles causing initial liquefaction (N) was plotted in Fig. 8 with contour lines of relative density for each kind of specimens.

For the purpose of clear examination of the effects of

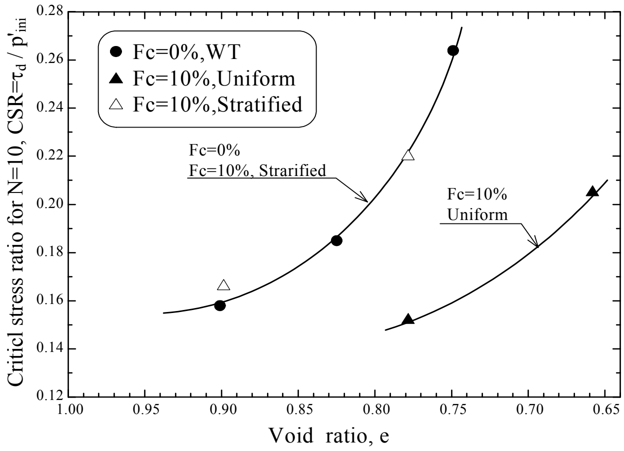

Fig. 10: Cyclic liquefaction strength versus void ratio

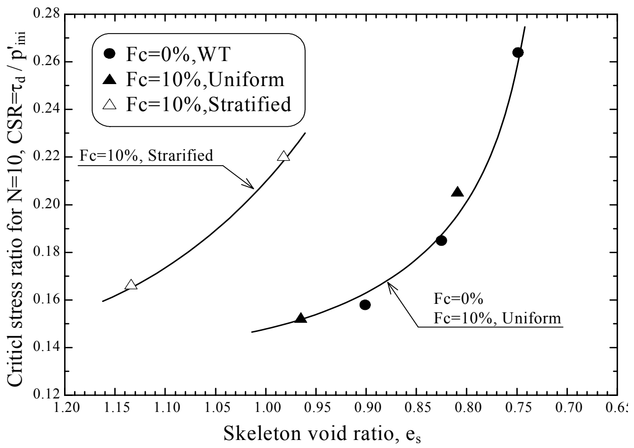

Fig. 11: Cyclic liquefaction strength versus skeleton void ratio

fines content and the layered structure due to segregation of silt content, critical stress ratios (*CSR*) which causes initial liquefaction at *N*=10 were readout from the plot of the contour lines in Fig. 8, and the *CSR* values were plotted versus the corresponding relative density in Fig.9. This figure indicates that the cyclic liquefaction resistance of stratified silty sand is higher than the resistance of uniformly mixed material. The strength of the uniform sample of D_r=70% was *CSR* = 0.14 whereas the stratified sample of the same relative density exhibited *CSR* = 0.195. The difference of the liquefaction strength due to segregation may be decreased if the relative density exceeded 85% to 90%, as suggested from the results from monotonic loading tests displayed on Fig. 5. The liquefaction strength of the clean sand with *FC*=0% was higher than both stratified and uniform with *FC*=10%.

The values of the relative density plotted in Fig. 8 were converted in void ratio (*e*) and the *CSR* – *e* relationship was plotted in Fig. 10. The cyclic liquefaction strengths (*CSR*) of the stratified silty sand and the clean sand were plotted around the same level in this figure, however the strength of stratified silty sand may be smaller than the clean sand if their densities were higher with smaller void ratios as suggested by Fig. 4.

Further more, the *CSR* – $e_{skeleton}$ relationship from the same tests was plotted in Fig. 11. In this case, the cyclic liquefaction strength of the uniformly deposited silty sand was in the same level as the strength of the clean sand in the range of $e_{skeleton}$ less than the maximum void ratio of clean sand which is e_{max} = 0.977. This coincidence is in harmony with the results of monotonic loading tests shown in Fig. 6. The cyclic liquefaction strength of the stratified silty sand was much higher than the uniform silty sand the clean sand, but the results of monotonic loading tests shown in Fig. 6 suggests that the difference may be diminished if $e_{skeleton}$ was decreased.

CONCLUSIONS

Effects of segregation of fine and coarse soil particles on the undrained behavior and liquefaction resistance of silty sand were verified by means of undrained triaxial tests. Perfectly segregated specimens were constituted by depositing Toyoura sand and kaolin silt separately in layers, and their undrained shear behavior was compared with the test results of uniformly deposited specimens of complete mixture of the same sand and silt content. Generally the stratified specimen exhibited much stiffer undrained response compared with uniform specimen, both in monotonic loading and cyclic loading conditions. The resistance to liquefaction of the stratified deposits were not so much affected by the amount of fines, whereas the resistance of the uniform deposits was drastically decreased with increasing fines content, thus the discrepancy of the behaviors of stratified and uniform materials was larger for higher fines content, especially if the skeleton void ratio of the deposit was greater than the maximum void ratio of the sand content. These facts indicate that the in situ liquefaction resistance of natural deposits with graded bedding could be highly underestimated by triaxial testing if remolded and uniformly reconstituted specimens were used in the laboratory.

REFERNCES

[1] Yoshimine, M. and Koike, R., “Liquefaction of clean sand with stratified structure due to segregation of particle size,” *Soils and Foundations*, Vol. 45, No. 4, pp. 89-98, 2005.

[2] Zlatovic, S. and Ishihara, K., “On the influence of nonplastic fines on residual strength,” *Proceedings of the first International Conference on Earthquake Geotechnical Engineering* (IS-Tokyo'95), Vol. 1, pp. 239-244, 1995.

[3] Kuwano, J., Nakazawa, H., Sugihara, K. and Yabe, H., “” (in Japanese), *Proceedings of the 31th Japan National Conference on Soil Mechanics and Foundation Engineering*, JGS, pp. 993-994, 1996.

(5) Performance based design and other related topics

Seismic Microzonation of Taipei Basin

C.H. Chen [1], C.C. Tsai [1], J.S. Chiou [2]
[1] Department of Civil Engineering, National Taiwan University, Taipei, Taiwan
[2] National Center for Research on Earthquake Engineering, Taipei, Taiwan

Abstract

A seismic microzonation map for the area of Taipei basin has been published in the 2005 version of Seismic Design Code for Buildings of Taiwan. The area of Taipei Basin is divided into four microzonations. It was developed primarily based on the contour map of parameter C_v, which is deduced from the normalized response spectra of past strong ground motions recorded in the Taipei basin. This paper is to investigate the suitability of zoning scheme by other available information. Firstly, the topography and geology of Taipei basin were reviewed and the averaged shear wave velocities of top 30 meters of soils at associated seismograph sites, Vs_{30}, were calculated for site characterization. Secondly, the ground periods deduced from spectral analyses of past earthquake data were compared with the values of C_v. It is found that the microzonation map developed on the basis of C_v values is generally consistent with the distributions of Vs_{30} and ground periods of Taipei basin. For the areas near the northwestern and southeastern fringes of the basin, they are specified as the high C_v zones in the microzonation map of the code. However, the results of Vs_{30} and ground periods distribution indicate that these areas are not appropriate to be categorized into long period zones. Some studies and further modifications are indeed necessary.

Keywords—*Seismic microzonation, response spectrum, shear velocity, ground period*

INTRODUCTION

The Taipei basin, located in northern Taiwan, is the most developed area in Taiwan. It is occupied with dense population and high-rise buildings. However, the Taipei basin is known as a soft-deposited basin. Considering the active collisions between the Philippine Sea Plate and the Eurasian Plate along the east coast of the Taiwan Island, the Taipei basin is continuously threatened by the attack of strong earthquakes. Therefore, the seismic design for structures and buildings in the basin is of great concern. For convenience of engineering design, the latest version of Seismic Design Code for Buildings [1] published a seismic microzonation map for the area of Taipei basin. This map was developed based on the contour of parameter C_v, which defines the shape of the normalized response spectrum deduced from past strong ground motions recorded in the area of the Taipei basin. According to this microzonation map, for a structure in the basin, engineers can easily choose the corresponding design spectrum for seismic design. Since this proposed microzonation is generated solely on the basis of response spectrum of past earthquakes, this study aims at further investigating this microzonation map with the site geological conditions.

TAIPEI BASIN

1) *Geology*

The Taipei basin is the second largest basin in Taiwan. It is a tectonic graben resulting from reverse and normal faults. Topographically, the Taipei basin is surrounded by mountains and high lands, and the ground surface in the basin is located on an elevation just a few meters above the sea level. Its shape is close to a triangle as shown in Fig. 1 [2]. The basin is bounded by Yangmingshan to the north, Linkou mesa to the west, and the Ridge of Syue Mountains to the southeast. Along the north fringe of the basin, the Tatun volcano group has an altitude of several hundred meters, formed by Pleistocene andesites and tuff breccias. The Linkou mesa on the west of the basin has an altitude ranging between 200 and 250 m, which is characterized by thick gravels overlain by several meters of laterite soils. To the southeast, there are foothills of several hundred meters high, the basement are alternate formations of sandstone, siltystone and shale, which are formed at the period from Miocene to Oligocene.

Within the basin, the land surface is very flat, tilting gently to the northwest. The total area of the Taipei basin with an altitude below elevation 20 meters is around 243 square kilometers. A swampy area of 19 square kilometers is distributed in the northwestern part of the basin. The main river flows through the Taipei basin is the Tamshui River. The Tahan Creek, the Hsintien Creek and the Keelung River are three major distributaries of the Tamshui River. These three distributaries are all from the southeastern mountain areas of Taipei basin and flowing through the western foothills belt. The deposits in the basin are primarily come from these three rives. The major alluvial deposits of the Tahan Creek, the Hsintien Creek and the Keelung River are sandy soils, gravelly soils and soft mud, respectively, which constitutes the unconsolidated layers in the basin.

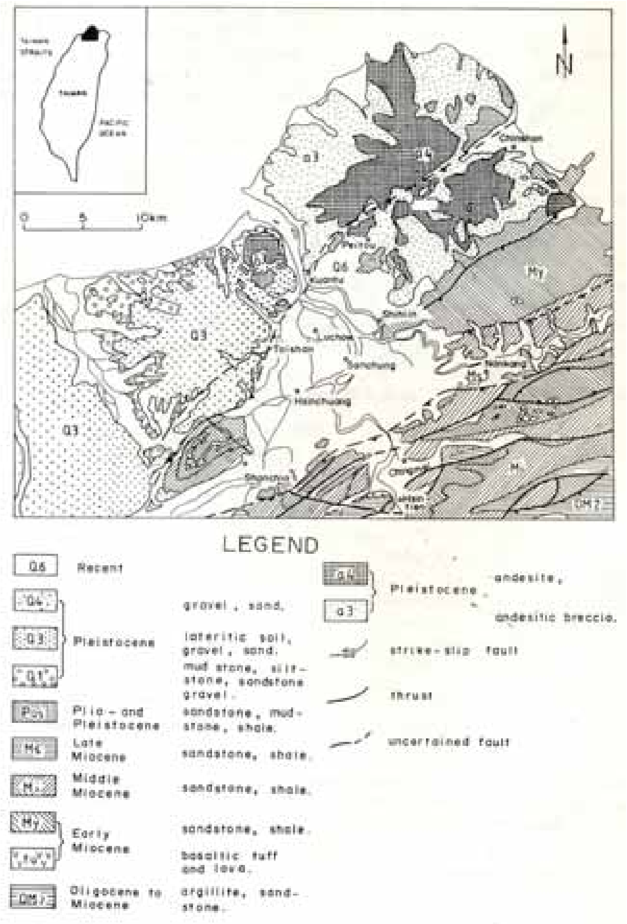

Fig. 1: Geological map of northern Taiwan [2]

2) *Baserock*

Since the Taipei basin is a tectonic graben resulting from reverse and normal faults, the depth of the base rock changes greatly in the basin. Based on large amount of geological explorations conducted by many organizations, the depth of the base rock surface can be depicted as shown in Fig. 2, which shows that the base rock surface of the Taipei basin is a northwestward dipping surface. At the southeast fringe of the basin, the outcrops of base rock can be found near the ground surface. The depth of base rock surface increases very rapidly toward the northwest region. The deepest location is at the Wuku area, about 700 meters below the ground surface.

3) *Unconsolidated sediments*

In the Taipei basin, the unconsolidated sediments overlying the basement can be divided, in the deposition order, into the Banqiao, Wuku, Chinmei and Sungshan Formations. The Banqiao and Wuku Formation are mainly composed of alternating beds of mud, sand and pebble. The Chinmei formation is mainly pebble with some sands and silts, while the Sungshan Formations consists of alternating layers of silty sand and silty clay.

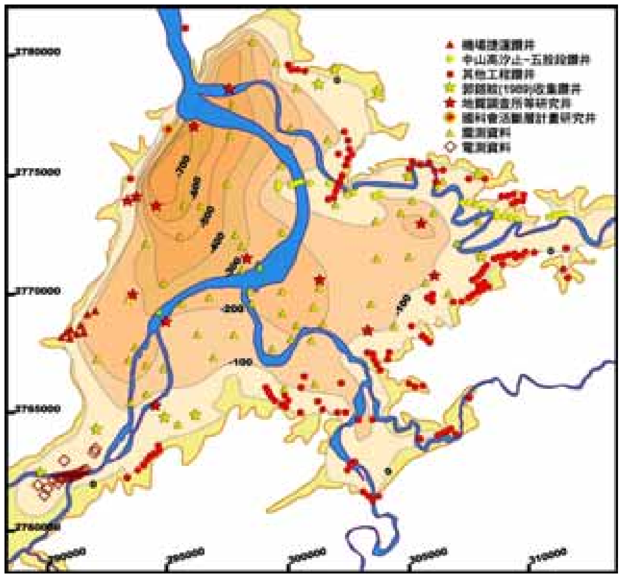

Fig. 2: Depth of baserock surface in Taipei basin

Basically, the Sungshan Formation has very low penetration resistance. Near the ground surface, the SPT-N values are usually less than five. In contrast, the gravels in the Chinmei Formation have a much higher SPT-N value, usually higher than 100. Therefore, the thick layer in the Chinmei Formation is usually regarded as a bearing stratum in engineering practices. Since the Sungshan Formation is significantly softer than the other formations in the basin, the unconsolidated sediment can thus roughly be divided into two main layers: the shallow layer is the Sungshan Formation, and underlain by gravelly layer, including the Chinmei, Wuku and Banqiao Formations.

4) *Thickness of each layer*

From the geological data collected in the database GEO2000 [3], which contains the boring data of major constructions in the Taipei area, the elevation of the bottom of the Sungshan Formation can be determined as shown in Fig. 3. Its thickness is about ten meters in the southern area of the basin and increases northwardly to more than 100 meters in the northwest margin of the basin. The thickness of the gravelly layer can be easily calculated by the difference between the elevation of the bottom of the Sungshan Formation and that of the basin basement.

5) *Velocity profile*

The velocity profiles of the Sungshan Formation have been reported in many investigations. In most areas of the basin, the shear wave velocity of the Sungshan Formation is around 200-300 m/s. However, the velocity of the eastern area and the zones deposited by Keelung River is relatively lower. The data for the velocities of the Chinmei and deeper formations are very limited. In most areas in the basin, shear wave velocity of gravelly layer is around 400-500 m/s.

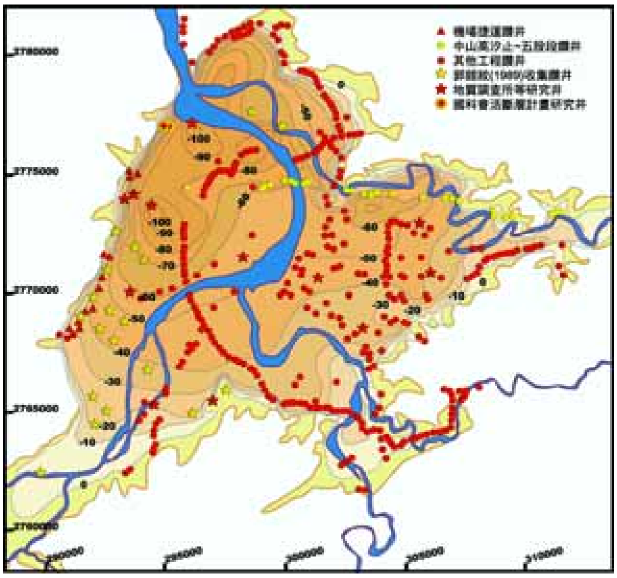

Fig. 3: Elevation of the bottom of the Sungshan Formation

STRONG MOTION OBSERVATION NETWORK

The Taiwan Strong Motion Instrumentation Program (TSMIP) had been conducted by the Seismological Observation Center of the Central Weather Bureau, Taiwan, R.O.C. A total of 1000 seismograph stations have been installed in the island. Among them, 43 free-field stations are in operation in the Taipei basin area. The station interval is about 2 km on the average. The position of stations is shown in Fig. 4, in which the stations are indicated by triangle symbols and station numbers. The boundary of the basin in this figure is set at an altitude of 20 meters above the sea level.

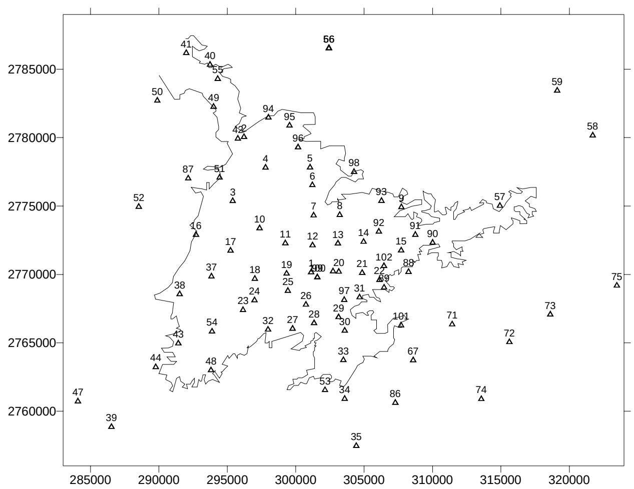

Fig. 4: Seismograph stations in the area of the Taipei basin

SEISMIC MICROZONATION MAP

Chai, Teng and Yeh [4] generated the microzonation map for the area of Taipei basin. They selected large amount of significant earthquake ground motions recorded in the area of the Taipei basin as the data base. Based on the average of the normalized acceleration response spectra, they defined the shape of the design acceleration response spectrum for the area of the Taipei basin as follows:

$$S_a = \begin{cases} 1.0 + 7.5T/T_0 & ; \quad 0 \le T \le 0.2T_0 & \text{(very short period)} \\ 2.5 & ; \quad 0.2T_0 \le T \le T_0 & \text{(short period)} \\ C_v/T & ; \quad T_0 \le T \le 2.5T_0 & \text{(medium period)} \\ 1.0 & ; \quad 2.5T_0 \le T & \text{(long period)} \end{cases} \qquad (1)$$

in which T is the period of structure and T_0 is the corner period between the short period and middle period of the spectrum, which is defined as $C_v/2.5$. In the above definition, only one parameter, C_v, is required to define the shape of normalized acceleration response spectrum for the area of the Taipei basin. It can be noted that when the value of C_v increases, the corner period T_0 increases.

To determine the C_v value at each seismograph station in the area of the Taipei basin, Chai, et al. [4] computed the response spectrums with one standard deviation (5% damping ratio) for past earthquake records from 1993 to 1999 and then deduced the corresponding C_v values. The contour map of C_v is shown in Fig. 5. It can be seen from Fig. 5 that two major regions of high C_v values are located at the northwestern (Wuku area) and northeastern (Sungshan area) within the Taipei basin.

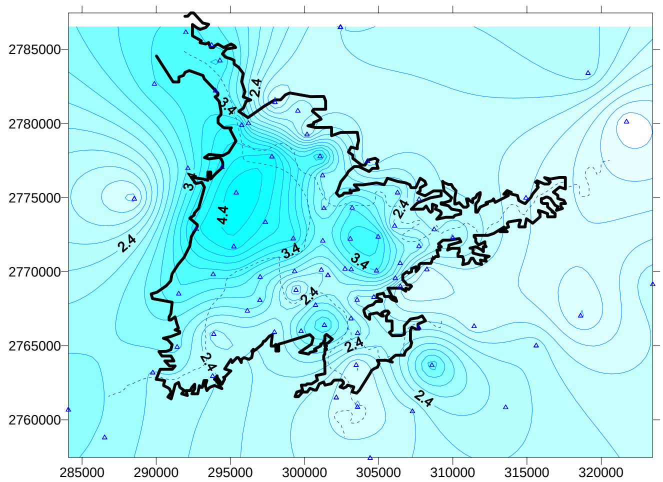

Fig. 5: C_v contour of the Taipei basin (After Chai, et al. [2])

Based on the distribution of C_v values obtained as above, Chai, et al. [4] suggested subdividing the Taipei area into four microzonations, as shown in Fig. 6, for the use of seismic design. The area with C_v values ranging from 3.4-4.6 is categorized as zone T1. For the areas with less C_v values are categorized as zone T2, T3 and T4, respectively, as shown in Table 1. Accordingly, the corner period T_0 for each zone can thus be calculated, also shown in Table 1. Based on Eq. (1), the normalized design response spectrum for each zone can be plotted as shown in Fig. 7. It can be seen that the design response spectrum will spread over to larger period for the zone with larger C_v value.

Table 1 Criteria of microzonation

Zone	Range of C_v	T_0
T1	3.6-4.6	1.60
T2	2.8-3.6	1.30
T3	2.2-2.8	1.05
T4	1.5-2.2	0.85

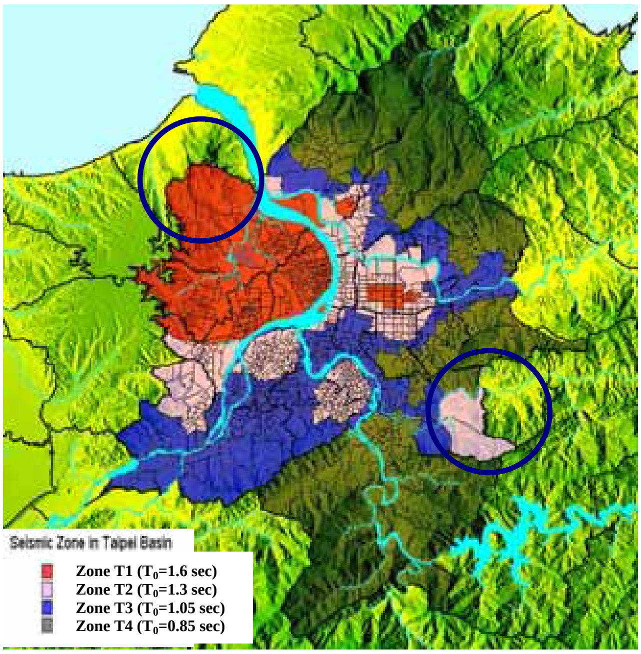

Fig. 6: Seismic microzonation of Taipei area (After Chai, et al. [4])

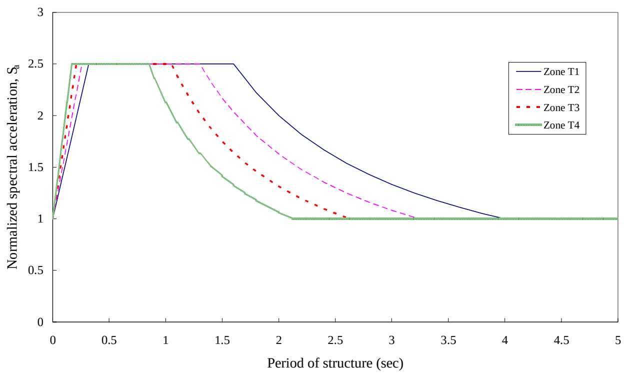

Fig. 7: Normalized response spectrum of Taipei basin

For the sake of building construction administration, the microzonation map shown in Fig. 6 was generated by using the administration district as the basic unit for zonation division. Under this circumstance, the northwest fringe of the basin (Linkou mesa and Kuan-yin Mountain, circled zone at upper-left side) is categorized into Zone T1 and the southeastern Chi-Nan mountain area (circled zone at lowe-right side) is categorized into Zone T2. However, the Linkou mesa is known as the thick gravel formation, the Kuan-yin Mountain is Pleistocene volcanic rocks, and the Chi-Nan mountain areas are the Miocene rocks. All these areas should be categorized as stiff sites. Therefore, the purpose of this paper is to further investigate the suitability of microzonation scheme as published in Fig. 6.

RELATIONSHIP BETWEEN Vs_{30} AND C_v VALUES

The microzonation map of Taipei basin shown in Fig. 6 is basically developed based on the distribution of C_v values (normalized velocity-response spectral coefficients). Therefore, it is interesting and important to investigate the relationship between those C_v values with the geological conditions at the site of seismograph stations. In engineering practices, it is very often to use the shear wave velocity of soils to categorize the site condition of a ground. Since the ground surface earthquake motions are significantly affected by the shear wave velocity of soils near the ground surface, ATC-32 [5] recommends that a parameter Vs_{30} can be used to roughly characterize the soil condition of a site. Vs_{30} is the averaged shear wave velocity of soil layers within 30 m below the ground surface, which is defined as

$$Vs_{30} = \frac{\sum d_i}{\sum d_i / V_{si}} \qquad (2)$$

in which d_i is the thickness of the ith soil layer, V_{si} is the shear wave velocity of the ith soil layer, and Σd_i=30m. Accordingly, the draft of Seismic Design Code for Railway Bridges of Taiwan [6] adopts the Vs_{30} for the classification of ground type as shown in Table 2.

Table 2 Ground classification on shear velocity

Ground classification	Velocity (m/s)
Type I	$Vs_{30} \geq 270$
Type II	$270 \geq Vs_{30} > 180$
Type III	$180 \geq Vs_{30}$

Since 2000, a program to start to investigate the site conditions of all free-field seismograph stations in Taiwan was co-conducted by the Central Weather Bureau (CWB) and the National Center for Research on Earthquake Engineering (NCREE) of Taiwan. For each exploration hole at the site of seismograph station, the shear and compressional wave velocities of soils were measured by the Suspension P-S Logging method. Up to date, a total of 23 stations in the Taipei basin area had been measured. Based on the data of shear wave velocities measured, the values of Vs_{30} are calculated and compared with the associated C_v values, as shown in Fig. 8. From this figure, it can be seen that the C_v values are correlated quite well with those of Vs_{30} for most stations. The lower the shear wave velocity, the higher the C_v value, which means that the soft ground will have more prominent long-period response during earthquake excitations. Also shown in Fig. 8, the ground classification based on Vs_{30} is consistent with the microzonation based on C_v, the Type 1 ground coincides with Zone T4, the Type 2 ground coincides with Zone T3, and the Type 3 ground coincides with Zones T2 and T1.

However, it can be found that there are three points (TAP002, 051 and 067) in Fig. 8 to have greater deviation from the trend. They are classified as Type 1 ground based on Vs_{30}; however, they have quite high C_v values and zoned into Zone T1 or T2. Examining the locations of these three stations, it can be found that all of them are located right on the boundary of the Taipei basin. The exploration loggings of these holes, as shown in Fig. 9, show that these sites are with very shallow soft-overburden on top of stiff gravels or rocks. For these stations, the in-consistency between the C_v values and the Vs_{30} is actually due to the shallow soft-overburden. These kinds of special cases need more studies to investigate the attributes for microzonation.

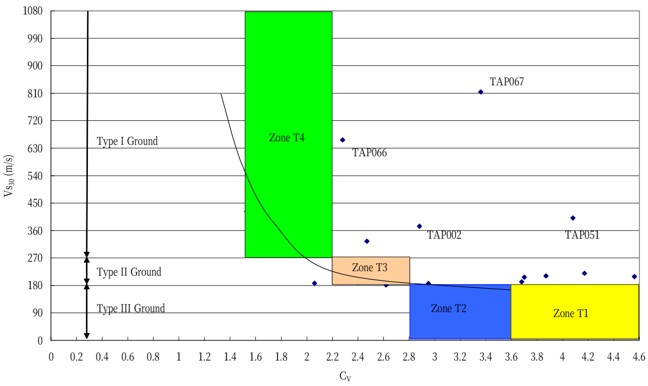

Fig. 8: Relationship of Vs_{30} and C_v

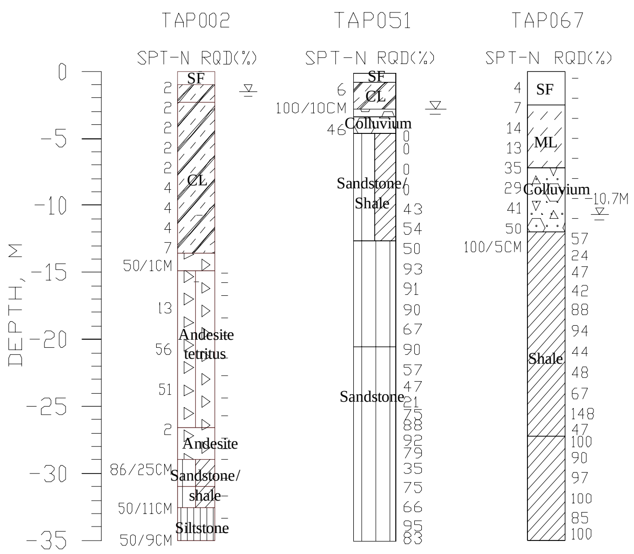

Fig. 9: Boring loggings of TAP002, 051 and 067

RELATIONSHIP BETWEEN GROUND PERIOD AND *Cv* VALUES

Another important parameter to represent the site condition is the ground period. A softer ground usually results in longer ground period. This study will use the spectral analyses of earthquake data to characterize the ground periods of Taipei basin.

1) *Earthquake Data*

On September 21, 1999, Taiwan suffered from the Chi-Chi earthquake, which caused 2450 deaths. The rupture line of the Julongpu fault stretched 108 km and destroyed thousands of nearby structures. In addition, the strong motion also induced extensive liquefaction and landslides. Although the Taipei basin was far away from the epicenter, it also suffered strong ground motion that caused casualties and damages of structures, including the collapse of two modern buildings and one school building. After the main shock, several aftershocks of magnitude larger than six were also recorded. On October 15, 1999, another earthquake, the Jia-Yi earthquake, also struck southern Taiwan. Here a total of six earthquakes, as shown in Table 3, recorded by TSIMP are selected for subsequent spectral analyses.

Table 3 Selected earthquake records

Event	Time	Epicenter	Depth (Km)	ML	PGA (gal)
1	1999/9/21 1:47	120.82°E23.85°N	7.3	7.3	80-120
2	1999/9/21 2:03	120.88°E23.79°N	3.5	6.6	4-8
3	1999/9/21 2:16	121.40°E23.87°N	2.0	6.8	20-30
6	1999/9/22 8:14	121.03°E23.82°N	15.6	6.8	15-20
7	1999/9/26 7:52	121.00°E23.85°N	9.9	6.8	15-20
8	1999/10/22 10:19	120.40°E 3.50°N	12.1	6.4	4-8

2) *Fourier Spectrum Method*

To investigate the frequency contents of an earthquake ground motion, it is often to transform an earthquake record into frequency domain by performing Fourier spectral analysis. On the basis of the maximum amplitude on Fourier spectrum, the corresponding predominant period can thus be determined. It should be noted that the ground period determined by the Fourier spectrum method is an approximated ground period, because the maximum amplitude of an earthquake record is influenced not only by the local soil condition, but also by the source and the traveling path of earthquake wave. Fig. 9 shows the averaged ground period contour of the Taipei basin determined by the Fourier spectrum method for six earthquakes described above. In this Figure, it can be seen that the Sungshan area and Wuku area are two zones with longer periods. These two zones are consistent with the zones of high C_v values and had been categorized as Zone T1. However, the ground period for the area on the northwestern fringe of Taipei basin (the circled zone at upper-left side of Fig.6) is quite low (less than 1 second), and should not be classified as Zone T4. Fig. 10 shows a good relationship between ground periods with C_v values. The C_v value increases with increasing ground periods. One station (TAP094, located on the north fringe of the basin) has greater deviation. The C_v value of this station is low, but its period is high, about one second.

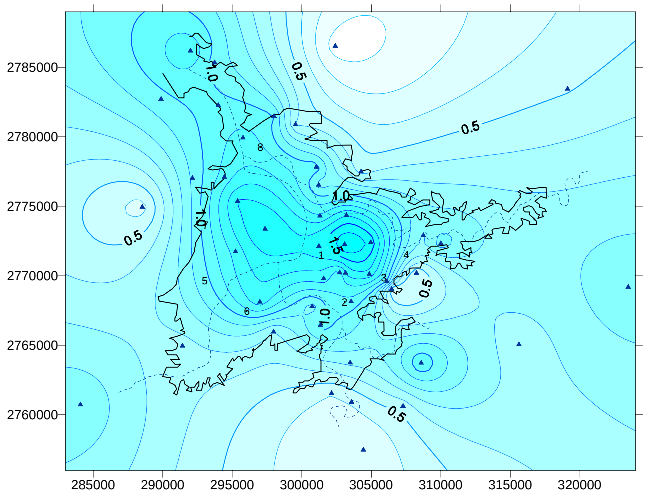

Fig. 9: Ground period from Fourier spectrum method

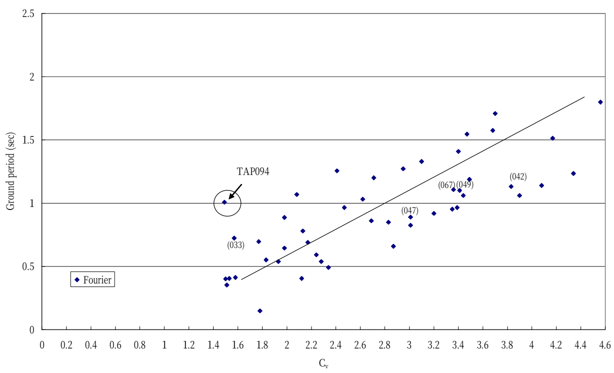

Fig. 10: Relationship of ground period by Fourier spectrum method and C_v

3) *HVSR Method*

Generally, to evaluate the real site amplification, we have to calculate the Fourier spectral ratios of ground surface motion to the rock base motion to remove the effects of the source and traveling path. However, the motion of rock base is lacking in most conditions. Nakamura [7] proposed a so-called HVSR method to calculate the ground period, which is determined by the frequency corresponding to the peak value of Fourier spectral ratios between the horizontal components (H) to vertical ones (V) of an earthquake recorded at the ground surface. The spectral ratio, SR, is defined as follows.

$$SR(f) = \frac{H(f)}{V(f)} \tag{3}$$

This study also applies the HVSR method to analyze six earthquake data described previously for evaluating the ground period. Firstly, the horizontal and vertical Fourier spectrums are computed and smoothed by a 0.8 Hz Parzen window. Then the horizontal Fourier amplitudes are divided by the vertical ones. The ground period can thus be identified corresponding to the peak value of spectral ratio.

Figure 11 shows the averaged ground periods of six earthquakes by HVSR method, in which the solid triangles locate the stations that had been triggered by these earthquakes. This figure also shows that Sungshan area and Wuku area are two major long-period zones in the basin. On the other hand, from Fig. 9, we can see that the ground period at the area near Station TAP 067 is low and quite uniform, unlike the C_v map and the ground period map determined by the Fourier spectrum method. Furthermore, it can also be seen that the ground period at the northwestern fringe of Taipei basin is quite low, which is not consistent the high C_v values used to generate the microzonation map.

Fig. 12 shows the relationship between ground periods from HVSR method and C_v values. In this figure, it can be seen that the C_v value also increases with increasing ground period. TAP033, 042, 047, 049 and 067 have greater deviation from the trend. All of them are located at the boundary of the basin. Again, this indicates that the characteristics of ground response at the basin boundary have to be carefully studied and then used as the basis for microzonation.

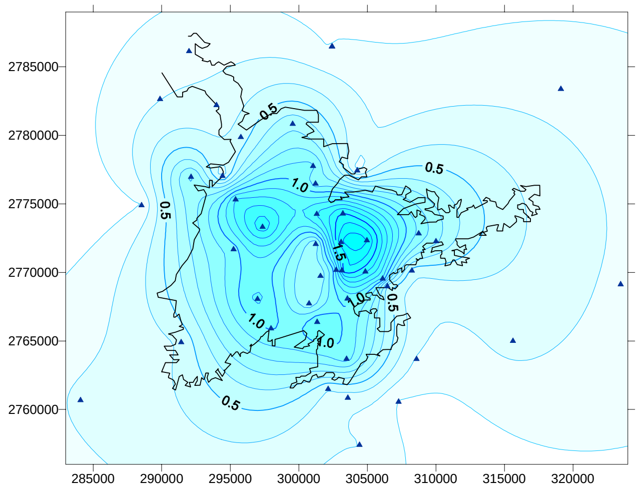

Fig. 11: Ground period from HVSR method

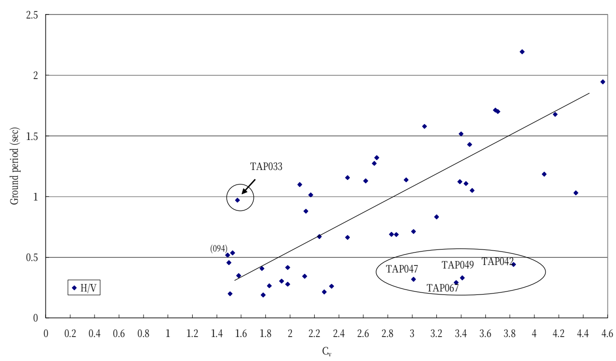

Fig. 12: Relationship of ground period by HVSR and C_v

4) ***Coda Method***

Coda wave means the vibrating wave at the end of an earthquake accelerogram. According to the single-scattering model proposed by Aki and Chouet [8], the amplitude of coda wave of an earthquake accelerogram can be expressed as

$$A_c(f,t) = S(f)R(f)C(f,t) \tag{4}$$

where $A_c(f,t)$ is the Fourier amplitude of a coda wave for a lapse time t greater than about twice the S-wave travel time, $S(f)$ is the source term, $R(f)$ is the site term, and $C(f,t)$ is the decay curve of coda, which is the function of time and frequency. According to Eq. (4), the frequency contents of coda are affected by the source factor and the site conditions. However, if the coda wave is picked at a quite long time after the main shock, the motion corresponding to a coda wave can be regarded as a free vibration, which in turn can be used to characterize the vibrational period of ground.

From the recorded ground motions of the Chi-Chi earthquake, it can be found that the Taipei basin was still vibrating after 90 seconds of the initiation of the earthquake. At that time, the ground motions at most areas of Taiwan had ceased. Therefore, we can assume the shaking after 90 seconds recorded at the Taipei basin was in a state of free vibration, so that the ground period can be identified by spectral analyses of these coda waves. The steps for coda analysis adopted in this study are shown below:

1. Starting from the end of record to look for the time (point) whose corresponding acceleration is greater than 4 gal, as shown in Fig. 13.
2. From this time point, to choose 4096 points (20.4 sec) backward as coda motion.
3. To perform Fourier spectral analysis for the coda motion.

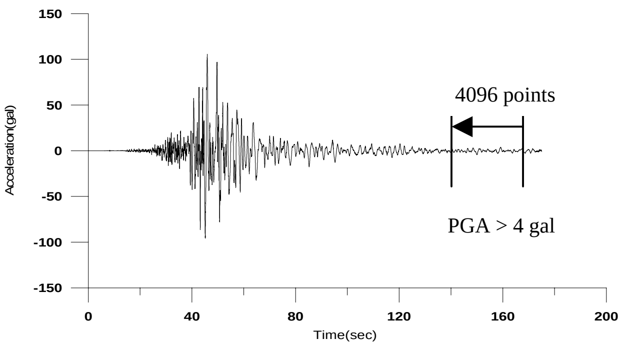

Fig. 13: Chi-Chi earthquake records of TAP003 for coda motions

The distribution of ground periods determined by the coda method is shown in Fig.14. Generally, the ground periods at most areas are longer than 1.0 sec. Two long-period zones in Sungshan area and Wuku area also exist, but the period of the west one is longer than that of the east one. In comparison with ground periods obtained by Fourier spectrum method and HVSR method, the period deduced from the coda method is generally longer.

Fig. 15 shows the relationship between ground period from HVSR method and the values of C_v. Generally, the C_v value increases with increasing ground period. Similar to the finding from Fourier spectrum method, TAP094 has greater deviation from the trend.

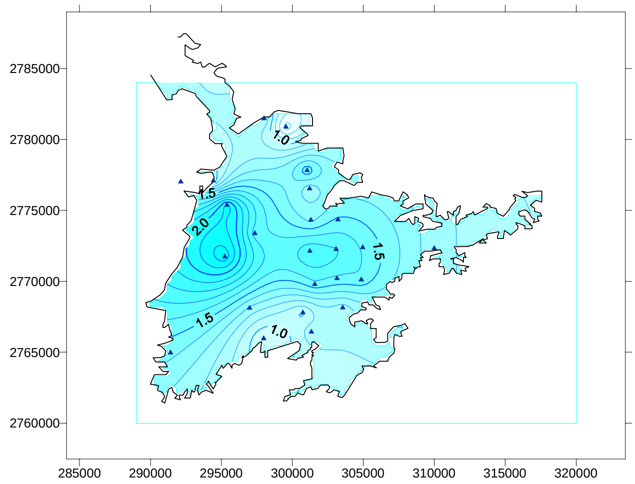

Fig. 14: Ground period from coda method

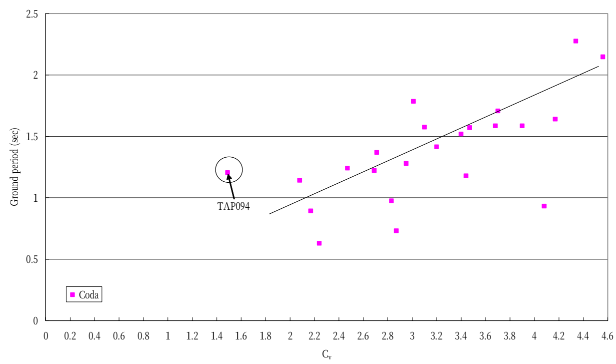

Fig. 15: Relationship of ground period by Coda and C_v

DISSCUSSIONS

This paper uses Vs_{30} and ground period to characterize the local soil conditions at the site of seismograph stations in the Taipei basin, and then compared them with the C_v values deduced from the normalized response spectrum of past earthquakes. Generally, there exists a common trend between C_v value and these two parameters: the C_v value increases with decreasing Vs_{30} and increasing ground period. In addition, comparison of the ground period contours from spectral analyses and C_v contour shows that two long-period zones at Wuku area and Sungshan area are consistent with high C_v zones. To some degree, the C_v value of response spectrum reflects the local soil condition. However, there still exists some obvious inconsistency among them.

Firstly, the ground period for the areas near the northwestern fringe of the Taipei basin (the Linkou mesa and Kuan-yin Mountain) is quite low as deduced from both the Fourier spectrum method and the HVSR method. However, these areas were specified as Zone T1 in the published microzonation map. It is thought that further modification is needed.

Secondly, the area near the Chi-Nan mountain (in the southeastern margin of the basin) was specified as Zone T2 in the published microzonation map, because the C_v value calculated from the earthquake records at TAP067 is quite high. However, the shear velocity at this site is relatively high and the ground period determined by the HVSR method is relatively short. It should be noted that all the results obtained above are based on the earthquake records recoded from only one station, TAP067, since it is the only one located at this area. Therefore, it is thought that more information is needed to investigate the characteristics of ground motion for this area.

CONCLUSIONS

This paper uses two parameters, Vs_{30} and ground period to investigate the present microzonation map developed on the basis of C_v contour, the following concluding remarks can be obtained:

1) The shape parameter of normalized response spectrum, C_v, can reflect the ground condition to some degree and therefore the distribution of the C_v values is suitable to be used as the basis for microzonation for the Taipei basin. However, for the areas near the boundary of the basin, this microzonation scheme maybe inappropriate since the C_v values obtained for these areas are not consistent with the information of measured shear wave velocities of soils and the ground periods deduced from spectral analyses.

2) There are two long-period zones in the Taipei basin where the period is longer than one second: one is in the Wuku area where the rock bed is very deep, and another is in the Sungshan area where the deposition of Sungshan formation is very soft. The long-period zones generally consist with high C_v zones.

3) Categorizing the northwest margin of the Taipei basin into Zone T1 is inappropriate since the ground period deduced from spectral analyses for this region is quite low.

4) The high C_v value at TAP067 is questionable since it is not consistent with the ground condition (shear velocity and ground period). More studies should be conducted to clarify this problem.

ACKNOWLEDGMENTS

The authors thank the Seismological Observation Center of the Central Weather Bureau, Taiwan, for providing the TSMIP earthquake data. Many thanks are also due to the National Center for Research on Earthquake Engineering, for providing the microzonation map of Taipei basin.

REFERENCES

[1] Architecture and Building Research Institute, *Seismic Design Code for Buildings*, Ministry of the Interior, Taiwan, 2005.

[2] Wang Lee, C. and Lin, T.P., “The Geology and Land Subsidence of the Taipei Basin,” Memoir of the Geological Society of China, No.9, 1987, pp447-464.

[3] Central Geological Survey, “Geological Data Base-GEO 2000,” 2000.

[4] Chai, J.F., Teng, T.J. and Yeh, C.S., “Seismic Microzonation and Design Response Spectrum in Taipei Basin,” *Proceedings o f the 7th National Conference on Structure Engineering*, Taiwan, 2004.

[5] ATC, ATC-32, *Improved Seismic Design Criteria for California Bridges: Provisional Recommendations*, Applied Technology Council, Redwood City, California, 1996.

[6] Bureau of High Speed Rail, Draft of *Seismic Design Code for Railway Bridges*, Ministry of Transportation and Communications, Taiwan, 2005.

[7] Nakamura, Y., “A Method for Dynamic Characteristics Estimation of Subsurface Using Microtremor on Ground Surface,” *QR of RTRI 30*, **1**, 25-33, 1989.

[8] Aki, K. and Chouet, B., “Origin of Coda Wave: Source, Attenuation, and Scattering Effects”, *J. Geophys. Res*., **80**, 3322-3342, 1975.

Performance Evaluation of Geotechnical Structures under Different Earthquake Motions

H. Hazarika[1], A. Nozu[1], T. Sugano[1], H. Suzuki[2]
[1]Geotechnical and Structural Engineering Department, Port and Airport Research Institute, Yokosuka, Japan
[2] Niigata Port and Airport Authority, Hokuriku Regional Development Bureau, Niigata, Japan

Abstract
A series of shaking table tests was performed on a model caisson quay wall by using a large underwater shaking table assembly. The seismic performance of the waterfront structure was evaluated by subjecting the soil-structure system into three different earthquake ground motions (two actual earthquake records and one scenario motion), and measuring the respective responses. Performance comparisons led to believe that for the same backfill, the types of strong motion will have a strong influence on the performance of the structure. A scenario motion created for the particular site, rather than the past strong motions at some other sites, thus can be the fitting answer to the new design trend.

Keywords— *Earthquake motion, Earthquake resistant structures, Gravity quay wall, Performance-based design, Shake table test*

Introduction

The destructive power of Mother Nature is irresistible. Increasing threats posed by devastating earthquakes are becoming matters of immense concern to lawmakers, planners, engineers and researchers worldwide. The only way to challenge posed by such natural catastrophes is to mitigate the disasters by protecting the existing and new infrastructures alike through some innovative and cost-effective means.

Retaining structures, a key element of infrastructure facilities, are prone to collapse accompanied with disastrous physical and economic consequences as is evident in many historical earthquakes. Selections of well-documented case histories of damage to port structures, for example, are presented in [1]. In seismically active zones, adequate design of such structures continues to be of utmost concern to the engineers and researchers. The devastations brought to many waterfront retaining structures by the 1995 Hyogo-ken Nanbu earthquake, Kobe can be found in [2] and [3]. Since the Kobe earthquake, significant theoretical and experimental works have been done on the subject ([4], [5], [6], [7], [8], [9]).

Lessons learned from the worldwide earthquakes in the 1990s have led to the emergence of a new design methodology called the performance-based design ([1], [10], [11]). In performance-based design, appropriate levels of design earthquake motions must be defined and corresponding acceptable levels of structural damage must be clearly identified. Dual approach are adopted in such design in which, Level 1 (L1) and Level 2 (L2) earthquake motions are typically used as design reference ground motions [12]. Until now, the trend was to adopt the past major historical earthquake record as the design ground motions. For example, past seismic design codes for Port and Harbor facilities in Japan, adopted any of the following three seismic motions; (1) The Hachinohe port wave record (The 1968 Tokachi Oki earthquake), (2) The Ofunato port wave record (The 1978 Miyagi-ken Oki earthquake) and (3) The Port Island wave record (The 1995 Hyogo-ken Nanbu earthquake). The design reference ground motions, however, will be different depending on the local seismological and soil characteristics of the site, where the target structure is intended to design or to retrofit. Consequently, the trend these days is towards creating a site-specific scenario motion based on the small motion records at the particular site.

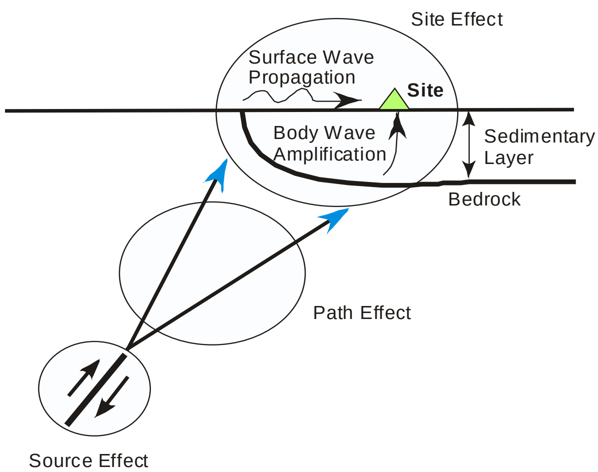

Fig. 1: Effect of source, path and site on strong ground motions

As shown in Fig. 1, earthquake ground motion is influenced by (1) source effect (2) path effect and (3) site effect [13]. Therefore, it is important to take into consideration these factors while constructing the earthquake ground motions adopted in the performance-based design. Reference [14] emphasized the importance of adopting the site-specific design ground motion reflecting the effects that emanates from such local seismological and ground characteristics. The new design codes for Port and Harbor facilities in Japan, which is expected to be released later this year and come into the force from the next fiscal year (2007), takes into account the earthquake ground motions and the site amplification factor of the particular sites, where the structure will be built [15]. The to be released design code suggests constructing original scenario motion at each site taking into consideration the local seismological and soil characteristics as illustrated in Fig. 1.

Therefore, it is important to evaluate the seismic performance of geotechnical structures, under different earthquake motions consisting of actual earthquake record of L1 and L2 motions as well as artificially constructed scenario motion reflecting small earthquake records at a particular site. The performance of the same type of structure will be different depending on the earthquake ground motion it is subjected to in a particular targeted site. The objective of this research is to evaluate the structural performance of gravity type waterfront structures, under different L1 and L2 type earthquake motions. A series of underwater shaking table tests was performed on a model caisson, for clarifying the seismic performance of the structure, which was subjected to ground motions that are characterized by different frequencies, amplitudes and durations.

Earthquake Ground Motions

Devastation caused to the waterfront retaining structures during the 1995 Kobe earthquake has led to an increasing concern about the seismic stability of the existing and newly built port and airport structures in Japan. In the future, large-scale devastating earthquakes (Tokai Earthquake, Tonankai Earthquake and Nankai Earthquake) are predicted to strike the Tokai and the Nankai region of Japan. Mitigating disaster and the economic implications from these predicted earthquakes are a major concern envisaged by the Central Disaster Management Council, Government of Japan [16]. In order to clarify the structural performance of a structure under different types of L1 and L2 earthquake motions, an extensive testing program using underwater shaking table test was undertaken, so that the soil-structure interaction behavior during any devastating earthquakes can be well understood and appropriate design methodology can be arrived at.

Three different earthquake loadings were imparted to a soil-structure system during the shaking table tests. The input motions selected were: (1) the N-S component of the earthquake motion recorded at the Hachinohe port, Hachinohe, Japan during the 1968 Tokachi-Oki earthquake (M 7.9), (2) the N-S component of the strong motion acceleration record at the Port Island, Kobe, Japan during the 1995 Hyogo-ken Nanbu earthquake (M 7.2), and (3) a scenario earthquake motion created artificially at Ohta ku, Tokyo, assuming an earthquake (M 7.9) that is presumed to occur in the southern Kanto region with its epicenter at Odawara, Kanagawa prefecture, Japan. This scenario record, in fact, is the product of the local seismological and ground characteristics (source, path and site effects) as illustrated in Fig. 1, which is obtained by using the empirical Green function [17]. These input motions are shown in Fig. 2.

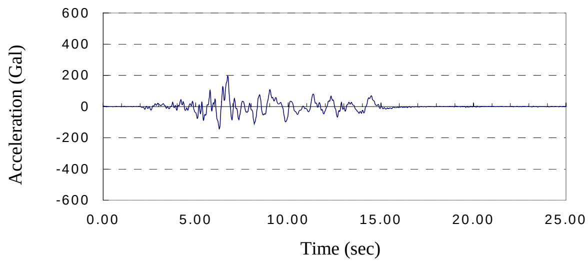

(a) Hachinohe (The Tokachi-Oki earthquake)

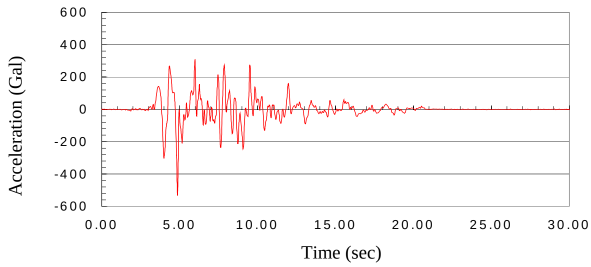

(b) Port Island, Kobe (The Hyogo-ken Nanbu earthquake)

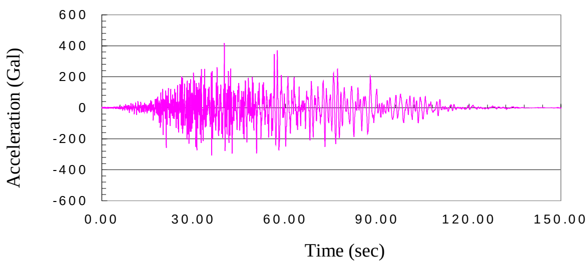

(c) Ohta ku, Tokyo (Simulated for the Southern Kanto earthquake)

Fig. 2: Input strong motion records

The Port Island wave record (named hereafter PI) of the 1995 Hyogoken Nanbu earthquake was adopted (Fig. 2b) because of the extensive damages brought by that earthquake to caisson type quay walls. This is also one L2 motion, which has already been adopted in the design codes. The Hachinohe port wave record of the 1968 Tokachi Oki earthquake (named hereafter HN) was used as another input motion (Fig. 2a) because it used to be the *de facto* standard for ground motion in the Japanese design standard of the Port and Airport structures

(Ministry of Transport, 1999) specified in [18]. The Ohta ku (Tokyo) scenario earthquake motion (named hereafter OK) was selected (Fig. 2c) because it is a L2 earthquake motion created based on the local seismological and ground characteristics of the Ohta ku area (Tokyo). Various design codes in Japan suggests that the design acceleration for L2 motion is about two to three times the acceleration for L1 motion [19]. Therefore, as a rule of thumb, the HN record can be presumed to be a L1 type motion, whereas the PI record is undoubtedly a L2 type motion. On the other hand, the OK wave is a scenario L2 motion. The L2 OK scenario wave is characterized by long duration in contrast to the L2 PI record, whose duration was small. The purpose of using these three different L1 and L2 earthquake motions was to investigate the structural performance depending on the earthquake intensity and severity.

SHAKE TABLE TESTING PROGRAM

The large three dimensional underwater shaking table assembly of Port and Airport Research Institute (PARI) was used in the testing program. The shaking table is circular with 5.65 m in diameter and is installed on a 15 m long by 15 m wide and 2.0 m deep water pool. The detailed specifications of the shaking table assembly can be found in [8] and [20]. A caisson type quay wall (model to prototype ratio of 1/10) was used in the testing. Fig. 3 shows the cross section of the soil box, the model caisson and the locations of the various measuring devices (load cells, pore water pressure cells, accelerometers and displacement gauges). The model caisson, made of steel, consists of three parts; the central part (width 50 cm) and two dummy parts (width 35 cm each).

All the monitoring devices were installed at the central caisson to eliminate the effect of sidewall friction on the measurements. The soil box was made of a steel container 4.0 m long, 1.25 m wide and 1.5 m deep. As shown in Fig. 3, the test model consists of 0.1 m of bedrock layer, 0.45 m of seabed layer of dense compacted sand, foundation rubble, and 0.85 m deep backfill. Bedrock layer was prepared using jet cement with a weight ratio of 10:3. The foundation rubble beneath the caisson was prepared using Grade 4 crushed stone with particle size of 13 mm ~ 20 mm. The backfill and the seabed layer were prepared using Sohma sand (No. 5). The end of the backfilling area in the steel container was sealed with unwoven textile to eliminate the effect of the rigid boundary. The sidewall of the container was made rigid, in order to achieve the plane strain conditions.

The dense foundation sand representing the seabed layer was prepared in two layers. After preparing each layer, the whole assembly was shaken with 300 Gal of vibration starting with a frequency of 5 Hz and increasing up to 50 Hz. Backfill was also prepared in stages using free falling technique, and then compacting using a manually operated vibrator (capacity 350W, frequency 191~217 Hz, diameter ϕ=32 mm, and length L=260 mm). The calculated relative density of the backfill was 45.94%, implying that the backfill soil is partly liquefiable. On the other hand, the seabed relative density was calculated to be 78.59 %, implying a non-liquefiable foundation deposit.

After constructing the foundation and the backfill, and setting up of the devices, the pool was filled with water gradually elevating the water depth to 1.3 m to saturate the backfill. This submerged condition was maintained for two days so that the backfill attains a complete saturation stage.

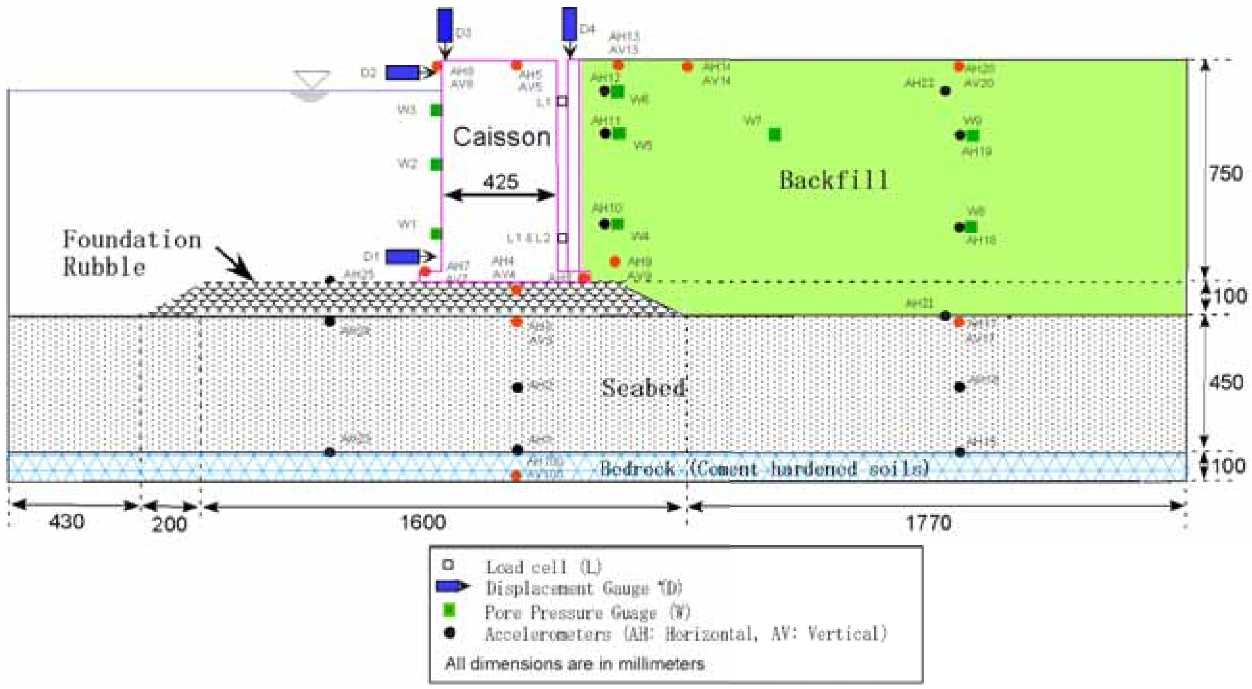

Fig. 3: Cross section of the test model

Durations of the shaking in the model testing were based on the time axes of the accelerograms shown in Fig. 2, which were reduced by a factor of 5.62 according to the similitude relationship [21] shown in Table 1.

Table 1. Similitude for 1g field

Items	Prototype／Model	Scale factor
Length	λ	10
Time	$\lambda^{0.75}$	5.62
Acceleration	1	1
Density	1	1
Stress, Water Pressure	λ	10
Displacement	$\lambda^{1.5}$	31.62

RESULTS AND DISCUSSION

Liquefaction Behavior

In order to elucidate the shear deformation behavior of the backfill during earthquakes, which may lead to the liquefaction, the excess pore water pressure measured by the installed water pressure gauges are plotted in Figs. 4(a) – (c) at a location 0.65 m away from the caisson back (W7 in Fig. 3) for each earthquake ground motion. It can be seen that, in the case of the PI wave and the HN wave, the pore water pressures develop appreciably that may trigger liquefaction in the backfill.

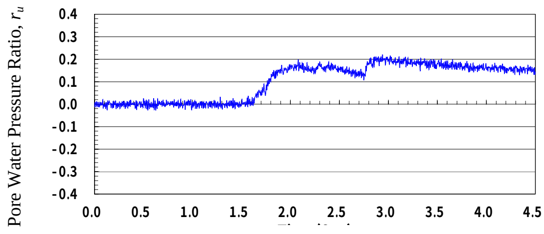

(a) HN wave (L1 motion)

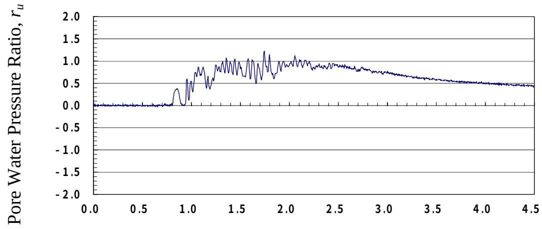

(b) PI wave (Actual L2 motion)

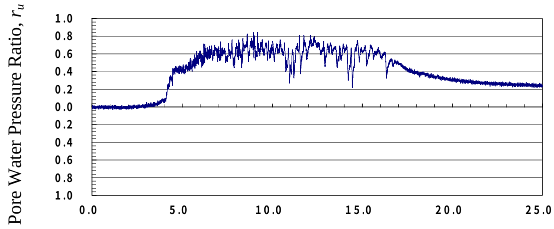

(c) OK wave (Scenario L2 motion)
Fig. 4: Excess pore water pressure generation

A careful observation indicates that, at this particular location, the HN wave generated the least pore water pressure ratio (maximum=0.2), followed by the OK wave (maximum=0.85). The PI wave generated the highest pore water pressure ratio (maximum=1.2). Therefore, as far as the present test conditions (type of soils, backfill soil density, are concerned, it can be said that while the HN type wave may not induce liquefaction at that location, the PI wave and OK wave is more likely to cause liquefaction. However, in practice, liquefaction is characterized in two ways [1]. Differences may arise regarding the liquefaction behavior depending on the definitions, especially if soil characteristics of the model are significantly different from those in the field.

An interesting observation, here, is regarding the rate of dissipation of the excess pore water pressure. The rate is low for the OK wave and the HN wave, and high for the PI wave. These observations lead to a conclusion that, the types of the strong motion wave can have an influence on the liquefaction behavior of the backfill soils. This particular investigation has also indicated that, for the particular backfill characteristics of the test program, the HN type record is less likely to cause liquefaction related damage. Therefore, performance of the structure will not be affected under L1 motion such as HN wave. However, substantial evidences are required to confirm this fact, taking into account the test conditions as well as the backfill soil properties of the prototype, and that is beyond the scope of this research.

Horizontal Displacements of the structure

During an earthquake, excessive structural deformations (like the ones during the 1995 Kobe earthquake) can be very detrimental. From the point of view of the performance-based design, it is of greatest importance whether the permanent structural deformation will lead to halting of the port operation in the event of a destructive earthquake. Evaluation of the residual deformation, thus, is an absolute requirement, in order to verify that structures will sustain their intended functions even after a L2 motion. The time histories of the horizontal displacements (displacement gauges D1 and D2 in Fig. 3) during the three earthquake loadings are compared in Figs. 5 to 7. In these figures, the negative displacement indicates a seaward displacement of the caisson. The figures reveal that the OK type earthquake record yields the highest residual displacement among the three motions. Another important observation is that, unlike the PI and the HN record, the OK record does not yield any positive displacement (towards the backfill). The caisson starts to move seaward right from the beginning of the oscillations for this particular motion. That perhaps is the reason for an unexpectedly higher residual displacement in this case as compared to the PI record and the HN record. In addition, unlike the other two motions, the PI wave results in predominant fluctuation (marked max and min in the figure) of the horizontal displacements at the beginning.

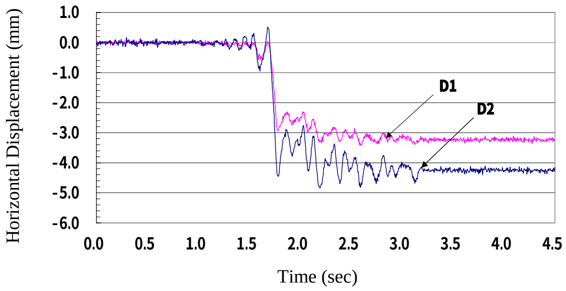

Fig. 5: Time histories of the horizontal displacements (HN wave)

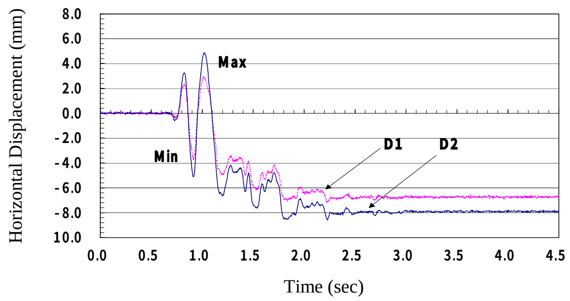

Fig. 6: Time histories of the horizontal displacements (PI wave)

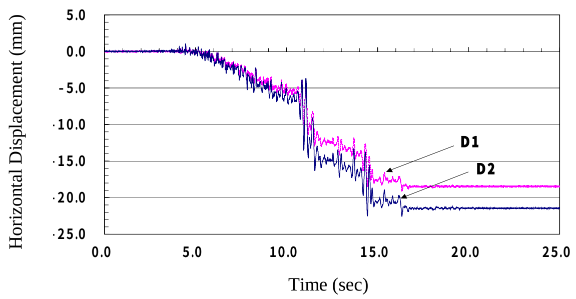

Fig. 7: Time histories of the horizontal displacements (OK wave)

Effect of Ground Motion on Structural Performance

The seaward permanent horizontal displacements of the prototype (calculated using the similitude relationship in Table 1) under the three earthquakes motions (PI, HN and OK) are compared in Fig. 8. This figure reveals that, under the L1 motion, the structure can perform satisfactorily, however, under L2 motions such as the PI wave and the OK wave, the function of the structure will be disrupted. This implies that, for the same soil type, depending on the design ground motion, the structural responses and performances will vary. Consequences in the design will be severe, if the PI wave record is adopted as the L2 design motion for a structure intended to perform under an L2 earthquake motion in Minami Kanto (Ohta ku) area. Local seismological and ground characteristics, emphasized in [13], thus, are likely to play a predominant role in the design. As discussed elsewhere, the L2 type motion is more likely to cause liquefaction in some parts of the backfill. In those locations, disaster mitigation measures against liquefaction will be required.

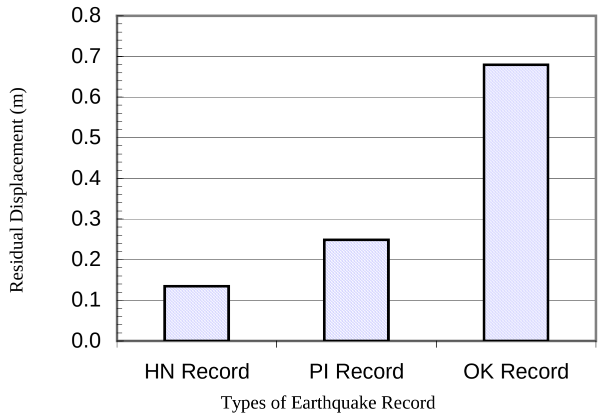

Fig. 8: Comparisons of the residual displacements (Prototype)

Enhancement Effect on Performance

In order to enhance the structural performances, the backfill soil was improved using a special earthquake resistant technique described in [22]. Fig. 9 compares the residual deformations of the structure (prototype) under the three earthquake ground motions. Naturally, the caisson with improved backfill experiences less residual displacements than the unprotected caisson displayed in Fig. 8 above. However, in the case of the OK record, even though the residual displacement itself is less (almost 1/3rd) compared to the unprotected case, the magnitude is relatively high as compared to the other two ground motions. It is difficult judge from this 1-g shaking table test alone, whether this amount of displacement will have any adverse effect on the intended performance. For such high intensity L2 motion, the zone of improved soil may have to be increased or some other protective measures need to be taken, so that the structural performances remain within the intended performance level as demanded by the performance-based design approach.

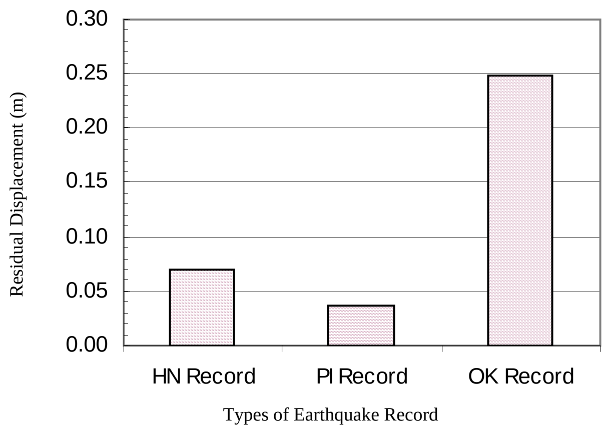

Fig. 9: Comparisons of the residual displacements of the caisson with improved backfill

Comparing the results of Fig. 9 with that in Fig. 8, it can also be said that the structure subjected to the PI wave performs very well, if enhancement measures are taken.

Interestingly, it performs better than under the HN type L1 motion. This particular example suggests that stronger L2 motion does not necessarily dictate the final design that is influenced by the high performance requirement for L1 motion. Therefore, the decision of the designer will have a strong influence on the performance-based design of structure. Such decision will dictate what kind of mitigation measures are to be taken for the same type of structure at the same locations for different earthquake motions.

SUMMARY AND CONCLUSIONS

A comparative study on the performances of a gravity type retaining structure under three different types of earthquake motions (L1 and L2) has been performed using underwater shaking table tests. The test results indicated the flaws of the present design codes, which blindly uses the past earthquake records without giving due considerations to the local seismological and site characteristics. The same structure under different L2 motions (with different site characteristics) may perform differently. It also divulges the difficulties associated with performance-based design, as the structural performances sometimes are dictated by the L1 motion rather than L2 motion. Thus, the responsibilities of the engineers matter a lot in the performance-based design. The type of strong motions will have a strong influence on the performance of the structure. Nevertheless, a scenario motion created for the particular site rather than the past strong motions at some other sites, thus, can be the fitting answer to the new design trend.

REFERENCES

[1] PIANC (International Navigation Association), "*Seismic Design Guidelines for Port Structures"*, Balkema Publishers, Rotterdam, 2001.

[2] Japanese Geotechnical Society (JGS) and Japan Society for Civil Engineers (JSCE), "Joint Report on the Hanshin-Awaji Earthquake Disaster (In Japanese)", 1996.

[3] Kamon, M., Wako, T., Isemura, K., Sawa, K., Mimura, M., Tateyama, K., and Kobayashi, S., "Geotechnical Disasters on the Waterfront", *Special Issue of Soils and Foundations*, Japanese Geotechnical Society, Vol. 1, pp. 137-147, 1996.

[4] Iai, S., Ichii, K., Liu, H., and Morita, T., "Effective Stress Analysis of Port Structures", *Special Issue of Soils and Foundations*, Japanese Geotechnical Society, Vol. 2, pp. 97-114, 1998.

[5] Inagaki, H., Iai, S., Sugano, T., Yamazaki, H., and Inatomi, T., "Performance of Caisson Type Quay Walls at Kobe Port", *Special Issue of Soils and Foundations*, Japanese Geotechnical Society, Vol. 1, pp. 119-136, 1996.

[6] Ishihara, K., "Geotechnical aspects of the 1995 Kobe earthquake", *Terzaghi Orientation, 14th International Conference of International Society of Soil Mechanics and Geotechnical Engineering*, Hamburg, Germany, Vol. 4, pp. 2047-2073, 1997.

[7] Ishihara, K., Yasuda, S., and Nagase, H., "Soil Characteristics and Ground Damage", *Special Issue of Soils and Foundations*, Japanese Geotechnical Society, Vol. 1, pp. 101-118, 1996.

[8] Sugano, T., Morita, T., Mito, M., Sasaki, T. and Inagaki, H., "Case Studies of Caisson Type Quay Wall Damage by 1995 Hyogoken-Nanbu Earthquake", Proc. of the *11th World Conference on Earthquake Engineering, WCEE*, Paper No.765, 1996.

[9] Towhata, I., Ghalandarzadeh, A, Sundarraj, K.P., and Vargas-Monge, W., "Dynamic Failures of Subsoils Observed in Waterfront Area", *Special Issue of Soils and Foundations*, Vol. 1, pp. 149-160, 1996.

[10] SEAOC, "Performance based seismic engineering of buildings", Structural Engineers Association of California, Sacramento, California, USA, 1995.

[11] Steedman, R.S., "Seismic design of retaining walls" , *Geotechnical Engineering*, Institution of Civil Engineers, Vol. 131, pp. 12-22, 1998.

[12] Japan Society for Civil Engineers (JSCE), "Earthquake Resistant Design Codes in Japan", 2000.

[13] Nozu, A., Fukuzawa, K., Sato, Y., and Sugano, T. , "Modification of the Empirical Green Function Method", *Report of the Port and Airport Research Institute (PARI)*, Yokosuka, Japan, Vol. 42(1), pp. 139-166 (in Japanese), 2003.

[14] Nozu, A., "Current Status of Strong-motion Earthquake Observation in Japanese Ports", *Special Issue of Journal of Japan Association for Earthquake Engineering*, Vol. 4(3), pp. 79-83, 2004.

[15] Nozu, A., and Nagao, T , "Site Amplification Factors for Strong-motion Sites in Japan Based on Spectral Inversion Technique", *Technical Note of the Port and Airport Research Institute*, Yokosuka, Japan, No. 1112 (In Japanese), 2005.

[16] Cabinet Office, Government of Japan: Central Disaster Management Council, Available: http://www.bousai.go.jp/jishin/chubou (in Japanese), 2006.

[17] Irikura, K., "Prediction of Strong Ground Motions Using Empirical Green's Function", *Proceedings of the 7th Japan Earthquake Engineering Symposium*, pp. 151-156, 1986.

[18] *Design Standard for Port and Harbour facilities and Commentaries*, Japan Port and Harbour Association, 1999 (In Japanese).

[19] Yasuda, S., "Recent Several Studies and Codes on Performance-based Design for Liquefaction in Japan", *Proceedings of Geotechnical Earthquake Engineering Satellite Conference, TC 4 of ISSMGE*, Osaka, Japan, pp. 46-53, 2005.

[20] Iai, S., and Sugano, T., "Shake Table testing on Seismic Performance of Gravity Quay Walls", Proc. of the *12th World Conference on Earthquake Engineering, WCEE*, Paper No. 2680, 2000.

[21] Iai, S., "Similitude for shaking table tests on soil-structure-fluid model in 1g gravitational field", *Soils and Foundations*, Vol. 29, No. 1, pp. 105-118, 1989.

[22] Hazarika, H., Kohama, E., Suzuki, H., and Sugano, T., "Enhancement of Earthquake Resistance of Structures Using Tire Chips as Compressible Inclusion", *Report of the Port and Airport Research Institute (PARI)*, Yokosuka, Japan, Vol. 45, No. 1, pp. 1-28, 2006.

Correlating DMT K_D and CRR of a Silty Sand through Laboratory Calibration Tests

A. B. Huang, Y.Y. Tai , C.H. Liu

Department of Civil Engineering, National Chiao Tung University, Hsin Chu, Taiwan

Abstract

The Flat Dilatometer Test (DMT) developed by Silvano Marchetti of Italy is a relatively new in situ test method. The DMT testing device consists of a 94-96 mm wide, 180-190 mm long and 14-16 mm thick blade with a 60 mm diameter inflatable membrane mounted on one side of the blade. The DMT blade is essentially a solid piece of stainless steel. The membrane is made of a thin stainless steel film. During the DMT, the blade is penetrated either by pushing or driving, to the desired depth and then record the two pressures required to lift off the membrane (p_o) and to further expand it by 1.1mm (p_1). Three parameters, the DMT modulus (E_D), material index (I_D) and horizontal stress index (K_D) are derived from p_o and p_1. For granular material, K_D is generally believed to be an amplification of K_o. The amount of amplification is related to the density state of the granular material. Based on this postulation, a few methods have been proposed to relate K_D to Cyclic Resistance Ratio (CRR) as a means to assess the liquefaction potential. Because of the limited database, the existing correlations are limited to clean sand. There has been little information as to the use of these correlations for sand with fines. The DMT method has not been well accepted as part of the simplified procedure.

Mai Liao Sand (MLS) is a typical silty sand found in Central Western Taiwan. MLS consists of relatively soft minerals and is significantly more compressible than clean quartz sand as typically reported in literatures. The in situ test results such as the blow counts (N) of SPT, cone tip resistance (q_c) of CPT, or shear wave velocity, may require a fines content adjustment when applying the simplified procedure of liquefaction potential for silty MLS. Earlier studies performed by the authors have shown that the use of different in situ test methods may lead to significantly different conclusions if the simplified procedure is followed. The problems with the use of simplified procedure in MLS may include the effects of soil compressibility (or lack of dilatancy) and partial drainage in the case of high fines content (fines contents in excess of 30%) in CPT.

Because the main part of DMT is inflation of the membrane, the problem of partial drainage during DMT penetration may be avoided by delaying the time period between end of penetration and membrane inflation. Without the partial drainage effects, it is possible that there is no need for different K_D-CRR correlation for MLS with different fines contents. The elimination of fines content adjustment should significantly streamline the procedure of liquefaction potential assessment and provide more consistent results. To verify this potential, a series of DMT calibration tests were

performed in a calibration chamber under stress controlled boundary conditions (B1). The calibration chamber specimen was prepared using a dry deposition method and the specimen remained dry during DMT. All specimens had a fines content of 15%. A series of monotonic and cyclic triaxial tests have been performed on MLS with fines contents and confining stresses comparable to those applied in DMT calibration tests. For MLS, the relationship between K_D and relative density (D_r) or state parameters are not nearly as consistent as those reported for clean quartz sand. Nevertheless, the K_D-CRR correlation for MLS did show a trend that is similar to those proposed earlier. However, the existing correlations may be too conservative to MLS. A tentative K_D-CRR curve for MLS is proposed. The validity of this proposed correlation has yet to be verified with field measurements.

Evaluation of subsurface ground softness layers of the eastern area of Sendai City based on the bore-hole data.

Tomohiro Mori, Motoki Kazama, Ryosuke Uzuoka and Noriaki Sento

Graduate School of Engineering, Dept. of Civil Engineering, Tohoku University, Sendai, Japan 980-8579

Abstract

It is known that engineering properties of subsurface layers are very important for evaluating the seismic wave amplification and the liquefaction damage, during an earthquake. In this study, to obtain the distributions of the subsurface ground softness, about 1200 bore-hole data of the eastern area of Sendai City were rearranged. And also, for studying the influence of the averaging method of soil profiles on the seismic response, an equivalent linear seismic response analysis was performed. The following results were obtained from this study: (1) In the Sendai plane, thick soft soil deposit is found in the eastern area of Nagamachi-Rifu active fault. (2) Liquefaction susceptive area is influenced from the representative soil profiles used for analysis. (3) The deviation to the average value of shear stress ratio is smaller than that of maximum acceleration response at the surface. (4) Averaging method of soil profiles from several bore-hole data used in the study is useful for practical engineering.

Keywords— *Bore-hole data, Geo Information System, soft ground,*

INTRODUCTION

It is well known that engineering properties of subsurface layers are very important for evaluating the seismic wave amplification and the liquefaction damage, during an earthquake. In recent years, using geo informatics technology, many bore-hole data have been used for practical evaluation of seismic hazard. However, the method is still research issue.

To study the seismic motion amplification and liquefaction susceptibility, in this study, about 1200 bore-hole data of the eastern area of Sendai City were rearranged under various conditions using GIS technique. Consequently, the distributions of the subsurface ground softness based on the soil kind, N-value and ground water level were evaluated.

REARRANGEMENT OF BORE-HOLE DATA AND EXTRACTION OF SOFT SUBSURFACE GROUND

Bore-hole data sets

The database consists of about 1200 bore-hole data which distribute in eastern area of Sendai City, the area is covered with about 6km in the east and west direction, and about 12 km in the north and south direction. Most of the depth of the bore-hole data is 10-20m, and average depth is 14.9m. The bore-hole data were obtained from the field investigations conducted from 1964 to 1995 for building construction.

Definition of soft ground

Earthquake damage is related to engineering properties of subsurface layers. According to the design manuals [1] [2] and the previous researches [3], soft grounds are categorized into clayey and sandy soft grounds. In this paper, these two kinds of soft layer were defined as follows;

1. Soft cohesive soil ground to be apprehensive for amplification of seismic wave, which satisfy the following two items.
- Cohesive soil (clay, silt, peat, organic soil and loam)
- N-value is less than four.

2. Soft sandy ground to be apprehensive for liquefaction, which satisfy the following three items.
- Sandy soil (sand and sandy silt)
- N-value is less than ten.
- Under the ground water level.

Input data items

Input data items for database from bore-hole data are shown in Table 1. When making database, in order to minimize the degradation of original soil information, soil kinds are classified into 14 kinds based on engineering soil classification system as shown in Table 2. In the table, E and R are added for representing the embankment with fills and rocks, respectively. Occasionally, the stratum has formed alternative strata and the soil of same kind may appear repeatedly. To distinguish gradations of strata, strata are named by three characters, as illustrated in Table 2. The first and second character expresses the kinds of soil, and third character express the gradations of stratum.

Table 1: Input data items for bore-hole database

Items	Contents
Persel's number of map ID of boring data	Persel's number of map I.D. of boring data (Example) 43-1-1
Coordinates (X, Y)	Cordinates of location about boring data based on Universal Tangential Merctor 54 system (UTM54)
Altitudes	The altitude obtained coordinates and digital elevation map
Depths	The depth from ground surface
Kinds of soil	Soil name and bottom depth of layer described in soil boring data
N-value	N-value based on Standard Penetration Test
Depths of penetration (in SPT)	The depth of penetration based on Standard Penetration Test
Ground water level	The depth of ground water level (under ground level)

Interpolation method

To illustrate the distribution of subsurface soft layers from limited number of bore-hole data, we used Inverse Distance Weighted (IDW) method as an interpolation method. IDW method weights the information in proportion to powers of the distance from the twelve nearest known points to an interpolating point. The equation of the interpolation is the following.

$$Z_j = \frac{\sum_{i=1}^{n} w_{ij} Z_i}{\sum_{i=1}^{n} w_{ij}} \tag{1}$$

$$w_{ij} = \left(\frac{1}{d}\right)^{\alpha} \tag{2}$$

Where w, d and alpha are the weight, distance from a known point to an interpolating point and the coefficient of powers, respectively. Subscriptions i and j represent a known data and interpolating data.
In the equation, we adopted the coefficient of alpha to be square. When selecting the basic bore-hole data, peculiar data due to a surrounding topographical feature was removed before interpolation.

The distribution of soft subsurface layers

Figure 1 shows the locations of bore-hole data in eastern area of Sendai City. The active fault line, Nagamachi-Rifu fault, is also plotted in the figure. The east side of Nagamachi-Rifu fault consists of strata with alluvial plane and loose sand deposits. In this area, the depth of ground water level is very shallow between 1m-2m. It seems that this area can be considered as the area having high liquefaction susceptibility.

Figure 2 shows the distribution related with the deepest depth of soft cohesive ground whose N-value is less than four. As shown in the figures, soft strata have deposited to depth of 10m from northeast to southwest along the Route-4 bypass.

Figure 3 shows the distribution related with the deepest depth of soft sandy ground with N-value less than ten. There is possibility that these areas may suffer serious damage from future earthquakes. However, liquefaction susceptive area predicted in this study is different from the result in liquefaction damage area predicted for expected Miyagiken-oki earthquake [4], indicating as the hatched area in Figure 3. Comparing to previous research [4], liquefaction susceptive area is shifted to 1.5km east from Route-4 bypass. The liquefaction possibility relates to the soil profiles and thickness of the soft layer. We will discuss this point in the next chapter using response analysis.

Table 2: Soil classified table and soil codes

First level classification			Second level classification			The codes of	Code
Soil character	name	Code	soil character	name	Code	layer's orders	(To distingish soils)
G	Gravel	1	G	Gravel	0	1～	101～
			GS	Gravel and sand	1	1～	111～
			GF	Gravel cantained fine-grained soil	2	1～	121～
S	Sand	2	S	Sand	0	1～	201～
			SG	Gravelly sand	1	1～	211～
			SF	Sand contained fine-grained soil	2	1～	221～
Cs	Cohesive soil	3	M	Silt	0	1～	301～
			C	Clay	1	1～	311～
Pt	Peat	4	Pt	Peat	0	1～	401～
O	Organic soil	5	O	Organic soil	0	1～	501～
V	Volcanic cohesive soil	6	V	Volcanic cohesive soil	0	1～	601～
R	Rock	7	R	Rock	0	1～	701～
E	Embankment and fill	8	E	Embankment and fill	0	1～	801～
A	Artificial materials	9	A	Artificial materials	0	1～	901～

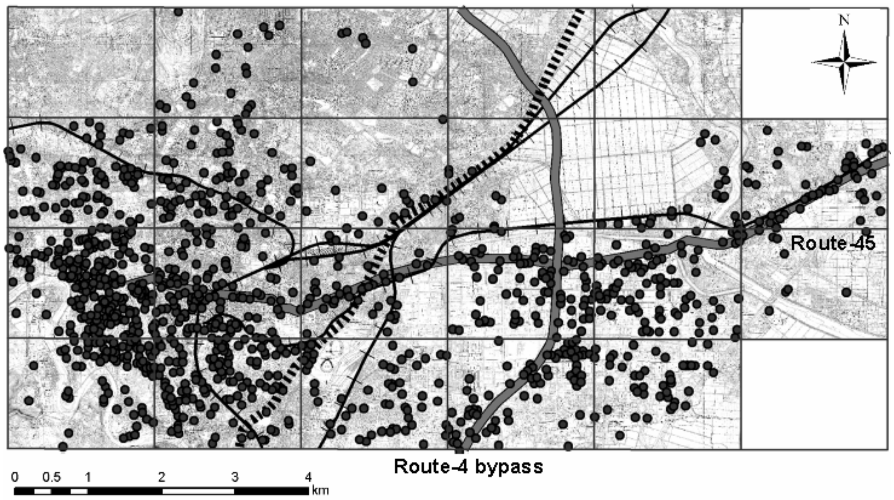

Fig.1: The location of bore-hole investigation data

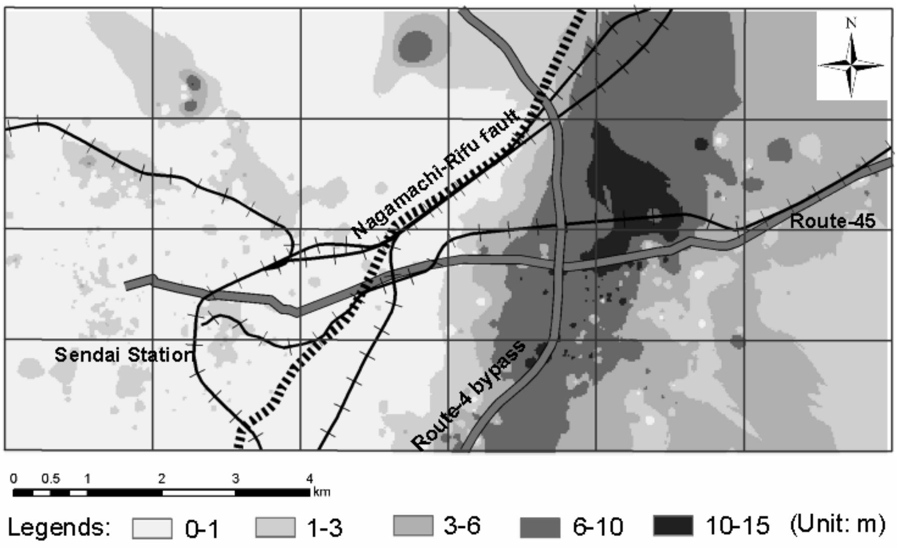

Fig.2: The depth of depositing soft cohesive ground of N-value less than four

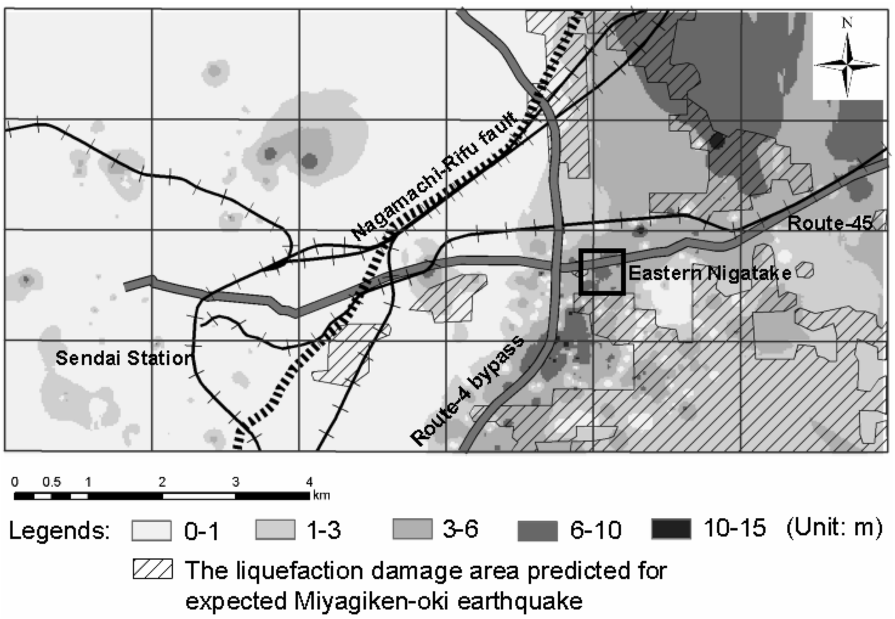

Fig.3: The depth of depositing soft sandy ground of N-value less than ten

STUDY OF THE REPRESENTATIVE SOIL PROFILES FOR DAMAGE EVALUATION CAUSED BY EXPECTED MIYAGIKEN-OKI EARTHQUAKE

The purpose

Occurrence of the next Miyagiken-oki earthquake is predicted in about ten years by the Headquarters for Earthquake Research Promotion, Japanese Government. For earthquake disaster mitigation, local city government made the prediction report in recent years [4]. In general, the degree of the damage is given by the mesh data. Therefore, it is necessary to make a representative soil profile for each mesh area based on the several bore-hole data. To study the representative soil profiles reflecting the average properties, we conducted the case study of the specific site in Sendai City.

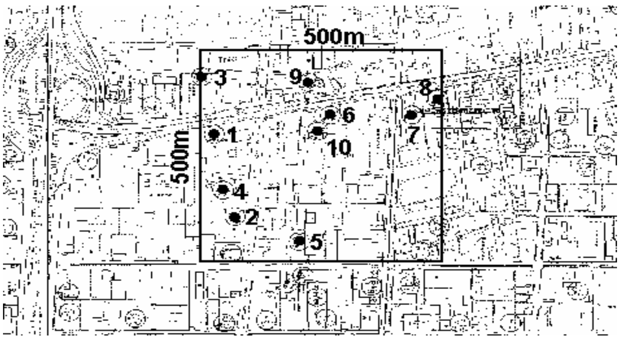

Fig.4: The detailed location of bore-hole data in Eastern Nigatake area (describing case numbers)

Target area and soils profiles used in the study

Eastern Nigatake area as shown in Figure 3 is selected for case study. According to the result in previous section based on the bore-hole data, this area was estimated to have high liquefaction potential. On the other hand, according to the local government report, this area is out of the liquefaction susceptive area. We have studied what is the cause of the difference between two.

Soil profile used in the local city report (named "case-Sendai") and the other 10 bore-hole point data (named "case-1 to case-10") located in the same area were chosen, its mesh size was 500m square. Figure 4 shows the position of case-1 to case-10. Figure 5 shows the soil information of case-Sendai and case-1 to case-10.

In Figure 5, it is found that the strata deposit consists of embankment, peat, sandy soil, cohesive soil, and gravel in order from ground surface. In case-1 to case-10, the strata include soft sandy soil layers in the range from the depth of 3.7m to 7.8m and its N-value is in the range from 1.5 to 10. Therefore, this soft sandy soil layers should be considered sufficiently to liquefy during earthquake. However, soil profiles in case-Sendai include strata only cohesive soil and gravel. It seems that the difference resulted from the method of selecting representative soil profiles for the mesh.

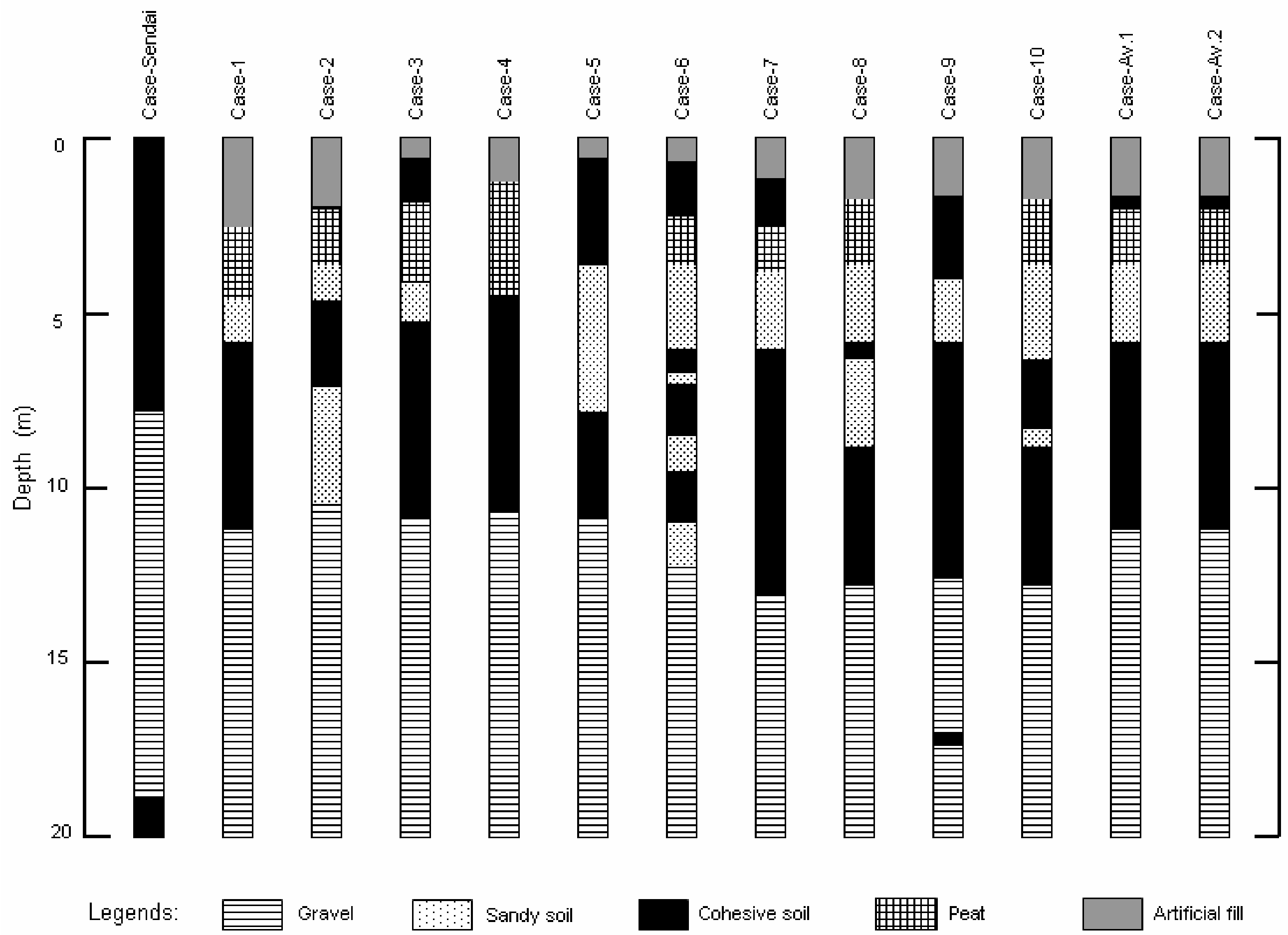

Fig.5: Comparison of bore-hole data

The relation between soil profiles and seismic response

For studying the relationship between the soil profiles of the mesh and seismic response, an equivalent linear seismic response analysis was performed with case-Sendai and case-1 to case-10. Dynamic soil properties used in the analysis was determined from two factors, kinds of soil and mean N-value. Table 3 shows the parameter of soils determined with kinds of soil and mean N-value. Figure 6-1 and 6-2 show the G-γ curves and h-γ curves of every kind of soils. According to Table 3 and Figure 6, wet unit weight of soils (γ_t), shear wave velocity (V_s), shear modulus (G) and damping factor (h) are determined.

Figure 7 shows the time history of the input seismic wave at a depth of 20m for all cases. The wave motion is the predicted engineering base motion for expected Miyagiken-oki earthquake with magnitude 7.4 at the study site. The wave was used for the seismic response analysis in local government report.

Figure 8 shows the frequency of maximum acceleration response at ground surface. In case-1 to case-10, mean maximum acceleration response at ground surface is 307.7cm/s^2 and standard deviation is 51.4cm/s^2. Solid line in the figure shows the normal distribution curve obtained from average value and standard deviation. When the distribution of maximum acceleration response follows normal distribution, 95% reliable range is 206.9cm/s^2 to 408.4cm/s^2. The error ratio with the mean value is ±32.7%.

Figure 9 shows the frequency of the maximum shear stress ratio (τ / σ_v') at the mid depth for 15 sandy soil layers included in case-1 to case-10. There is no stratum of sandy soil in case-Sendai. In case-1 to case-10, mean maximum shear stress ratio is 0.513 and standard deviation is 0.052. When the distribution of maximum shear stress ratio follows normal distribution, 95% reliable range is 0.411 to 0.615. The error ratio with the mean value is ±19.9%.

From the Figures 8 and 9, the maximum acceleration response varies widely comparing to the maximum shear stress ratio. When we consider the seismic response, we should note that there is 20-30% deviation. Furthermore, for liquefaction assessment, the shear stress ratio obtained from response analysis is more reliable information than maximum acceleration response at the ground surface.

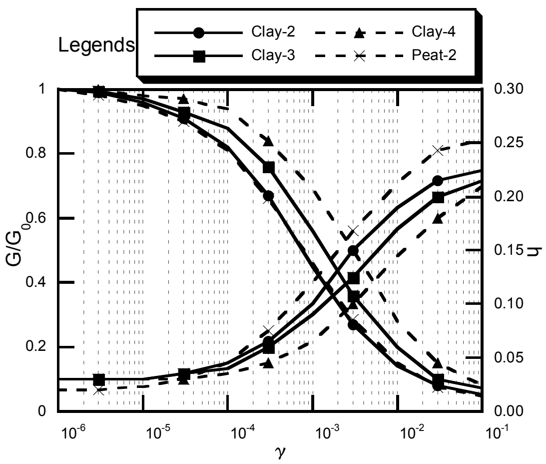

Fig.6-1: Shear strain dependent of shear modulus / damping factor for cohesive soils

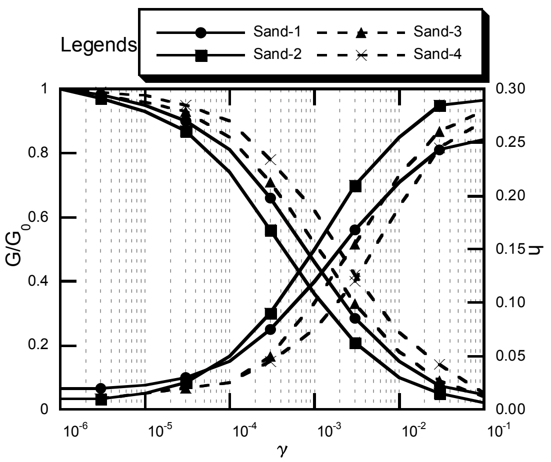

Fig.6-2: Shear strain dependent of shear modulus / damping factor for sandy soils

Table 3: The parameter of soils for an equivalent linear seismic response analysis

Kinds of soils	Parameters of soils					Shear strain dependence of shear modulus / dampingfactor
	N-value (-)	γt (g/cm3)	Vs (m/s)	G0 (tf/m2)	h0 (-)	
Embankment and fill (E)	5-20	1.90	280	15200.00	0.01	Sand-4
Artificial materials (A)	0-8	1.70	110	2098.98	0.01	Sand-1
Peat (Pt)	0-1	1.10	50	280.61	0.02	Peat-2
Organic soil (O)	1-5	1.30	90	1074.49	0.02	Peat-2
Silt (M)	0-1	1.40	80	914.29	0.03	Clay-2
Clay (C)	1-3	1.50	100	1530.61	0.03	Clay-2
Volcanic cohesive soil (V)	3-6	1.65	150	3788.27	0.03	Clay-3
	6-15	1.70	200	6938.78	0.03	Clay-4
Sand (S)	2-10	1.70	110	2098.98	0.01	Sand-1
Sand contained	10-20	1.70	200	6938.78	0.01	Sand-2
fine-grained soil (SF)	20-40	1.80	250	11479.59	0.01	Sand-2
Gravel (G) Gravel and sand (GS)	20-50	1.80	300	16530.61	0.01	Sand-2
Gravel cantained fine-grained soil (GF) Gravelly sand (SG)	50-	2.00	450	41326.53	0.01	Sand-3

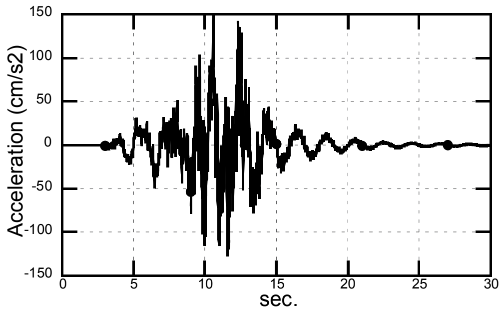

Fig.7: Input seismic motion at the depth of G.L.-20.0m

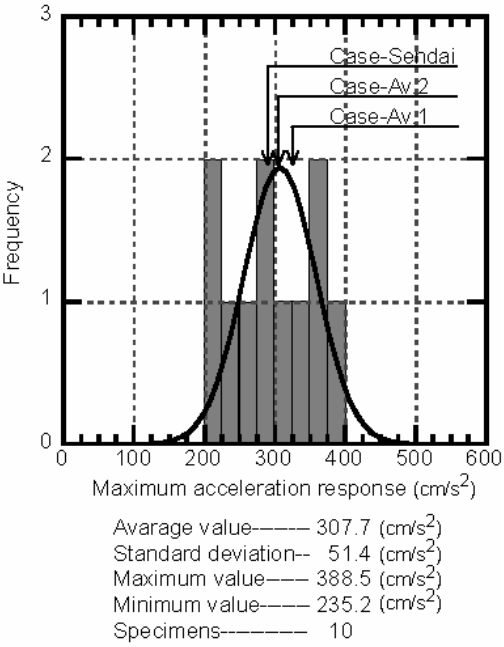

Fig.8: Frequencies of maximum acceleration response at ground surface

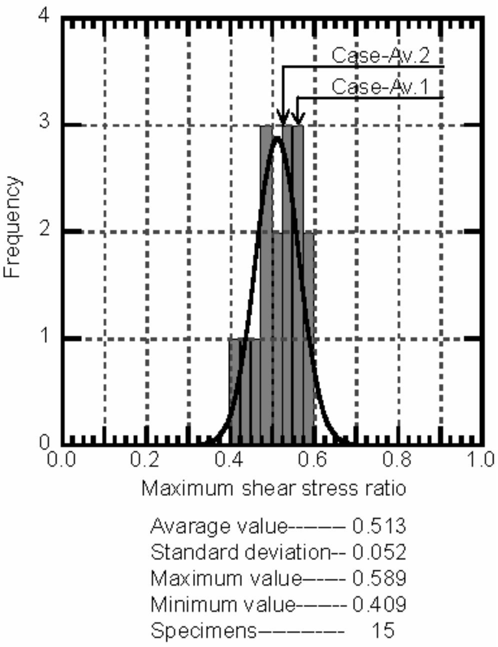

Fig.9: Frequencies of maximum shear stress ratio at the central depth of stratum of sandy soil

The influence of the averaging of soil profiles on the seismic response

In order to study the averaging methods of soil profiles, the influence of the averaging method on the seismic response was studied to consider the following two different averaging methods. Here, we consider the problem that representative soil profiles such as N-value and soil kinds at every ten centimeters will be determined by averaging the several bore-holes data.

Method 1: The soil kind at a certain depth is determined as the one most frequently appeared at the depth. The average N-value is determined by averaging the N-value only with the selected soil kind layer.

Method 2: The soil kind at a certain depth is determined from the same method above. The average N-value at the depth is determined by averaging the all N-value.

Henceforth, the soil information made by method 1 express as case-Av.1, and made by method 2 express as case-Av.2. Using the determined soil profiles as explained in case-Av.1 and case-Av.2, equivalent linear seismic response analysis was performed under the same condition as previous section. Maximum acceleration response at ground surface in case-Av.1 and case-Av.2 are shown in Figure 8. Maximum shear stress ratio at the central depth of stratum of sandy soil in case-Av.1 and case-Av.2 are shown in Figure 9.

Maximum acceleration response for case-Av.1 and case-Av.2 located nearly average value for case-1 to case-10. In this calculation condition, even if calculating after averaging soil profiles, the value is almost identical to mean acceleration response. Since the value in case-Av.2 is close to mean value than that in case-Av.1, method 2 seems superior to method 1. Furthermore, the deviation to the mean value of shear stress ratio has less than that of the maximum acceleration response at ground surface. Therefore, it is likely that, for liquefaction assessment, the method based on shear stress response has high accuracy than the one based on the acceleration response.

Figure 10 shows the relation between the maximum shear stress ratios in the depth direction for all soil profiles. On the whole, the trend can be seen that the maximum shear stress ratio developed in the range from 5.0 to 10.0 m depth, and decreasing as close to ground surface. When the existence of soft sandy soil layer and the maximum shear stress ratio is taken into consideration, the possibility of liquefaction in the area is not small for the expected next Miyagiken-oki earthquake. Among the calculation results, the result in case-4 has different pattern from others, case-4 shows the smallest maximum shear stress ratio at the depth around 5 m and the largest value at ground surface. It is noted that stratum of sandy soil does not exist in the only case-4. Considering these results, the selection of soil kind is more influential factor.

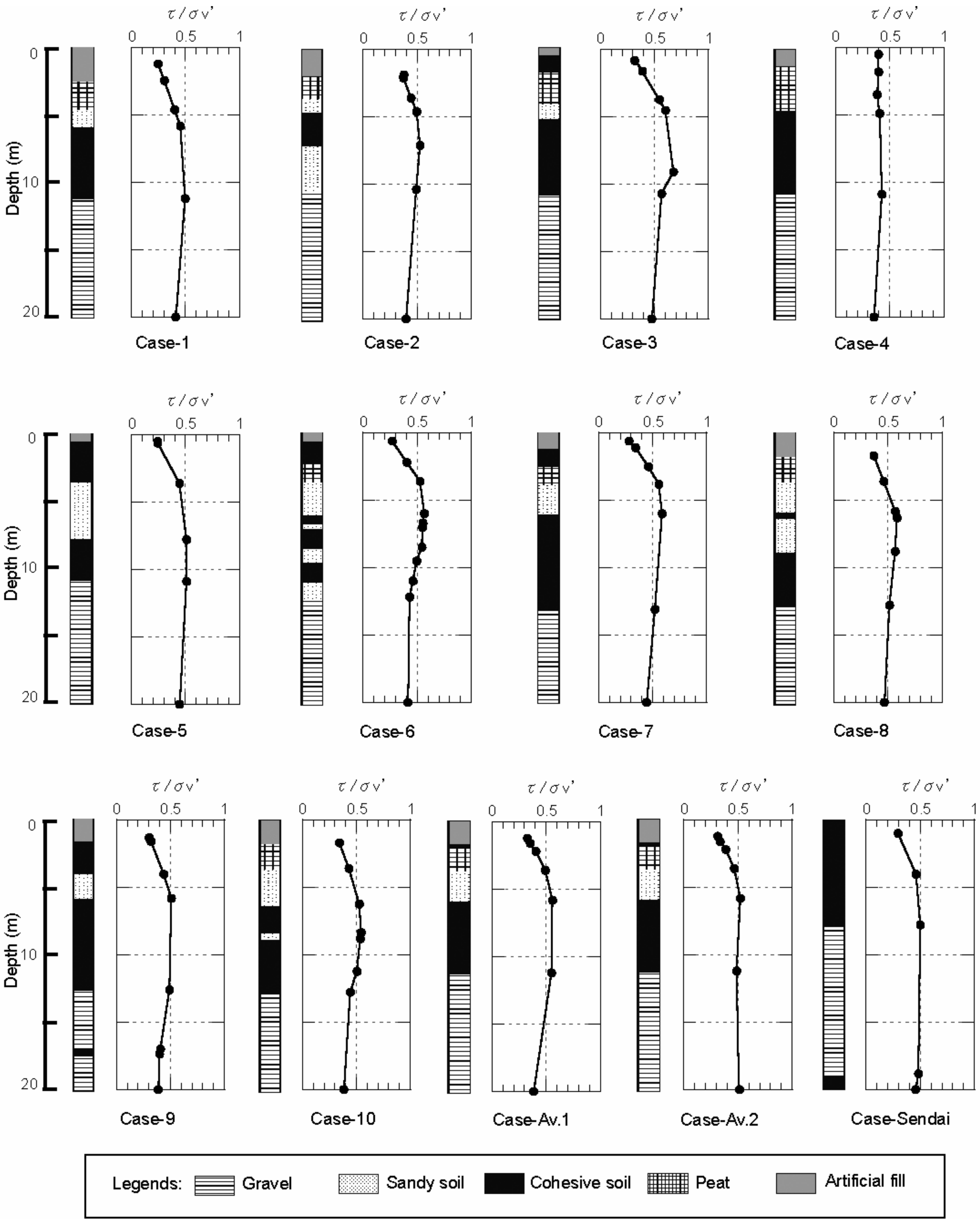

Fig.10: The relation between maximum shear stress ratio and the depth

CONCLUSION

1. Soft subsurface ground distribution can be obtained from about 1200 bore-hole data in eastern area in Sendai City, covering the 6 X 12 km area. In the Sendai plane, thick soft soil deposit is found in the eastern area of Nagamachi-Rifu active fault.
2. Liquefaction susceptive area obtained from the bore-hole data in this study was different from the area reported by local government damage prediction. The cause of the difference between two is the representative soil profiles used.
3. From the study of the averaging method of soil profiles, the deviation to the average value of shear stress ratio is smaller than that of maximum acceleration response at the surface. For liquefaction assessment, stress ratio is more reliable than the acceleration response at the surface.
4. Averaging method of soil profiles from several bore-hole data used in the study is useful for practical engineering.

REFERENCES

[1] Japan Federation of Architect and Building Engineers Associations. 1981. Explanation for the law about to regulate developing residential area.
[2] Japan Highway Public Corporation. 1976. New method of soil improvement for soft ground, 5-13.
[3] Public Works Research Institute of Tokyo metropolitan government. 1987. Prospect of liquefaction about Tokyo low land, 7-17.
[4] Sendai City. 2002. The research reports about predicted seismic hazard of Sendai City, 2-4-1 - 2-4-12.

The Performance-oriented Aspects for the Geotechnical Engineering

C.H. Wang[1] and J.R. Chen[2]
[1]*Taiwan Construction Research Institute, Taipei, Taiwan*
[2] *MAA Group Consulting Engineers, Taipei, Taiwan*

Abstract

In the traditional approaches for the hazard/risk evaluation/retrofitting and the design methodology, geotechnical engineers usually use the factor of safety to solve most of the problems. In the modern new era, the society demands for increasing of mega facilities and structures are threatened by several challenges, such as the natural hazard, human crisis, and engineering difficulty. In order to solve the challenges with sufficient safety and reasonable budge, a performance-oriented problem-solving has been immerged among the geotechnical engineering. To introduce the performance-oriented aspects for the geotechnical engineering, this article concentrates the discussions on two aspects: the hazard/risk evaluation/retrofitting and the new generation geotechnical structure design methodology.

Keywords—*performance, hazard, retrofitting strategy, design, Taiwan Power Company, Taiwan High Speed Rail*

INTRODUCTION

In the past history of geotechnical engineering development, because of the difficulty to fully understand the true behavior of soil, geotechnical engineers usually use certain amount of assumptions with previous experience to apply on the design and hazard evaluation. This approach causes a great level of uncertainty, including the unknowns of soil and geotechnical structure itself. On the other hand, the purpose of make the safety design in to make the structure can sustain a certain safe level under the destructive force produced by nature or human. It also require a great effort on understand the uncertainty on those destructive forces.

In the recent progress on the society development, the high demand on constructing new structures leads the needs of improvement of a more efficient method on the design specification. This problem can be enlarged especially when engineer is confronted to the mega project. The complexity of constructing a mega project is not only on the design of the structure itself, but also the necessity to meet the functional requirement. On the other hands, the large amount of existing structures are also challenged by the natural and man-made hazard. When natural force or human produce destructive force to the existing structures, the capacity of the structure may not be high enough to stand. For such reason, a reasonable risk assessment procedure followed by the retrofitting strategy should be thoughtfully established.

In order to resolve the challenges for both the existing and new structure, the new trend for the geotechnical engineering is to involve the performance-oriented aspect for treating the problem. For the existing structure, the performance requirement should be identified by retrofitting strategy on various risk levels produced by the natural and man-made hazards. For the new designed structure, the performance requirement should be defined by the safety level on the daily usage basis. In this article, two cases will be study for their performance-oriented design and retrofitting approach.

1. Study of risk assessment and retrofitting strategy for the soil foundation of power transmission tower on slope
2. Design consideration for mega project – the seismic design concept of the Taiwan High Speed Rail

STUDY OF RISK ASSESSMENT AND RETROFITTING STRATEGY FOR THE SOIL FOUNDATION OF POWER TRANSMISSION TOWER ON SLOPE

The target of this case study is the risk assessment and retrofitting strategy for the soil foundation of power transmission tower on slope. The electricity power network system is an essential industry that provides sufficient power for the entire country. The Taiwan Power Company is responsible for this duty to safely deliver electricity to all necessary corners among the island of Taiwan. Besides, to maintain the electricity power facility in a safety level to against all possible threats from hazards is also an important issue. In the past history of Taiwan, majors hazards can be produced from earthquake events and landslide hazards. In 1999, two major failure events seriously damaged the electricity power system and brought the entire society into dangers. One of the hazard was caused by the heavy rainfall-triggered landslide, which collapsed a transmission tower and led to the power blackout at the most part of north island. At the same year, the 921 Chi-chi earthquake with magnitude of 7.6 caused more than 600 collapsed towers, which again put the society into great dangers.

Among those power transmitting routs, the No.1 north-south direction 345kV line was first constructed in 1974, which was about 30 years ago. The main duty of this line is to transmit and re-rout electric power within the northern and southern island. From the current engineering concerns on risk assessment, this line usually cross a long distance (500m to 800m) on the slopes of hills within the sliding-suspected area. Furthermore, due to the restrain on technology and knowledge, the design of this line used soil foundation built on slop. The design of soil foundation is the assembled metal frames buried with graded rocks and soils, which is now considering a less reliable design to against the earthquake force and landslide hazard. From the performance-oriented viewpoint, the environmental effects and the material degrading in the past service life may seriously threat the future safety. In order to ensure the safety of these transmission towers, this study aims to evaluate the earthquake and landslide risk assessments of the soil foundation of the No.1 north-south direction 345kV line. Furthermore, the adequate retrofitting strategy is established to ensure the safety in the future service life.

For the No.1 north-south direction 345kV line, in total there are 1288 tower, in which 566 of them are made of soil foundation. As shown in Fig. 1, the extend of this line almost covers the entire west island. From the records, it shows that 92 of the 566 soil foundation tower have experienced failure in the past. Besides the serious failures triggered by the 1999 Chi-chi Earthquake, fortunately there were only minor failure have been observed.

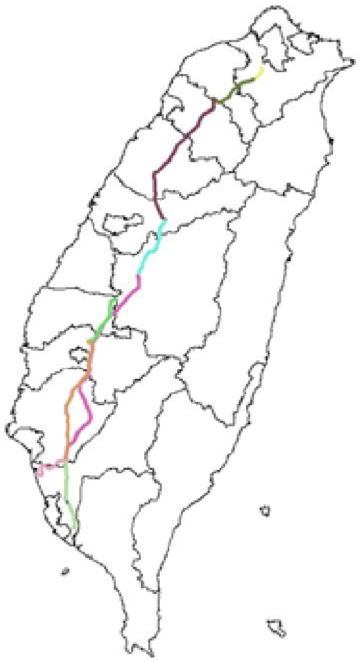

Fig. 1: The distribution of electric transmission tower of the No.1 north-south direction 345kV line

Performance-oriented Risk Assessment and Retrofitting Strategy

In the human history, the hazard events happened frequently, such as earthquake and heavy rainfall induced structure and facility failures. The consequence of those failures may produce various damage levels on human life and prosperities loss. Furthermore, some devastating event may cause a long term society trauma. For example, one of the most serious events struck Taiwan was the 1999 Chi-chi earthquake, which killed more than two thousand people and produced great society loss. For evaluating the possible future hazard and the reasonable risk assessment procedure, a properly defined approach for risk analysis is an important thing to be completed. In this article, in order to demonstrate the importance of the performance-oriented risk assessment, a four-staged strategy is introduced followed by a case study.

With progressing on the modern practice, the performance requirement has been considered as one of the most important and challenge issue for the risk assessment. In the previous works, Chen et al. (2005) [1] proposed for the seismic risk assessment procedure that described a proper way to characterize elements that need to be considered in the risk assessment. In this article, continuing on the previous efforts, a proposed performance-oriented procedure for the risk assessment is presents for the general geotechnical structures, especially for the existing structures. This procedure emphasized on four important stages (shown in Fig. 2), including the initial condition assessment, the risk assessment, the impact and retrofitting assessment, and the long term performance maintaining strategy.

In the first stage, in order to completely understand the initial design purpose, the past maintenance and hazard history, and the current performance of the structure, the basic information collecting on design, construction records, and the history on the requirement and mitigation records are fully desired. Besides, a proper investigation and monitoring approach can be great helps to understand the current safety level of the structure itself. Furthermore, with the help on the modern technology, a proper database system should also be established to store and maintain the accumulated information.

Based on the information from the first stage, the second stage emphasizes on analyzing the possible threats that producing the various hazard scenarios. In the beginning, all possible factors that may affect the safety of the structure should be analyzed. For example, potential factors include earthquake, rainfall, geology, tomography, previous hazard region, etc. By assembling factors to potential hazard scenarios, the possible failure modes and its extend on the geotechnical design can then be estimated, which also includes the various risk level.

In the third stage, the possible impact or consequence produced by various levels of risk is estimated, impact or consequence including the damages to human lives, economy loss, society disaster, etc. Before the final retrofitting program can be finalized, two major criteria should be further examined. The first criteria is the prioritization. This prioritization represents the importance of components within the structure, also the structure itself among the authority decision-making process. This prioritization will decided the retrofitting or re-construction sequence of the component or the structure. Another important criteria is the performance requirement of the component and the overall structure serviceability. Based on different failure types, risk, and performance requirement, the retrofitting feasibility study can then conclude several possible retrofitting techniques.

Combining the overall results of the previous 3 stages, the fourth stage not only generates the final optimized retrofitting program, but also provides the plan for the future maintenance plain. The retrofitting program optimization process evaluates all the possible retrofitting techniques, as well as to evaluate the possible performance upgrade. Finally, the long term maintenance plan provides the regulation of continuing maintenance schedule, hazard response procedure, and structure safety monitoring system.

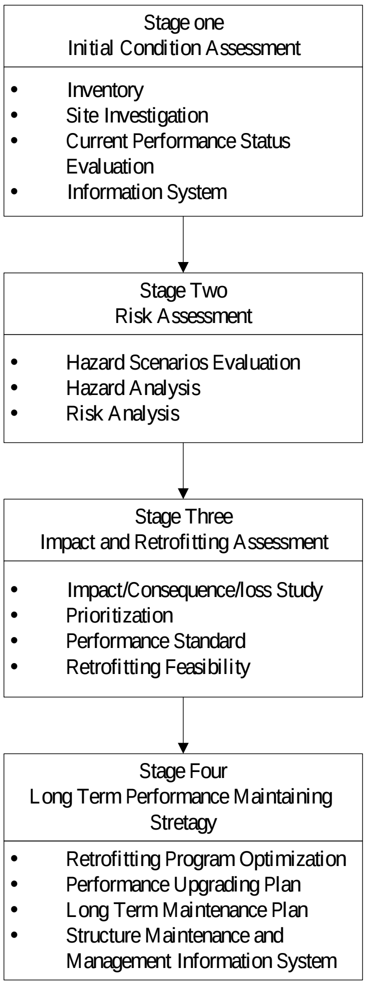

Fig. 2: Proposed Performance-oriented Risk Assessment Procedure

Case Study

In the first stage on the initial condition assessment, the basic information of the No.1 north-south direction 345kV line were collected, including the basic identification, the environmental investigation report, tower monitoring records, the past failure records, and the site investigation report. The basic identification includes the tower identification number, the constructed date, the type of foundation, and global positioning system (GPS) location. In the environmental investigation reports, the content was filed by previous site investigation. The content describes the rating on the geology condition, the slope angle, the adjacent cliff height, the nearby river system, and the surrounding vegetation condition. In the tower monitoring records, it show the periodically monitoring records on the settlement of the 4 soil foundation of each tower. In the past failure records, each failure event is described by the cause of failure (e.g. 1999 Chi-chi earthquake), the type and extent of failure (e.g. foundation settlement of 10 cm), and the mitigation records (e.g. re-leveling soil on foundation). Finally, in the site investigation report, it documents not only the condition assessment of the foundation and surrounding environment, but also the failure and possible threats to the safety. An example of the site investigation shows that the existing soil foundation was retrofitted by the 6 m diameter caisson foundation (shown in Fig. 3)


Fig. 3: Soil foundation retrofitted by caisson foundation

In the second stage of the risk assessment of this project, the process include the hazard scenarios analysis, slope hazard and risk analysis. For the observations of the past failures, the possible slope hazards (as shown in Fig. 4) include deep and shallow slope failure, settlement and lateral displacing of foundation, slope cracking, slope surface erosion, and damages caused by debris flow. By analyzing the hazard phenomena, there are several factors that may relate to the risk of slope instability, including the geology, tomography, nearby river system, slope vegetation condition, earthquake, rainfall, and debris flow. In the future development of this project, all of the factors above will be mapped by using the Geographic Information System (GIS) with the microzonation method. By correlated with the actual failure cases, various risk level can then be classified.

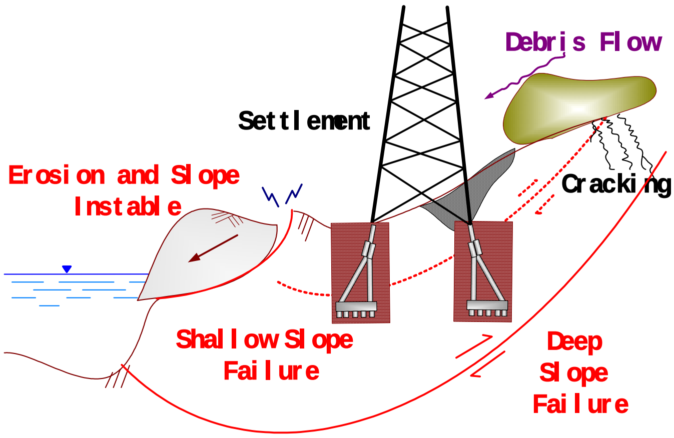

Fig. 4: Possible failure scenarios of the soil foundation of the electric power transmission tower

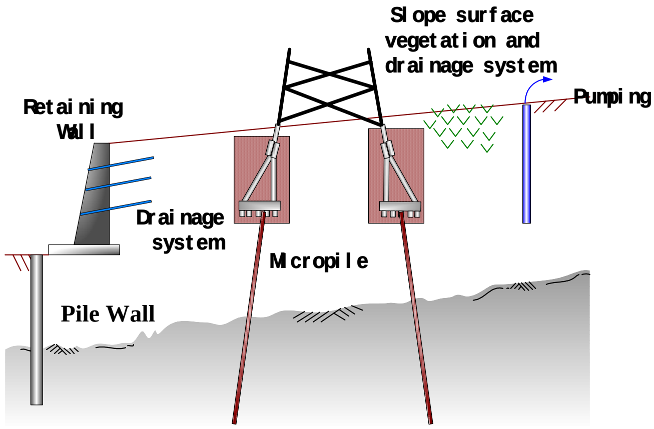

Fig. 5: Possible retrofitting programs for the soil foundation and surrounding slope

In the third stage of the impact and retrofitting assessment, the major works involve the classification of failure type and the corresponded retrofitting program. In the original retrofitting program of the Taiwan Power Company, most of the approaches use the foundation modification, such as installing of pile foundation. However, from the viewpoint of retrofitting feasibility study, the pile foundation usually involve a heavy construction efforts, also with higher cost. In order to use the best cost-effect technique to solve the actual problem, before choosing the final retrofitting program, the first thing to understand is the all possible retrofitting techniques. By observing the failure condition, the corresponding retrofitting techniques can be classified into the techniques for the soil foundation and for the surrounding slope. According to the failure types illustrated in Fig. 4, Fig. 5 shows some major types of retrofitting techniques. To solved the instability of soil foundation itself, the micro-pile or regular pile foundation can be chosen. For the slope surface water runoff and erosion problem, improving the surface vegetation condition and drainage system can prevent the water accumulation. By doing so, the risk of slope instability can decreased by decreasing the amount of surface infiltration. Some slope instability can also be triggered by the high or fluctuated groundwater table. For this situation, the groundwater table can be lowered or stabilized by either from the upper part of slope by using pumping, or from the lower part of slope by using drainage system. For the overall slope instability problem, the retaining watt and the piles can be used at toe of slope. By doing this, it can decrease the risk for the shallow and deep slope failure.

In the four stage of this project, the efforts will be emphasized on the retrofitting strategy. After analyzing the risk of slope failure , several approaches can be used. For the slope with high risk, it will be recommended to relocate the existing tower to a safer location. For the moderate risk level, the proper retrofitting program can be chosen for the soil foundation and surrounding slope. Furthermore, in order to make proper respond to the future hazard, a proper procedure of investigation and monitoring schedule should also be arranged. For those locations with none to low risk level, the regular inspection should be sufficient for the safety purpose. For those various approaches stated above, a appropriate strategy should match the balance between various risk levels and the current safety condition.

When considering the performance requirement of the seismic risk assessment, Vision 2000 (SEAOC, 1995) [2] defines the performance level according to three factors. First factor is the earthquake performance level, which describes the required condition (e.g. fully operational, operational, life safe, and collapse) after the structure suffered from the earthquake damage. Second factor is the earthquake design level, which involves the magnitude of design earthquake (e.g. reoccurrence period of 970, 475, 72, or 43 years). Third factor is the importance of the structure, which is defined in terms of basic objective, essential/hazardous objective, and safety critical objective.

Based on a similar consideration, the retrofitting strategy for this project is shown in Fig. 6. The risk and safety levels are divided into four levels, including high, medium high, medium low, and low. In the remaining works of this project, those 566 towers with soil foundation will be distributed into those 16 grids, based on the current condition of the safety level and their risk level on slope hazard. The type of retrofitting approach will be generalized in to Level 1 to Level 5. Those 5 levels are described as:

Level 1: only regular inspection required

Level 2: regular inspection with moderate retrofitting program after proper site investigation

Level 3: monitoring system with retrofitting program after detailed site investigation

Level 4: monitoring system with intensive retrofitting program (including foundation modification) after detailed site investigation

Level 5: re-locating tower

Safety Level \ Risk Level	Low	Medium Low	Medium High	High
Low	Level 3	Level 4	Level 4	Level 5
Medium Low	Level 2	Level 3	Level 4	Level 4
Medium High	Level 2	Level 2	Level 3	Level 4
High	Level 1	Level 2	Level 2	Level 3

Fig. 6: Retrofitting Strategy for the electric transmission tower on slope

In the following stage of this remaining project, the appropriate retrofitting program will be classified among those 566 tower based on the proposed retrofitting strategy.

DESIGN CONSIDERATIONS FOR MEGA PROJECT – THE SEISMIC DESIGN CONCEPT OF THE TAIWAN HIGH SPEED RAIL

The Taiwan High Speed Rail (THSR) Project is a mega size infrastructure development in terms of investment, construction size, and complexity, and it was handled by the BOT contract pattern. To meet the operation time target, this project was carried out on a fast track turn-key basis, and the design and construction had to be proceeded at about the same timeline. This requires extremely close coordination between designers and constructors. Due to the high operation speed, safety becomes the top concern. Because of the importance of this infrastructure, all the structures were designed with a life of 100 years. In addition, the trains were set to operate at a high speed (the maximum design speed = 350 km/hr) while maintaining running safety and comfort level for passengers, more stringent criteria than regular railways and highways were adopted in the design (Moh, 2004) [3].

Performance Requirements of THSR

Since Taiwan is highly susceptible to earthquakes, seismic resistance design is of great importance to the THSR infrastructure. To prevent over-conservatism in design, it is rational considering different performance requirements under different levels of earthquake excitation. This concept was considered in the seismic design of the THSR structures, where two types of earthquakes with different performance requirements were specified in the design specifications. For the THSR project, the primary purpose of earthquake design is to safeguard against major failures and loss of life, and two levels of earthquakes are specified in the design specification (THSRC, 2001) [4]:

(a) Type I Earthquake – Design for repairable damage: Type I Earthquake is the ground acceleration corresponding to a return period of 950 years, which has a 10% probability of exceedance in 100 years. In this earthquake level, structures are allowed to yield but damages to structures, if any, shall be repairable. The design peak ground accelerations (PGA) in the horizontal direction for type I earthquake is different for different zones in Taiwan, as shown in Fig. 7. The peak ground accelerations in the vertical direction are two-third of those in the horizontal direction.

(b) Type II Earthquake – Design for safe operation at maximum speed and no yielding: Type II Earthquake is intended for the serviceability limit state design for structures carrying THSR tracks, in which no yielding are allowed and the operation of the system subsequent to earthquakes is expected to be unaffected. To make sure that trains still can run at their full speed of 350 km/hr, it is mandatory to inspect the deformations of tracks after earthquakes and make sure they are within allowable ranges. The design PGA in the horizontal direction for Type II earthquakes are one-third of those specified for the Type I earthquakes and the design ground acceleration in the vertical direction are two-thirds of those in the horizontal direction.

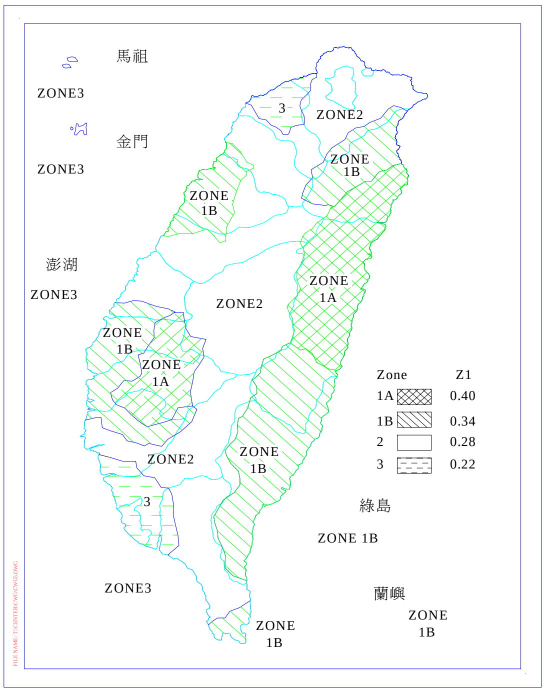

Fig. 7 Design Ground Acceleration for Type I Earthquake (THSRC, 2001) [4]

For the design of foundation capacity and stability and for the settlement design, five unfactored loading combination cases were specified. Case 1 is the combination for "Normal Load" condition, Cases 2 and 3 are combinations for "Exceptional Load" conditions, while Case 4 is the combination for "Ultimate Load" condition. All these load cases are essentially design conditions corresponding to the ultimate limit state. Case 5 is the loading combination for verification of settlement criteria. For the safety measure of pile foundations and barrettes, some empirical safety factors were specified, as shown in Table 1. For the structural design of foundation components, factored loading combinations along with the load and resistance design may be used.

Table 1 Safety Factors for design of pile foundations and barrettes (THSRC 2001)

	Safety Factor		
	Normal Load	Exceptional Load	Ultimate Load
End Bearing Capacity	3.0	2.0	1.25
Skin Friction	2.0	1.5	1.25
Pullout Resistance	No tension forces are permitted on piles.	2.5	1.5

One of the significant requirements for the foundation design is to meet the strict deflection control, vertical settlement and horizontal displacement criteria, to ensure running safety of trains at their maximum speed of 350 km/hr. It is prescribed in the design specification of bridge and viaduct foundations that the differential vertical settlements between adjacent piers after completion of construction shall not exceed 1:1000 for simply supported spans and 1:1500 for continuous spans (THSRC, 2001). For the computation of the vertical settlements, all superimposed dead loads including trackwork shall be accounted for, which also are stipulated to ensure that the vertical alignment of rails meets the criteria. As a serviceability limit state criterion under Type II earthquakes, maximum lateral displacement shall not exceed: 50 mm tilt from vertical axis at top of caissons, 50 mm relative displacement between pile head and pile toe, and 50 mm relative displacement between barrette head and barrette toe.

The design of the THSR structures has the basic concept of performance-based design, in which different performance requirements were considered for different earthquake levels. However, the performance requirements were not implemented in an explicit form of performance matrix. Table 2 attempts to summarize the loosely specified design requirements in the context of the performance matrix.

Although the basic performance-based design concept was attempted in the THSR design of civil works, some redundancy may still exist because performance requirements and verification methods were not addressed in a systematic manner. With experiences of the THSR design, it seems importance considering the essence of performance-based design concept and making critical review on current practice. The result of retrospective evaluation on the design code concept would provide useful information for future upgrade of the seismic design code.

Table 2 Performance Matrix Attempted to Summarize Foundation Design Requirements

Limit State	Serviceability	Ultimate (Repairable)
Long Term Condition	Case 5	Cases 1, 2, 3
Type II Earthquake	*specified for structural design	
Type I Earthquake		Case 4

Design Code Concept

The performance-based engineering and the development of performance-based design code have been a major pursue in earthquake countries (especially U.S. and Japan) in the past decade. Buckle (2002) [5] stated that there are two fundamental issues that should be addressed for the performance-based design:

1. Selecting the specified ground motions (hazard level) and the corresponding damage states (performance objectives)
2. Developing methods of evaluation for the verification of damage states and performance objectives

An effective way to organize the desired performance requirements is arranging them in a performance (criteria) matrix. This concept has been implemented by Caltran and considered by AASHTO for the seismic design specification (Buckle, 2002) [5]. In Japan, the performance matrix also has been used in recently developed geotechnical engineering and civil engineering codes, respectively Geo-code 21 and PLATFORM (Honjo, 2004) [6]. Both codes are fully performance-based, and the performance matrix used in Geo-code 21 is shown in Fig. 8. This matrix consists of three levels of design situations in the vertical axis and three limit states in the horizontal axis, and performance requirements to be specified can be clearly identified based on importance of the structure. In Geo-code 21, serviceability limit state requirements must be specified for both high and low frequency earthquakes, and repairable limit state requirements must be specified for low frequency earthquakes. An attempt to summarize the performance requirements specified in the THSR design specifications into a performance matrix was given in Table 2. With that, it can be compared to the performance matrix of Geo-code 21, and it is suggested that some load cases can be modified and reallocated so as to attain a more complete and effective design consideration.

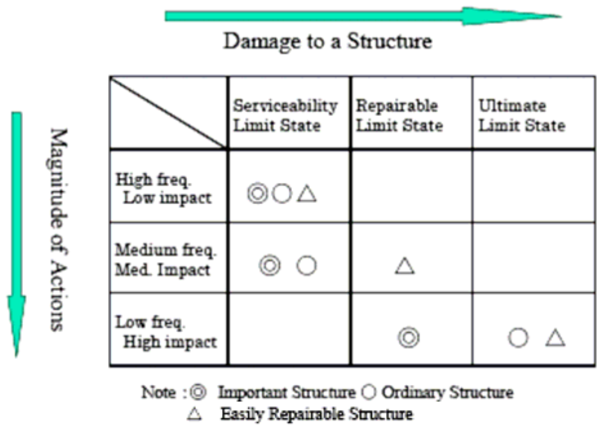

Fig. 8 Performance Matrix for Japanese Geo-code 21 and PLATFORM (Honjo, 2004) [6]

In addition, safety measures stipulated in the THSR design specifications are not consistent for structural and geotechnical design. Empirical safety factors were used for the geotechnical design, whereas the load factored design may be used to design the structural component. Essentially, reliability levels associated with these two safety measures are different, which may lead to an over-conservative design either on the geotechnical or the structural component. To attain a harmonized design, it is required that the reliability levels of both the structural and geotechnical designs be known explicitly. It should be known that theoretical developments in structural reliability and applications of probabilistic design are being pursued actively in the structural community (Phoon, 2004) [7]. Therefore, it warrants that the geotechnical community takes serious efforts in similar endeavor, so that a rational and harmonized design may be achieved in both geotechnical and structural aspects.

CONCLUSIONS

In the new era for the geotechnical engineering, to meet the performance requirement for the existing and new design will be a challenged work. In this article, two case studies are presented for both cases.

The fist case is the "Study of Risk Assessment and Retrofitting Strategy for the Soil Foundation of Power Transmission Tower on Slope". The main concerns of this project is to characterized the risk levels with their corresponded retrofitting strategy for the soil foundations on slope. In the beginning of this case study, a four-staged strategy of the risk assessment approach is presented. By following this approach, the possible risk produced by slope instability was first characterized by all possible failure type. Then, the corresponded retrofitting method are discussed. Finally, in order to decide the most appropriate retrofitting method and schedule, the retrofitting strategy is proposed for the future works.

The THSR project is a mega size development, and its infrastructure is designed to be seismicity resistant. For rational design, performance requirements are considered in the design specification, however the completeness of performance based design is just loosely kept. The project revealed the need for sound and realistic design concepts in geotechnical engineering, and the performance-based design with due considerations of explicit reliability levels should be the framework for implementation in future geotechnical seismic design. The geotechnical community is way behind the structural community in this subject area. It calls for serious efforts in conducting relevant investigations and developments such that a harmonized design on both structural and geotechnical aspects may be achieved.

ACKNOWLEDGMENTS

The project of "Study of Risk Assessment and Retrofitting Strategy for the Soil Foundation of Power Transmission Tower on Slope" is finically supported by the Taiwan Power Company.

REFERENCES

[1] Chen,C.H., Wang, C.H., Lee, Wei. F., Meu-, H-T, and Chang, C.-F. (2005). "Procedure of Seismic Risk Assessment for Underground Transportation Structure," Proceeding of Geotechnical Earthquake Engineering Satellite Conference, Osaka, Japan, 10 September, 2005, pp 236-243.

[2] SEAOC, VISION 2000 – Performance based seismic engineering of buildings. Structural Engineering Association of California, Sacramento, California, USA, 1995.

[3] Moh, Z. C. (2004). "Geotechnical issues in design and construction of viaducts of the Taiwan High Speed Rail." Proc., 12th Asian Regional Conference on Soil Mechanics and Geotechnical Engineering, Singapore.

[4] Taiwan High Speed Rail Corporation. (2001). Design Specifications, Civil Works, Vol. 9. Taiwan High Speed Rail Corporation, Taipei.

[5] Buckle, I. G. (2002). "AASHTO LRFD limit state design of bridges with emphasis on seismic performance." Proc., International Workshop on Foundation Design Codes and Soil Investigation in view of International Harmonization and Performance Based Design, Tokyo, Japan, 17 –30.

[6] Honjo, Y. (2004). "Comprehensive design codes development in Japan: Geo-code 21 ver.3 and code PLATFORM ver.1." Proc., International Workshop on Limit State Design in Geotechnical Engineering Practice, Boston.

[7] Phoon, K. K. (2004). "Towards reliability-based design for geotechnical engineering." Special Lecture at Korean Geotechnical Society, Seoul.

Framework of Design Procedures of Pipeline Structures Against Surface Earthquake Faulting

S. Yasuda[1] and M. Hori[2]

[1]*Department of Civil Engineering, Tokyo Electric University, Tokyo, Japan*

[2]*EarhtquaekeResearch Institute, University of Tokyo, Japan*

Abstract

This paper explains framework to establish deign procedures of pipeline structures against possible surface earthquake faulting. Such procedures will be needed due to the increase of the public concern for faulting. Key items of the fault resistance design are summarized. A model for the critical state of the pipeline structure subjected to faulting is presented, and measures which increase the safety against faulting are considered.

Keywords—*Faulting Surface earthquake fault, pipeline structures, design procedures*

INTRODUCTION

The four Japanese Islands, which are located near the four plates, have more than 2,000 active faults, all of which are the remaining of past earthquake events. There are some other faults which are hidden under sedimentary ground layers; see [1] for a list of related references. While the interval of intra-plate earthquakes is of the order of 1,000 years, when an intra-plate earthquake of large scale happens, surface ground faulting is induced so that near-by buildings and structures are damaged by ground deformation besides strong ground motion.

There have been public concerns for possible faulting since 1995 Great Hanshin Awaji Earthquake. It should not be overlooked that two earthquakes in 1999 have induced large ground deformations so that infrastructures such as dams and highways are damaged. At this moment, no regulation is established for possible faulting in designing structures and the number of structures which prepared faulting is limited. However, the preparation of possible faulting will be a social responsibility for lifeline companies.

Based on these backgrounds, the authors are studying design procedures for pipeline structures; see [2-6]; see also [7]. The procedures are standard; they consist of survey, estimate of possible faulting, and the examination of structure safety against estimated faulting. However, some detail of these procedures need attention since no general agreement has been made on constructing a design model to considering faulting. This paper proposes a model which, the authors believe, is suitable for lifeline structures.

DEIGN PRINCIPLE

In designing pipeline structure for faulting, the following items will be of major concern: 1) the vulnerability of faulting at a site; 2) the type, degree and area of ground deformation induced by faulting; 3) a possible failure mode of the structure for which a design model will be constructed; and 4) measures which prevent the failure. The flowchart of the basic design procedures are shown in Fig. 1 The flowchart consists of the evaluation of fault presence including hidden faults and the four procedures that correspond to the item of major concern.

Another item is setting of safety factors. Compared with the occurrence of strong ground motion, the occurrence of faulting at a particular site is small by the order of magnitude even when an earthquake of large scale takes place. In general, therefore, safety factors ought to be smaller if they are somehow related to the possibility.

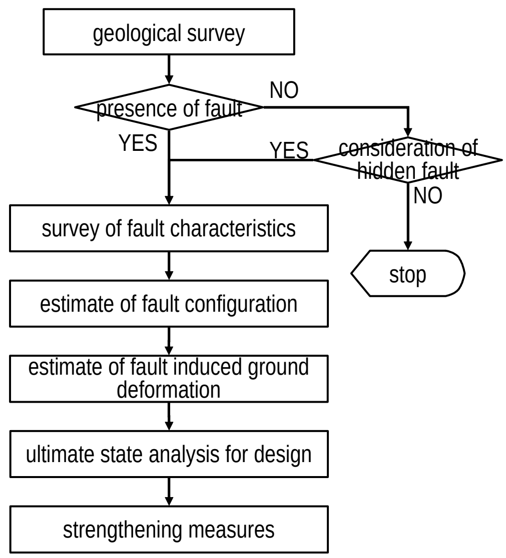

BASIC DESIGN PROCEDURES

Some detailed explanations are given to the design procedures which are explained in the preceding section. These explanations are aimed not to provide specific description of the procedures. They point out issues which, the authors believe, need to be clarified in making actual design codes or guidelines for pipeline structures against faulting.

Survey of fault presence

In Japan, surface ground faults are identified by geological study which mainly uses maps and aerial photos and geophysical survey which determines underground structures; trench survey are carried out to estimate past events of faulting.. The most results of the geological study are archived in a form of GIS. There is limitation of the geological study in clarifying the fault properties since it gathers information which can be seen from the surface. The geophysical survey is made to see the underground though it is expensive.

When the sedimentation layers are thick, it is not easy to identify the presence of surface ground fault; man-made structures hide records of past events. Thus, there is some possibility of hidden faults. Also, a new surface ground fault sometimes appears when rupture processes from the source fault change their direction in undergrounds. Even for well-identified faults, some attention needs to be paid on the appearance of such a new fault near the past fault.

Estimate of fault characteristics

When the location of a fault is known, it is necessary to judge whether some countermeasures should be taken or not. This judge is made by considering the past activity. In Japan, there are three categories for the degree of activity, and known faults are classified into three. The most active category is a fault which may move in around 1,000 years. Design against an active fault should be taken if the fault belongs to this category.

Surface ground fault is formed when rupture processes starting from this source fault reach ground surface. Thus, the characteristics of a source fault will be of primary importance for the design purpose. The characteristics are the fault type (normal/reverse/lateral), the amount of slip, and the magnitude of a possible earthquake.

Estimate of ground deformation

While the previous two procedures are related to earth science such as geology and seismology, the current procedure is for geotechnical issues which are related to the ground deformation induced by surface ground fault; see [8-11]. A key point is that the ground deformation could be fatal for structures since it produces permanent and large displacement gap even though deformation is spatially limited.

The configuration of ground deformation due to reverse faulting is studied as an example; see Fig. 2. It is assumed that bedrock, which is brittle, has sharp displacement gap that is caused by the rupture processes running in the crust. The displacement gap may not grow in the same manner in ground layers, which are more ductile. Somehow, the gap is spread in the layers, and a certain conjugate fault is formed. Thus, the ground surface deformation is smoothened, even though the deformation is limited to a certain zone.

Ultimate state analysis for faulting

Figure 3 shows a design model of a pipe structure subjected to ground deformation induced by surface earthquake faulting of a reverse type. Displacement gap, or often called off-set, in the ground layers is transmitted to the structure. The effect of the gap on the structure changes depending on the relative direction of the pipe with respect to the fault plane.

Subjected to the ground deformation, the pipe structure is deformed as well as moved; it is known that the structure goes up when it is located shallowly and ground pressure is low. The model needs to examine local non-elastic deformation and structure response which leads to buckling. The prevention of buckling will be a key issue since the structure will suffer fatal damage. Non-linear FEM analysis is used to study these deformation and response; both the material and kinematic non-linearities should be adopted in FEM.

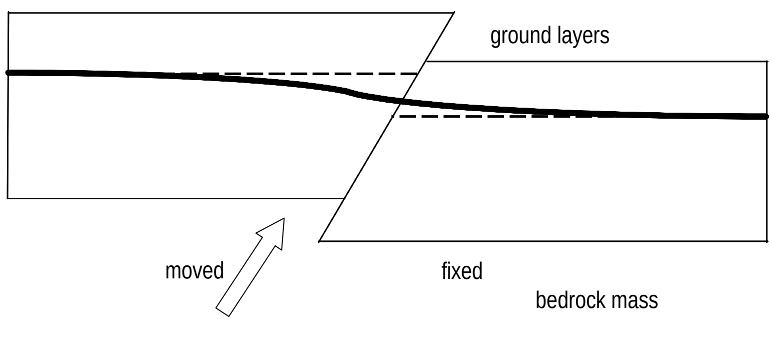

Fig. 2 Reverse faulting and deformation of pipeline structure.

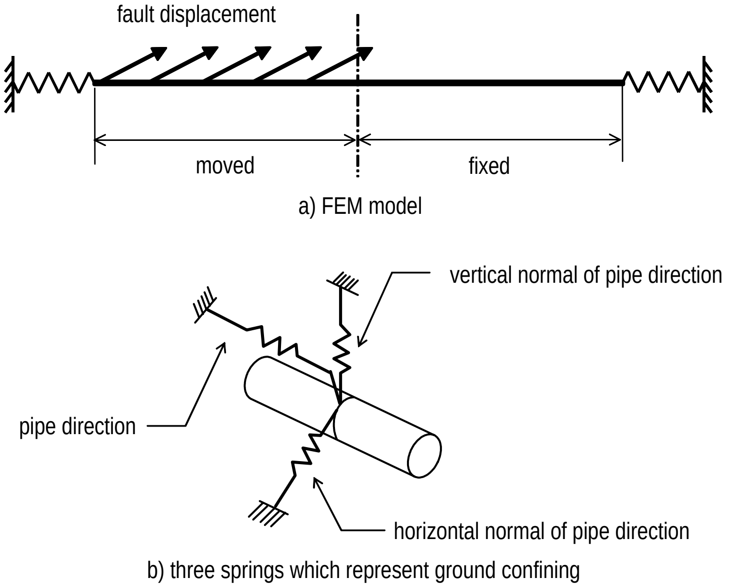

Fig. 3 Analysis model of pipeline structure subject to reverse faulting.

In analyzing the model, the structure safety is checked with respect to the deformation. Since pipelines are used to deliver energy or water, the critical state will be large deformation that leads to leak. Hence, just like other state, the deformation should be measured with respect to strain that is accumulated in the pipe structure. In Fig. 4, a kind of averaged strain of pipe structure deformation induced by faulting is presented. This strain could be a good measure in examining the safety of the pipe structure.

As earthquake resistance deign of pipe structure assumes quasi-static state, the model used in analyzing the deformation of pipe structure due to fault ground deformation ignores inertia effects. Also, the fault ground deformation is not coupled with strong ground motion in the model. This is because the amplification is not large in the ground layers and the speed of the rupture processes running in the ground is slower than the earthquake wave velocity.

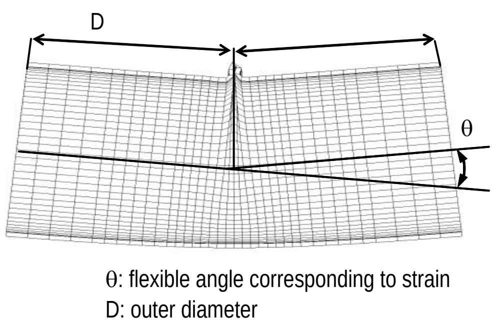

Fig. 4 Definition of strain of pipe deformation induced by faulting.

Strengthening measures

There are several suggestions to strengthen a pipeline structure against faulting; these suggestions should be considered in designing the structure. The key design variables of the pipeline structure are the radius and thickness of the configuration and the stiffness and strength of the material. The structure will be stronger for faulting if these variables are increased.

Other suggestions are summarized as follows: 1) increase of the deformation capacity of the structure; 2) the cut-off of the ground deformation from the structure; and 3) the release or weakening of the deformation transmitted from the ground to the structure.

CONCLUDING REMARKS

Surface earthquake faulting is an event of extremely low possibility; faulting is formed along line segments only when a large earthquake happens in a shallower crust. The first step of establishing the design procedures against faulting is thus to understand the difference between faulting and strong ground motion.

While surface earthquake faults in Japan are those which are induced by an intra-plate earthquake, some countries have faults which are induced by an inter-plate earthquake. The return period of intra-plate and inter-plate earthquakes are different. Hence, the possibility of surface faulting is larger for inter-plate earthquakes and more attentions should be paid in designing pipeline structures against this kind of faulting.

Table 1 Several countermeasures of pipeline structures against faulting.

objectives	countermeasures
increase of strength	increase of thickness, diameter use of better material
increase of deformability	use of flexible joint and joint set use of curved pipe
cut-off of ground deformation	shielding of pipe; several structures and apparatus are available
release of force due to ground deformation	use of light weight mixtures

ACKNOWLEDGMENTS

The authors wish to express their thanks for valuable comments made by Prof. Tani (Yokohama National University) and Dr. Taniyama (Saitama University) and Prof. Yoshida (Tohoku Gakuin University).

REFERENCES

[1] Konagai, K.: *Proceedings of International workshop for seismic fault-induced failures*, JSCE, 200..Sakanoue, T. and Yoshizaki, K.: A Study on Earthquake-Resistant Design for Buried Pipelines Using Lightweight Backfill, *Proc. of 13th World Conference on Earthquake Engineering*, 2004.

[2] Trautmann, C.H. and O'Rourke, T.D.: Lateral Force-Displacement Response of Buried Pipes, *Journal of Geotechnical Engineering*, ASCE, Reston, VA, Vol.111, No.9, pp.1077-1092, 1985.

[3] Alaska Pipeline Service Company: http://www.alyeska-pipe.com/, 2003.

[4] Hall, W.J., Nyman, D.J., Johnson, E.R. and Norton, J.D.: Performance of the Trans-Alaska Pipeline in the November 3, 2002 Denali Fault Earthquake, *Proc. 6th U.S. Conference and Workshop on Lifeline Earthquake*, ASCE Technical Council on Lifeline Earthquake Engineering, 2003.

[5] Kropp, A.G.E. and Lott, J.G.E.: Residential design approaches over earthquake-induced ground shearing", *Proceedings of 11th International Conference on Seismic Design Earthquake Engineering/3rd International Conference on Earthquake Geotechnical Engineering*, Vol.1, pp.334-339, 2004.

[6] Doolin, D.M. and Wells, D. L.: Constraining the location of the Hayward fault at California Memorial Stadium using structural fracture pattern", *Proceedings of 11th International Conference on Seismic Design Earthquake Engineering/3rd International Conference on Earthquake Geotechnical Engineering*, Vol.1, pp.605-612, 2004.

[7] Ohmatchi, T., Kojima, N. and Murakami, A.: Ground displacement and change in reservoir water level due to seismic rupturing of a hidden fault underlying a dam site, *J. Struct. Mech. Earthquake Eng.*, Vol. 710/I-60, JSCE, 337-346 (in Japanese), 2002.

[8] Onizuka, N. Hakuno, M. Suzuki, T., Iwashita, W. and Hori, M.: Model experiment on rupture propagation of surface grounds due to dip-slip fault movements of bacements, *J. Geotech. Eng.*, Vol. 701, No. 58, JSCE, 29-38 (in Japanese), 2002.

[9] Tani, K. and Ueta, K.: Shape and location of discontinuity in sand induced by fault displacement in bed rock," in *Proc. 26 Japan National Conf. on Geotech. Eng.*, 1185-1188, JSGE (in Japanese), 1991.

[10] Tani, K., Ueta, K. Abe, S., Nakada, Y. and Hayashi, Y. (1997). Deformation structure of surface unconsolidated layer along the Nojima Earthquake Fault, *J. Geotech. Eng.*, Vol. 568/III-39, JSCE, 21-39 (in Japanese), 1997.

[11] Taniyama, T. and Watanabe, H.: Deformation of sandy deposits by reverse faulting, *J. Struct. Mech. Earthquake Eng.*, Vol. 591/I-43, JSCE, 313-3258 (in Japanese), 1998.

(6) Damages during recent earthquakes

Cause of Earthquake Induced Damage of Building No.3 at NNCT

A. Onoue[1], K. Fukutake[2], H. Hotta[2], H. Nagai[3]

[1]*Department of Civil Engineering, Nagaoka National College of Technology, Niigata, Japan*
[2]*Institute of Technology, Shimizu Corporation, Tokyo, Japan*
[3]*Sceience System Division, CRC Solutions Co. Ltd., Tokyo, Japan*

Abstract

Building No.3 of Nagaoka National College of Technology (NNCT) was disconnected at its middle part due to the strong vibrations during the 2004 Niigata-ken Chuetsu Earthquake. The cause of this destruction was investigated from a landslide view point through an erasto-plastic effective stress dynamic FEM after examining the precise configuration of soil strata. The examination revealed that the building has been built on the boundary of cutting and filling soils and the fill material has been banked on the weak organic soil which was originally the old surface layer before filling the valley. According to the analysis, it was confirmed that the building was pulled and twisted by landslide of the bank shotcrete accompanied with pile fructure.

Keywords—*cutting and filling ground, dynamic analysis, effective stress, earthquake, finite element method, organic soil*

INTRODUCTION

Nagaoka National College of Technology was suffered serious damages by the 2004 Niigata-ken Chuetsu Earthquake. Since the site where Building No.3 located consisted of cutting and filling ground at the exit of old valley topography, the vibration of the ground was considered to be complicated. Many damaged buildings and facilities located the peripheral zones of the campus that were made by filling of soil. Most of the peripheral slopes slid and deep and wide cracks appeared just after the main shock. Although large cyclic inertial force must have acted to Building No.3, the cause of disconnection and torsion of the building was supposed to be landslide of the filling ground because the other half of the building that located on the cutting ground was not damaged at all.

For the first step to make such complicated vibration of the ground clear, the seismic response of the ground is simulated by a nonlinear effective stress dynamic finite element analysis. The cause of disconnection of Building No.3 is next investigated through comparing observed results and the analyzed ones.

SEISMIC DISASTER INDUCED TO NNCT BY EARTHQUAKE

Outline of the site

The campus of NNCT at Nishikatagai, Nagaoka-city locates at a corner of Mt. Yukyu which is situated on the west edge of the Higashiyama hills. It was originally a small hill with a summit having an elevation of 75 m and its axis of the ridge was almost Northwest-Southeast in compass as seen in Fig. 1. Several buildings along the southeast edge of the campus are superimposed in the contour lines of original geography in this figure. The original stratigraphy was composed of the volcanic ash cover, Oyama layer of Pleistocene deposit and Uonuma layer sedimented by early Diluvium, from the top to downward. The hill was cut to be terraced at the elevation (hereafter: EL) of 62.8 m for forming athletic field at the northwest portion, at EL=65 m for the center campus and at EL= 68.2 m for the slightly higher ground at the southeast portion in 1960. The gray color area in Fig. 1 shows the cutting ground and white area shows the filling ground. The west slopes and valleys were filled with cut soil to enlarge the area of each terrace toward west and southwest in direction for the first cutting and filling ground construction. The present campus shown in Fig. 2 was completed after the second filling construction for further expansion of the site at each elevation in 1968. The figures in ellipse in Fig. 2 indicate the elevation at respective area. The Northeast slope and the Northwest slope are partially shaped natural slopes of original hill.

It can be found through comparing Fig. 1 with Fig. 2 that there are tow deep and long hidden valleys which have been already filled. One is berried below the athletic field and the other is below the middle of campus. Both old valleys open to the southwest edge of present campus. The filling ground spreads to the area where the elevation of original ground surface is lower than 65 m at the southwest side of the line which connects the southwest corner of Building No.6 - almost all of Computer center – the southeast edge of Library – the north end of Connection passage between Buildings No.2 and No.3 – the northwest portion of Building No.3 – the northwest edge of Athletic club house - the northeast part of Second gymnasium – the southwest edge of Snow and Ice Lab. Center. Incidentally, Connecting passage and the southwest half of Building No.3 locate at the exit of the old valley which sweeps deeply off to east direction. All buildings that locate on the filling ground are supported by bearing piles except for Connecting passage and Machinery factory.

Feature of Building No.3 and its ground

Fig. 3 (a) is a picture of Building No.3 behind the parking lot for bicycles taken from southwest direction.

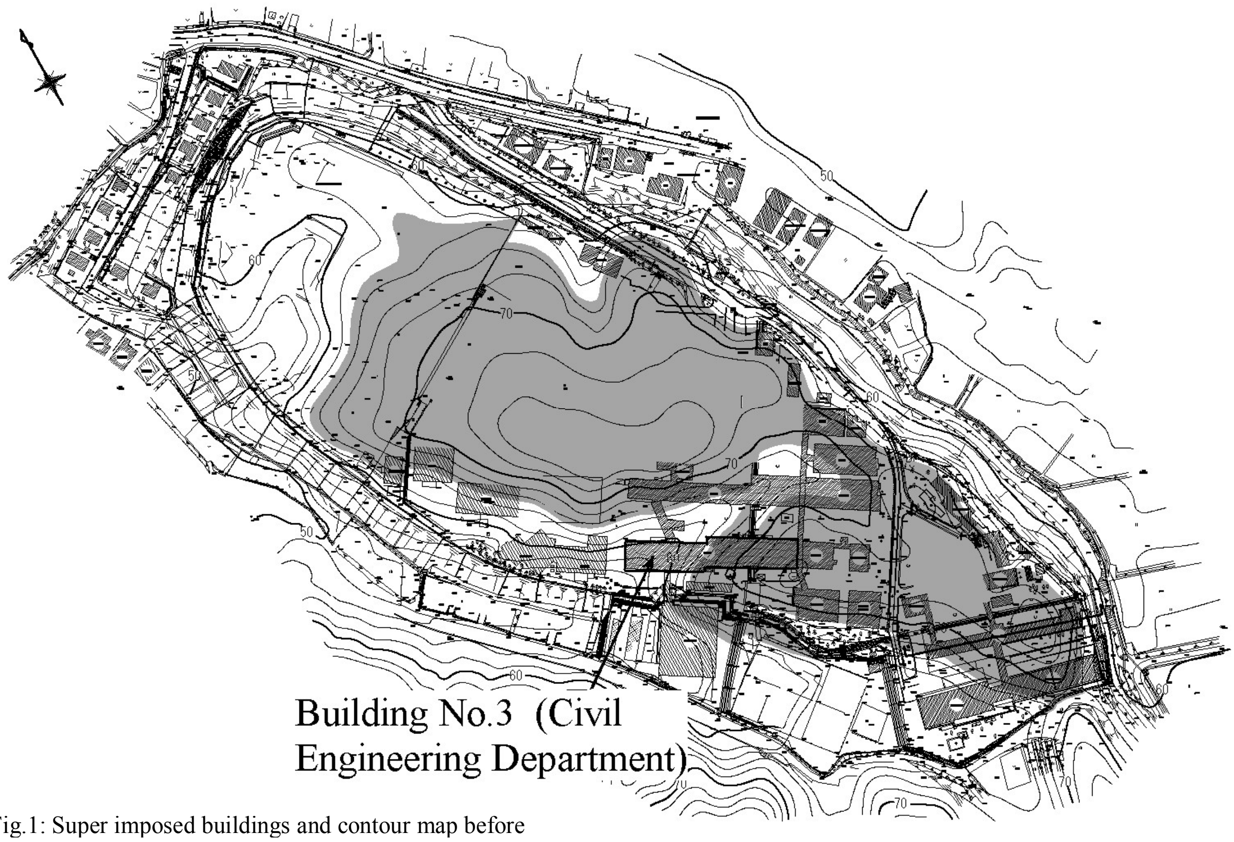

Fig.1: Super imposed buildings and contour map before construction of the site by cutting and filling

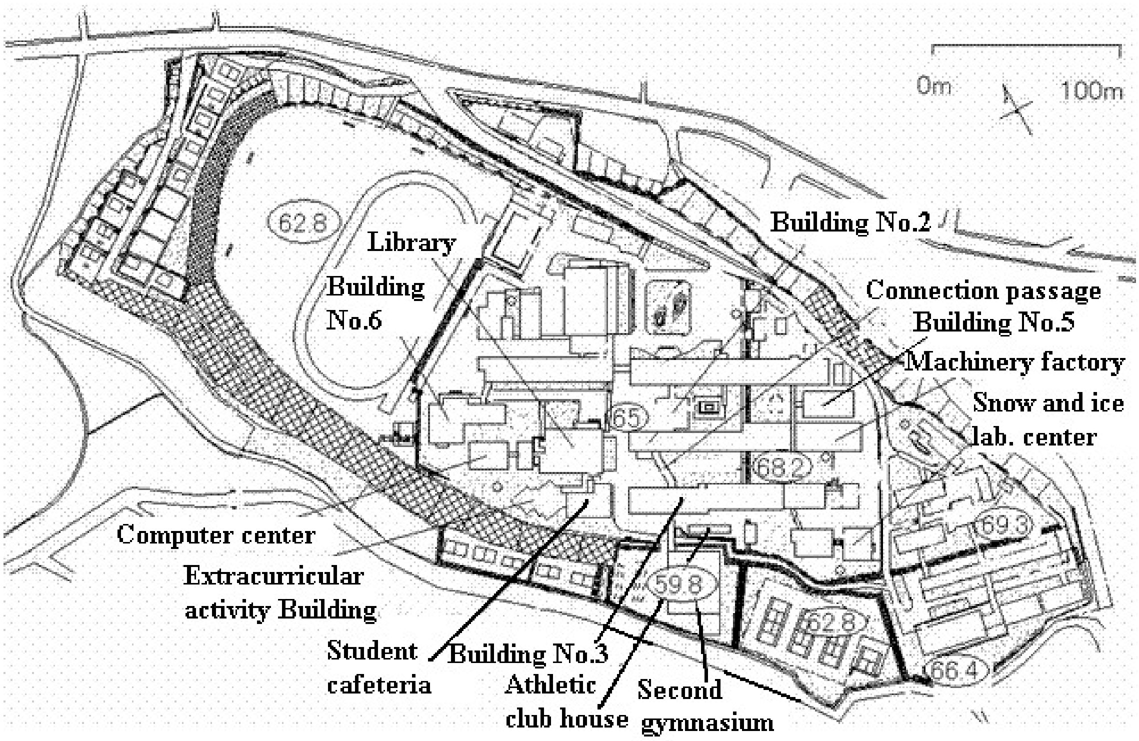

Fig.2: Plan of campus (Figure in ellipse: Elevation (m))

Second gymnasium is seen on the right. Note that there is a difference of 5.2 m in ground elevation between the front and the back, both of which are filling ground. Fig 3 (b) is a view from south direction. The far side of Building No.3 is of three stories and this side of it is 2-stories high. The 2-stories portion of Building No.3 and Athletic club house at the front locates the cutting ground, whereas the 3-stories portion is on the filling one.

Damage of Building No.3 caused by the earthquake

Fig. 4 is the plan of damaged Building No.3 after the earthquake. The 3-stories portion of 40 m long at northwest side and the 2-stories portion of 24 m long at the middle stand on the ground of EL = 65 m, and the single story portion of 16 m long at southeast side stands on EL = 68.2 m for connecting to the second floor at the middle of the building. The 3-stories portion turned anti clockwise and the northwest end displaced 77 cm to southwest direction by the earthquake. Since the crack of 18 cm wide was occurred beside the great beam, displacement of the ground amounts to 95 cm to southwest direction there. At the same time, the ground subsided 47 cm and 59 cm at Points b and c, respectively. Fig. 5 shows the footing and the tow piles out of the 3-combined piles at the corner. They are reinforced concrete piles having a diameter of 30 cm. As is evident from the pictures, the piles moved larger than the footing. The piles displaced under 20 cm toward southeast and over 35 cm toward northwest more than the footing together with the ground, and the pile heads were destroyed as long as 60 cm. This means that the ground moved accompanied by the piles. Fig. 6 is a photograph of the column and the second floor at Point A taken from the direction of the arrow shown in Fig.4. The column displaced 26 cm resulting an opening in the floor. A part of column belonging to the first floor can be seen from the second floor. The floor is made of double reinforced concrete having a thickness of 13 cm, a rebar diameter of 9 mm and a rebar spacing of 17 cm.

SEISMIC RESPONSE ANALYSIS OF THE GROUND

Analysis model

The ground in the vicinity of Building No.3 was turned into the analysis model shown in Fig. 7 (a). Fig. 7(b) shows the FEM mesh configuration. Note that viewing directions are different between (a) and (b). The gradient of the slope in the third quadrant ranges from 25 ° to 28 ° and the high step between Building No.3 and the bicycle parking lot is retained by the stone block

(a) View from southwest direction

(b) View from south direction

Fig.3: Building No.3

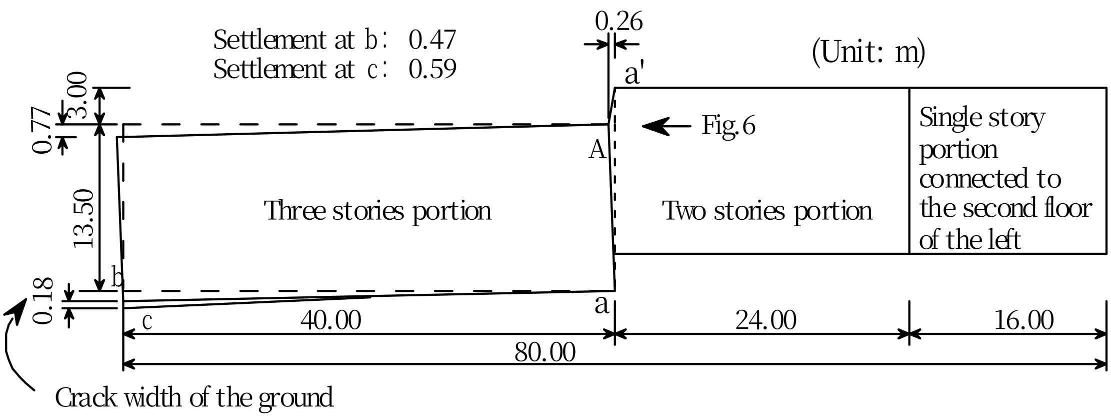

Fig.4: Disconnection of Building No.3 and displacements

retaining wall. The boring log at the point indicated in (a) is shown in Table 1 together with the input soil properties for FE analysis. There is an extremely weak organic soil layer having an N value of 0 just under the filling loam layer of about 8 m thick having a N value of less than 6. This organic soil had covered the original hill of Oyama layer before the filling construction for campus extension, and spreads to the border between the cutting and filling ground. The depth of water table is 3.5 m.

(a) Footing at the southeast corner with three piles

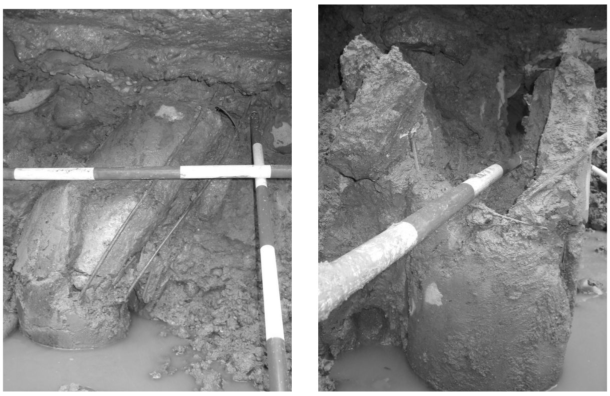

(b) Fracture of the right pile's head (c) Fracture of the left pile's head

Fig. 5: Footing and piles at Southeast corner

Fig. 6: Disconnected second floor at point A in Fig.4

It was assumed that the side boundaries of the analysis model in Fig. 7(a) go on forever and the elements of deformable only for shear were set up. In other words, the displacements in three directions of the all peripheral nodes were assumed to be equal to those of the corresponding nodes at one line inside by applying the Multi-Point Constraint function.

Analysis method

The 3-D dynamic analysis conducted here is an elasto-plastic effective stress analysis using "HiPER" [1]. The modified R-O model extended to three dimensions was used for the stress-strain relationship, and the bowl model was used for the strain-dilatancy relationship [2]. In the bowl model, the monotonously compressive component of dilatancy was expressed by the following cumulative shear strain, *G**, and the reversibly dilative component, namely the vibration component, was expressed by the following resultant shear strain, *Γ*.

$$\Gamma = \sqrt{\gamma_{zx}^2+\gamma_{zy}^2+\gamma_{xy}^2+(\varepsilon_x-\varepsilon_y)^2+(\varepsilon_y-\varepsilon_z)^2+(\varepsilon_z-\varepsilon_x)^2} \qquad (1)$$

$$G^* = \sum \Delta G^*$$

$$= \sum \sqrt{\Delta\gamma_{zx}^2+\Delta\gamma_{zy}^2+\Delta\gamma_{xy}^2+\Delta(\varepsilon_x-\varepsilon_y)^2+\Delta(\varepsilon_y-\varepsilon_z)^2+\Delta(\varepsilon_z-\varepsilon_x)^2}$$

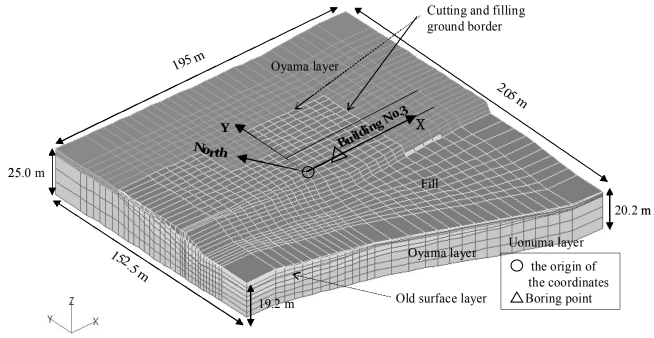

(a) Analysis area (view from west direction)

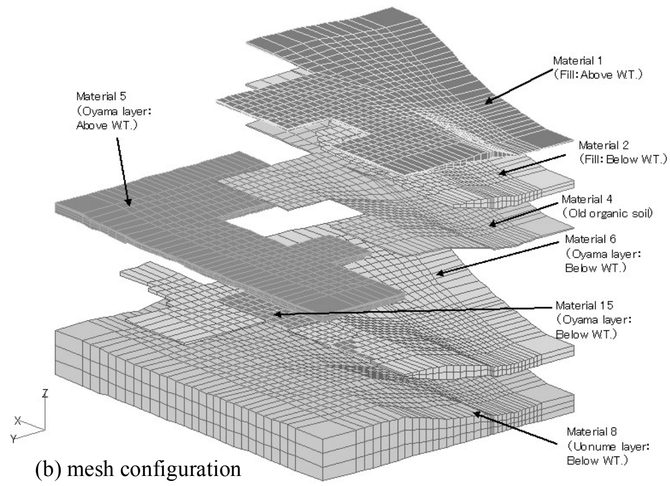

(b) mesh configuration

Fig. 7: Configuration of FEM mesh and material types
(View from north direction)

(2)

The dilatancy, ε_V^s, is accordingly expressed as Eq. (3).

$$\varepsilon_V^s = A \cdot \Gamma^B + \frac{G^*}{C + D \cdot G^*} \tag{3}$$

The values of A, B, C and D used in the present analysis are -0.2,1.4, 2.5 and 40.0, respectively and the value of $C_s/(1+e_0)$ is assumed to be 0.05 for all layers, where C_s is the swelling index. The minimum value of the liquefaction resistance R, namely X_l, is 0.05 for the organic soil and 0.1 for all other layers. The shear modulus for each layer is calculated from the *Vs value*.

The seismic waves observed at the base rock of 100 m deep in the ground at the KiK-net station [3] in Nagaoka Institute of Snow and Ice Studies which is very near, i.e., about 700 m in distance from NNCT, were used after slightly correcting from compass direction to coordinate direction (see Fig. 7(a)). Fig. 8 shows the input horizontal accelerations being input as E+F waves at the base of the analysis model. The long period components due to surface waves can be seen at latter half in this figure. The vertical acceleration was disregarded because of its negligible influence on the calculation results according to the previous study [4]. The major axis of the input acceleration almost coincides with y-direction, and the maximum acceleration values in x- and y-components are 313 gal and 477 gal, respectively. The predominant frequencies of x-direction are 0.5 Hz and 2.0 Hz, and those of y-direction are 0.6 Hz and 2.0 Hz.

Analysis results and discussions

The results of modal analysis are shown in Fig. 9. The x-direction and the y-direction displacements at the slope in the third quadrant are distinguished in the first and the second inherent modes, respectively. Fig. 10 shows the distribution of the maximum accelerations in the entire period of duration. The y-components almost coincide the major axis and are larger than the x-components. The largest acceleration was 720 gal, which occurred along the top of the high step of Oyama layer between Building No.3 and the tennis court in the fourth quadrant. The maximum accelerations are relatively small at the filling ground which has been filled on the Old surface layer of weak organic soil, in comparison with those at the cutting ground. This means that the Old surface layer worked as an isolation layer. Fig. 11 is the panel diagram showing the distribution of the maximum pore water pressure ratio. This ratio exceeds 50 % at the bottom of the filling loam and the top of Oyama layer between which the Old surface layer is sandwiched, as well as in the Old surface layer in between. The largest value exceeds 70 % in the Old surface layer. Fig. 12 shows the distribution of the maximum resultant shear strain, Γ. The largest value of Γ reached as large as15% in the Old surface layer, which indicates the occurrence of a land slide in this layer. Fig. 13 shows the deformation of the ground surface at the end of vibration, t = 15 sec. Two third in the left hand of the rectangular which indicates a portion of Building No.3 illustrated in Fig. 4 locates on the filling ground, whereas one third of it stand on the cutting one. Though the deformation of the cutting ground is small, the filling ground moved remarkably to both left and lower directions in this figure. This means that the filling ground moved together with piles and the piles pulled and had the left portion of the building turn anti-clock wise. During the process of such movement, the pile heads broke as seen in the Fig. 5(b) and (c). The analyzed deformation of the ground is similar to the actual one, the maximum displacement at the origin of the coordinates is 11 cm whereas the actual movement was more than 95 cm there though. The reasons of this discrepancy are considered to be following limits in this particular analysis;

1) Cracks in the model ground can not be evaluated in the analysis.

2) The all layers above the water table are united as a continuum.

3) Discontinuous displacement like a sliding failure is difficult FEM.

Figs. 15 and 16 show the time histories of ground surface displacement and the orbit of horizontal displacement .at the origin of the coordinates, respectively. As is clear from these figures, the ground at the northwest corner of Building No.3 moved mainly toward y-direction, namely down stream of the berried valley, being accompanied by subsidence. Fig. 16 shows the stress-strain relationships in the Old surface layer just below the origin of the coordinates. The both shear strains, especially γ_{yz}, increased in the direction along which the initial shear stresses had acted before the event. Fig. 17 shows the time history of excess pore water pressure ratio in the Old surface layer just below the origin of the coordinates. It had rapidly reached 60 % by an elapse time of 4.5 sec, namely soon after the beginning of the seismic motion and before starting the following several large shocks.

CONCLUSIONS

The cause of the damage induced to Building No.3 at Nagaoka National College of Technology by the 2004 Niigata-ken Chuetsu earthquake was investigated from a land slide view point based on an elasto-plastic effective stress dynamic FEM. The following conclusions were obtained from the present work;

1) A land slide occurred at the filling ground where the half building located whereas the other half stand on the neighboring cutting ground with no sliding. The sliding occurred in the Old surface layer of weak organic soil which had covered the original hill before filling construction on it. The filling ground took piles with its sliding and the piles pulled and twisted the building resulting disconnection of it at the border between the cutting and filling ground.

2) The sliding is considered to have occurred very early by approximately 4 sec after the beginning of the earthquake and before the main shocks of the event.

The horizontal accelerations at the base rock is considered to be doubled at the ground surface.

Table 1: Boring log and soil properties

m	Layer	Soil type	V_s (m/s)	γ_t (kN/m^3)	$\gamma_{0.5}$ ($\times 10^{-4}$)	h_{max}
0–3	Fill	Fill	100	16.2	8.7	0.20
	Water table: GL -3.5 m					
4–7	Fill	Filling loam	130	16.2	14.3	0.20
8	Old surface soil	Organic soil	60	13.7	16.2	0.20
9–12	Oyama layer	Volcanic clay, Medium sand	150	16.7	Above water table: 17.7 Below w.t.: 8.8	0.20
13–15	Uonuma layer	Clayey sand and gravel	300	17.6	Above: 4.3 Below: 1.8	0.22

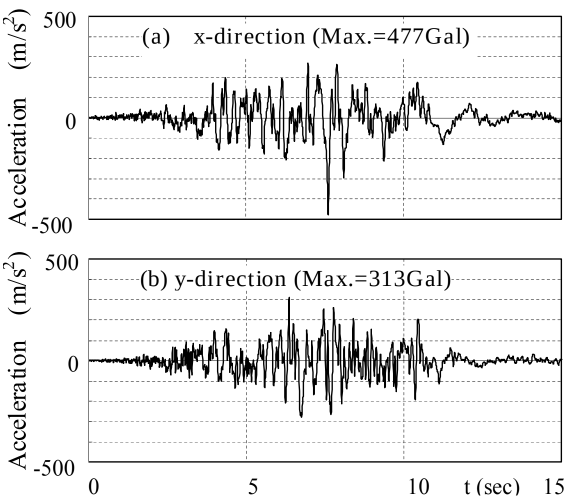

Fig. 8: Input seismic wave (*E+F* wave)

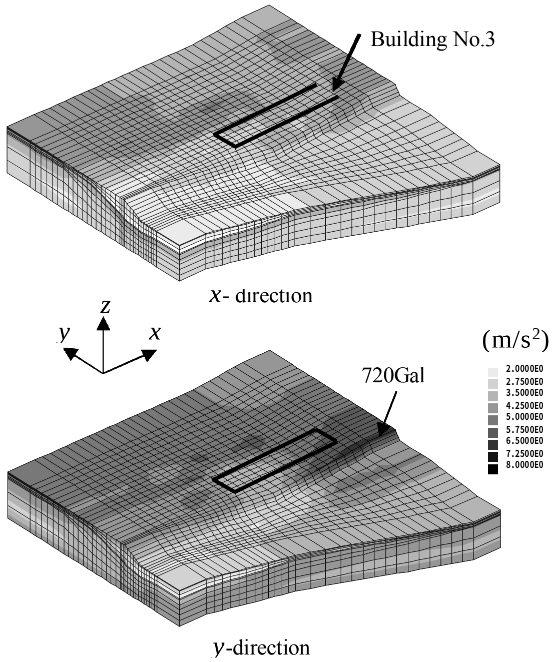

Fig.10: Distribution of maximum acceleration

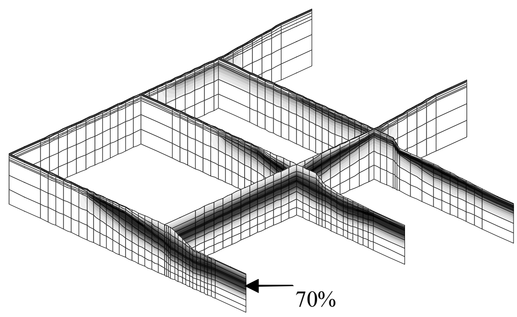

Fig.11: Distribution of maximum pore pressure ratio

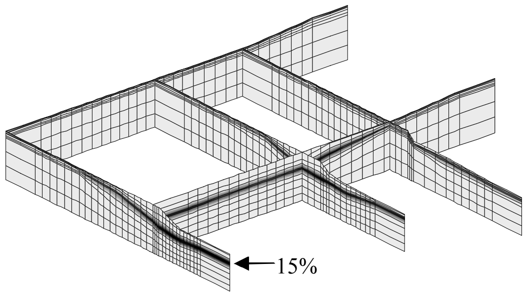

Fig.12 Distribution of resultant shear strain

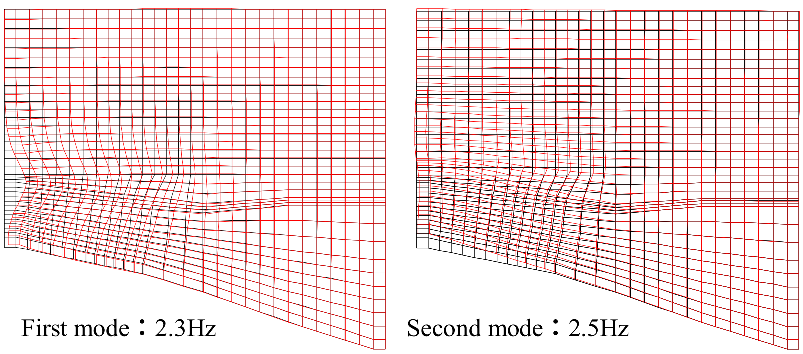

Fig. 9: Plan of 1st and 2nd modes

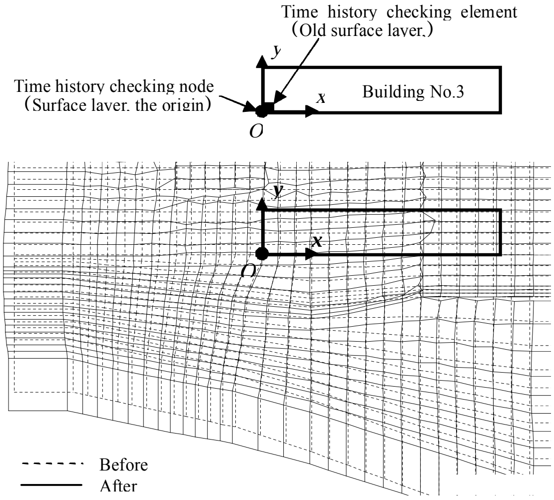

Fig.13: Plan of deformation at 15 sec after the beginning of the earthquake

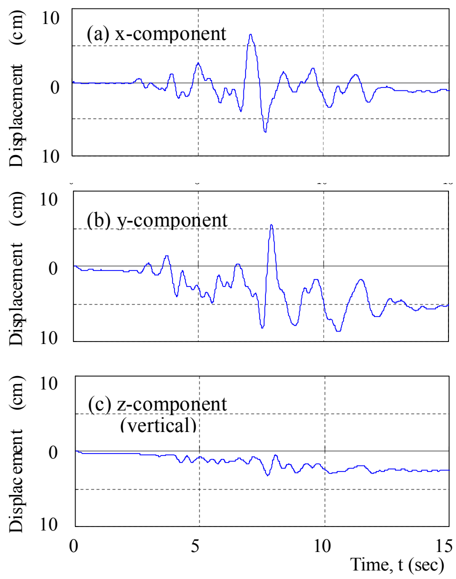

Fig.14: Time history of ground surface displacement at the origin of the coordinates

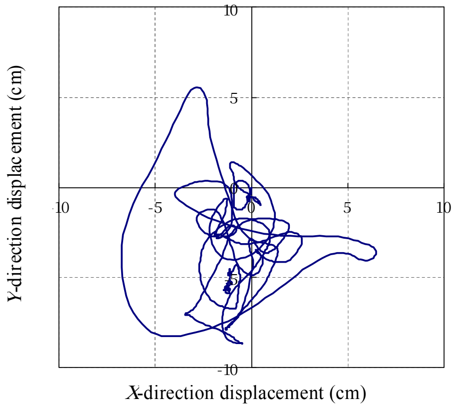

Fig.15: Horizontal displacement orbit of ground surface at the origin of the coordinates

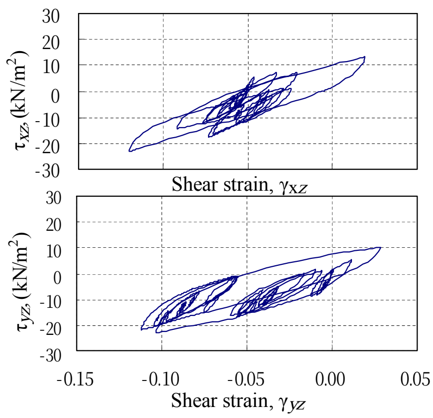

Fig.16: Stress-strain relationship of Old surface layer at the southwest corner of Building No.3

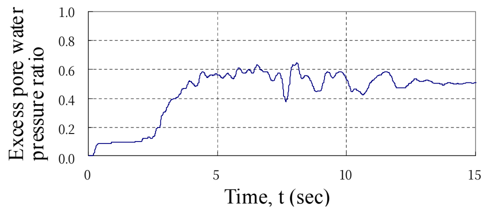

Fig.17: Time history of excess pore water pressure ratio of Old surface layer at the southwest corner of Building No.3

Acknowledgments

The authors wish to thank Dr. Tomomi Sato for her advise on the input seismic wave. This study was conducted in "Emergency research on the 2004 Niigata-ken Chuetsu Earthquake" based on the Special Coordination Funds for Promoting Science and Technology (MEXT).

References

[1] Fukutake, K., "Studies on three-dimensional liquefaction analyses of soil-structure system considering multi-directional shearing of soil" (in Japanese), doctoral thesis of Nagoya Institute of Technology, 1997.

[2] Fukutake,K.and Matsuoka,H., "Stress-strain relationship under multi-directional cyclic simple shearing"(in Japanese), Proc. Annual congress of Japan Society of Civil Engineers, No.463/III-22, pp.75-84, 1993.

[3] http://www.kik.bosai.go.jp/kik/

[4] Fukutake K., Hotta H. and Onoue A., "Stability of cutting and filling ground using 3-dimentional equivalent linear analyses during Chuetsu Earthquake", Proc. Proc. Simpojium on safeness and performance evaluation of ground for hausing, JGS, pp.39-46,2005.

Report on the sluice damage caused by the 2003 Tokachi-oki Earthquake

M.Kawai[1], T.Takebe[1], K.Satou[1], N.Minobe[2], S.Kakubari[2], M.Shiwa[2], Y.Sasaki[3]

[1]*OYO Corporation, Sapporo, Japan*

[2]*IKEDA River Office, Obihiro Development and Construction Department, Ministry of Land, Infrastructure and Transport , Obihiro, Japan*

[3]*Japan Institute of Construction Engineering, Tokyo, Japan*

Abstract

Serious damage was caused to many civil engineering structures by the 2003 Tokachi-oki earthquake that recorded magnitude 8.0 in the Pacific side of Hokkaido. In the downstream area of the Tokachi River which was close to the epicenter, more than 16km of river dike at 26 places was damaged. Damage of river dike was caused mainly by soil liquefaction in ground and/or embankment due to the high level of earthquake shaking. The Ohtsu-shigai sluice which is located near the river mouth of the Tokachi River was expanded in length horizontally by opening at coupling portion, though there was no apparent crack nor deformation of the dike was observed on the dike surface at this section. The serious structural damage such as a slant of a foundation pile or a break of the pile head were found from open cut investigation. This paper describes the damage feature of this sluice, which is rarely seen at field in the past.

Keywords—2003 Tokachi-oki earthquake, River dike, sluice, liquefaction

INTRODUCTION

Damage was caused to many civil engineering structures mainly on the East Coast of Hokkaido by the 2003 Tokachi-oki earthquake that occurred on September 26, 2003. In the Tokachi River downstream area which was close to the epicenter, 26 places or a length of 16km of the river dike were damaged by this earthquake. Damage to the river dike was mainly caused by liquefaction within ground and/or embankment due to earthquake shaking. Although large deformation was not recognized at the dike section where the Ohtsu-shigai sluice was located near the river mouth of the Tokachi River, but as a result of inspection from inside, large openings of joints of sluice segments were found which implied the displacement of sluice segments. Adding to these joint openings, serious structural damage to foundation piles such as a slant and a breaking of the pile heads were detected from both a partial open cut investigation which was carried out after the preliminary inspection and a full open cut investigation during reconstruction of the sluice. These damage features apparently indicated the horizontal displacement of sluice segments due to the axial elongation of the sluice.

In Japan, there are many experiences on earthquake damage to river dikes, but there is almost no report on the damaged sluices by earthquakes.

This paper shows about the damaging situation of the Ohtsu-shigai sluice which was obtained from the field investigation.

OUTLINE OF THE 2003 TOKACHI-OKI EARTHQUAKE

"The 2003 Tokachi-oki earthquakes", which occurred at 4:50 on September 26 in 2003, recorded magnitude 8.0. This was since "1994 Hokkaido Toho-oki earthquake" in Japan. And ground motion larger than the seismic intensity 1 was felt in wide area from Hokkaido to the Kanto region. The details of this earthquake were as follows.

【Main shock】

Time: 26th September 2003 AM4:50:076

Location of epicenter:Lat. 41degrees N 46.7 minutes
Long. 144 degrees E 4.7 minutes

Depth: 42km

Magnitude: 8.0

Seismic intensity 6-; Niikapu town, Shizunai town, Urakawa town, Toyokoro town etc.

Seismic intensity 5+; Atsuma town, Asyoro town, Obihiro city, Honbetsu town etc.

【largest aftershock】

Time: 26th September 2003 AM6:08:018

Location of epicenter: Lat. 41degrees N 42.4 minutes
Long. 143 degrees E 41.7 minutes

Depth: 21km

Magnitude: 7.1

Seismic intensity 6-; Urakawa town

Seismic intensity 5+; Niikappu town

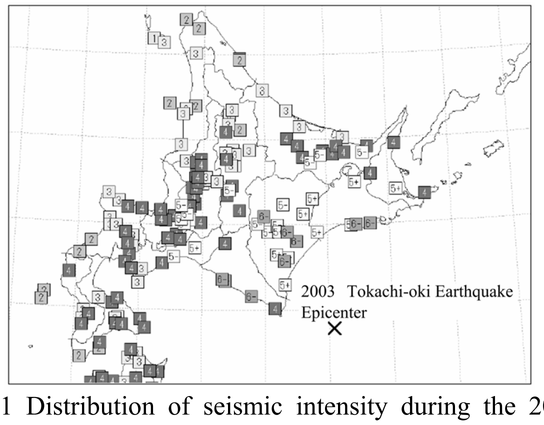

Fig.1 Distribution of seismic intensity during the 2003 Tokachi-oki Earthquake

DAMAGE OF THE TOKACHI RIVER

Distribution of maximum acceleration in the downstream area of the Tokachi River is shown in Fig.2, at many locations the acceleration exceeded 468 gal which had been observed during “the 1993 Kushiro-oki earthquake”. And many infrastructure facilities, such as road, bridge and river bank etc., were damaged during this event.

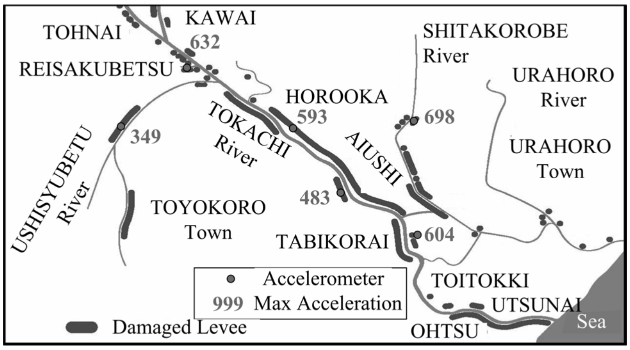

Fig.2 Distribution of maximum acceleration in the downstream area of the Tokachi River

In the Ohtsu section of the Tokachi River dike that is located near the river mouth, the inspection passage on the land side berm was slid (Photo.1), and traces of sand boiling around the toe of the bank slope showed outbreak of soil liquefaction.

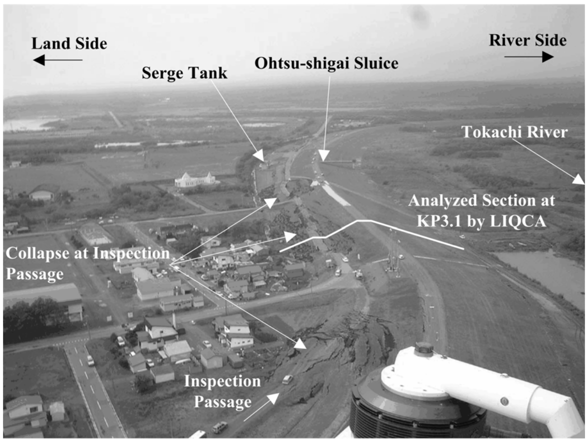

Photo.1 Damage of inspection passage in the Ohtsu bank

According to the acceleration record at the Ohtsu water level observatory, which is located in downstream of the damaged section, the recorded motion continued for 265.9 seconds, and the maximum accelerations were 424gal in N-S direction, 526gal in E-W direction and 191 gal in U-D direction.

OUTLINE OF THE OHTSU-SHIGAI SLUICE

The Ohtsu-shigai sluice is located at about 3.3km upstream from the river mouth. And a village of the Ohtsu district whose main industry is fishery is located in the land side of the dike.

This sluice was constructed in 1995 for discharging the inland water. Outline of the sluice is as follows;

Construction year: 1995
Type of foundation: PHC Pile φ 350mm,L=33m
Dimensions: □1.5m*1.5m L=80.85m
Plan flow quantity: Q=1m^3/sec

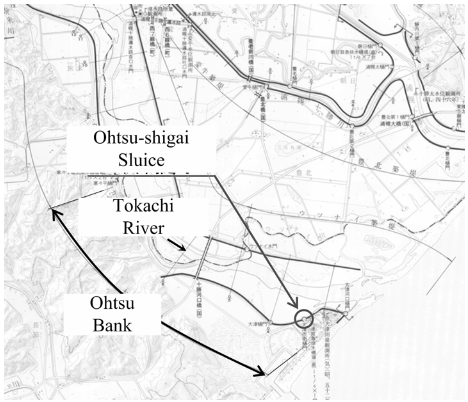

Fig.3 Location of the Ohtsu-shigai sluice

OBSERVED DAMAGE

The damage such as the slope failure of dike shown in Photo.1 was remarkable in the Ohtsu section of the Tokachi River, and the restoration measure for bank was conducted rapidly after the earthquake.

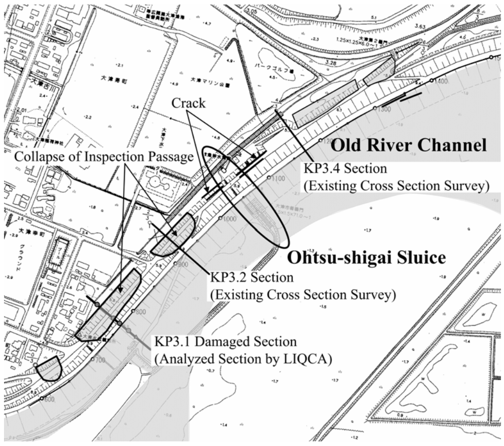

Fig.4 Damage of the Ohtsu bank around the Ohtsu-shigai sluice

However, for the sluice, the detailed investigation was conducted in the spring of 2004, because the apparent damage was not detected from outside of the sluice and it was difficult to assure the safety during inspection under the actively occurring condition of aftershocks.

The observed damage of the Ohtsu-shigai sluice in each stage of inspection is summarized as follows.

(1) Preliminary inspection

The vertical difference of 41cm at the maximum was found on the dike surface at slope, and the opening between sluice body and wing wall to reach about 70cm was detected mainly at the river side of the dike section by appearance inspection as shown in Fig.5.

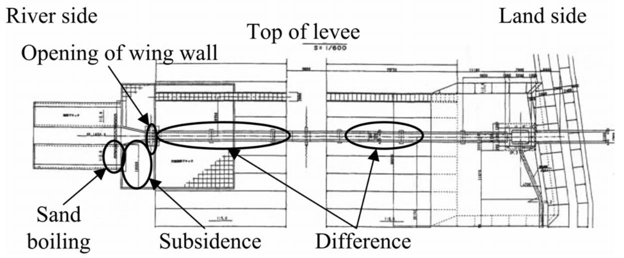

Fig.5 Observed deformation by appearance inspection

Because the result of this appearance inspection showed that it was very likely that damage extended to the sluice body, more detailed inspection from inside was carried out. The result of inside inspection is shown in Fig.6, and the deformation of joints and cracks are shown in Photos.2- 5.

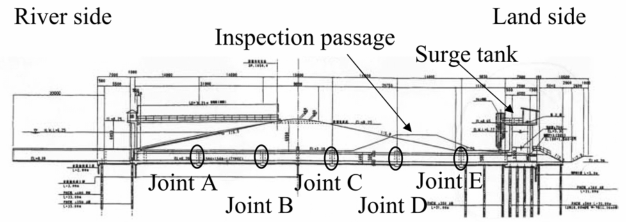

a) Cross Section of the Ohtsu-shigai Sluice

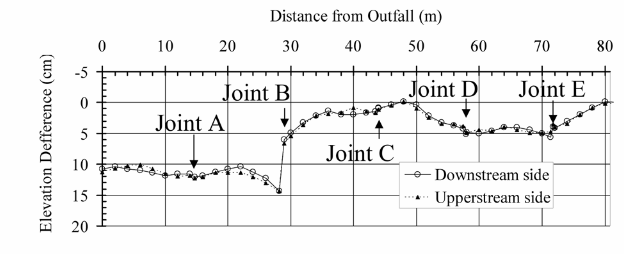

b) Distribution of Elevation Difference along the Sluice

Fig.6 Result of sluice inspection

Table.1 Difference of each joint

	Horizontal Displacement (cm)	Vertical Displacement (cm)
Joint A	30(75-45)	0.4-0.5
Joint B	43(88-45)	7.7-8.3
Joint C	6(51-45)	0.4-0.5
Joint D	8(53-45)	0.9-1.0
Joint E	-1(44-45)	1.2-1.7

Initial horizontal difference is around 45cm

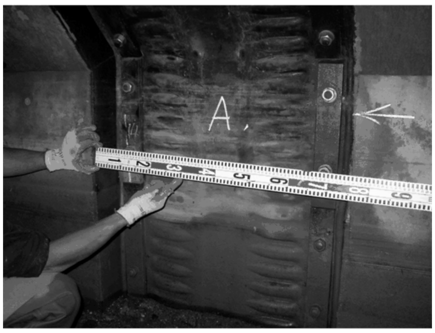

Photo.2 Horizontal displacement at joint A

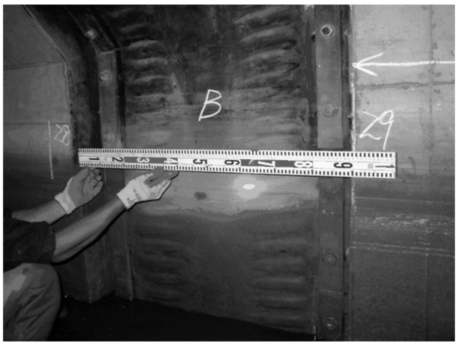

Photo.3 Horizontal displacement at joint B

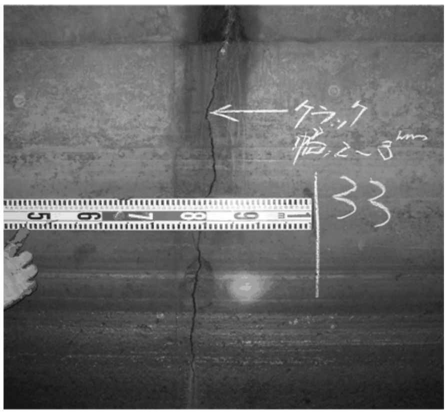

Photo.4 Open crack located 32.75m from outfall

Photo.5 Open crack located 35.05m from outfall

As the detected results of the above inspection had shown the possibility of serious damage to the sluice, the first-stage investigation that included the partial open cut to inspect the piles was carried out to judge the necessity of reconstruction.

(2) First-stage investigation

In the first-stage investigation the water head transmission test was conducted for checking sealing function via the grout holes which bored in the sluice, and the partial open cut investigation to observe foundation pile situation at river side were carried out.

The transmission test did not show a clear longitudinal transmission of water head beneath the sluice, it meant the sealing function did not received serious damage even the sluice segments had largely displaced from each other.

From the partial open cut investigation, it was observed that the foundation pile located in river side was completely broken at the top and slanted toward nine degree to the river side and four degree to the downstream side (shown in Fig.8).

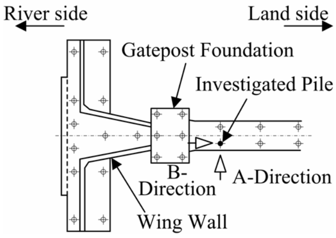

Fig.7 Location of investigated pile for partial open cut investigation

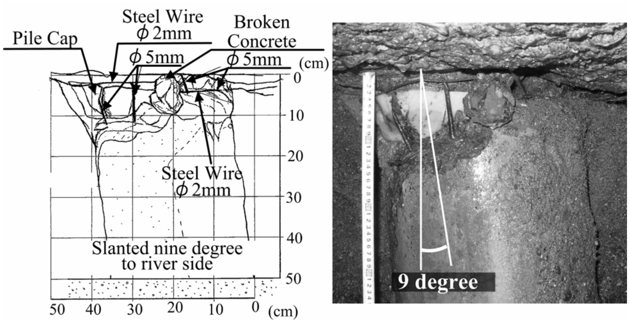

a) A-Direction

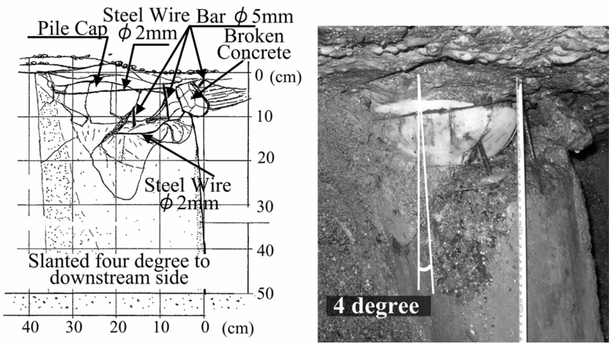

b) B-Direction

Fig.8 Damaged pile in river side of the sluice

The result of the integrity test, which is one of Non Destructive Inspection using elastic wave, on foundation pile showed that the foundation piles were damaged at not only their heads but also in the ground.

The inspection and the first-stage investigation results are summarized as follows;

- Two flexible joints located in the river side were found deformed more than the allowable extent, namely the breaking risk is high.
- The foundation piles were found to have been badly damaged, namely their bearing capacity was almost lost.
- Some of the opening cracks around the sluice body were observed, and the damage of the sluice itself was also noticed to be serious.

From these, it was judged that damage could not be recovered by repair work, and the reconstruction of the sluice was inevitable.

(3) Second-stage investigation

By the judgment based on the first-stage investigation, the Ohtsu-shigai sluice was decided to be reconstructed. It was an extremely rare example that a sluice suffered damage by an earthquake. And it would give valuable information from the detailed inspection for establishing better methods of designing sluices against earthquake.

Therefore, the full open cut investigation was performed to observe the breaking situation of piles and the sluice body by taking advantage of reconstruction which exposed the whole parts of the damaged sluice.

1) Damage of foundation piles

The inspection of foundation piles in the second-stage investigation was carried out for 12 piles which existed at sluice joint location. Photos.6 and 7 show examples of the damaged pile. It was obtained that the breaking of pile top and the slanting of pile took place mainly at river side in below the damaged sluice body. And the piles that were located from the center of bank to land side were little slanting, but the top of all piles were broken. In addition, the pile below the serge tank was damaged like a shear destruction which is applied compression load as shown in Photo.7.

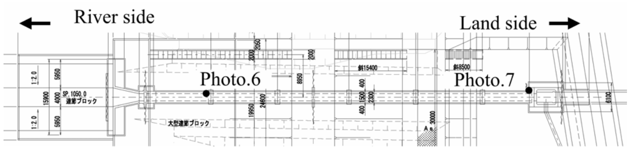

Fig.9 Location of investigated pile for full open cut investigation


Photo.6 Example of damaged pile


Photo.7 Damaged pile below serge tank

2) Damage of sluice body

The inspection of the sluice body was carried out to check the deformation of joint and the situation of crack.

The observed result is shown in Fig.10. It shows the two blocks in the river side sank greatly, and that the sluice body was bent at a crack position was obtained.

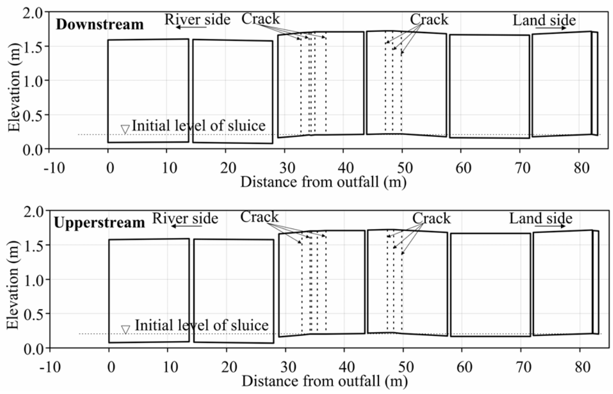

Fig.10 Deformation of sluice body

At the joints A and B, which had been found seriously damaged during inside inspection, it was found that the concrete collar were slanted two degree to four degree as shown in Photos.8 and 9.

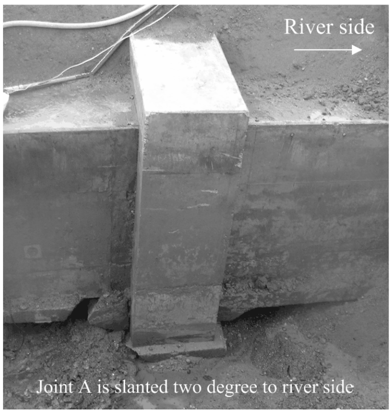

Photo.8 Deformation of joint A

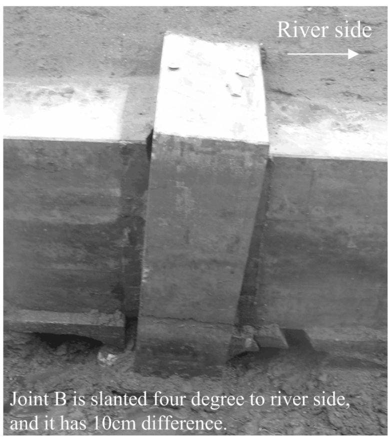

Photo.9 Deformation of joint B

3) Full open cut investigation

Fig.21in the last page shows the soil condition of the embankment and foundation ground observed at about 30m downstream point from the damaged sluice. It was found that there was an old dike inside the current embankment at the land side, and the reclaimed soil layer beneath the river side slope of the dike. This is to fill the edge of the river channel so that the dike was widened towards the water. It was also found that laminae in the reclaimed soil layer were apparently distorted as shown in Fig. 21 b) evidencing the large deformation of this layer.

Furthermore, the slanted collars and the slanted piles are found to be located in the area where the reclaimed soil is distributed beneath the dike.

ESTIMATION OF DAMAGE MECHANISM

(1) History of embankment

Fig.11 shows the change of aerial photos around the Ohtsu-shigai sluice, and Fig.12 shows the cross section drawn from existing surveying result near the sluice. According to these figures, part of the bank around the Ohtsu-shigai sluice is situated on the ground which fills the periphery of an old river channel, and the river bank had been built on it as observed during the open cut investigation.

Fig.11 The change of river channel by aerial photo

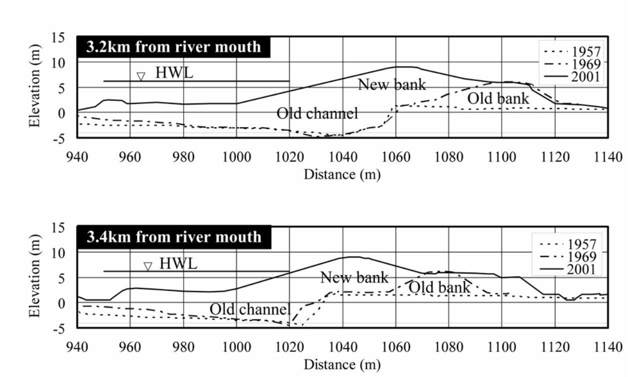

Fig.12 Result of existing cross section survey

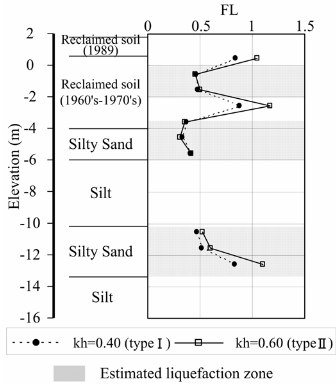

Fig.15 Evaluation of liquefaction susceptibility at B-1

(2) Evaluation of liquefaction susceptibility

As described above, foundation ground is susceptible to liquefaction, and the traces of sand boiling were observed in the Ohtsu section of the dike. From the result of the liquefaction evaluation as shown in Figs.15- 17, it was confirmed that the reclaimed soil and the sand layers which were deposited beneath bank had a possibility of liquefaction against the recorded ground motion.

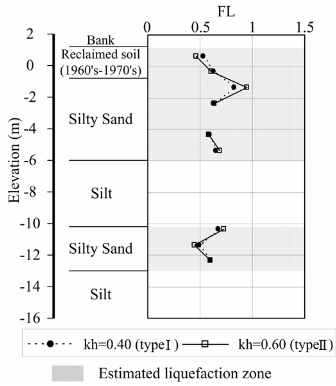

Fig.16 Evaluation of liquefaction susceptibility at B-2

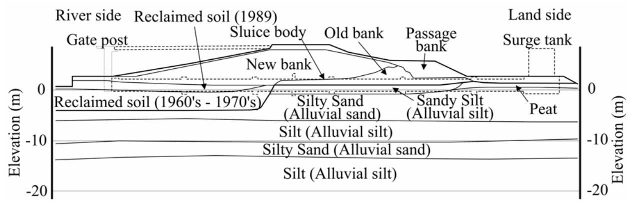

Fig.13 Geological profile of the Ohtsu-shigai sluice

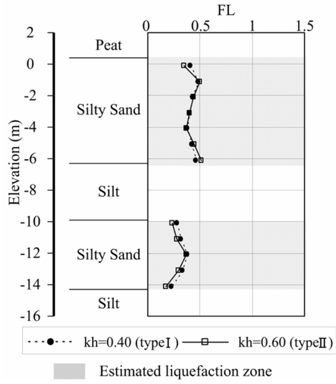

Fig.17 Evaluation of liquefaction susceptibility at B-3

Table.2 Geotechnical characteristic of stratum

Stratum	γ_t (kN/m^3)	D_{50} (mm)	Fc (%)	Average N value
New bank	19.0	0.259	19.3	13 (8-16)
Old bank				
Reclaimed soil (1989)	17.0	0.985	4.8	10
Reclaimed soil (1960's-1970's)	17.0-19.0	0.025-0.407	9.0-76.3	7(2-13)
Alluvial sand (upper)	17.0	0.07-0.406	9.0-51.8	9(5-14)
Alluvial silt (upper)	16.0	0.004-0.008	97.0-98.4	4(2-6)
Alluvial sand (lower)	18.0	0.107-0.149	18.7-35.5	12(4-21)
Alluvial silt (lower)	16.0	0.004-0.008	97.0-98.7	5(3-5)

(3) The breaking depth of piles

Fig.18 shows the breaking depth of piles which is obtained from the integrity test, and the estimation of liquefaction result. It was revealed that there were many break points at the river side, and the breaking depths were located at the top or the bottom of the liquefiable stratum.

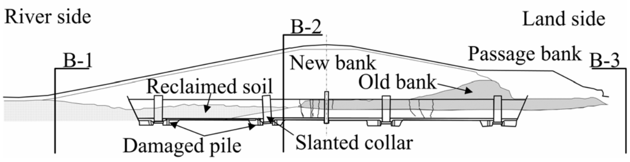

Fig.14 Location of liquefaction estimate point

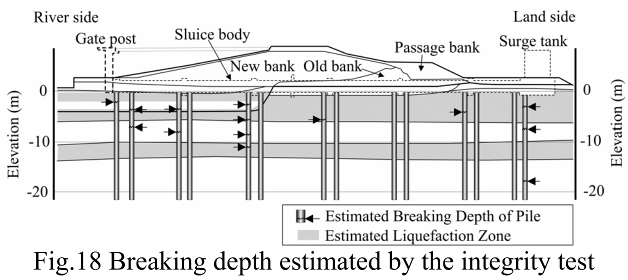

Fig.18 Breaking depth estimated by the integrity test

(4) Numerical analysis results

Figs.19 and 20 show the result of dynamic analysis against the recorded ground motion by a cord named LIQCA on the cross section of the dike at about 200 m downstream of the sluice point. In this analyzed section, reclaimed soil layer in the old river channel is modeled beneath the river side slope, which is same as the section of the sluice shown in Fig.4. However, the sluice is not included in this analyzed section. It should be noted that this analysis shows deformation of the dike without sluice.

From this result, in case there is no sluice, the bank sank around 2.7m at the maximum and the large horizontal displacement was caused. In addition, the tensile strain was induced in wide area from the river side to the center of bank. This shows a potential of stretch of the bank is high.

The observed damage at analyzed section was mainly a failure at the inland slope due to liquefaction in the old bank. And the some cracks and the trace of liquefaction were observed at the river side. It shows liquefaction was occurred in the reclaimed soil. The analyzed result coincides with the actual failure well, but not matches to the section of the sluice as for the failure in inland side slope. This is considered due to the difference of groundwater level inside the dikes. However, it should be noted that the deformed mode of the riverside half of the dike apparently shows the potential of sluice elongation through dike stretching.

Table.3 Model parameter for LIQCA analysis

Stratum	Vs (m/s)	Vp (m/s)	Go (kPa)	Eo (kPa)	ν
New bank	130	260	30400	40500	0.333
Old bank	130	260	30400	40500	0.333
Reclaimed soil (1989)	130	260	30400	40500	0.333
Reclaimed soil (1960's-1970's)	130	260	30400	40500	0.333
Alluvial sand (upper)	170	340	52000	69300	0.333
Alluvial silt (upper)	170	340	49100	65500	0.333
Alluvial sand (lower)	170	340	52000	69300	0.333
Alluvial silt (lower)	170	340	49100	65500	0.333

The ground water level is located below around 1.0m below surface at the river side and the land side which obtained by field investigation.

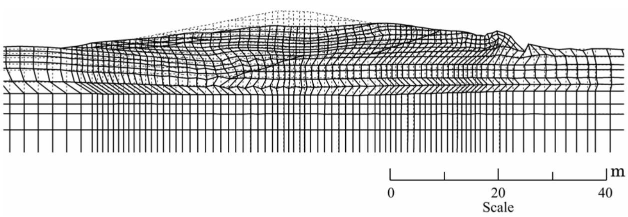

Fig.19 Residual deformation of the Ohtsu-bank at KP3.1 section by LIQCA

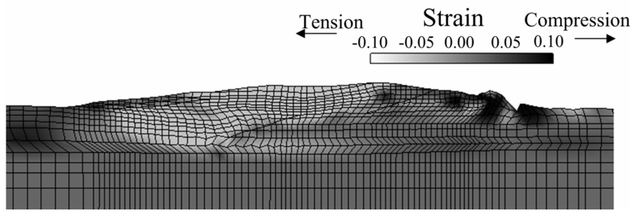

Fig.20 Distribution of strain at KP3.1 section

(5) Presumed deformation mechanism

It became clear from the study that;

-The sandy soil which filled old river channel was deposited at the river side of the Ohtsu-shigai sluice.

-It is very likely that this sandy soil was liquefied.

-The sandy soil which was deposited under the reclaimed soil was also very likely to liquefaction.

-From numerical analysis, it was apparent that the tensile strain was induced beneath the dike slope from the bank center to the river side due to the liquefaction of the reclaimed soil layer.

From the above, the mechanism of deformation can be estimated as follows;

-The reclaimed soil which was distributed in the river side had been liquefied by the strong earthquake.

-By this liquefaction, the dike was forced to stretch to the river side largely, and this caused elongating force acted on the sluice.

-By this force acted to the sluice and the deformation of the reclaimed layer, joint openings of sluice segments and vertical difference were caused from the center to the river side, and the collar of joint was pushed and slanted.

-The foundation piles were pushed to river side by the displacement of sluice segments, resulting the breaking of pile heads and the slanting of piles.

CONCLUSION

The experience of the Ohtsu-shigai sluice damage implies that there is a possibility of deformation of the embedded sluice when liquefaction took places at shallow ground below sluice, even when the damage was not observed at the surface of bank.

And the sluices constructed on the old river channel need to be paid careful attention against seismic damage. Such a kind of elongated damage seen in the Ohtsu-shigai sluice case could be evaluated through the examination of the stretching amount of dike without sluice.

REFERENCES

[1] M.Shiwa, S.Kakubari, Y.Igarashi, "Study on the damage of river structure in downstream of the Tokachi River by the 2003 Tokachi-oki earthquake – The damage situation of the Ohtsu-shigai sluice –", 49th technical meeting on research and development of Hokkaido Regional Development Bureau, 2006

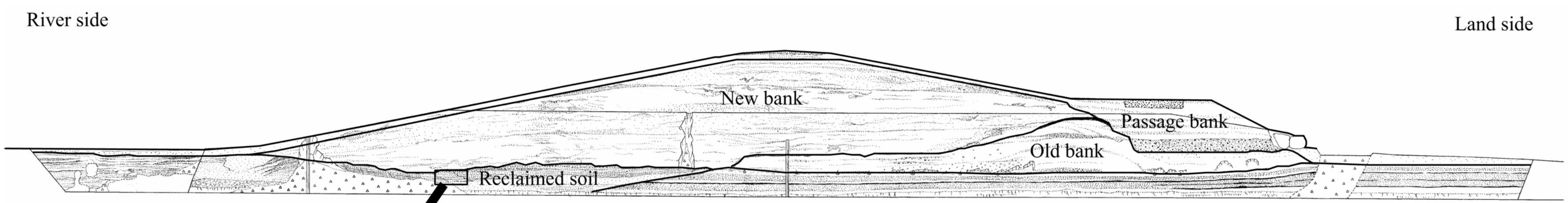

a) Sketch of open cut investigation for New sluice (sketched by H.Satou)

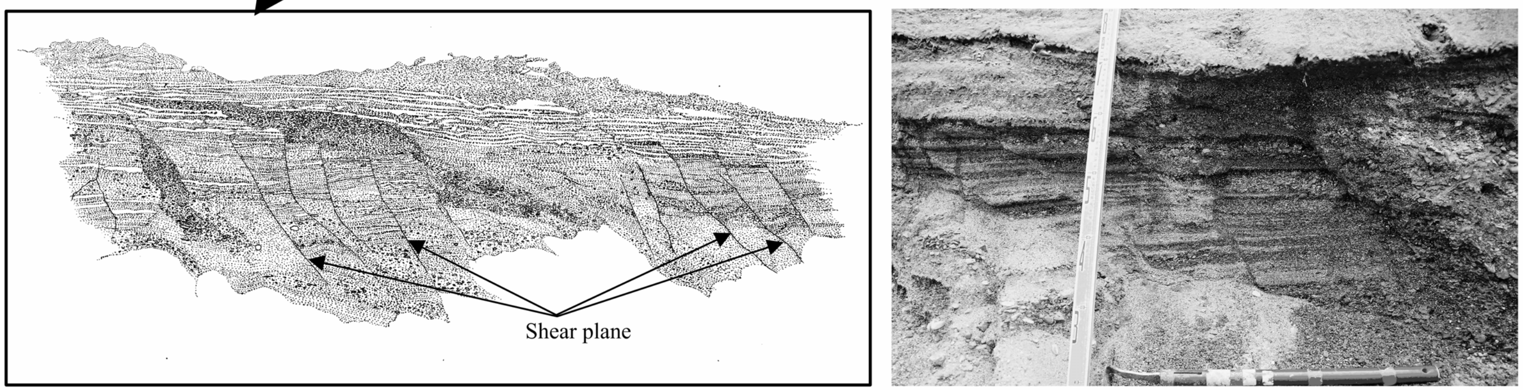

b) Sketch and photo of the details of sedimentation in reclaimed soil (sketched by H.Satou)

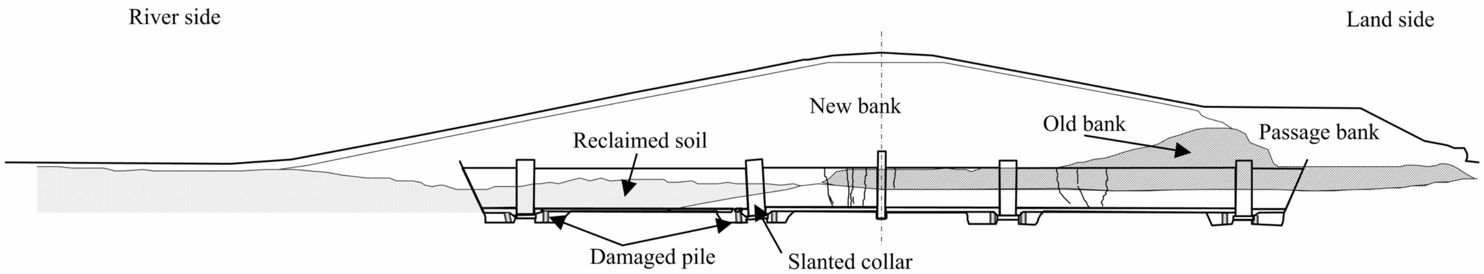

c) Relations of the bank classification and sluice deformation

Fig. 21 Result of open cut investigation at new sluice location

Restoration of a Tilted Three-Story RC Building via Grouting

Yung-Kuang Lin[1], Chin-Jung Kuo[1], Hsii-Sheng Hsieh[2], and San-Shyan Lin[3]
[1]*Mice Consultants Co., Ltd, Taipei, Taiwan.*
[2]*Trinity Foundation Engineering Consultants Co. Ltd., Taipei, Taiwan.*
[3]*Dept. of Harbor and River Eng., National Taiwan Ocean University, Keelung, Taiwan 20224.*

Abstract

This paper studies the restoration of a tilted three-story reinforced concrete building that was the result of earthquake-induced soil liquefaction during the Chi-Chi earthquake in 1999, using low-pressure cement-water glass grout. The restoration plan, which includes layout of micropiles and jet grouting piles to serve as curtain wall and layout of grouting locations, is described first. Effectiveness of the adopted restoring plan is then evaluated by comparing the relative settlement of the ground floor slab, before and after the grouting. Comparison on shear wave velocity of the site, before and after grouting, confirms the effectiveness of the restoring plan.

Keywords—Restoration, Liquefaction, Tilted building, Grouting

INTRODUCTION

A reinforced concrete house (Fig. 1), two stories in the front and three stories in the back, located at Yuan Lin Towanship was tilted as a result of the Chi-Chi Earthquake of September 21, 1999. Site reconnaissance in the surrounding area was conducted after the earthquake. Many sand boiled holes were observed. As a matter of fact, the owner of the house observed sand boiling phenomena in the nearby open space of the house during the earthquake. It's believed that tilting of the house was mainly caused by soil liquefaction, although a one-story steel frame factory (Fig. 2), located at about 2 meters to the left of the building appeared to have remain unharmed after the earthquake.

This paper studies the restoration plan adopted for this particular house, including layout of micropiles and jet grouting piles serving as curtain wall and layout of grouting locations. Effectiveness of the restoration method adopted is then evaluated by comparing the relative settlement of the ground floor slab, before and after the grouting. In addition, comparison on shear wave velocity of the site, before and after grouting, is also evaluated for the effectiveness of the restoration plan.

SITE INVESTIGATION

Based on SPT tests conducted on January 26, 2002, the soil profile can roughly be divided into four layers and is given in Table 1. The water table was found to be at 4.0m below ground surface. The nearest building to the house is a one-story steel frame factory, located at about 1.9m to 2.8m away from the left side of the inclined house. The remaining three sides of the inclined house are open spaces.

Some measurements and investigation for the house were conducted on March 18, 2002. In general, the house was tilted on the back left corner of the building, with angular rotation between 1/110 and 1/150. Foundation of the building is a 25cm thick raft foundation with embedded depth of 150cm to 200cm (Fig. 3). Differential settlement in the transverse direction of the ground floor slab was 8.1cm and the maximum differential settlement of the ground floor slab was 17.3cm.

A water pipe (Fig. 4) almost parallel to the building was found on the left side of the building and was embedded at 70cm to 150cm below the ground surface. Sewage pipeline, with embedded depth of 30cm to 50cm was found at the back right corner of the building.

RESTORATION VIA GROUTING

Low-pressure cement-water glass mixture grout was used for the purpose to restore the tilted building. In general, low pressure means grouting pressure can be as low as 20 kg/cm^2. Micropiles and jet grouting were used and installed, respectively, on the left side and in back of the building as curtain wall. The purpose of the curtain wall installation is to control effectiveness of grouting and to reduce its effect on the neighboring building. Fifty-six micropiles, 10cm in diameter and 10m in length, were installed between the tilted house and the neighboring factory with center-to-center of 40cm. Since no other structure is behind the building, 9 jet grouting piles, with diameter of 50cm, were installed from depth of 2.5m to 9.0m. Set up of the curtain wall is indicated in Fig. 5.

Thirteen inclined injection holes were used, as shown in Fig. 6, for low-pressure cement-water glass mixture grouting. A two-inch wide PVC tube with pre-drilled holes at every 50cm was used and embedded about 6.5m below ground surface.

To prevent induction of excessive upheaval of the ground and excessive distortion of the building during the process of grouting, the incremental angular distortion of the building and the maximum uplift of the ground were controlled within the limit of 1/500 and 2cm, respectively. The grouting process was set to stop once the angular rotation of 1/360 of the building was reached. The grouting process started from the back left of the building. LW (Labile Wasserglas) grout, a mixture of cement and water glass, was adopted for this. Some material properties of the water glass is given in Table 2. Each cubic meter of cement grout contains 16 to 18 packs of cement (50kg/pack) and 250 to 350 liter of water glass. Grouting pressure was maintained around 10 to 20g/cm^2. In addition, the volume of grout injection was controlled betweem 2.0L/min to 30L/min. Altogether, it took 15 days to finish the job, and 910 packs of cement were used.

RESTORATION RESULTS

The maximum differential settlement of the ground floor slab reduced to 2.5cm after restoration, or 1.4cm and 1.5cm in the transverse and in the longitudinal direction, respectively. Comparisons on the values of the differential settlement before and after restoration are given in Figs. 7 and 8, in which the reference point is set at SM1. In addition to the performance of the building after restoration, comparison on shear wave velocity of the ground before and after restoration is also made and is given in Table 3.

SUMMARY AND CONCLUSIONS

A case study for restoration plan of a tilted three-story building caused by the Chi-Chi Earthquake has been studied in this paper. Success of the restoration plan, via low pressure cement-water glass mixture grout, is demonstrated by comparing the differential settlement of the ground floor slab of the building and the shear wave velocity of the ground before and after the restoration. The building is still performing very well after the restoration work.

Table 1: Simplified Soil Profile

Layer	Depth(m)	Soil description	N value
I	0.0~3.0	backfill gravel/sand mixture	9~36(23)
II	3.0~6.8	SM or MS	5~12(8)
III	6.8~9.4	MC	7~16(12)
IV	9.4~20	SM or MS	11~27(18)

Table 2: Main Constituents of Water Glass

Specific Gravity	33-42
SiO_2（%）	21-36
Na_2O（%）	6-12
Fe（%）	below 0.05
Insoluble（%）	below 0.4

Table 3: Comparison of Shear Velocity before and after Grouting

Before		After	
Depth (m)	Shear wave velocity (m/s)	Depth (m)	Shear wave velocity (m/s)
0.426	176.711	0.543	384.700
0.959	176.747	1.221	391.832
1.625	176.509	2.069	332.951
2.458	176.219	3.129	263.744
3.499	176.043	4.454	337.615
4.800	180.131	6.110	510.493
6.426	184.314	8.180	519.271
8.459	189.513	10.767	694.659
11.000	189.638	14.001	693.732
13.750	189.449	17.501	582.402

Fig. 1: Tilted house before retrofitting

Fig. 2: Steel frame factory

Fig. 3: Foundation of the building

Fig. 4: Pipe lines on the LHS of the building

Fig. 5: Layout of micro piles, jet grouting piles and grout points

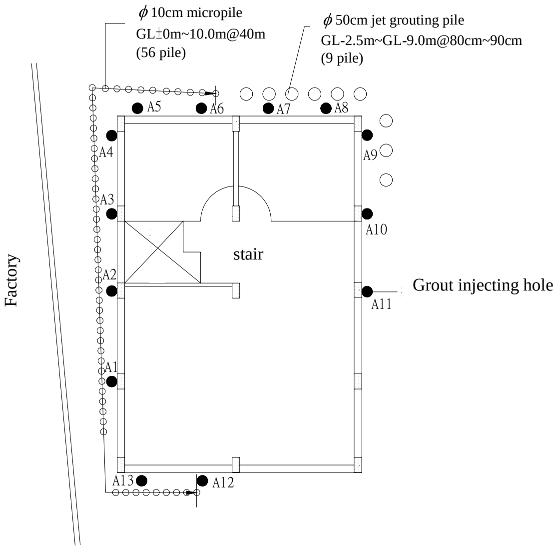

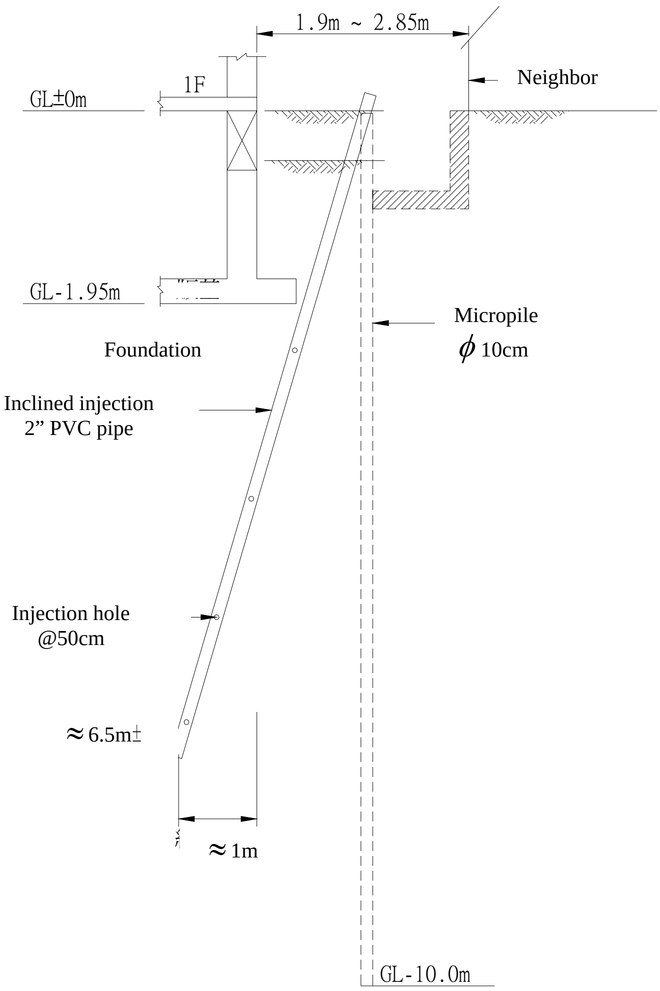

Fig. 6: Layout of instillation of injection pipe

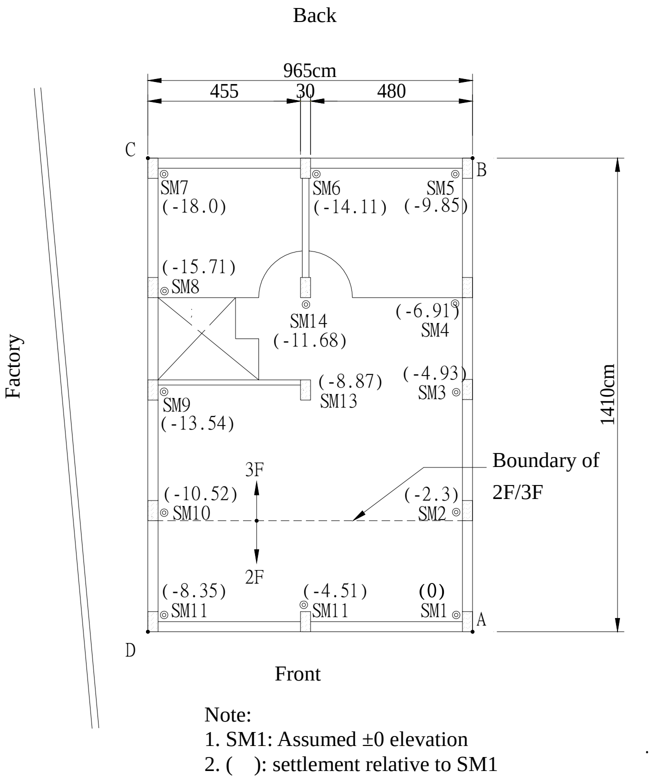

Fig. 7: 1st Floor slab settlement before grouting

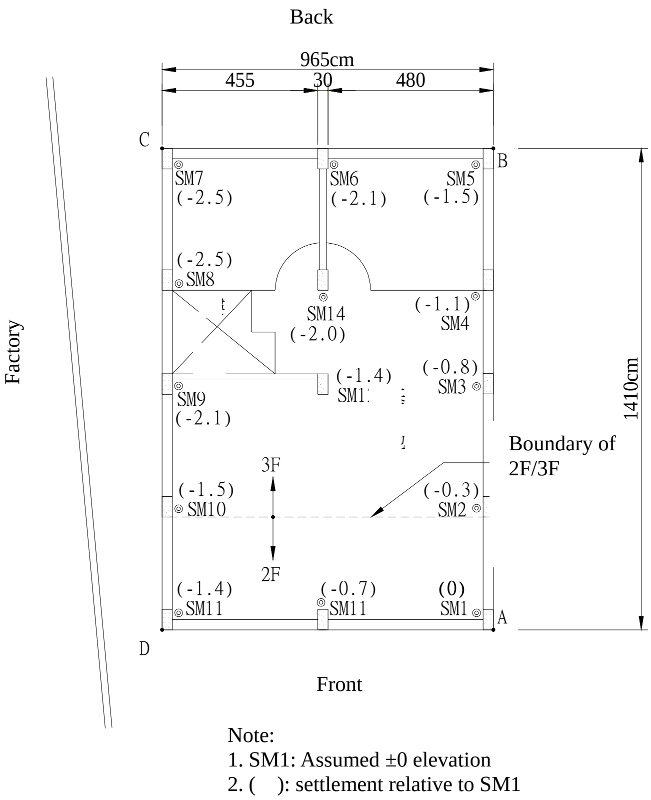

Fig .8: 1st Floor slab settlement after grouting

Fig. 9: Building after retrofitting

Damage of embankment and Reconstruction by the RRR method in Joetsu Line by Niigata-ken Chuetsu Earthquake in 2004

M.Kikkawa[1], F. Aizawa[2] , K.Saruya[3] , H.Morishima[1]

[1]*Structure Maintenance Division ,Niigata Branch , East Japan Railway Company, Japan*

[2] *Niigata Civil Ehg. Center, East Japan Railway Company, Japan*

[3] *Reconstruction Project Team(Structure Maintenance Division ,Hachioji Branch ,East Japan Railway Company, Japan)*

Abstract

By Niigata-ken Chuetsu Earthquake, lot of damage occurred in a railroad and a road, lifelines such as electricity or gas. In soil structure section of the existing line, the damage such as embankment collapse or slope collapse occurred. Especially, the embankment of the Joetsu line suffered damage, which was built on the valley side formed by erosion from the Shinano River. The failed railway embankment would have to be restored and reinforced as early as possible to resume the railway service that plays a critical role in the region's mass transit. The Reinforced Railroad/Road with Rigid facing (RRR) method was adopted.

This paper describes the damage outline of two embankment with serious damage of Joetsu Line and The RRR method of reconstruction.

Keywords— *railway, embankment, reconstruction, RRR method*

INTRODUCTION

At 17:56 on October 23, 2004, an earthquake with a moment magnitude of 6.8 occurred directly above its hypocenter in Niigata Prefecture (Chuetsu district) located approximately 195km north-northwest of Tokyo.

When the seismic motion that has certain volume is detected, Shinkansen trains stop by the feeding stop immediately, and the existing trains stop by the train protection radio or the train radio. A measurement value recorded by each observation point is sent to command room and judged train operating restriction based on those values. At the time when NIIGATA-KEN Chuetsu Earthquake has occurred, the train operating restriction was judged by using the maximum acceleration of an earthquake in Shinkansen and using the spectrum intensity of an earthquake in the existing line.

Figure 1 shows the data in this earthquake for the restriction of Shinkansen and the existing line. These values are more than train operating stop value. The maximum acceleration for the restriction of Shinkansen operation is a composite value of two horizontal vectors filtered to cut the high and the low frequency elements. Therefore, these values are smaller than the maximum acceleration recorded by the seismograph and the acceleration recorded by other institutions.

The hypocenter was near from railway side. The damage occurred in tunnels and viaducts at Shinkansen, and bridges, tunnels, embankments and cuts at the existing line. Especially, in Shinkansen, it was the first time after its operation that the operating train derailed when it stopped urgently even though the passengers have not damaged. And, trains in the existing line had stopped safely and train and passenger's safety was secured despite of extensive structure damage.

Afterwards, Shinkansen reconstructed on December 28, 2004, and then train operations have been resumed. The reconstruction methods of the existing line have been decided in order to reconstruct coming snowfall season, and executed the engineering work all days. As a result, Shinetsu line resumed operations on November 29, 2004, the single track of Joetsu Line on December 27. snowfall term. By Joetsu Line, it was continued reconstruction of the tunnel bank upper part slope that collapsed and opened a double track on March 25, 2005.

In this paper, The damage outline of two embankment with serious damage of Joetsu Line and The RRR method of reconstruction is reported.

Damage of the existing line soil structure section

At the existing line, Embankment collapse, track bed settlement and cut collapse occurred at 86 places in four lines in this district as well as the Shinetsu line and Joetsu Line. Large-scale collapse of embankment occurred in two places on Shinetsu line and in five places on Jouetsu Line.

Damages of the most parts were: ①boundary parts between cut and embankment; ②catchments which valleys and swamp were reclaimed; ③boundary parts of embankment to increase a line; ④embankment on inclined ground; (Especially, the collapse of Joetsu Line had concentrated on the section of about 2km between Ojiya and Echigo-Kawaguchi nearing to the epicenter. The embankment of this section was constructed by

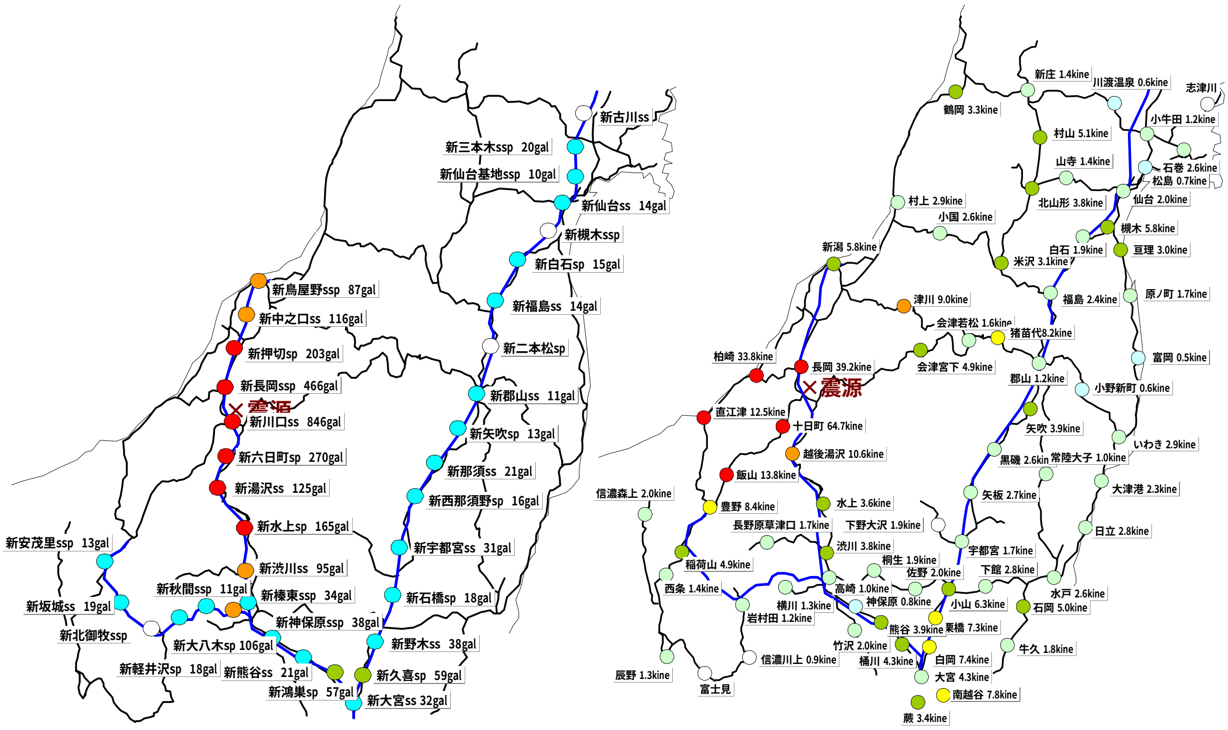

Fig. 1: The data for the restriction of Shinkansen and existing line (10/23 tremble M6.8 by 17:56)

reclaiming from the valley where small river flowed from Shinano River, and a double-track had constructed afterwards). None of the following effect has happened: ①the collapse according to the rise of the excess pore water pressure that was the principal cause of the collapse at the earthquake; ②the base destruction of the ground; ③ the embankment outflow according to the lateral spreading; Collapsed embankment materials contain viscous soil mainly composed of fine-grained fraction. In “Railway Structures Design Standard (Soil Structure)" (Hereafter, it is said, "Soil Structural Standard"), Most of embankment materials belong to B to D group, and the compaction degree is not high.

Selection of Reconstruction method

In view of the seriousness of the damage, failure-restraining structures with piles or bridge construction was originally considered to provide resistance to earthquakes and rainfall performance. It takes a considerable period for reconstruction as the method needs large-scale temporary facilities, to bring in large equipment like the pile driver because the area was a scarp. That was why this method might require the enormous costs and term of works. Reconstruction was made by embankment in consideration of the safety while the aftershock was continuing.

A basic policy of embankment reconstruction is as follows: ① early reconstruction, ② basing on Soil Structural Standard; ③having earthquake resistance and the rainfall resistance; Based on the above policy, embankment is selected. At first, it was considered to remove soil and sand collapsed, and pile up according to regulated stable gradient. However, it was assumed that the amount of the embankment become huge and takes long time in this methods. Therefore, it was examined to minimize the amount of the embankment that greatly influences the term of works.

As a result, it is examined to pile up the embankment wall by the severe gradient in order to reduce the amount of the treatment soil, and it made possible to reduce the term of works and the construction cost. The RRR method using reinforcing the backfill soil with a geotextile and rigid facing construction having bend rigidity had been selected. The reasons are as follows:

①The amount of the treatment soil can be reduced because it could construct the embankment grade with rapid incline;.

②The coverage of the embankment material is wide because a geotextile is closely arranged;

③The stability of the embankment and earthquake resistance is high because an integrated wall has a high rigidity;

④There are enough cases as a railway embankment;.

It is necessary to control the amount of the embankment as much as possible and construct faster because immediate reconstruction is the most important purpose. That was why the RRR method was considered to be effective to pile up the embankment rapidly and satisfying the purpose. Moreover, this method has excellent performance such as stability, earthquake resistance and rainfall resistance. Therefore, it made the performance improvement of the restored embankment and works for reconstruction at the early and permanent stage.

Around Joetsu Line 220k500m (Near the exit of The TENNO tunnel)

Damage of embankment

The collapsed part lies on the upper part of the rapid grade cliff that faces Shinano River. The base is mudstone of the upper part of Kawaguchi layer and inclines toward the Shinano River; it is so-called flow board structure. Unconformable Uonuma layer, which is shallow sea and river sedimentary layer of Quartemary Pleistocene, Uonuma layer covers with the mudstone. The opening line is down-track that cut Kawaguchi layer, the Uonuma layer, and the talus sedimentary layer on the grade of a rapid cliff. Up-track was constructed with the double-track electrification, and has the Tenno tunnel and snow shelter of consecutive concrete box along with the down-track .The national road goes the upper part of the grade.

The most upper part of collapse was the part of crack of the national road. The width of the collapse was about 55m in the direction of the down-track. The earth cover collapsed and a part of concrete lining was exposed around connected part between the snow shelter and the tunnel on the up-track. The cast-in-place concrete cribwork on the upper part of the grade, and the retaining wall of gravity type under the grade, also flowed down with the collapsed soil and sand. The maximum collapse depth was about 7m and the amount of the collapse soil was about 9,900m^3. (Picture 2)

Pic.2: Embankment collapse (around 220k500m Joetsu Line)

Reconstruction works

The collapsed soil was piled up 70-80m in length and 55m in width from collapsing down-track. The collapse area continues on the slope failure, and it was seriously a dangerous situation to go there the stream bottom. We examined to decrease of the embankment volumes, which influences on the construction works. As a result, the cement stabilization was made on the collapse soils, and the soil was utilized the bearing ground of embankment. In order to control the ground displacement of the embankment and the up-truck tunnel using the ground anchor was utilized because the bearing ground was the flow ground at a deep position.

The ground anchor was designed modeling collapse condition and the physical properties of the foundation ground using the inverse analysis by the slip circle analysis. Then, we assumed the slip circle including the reinforced embankment, and set number of the ground anchor and tension force as over 1.4 safe rate on a steady basis. (Figure 2)

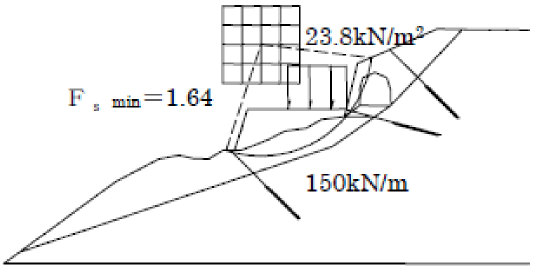

Fig. 2: The ground anchor's examination (down-truck)

(1)DESIGN OF REINFORCED EMBANKMENT

As the physical properties for the embankment material, a specific weight per volume γ =20kN/m^3 and an internal friction angle is ϕ=30° (cohesion is c=0kN/m^2) , a design strength of reinforcing material Ta=31kN/m and vertical interval of reinforcing material of 0.3m were specified and a cross section with the designated safety factor was determined . (Figure 3)

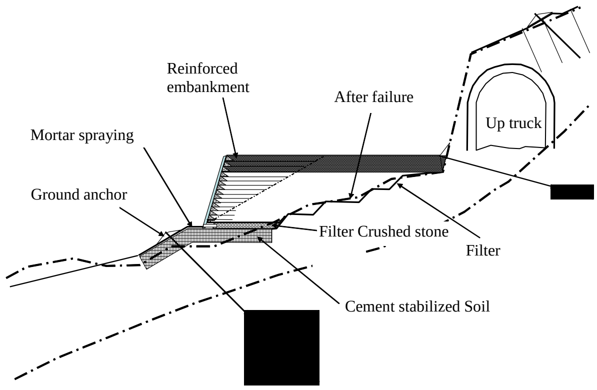

Fig. 3: Reconstruction section (220k500m)

(2)REINFORCEMENT OF BEARING GROUND

To reinforce the bearing stratum of reinforced embankment and to secure the operation yard for heavy equipment, the soil was stabilized for a depth of 1m by applying cement-type solidifiers. As a result, the coefficient of subgrade reaction K_{30} was satisfied with 70MN/ m^3 by the plate loading test.

(3) GROUND ANCHOR WORK

After the soil was stabilized with cement, a soil platform for anchor work was built for installing fourteen 15-m-long ground anchors with pretension of 600KN/ per rod at intervals of 4m.

(4) DRAINAGE WORK

In order to drain seepage water out of embankment, perforated polyethylene pipe (diameter of 65mm) were laid. Then, they were connected to drain pipes of the embankment. And, the filter drain layer were spread by intervals of 2m (width: 0.5m, thickness: 4mm). Material against sand outflow was attached throughout the ground to prevent fine soil particles from entering the crushed-stone embankment from the ground.

(5) EMBANKMENT MATERIALS

As the embankment materials the grading of grains crushed-stone C-40 were used. They were banked using 1t or 4-ton roller with doing the compaction administration. The anchors bars for wall were piled according to the progress of embankment and the laying of reinforced material. The coefficient of subgrade reaction K_{30} of 139-184MN/m^3 was obtained in plate loading test at crown of the embankment.

(6) CONCRETE WALL WORK

After placing 900mm-thick concrete foundation, a 300m-thick concrete wall was placed. At the base of the wall, 1m-long D22 anchor bars were installed at an embedded depth of 600mm.

As the existence of a large slip surface under the national road and tunnel of the up-truck was great concern, borehole inclinometers and extensometers were installed in the reconstruction section to allow for dynamic field observations during construction. Only minor displacements were observed, which subsided during construction, and the work was completed without any problems (volume of embankment material: 1767m^3, scale of concrete wall work: 81m^3). (Picture 2)

Pic.2: View of the reconstruction structure
(220k500m)

Around Joetsu Line 221k000m

Damage of embankment

This area is the upper part of the streamside terrace of the Shinano River, and the bedrock is Kawaguchi layer the same as Tenno Tunnel. There is the retaining wall (h=2m) next to the main line, and the national road is along the line. This area has the talus where Ishida River flows into Shinano River, and a slope extension including the embankment is about 120m.The upper collapse part was a surface of the national road, the pavement of the center of the road had sunk. The retaining wall between the national road and Jouetsu Line was also collapsed. And, the railway track bed was flowed out to 65m in the direction of the railway, and it was collapsed 12m in maximum depth and the collapse grade extension 120m. The gravity retaining concrete wall (h=4m) had collapsed on the construction joint. The collapsed earth volume was about 13000m^3. This area collapsed between the up-truck and the down-truck. Therefore, we had to restore the embankment when the single line was restored, and this reconstruction works became the most critical on the reconstruction process in a single track operating. (Picture 6)

Pic.3: Embankment collapse
(around 221k000m Joetsu Line)

Reconstruction by the RRR method

Judging from the result of affected condition, periphery topography and geological boring, it was assumed that the collapse of the embankment was not by sliding in the sedimentary rock layer which was composed the foundation ground but it was resulted from the shear deformation of embankment by the seismic motion. Therefore, as far as the embankment foundation ground concerned, it was assumed that the methods of deterrence works did not have to be done, and the restoration only of the roadbed was advanced. (Figure 4)

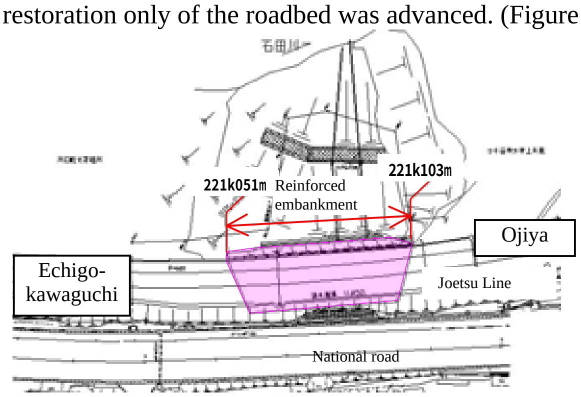

Fig. 4: Reconstruction position (221k000m)

(1)DESIGN OF REINFORCED EMBANKMENT

In parts of RRR method, the height was 13m, and the maximum layer thickness was 41 layers. The length of geotextile (vertical interval 0.3m, design strength Ta=52kN / m) was 5.0～13.0m, and it interval was 1.5m. (Figure 5)

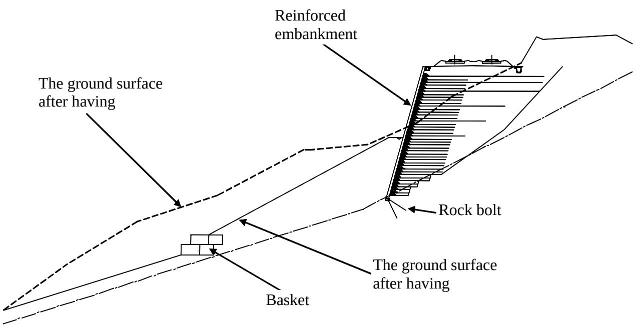

Fig.5: Reconstruction section (221k000m)

(2)EMBANKMENNT MATERIALS

The embankment materials were based on the Design Standard of Railway Structure. These materials have a good permeability and Crushed stone (G-CLS). Thus, it was possible to embankment materials over both of the drain layer part. We could make the reinforced materials short and to decrease the ground excavation quantities for shortening work periods. The excavation quantity of the embankment was 4000m^3.

(3) CONCRETE WALL WORK

The concrete wall was started-up from the foundation ground at a grade of 1:0.3, and it was built by cast in-pile RC (the thickness 300mm, the maximum wall 3.18m). The wall foundation and the bearing ground were united. The horizontal force which works the wall is supported by the bearing ground. We aimed to stabilities the embankment and foundation on the grade by arranging the lock bolts in the wall foundation. The wall was designed including the load which works on the road as the embankments were next to the roadway.

As the construction procedure, firstly, the collapse soil and the upper layer were excavated and took away. Secondly, the rock bolts (L=2.0m and 2.0m pitch) were driven into the soft rock of bearing ground. Finally, the foundation of reinforced retaining wall was cast.

Because of the water catchment geography, we set up the filter layers into the reverse of foundation to enhance drainage. In front of the foundation were set up underdraines. We banked the embankment with laying the reinforced materials to the certain higher (the maximum height 13m). The execution quantity of concrete wall was 159m^3. Concerning the embankment made with the collapse soil of under the reinforced embankment, we set up the mattress shaped gabion in the top of slope and the drainage works in the slope in consideration of drain. (Picture 4)

Pic.4: View of the reconstruction structure (220k000m)

CONCLUSIONS

In this disaster restoration, because of heavy snow region, it was impossible to do emergency restoration works if it snowed heavy. Thus, we selected the most efficient method as possible as we could. As a result, the embankment works were completed for about one month because it was sun-blessed.

Moreover, as for disaster restoration works, the emergency is very important, and it was the emergency structure was adopted. It is usual to perform the restoration works again to fulfill the performance requirement as the permanent structure. In this disaster, we were able to build the permanent structure with enough performance requirements (earthquake-proof and rainfall) by using reinforced embankment method despite of the bad condition of the steep bearing ground. Moreover, it was evaluated that we could shorten the shortening work periods by decreasing the excavation soil at the same time.

Thank you for cooperation and an effort of the general construction contractor and person concerned.

REFERENCES

[1] Y. Taniguchi, H. Morishima, " The damage and reconstruction of railway embankment by Niigata-ken Chuetsu Earthquake ," Geosynthetics Technical Infomation , Mar.2005.

[2] Y. Hagiwara, K. Takamura, " Reconstruction of Joetsu Line embankment by Niigata-ken Chuetsu Earthquake," , TEKKEN CO. Technical Report, Oct. 2005.

[3] F. Aizawa, H. Morishima, " Summary of Niigata-ken Chuetsu Earthquake ," The Journal of Japan Railway Civil Engineering Association, Sep. 2005.

[4] T. Imai, M. Kikkawa, "The damage and reconstruction of the existing line (soil structure) ," The Journal of Japan Railway Civil Engineering Association, Sep. 2005.

[5] H. Morishima, K. Saruya, F. Aizawa, " The damage and reconstruction of soil structure section of the existing line ," The Foundation Engineering & Equipment, Oct. 2005.

Damage of the Shinano River Dike due to The Niigata-ken Chuetsu Earthquake

H.Oshiki[1] and Y. Sasaki[1]
[1]*Japan Institute of Construction Engineering, Tokyo, Japan*

Abstract

This paper describes the damage to the Shinano River dike during the Niigata-ken Chuetsu Earthquake. Those seriously damaged sections of the dike were situated fairly short distance from the epicenter and believed to suffer strong shaking. The dike damage was caused significantly at 17 places reaching total length of 19km. At 3 sections out of 17 sections, the dike damage was apparently induced by soil liquefaction. Besides seriously damaged sections of dike, there was an undamaged section where had been suffered damage during the Niigata Earthquake in 1964. The undamaged section had been strengthened against seepage failure by widening its cross sectional area, and installed gabion at the toe of inland side slope to increase draining function.

Repair works of damaged facilities by this earthquake was conducted smoothly by utilizing classification results of damage focusing on their failure modes.

Keywords— earthquake, soil liquefaction, river dike, damage ratio, repair works

INTRODUCTION

An earthquake named the Niigata-ken Chuetsu Earthquake hit southern area of Niigata Prefecture on October 23, 2004. Main feature of this earthquake is shown in Table 1. Figure 1 shows the location of the epicenter of this earthquake together with the epicenter of the Niigata Earthquake in 1964.

It should be noted that intense aftershocks repeatedly hit the affected area as shown in Fig. 2.

It was reported that 49 persons were killed, 4,794 were injured and 120,391 dwelling houses were damaged during the event in 2004 [1].

This earthquake caused damage to river facilities of the Shinano River as well. This paper summarizes the damage features of the Shinano River dikes.

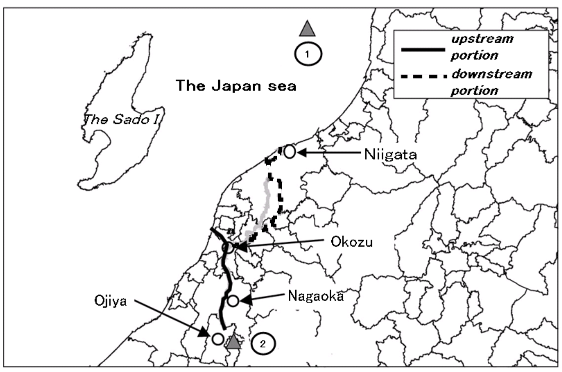

① Epicenter of the Niigata Earthquake in 1964
② Epicenter of the Niigata-ken Chuetsu Earthquake in 2004

Fig. 1 The Epicenters and the Shinano River

Table 1 Main feature of the Niigata-ken Chuetsu Earthquake

Origin Time	17:56, October 23, 2004
Location	37.3N, 138.8E
Depth	13 km
Magnitude	6.8
Max. Intensity	7

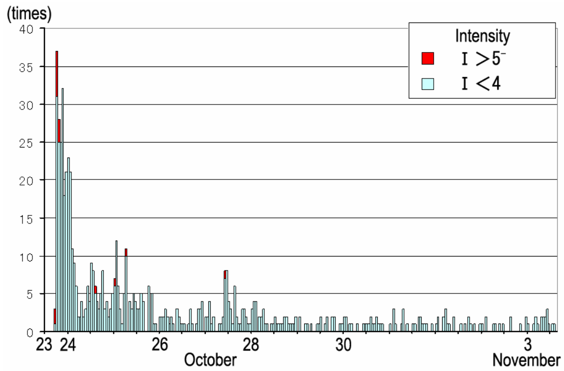

Fig. 2 Frequency of aftershocks

DAMAGED SECTIONS OF THE SHINANO RIVER

Location of Damaged Sections

The Shinano River has its origin at Mt. Hotaka of the Northern Alps in central Honshu and flows into the Japan Sea at Niigata city. The length of 367 km along its river course is the longest in Japan. This river changes its name from the origin to its river-mouth as the Azusa River, the Sai River, the Chikuma River, and the Shinano River.

Niigata district has been hit by large earthquakes two times in these 42 years, namely one was the Niigata Earthquake in 1964 and the other was the Niigata-ken Chuetsu Earthquake in 2004.

Significant damage in 1964 to the river facilities of the Shinano River was seen in the lower reach of the stream illustrated by dashed line in Fig. 1. On the contrary to this, critical damage to the river facilities in the case in 2004 was distributed in fairly limited area of the mid to upper reach of the stream as illustrated by solid line in Fig. 1.

Outline of the damage

Damage detection survey conducted just after the earthquake in 2004 revealed that the Shinano River facilities were damaged more or less at 171 places as shown in Table 2. Fig. 3 shows schematically the location of damaged spots.

Typical damage is shown in Fig. 4. Severe damage to river facilities other than dike was the exfoliation of concrete of the gate pier of the Myoken weir to expose its iron-bars as shown in Fig. 4. The gate was controllable even after this much critical damage.

Table 2 Outline of damage to river facilities

river	Damaged place				
	crack	settlement	Slope failure	weir etc.	total
Kyu Shinano river	1	0	0	0	1
Shinano river	93	16	1	5	115
Uono river	42	6	2	5	55
total	136	22	3	10	171

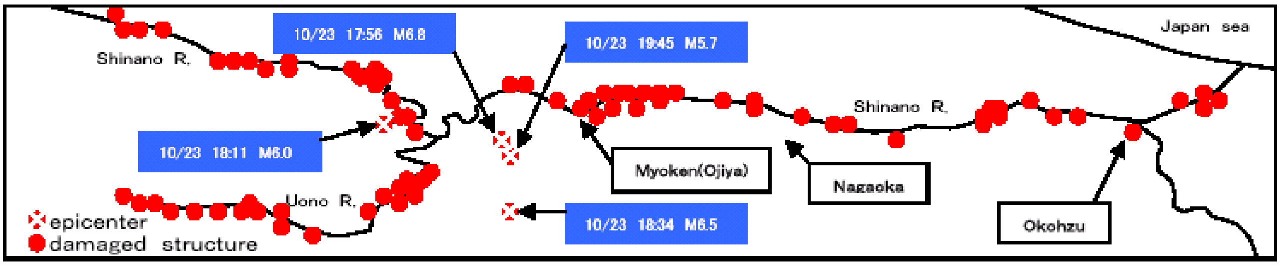

Fig.3 Location of damaged river facilities

a) Nagaro dike

b) Sanbyono revetment

c) Chagogawa sluice

d) Myoken weir (No.8 gate pier)

Fig. 4 Damaged River facilities during the Niigata-ken Chuetsu Earthquake

Precipitation and Water Level in the River Channel

Fig. 5 shows the precipitation observed at Nagaoka in October, 2004 and the water level in the river channel. Typhoon 0423 caused rainfall from October 19 to 21, prior to the occurrence of the earthquake, this was thought to affect the occurrence of slope failure and its inducing disaster [2]. Highest water level in the river due to this rainfall exceeded the altitude of high water channel by about 1-2 m at around midnight of October 21.

It was lucky that the water level rising did not appear after the damage to dikes by earthquake but before the earthquake.

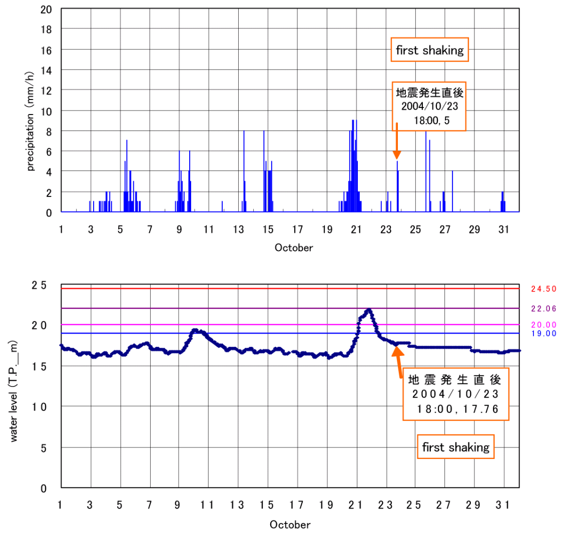

Fig. 5 Precipitation and Water Level (Nagaoka)

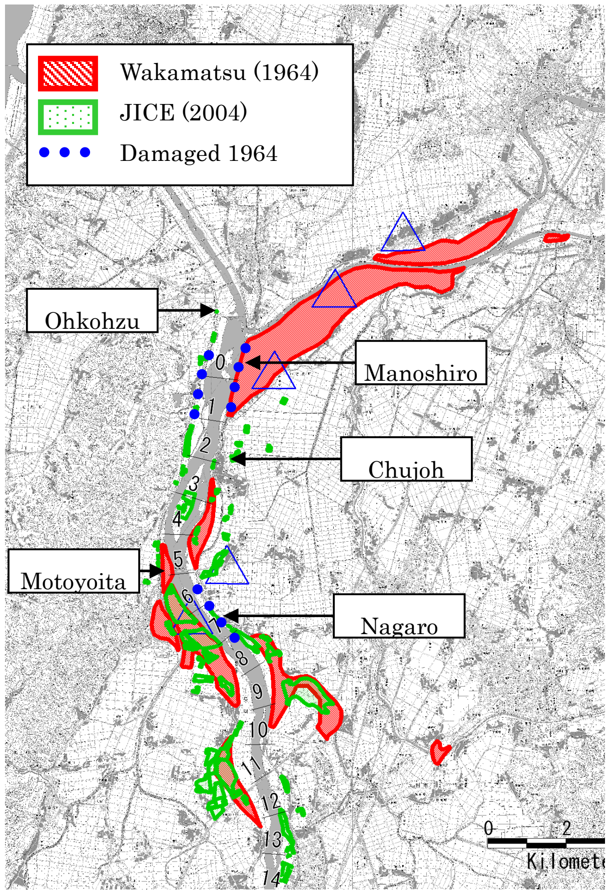

Fig. 6 Liquefied area

Topography, Geology and Soil Conditions around the Affected Sections of the Shinano River

The Shinano River runs together with the confluent stream of the Uono River from Echigo-Kawaguchi and flows in mountainous area down to the entrance of the alluvial fan at around the Myoken weir in Ojiya, from there the river course is surrounded by flood protection dikes in both sides.

Tentative heliport was set on left side high water channel of the river near the Myoken weir for transporting disaster recovery goods to the community of the isolated Yamakoshi village. Downstream from Nagaoka, about 13 km distant from the weir, topography of the surrounding land becomes flat on both sides.

Although thin sand and gravelly layer is deposited around the Myoken weir, alluvium consisting of alternative layers of fine sand, silt and clay becomes thicker gradually towards the downstream from Nagaoka. Thickness of soft soil layer of this alluvium having N value less than 10 is about 15 m at around Ohkohzu.

Fig. 6 shows the distribution of sand boiling spots read from aerial photo nearby the severely damaged dike sections [3]. This figure also shows the area where soil liquefaction was obvious during the Niigata earthquake in 1964 [4].

In the case of 1964, it is well known that soil liquefaction was observed in vast extent in Niigata city from the river mouth of the Agano and the Kyu-Shinano Rivers to 10 km upstream of the Kyu-Shinano River. Comparing to this past case, it is noticed that the liquefied spots during the event in 2004 were distributed more in upstream area from Ohkohzu but did not found in downstream area from Ohkohzu.

DAMAGE TO RIVER DIKES

Failure Mode of Severely Damaged Sections

Among the damage caused to river facilities shown in Fig.-3 and Table 2, severely damaged sections of dike were found at 13 sections on the main stream and at 4 sections on the confluent stream of the Uono River, totally at 17 locations. Out of these 13 sections on the main stream, 10 sections were located between Ohkohzu and Ojiya. Details of those 17 heavily damaged sections are summarized in Table 3. Total length of them reached 19 km as shown in this Table. Those 17 sections of dike were rehabilitated by the aid of the natural disaster relief expenditure.

Dike crest was subsided at 3 sections and part of the crest was settled due to slide of side slopes at 5 sections. Longitudinal cracks were observed on their crest and/or side slopes at almost all sections shown in Table 3. It was judged that those cracks were shallower than HWL at 8 sections, though a section where the cracks were deeper than HWL. Following these damage features, above mentioned 17 sections were classified into six types of failure mode as shown in Table 4. This classification was utilized in selecting repair method.

It should be noted that the Nagaro section damaged in 2004 was also damaged in 1964, and the Manoshiro section shown in Fig. 5, which was located in downstream of the Chujoh section, was not damaged in 2004. This section had been damaged in 1964 and widened its cross section later in 1989.

Three sections of dike classified in Type F (crest subsidence) in Table 4 were considered to suffer from their damage due to soil liquefaction of foundation ground. Those sections are Chujoh, Nagaro, and Motoyoita sections.

Fig. 7 shows the history of the river course movements in these 100 years around these sections. From this figure, it is known that these three sections had experienced following situations in these 100 years.

The Chujoh dike had existed as is situated at same location as present. This part of river course had been

Table 4 Classification of failure mode of dikes

type	failure mode	features	places	distance (m)	
A	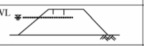 HWL	longitudinal cracks (shallower than H.W.L)	8	6,997	
B	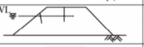 HWL	longitudinal cracks (deeper than H.W.L)	1	449	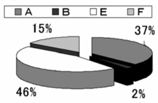
C	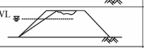 HWL	transverse cracks (shallower than H.W.L)	—	—	
D	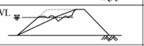 HWL	transverse cracks (deeper than H.W.L)	—	—	
E	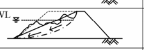 HWL	slide of slope (failure of crest)	5	8,659	
F	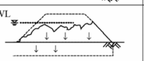 HWL	total collapse of crest no original shape remaining (liquefaction of foundation)	3	2,871	
			17	18,976	

Table 3 Severely damaged sections

No	Location	L: Left bank R: right bank Distance mark	Length (m)	Damage features	Type			
					A	B	E	F
1	南蒲原郡中之島町真野代新田～中条地先	R NO.10k+0～NO.2.5k-27m	1,422	Longitudinal cracks on crest (deeper than HWL) Slide of slope and bulging	○	○	○	○
2	三島郡与板町本与板地先	L NO.4.0k-20～NO.4.5k+334m	889	Longitudinal cracks on crest and slope (both shallower and deeper than HW L) subsidence of crest (bulging)	○	○	○	○
3	長岡市李崎地先	L NO.6.0k+380～NO.6.5k+70m	310	Longitudinal crack on crest, slide of slope and berm (shallower than HWL)	○	○	○	
4	南蒲原郡中之島町長呂地先	R NO.6.0k+215～NO7.0k-100m	520	Longitudinal cracks on crest (deeper than HWL) Slide of slope and bulging	○	○	○	○
5	長岡市山田町地先	R NO.18.0k+100～NO.18.0k+150m	50	Slide of slope			○	
6	長岡市草生津～大宮地先	R NO.18.2k-80～NO.19.5k-40m	1,530	Longitudinal crack on crest	○			
7	長岡市水梨地先	R.20.5k+50～NO.20.75k+80m	240	Longitudinal crack on crest	○			
8	長岡市南陽～前島地先	R NO.22.0k-120～NO.23.25k+90m	1,470	Longitudinal cracks on crest	○			
9	三島郡越路町浦～長岡市三俵野地先	R NO.24.5k-50～NO.29.5k-53m	5,050	Longitudinal cracks on crest (deeper than HWL) Slide of slope and bulging	○	○	○	
10	三島郡越路町釜ヶ島～小千谷市五辺地先	L NO.25.5k+95～NO.28.5k+198m	3,055	Longitudinal cracks on crest (lower than HW L) Slide of slope and bulging	○		○	
11	小千谷市上片貝地先	L NO.38.5k+165～NO.39.0k+108m	365	Longitudinal cracks on crest	○			
12	北魚沼郡川口町西川口地先	Uono r, L NO.0.75k+99～NO.42.0k+385m	707	Longitudinal cracks on crest	○			
13	小千谷市川井（下流） 地先	R NO.45.0k-70～NO.45.0k+425m	495	Longitudinal crack on crest (shallower than HWL) Sliding failure of revetment of 290m	○			
14	小千谷市川井（上流） 地先	R NO.45.5k-180～NO.46.5k+260m	1,340	Longitudinal cracks on crest		○		
15	北魚沼郡川口町西川口地先	Uono r, L NO.1.5k+65～NO.1.75k+55m	194	Longitudinal cracks on crest		○	○	
16	魚沼市新道島地先	Uono r, R NO.6.0k-348～NO7k+96m	836	Longitudinal cracks on crest (shallower than HWL) sliding failure of revetment of 655m（1200m）		○		
17	魚沼市下島地先	Uono r, L NO.6.75k-5～NO.7.0k+200m	449	Longitudinal cracks on crest (shallower than HWL)		○		

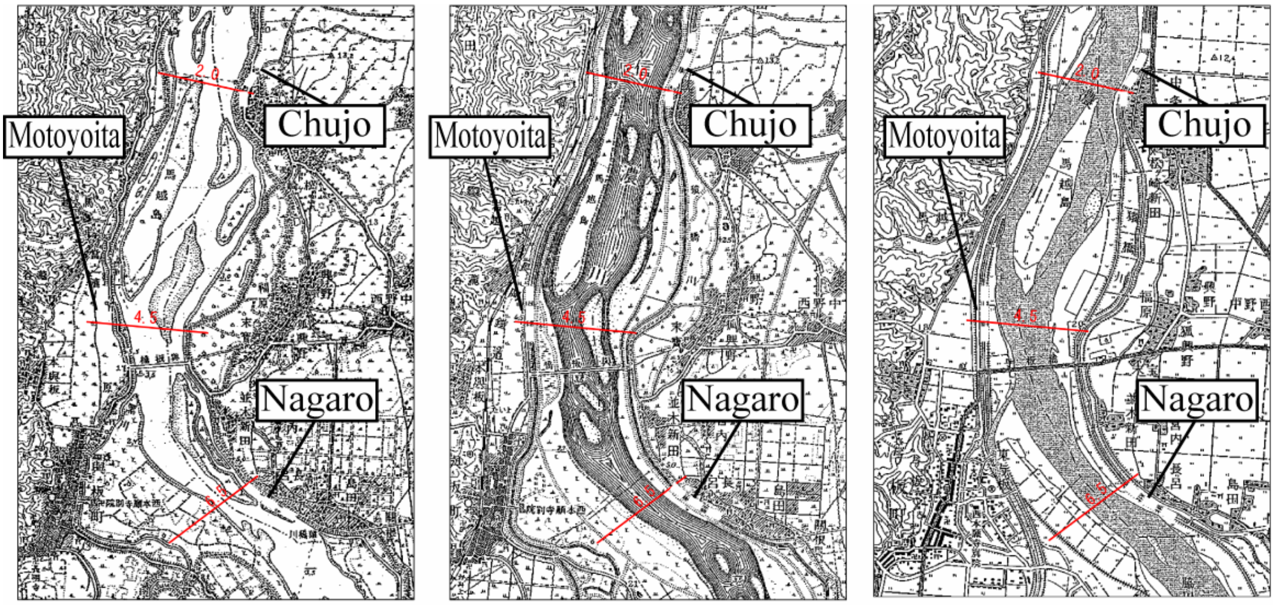

a) 1911 b) 1952 c) 1995

Fig. 7 History of river channel and the 3 sections

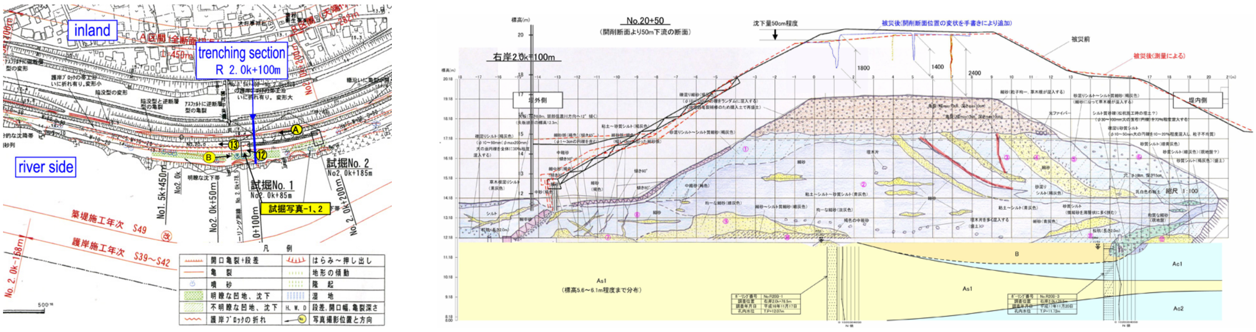

Fig. 8 Trenching survey at the Chujoh section

water colliding front 100 years ago too. Current location of the Nagaro dike had been a confluence place of the Saruhashi River 100 years ago, so no dike had been located at this place at that time. Present location of the Motoyoita dike had been on paddy field in mid of backswamp100 years ago.

Damage features at these three sections are summarized below.

Chujoh Section (2 km on right bank)

Figs. 8 and 9 show the results of trenching survey and damage features at this section.

Many longitudinal cracks were caused on top crest and side slopes in this section. Maximum depth of these fissures was 220 cm. Continuous cracks and sand boiling were also seen at river side toe of the dike. River side shoulder subsided by about 45 cm. Revetment on river side slope opened at its joints and bulged as shown in Fig. 9.

The high water channel at this section is formed by loosely deposited soil due to sedimentation effect of series of groynes. Several widely opened cracks and sand boiling were also seen on this high water channel.

The F_L value of foundation ground indicated that sand layer about 6 m thick (N<10) beneath the dike had been caused liquefaction against 400 cm/sec^{2}of PGA, which was estimated from epicentral distance and main shock magnitude.

Nagaro Section (6.5 km on right bank)

Center of the top crest subsided by more than 1 m, and many longitudinal fissures were observed at this section. A fissure on land side berm was 20 cm wide and 200 cm deep. Land side slope was deformed as if it slid towards the Saruhashi River which is flowing nearby the toe of the dike section parallel to the Shinano River.

Figs. 10 and 11 show the results of trenching survey and damage features at this section. It was judged that the sand layer (N<10) beneath the dike was caused liquefaction for about 2 m because the F_L value of this layer was less than 1.0.

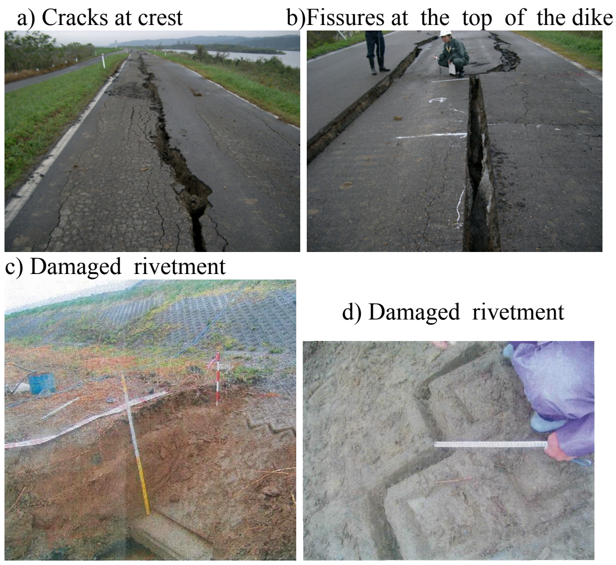

Fig. 9 Damage at the Chujoh section

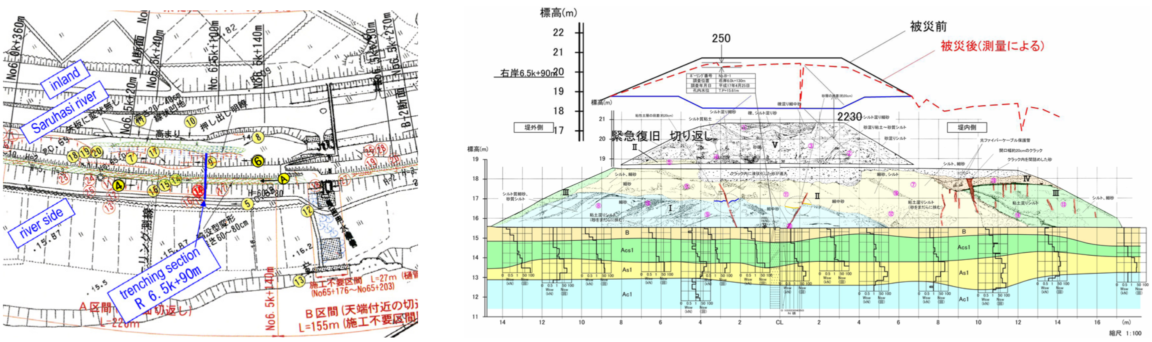

Fig. 10 Trenching survey at the Nagaro section

Motoyoita Section (4.5 km on left bank)

Large scale cracks were found on both shoulders at crest accompanied by crest settlement by 80-100 cm at this section. Many more fissures and bulging were seen at river side slope than at land side slope. Sand boiling was observed around the river side toe. And at land side toe, concrete made sheet piles were inclined by being pushed towards the Kyu-Kuro River which is flowing nearby the toe of the dike section parallel to the Shinano River.

Figure 12 and 13 show the results of trenching survey and damage features at this section. It was known that the construction material of this dike was sandy soil and the foundation ground was covered by soft compressible clay layer at its surface. So it was judged that the subsided sandy soil of dike bottom about 2 m thick (N<10) was caused liquefaction because the F_L value of this layer was less than 1.0.

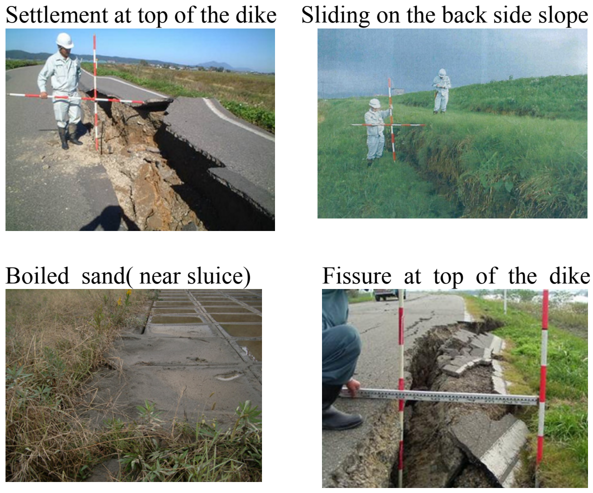

Fig. 11 Damage at the Nagaro section

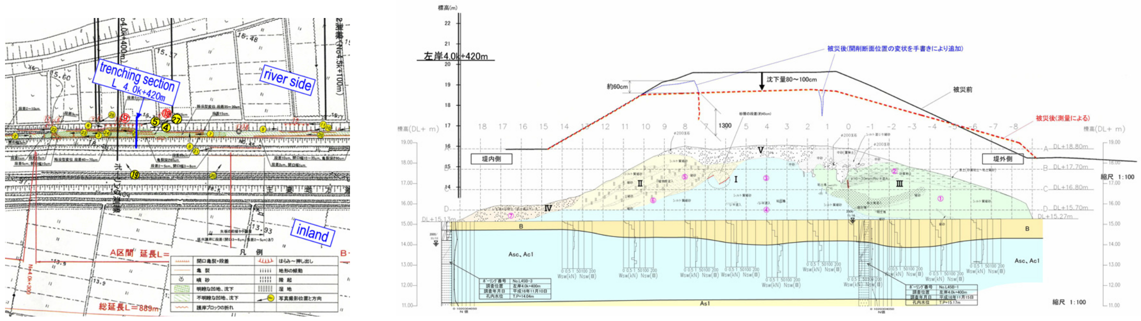

Fig. 12 Plan of the Motoyoita section

Undamaged Dike (Manoshiro Section)

Other than damaged sections, there was an undamaged section where failure of dike had been experienced during the Niigata Earthquake in 1964 as mentioned before. That is the Manoshiro Section located downstream of the Chujoh section. This section had been constructed in an old river channel as shown in Fig.14 during the construction the Ohkohzu discharging bypass channel.

After the repair work of the damage caused by the Niigata Earthquake in 1964, this section of dike had been strengthened by widening its cross sectional area in 1989 as shown in Fig. 15. Although the purpose of this

Fig. 13 Trenching survey (Motoyoita section)

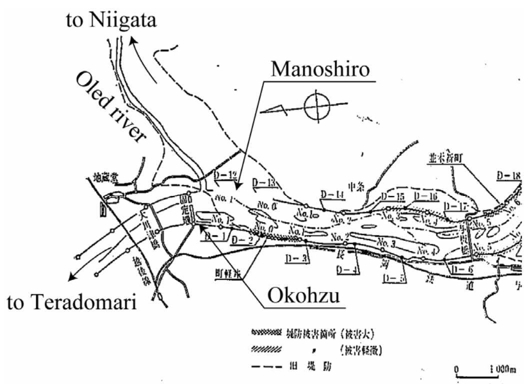

Fig. 14 Location of the Manoshiro Section

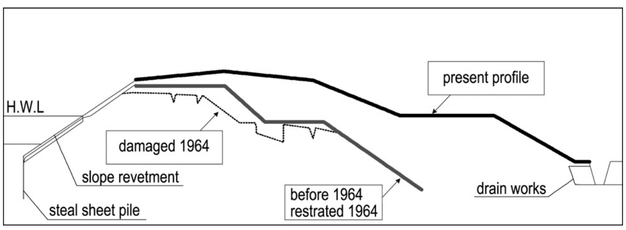

Fig. 15 Cross section profile of Manoshiro section

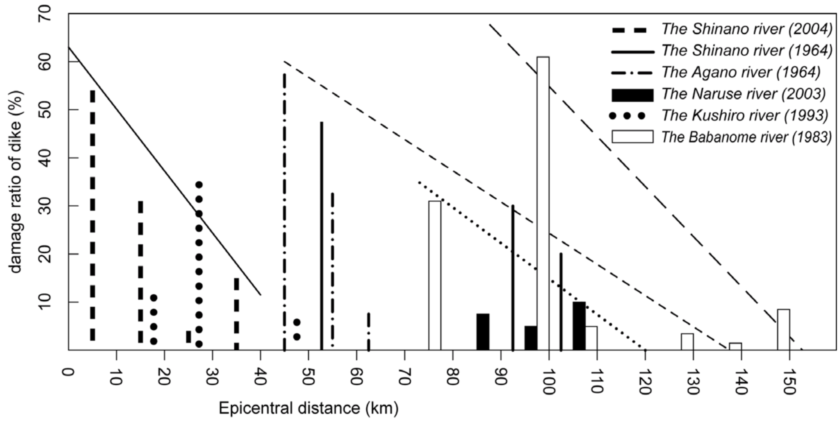

Fig.16 Damage Ratio of Dike versus Epicentral Distance

strengthening was to give more resistance against seepage failure, it was known that a widened dike behaved well against earthquake.

Damage ratio of the Shinano River Dike during the Niigata-ken Chuetsu Earthquake

Fig. 16 shows damage ratio of the Shinano River dikes during the earthquake together with other cases in the past. Damage ratio in this figure is gained as a ratio of lengths of restored section by the natural disaster relief expenditure over lengths of existing dikes in 10 km interval of epicentral distances.

It is known from this figure that the decreasing tendency of the damage ratio with epicentral distance in the case of the Shinao River in 2004 was similar to past experiences. However, quantitative amount of them were smaller than that in the past cases. Although it might be brought from the situation that the liquefiable deposit of alluvium was not thick beneath the dike, the clear reason of this is not known at this stage.

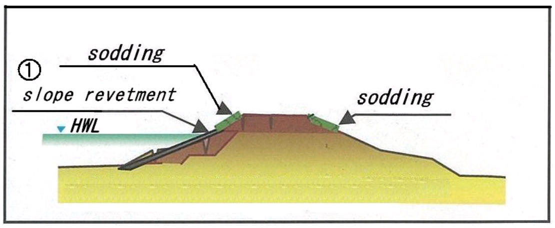

a) type A,B,C,D and E
(① : above mentioned 2))

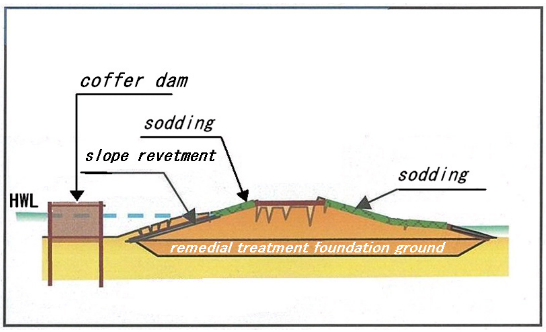

b) type F

Fig.17 Schematic illustration of repair methods for damaged dike

REPAIR WORKS OF DAMAGED DIKE

Repairing strategy

Selection of the method of repair works for each damaged section of dike was conducted smoothly by utilizing the classification of dikes by failure mode shown in Table.4.

Followings are the outline of the repair method for each type of damaged mode:

1) Type A and C: to ditch cracked portion of the damaged dike to bottom of cracks and re-compact the filled materials as was before.
2) Type B, D and E (river side slope): same as above 1) + installation of revetment.
3) Type B, D and E (other than river side slope): same as above 1).
4) Type F: to remediate liquefiable foundation soil, then reconstruct the dike.

Figure 17 shows schematic illustration of these repair methods.

Repair methods for three sections where damage was apparently caused by soil liquefaction are as follows:

Chujo section

Sand compaction pile method was selected for this section. Treated distance was 450m long along the axis of dike, and treated depth was 6.25 ～7.0m.

Fig. 18 shows the repair works at this section.

Fig. 18 Repair works (Chujoh section)

Nagaro section

The remedial treatment of this section was decided to conduct with the stabilization by cement mixing, because the liquefiable layer was considered to exist only in shallow part of the ground. Treated length of the section was 220 m and the treated thickness was 3 m.

Repair works at this section is shown in Fig. 19.

Fig. 19 Repair works (Nagaro section)

Motoyoita section

The remedial treatment of this section was decided to use the stabilization by cement mixing too. Treated length of the section was 225 m and the treated thickness was 2.6 m.

Repair works at this section is shown in Fig. 20.

Fig. 20 Repair works (Motoyoita section)

CONCLUSION

It was shown that the affected dikes of the Shinano River were suffered to earthquake damage twice in these 42 years. Damage features of these cases are summarized as follows:

- By the event in 1964, river dikes located in northern district in Niigata Prefecture were damaged at many places in vast extent. Those damaged sections had been concentrated mostly to downstream of the Shinano River, namely Kyu-Shinano River, Agano River and others.
- During the earthquake in 2004, most of the river dike damage was found in comparatively limited area in mid to upstream of the Shinano River, where the thickness of the alluvium was comparatively thin.

As for the case in 2004, damage features of river dikes are summarized as followings.

- Severely damaged sections of dike were found at 17 locations out of more than 100 spots where damage was detected.
- At three sections out of above 17 sections, it was known that the dike damage was apparently induced by soil liquefaction.
- At the Manoshiro section where the cross sectional area had been enlarged did not suffered any deformation during the event in 2004, though had been caused significant deformation in 1964.
- Location of these 17 sections can be summarized in damage ratio against epicentral distance graph as shown in Fig. 16.
- Classification of damaged sections according to their failure mode effectively aided to make decision on the repair methods in such a confused state after the big earthquake.

ACKNOWLEDGMENTS

Damage detection survey on river facilities of the Shinano River was basically conducted under the direction of the Shinano River Work Office, Ministry of Land Infrastructure and Transportation. Permission to use the investigated results given to authors by the Shinano River Work Office is gratefully acknowledged.

REFERENCES

[1] Niigata Prefecture," Information about the Niigata-ken Chuetsu Earthquake", http: // saigai.pref.niigata.jp / content /jishin/ jishin_1.html 2005

[2] Nakai, S., Kaibori, M., Sasaki, Y., Moriwaki, T. and Kano, S., "Applicability of Rainfall Index R' for Recent Cases in 2004 - 2005" , 2nd Japan - Taiwan Joint Workshop on Geotechnical Hazards from Large Earthquakes and Heavy Rainfall, May 18 - 20, 2006, Nagaoka, Japan

[3] Japan Institute of Construction Engineering ,"The Report on the Technical Investigations and Analysis on Damage of the Shinano River Dike due to the Niigata-ken Chuetsu Earthquake", report to The Shinano River Work Office, Ministry of Land Infrastructure and Transportation (in Japanese), 2005.

[4] Wakamatsu, K., "Map of soil liquefaction spots during past earthquakes in Japan", 1991.

Analyses for the Settlement of Damaged Embankments during the Niigataken-chuetsu Earthquake based on a Unified Stress-strain Relationship of Liquefied or Softened Soils

S. Yasuda[1], M. Inagaki[2] , H. Itakiyo[3], S. Yamada[4] and K. Kasuda[4]
[1] *Tokyo Denki University, Saitama, Japan*
[2] *Central Nippon Expressway Company, Ishikawa, Japan*
[3] *Central Nippon Expressway Company, Tokyo, Japan*
[3]*Kiso-jiban Consultants, Co., Ltd., Tokyo, Japan*

Abstract

The 2004 Niigataken-chuetsu earthquake brought large settlement of highway embankments of Kan-etsu Express Way in Japan. The authors tried to evaluate the settlement of the embankments by an analytical code ALID to study the mechanism of the settlement. In the analyses, a unified relationship among shear modulus of liquefied sands or softened clays, undrained cyclic shear strength and safety factor against failure, was used. The unified relationship has been obtained by cyclic torsional shear tests for many undisturbed and disturbed samples. Analyzed results showed that the evaluated deformation was fairly coincided with the measured deformation.

Keywords—*Embankment, analysis, earthquake*

INTRODUCTION

During the 2004 Niigataken-chuetsu earthquake, highway embankments of Kan-etsu Express Way settled several ten cm at many sites in Ojiya City. Sand boils were not observed at the damaged sites. Soil investigation at the damaged two sites showed that the surface soils were mainly clayey soils.

Then, the authors tried to evaluate the settlement by using an analytical code "ALID" to study the mechanism of the settlement. In the analyses, a unified relationship among shear modulus of liquefied sands or softened clays, undrained cyclic strength and safety factor against failure, was used. The unified relationship has been obtained by cyclic torsional shear tests for many undisturbed and disturbed samples, which were taken at 24 sites in Japan.

DAMAGE TO HIGHWAY EMBANKMENTS OF KAN-ETSU EXPRESS WAY DURING THE 2004 NIIGATAKEN-CHUETSU EARTHQUAKE

On October 23 in 2004, the Niigataken-chuetsu earthquake, of Magnitude 6.8, occurred in Japan. The maximum surface acceleration recorded at Kawaguchi town was 1722 Gals. Many railways including Shinkansen, roads, houses, pipelines and other structures were severely damaged. Moreover, huge number of landslides, more than 1700, occurred and hit many towns and villages, including Yamakoshi village. The slid soils dammed up rivers and made natural dams.

In Kan-etsu Expressway, highway embankments between Horinouchi IC and Nagaoka IC were damaged. Especially, the damages in two areas; "A" aria and "B" aria, as shown in Fig.1, were serious. In the "A" Aria, the

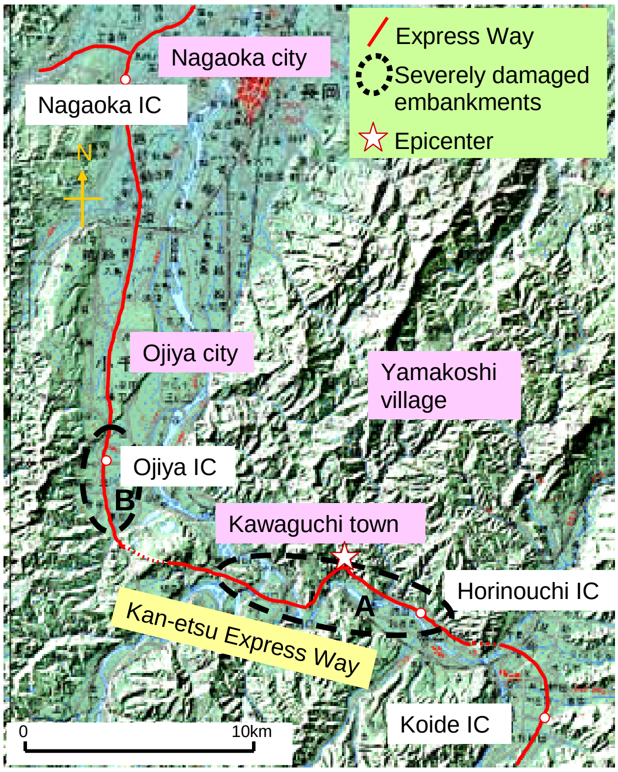

highway between Horinouchi IC and Kagaguchi IC road was constructed by cut and fill method on the slope of hill. Sliding of filled embankments occurred at several sites.

On the contrary, in the "B" area, the highway between Kawaguchi IC and Nagaoka IC was constructed

Photo 1 Damaged highway embankment of Kan-etsu Express way in Ojiya city

Photo 2 Settlement of the surface of highway (Gravelly ground)

Photo 3 Settlement of the surface of highway (Clayey ground)

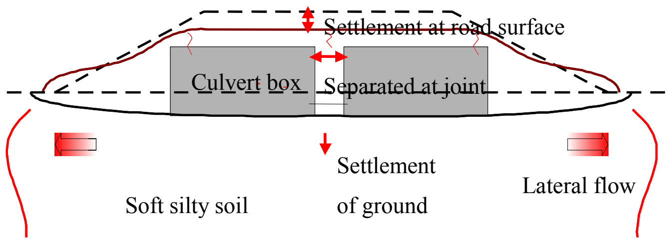

Fig.2 Schematic diagram of deformation of damaged road embankments (Clayey ground)

by filling soils on lowland plain as shown in Photo 1. Surface soil of the plane is gravel, sand or clay. Height of the embankment is 5 to 9 m. Many underpasses cross the road embankment. Underpasses were constructed by concrete culvert boxes. Due to the Niigataken-chuetsu earthquake, highway embankments settled several ten cm as shown in Photos 2 and 3. In clayey ground, near Ojiya IC, culvert boxes and grounds deformed as schematically shown in Fig.2. Both side of toes of the road embankment spread in lateral direction as shown in Photo 4. Culvert boxes settled and separated at joints as shown in Photo 5. Embankment soil fell down through the opened joints Due to the spread, the ground adjacent the embankment moved laterally as shown in Photo 6.

CYCLIC TORSIONAL TESTS TO OBTAIN STRESS-STRAIN CURVES OF LIQUEFIED SANDS OR SOFTEND CLAYS

Yasuda et al. (1999) proposed a static analysis method named "ALID (Analysis for Liquefaction-Induced Deformation)" to estimate large deformation of liquefied ground. In the method, stress-strain curves of liquefied soils are used. They conducted cyclic torsional tests to obtain the stress-strain curves of liquefied sands (Yasuda et al. (1999)). In the test, three reconstituted samples and a series of undisturbed samples were tested. In addition, many undisturbed samples of sandy soils and clayey soils were taken for tests (Yasuda et al., 2004). Then test results were combined and proposed a unified relationship. Total number of tested samples and specimens were 53 and about 400, respectively.

In the tests, samples were trimmed to become hollow cylindrical specimens. Outer diameter, inner diameter and height of the specimen were 7 cm, 3 cm and 7 cm, respectively. Then the specimens were saturated and consolidated. Confining pressure, σ_c' was adjusted as in-situ effective overburden pressure. After the consolidation, 20 cycles of cyclic loading with 0.1 cycles/sec. was applied to the specimens as shown in Fig.3 under undrained condition. Then, a monotonic loading was applied under undrained condition with a speed of 10 % of shear strain/minute.

Photo 4 Lateral spread of highway embankment (Clayey ground)

Photo 5 Separated joint of culvert boxes and fallen soils of embankment (Clayey ground)

Photo 6 Moved adjacent ground (Clayey ground)

Time histories of shear stress, shear strain and pore water pressure during the monotonic loading were measured. About 4 to 8 specimens were used in one sample. And, different amplitude of cyclic loading was applied to each specimen to control safety factor against

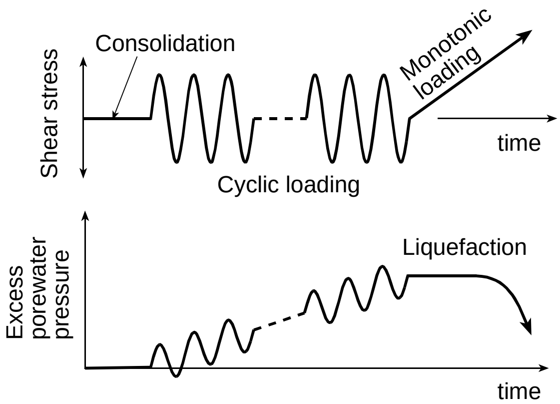

Fig.3. Procedure of cyclic and monotonic loading

liquefaction, F_L, which implies severity of liquefaction or failure, mentioned later. In addition, static tests to apply monotonic loading only were carried out. These tests were called as "static" in this paper.

As mentioned above, different amplitude of cyclic loading was applied to each specimen. Then, relationships between cyclic stress ratio, τ_d/σ_c' and double amplitude of shear strain at 20th cycle, γ_{DA} (N=20) were plotted. And, the stress ratio to cause 7.5 % of shear strain by 20 cycles, R_L(γ_{DA}=7.5 %, N_L=20) was estimated. This stress ratio is same as the stress ratio to cause liquefaction, R_L(ε_{DA}=5 %, N_L=20) in cyclic triaxial tests for sandy soils. Therefore, this stress ratio means liquefaction strength in sandy soils. In clayey soils, this must imply a stress ratio to cause a kind of failure and must be said as undrained cyclic shear strength.

Figure 4 shows relationships between R_L(γ_{DA}=7.5 %, N_L=20) and fines content, F_C. The R_L(γ_{DA}=7.5 %, N_L=20) increased with F_c.. Figure 5 shows relationships between R_L(γ_{DA}=7.5 %, N_L=20) and Plasticity Index, I_p. The R_L(γ_{DA}=7.5 %, N_L=20) increased with I_P also. These two relations mean the R_L(γ_{DA}=7.5 %, N_L=20) of clayey soils is greater than the R_L(γ_{DA}=7.5 %, N_L=20) of sandy soils. However, if a very strong earthquake hit a clayey ground, large stress ratio such as 0.5 induces in the ground. This means that some failure may occur in clayey grounds same as liquefaction in sandy grounds.

To clarify what kind of failure occurs in clayey grounds, excess pore water pressure ratios at 20th cycle of just liquefied or failed specimens (F_L=1.0) were plotted with Fc in Fig.6. Here F_L was defined as follows:

$$F_L=R_L(\gamma_{DA}=7.5\ \%, N_L=20)/(\tau_d/\sigma_c') \qquad (1)$$

where, τ_d/σ_c': applied stress ratio.

The excess pore water ratio decreased with F_c. as shown in Fig.6. It is clear that the pore water pressure ratio decreased with F_c. up to 0.2. This means that, in clayey soils, effective stress in the soil does not decease to zero due to cyclic loading, even though large shear strain occurs. Therefore, some resistance or shear modulus

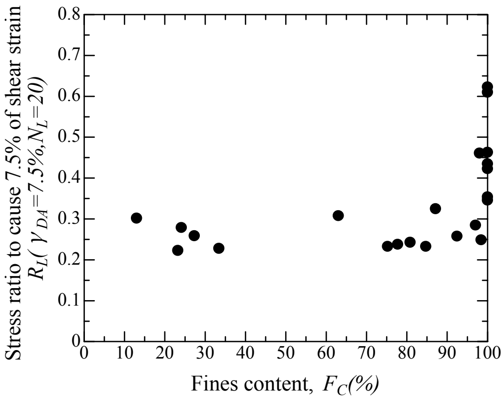

Fig.4. Relationship between R_L and F_c

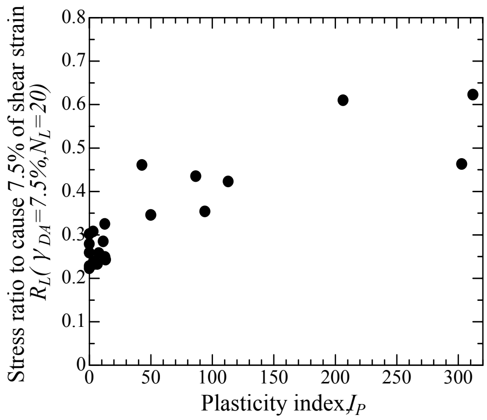

Fig.5. Relationship between R_L and I_P

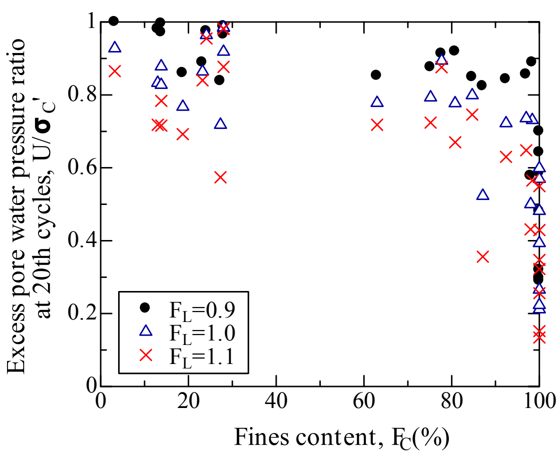

Fig.6 Relationship between F_c and excess pore water pressure ratio of liquefied or failed specimen

would remain in clayey ground even if very strong earthquake hit the ground. This phenomenon must be called not "failure" but "softening".

STRESS-STRAIN CURVES OF LIQUEFIED SANDS OR SOFTENED CLAYS

Typical time histories of shear stress and excess pore water pressure during monotonic loading for silty sand, sandy silt and peat are shown in Figs.7 to 9. Scales of axes in (c) are enlarged ones of (a). In silty sand, stress-strain curve under static loading was normal. Namely shape of the curve was convex. However, the shapes of stress-strain curves of liquefied specimen (F_L <1.0) were different. Shear strain increased with very low shear stress up to large strain. Then, after a resistance transformation point, the shear stress increased comparatively rapidly with shear strain, following rapid decrease of pore water pressure. The shear strain up to the resistance transformation point increased with the decrease of F_L. This behavior is similar as the one in clean sand (Yasuda et al., 1998, 1999).

In peat, shear stress at certain shear strain slightly decreased with F_L as shown in Fig.9 However, stress-strain curves of the peat were normal even F_L <1.0. And, stress strain curves of softened specimens were not so different from that of the specimen tested under static loading only. This behavior is different from the behavior of liquefied sands.

Stress-strain curves for sandy silt were intermediate between those of silty sands and peat.

Then the authors classified the shape of the stress-strain curves into two types as shown in Fig.10. Type A corresponds to the stress–strain curve for liquefied sandy soils. Type B is the stress-strain curve for softened clays or peat. In type A, stress-strain curves before and after the resistance transformation point can be presented approximately by a bilinear model with G_1, G_2 and γ_L as same as for clean sand (Yasuda et al., 1999). The G_1

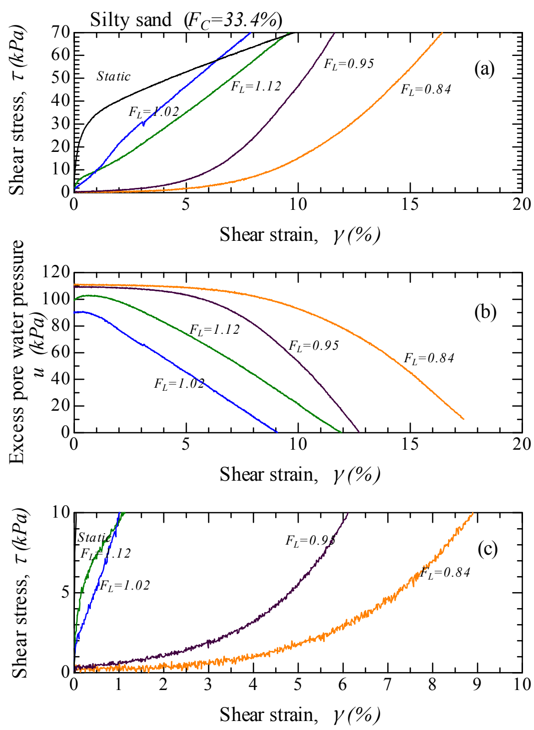

Fig.7. Time histories of shear stress and pore water pressure for a silty sand

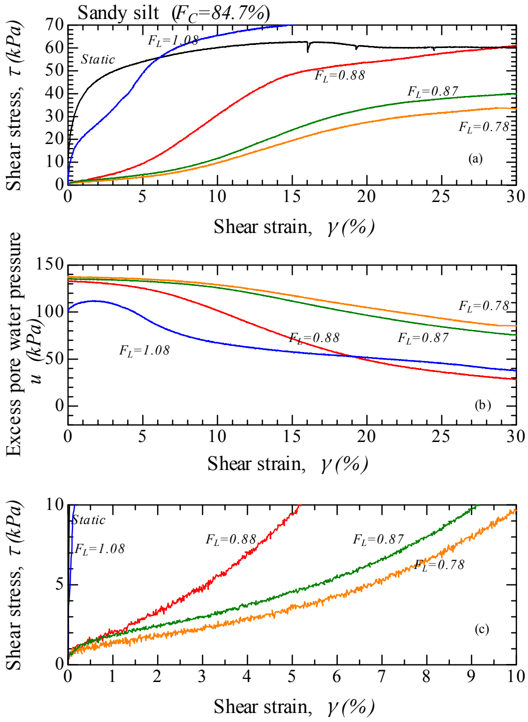

Fig.8. Time histories of shear stress and pore water pressure for a sandy silt

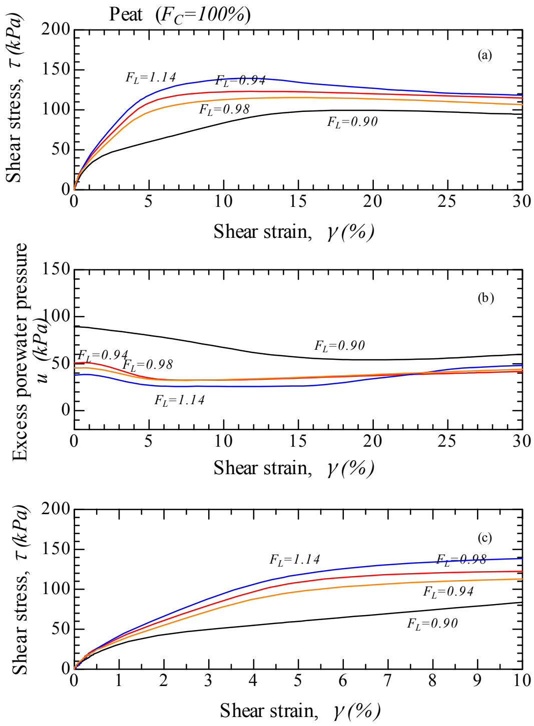

Fig.9. Time histories of shear stress and pore water pressure for a peat

means shear modulus of a liquefied soil. The γ_L is influenced by grain size, density, F_L and other factors. When F_L=0.9, it was about 5 to 20 % for loose sands. In type B, it is necessary to select reference strain to define

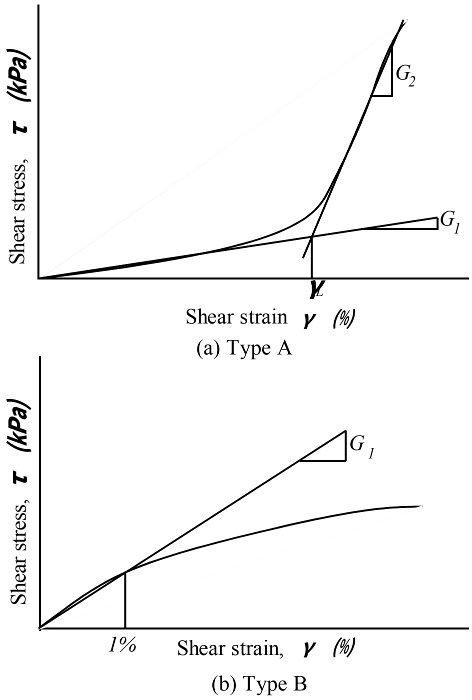

Fig.10. Classification of stress-strain curves of liquefied sandy soils and softened clayey soils

shear modulus, G_1. In clayey ground, it seems that large shear strain does not induce due to earthquake because some amount of resistance remains after cyclic loading, mentioned before. Therefore the authors defined shear modulus of softened soil, G_1 as the secant modulus at 1% of shear strain as shown in Fig.10 (b).

Then the liquefied or softened shear moduli, G_1, were estimated for all stress-strain curves. In sandy silt, two values of G_1 defined by Type A and Type B were estimated. And, smaller value was judged as G_1. Then, by plotting the relationships between G_1 and F_L, G_1 at F_L=0.8, 0.9, 1.0, 1.1 were estimated.

A UNIFIED RELATIONSHIP AMONG G_1/σ_c', R_L AND F_L

Yasuda et al.(1998, 1999) proposed a relationship among reduction rate of shear modulus G_1/G_0, F_L, and F_c. However, this relationship cannot be extended to clayey soils because the parameter of F_C is not suitable for clayey soils.

Then the authors tried to find out a new relationship. As shown in Fig.5, R_L(γ_{DA}=7.5 %, N_L=20) increased with I_P. Though a figure is not shown in this paper, G_1 increased with I_P also. Then, it seemed the parameter R_L(γ_{DA}=7.5 %, N_L=20) must be introduced in the new relationship. This value is easy to evaluate because many simple formula to estimate R_L(γ_{DA}=5 %, N_L=20) based SPT N-value have been proposed. One more parameter to be introduced in the relationship must be σ_c'.

Then, the authors selected the relationship between

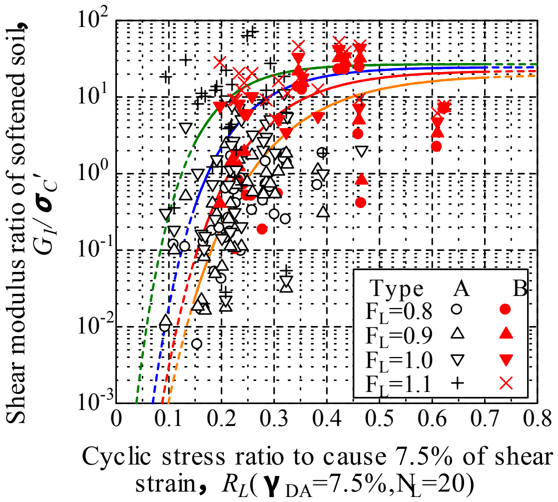

Fig.11 Relationship between G_l/σ_c' and R_L for F_L=0.8, 0.9,1.0 and 1.1 (Yasuda et al., 2004)

Fig.12 Location of detailed investigated sites

G_l/σ_c', $R_L(\gamma_{DA}$=7.5 %, N_L=20) and F_L, and plotted on Fig.11. In these figures, all data conducted by Yasuda et al.(1999) and Yasuda et al.(2004) are plotted. As shown in these figures, G_l/σ_c' increased with $R_L(\gamma_{DA}$=7.5 %, N_L=20) and F_L. And, all plotted points were concentrated in comparatively narrow bands in each F_L. Thus a unified relationship for all samples can be derived as follows:

$$G_1/\sigma_c' = ae^{(-\exp(-b(R_L-c)))} \qquad (2)$$

where,

$$a = 23.6F_L + 0.98,$$
$$b = 9.32F_L^3 - 10.8F_L^2 + 13.27F_L - 0.806,$$
$$c = -1.40F_L^3 + 3.87F_L^2 - 4.14F_L + 1.95$$

DETAILED SOIL INVESTIGATION AND ANALYSES FOR THE SETTLEMENT OF DAMEGED EMBANKMENTS

To demonstrate the mechanism of the settlement of the highway embankments during the 2004 Niigataken-chuetsu earthquake, the authors selected two sites; Ojiya No.2 and Kawaguchi No.22 between Kawaguchi IC and Nagaoka IC, for detailed soil investigation. Figure 12 shows locations of two sites, together with K-net Ojiya Site, where accelerograph is installed. The maximum surface acceleration recorded at K-net Ojiya Site was 1314 cm/s^2 in EW direction. Surface soil conditions at Ojiya No.2 and Kawaguchi No.22 sites, investigated after the earthquake, are shown in Fig.13 and 14. Soils for embankments at two sites are clayey soils with 70 % of fines. Heights of the embankments at two sites are 5.3 to 5.6 m and 5.6 to 6.8 m, respectively. A thin soft silt layer with 2 m thickness is deposited under the embankment at Ojiya No.2. Then, silty sand, silt, sandy silt and silt layers, with 10 to 20 of SPT *N*-values, were underlaid to the depth of 24 m. At Kawaguchi No.22, thick soft silty layers, with about 5 of SPT *N*-values, are deposited to the depth of 16 m. As mentioned before, large settlement and spread occurred at this area. The settlement of surface of road at Ojiya No.2 and Kawaguchi No.22 were 65 cm and 70 cm, respectively. Opening of the joints of culvert boxes at Ojiya No.2 and Kawaguchi No.22 were 75 cm and 30 cm, respectively.

Based on the soil conditions, analyses for deformation due to the earthquake were conducted by using analytical code “ALID/Win (Yasuda et. al., 1999) ”. In this code, finite element method is applied in the following steps:

i) In the first step, the deformation of the ground before earthquake is calculated by using the stress-strain relationships of intact soils.

ii) The deformation of the ground due to liquefaction or softening is calculated in the second step, by using the stress-strain relationship of liquefied or softened soils.

iii) Finally, deformation of the ground due to the dissipation of excess pore pressure is calculated based on the simple relationships among volumetric strain, F_L and relative density proposed by Ishihara & Yoshimine(1992). The author studied the adaptability of the ALID/Win to various structures, such as settlement of raft foundations, floatation of buried structures and flow of the ground behind sea walls.

In the analyses for the damaged embankments, cyclic shear stress induced in the grounds and embankments during the Niigataken-chuetu earthquake were estimated by the simple method introduced in the specification for highway bridge (2002) based on the recorded maximum surface acceleration. As the grounds at two sites are silty soil, stress ratio to cause failure, R_L was estimated from unconfined compressive strength q_u by using the relationship between R_L and $(q_u/2)/\sigma_v'$ as show in Fig.15, which was derived by the authors. Then the distribution of F_L values was estimated for two sites.

Reduction rate of shear modulus of embankment and unsaturated layer upper layer due to shaking, were assumed as 1/40 and 1/10, respectively base on the previous study (Yasuda et al., 2003).

Deformations of embankments and grounds before and after earthquake are shown in Fig 16(a) and 16(b).

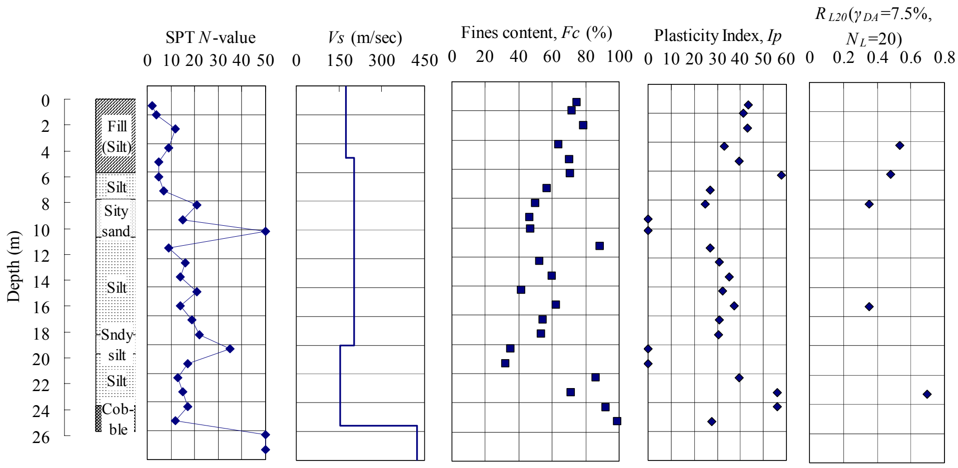

Fig.13 Soil profile and tests results at Ojiya No.2

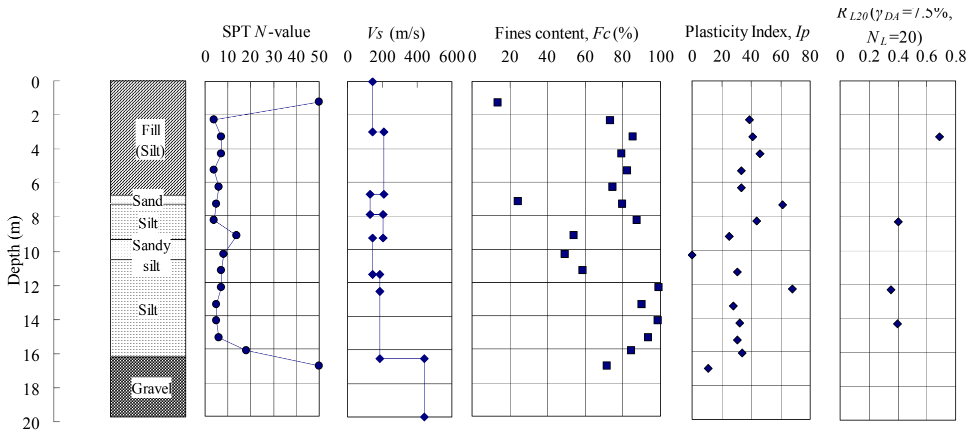

Fig.14 Soil profile and tests results at kawaguchi No.22

Grounds under the embankments spread laterally, and embankments stretched and settled as same as the actual deformation shown in Fig.2. Analyzed settlement at the center of surface of roads at Ojiya No.2 and Kawaguchi No.22 were 26.6 cm and 52.1 cm, respectively. Figures 17 (a) to 17(c) compare analyzed settlements and horizontal displacements at both toes, with the measured ones, respectively. As shown in these figures, analyzed settlements and horizontal displacements were fairly coincided with the measured values.

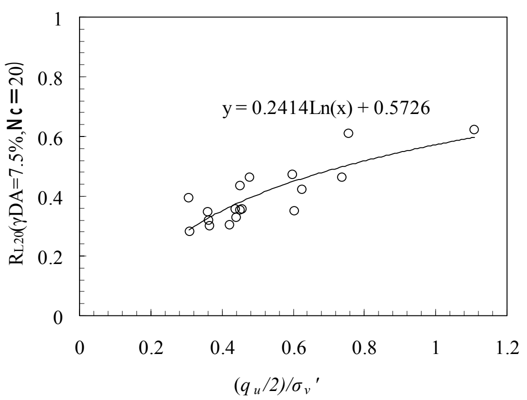

Fig.15 Relationship between R_L and $(q_u/2)/\sigma_v'$

CONCLUSIONS

Cyclic torsional tests were carried out to demonstrate the stress-strain curves of liquefied sands or softened clays. Then a unified relationship among shear modulus ratio after cyclic loading, G_l/σ_c', $R_L(\gamma_{DA}=7.5\ \%, N_L=20)$ and F_L was derived. Analyses for the deformation of highway embankments damaged due to Niigataken-chuetsu earthquake, were conducted based on the unified relationship. Analyzed deformations were fairly coincided with the actual deformations.

ACKNOWLEDGMENTS

The authors would like to express their thanks to Messrs T. Ideno, Y. Sakurai, S. Nakao, former students at Tokyo Denki University, for their cooperation in carrying laboratory tests.

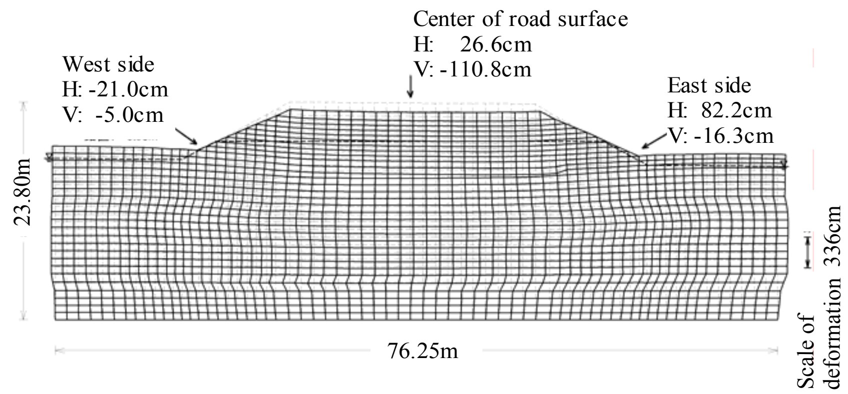

(a) Ojiya No.2

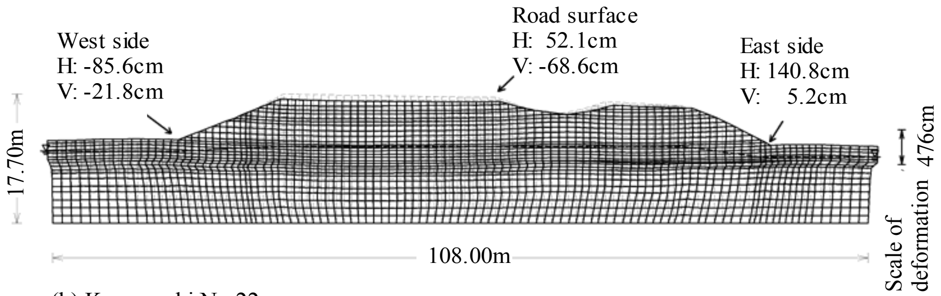

(b) Kawaguchi No.22

Fig.16 Analyzed deformation of embankments and grounds

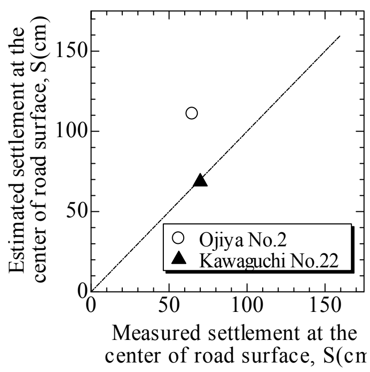

(a) Surface of road

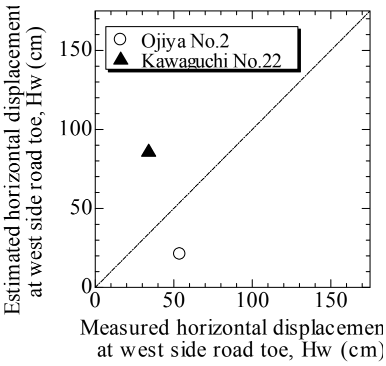

(b) West side toe

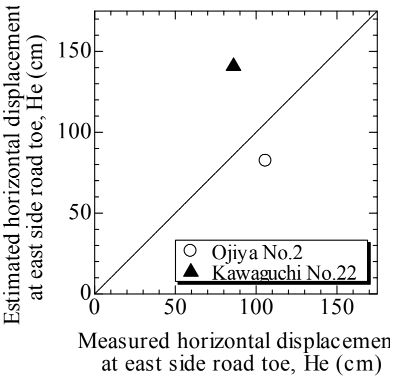

(c) East side toe

Fig.17 Comparison of analyzed and measured displacements

REFERENCES

[1] Ishihara, K. and Yoshimine, M.: Evaluation of settlements in sand deposits following liquefaction during earthquakes, *Soils and Foundations*, Vol.32, No.1, pp.173-188, 1992.

[2] The Japan Road Association: Specification for Highway Bridges , 2002. (in Japanese)

[3] Yasuda, S., Terauchi, T., Morimoto, H., Erken, A. and Yoshida, N.: Post liquefaction behavior of several sands, *Proceeding of the 11th European Conference on Earthquake Engineering*, 1998.

[4] Yasuda, S., Yoshida, N., Adachi, K., Kiku, H. and Gose, S.: A simplified analysis of liquefaction-induced residual deformation, *Proceedings of the 2nd International Conference on Earthquake Geotechnical Engineering*, pp.555-560, 1999.

[5] Yasuda, S., Ideno, T., Sakurai, Y., Yosida, N. and Kiku, H.: Analyses of liquefaction-induced settlement of river levees by ALID, *Proceedings of the 12th Asian Regional Conference on SMGE*, pp.347-350, 2003.

[6] Yasuda, S., Inagaki, M., Yamada, S. and Ishikawa, K.: Stress-strain curves of liquefied sands and softened clays, *Proceedings of the International Symposium on Engineering Practice and Performance of Soft Deposits*, pp.337-342, 2004.

Three-dimensional analysis of liquefaction-induced flow at Koshien-hama during the 1995 Hyogoken-nambu (Kobe) earthquake.

S. Yasuda[1], N. Yoshida[2], Y. Ohya[3]
[1]*Department of Civil Engineering, Tokyo Denki University, Japan*
[2]*Department of Civil and Environmental Engineering, Tohoku Gakuin University*
[3]*Structural Engineering Division, JIP Techno-Science, Japan*

Abstract
A three-dimensional finite element analysis is conducted in order to investigate three-dimensional effect on ground displacement caused by liquefaction-induced flow. The ALID method is used in the analysis, in which mechanical property of the liquefied sand is modeled into a concave bi-linear model whose stiffness is evaluated from the F_L value. Two tow-dimensional analyses and a three-dimensional analysis are carried out. Two-dimensional analyses showed that displacement of quay walls are almost identical regardless the region in the back ground, and it agrees with the observed displacement. Two and three-dimensional analyses showed similar quay wall displacement although FE mesh is different to each other. The differences appear near the corner of quays, and when there are structures near the back ground.

Keywords—*Liquefaction-induced flow, Kobe earthquake, fill, quay wall, three-dimension*

INTRODUCTION

Soil liquefaction has brought significant damage not only to earth-structures but also super structures. At the beginning when soil liquefaction was found to bring damage to various structures, loss of load carrying capacity was of primary interests. Then large amount of horizontal displacement was found to occur in the wide area where soil liquefaction was found. It was called permanent displacement or lateral spreading, but recently the term liquefaction-induced flow becomes popular.

There are significant differences between the conventional concept of soil liquefaction and liquefaction-induced flow from the point of view of the design. The ground loses its capacity to carry structures in the conventional concept, but the ground works as external load to structures by the liquefaction-induced flow. In this sense, the ground works passively in the conventional concept, but it works active in the liquefaction-induced flow. Therefore, prediction of the displacement caused by liquefaction-induced flow is very important in the engineering practice.

The most possible geological conditions that liquefaction-induced flow occurs are cases that the ground surface or upper boundary of the liquefied layer tilts and the case that the lateral side opens such as back ground of a quay wall. These topographies are easily modeled into two-dimensional model in many cases. There are cases, however, where three-dimensional treatment may be necessary, but research on the three-dimensional behaviour has been hardly carried out.

The three-dimensional effect will be investigated in this paper by using the simulation of the damaged fill land during the 1995 Hyogoken-nambu (Kobe) earthquake as an example.

INVESTIGATED SITE

Almost all the shore was fill in and near the Kobe city as seen in Figure 1, and soil liquefaction occurred in almost all the fill. The site used in this paper, Koshien-hama, is located in the east of the figure. A detailed map of north-western part of the Koshien-hama is shown in Figure 2. Allows in the figure are residual displacement vectors obtained by comparing the aerial photos taken before and after the earthquake [1]. All the quay walls moved for about 1 to 1.5 meters towards the sea, and displacement of the back ground occurred associated with the movement of the caisson.

One of the most significant events in Koshien-hama is damage to the Nishinomiyako Bridge. As shown in Photo 1, the bridge slab fell down. However, this damage is said not be caused by liquefaction-induced flow which is dealt with in this paper, but it felled because of inertia effect [2].

Photo 1 Nishinomiyako Bridge and Koshien-hama (right side)

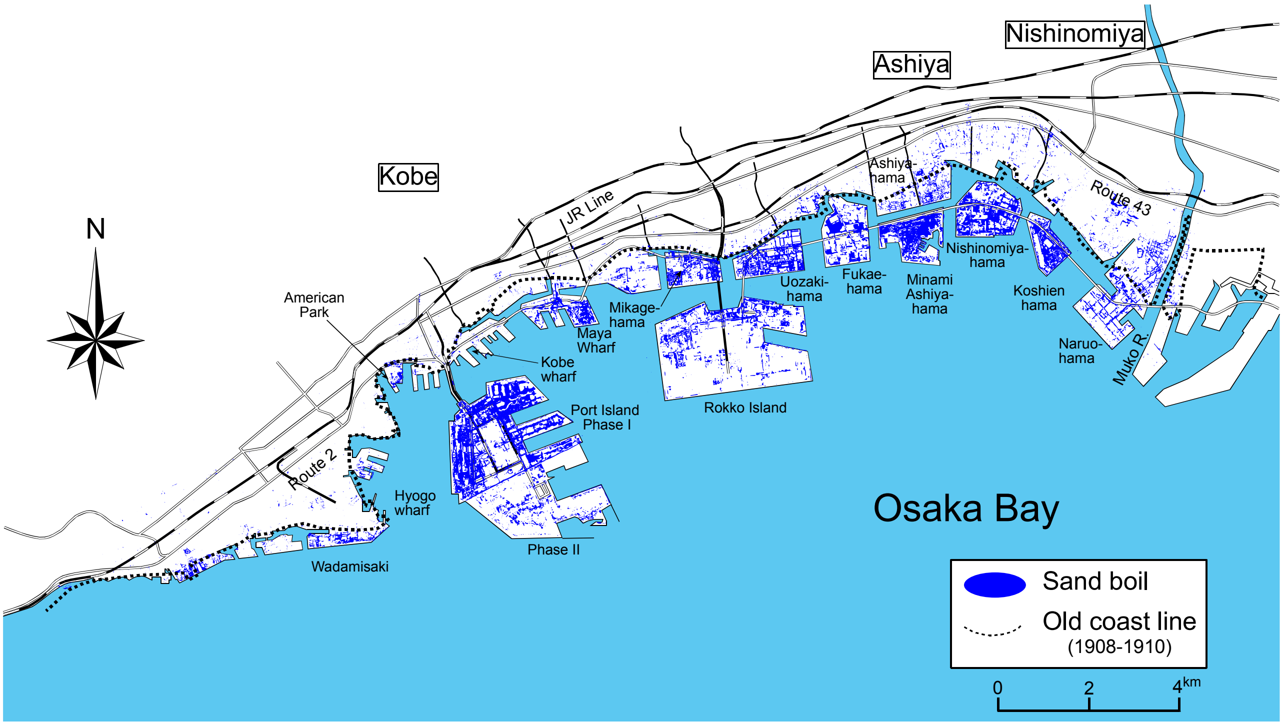

Figure 1 Fill in the Kobe area

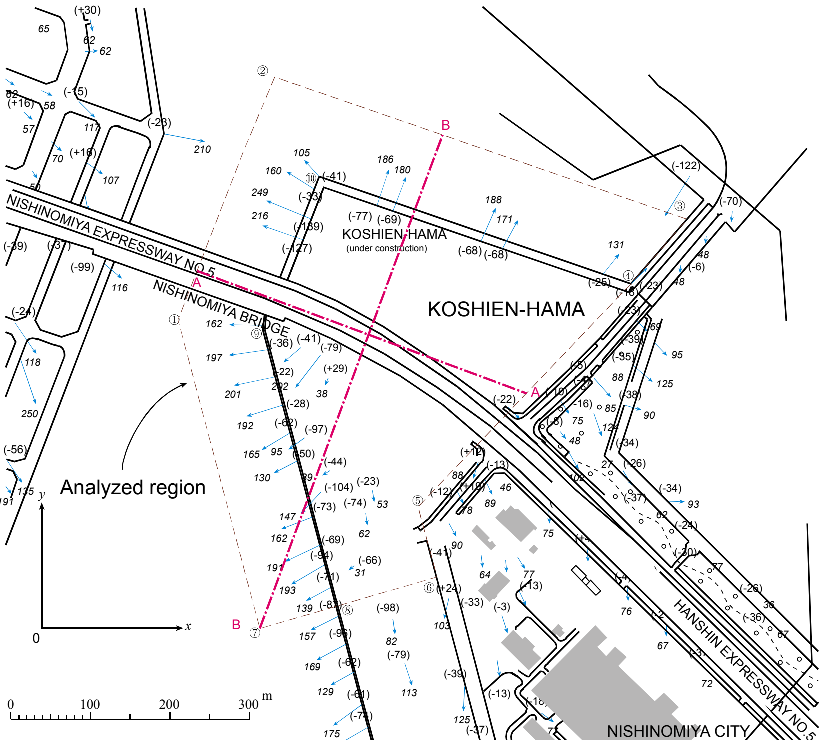

Figure 2 Map of Koshien-hama.

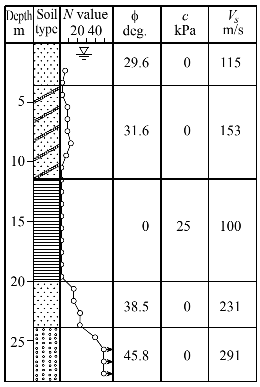

Figure 3 Soil profiles

As seen in Figure 1, this fill area is surrounded by the sea and the shape is narrow. Therefore, ground movement towards the north-west direction may be affected not only by the movement of quay wall in this direction, but also by that in the perpendicular direction, which is the reason why we chose this site as a target to investigate three-dimensional effect.

Soil profile of the site is shown in Figure 3.

METHOS OF ANALYSIS

Fundamental concept

The method named ALID [3] (Analysis of Liquefaction Induced Displacement) is employed in analyzing this site. The fundamental assumptions employed in ALID are

1)Liquefied sand behaves as solid.

2)Stress-strain curve of liquefied sand under monotonic

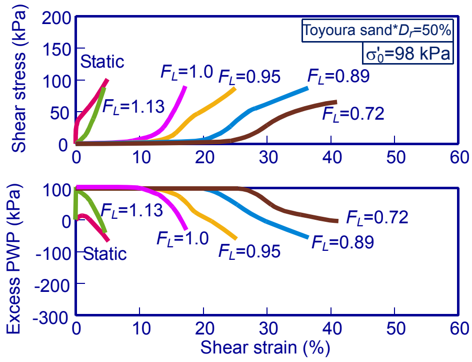

Figure 4 Stress-strain curve after liquefaction

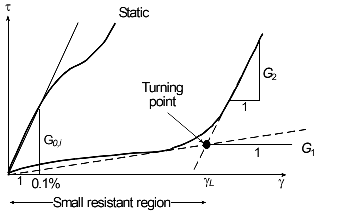

Figure 5 Bi-linear model of stress-strain curve

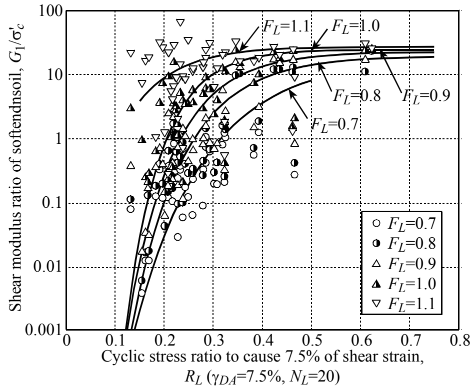

Figure 6 Residual shear modulus during flow

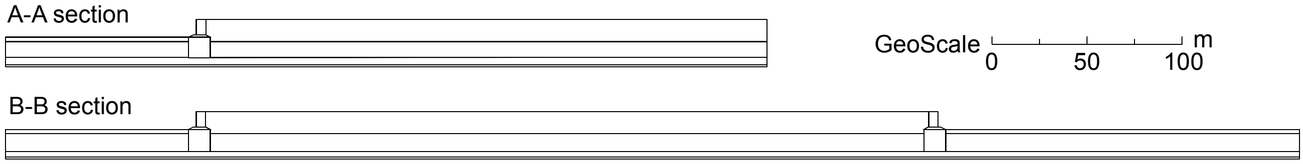

Figure 7 FEM model in two-dimensional analysis

loading can be evaluated from the F_L value, resistance factor against soil liquefaction.

Figure 4 shows stress-strain curve of liquefied sand. These curves are obtained by increasing strain monotonically after several cycles of loading after the soil liquefy. The F_L values in the figure are indices showing how many cyclic loads are applied after the onset of liquefaction; the smaller F_L value indicates larger amount of loading after the liquefaction.

The stress-strain curve have characteristics that 1) Stiffness is very small, but not zero in the beginning of loading during which flow is supposed to occur, 2) The stiffness increases very rapidly and excess porewater decreases at certain strain, which indicates cyclic mobility occurs, and 3) Zones with very small stiffness is larger in the specimen which was subjected more cycles after the liquefaction.

The stress-strain curve is modeled to be a concave bi-linear model in ALID, as schematically shown in Figure 5. The stiffness during the flow or in the low stiffness region again relates the amount of loading after liquefaction or F_L value. Typical relationships are shown in Figure 6 [4].

At least two static analyses are usually made to evaluate displacement after the flow in ALID. The first analysis is made in order to obtain initial stress states as well as initial displacement. This analysis is either switch-on-gravity analysis or layer-by-layer construction analysis. The second analysis is carried out by two ways. The one is a switch-on-gravity analysis in which only shear modulus is replaced from the first analysis keeping other property constant. Liquefaction-induced residual deformation is calculated by subtracting the deformation of the first analysis from that of the second analysis. This method is called a switch-on-gravity method. In another method, stress-strain curve is changed by constraining the deformation or strain in all elements. Then equivalent nodal force required to constrain the displacement is released, resulting in the deformed shape after the flow.

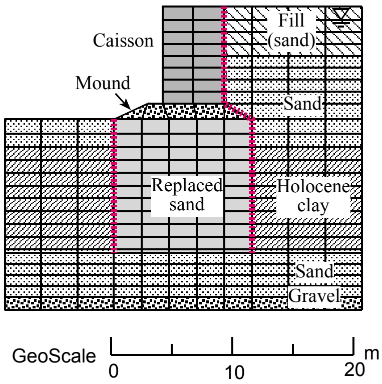

Figure 8 Details of model near caisson

Displacement by flow is directly obtained by the second analysis. Both methods give nearly the same deformation in many cases, but the latter method is necessary when initial state is computed by layer-by-layer construction analysis or nonlinear analysis.

Numerical analysis

The F_L value is evaluated based on the JRA design specification [5]. Here horizontal seismic coefficient at the ground surface is evaluated from the peak ground acceleration of 411.5 cm/s^2, which is the peak ground acceleration observed at the Higashi-Kobe Bridge located nearby this site.

Two computer codes are used in the analysis. The one is ALID/Win [6], which is used for the two-dimensional analysis, and the other is DIANA [7], which is used for the three-dimensional analysis.

The shear stiffness after the liquefaction is evaluated from the empirical equation proposed by Yasuda et al. [4] when comparing the result of analysis with observed displacement. The shear modulus during flow, G_1, is expressed as

$$G_1 / \sigma'_c = a \exp(-\exp(b(R_L - c))) \quad (1)$$

where σ'_c is initial effective confining stress, R_L is liquefaction strength, and a, b, and c are parameters depends on F_L value.

The shear modulus ratio of 1/2000 is used when comparing two and three-dimensional analyses. The reason why different moduli are used is that in the ALD/Win, the procedure to calculate shear modulus during flow is automatically done in the computer, whereas it should be made by hand through the input data in DIANA and it is difficult to define shear modulus element by element for three-dimensional analysis because of huge number of element.

North-western part of the Koshien-hama is analyzed. The analyzed area is shown in Figure 2 with dashed line. It is a hexagonal shape and includes sea area up to 100 m far from the shore.

Two sections, A-A and B-B, are analyzed in the two-dimensional analysis, which is also shown in Figure 2. The A-A section runs from east to west. There exists caisson quay wall in the west end, whereas displacement at the east end is fixed against horizontal displacement. Figure 7 shows the model, which is composed of 3236 nodes and 3078 elements. It is noted that this section passes bridge piers, but it is not considered in the two-dimensional analysis. The B-B section runs in the north-south direction and there are caissons at both ends in this caisson. In other words, both ends have free surface. The FE model is also shown in Figure 7, which is composed of 4944 nodes and 4693 elements.

Figure 8 shows details of FE mesh near the caisson and soil profiles. All caissons are the same structure. Joint elements are installed between the surface of the caisson and neighboring soil in order to allow tangential relative displacement; locations of the joint elements are shown as dashed line.

The 3-dimensional mesh is shown in Figure 9. This model is composed of 85611 nodes and 74294 elements. The seabed is shown in green, the ground surface is shown in yellow, the top surface of the caisson is in blue and the surface of the caisson is in purple color. In addition, pier of the bridge is shown in red color. Joint elements are inseted between the caissons at every 10 elements so that caissons can move in the longitudinal direction easily.

RESULTS AND DISCUSSIONS

Figure 10 shows displacements of A-A and B-B sections obtained by two-dimensional analysis. The maximum displacements are about 1 meter, which agrees with observed displacement.

The horizontal displacements of A-A section and B-B section are almost the same. This indicates that deformation of the quay wall is controlled only by the ground condition near the caisson and not by the ground condition or boundary condition of the backfill ground.

The tilt of the caisson is clockwise, which is different from the observed one. The stiffness of the non-liquefied layer above the liquefied layer seems to affect this, because stiffness of the nonliquefied layer constrains movement of caisson at the top. In order to avoid this inconveniency, no-tension elements are used in the nonliquefied layer. The result is shown in Figure 11. The overall displacement does not change although deformed shape is sometimes different, but the tilt of the caisson is counter-clockwise, and agrees with observed rotation. This fact again indicates that deformation of the caisson is significantly controlled by the ground condition near the caisson.

Figure 12 compares deformation between 3-dimensional analysis and 2-dimensional analysis. Since it is difficult to retrieve the displacement at the specified section, deformation along the south end is shown in Figure 12(a) as displacement by 3D analysis. The deformed shapes are similar to each other, although FE mesh is different. Note that difference of displacements between Figure 10 and Figure 12(a) comes from the

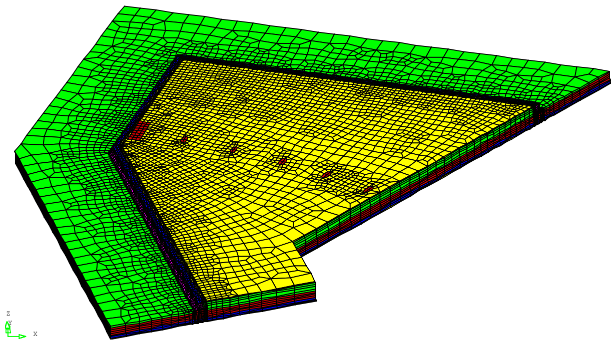

Figure 9 FEM model in three-dimensional analysis

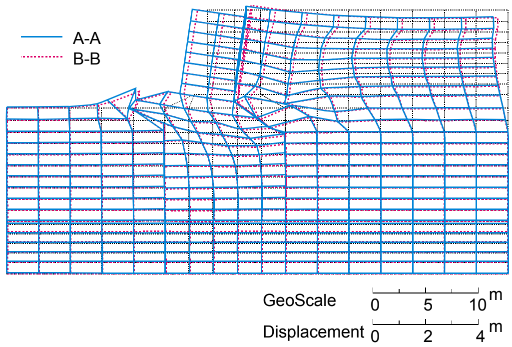

Figure 10 Displacements

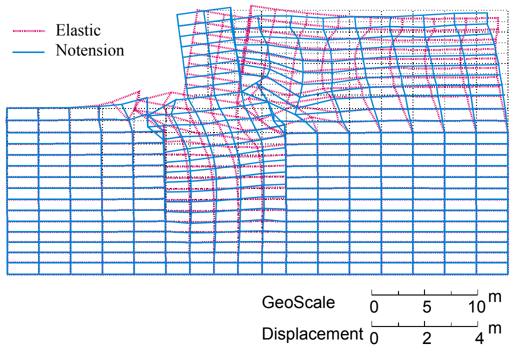

Figure 11 Effect of no-tension (A-A section)

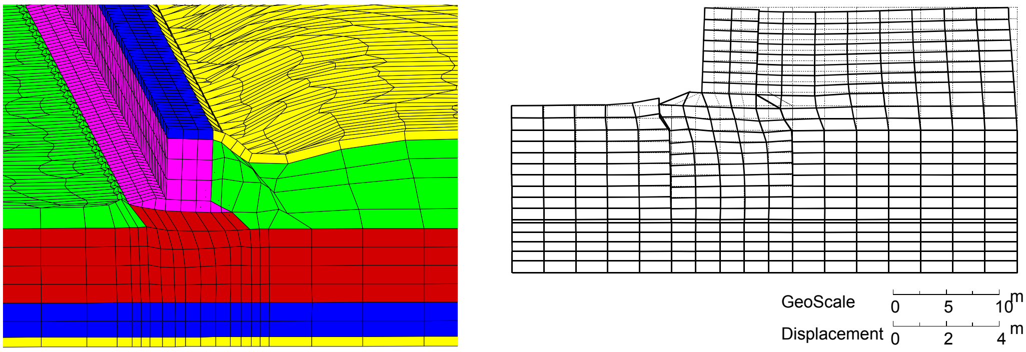

(a) 3D analysis (b) 2D analysis (A-A section)

Figure 12 Deformed shape by 3D analysis

difference of shear modulus during flow as described in the preceding. This difference indicates that stiffness of the sand during flow has strong effect to the deformation after flow.

Displacement of horizontal displacement of the caisson in the three-dimensional analysis is shown in Figure 13. In order to see the displacement vectors, highway is removed from the figure. Generally, all displacement is almost the same order, which agrees with the previous finding. Detailed investigation, however, shows non-unique displacement pattern at three places.

The displacement at the corner of the caisson is smaller than the one of ordinary portion. This may be the result that the displacement of the caisson in the normal direction is constrained by the caisson crossing it.

Displacement is also smaller at the right end. The boundary condition of the right end is set so that horizontal displacement occurs in the direction along the boundary of the backfill ground. However, direction of the caisson and boundary of the backfill ground is not right angle, displacement of the caisson in the normal direction is somewhat constrained because of the longitudinal stiffness of the caisson. On the other hand, caisson and boundary of the backfill ground is almost perpendicular to each other. Therefore constraint discussed above does not occur, resulting in almost the same displacement with other place.

These two observations indicates importance of modeling on the longitudinal stiffness of the caisson, and that used in the analysis may be larger than the actual one

Another difference occurs at the left end below the road bridge. Note that the bridge is not shown in Figure 13; it is shown in Figure 2. Displacement here is very small or nearly zero. This is caused by the existence of bridge pier just behind of the caisson. Same as discussion in the preceding, it is obvious that stiffness of the unliquefied layer constrain the horizontal displacement of the caisson. In the preceding discussion, we conclude that boundary condition of the backfill ground hardly affect the displacement of the caisson. This conclusion, however, cannot be applied to this case because the bridge pier is located only about 10 meters from the quay wall and it is assumed not to move in the analysis.

Figure 14 compares horizontal displacement at the ground surface along the B-B section. Displacements at

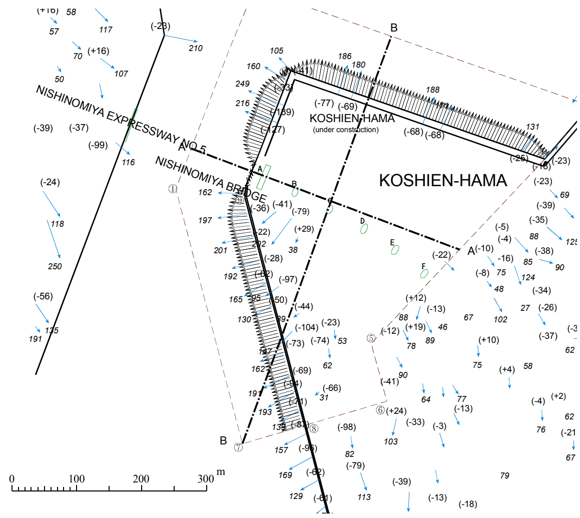

Figure 13 Horizontal displacement of caissons

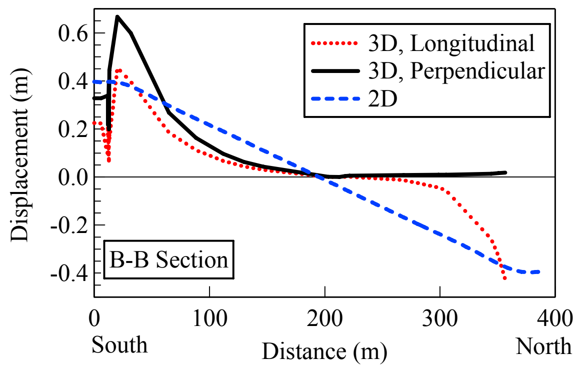

Figure 14 Comparison of horizontal displacement along B-B section.

the north caisson are nearly the same for 2-D and 3-D analyses. Here longitudinal and perpendicular indicates displacement along and perpendicular to the B-B line. Displacements are nearly the same at the north end; displacements in the direction normal to the caisson are about 40 cm in both analyses and displacement tangential to the caisson is nearly zero in the three-dimensional analysis. However, significant difference is seen at the south just behind the caisson. Three-dimensional analysis shows increase of the displacement of the ground surface, but it is not observed in two-dimensional analysis. Large displacement is also seen in Figure 12(a); large settlement is seen just behind the caisson.

CONCLUDING REMARKS

Both two-dimensional and three-dimensional analyses are carried out at the Koshien-hama site where liquefaction-induced flow was observed during the 1995 Hyogoken-nambu earthquake. The following conclusions are obtained.

1) Displacement of the caisson is strongly controlled by the ground condition near the caisson, and backfill ground far from the caisson hardly affects it. Evaluation of stiffness of sand during flow is important.
2) Treatment of the nonliquefied layer near the ground surface is one of the key issues in evaluating the displacement of the caisson, and consideration of nonlinear or no-tension will be required.
3) Both two- and three dimensional analyses give almost the same caisson displacement in the ordinary configuration of the caisson, but does not agree when geometrical configuration is complex.
4) Existence of the rigid structure near the caisson affects the prediction of displacement. The two-dimensional analysis cannot consider its effect.

In conclusion, two-dimensional analysis may be sufficient in predicting the displacement of the caisson, but local effect such as corner or existence of the rigid structure cannot be considered in the two-dimensional analysis.

In the comparison between two- and three-dimensional analyses in this paper, shear modulus during flow is assumed to be the same in order to make the analysis simple. However, initial condition, especially initial stress state, may be different in the three dimensional configuration in the actual situation. This effect must be examined in future.

ACKNOWLEDGMENTS

The work presented in this paper was supported by the Special Project for Earthquake Disaster Mitigation in Urban Areas from the Ministry of Education, Culture, Sports, Science and Technology of Japan.

REFERENCES

[1] Hamada, M., Isoyama, R. and Wakamatsu, K.: The 1995 Hyogoken-Nanbu (Kobe) earthquake, Liquefaction, ground displacement and soil condition in Hanshin Area, ADEP, 1995, 194pp.

[2] Hanshin Expressway Public Corporation: Overcoming the earthquake disaster, Report of damage and restoration against earthquake damage, 1997, 786pp. (in Japanese)

[3] Yasuda, S., Yoshida, N., Adachi, K., Kiku, H., Gose, S. and Masuda, T.: A simplified practical method for evaluating liquefaction-induced flow, Journal of Geotechnical Engineering, Proc. JSCE, No. 638/III-49, 1999, pp. 71-89 (in Japanese)

[4] Yasuda, S., Nagao, K., Inagaki, M. and Ishikawa, K.: Relationship between shear modulus ratio of liquefied soils and cyclic strength, Proc., The 39th Japan National Conference on Geotechnical Engineering, JGS, 2005, pp. 423-424 (in Japanese)

[5] Specifications for Highway Bridges, Part V, Seismic design, Japan Road Association, 2002

[6] ALID Study Group: ALIF/Win, Computer code for liquefaction-induced flow by two-dimensional finite element method, 2005

[7] JIP Techno-Science: DIANA 8.1 Basic course, 2005